ISSN 1580-3155 Pages 179–436 ■ Year 2024, Vol. 71, No. 2

Slovensko kemijsko društvo
Slovenian Chemical Society

Acta Chimica Slovenica

2

71/2024

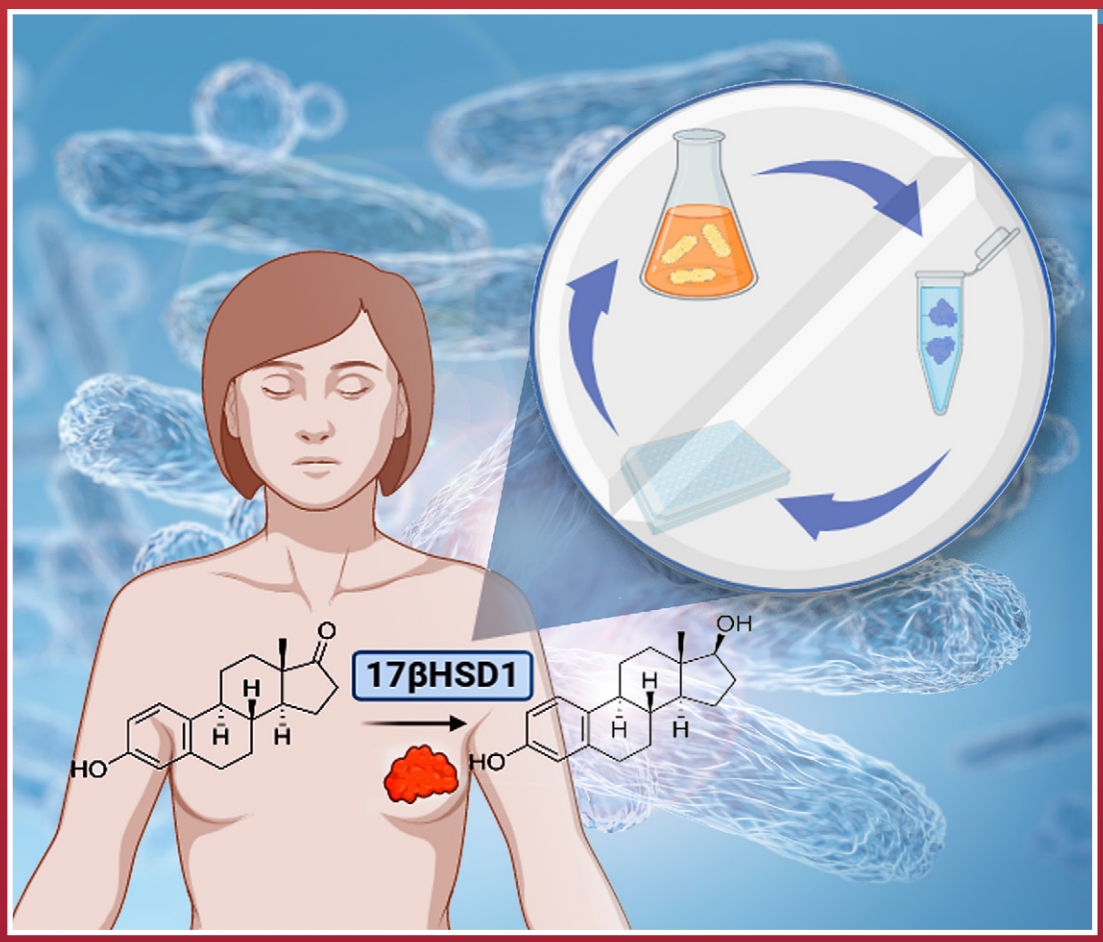

http://acta.chem-soc.si

Acta Chimica Slovenica is indexed in: *Academic Search Complete, Central & Eastern European Academic Source, Chemical Abstracts Plus, Chemical Engineering Collection (India), Chemistry Citation Index Expanded, Current Contents (Physical, Chemical and Earth Sciences), Digitalna knjižnica Slovenije (dLib.si), DOAJ, ISI Alerting Services, PubMed, Science Citation Index Expanded, SciFinder (CAS), Scopus, Web of Science and Portico.* Impact factor for 2022 is IF = 1.20.

Izdaja – Published by:
SLOVENSKO KEMIJSKO DRUŠTVO – SLOVENIAN CHEMICAL SOCIETY
Naslov redakcije in uprave – Address of the Editorial Board and Administration
Hajdrihova 19, SI-1000 Ljubljana, Slovenija
Tel.: (+386)-1-476-0252; Fax: (+386)-1-476-0300; E-mail: chem.soc@ki.si

Izdajanje sofinancirajo – Financially supported by:
National Institute of Chemistry, Ljubljana, Slovenia
Jožef Stefan Institute, Ljubljana, Slovenia
Faculty of Chemistry and Chemical Technology, University of Ljubljana, Slovenia
Faculty of Chemistry and Chemical Engineering, University of Maribor, Slovenia
University of Nova Gorica, Slovenia

Acta Chimica Slovenica izhaja štirikrat letno v elektronski obliki na spletni strani http://*acta.chem-soc.si*. V primeru posvečenih številk izhaja revija tudi v tiskani obliki v omejenem številu izvodov.

Acta Chimica Slovenica appears quarterly in electronic form on the web site *http://acta.chem-soc.si*. In case of dedicated issues, a limited number of printed copies are issued as well.

Transakcijski račun: 02053-0013322846 Bank Account No.: SI56020530013322846-Nova Ljubljanska banka d. d., Trg republike 2, SI-1520 Ljubljana, Slovenia, SWIFT Code: LJBA SI 2X

Oblikovanje ovitka – Design cover: KULT, oblikovalski studio, Simon KAJTNA, s. p. Grafična priprava za tisk: OSITO, Laura Jankovič, s.p.

Graphical Contents

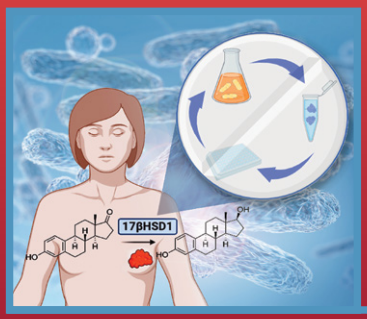

Acta Chimica Slovenica

Year 2024, Vol. 71, No. 2

SCIENTIFIC PAPER

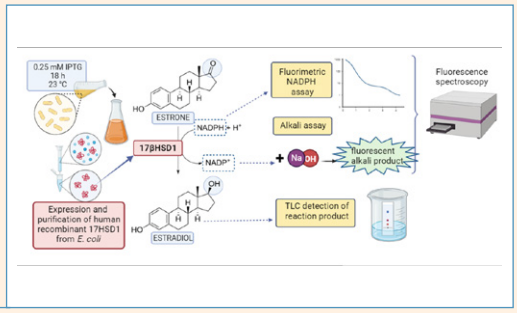

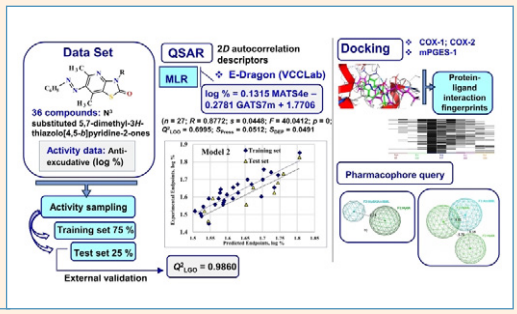

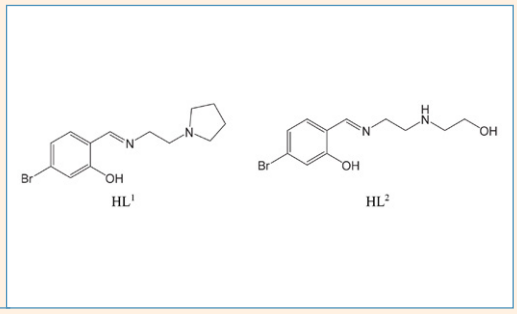

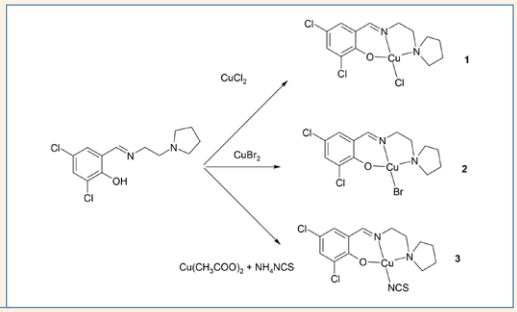

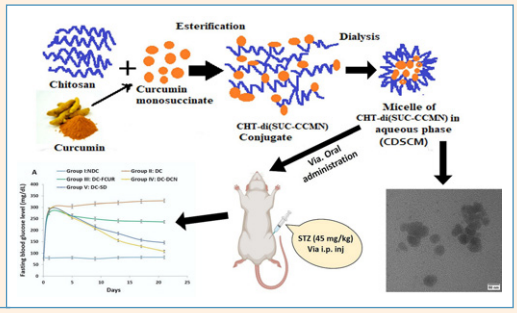

Scientific paper

New Compounds Derived from Nitrophenol Synthesis, Structural Investigation and Anticorrosion Properties

Ali Mahdi Farhan,[1,*] Hanaa Kadtem Egzar[2] and Hawraa Mahdi Alabidi[2]

[1] *Ministry of Education, Al-Najaf, Iraq*

[2] *Department of Chemistry, College of Science- University of Kufa*

* *Corresponding author: E-mail: aliphd256@gmail.com*

Received: 10-03-2023

Abstract

A new azo compound **3** [2-((4-hydroxy-3-(*E*)-(2-hydroxy-5-nitrophenyl)diazenyl)benzaldehyde] and the azo-Schiff derivative **4** [2-((4-hydroxy-3-((*E*)-(2-hydroxy-5-nitrophenyl)diazenyl)benzylidene)amino)-4-nitrophenol[(azo-Schiff **4**) have been synthesized. ^{13}C-NMR, ^{1}H-NMR, FT-IR, mass spectroscopy and UV-Vis analysis was used to characterized new compounds. The new synthesized compound azo-Schiff **4** was utilized to inhibit mild steel (MS) corrosion at little concentrations (0.001–0.006 M). Weight loss measurements studies in 1 M HCl and at 298 K showed that azo-Schiff **4** has a good corrosion inhibition efficiency, 75% at 0.002 M of inhibitors. It was found that adsorption methods follow Langmuir isotherm with ΔG values around –23.8 kJ/mol; this confirms that a stable protective film is formed spontaneously during physical adsorption on the mild steel.

Keywords: Azo compounds, Schiff base, anticorrosion, spectral identification.

1. Introduction

In most manufacturing methods, hydrochloric acid (HCl) is utilized as a washing and cleaning solution to remove rust from mild steel (MS). The acidic medium causes the evolution of hydrogen and formation of chloride ions dissolved in water, which accelerate corrosion. To prevent the effect of the HCl acid, effective and influential additives are added to protect the surfaces of the alloys and metals from corrosion.[1–3] Among the most often used inhibitors to protect metals from the effects of acids are organic inhibitors because they are some of the most effective, practical, efficient and low-cost techniques.[4] Organic inhibitors, for example those containing conjugate π bonds, aromatic nuclei, and heteroatoms (oxygen, nitrogen, carbon or sulfur), are one of the broadly utilized inhibitors used to the resist metal corrosion.[5–12] Organic inhibitors lower the rate of metal corrosion by inhibiting the active sites when the inhibitor is adsorbed on the metal surface thus creating a protective barrier between the electrolyte and the metal surface that displaces water molecules.[13,14] Studies have shown the effectiveness of Schiff bases in inhibiting corrosion in an acidic medium because of its –C=N– group. The π-bond in –C=N– group is able to interact with surface of the metal and nitrogen atoms are capable to form coordinate covalent bonds by its unshared electrons.[15,16] Azo compounds are used as corrosion inhibitors due to their ability to form a protective layer and a chelating complex with the surface of the metal due to the presence of an active group (–N=N–).[17–20]

A number of researchers already synthesized new azo compounds and tested them as anticorrosion chemicals. For example, a new azo-coumarin dye was created by Yusoff et al.,[21] and it was discovered that the new compounds work well as anticorrosion agents. On the other hand, Schiff base compounds are also used as anticorrosion chemicals. For instance, Madani et al.[22] prepared two Schiff base compounds from benzidine and found that these compounds, even at low concentrations, showed a good inhibitory action in the tested medium and that the increase in inhibitors concentrations increased the effectiveness of their inhibition activity. Because of this, our work included developing novel azo-Schiff compounds derived from nitrophenol compounds and screening them for anticorrosion properties to obtain promising results in this area.

2. Experimental Part

2. 1. Materials and Instruments

All organic chemical, solvents and inorganic salts these utilized in this work were provided by Merck, Sigma Aldrich, Fluka, and BDH.

Mass spectra were measured by AB SCIEX (3200) Mass analyzer, UV-Vis spectra were measured in ethanol using a Shimadzu UV-1650 instrument (Japan) and IR spectra were obtained as KBr disks using a Shimadzu FT-IR 8400 instrument in the range 400–4000 cm^{-1}. ^{1}H-NMR spectra of ligand were recorded by using Bruker Avance-111 (300 MHz) spectrometer using DMSO-d_6 as the solvent for measurement; chemical shifts are given relative to the internal standard tetramethylsilane (TMS). Melting points were determined using a melting point apparatus.

Mild steel plates (1 cm × 1 cm × 0.1 cm) were used for weight loss. The plates were washed with acetone , distilled water and desiccated prior any experiment. The HCl solution was utilized with concentration of 1 M as corrosive medium.

2. 2. Synthesis of Azo Compound 3[23,24]

To obtain the azo compound **3**, 2-amino-4-nitrophenol (**1**) (154 mg, 0.01 mmol) was dissolved in 25 mL of absolute ethanol. After adding 2 mL of concentrated HCl, following 25 minutes of stirring in an ice bath, 25 mL of an ice-cold sodium nitrite solution, $NaNO_2$ (10%) was added drop wise, over the time of 35 minutes. The reaction mixture became reddish brown and was added drop by drop to a second ice-cold solution of 3-hydroxybenzaldehyde (**2**) (122 mg, 0.01 mmol) in 20 mL of alkaline ethanol, which was then stirred continuously at 45 °C overnight. The reaction mixture was neutralized using diluted ammonia and hydrochloric acid until pH 7, then the target product was washed in cold distilled water, filtrated and dried.

Yield: 350 mg (74%), deep brown powder, m.p.< 300 °C, FT-IR (KBr) (cm^{-1}): 3396 (OH), 2929 and 2889 (C-H aliph), 2833 and 2752 (C-H aldehyde), 1674 (C=O, aldehyde), 1594 (C=C, arom), 1496 (N=N), 1308 and 1163 (NO_2). ^{1}H-NMR (300 MHz, DMSO-d_6) δ 9.43 (s, 1H, CHO), 8.51 (s, 1H, H3-arom A), 8.22 (s, 1H, OH- arom A), 8.19 (s, 1H, OH- arom B), 7.74–7.71 (d, 2H, H5-arom A + H2-arom B), 7.47 (s, 1H, H6-arom B), 6.43–6.42 (d, H3-arom B), 5.94–5.91 (d, H6-arom A).

2. 3. Synthesis of Azo-Schiff Base Compound 4[25,26]

Schiff base compound **4** was prepared by dissolving azo compound **3** (600 mg, 2.09 mmol) in 40 mL of ethanol containing 2-amino-4-nitrophenol (**1**) (321 mg, 2.09 mmol) and a few drops of glacial acetic acid; the mixture was heated under reflux for 7–9 hours. TLC was used to check the progress of the reaction (mobile phase: chloroform/methanol (3:1.5)). After cooling, the solid product that precipitated from the ethanol was collected by filtration, and purified by recrystallization to obtain the desired product.

Yield: 850 mg (82%), pale yellow powder, m.p. 271–273 °C, R_f 0.38, FT-IR (KBr) (cm^{-1}): 3402 (OH), 2918 and 2896 (C-H aliph), 1643 (C=N), 1594 (C=C, arom), 1498 (N=N), 1309 and 1161 (NO_2).^{13}C-NMR (75.5 MHz, DMSO-d_6) δ 155.9 (C=N), 138.3 (C-OH), 137.9 (C-NO_2), 130.4 (C1- arom B), 126.9 (C4- arom B),119.8 (C5- arom B), 117.2 (C3- arom A + C3- arom C), 115.9 (C2- arom A + C2- arom C), 115.2 (C5- arom A + C5- arom C), 113.7 (C2+5- arom B), 107.2 (C6- arom A + C6- arom C).

2. 4. Weight Loss Measurements

The gravimetric measurements were carried out for mild steel plates in 1 M HCl solution in the absence and presence of the azo-Schiff **4** solution. After washing and weighting, the MS plates were immersed in corrosive environment for 1080 h at 298 K, then the loss in weight was determined by the change in MS plate's weights. MS surface coverage (θ), rate of corrosion (*CR*) and efficiency of inhibition (*IE* %), were calculated by equations 1–3.

$$CR = \frac{W}{At} \quad (1)$$

$$IE\% = \frac{CR^\circ - CR}{CR^\circ} \times 100 \quad (2)$$

$$\theta = \frac{CR^\circ - CR}{CR^\circ} \quad (3)$$

Where A is the area of MS plates in cm^2, W represents the lost weight of MS plates in mg, CR is the rate of corrosion, and t is the time of immersion in h in the presence of azo-Schiff **4** solution.

3. Results and Discussion

3. 1. Characterization of Azo 3 and Schiff base 4 Compounds

A new azo compound **3** was successfully synthesized by the coupling reaction between 2-amino-4-nitrophenol (**1**) and 3-hydroxybenzaldehyde (**2**) in a basic medium as shown in scheme 1.

By using spectral methods such as FT-IR, the azo compound **3** was characterized, which showed clear bands absorption due to stretching vibration of functional groups, for instance, the band of the hydroxyl group was observed at 3396 cm^{-1}, while the carbonyl aldehyde absorbed at 1674 cm^{-1}; furthermore, the C–H of the aldehyde group appeared as a double band at 2833 and 2752 cm^{-1}; the other absorptions of the compound **3** are listed in Table 1.

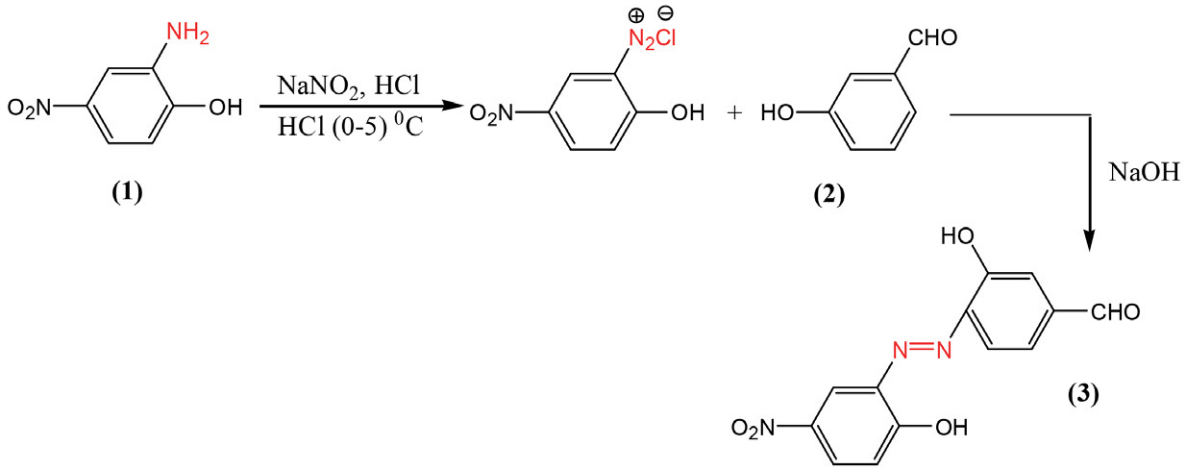

Scheme 1. Synthesis azo compound **3**.

Also, the new compound **3** was characterized by its ^{1}H-NMR spectrum, displaying a singlet at 9.43 ppm due to an aldehyde group proton, whereas the proton of the phenol group appeared at a chemical shift of 8.22 ppm, whereas the aromatic protons were observed at downfield in the range of 8.51–5.91 ppm as a result of the nitro group having electron withdrawing characteristics (Figure 1).

In the second step of the synthesis, Schiff base derivative **4** is prepared by reacting an azo molecule **3** with 2-amino-4-nitrophenol (**1**) in an acidic medium, as shown in Scheme 2.

In the FT-IR spectrum of the azo-Schiff derivative **4** new absorption bands belonging to azo-methane group appeared at 1643 cm^{-1}, also the stretching vibration of azo

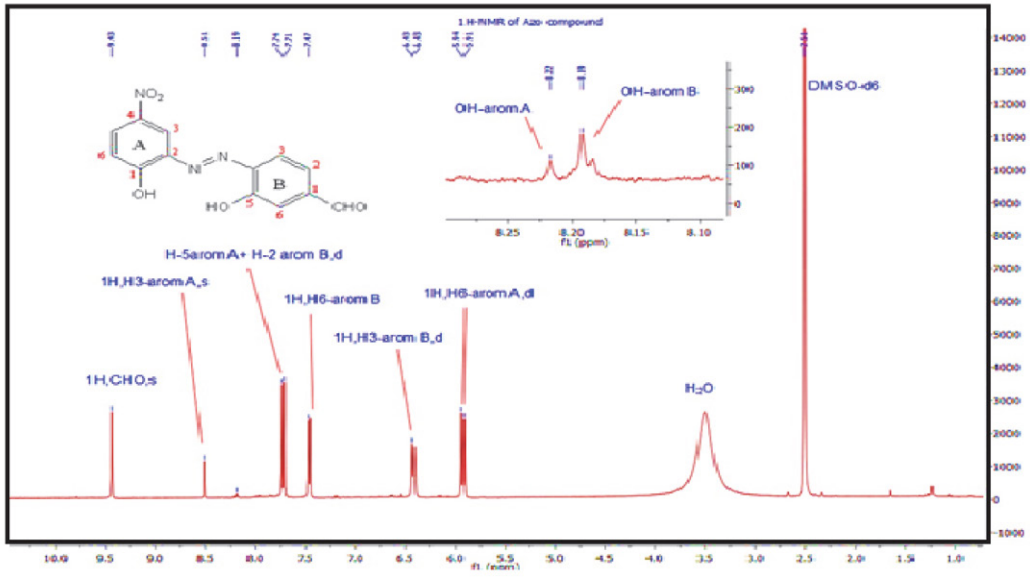

Figure 1. ^{1}H-NMR of azo compound **3**.

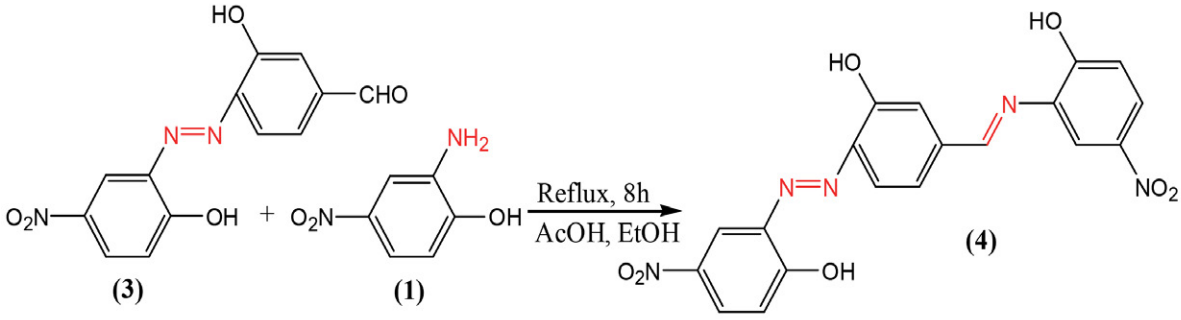

Scheme 2. Synthesis of the azo-Schiff derivative **4**.

group was observed at 1498 cm^{-1}, the other absorption bands of this compound are listed in Table 2.

The newly formed compound **4**, on the other hand, was identified by its ^{13}C-NMR spectrum, which also revealed a clear signal at 155.9 ppm caused by a resonant azo-methane group. The aromatic carbon atoms were observed in the range of 138.3–107.2 ppm as a result of the electronic effect of the neighboring group to the carbon atom (Figure 2).

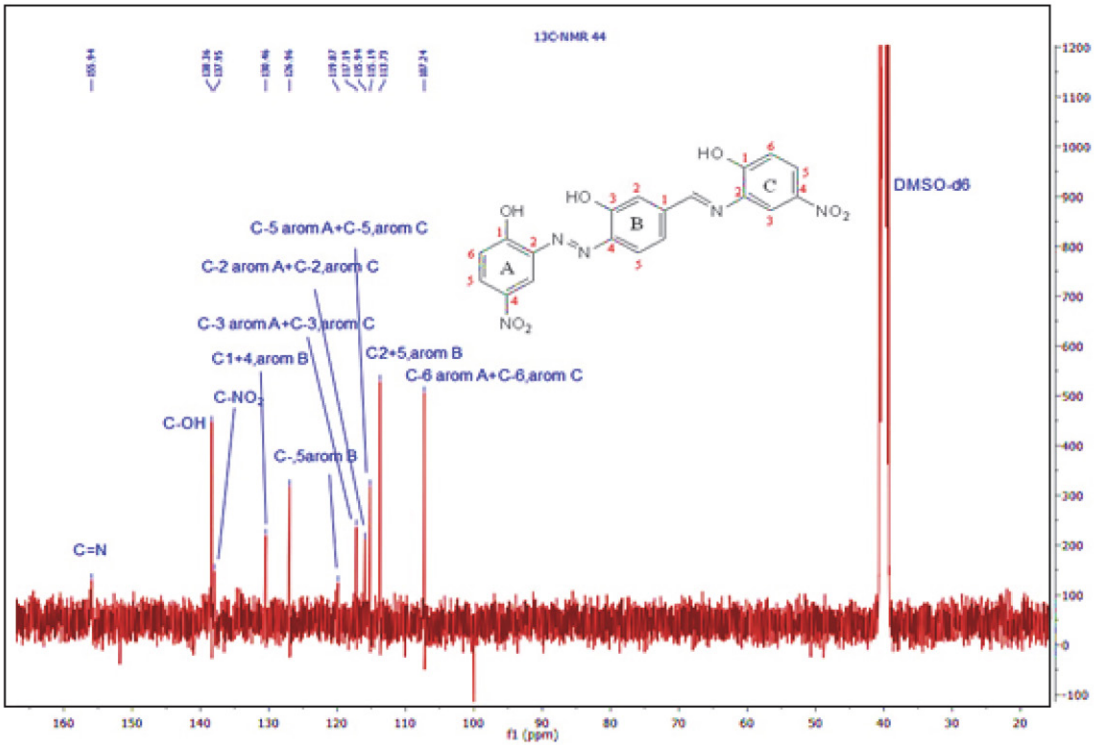

Figure 2. ^{13}C-NMR of azo-Schiff compound **4**.

Table 1. Characterization of azo compound **3** and azo-Schiff compound **4** by FT-IR

Compound	ν OH	ν C-H aliph	ν C-H aldehyde	ν C=O	ν C=N	NO_2
Azo compound	2290	2920	2833 – 2752	1574	–	1308 – 1163
Schiff compound	3402	2918	–	–	1643	1309 – 1161

3. 2. Mass Spectra

Mass spectrum for compound **3** showed a peak at *m/e* 285 confirming the molecular ion of the azo compound **3**, the primary fragmentation takes place in two ways, with the first route being the loss of N_2 of the azo group giving a peak at *m/e* 259; the other path starts by the elimination of two OH groups giving a peak at *m/e* 255 (Scheme 3).

3. 3. UV-Vis Spectrum

The electronic absorption spectra of the prepared compounds were measured in ethanol as the solvent. The essential absorption of the azo compound **3** and azo-Schiff derivative **4** appeared at 401 nm and 480 nm, respectively. The spectral data and some physical properties are listed in Table 2.

Table 2. Electronic spectral data of prepared compounds **3** and **4**.

Compound	color	Value of λ *max* (nm)	Type of transition
Azo compound **3**	Brown	286, 291	π–π*
		335	n-π*
		401	CT
Azo-Schiff base **4**	Dark brown	212,234	π–π*
		340	n-π*
		480	CT

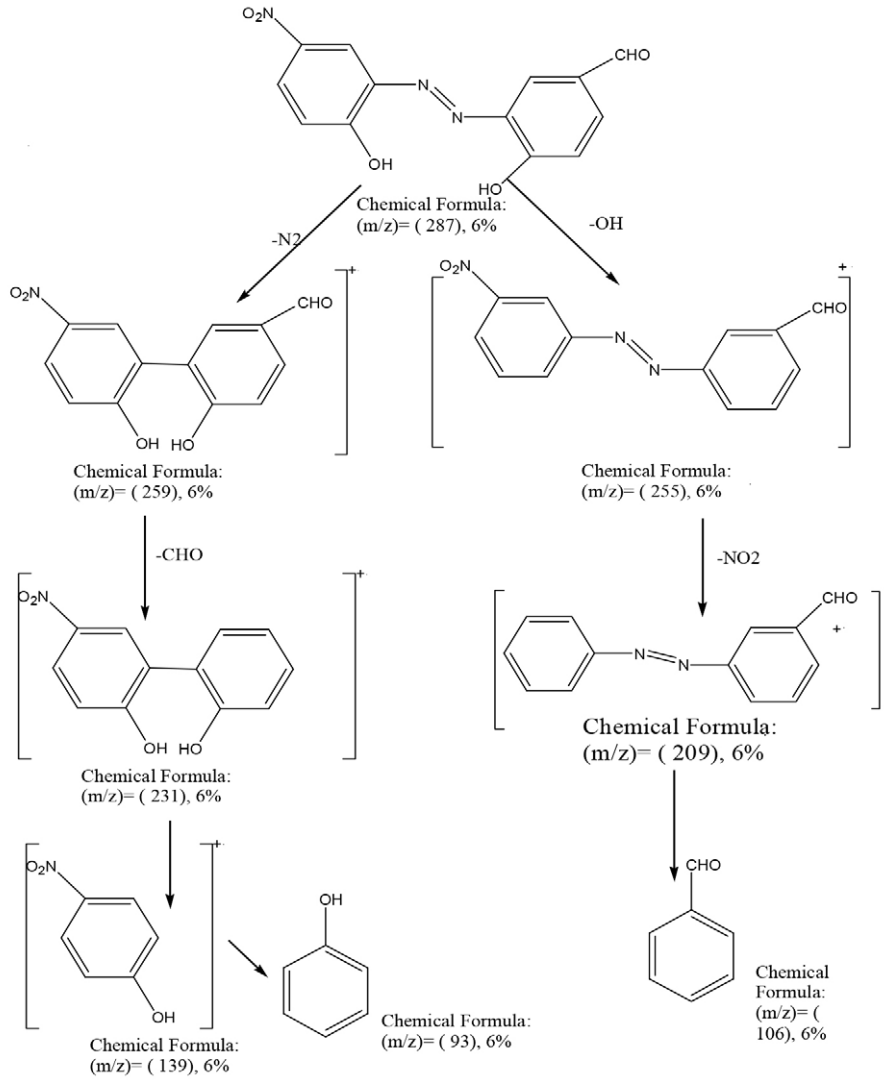

Scheme 3. A proposed pathway for MS fragmentation of the azo compound **3.**

3. 4. Gravimetric Measurements

Figures 3 and 4 demonstrate the weight loss results of MS plates in the presence and absence of the solution of azo-Schiff **4** in the acidic environment. The inhibition activity of azo-Schiff compound **4** to the corrosion of MS in 1 M HCl might be attributed to the existence of various groups having an evident effect on the inhibition efficiency produced by electron donating groups (–N=N–, HC=N, –OH); this adsorption centers (*i.e.* electron donating) increase adsorption and enhance the surface area covered by the compound and thus increase the efficiency of inhibition. Presences of –OH (electron donor) group in the azo-Schiff **4** enhanced the conjugation and facilitated bonding of the benzene ring. $-NO_2$ group in the azo-Schiff **4** decreases the inhibition efficiency, because of the electron withdrawing effect of nitro group, which decrease the electron density on the ring, and therefore the efficiency of the inhibition as well.[27]

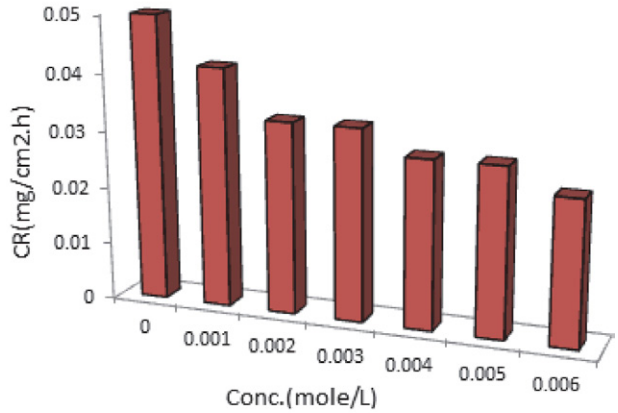

Figure 3. Effect of azo-Schiff **4** solution concentration on the corrosion rate of mild steel plates in 1 M HCl at 303 K.

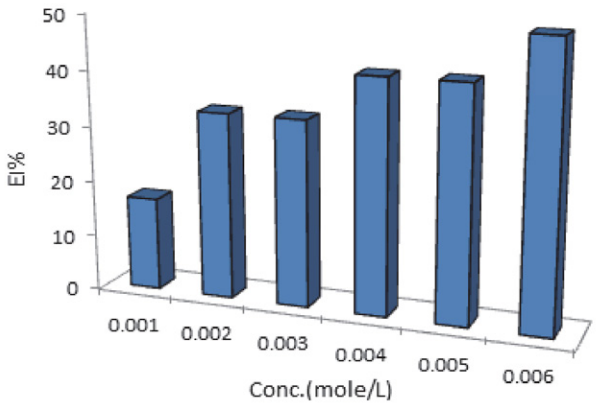

Figure 4. Influence of concentrations of azo-Schiff **4** solution on the efficiency of inhibition of MS plates corrosion in 1 M HCl at 298 K.

3. 5. Adsorption Isotherms

To find the most suitable and the best adsorption isotherm we used values of surface coverage (θ) that were obtained from the weight loss results (Figure 5). The adsorption isotherm assists to achieve the bonding between the surface of the plates and the azo-Schiff **4** molecules. The azo-Schiff **4** molecules are adsorbed physically or chemically on the surface of the plates. To recognize the adsorption type, the isothermal adsorption Freundlich, Temkin, and Langmuir isotherms were applied to methodological results. It was noticed that the mechanism of adsorption of azo-Schiff **4** on the MS surfaces obeyed Langmuir adsorption isotherm as shown by the high value of the regression coefficient (R^2 = 0.9295) indicating a good fitting; the obtained values of the intercept and slope were 0.0042 and 1.3888, respectively; the slope value being close to the unity thus suggesting a homogenous distribution and monolayer coverage of the azo-Schiff **4** molecules on the surface as supposed by Langmuir equation.

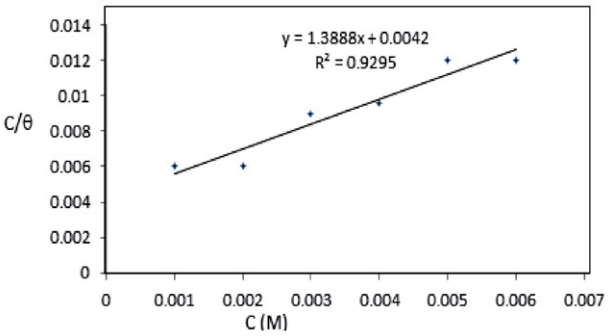

Figure 5. Langmuir isotherm of MS plates in the presence of the azo-Schiff **4**.

The value of the adsorption equilibrium constant (K_{ads}) equals 234.09; it was obtained from the straight line of C/θ and concentrations (C) as shown in the Equation 4.

$$\frac{C}{\theta} = \frac{1}{K_{ads.}} + C \quad (4)$$

To find the value of the adsorption free energy (ΔG_{ads}) we used the Equation 5.

$$\Delta G_{ads} = -RTln55.5K_{ads} \quad (5)$$

The ΔG_{ads} value for azo-Schiff **4** (–23.8 kJ/mol) indicates physisorption adsorption, because its value is a less negative value and is around –20 kJ/mol.[28–30]

4. Conclusion

By measuring the anti-corrosion properties of the azo-Schiff compound **4**, it was discovered that this is a more effective compound than the initial azo compound **3**. This is likely because **4** contains additional heteroatoms, which are able to donate unpaired electrons to metals and inhibit corrosion.

Supplementary Material

FT-IR of azo compound **3** and azo-Schiff derivative **4**, MS spectrum of **3** and UV-Vis spectra of **3** and **4**.

Declaration of competing interest

The authors declare that they have no conflict of interest.

This study was not supported by any organization.

5. References

1. M. Abdulhussin Enad, M. Y. Kadhim, A. S. Abdulnabi, *J. Glob. Pharma Technol.* **2020**, *12*, 651–656.
2. M. S. Mezhr, *Ann. Rom. Soc.* **2021**, 910–928. **DOI:**10.1088/1757-899X/928/2/022037
3. H. Khaleel, A. A. Ateeq, A. A. Ali, *Int. J. Appl. Eng. Res.* **2018**, *13(6)*, 3638–3647.
4. S. Bashir, V. Sharma, H. Lgaz, I. M. Chung, A. Singh, *J. Mol. Liq.* **2018**, *263*, 454–462. **DOI:**10.1016/j.molliq.2018.04.143
5. A. Nasima, A. K. Singh, B. Chugh, M. Akram, F. Perveen, I. Rasheed, F. Altaf, P. A. Channar, A. Saeed, *Ionics* **2019**, *25*, 5057–5075. **DOI:**10.1007/s11581-019-03028-y
6. I. B. Obot, S. A. Umoren, N. K. Ankah, *J. Mol. Liq.* **2019**, *277*, 749–761. **DOI:**10.1016/j.molliq.2018.12.108
7. A. K. Singh, S. Thakur, B. Pani, G. Singh, *New J. Chem.* **2018**. *42(3)*, 2113–2124. **DOI:**10.1039/C7NJ04162D
8. R. Yıldız, *Ionics.* **2019**, *25(2)*, 859–870. **DOI:**10.1007/s11581-018-2649-5
9. H. M. Elabbasy, H. S. Gadow, *J. Mol. Liq.* **2021**, *321*, 114918. **DOI:**10.1016/j.molliq.2020.114918
10. H. S. Gadow, M. Fakeeh, *RSC Adv.* **2022**, *12(15)*, 8953–8986. **DOI:**10.1039/D2RA01296K

11. T. E. Schmitzhaus, M. R. Vega, R. Schroeder, I. L. Muller, Mattedi, C. F. Malfatti, *Corros. Mater*. **2020**, *71(7)*, 1175–1193. **DOI:**10.1002/maco.201911347
12. O. O. Ogunleye, A. O. Arinkoola, O. A. Eletta, O. O. Agbede, Y. A. Osho, A. F. Morakinyo, J. O. Hamed, *Heliyon*. **2020**, *6(1)*, e03205. **DOI:**10.1016/j.heliyon.2020.e03205
13. I. Danaee, S. Ramesh Kumar, M. Rashvand Avei, M. Vijayan, *Mater. Res*. **2020**, *23*, e20180610.
14. H. S. Gadow, M. Fakeeh, *RSC Adv*. **2022**, *12(15)*, 8953–8986. **DOI:**10.1039/D2RA01296K
15. M. E. Moustafa, A. I. Ali, A. Y. El-Etre, H. A. Ibrahim, *Benha. J. Appl. Sci*. **2019**, *4(2)*, 167–187. **DOI:**10.21608/bjas.2019.187205
16. P. Kumari, M. Lavanya, *J. Bio- Tribo-Corros*. **2021**, *7(3)*, art. no. 110. **DOI:**10.1007/s40735-021-00542-3
17. D. Clofent, M. de Homdedeu, M. Muñoz-Esquerre, M. J. Cruz, X. Muñoz *Allergy Asthma Clin. Immunol.* **2020**, *16*, art. no. 7. **DOI:**10.1186/s13223-020-0404-8
18. F. Vázquez-Ortega, I. Lagunes, Á. Trigos, *Dyes Pigments*, **2020**, *176*, 108248. **DOI:**10.1016/j.dyepig.2020.108248
19. L. H. Madkour, S. Kaya, L. Guo, C. Kaya, *J. Mol. Struct*. **2018,** *1163*, 397–417. **DOI:**10.1016/j.molstruc.2018.03.013
20. H. M. Alabidi, A. M. Farhan, N. S. Salh, A. A. J. Aljanaby, *Curr. Appl. Sci. Technol*. **2023**, *23(4),* art. no. 7.
21. M. H. Yusoff, M. N. Azmi, M. H. Hussin, H. Osman, P. B. Raja, A. Abdul Rahim, K. Awang, *Int. J. Electrochem. Sci*, **2020**, *15(12)*, 11742–11756. **DOI:**10.20964/2020.12.43
22. A. Madani, L. Sibous, A. Hellal, I. Kaabi, E. Bentouhami, *J. Mol. Struct*. **2021**, *1235*, 130224. **DOI:**10.1016/j.molstruc.2021.130224
23. H. M. Alabidi, A. M. Farhan, M. M. Al-Rufaie, *Curr. Appl. Sci. Technol*. **2021,** 176–187.
24. H. M. Alabidi, A. M. Farhan, H. M. Y. Al-Laban, A. A. J. Aljanaby, *Egypt. J. Chem*. **2023**, *66(1)*, 175–181.
25. N. A. Abdul-Rida, A. M. Farhan, N. A. Al-Masoudi, B. A. Saeed, D. Miller, M. F. Lin, *Mol. Divers*. **2021**, *25*, 661–671. **DOI:**10.1007/s11030-020-10038-w
26. N. A. AL-Rida, A. M. Farhan, *J. Phys. Conf. Ser*. **2019**, *1294, 5*, 052002. **DOI:**10.1088/1742-6596/1294/5/052002
27. S. Benkhaya, S. M'rabet, A. El Harfi, *Heliyon* **2020**, *6*, e03271. **DOI:**10.1016/j.heliyon.2020.e03271
28. A. Singh, K. R. Ansari, J. Haque, P. Dohare, H. L. Gaz, R. Salghi, M. A. Quraishi, *J. Taiwan Inst. Chem. Eng*. **2018**, *82*, 233–251. **DOI:**10.1016/j.jtice.2017.09.021
29. C. Verma, L. O. Olasunkanmi, E. E. Ebenso, M. A. Quraishi, *J. Mol. Liq* **2018**, *251*, 100–118. **DOI:**10.1016/j.molliq.2017.12.055
30. P. Singh, E. E. Ebenso, L. O. Olasunkanmi, I. B. Obot, M. A. Quraishi, *J. Phys. Chem. C*. **2016**, *120(6)*, 3408–3419. **DOI:**10.1021/acs.jpcc.5b11901

Povzetek

Pripravili smo dve novi spojini: azo spojino **3** [2-((4-hidroksi-3-(*E*)-(2-hidroksi-5-nitrofenil)diazenil)benzaldehid] ter njen Schiffov derivat **4** [2-((4-hidroksi-3-((*E*)-(2-hidroksi-5-nitrofenil)diazenil)benziliden)amino)-4-nitrofenol] (azo-Schiff **4**). Za karakterizacijo novih spojin smo uporabili ^{13}C-NMR, ^{1}H-NMR, FT-IR, masno spektroskopijo in UV-Vis analizo. Novo, sintetizirano azo-Schiffovo spojino **4** smo v nizkih koncentracijah (0.001–0.006 M) uporabili kot inhibitor korozije mehkega jekla (MS). Študije izgube mase v 1 M HCl pri 298 K so pokazale, da azo-Schiffova spojina **4** izkazuje dobro protikorozijsko učinkovitost, t.j. 75 % pri njeni koncentraciji 0.002 M. Ugotovili smo, da adsorpcija poteka skladno z Langmuirjevo izotermo, kjer je ΔG približno –23.8 kJ/mol, kar potrjuje, da s fizično adsorpcijo preiskovane spojine na mehko jeklo nastane stabilen zaščitni sloj.

DOI: 10.17344/acsi.2023.8517 *Acta Chim. Slov.* **2024,** *71,* 186–196

Scientific paper

Extraction and Characterization of Nanocellulose from Waste of Date Palm "*Phoenix Dactylifera*" as Reinforcement of Polymer Composites

Meriem Kadri,[1] Nebia Bouzidi,[2,*] Toufik Chouana,[3] Hakim Belkhalfa,[4] Abdellah Henni[5] and Youcef Bouhadda[2]

[1] *Laboratory Research on Biological Systems and Geomatics, University Mustapha Stambouli of Mascara, Mascara 29000, Algeria*

[2] *Laboratory of Physical Chemistry of Macromolecules and Biological Interfaces, Faculty of Sciences, Department of Biology, University Mustapha Stambouli of Mascara, Mascara 29000, Algeria*

[2] *Laboratory for the protection of ecosystems in arid and semi-arid zones. University Kasdi Merbeh of Ouargla, Ouargla 30000 Algeria*

[4] *Scientific and Technical Research Center in Physicochemical Analysis, CRAPC, Bou-Ismail, Tipaza, Algeria*

[5] *Laboratory of Dynamic Interactions and Reactivity of Systems, University Kasdi Merbah of Ouargla, Ouargla 30000, Algeria*

** Corresponding author: E-mail: lina_kholoud@yahoo.fr*
Tel.: +213791182816

Received: 16-10-2023

Abstract

Cellulose is the most abundant and renewable polymer in nature. It is characterized by its biodegradability which helps create a friendly environment. This study seeks to describe the nanocellulose obtained from waste date palm, within the dried palms (DP) and the fresh palms (FP) through implementing chemical methods (hydrolysis with H_2SO_4). Physical properties, morphology, the elemental composition and the thermal stability were determined by Fourier transform infrared spectroscopy (FTIR), X-ray diffraction (XRD), zeta sizer, scanning electron microscopy (SEM), whereas energy dispersive X-ray (EDX) and thermogravimetric analysis (TGA), respectively. FTIR, SEM and EDX results revealed the effective removal of impurities, hemicellulose and lignin. After treatment, the dried palm (DR) samples contained 35.99% of cellulose and 33.12% of cellulose nanocrystals (CNC), while fresh palm (FP) samples 36.17% of cellulose and 34.35% of CNC. The CNCs have higher crystallinity than the raw fibers and Zeta sizer was between 25 and 1150 nm. TGA analysis showed that DP demonstrated noticeable thermal resistance.

Keywords: Nanocellulose; Date palm waste; Fibers; Extraction; Leaves of the date palm

1. Introduction

The depletion of fossil resources and the search for alternative solutions with an aim to secure the environment have stimulated interest towards the development of renewable and eco-friendly sustainable materials.[1–4]

Natural fiber composites, also known as natural fiber reinforced polymer composites have recently become highly valued materials. Aside from the expanding ecological, social, and economic awareness.[5] Natural fibers from residues and agricultural waste (e.g. flax, kenaf, hemp, sisal, jute) incorporated into these products either as fillers or reinforcement components within polymer matrices, opening avenues for diverse applications,[5,6] for example the paper industry, composites, biomedicine, textiles, construction, aerospace, automotive, to sensors, etc.[2]

Cellulosic fiber related to the main chemical constituent, cellulose, or lignocellulosic fibers, are amorphous matrices mostly composed of semi-crystalline cellulose microfibrils supported by hemicellulose, lignin, waxes, extractables and trace elements.[7–9] The materials based on cellulose, hemicelluloses and lignin, have several advantages for being renewable, biodegradable, and they do not

harm our environment. They are used to substitute petroleum materials.[10–12]

The cellulose is one of the most important natural resources. It is derived from plant cell walls and can be found in different sources like bacteria, algae, fungi, and some animals like tunicates.[13–17] Cellulose is found in the form of microfibril bundles oriented in various helical structures. Nanocrystalline celluloses (NCCs), or cellulose nanocrystals (CNCs) have generated a significant interest in the domain of materials science due to their intrinsic attractive properties, which include nanodimension, high surface area, high aspect ratio of 100, high crystallinity, low density, high mechanical strength, high dispensability in aqueous solutions, and unique morphology. Consequently, CNCs can be employed in various applications, such as reinforcement and support materials for nanocatalysts.[9,18–233, 5, 7, 9, 11, 13, and 15 m] In addition to films, hydrogels, and aerogels.[2]

Date palm (*Phoenix dactylifera*) belongs to the family *Plamae* (*Arecaceae*) and it is a tropical tree. The *Palmae* family comprises around 220 genera and about 2600 species.[24] It is the most significant agricultural crop, found abundantly in Northern. The date palm is an essential part of the flora of all Middle East and North Africa (MENA) countries. It plays a crucial role in the social, economic and cultural life of the region,[25] and it proves highly effective in the ongoing battle against desertification by providing a microclimate which prevents the long-term deterioration of ecologically fragile environments.[26,27] Furthermore, every tree lives for over than 100 years, yielding fruit and waste products, and large quantities of residues that are undoubtedly accumulated in agricultural lands, every year after date palm harvesting.[26–29] Each date palm tree generates about 30 kg of biomass with dry leaves contributing roughly 20 kg per year.[30] Waste is often disposed of by burning or in landfills, leading to significant environmental issues. Therefore, using specific natural fibers will not only minimize waste disposal challenges, but also environmental pollution.[5,6] The waste of date palm is interesting because of its abundance and relatively low cost in the manufacturing and industrial sector, in comparison to other vegetal fibers, which are currently used in the industrial fields.[6]

With the aim of the industrial exploitation this study investigates nanocellulose extracted from the leaves of the date palm tree (*Phoenix dactylifera* L). The leaves of the date palm were used as a source of cellulose in this work. We employed two types of waste materials, dried palm (DP) and fresh palm (FP), to examine the influence of maturation status on the properties of the extracted cellulose. Cellulose nanocrystals (CNCs) are derived from native cellulose by acid hydrolysis, which removes the amorphous parts. The resulting CNCs were characterized for their physicochemical, structural, morphological, and thermal properties to assess their potential as reinforcing materials in biocomposites.

2. Materials and Methods

2. 1. Plant Material

The samples of leaves (dry palm (DP) and fresh palm (FP)) of the date palm (*Phoenix dactylifera L*) were collected during the harvest period in their natural habit from Ouargla in the South-East of Algeria (31°54' to 32°1' North, 5°15' to 5°27' East).

2. 2. Chemical Reagents

Various chemical reagents were employed in the extraction and characterization process. These reagents included toluene, ethanol, sodium chlorite, acetic acid, sodium hydroxide, and sulfuric acid. All the chemicals were procured from Sigma-Aldrich.

2. 3. Chemical Compositions

The α-cellulose content, the acid-insoluble lignin and the ash content of specimens were determined according to the ASTMD 1103 – 55 T, ASTMD 1106-56 standard and ASTMD 1102-56 standard, respectively.[31]

2. 4. Isolation of Cellulose Fibers

The cellulose fibers were isolated as described by Mehany et *al.*[32] The palm residues were cleaned carefully three-four times under hot water to eliminate any dirt and other water-soluble compounds, and then dried in the open-air environment (between 25 and 30 °C). The residues were crushed then sieved a 60-mesh screen (250 µm) to cellulose fibers (Retch Control, model AS 200).

The extraction of cellulose was carried out following the methods outlined by Lu & Hsieh[33] Mellissa et *al.*[34] and Lu et *al.*[35] with some modifications (Figure 1):

10 g of palm powder were immersed in 150 ml of mixture of toluene and ethanol (2:1 v/v) for 20 hours. This step aimed to eliminate wax, pigments, and oils present in the palm powder. The resulting material from extraction was dried in an oven at 55 °C for 24 hours to remove any residual solvents and moisture. The dried palm powder was mixed with 10% NaOH solution (1 g/10 mL) at 75 °C for 1 hour. This treatment produced alkali-treated fibers by breaking down non-cellulosic components. The alkali-treated fibers, which constituted the insoluble pulps rich in cellulose, were subjected to a bleaching process. A 150 mL solution of 1% v/v sodium hypochlorite / deionized water, buffered to pH 5 using an acetate buffer, was used for bleaching. The mixture was stirred at 70 °C for 1 hour. The bleached fibers were washed at least three times with distilled water, or until the pH of the wash became neutral. Finally, the cellulose fibers were air-dried and weighed to obtain the final yield of extracted cellulose fibers.

2. 5. Isolation of Palm Nanocrystalline Cellulose

Isolation of palm nanocrystalline cellulose was performed using the method of Madureira et *al.* [36] with slight modification; the isolated cellulose was hydrolyzed with 64% wt sulfuric acid at an acid/cellulose ratio of 10 mL/g and at a temperature of 45 °C for 45 minutes. The acid hydrolysis was stopped by diluting with cold water (between 0 and 2 °C) for 10 times. The resulting cellulose nanocrystal gel was washed twice, centrifuged (Hettich Rotina, model 380R) at 5000 rpm for 30 min at 10 °C, and then dialyzed with regenerated cellulose dialysis membranes with a molecular weight cutoff of 12–14 KDa, against ultrapure water for 4 days and until neutral pH was achieved. The suspension was sonicated (53Church Hill Newtown, model VC505) in an ice bath for 30 min, then frozen at –30 °C, and freeze-dried. The dried product was stored for subsequent characterizations. The values were determined in triplicate.

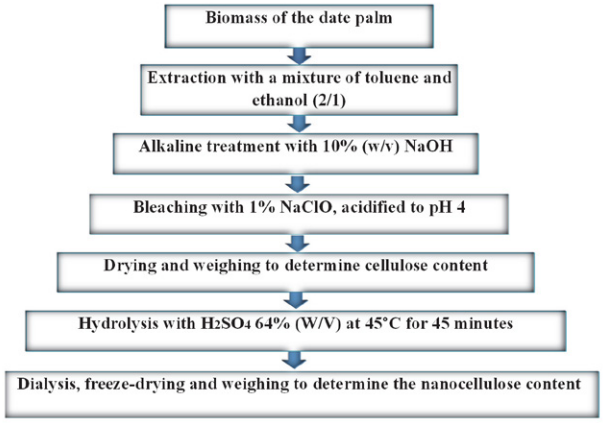

Figure1. The extraction process of nanocellulose from palm fibers

2. 6. Characterization of Nanocellulose

Fourier Transform Infrared (FTIR)

Infrared spectroscopy was performed using an FTIR spectrometer (Cary 660 FTIR). The measurements were conducted in the range of 4000–400 cm^{-1} with a resolution of 8 cm^{-1}

X-ray diffraction (XRD)

XRD measurements were carried out using a Proto Benchtop XRD instrument under room conditions. The analysis was performed at 2θ ranging from 5° to 40° with a step of 0.02° and a scan rate of 2 s/step. XRD analysis provides information about the crystalline structure of the nanocellulose.

Crystalline Index (CrI) values were calculated using two equations (Eq 1 and Eq 2).[37,38]

$$CrI = [(I_{max} - I_{am})/ I_{max}] \text{ X } 100 \quad (1)$$

$$CrI = (A_{Cry} / A_{Total}) \text{ X } 100\% \quad (2)$$

where I_{max} is the peak intensity at the crystalline plane (2θ = 22.6°), and I_{am} is the minimum intensity located between the two most distinct peaks (2θ = 18.7°). A_{Cry} is the sum of crystalline band areas, and A_{Total} is the total area under the diffractograms. The calculated crystallinity index provides a measure of the degree of crystallinity in the nanocellulose sample.

The crystal size (D) of the nanocellulose was estimated using the following equation (Eq 3).

$$D = (K \lambda) / \beta \cos\theta \quad (3)$$

where K is the Scherrer constant, λ is the wavelength of X-ray radiation, β is the full width at half maximum (FWHM) of the peak, and θ is the diffraction angle.

Thermogravimetric analysis (TGA)

The thermal stability of the cellulose nanocrystals (CNCs) was analyzed using a TGA instrument (differential thermogravimetry) –51H. The specimens were heated from room temperature to 700 °C at a heating rate of 10 °C/min under a N_2 gas flow rate of 60 mL/min.

Scanning electron microscopy (SEM)

The microstructural analysis of the raw fibers and CNCs of palm fibers was carried using the scanning electron microscope (EVO15, smart EDX Zeiss). The dried sample powder was placed on carbon strips and coated with a thin gold layer under an argon atmosphere. Micrographs were taken at an accelerating voltage of 15 kV.

Zeta sizer

The suspensions of CNCs (0.05% w/v) were examined using a Zetasizer HORIBA Scientific SZ-100 for zeta size analysis.

3. Results and Discussion

3. 1. Isolation and Purification of Cellulose

The chemical compositions of the fibers obtained before the purification is shown in table 1. These results are consistent with findings from other researchers.

The obtained results showed that the cellulose is the most chemical constituent of date palm fibers. The cellulose was isolated from palm fibers with an interesting rate of 35.99% ± 2.64 for DP and 36.17% ± 0.66 for FP. According to Astruc et *al.*[39] the cellulose yield of the fibers, the level of polymerization of the cellulose and the angle of the

spirals in each wall vary for each plant and have a direct influence on their physical and chemical properties**.**

The standard deviations associated with the cellulose yield percentages indicate possible measurement errors. However, these values obtained through the purification process demonstrate its effectiveness in isolating cellulose from palm fibers. Additionally, the chemical compositions of the fibers before the purification processes were consistent with previous research, confirming the reliability of the obtained results. Further analysis and characterization of the isolated cellulose will provide more insights into its properties, allowing for a comprehensive understanding of its potential applications in various fields.

Table 1. Chemical compositions of different palm fibers

Component	Present work		Sbiai et *al.* (2010)[40]	Gouamid (2015)[41]	Jonoobi et *al.* (2019)[28]
	DP	FP			
Cellulose (%)	35.99	36.17	54.75	38.10	40.21
Lignin (%)	18.07	16.45	15.30	11.95	32.2
Extractible (%)	20.16	24.10	8.2	19.46	4.24
Ashes (%)	8.21	8.78	1.75	7.75	10.54
Moisture (%)	4.89	4.21	/	/	/
Hemicellulose(%)	/	/	/	22.7	12.8

Alkaline dilute treatment was used to mainly dissolve lignin, pectin, hemicelluloses and proteins. Furthermore, a bleaching step was carried out to eliminate any remaining lignin residues.[42]

The isolation and purification of cellulose from palm fibers followed a three-step procedure consisting of dewaxing, delignification, and hemicellulose elimination. Each step contributed to transforming palm fiber into a clean white color. The physical appearance of palm fibers before and after purification is illustrated in Figure 2(d). The palm fibers appear as white cottony fibers, after alkali and bleaching process. The change in color indicates the effective removal of a significant amount of non-cellulosic components during the purification process.

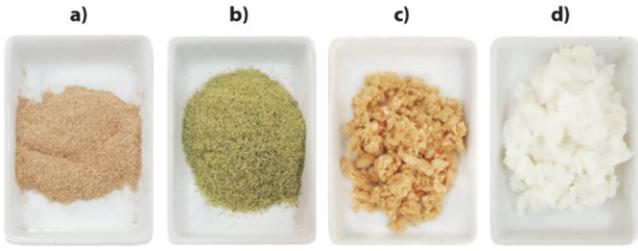

Figure 2. Raw fibers of DP (a), raw fibers of FP (b), delignified fibers (c) and bleached fibers (d)

3. 2. Preparation of the Cellulose Nanocrystals

The purified cellulose was further treated by sulfuric acid hydrolysis in the following conditions: 45°C, 45 min and 64% (wt) H_2SO_4 concentration. These conditions were determined based on research by several authors,[33,36,43,44] who emphasized the critical role of acid concentration, hydrolysis temperature, and time as crucial parameters in CNCs isolation.

According to Lu et *al.*[35] the yield of CNCs by sulfuric hydrolysis ranged from 10% to 80%. The yield of CNCs in this work is in this range with 33.12% ± 2.51 for DP and 34.35% ± 0.18 for FP.

The yield is attributed to the additional hydrolysis of the amorphous regions of the cellulose, according to Nang et *al.*[45] Acid hydrolysis is a widely utilized method for manufacturing nanocrystalline cellulose (NC). It proves to be effective due to its ability to selectively degrade the amorphous regions of cellulose microfibrils, while preserving the crystalline domains. Consequently, these preserved crystalline domains can be isolated and obtained as monocrystals. In general, there are numerous factors that influence the yield, not just the reaction conditions like the acid type and concentration, the time of hydrolysis and temperature, also the mechanic treatments, the centrifugation throughout the procedure and fibers characteristics.[35]

3. 3. Fourier Transform Infrared (FTIR)

The Fourier transform infrared (FTIR) analysis provided valuable information about the chemical changes that occurred during the purification and isolation of cellulose nanocrystals (CNCs). Figure 3 shows the comparison of the FTIR spectra of various stages of the process, including raw fibers, dewaxed fibers, delignified cellulose, and CNC.

The presence of a peak at 2849 cm^{-1} in the FTIR spectrum of raw fibers, attributed to waxes, indicates the presence of extractable materials in the initial fibers. However, after the dewaxing step, this peak is absent, confirming the effective removal of waxes and other extractables from the fibers.

Regarding lignin, characteristic peaks were observed in the FTIR spectra of raw fibers, including peaks at 1516 cm^{-1} (aromatic backbone vibration), 1508 cm^{-1} (C=C vibrations of aromatic rings), and 1243 cm^{-1} (C-O bonds of carboxylic and ether groups). These peaks are

indicative of the presence of lignin. However, after the delignification stage, these peaks diminish or disappear completely, indicating the successful elimination of lignin from the cellulose structure. The presence of specific peaks at 1230 cm^{-1}, 1461 cm^{-1}, and 1517 cm^{-1} in the FTIR spectra confirms the complete sequential removal of lignin during the purification process. These results align with previous studies by Astruc et *al.*[3] and demonstrate the effectiveness of the purification steps in eliminating lignin from the cellulose fibers. Generally speaking, the FTIR analysis provides strong evidence of the successful purification of cellulose and the removal of waxes and lignin, validating the purity of the obtained cellulose and its suitability for further processing into cellulose nanocrystals.

The presence of characteristic peaks at 1729 cm^{-1} and 1700 cm^{-1} in the FTIR spectrum indicates the presence of carbonyl stretching vibrations, which are attributed to hemicelluloses.[33,36] Additionally, the peak at 1700 cm^{-1} is associated with acetyl and ester groups in hemicellulose, or carboxylic acid groups.[35] The disappearance of these peaks in the FTIR spectra of delignified cellulose and CNCs indicates the successful removal of hemicellulose from the palm fibers. The purification process effectively eliminates hemicellulose, resulting in the isolation of cellulose-rich materials. The removal of hemicellulose is crucial for obtaining purified cellulose materials since hemicellulose contributes to the amorphous regions of the fibers and can affect the properties of the final product. By eliminating hemicellulose, the delignified cellulose and CNCs obtained have a higher cellulose content and enhanced crystallinity, making them suitable for reinforcement application.

The band observed in the range of 3400–3000 cm^{-1} corresponds to the stretching vibrations of hydroxyl groups (-OH) present in cellulose, as noted by Astruc et *al.*[43] The FTIR spectra of cellulose typically exhibit several distinct bands that can be attributed to specific functional groups within the cellulose structure. These include the stretching of OH bonds at 3362 cm^{-1}, the asymmetric angular deformation of C-H bonds at 1429 cm^{-1}. The symmetric angular deformation of C-H bonds at 1371 cm^{-1}.The stretching of C-OH and C-C-OH bonds in secondary and primary alcohols at 1110 cm^{-1} and 1059 cm^{-1}, respectively, and the angular deformation of C-H bonds at 897 cm^{-1}, as reported by Vasconcelos et *al.*[46] Additionally, Madureira et *al.*[36] identified peaks at 3310 cm^{-1} and 1640 cm^{-1}, respectively, associated with cellulose, as well as a peak at 2900 cm^{-1} attributed to C-H stretching vibrations, which are present in all samples.

The presence of peaks at 3400–3000 cm^{-1}, 2900 cm^{-1}, 1110.9 cm^{-1}, 1059 cm^{-1}, and 897 cm^{-1} in the FTIR spectrum (as shown in figure 3) confirms the presence of cellulose throughout the purification and extraction processes of CNCs. These results indicate that cellulose is retained and not eliminated during the purification and extraction steps; supporting the successful isolation of CNCs while maintaining the cellulose structure.

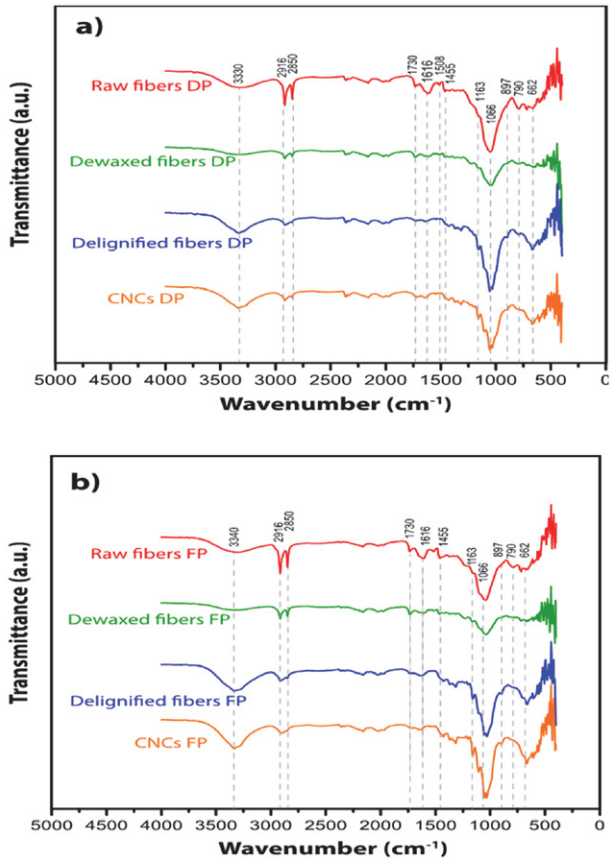

Figure 3. FTIR spectroscopy of DP (a) and FP (b) at different stage of treatment

3. 4. X-ray Diffraction (XRD)

The crystallinity of nanocellulose is a main factor in determining its thermal stability and mechanical properties.[47] The crystallinity study allows to determine the effect of extraction methods on the crystal structure of the cellulose. X-ray diffraction (XRD) technique was utilized to identify the CrI of raw fibers and nanocrystals (Figure 4).

Studies by Culsum et *al.*[23] and Lu et *al.*[35] report that the characteristic diffraction peaks of cellulose appear at $2\theta \approx 15.71$, 16.48 and 22.50, representing different crystallographic planes. Similarly, the XRD patterns of bacterial cellulose from Vasconcelos et *al.*[46] align with these characteristic peaks.

As shown in figure 4, the XRD patterns of the samples also reveal these characteristic diffraction peaks of cellulose at 2θ values of approximately 15, 17, and 22°. Additionally, a distinct peak at $2\theta \approx 22$ indicates the presence of a crystalline region.

Table 2 provides the measured values for the crystallinity index (%), and crystallite size obtained from X-ray

diffraction curves. The CNCs fibers exhibited the highest crystallinity index value, while the lowest value was observed for the raw fibers. These results are well correlated with values of Rajinipriya et *al.*[2] Dahlem et *al.*[48] and Gond et *al.*[49]

Dahlem et *al.*[48] reported that the raw fibers had a crystallinity index of 40.62%, while the CNC exhibited a higher value of 66.19%. Similarly, Gond et *al.*[49] found that the raw fibers had a crystallinity index of 32.4%, whereas the CNC showed a higher value of 53.02%. Both studies concluded that the crystallinity of the nanocellulose (NC) was higher compared to that of the initial material. This increase in crystallinity can be attributed to the application of a chemical treatment, which effectively eliminated the non-cellulosic components of the fibers.

According to Vasconcelos et *al.*[46] the increasing crystallinity following the acid hydrolysis reaction is a result of a decrease in amorphous content, because this region is more available to acid attack.

The obtained crystallite size values are in close agreement with those reported by Gondet*al.*[49] who found a size of 3.74 nm for raw fibers and 3.4 nm for CNC.

A number of parameters such as the source of cellulose, isolation process conditions and various pretreatments determine the final crystallinity of nanocellulose in either crystal or fiber form.[50]

Biomass of lignocellulosic components consists of amorphous and crystalline regions. The amorphous region is mainly due to lignin and hemicellulose, while the crystalline region is attributed cellulose. Therefore, the treatment that is done chemically leads to the depolymerization of hemicellulose and the delignification of fibers, which tends to increase the crystallinity of cellulose obtained.[51]

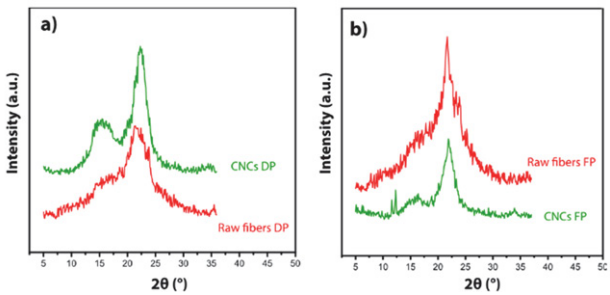

Figure 4.DRX of DP (a) and FP (b)

Table 2. The results of crystallinity index and crystal size of studied raw fibers and CNC

	Crystallinity index (%)	Crystal size (nm)
Raw fibers DP	35.09	5.85
CNCs DP	53.34	3.03
Raw fibers FP	28.0	5.53
CNCs FP	57.7	3.48

3. 5. Zeta Sizer

Particle size measurement using a Zetasizer or Nanosizer is commonly used to determine the size distribution and assess the dispersion and stability of CNCs in aqueous solutions.[20,23] The analysis provides information on the size range and distribution of the particles. In the Figure 5, it is evident that the size of CNC particles obtained from DP ranges from 25 to 1000 nm with an average of 512.5 nm. In contrast, for CNC particles obtained from FP, the size range is 76 to 1150 nm, with an average of 613 nm. These findings are consistent with previous studies that have reported CNC sizes ranging from 5.6 to 1106 nm; 30 nm to 1 µm.[43]

The broad distribution observed can be attributed to the anisotropic properties of the CNC suspension in solution.[43] It is important to note that the size distribution obtained from light diffusion techniques like the Zeta sizer may not provide precise and accurate measurements of particle size, as it measures the length and diameter of particles. However, the results can still provide valuable information about the general size range and distribution of the CNC particles. For more detailed and accurate information about the particle size and morphology of CNCs, microscopy techniques are recommended. The size distribution obtained from the Zeta sizer analysis often aligns well with the results obtained by microscopy, further confirming the overall size range and distribution of CNC particles.

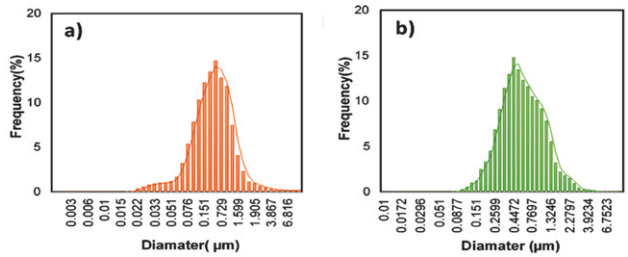

Figure 5. Zeta sizer of CNCs-DP (a) and CNCs-FP (b)

3. 6. Scanning Electron Microscopy (SEM) Analysis

SEM images (figure 6) provide valuable insights into the surface morphologies of palm fibers before and after chemical treatments. The untreated palm fibers (Figure 6 a1 and b1) appear as large bundles with rough surfaces. The presence of wax, oil, and surface impurities is clearly visible, indicating the presence of cellulose fibers embedded in hemicelluloses and lignin. These substances are effectively removed during the delignification process, as shown in Figure 6 (a2 and b2), resulting in a more defined and shorter cellulose fiber size with an approximate diameter of 4.98 µm.

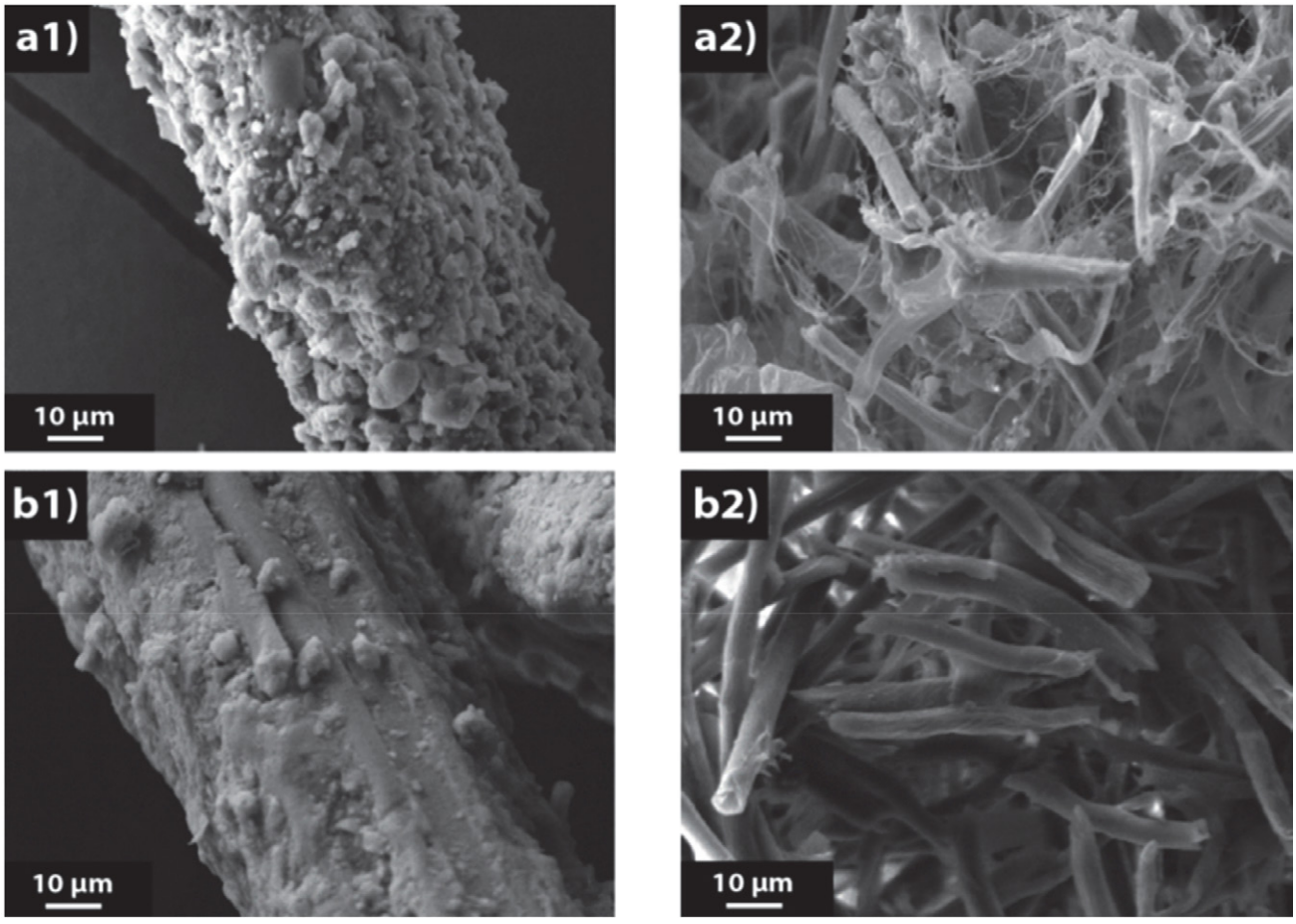

Figure 6. SEM micrographs of raw fibers of DP (a1), CNCs-DP (a2), raw fibers of FP (b1) and CNCs-FP (b2)

According to Ali et *al.*[52] alkaline and acid treatments of cellulosic fibers generally result in a more transparent, clearer, and harder surface with dispersed fibers compared to the raw form. in this study, the sulfuric acid treatment (64%) effectively disintegrates the palm fibers, reducing their size to nanocrystalline cellulose.

The presence of wax, oil, and impurities on the surface of untreated fibers is clearly observed. The treated fiber clusters, shown in Figure 6, exhibit a smoother surface, indicating the removal of hemicelluloses, lignin, wax, oils, and other impurities. This improvement in surface morphology is consistent with the results reported by Zarina and Ahmed.[53]

Overall, SEM analysis reveals the morphological changes that occur after the chemical treatments, confirming the removal of impurities and the transformation of palm fibers into nanocrystalline cellulose with improved surface characteristics.

3. 7. Energy Dispersive X-ray Spectroscopy (EDX)

The EDX spectrum shows the spectra peaks that correspond to the binding energies of carbon, oxygen and other elements as the major components. The EDX spectrum reveals the presence of trace elements and impurities in the treated cellulose material. This is not unusual and can be influenced by various factors, including the source of the cellulose, the purification process, and the specific treatment methods employed. The detection of calcium (Ca), chlorine (Cl), and silicon (Si) as impurities indicates the presence of these elements in the treated cellulose. These impurities could arise from the raw material itself, such as minerals present in the plant fibers used for cellulose extraction. They can also originate from the processing methods used, including the chemicals and equipment employed during the treatment process. The presence of these trace elements does not necessarily indicate a negative aspect, but their quantities should be evaluated to ensure they are within acceptable limits for the intended applications of the cellulose material. The presence of residual sulfur (S) in small amounts can be attributed to the H_2SO_4 acid hydrolysis process used for the extraction of cellulose nanocrystal (CNC). The sulfuric acid used in the hydrolysis process can leave residual traces in the final CNC product. While efforts are made to minimize residual impurities during purification and extraction processes, the detection of sulfur suggests that some residual

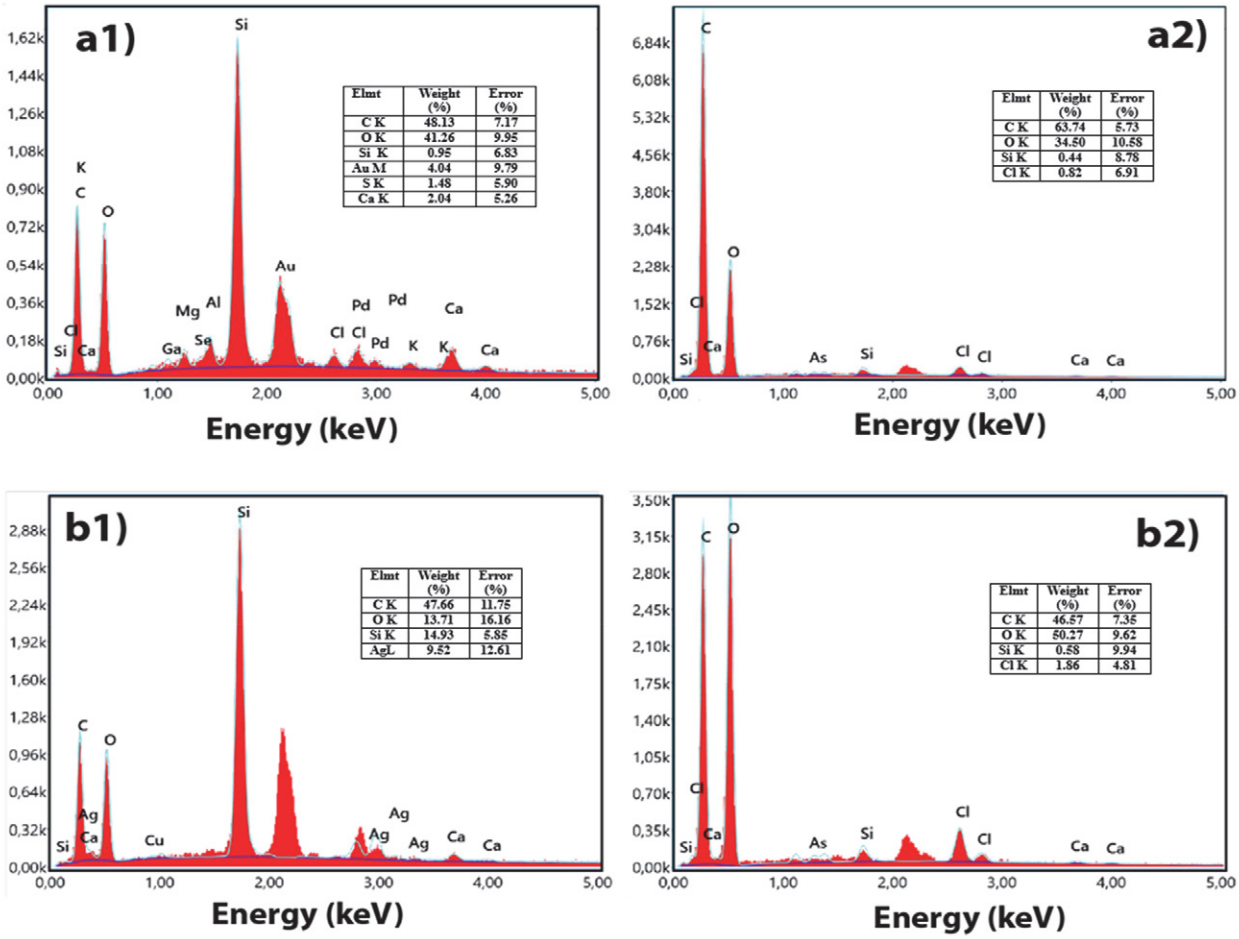

Figure 7. EDX of raw fibers of DP (a1), CNCs-DP (a2), raw fibers of FP (b1) and CNCs-FP (b2)

impurities from the acid treatment remain. These residual impurities should be considered when evaluating the purity and suitability of the CNC for specific applications. It's worth noting that the EDX spectrum provides qualitative elemental analysis, indicating the presence of different elements in the sample. For more accurate quantification of these elements, additional analytical techniques such as atomic absorption spectroscopy or inductively coupled plasma mass spectrometry may be employed. It's worth mentioning that in the raw fibers, elements such as calcium (Ca), silicon (Si), chlorine (Cl), magnesium (Mg), and potassium (K) are also present. These elements may be naturally present in the palm fibers or could be introduced during the growth or processing stages. The EDX analysis provides valuable information about the elemental composition and impurities present in the cellulose samples, confirming the effectiveness of the treatment in removing certain impurities while also indicating the residual presence of some elements originating from the extraction process.

Considering both the natural presence of certain elements in the raw fibers and the residual elements from the extraction process, it is important to determine the acceptable limits for these impurities based on the specific applications of the cellulose material. Quality control measures and appropriate purification techniques can help ensure that the final cellulose product meets the required standards for its intended use. These results and observations are in accordance with the results carried out by Ali et *al.*[52]

3. 7. Thermogravimetric Analysis (TGA)

The thermogravimetric analysis allows for measurement of the degradation of a sample according to the temperature end /or time.[54] Concerning the thermogravimetric analysis of the date palm fibers, results are illustrated in figure 8.

The initial weight decrease observed in the TGA measurement of CNCs in the range of 25–220 °C is likely due to the evaporation of water absorbed on the surface of CNCs. The subsequent weight loss observed between 220 °C to 360 °C can be attributed to the breaking or rearranging the glycosidic bonds of the CNCs, leading to cellulose degradation processes such as depolymerization, dehydration, and decomposition of glycosyl unit.[23]

Our results (Table 3) reveal that date fibers show two distinct degradation peaks with confirm the results reported by Bourmaude*t al.*[30] who reported that the date palm

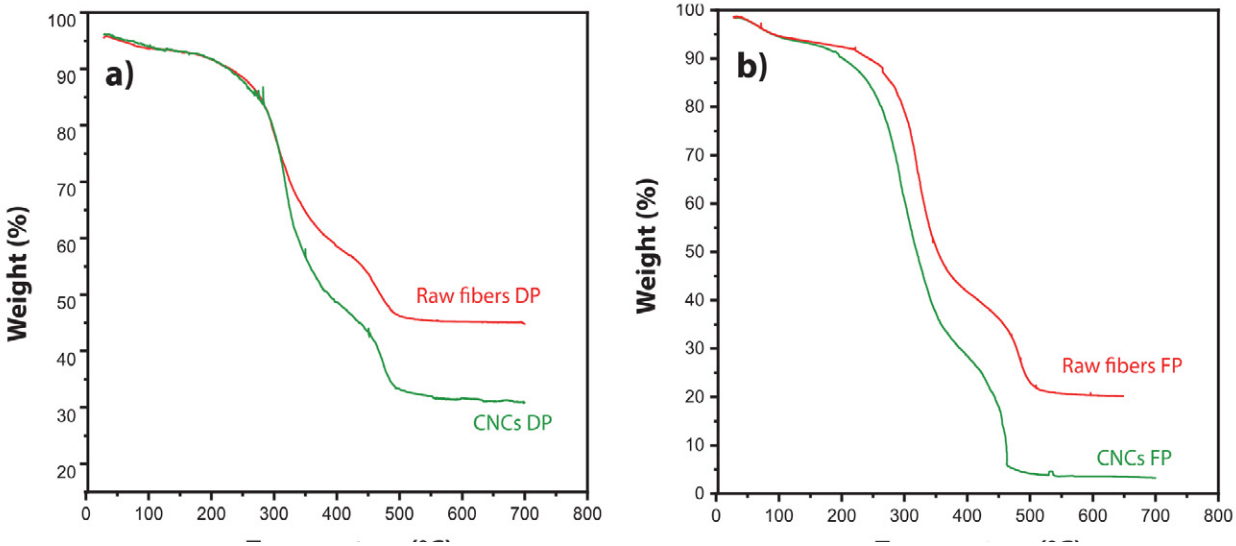

Figure 8. TGA of DP (a) and FP (b)

fibers have better thermal stability compared to other natural fibers.

According to Ali et *al.*[52] the thermal degradation of cellulose generally occurs in three phases. The initial weight losses for the samples were due to the evaporation of absorbed or surface-bound moisture (H_2O), which was evaporated below 100 °C. The degradation of CNC began at 259 °C, with the onset and offset temperatures for cellulose degradation occurring between 277 °C and 387 °C as measured by TGA.

The thermal degradation behavior of the samples can be further explored by referring to Table 3, which presents the specific onset and offset temperatures associated with weight loss and the degradation of the cellulose material.

Figure 8 and Table 3 clearly demonstrate that the CNC-DP exhibits significantly higher thermal stability compared to CNC-FP, with a weight loss of 14.74% for DP and 30.67% for FP. The disparity in thermal stability can be attributed to differences in the size, structure, and surface properties of the CNCs.

In terms of the thermal stability of the chemical components present in lignocellulosic materials, Raju et *al.*[9] indicate that hemicellulose, lignin, and cellulose exhibit different levels of thermal stability. Generally, hemicellulose is less thermally stable compared to lignin and cellulose. In the case of treated fibers, the removal of impurities, such as lignin and hemicellulose, during the chemical treatment process can lead to an improvement in thermal stability compared to untreated fibers. These findings highlight the influence of chemical treatments on the thermal stability of cellulose and lignocellulosic materials, with the potential to improve their thermal properties and expand their application possibilities

4. Conclusion

This study explored the potential of the date palm (*Phoenix dactylifera L*) waste leaves as a source of nanocellulose (CNC) with tailorable properties. Agricultural wastes represent an immense source of natural fibers, and utilizing them for CNC production offers a sustainable and cost-effective approach. In order to study the influence of the degree of maturity on the properties of the extracted nanocellulose, two types of waste material were used, that is dried palm (DP) and fresh palm (FP).

Alkaline and bleaching treatments effectively removed lignin, hemicellulose and impurities, as confirmed by FTIR and SEM micrographs. While EDX revealed traces of chemical impurities on the treated nanocellulose. XRD analysis revealed a higher degree of crystallinity for the CNCs compared to the raw fibers. Zeta sizer results

Table 3. The thermal degradation of studied raw fibers and CNCs

Samples	1st thermal degradation			2nd thermal degradation			Char yield
	T Onset (°C)	T Offset (°C)	WL (%)	T Onset (°C)	T Offset (°C)	WL (%)	(%)
Raw fibers DP	266.91	372.13	25.32	423.87	493.00	10.13	**15.19**
CNC DP	263.17	349.91	28.01	421.72	495.01	13.27	**14.74**
Raw fibers FP	265.22	375.99	43.26	451.28	511.93	14.35	**28.91**
CNC FP	226.61	353.50	51.24	414.65	464.82	20.57	**30.67**

showed that the size ranging was between 25 and 1150 nm. The TGA showed a high thermal stability for DP compared with FP.

Based on the findings, comparatively, more mature date palm leaves (DP) demonstrate slightly superior characteristics especially in terms of crystallinity and thermal stability when compared to fresher palm leaves (FP). This suggests that the degree of maturity can influence the final properties on the CNCs. The study emphasizes the significance of particle characteristics, including crystallinity, size, as well as the thermal stability of CNC particles, coupled with the low cost and abundant availability of the source material, date palm CNC emerges as an appealing option for reinforcing polymer materials.

5. References

1. H. Kargarzadeh, M. Ioelovich, I. Ahmad, S. Thomas, A. Dufresne, Handbook of Nano-cellulose and Cellulose Nanocomposites, Wiley-VCH, Verlag. **2017**, 23. **DOI:**10.1002/9783527689972
2. M. Rajinipriya, M. Nagalakshmaiah, M. Robert, S. Elkoun, *ACS Sustain. Chem. Eng.* **2018**, *6*, 2807–2828. **DOI:**10.1021/acssuschemeng.7b03437
3. J. Astruc, M. Grandbois, G. Laroche, M. Robert, S. Elkoun, *Can. J. Chem*. **2021**, *99*, 1–25. **DOI:**10.1139/cjc-2020-0371
4. K. J. Nagarajan, N. R. Ramanujam, M. R. Sanjay, S. Siengchin, B. Surya Rajan, K. SathickBasha, P. Madhu, G. R. Raghav, *Polym. Compos*. **2021**, *42*, 1588–1630. **DOI:**10.1002/pc.25929
5. F. M. Al-Oqla, S. M. Sapuan, *J. Clean. Prod.* **2014**, *66*, 347–354. **DOI:**10.1016/j.jclepro.2013.10.050
6. B. Chihaoui, F. S. Parareda, Q. Tarrés, F. X. Espinach, S. Boufi, M. Delgado-Aguilar, *Polym*. **2020**, *18*, 1693. **DOI:**10.3390/polym12081693
7. S. Azizi, F. Alloin, A. Dufresne, *Biomacromolecules* **2005**, *6*, 612–626. **DOI:**10.1021/bm0493685
8. Y. Habibi, L. A. Lucia, O. J. Rojas, *Chem. Rev*. **2010**, *110*, 3479–3500. **DOI:**10.1021/cr900339w
9. V. Raju, R. Revathiswaran, K. S. Subramanian, K. T. Parthiban, K. Chandrakumar, E. V. Anoop, C. J. Chirayil, *Sci. Rep*. **2023**, *13*, 1199. **DOI:**10.1038/s41598-022-26600-5
10. A. Dufresne, *Mater. Today* **2013**, *16*, 220–227. **DOI:**10.1016/j.mattod.2013.06.004
11. B. Thomas, M. C. Raj, B. K. Athira, H. M. Rubiyah, J. Joy, A. Moores, G. L. Drisko, C. Sanchez, *Chem. Rev.* **2018**, *118*, 11575–11625. **DOI:**10.1021/acs.chemrev.7b00627
12. C. R. Contessa, G. S. Da Rosa, C. C. Moraes, *Int. J. Mol. Sci.* **2021**, *22*, 10628. **DOI:**10.3390/ijms221910628
13. H. Ng, L. T. Sin, T. Tee, S. Bee, D. Hui, C. Low, A. R. Rahmat, *Compos. B* **2015**, *75*, 176–200. **DOI:**10.1016/j.compositesb.2015.01.008
14. N. Kanai, T. Honda, N. Yoshihara, T. Oyama, *Cellulose* **2020**, *27*, 5017–5028. **DOI:**10.1007/s10570-020-03113-w
15. L. Y. Ng, T. J. Wong, C. Y. Ng, C. K. M. Amelia, *Arab. J. Chem.* **2021**, *14*, 10339. **DOI:**10.1016/j.arabjc.2021.103339
16. D. K. Arserim-Uçar, F. Korel, L. S. Liu, K. L. Yam, *Food Chem.* **2021**, *336*, 127597. **DOI:**10.1016/j.foodchem.2020.127597
17. N.E.A. El-Naggar, A.B.A. Mohammed, S.E. El-Malkey, *Sci. Rep*. **2023**, *12*, 18533. **DOI:**10.1038/s41598-022-26642-9
18. M. R. Ishak, S. M. Sapuan, Z. Leman, M. Z. A. Rahman, U. M. K. Anwar, *J. Therm. Anal. Calorim*. **2012**, *109*, 981–989. **DOI:**10.1007/s10973-011-1785-1
19. S. Mondal, *Carbohydr. Polym*. **2017**, *163*, 301–316. **DOI:**10.1016/j.carbpol.2016.12.050
20. R. A. Ilyas, S. M. Sapuan, M. R. Ishak, *Carbohydr. Polym.* **2018**, *181*, 1038–1051. **DOI:**10.1016/j.carbpol.2017.11.045
21. J. H. Jordan, M. W. Easson, B. Dien, S. Thompson, B. D. Condon, *Cellulose* **2019**, *26*, 5959–5979. **DOI:**10.1007/s10570-019-02533-7
22. I. Uddin, S. Thomas, R. K. Mishra, A. M. Asiri (Ed.) : Sustainable polymer composites and nanocomposites, Springer, **2019**, pp. 37–65. https://link.springer.com/book/10.-1007/978-3-030-05399-4
23. N. T. U. Culsum, C. Melinda, I. Leman, A. Wibowo, Y. W. Budhi, *Mater. Today Commun.* **2021**, *26*, 101817. **DOI:**10.1016/j.mtcomm.2020.101817
24. A. Faiad, M. Alsmari, M. M. Z. Ahmed, M. L. Bouazizi, B. Alzahrani, H. Alrobei, *Sustain*. **2022**, *14*, 1134. **DOI:**10.3390/su14031134
25. R. A. Nasser, H. A. Al-Mefarrej, *World Appl. Sci. J.* **2011**, *15*, 1651–1658
26. A. Bendahou, H. Kaddami, M. Raihane, Y. Habibi, A. Dufresne, *Rev. Roum. Chim*. **2009**, *54*, 571–575.
27. W. Ghori, N. Saba, M. Jawaid, M. Asim, *IOP Conf. Mater. Sci. Eng.* **2018**, *368*, 012009. **DOI:**10.1088/1757-899X/368/1/012009
28. M. Jonoobi, M. S. H. *J. Renew. Mater.* **2019,** *7*, 1055–1069. **DOI:**10.32604/jrm.2019.08188
29. S. Awad, Y. Zhou, E. Katsou, Y. Li, M. Fan, *Waste Biomass Valori* **2020**, *12*, 2853–2887. **DOI:**10.1007/s12649-020-01105-2
30. A. Bourmaud, H. Dhakal, A. Habrant, J. Padovani, D. Siniscalco, M. H. Ramage, J. Beaugrand, D. U. Shah, *Comps. A: Appl. Sci. Manuf.* **2017**,*103*, 292–303. **DOI:**10.1016/j.compositesa.2017.10.017
31. American Society, "ASTM Standards On Wood, Wood Preservatives, And Related Materials" **1959**, 139–150. http://archive.org/details/astmstandardsonw00amer
32. S. Mehanny, E. E. Abu-El Magd, M. Ibrahim, M. Farag, R. Gil-San-Millan, J. Navarro, A. E. H. El Habbak, E. El-Kashif, *J. Mater. Res. Technol.* **2021**, *10*, 526–537. **DOI:**10.1016/j.jmrt.2020.12.027
33. P. Lu, Y. L. O. Hsieh, *Carbohydr. Polym.* **2012**, *81*, 564–573. **DOI:**10.1016-/j.carbpol.2011.08.022
34. B. A. Melissa, S. M. M .A. Bashir Ahmmad, *J. Reinf. Plast. Compos.* **2014**, *33*, 2205–2213. **DOI:**10.1177/0731684414558325
35. S. Lu, T. Ma, X. Hu, J. Zhao, X. Liao, Y. Song, X. Hu, *J. Sci. Food Agric.* **2022**, *102*, 312–321. **DOI:**10.1002/jsfa.11360
36. A. R. Madureira, T. Atatoprak, D. Çabuk, F. Sousa, R. C. Pul-

lar, M. Pintado, *Int. J. Food Stud.* **2018**, *7*, 24–33. **DOI:**10.7455/ijfs/7.1.2018.a3
37. L. Segal, J. J. Creely, A. E. Martin, C. M. Conrad, *Text. Res. J.* **1959**, *29*, 786–794. **DOI:**10.1177/004051755902901003
38. H. Hermans, J. J. Hermans, A. Weidinger, *J. Polym. Sci.* **1948**, *169*, 1–9. **DOI:**10.1002/pol.1948.120030101
39. J. Astruc. Extraction et compatibilisation de nanocristaux de cellulose issue de résidus lignocellulosiques pour le renforcement de biocomposites, Québec, Canada, **2018**, 1–150. https://core.ac.uk/download/pdf/199228206.pdf
40. A. Sbiai, A. Maazouz, E. Fleury, H. Sautereau, H. Kaddami, *Bioresources* **2010**, *5*, 672–689. **DOI:**10.15376/biores.5.2.672-689
41. M. Gouamid, Contribution of the study of diagnosis and valuation of El ghars palm waste, Ouargla, Algeria, **2015.** https://search.mandumah.com/Record/944117
42. W. P. F. Netoa, H. A. Silvérioa, N. O. Dantasb, D. Pasquini, *Biomass. Bioenerg.* **2012**, *46*, 555–563. **DOI:**10.1016/j.biombioe.2012.06.039
43. J. Astruc, M. Nagalakshmaiah, G. Laroche, M. Grandbois, S. Elkoun, M. Robert, *Carbohydr. Polym*. **2017**, *178*, 352–359. **DOI:**10.1016/j.carbpol.2017.08.138
44. T. Gabriel, A. Belete, G. Hause, R. H. H. Neubert, T. Gebre-Mariam, *J. Polym. Environ*. **2021**, *29*, 2964–2977. **DOI:**10.1007/s10924-021-02089-3
45. N. An, H. T. Chi Nhan, T. D. Tap, T. T. T.Van, V. P. Van , L. Van Hieu, *J. Polym. Environ*. **2020**, *28*, 1465–1474. **DOI:**10.1007/s10924-020-01695-x
46. N. F. Vasconcelos, J. P. A. Feitosa, F. M. P. da Gama, J. P. S. Morais, F. K. Andrade M. S. M. de Souza Filho, M. F. Rosa, *Carbohydr. Polym.* **2017**, *155*, 425–431. **DOI:**10.1016/j.carbpol.2016.08.090
47. E. Dinçel Kasapoğlu, S. Kahraman, F. Tornuk, *Foods* **2023**, *12*, 746. **DOI:**10.3390/foods12040746
48. M. A. Dahlem, C. Borsoi, B. Hansen, A. L. Catto, *Carbohydr. Polym*. **2019**, *218*, 78–76. **DOI:**10.1016/j.carbpol.2019.04.064
49. R. K. Gond, M. K. Gupta, M. Jawaid, *Polym. Compos.* **2021**, *42*, 5400–5412. **DOI:**10.1002/pc.26232
50. M. Jonoobi, *Cellulose* **2015**, *22*, 935–969. **DOI:**10.1007/s10570-015-0551-0
51. S. A. Wahib, D. A. Da'na, M. A. Al-Ghouti, *Arab. J. Chem.* **2022**, *15*, 103650. **DOI:**10.1016/j.arabjc.2021.103650
52. A. J. Ali, A. Danladi, M. M. Bukhari, B. B. Nyakuma, *J. Nat. Fibers* **2020**, *19*, 2756–2771. **DOI:**10.1080/15440478.2020.1856279
53. S. Zarina, I. Ahmad, *BioRes.* **2015**, *10*, 256–271. https://bioresources.cnr.ncsu.edu-/resources/biodegradable-composite-films-based-on-k-carrageenan-reinforcedbycellu-losena-nocrystal-from-kenaf-fibers/
54. K. Benhamou. Extraction de nanofibrilles de cellulose à structure et propriétéscon-trôlées : caractérisation, propriétésrhéologiques et application nanocomposites, Gre-noble Alpes, Maroc, **2015**, 173- 240. https://theses.hal.science/tel-01260323

Povzetek

Celuloza je najbolj razširjen in obnovljiv polimer v naravi. Odlikuje ga biorazgradljivost, ki pomaga ustvarjati prijazno okolje. Ta študija želi opisati nanocelulozo, pridobljeno iz odpadkov datljeve palme, tako posušenih (DP) kot svežih palm (FP) z uporabo kemijskih metod (hidroliza s H_2SO_4). Fizikalne lastnosti, morfologijo, elementarno sestavo in termično stabilnost smo določili s Fourierjevo transformacijsko infrardečo spektroskopijo (FTIR), rentgensko difrakcijo (XRD), zeta sizerjem, vrstično elektronsko mikroskopijo (SEM) in energetsko disipativno rentgensko *analizo* (EDX) in termogravimetrično analizo (TGA). Rezultati FTIR, SEM in EDX so razkrili učinkovito odstranjevanje nečistot, hemiceluloze in lignina. Po obdelavi so vzorci posušene palme (DR) vsebovali 35,99% celuloze in 33,12% celuloznih nanokristalov (CNC), vzorci sveže palme (FP) pa 36,17% celuloze in 34,35% CNC. CNC ima večjo kristaliničnost kot surova vlakna in Zeta potencial je bil med 25 in 1150 nm. Analiza TGA je pokazala dobro toplotno odpornost DP.

Scientific paper

Insight Into the Interaction of Quinizarin with SDS Micelles – Effects of Additives

Ana Maria Toader,[1] Izabella Dascalu,[1] Petruta Oancea[2] and Mirela Enache[1,*]

[1] *Institute of Physical Chemistry "Ilie Murgulescu", Romanian Academy, Splaiul Independentei 202, Bucharest 060021, Romania*

[2] *Department of Physical Chemistry, University of Bucharest, Blvd. Elisabeta 4-12, Bucharest 030018, Romania*

* *Corresponding author: E-mail: enachemir@yahoo.com*

Received: 11-15-2023

Abstract

Association behavior between quinizarin (1,4-dihydroxy-9,10-anthraquinone, Q), an analogue of the chromophore of anthracycline anticancer drugs and sodium dodecyl sulfate (SDS) micelles in the presence of glucose, NaCl and urea additives was studied using absorption spectroscopy and conductometric techniques. The spectral results indicate an increase of binding constant and partition coefficient values in the presence of glucose and NaCl whereas the addition of urea leads to a decrease of binding strength and quinizarin partitioning into SDS micelles. Thus, the rise of NaCl and glucose concentrations is favorable for the quinizarin distribution into SDS micelles. From electrical conductivity measurements it was found that the critical micelle concentration (CMC) of SDS/quinizarin system decreases by adding NaCl and glucose whereas urea has not influence on the micelization process at the concentrations used in the present study. Since biologically compounds like glucose, NaCl and urea are found in the human body, the attained outcomes can be important in finding of effective drug delivery systems.

Keywords: Quinizarin, SDS micelles, glucose, NaCl, urea

1. Introduction

Quinizarin (1,4-dihydroxy-9,10-anthraquinone, Q) is a synthetic anthraquinone used as fungicide and pesticide, antioxidant, additive in lubricants to check oxidation and corrosion in engines, and as dye.[1,2] Quinizarin inhibits HIV proteinase[3] and possess significant antiproliferative and antimetastatic properties by the induction of intracellular transglutaminase activity.[4,5] From pharmaceutical point of view, quinizarin molecule contains the planar anthraquinone unit typical of some biologically and pharmaceutically significant compounds, including several antitumor drugs such as doxorubicin, daunorubicin and mitoxantrone which are widely used in clinical practice. The anthraquinone chromophore is responsible both for antitumor activity of these drugs by the intercalation between the DNA base pairs and cardiac toxicity by the generation of reactive oxygen species. Taking into account the above, different simpler and cheaper anthraquinones (quinizarin, danthron, purpurin) have been investigated and compared with the known drugs.[6–9]

Surfactants with their unique structure that contains both hydrophilic and hydrophobic moieties in the same molecule can form aggregates (micelles) at a certain concentration (known as critical micelle concentration, CMC) due to a delicate balance between the interactions of polar and non-polar parts. Besides their extensively use in the textile and pharmaceutical industries as solubility enhancers, diluents or emulsifying agents, surfactant micelles can be used in drug delivery systems to increase the solubility and bioavailability of hydrophobic drugs and to protect the drug molecules from adverse effects of the biological environment.[10–13] The solubilization of drug molecules into micelles depends on its polarity: nonpolar molecules will be solubilized in the micellar core while the drug molecules with intermediate polarity will be distributed in the interfacial region of the micelle in certain intermediate positions.[14–16]

The development of an effective drug delivery system demands in-depth knowledge of the interaction of drug molecules with surfactant micelles and the effect of several factors like pH, temperature, additives, ionic strength, etc.[17,18] Due to their structure, the surfactant micelles mimic the native lipid bilayer environment and are used to study the interactions of different drugs with membranes.[19,20]

Sodium ions, glucose and urea are present in blood plasma in variable quantities and their presence may influence the drug biological activity. In addition, the administration of anthracycline drugs is given as slow infusion in 0.9% NaCl or 5% glucose solutions and glucose is used as a preferred source of carbohydrate in parenteral nutrition regimens, being rapidly absorbed from the gastrointestinal tract. It is well documented that the addition of various additives like electrolytes, carbohydrates, alcohols, aminoacids, etc. can affect the association behavior of ionic and nonionic surfactants either through specific interactions with the surfactant molecules or by changing the solvent nature.[21–24] The presence of these compounds not only changes the micellar parameters but also can modulate the interaction pattern of micelles with drugs. Hence, it is important to get knowledge of drug–micelle association behavior in the presence of different physiological additives.

We previous investigated the interaction of quinizarin with SDS micelles in 0.1 M phosphate buffer (pH 7.4) and at different temperatures, using spectrophotometric and conductometric techniques.[25] The results showed a strong interaction between quinizarin and SDS micelles and both binding and partition processes are spontaneous and entropy driven. Also the hydrophobic interactions are the main forces involved in binding and partition processes.

Considering the above aspects and in extension to our prior study concerning the interaction of antitumor drugs with biomimicking organized assemblies like surfactant micelles, the current paper aims to investigate the influence of glucose, NaCl and urea on the interaction of quinizarin with SDS micelles. The studies were carried out using absorption and electrical conductance measurements.

2. Experimental

2. 1. Materials

Quinizarin (96% purity), sodium dodecyl sulfate (SDS, 97%), sodium chloride (NaCl, 99%), glucose (99.5%), urea (99%), sodium phosphate dibasic (99%) and sodium phosphate monobasic (99%) were purchased from Sigma Aldrich and used as received without further purification. All solutions were prepared using deionized water of 18.2 MΩcm resistivity (Direct-Q 3UV System, Millipore). Experiments were performed in 0.1 M phosphate buffer, pH 7.4 in order to mimic physiological conditions. Due to the low solubility of quinizarin in water, a concentrated stock solution was prepared by dissolving quinizarin in methanol. Then, small aliquots of this stock were diluted with phosphate buffer such that the methanol content in the investigated solutions was always below 1%. The solutions were prepared just before experiment and kept in the dark because the quinone unit is sensitive to the light.

2. 2. UV-Visible Measurements

Absorption spectra were taken on a JASCO V-630 spectrophotometer equipped with a Peltier controlled ETCR-762 model accessory (JASCO Corporation, Tokyo, Japan) using quartz cuvette with a path length of 1 cm. The absorption spectra of quinizarin in 0.1 M phosphate buffer, pH 7.4 and different concentrations of glucose, NaCl and urea have been recorded in the range of wavelength λ = 350–700 nm after the successive additions of concentrated SDS solution.

2. 3. Conductivity Measurements

Specific conductivities were performed on Consort K912 conductivity meter (Parklaan 36, B-2300 Turnhout, Belgium). This instrument has auto ranging from 0 to 1000 mS/cm and conductivity control with accuracy of ± 0.5%. The electrode used had a cell constant of 0.98 cm^{-1} and was calibrated using KCl over the appropriate concentration range. A concentrated SDS solution was gradually added to phosphate buffer containing quinizarin and different concentrations of additives and the conductivity of the ensuing solution was noted, after appropriate mixing. Subsequently, CMC values were determined by using the conventional method based on the plot of conductivity (k) against the surfactant concentration.

3. Results and Discussion

3. 1. Absorption Spectroscopy

Our previous spectral investigation on the interaction of quinizarin with SDS micelles in 0.1 M phosphate buffer (pH 7.4) at different temperatures revealed a strong interaction between quinizarin and SDS micelles.[25] In order to find out the effect of physiologic additives such as glucose, NaCl and urea on the interaction of quinizarin with SDS micelles, similar experiments were performed in the presence of 1%, 5% glucose, 0.5%, 0.9% NaCl and 0.6%, 1.2% urea.

Fig. 1 shows the absorption spectra of quinizarin in the presence of additives (5% glucose (Fig. 1a) and 0.5% NaCl (Fig. 1b)) and increasing concentrations of SDS. In our experimental conditions (0.1 M phosphate buffer, pH 7.4), quinizarin is in neutral form and the visible absorption spectrum shows a broad absorption maximum at ~ 470 nm and a shoulder at about 535 nm. The changes in the spectral behaviour of quinizarin for increasing SDS concentrations are the same for glucose, NaCl and urea, respectively the increase in absorbance and the splitting of the absorption maximum in three peaks. Also, a new peak appears around 515 nm and the shoulder at about 535 nm disappears. Addition of glucose, NaCl and urea does not affect the characteristics of absorption spectra of quinizarin in SDS micelles, which would imply the presence of the same kind of interactions and the same location of

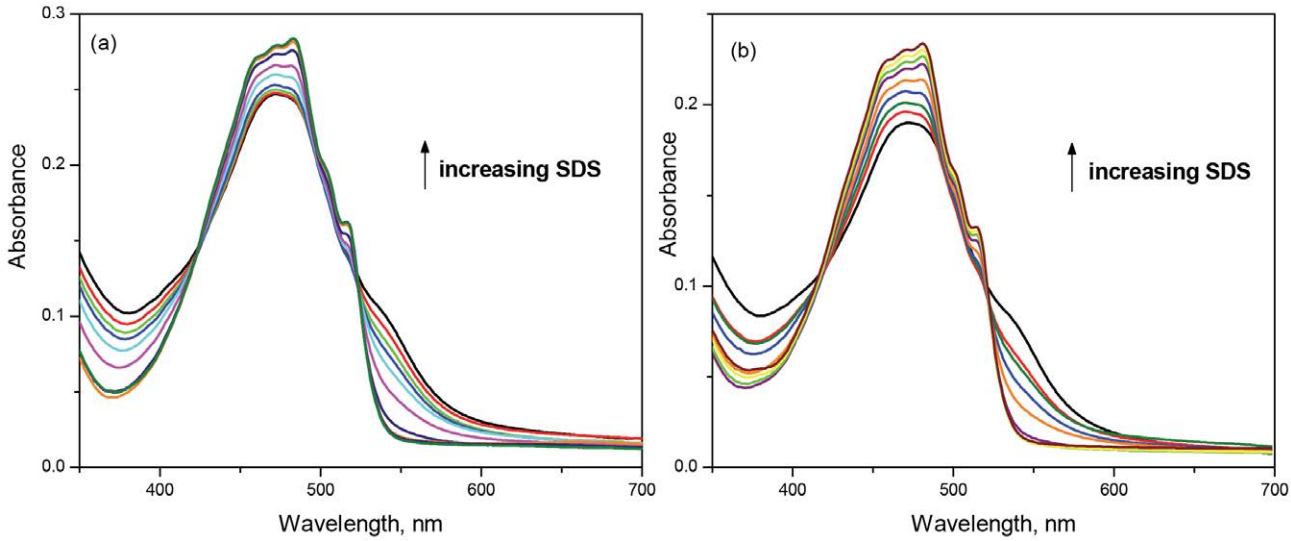

Figure 1. Visible absorption spectra of quinizarin at various concentrations of SDS in the presence of: (a) 5% glucose and (b) 0.5% NaCl.

quinizarin molecules into SDS micelles as compared with the absence of these additives.

Further, the absorbance values at 470 nm were used to calculate the binding constant (K_b) and the partition coefficient (K_x), and the respective thermodynamic parameters in order to evaluate the influence of glucose, NaCl and urea additives on the interaction of quinizarin – SDS micelles. The binding constant was determined using the Benesi–Hildebrand equation:[26,27]

$$\frac{1}{A - A_0} = \frac{1}{K_b(A_1 - A_0)[SDS]} + \frac{1}{A_1 - A_0} \quad (1)$$

where, A_0 is the absorbance value in the absence of SDS, A is the absorbance value in the presence of SDS and A_1 is the absorbance value at high concentration of SDS. From the linear plots between $1/(A–A_0)$ and 1/[SDS] (Fig. 2), the values of K_b were evaluated using the intercept and the slope and are given in Table 1.

The binding constant of quinizarin to SDS micelles was previous found to be 2524 M^{-1}.[25] From Table 1 it can be observed that glucose and NaCl enhance the binding of quinizarin to SDS micelles and this increase is higher for higher concentrations of glucose and NaCl. The high-

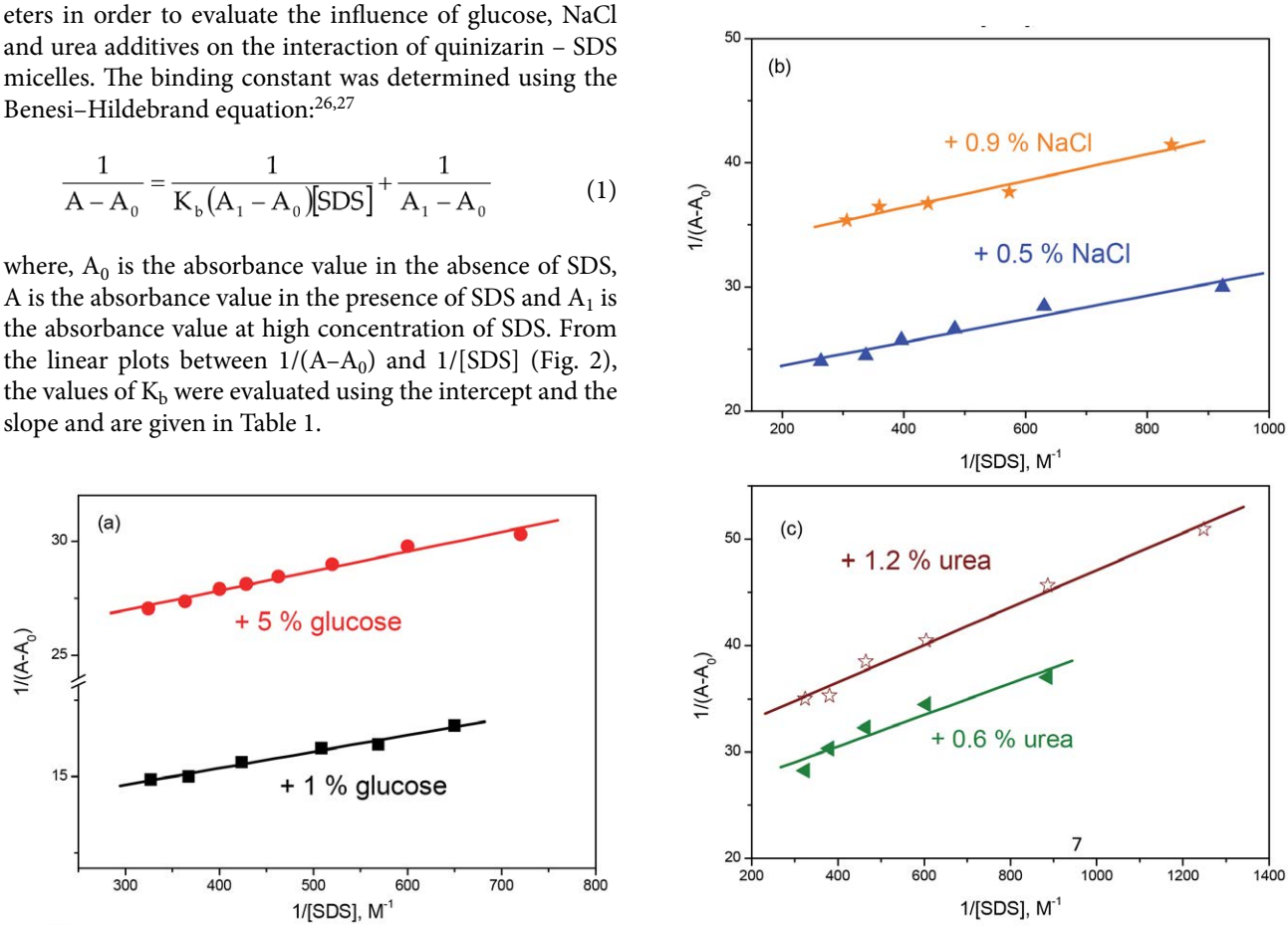

Figure 2. Benesi–Hildebrand plots for the calculations of binding constant (K_b) for quinizarin/SDS micellar system in the presence of additives: a) glucose, b) NaCl and c) urea.

est binding constant was obtained for 0.9% NaCl. Banipal *et al.* reported that the presence of NaCl increases the binding and partitioning of ciprofloxacin hydrochloride to SDS and hexadecyltrimethylammonium bromide (HTAB) micelles because NaCl enhances the hydrophobic interactions between the drug and both surfactants.[28] We have reported that the hydrophobic interactions are the main forces involved in the binding of quinizarin to SDS micelles.[25] Therefore, the increase of hydrophobic interactions can account for higher binding constants observed for quinizarin/SDS micelles in the presence of NaCl.

An increase of the interaction strength in the presence of glucose, galactose, sucrose and maltose carbohydrates was found for the binding of safranine T dye with different micelles.[20] Glucose is a hydrophilic molecule containing six hydroxyl groups that appears to be responsible for making strong cooperative hydrogen bonds with the surfactant molecules which is manifested by dominance of electrostatic interactions at pre-micellar SDS concentrations whereas hydrophobic interactions play a greater role at micellar SDS concentrations.[29]

Unlike glucose and NaCl, the presence of urea leads to a decrease of the binding constant of quinizarin to SDS micelles. The decrease of the binding constants on addition of urea was also observed in the case of the binding of the charged and uncharged forms of the local anesthetic tetracaine to zwitterionic micelles.[30] Electron spin resonance spectroscopy investigation on the effect of urea on SDS micelles showed a decrease of the polarity and a strong increase of the microviscosity of the micellar interface.[31]

The negative values of ΔG_b indicate the spontaneous nature of quinizarin-SDS micelles binding process in the presence of glucose, NaCl and urea additives and the spontaneity of this process is enhanced in the presence of higher glucose and NaCl concentrations.

Along with the determination of binding constant, the quinizarin–SDS micelles interaction was further characterized by determining the partition coefficient (K_x) which is a thermodynamic parameter representing the ratio of concentration of drug molecules in micelle to that in aqueous solution and provides information about the extent of solubilization. The partition coefficient was determined according to the pseudo-phase model using the following equation:[32,33]

$$\frac{1}{\Delta A} = \frac{1}{\Delta A_\infty} + \frac{n_W}{K_x \Delta A_\infty ([SDS] + C_T - CMC)} \quad (2)$$

In eq. (2), $\Delta A = A - A_0$, $\Delta A\infty = A_1 - A_0$, C_T is the total drug concentration and $n_w = 55.5$ M is the molarity of water. The values of K_x are obtained from the slope of the plot of $1/\Delta A$ versus $1/([SDS] + C_T - CMC)$, as is shown in Fig. S1 (Supplementary Material).

Our previous investigation showed that quinizarin presents large positive values of K_x (3.44×10^5) indicating that quinizarin molecules prefer to move from aqueous environment to more hydrophobic environment of SDS micelles.[25] As seen from Table 1, NaCl, glucose and urea exert a strong influence on the degree of partitioning of quinizarin molecules. The presence of NaCl and glucose leads to higher partition coefficients, meaning large-scale transfer of quinizarin molecules from the aqueous to the micellar media. The K_x values decrease in the presence of urea. The large negative values of ΔG_x are indicative of the spontaneous nature of partitioning process in the presence of these additives.

The radius of SDS micelles, the aggregation number and the packing parameter increase with increasing NaCl concentration.[21] This means that larger spherical micelles are formed which in turn helps to accommodate more drug molecules per micelle. Also, the aggregation number of SDS increase in the presence of different sugars (glucose, galactose, sucrose, maltose).[22] Therefore, the higher micellar partition coefficients achieved in the presence of increasing concentrations of glucose and NaCl can be related to the greater micellar size of SDS micelles.

3. 2. Conductivity Measurements

The conductivity of quinizarin/SDS solutions as a function of surfactant concentration is viewed in Fig. 3 for different concentrations of glucose, NaCl, and urea. From the sudden change of the slope in these plots the CMC values were obtained and included in Table 2.

The CMC of SDS in pure water at 298.15 K is between 8.00 and 8.30×10^{-3} M depending on the exper-

Table 1. Values of binding constant (K_b), partition coefficient (K_x) and free energy of binding (ΔG_b^0) and partition (ΔG_x^0) for quinizarin/SDS micellar system in 0.1 M phosphate buffer (pH 7.4) and different additives.

Additive	K_b / 10^3 (M^{-1})	ΔG_b^0 (kJ mol^{-1})	K_x / 10^5	ΔG_x^0 (kJ mol^{-1})
glucose 1%	2.62 ± 0.05	–19.17	5.11 ± 0.03	–32.02
glucose 5%	2.83 ± 0. 07	–19.36	6.70 ± 0.05	–32.68
NaCl 0.5%	2.53 ± 0.02	–19.09	4.40 ± 0.04	–31.66
NaCl 0.9%	2.97 ± 0.03	–19.48	6.98 ± 0.07	–32.78
urea 0.6%	1.76 ± 0.02	–18.20	1.13 ± 0.05	–28.34
urea 1.2%	1.57 ± 0.04	–17.93	1.42 ± 0.04	–28.90

imental method used.[34–36] In phosphate buffer at pH 7 and 298.15 K, CMC values of SDS decrease from 6.09 × 10^{-3} M (5 mM phosphate buffer) to 1.99 × 10^{-3} M (50 mM phosphate buffer).[37] In our previous investigations, it was found that the presence of quinizarin increases the CMC of SDS in 0.1 M phosphate buffer, pH 7.4 from 9.28 × 10^{-4} M to 1.06 × 10^{-3} M and this increase was explained by the possibility of hydrogen bonding between hydrophilic parts of drug and water, as the location of drug molecules in the outer portion of micelle close to micelle water interface leads to decrease in entropy thus making process of micellization less convenient.[25,38,39]

The results in Table 2 indicate that the presence of glucose leads to a decrease of CMC and increasing the concentration of glucose from 1% to 5% increases the reduction in CMC. These results are in agreement with literature results which indicate a decrease of CMC of SDS with gradually increasing concentrations of different sugars (glucose, galactose, sucrose, maltose).[22] Also, CMC values of SDS showed a regular decrease with increase in sugar concentration as well as with the size of the hydrophobic group of sugar molecule.[40] Glucose is a hydrophilic molecule containing six hydroxyl groups which strongly attract water molecules, thus the water – water interaction is replaced by water – sugar interaction and therefore the formation of iceberg structure around surfactant monomers due to hydrophobic interaction is prohibited and the micelle formation is favoured and CMC is lowered.[22]

A more pronounced decrease in CMC was observed by adding NaCl at SDS solutions containing quinizarin drug (Table 2). This indicates that higher concentration of NaCl provides a convenient environment for micellization of our studied quinizarin/SDS system. In the case of ionic surfactants such as SDS, a decrease of CMC values was observed for the micellization of pure ionic surfactants and also for drug-surfactant systems as the inorganic salt concentration increases.[18,21,41–43] The decrease in the CMC value is mainly due to the decrease in the thickness and potential of the electric double layer at the interface, and consequently, the electrical repulsion between charged head groups are reduced and the micellization process starts at lower surfactant concentration.[41–43]

Regarding the influence of urea, it can be observed that the presence of 0.6% and 1.2% urea does not change the CMC value of quinizarin/SDS solution. Reports on urea effects on SDS micellization in aqueous solution indicate that the CMC increased upon 2, 4 or 6 M urea concentrations addition, whereas the micellar aggregation number and the polarity the micellar interface decreased.[44] The lower urea concentrations used in our investigations has not influence on the micellization of quinizarin/SDS system, in agreement with studies performed by Kancharla et al. which showed that the CMC of SDS in aqueous solution did not change much at low urea concentrations, but increased by 11% in the presence of 4 M urea.[45]

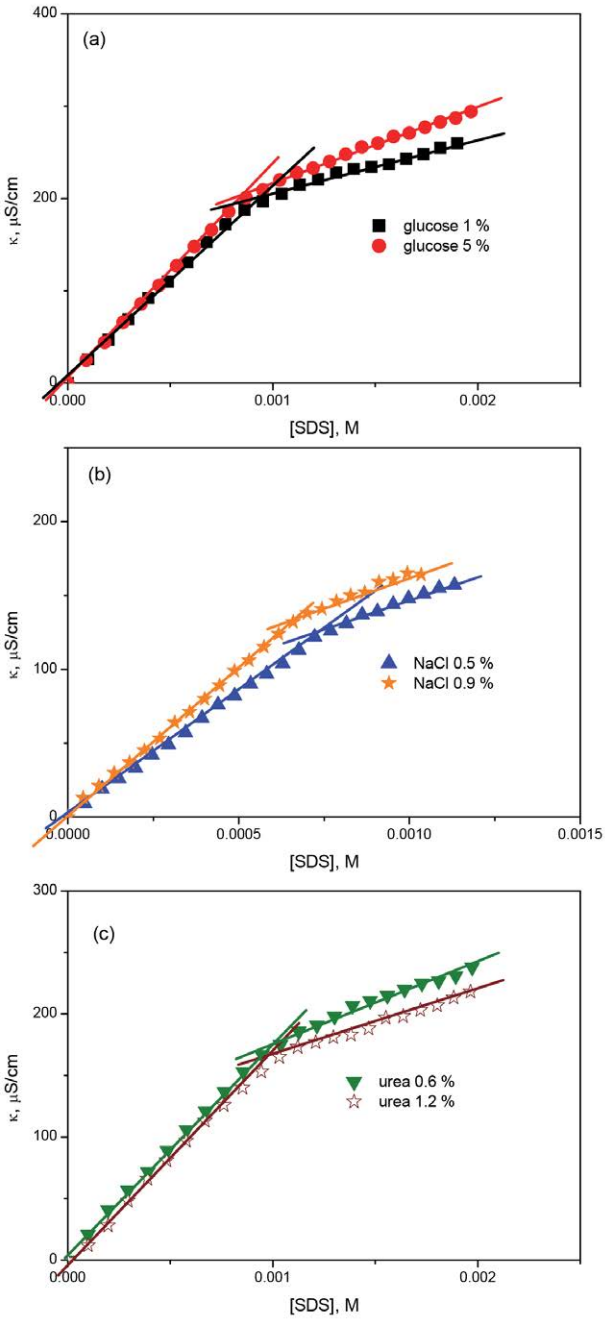

Figure 3. Dependence of specific conductivity, κ, on the concentration of SDS in solution of 2.15 × 10^{-5} M quinizarin in 0.1 M phosphate buffer in the presence of different concentrations of (a) glucose, (b) NaCl and (c) urea.

4. Conclusions

The present study focuses on the effects of glucose, NaCl and urea additives on the interaction between quinizarin, an analogue of the chromophore of anthracycline anticancer drugs and SDS micelles, as a model drug delivery system and the most accepted model system for studying different aspects of membrane interactions with

Table 2. Critical micelle concentration (CMC) for SDS in: water, 0.1 M phosphate buffer (pH 7.4), 0.1 M phosphate buffer (pH 7.4) and 2.15×10^{-5} M quinizarin, and 0.1 M phosphate buffer (pH 7.4), 2.15×10^{-5} M quinizarin and different additives (NaCl, glucose, urea).

Medium	CMC, M
water[36]	8.00
0.1 M phosphate buffer (pH 7.4)[25]	$(9.28 \pm 0.11) \times 10^{-4}$
0.1 M phosphate buffer (pH 7.4)[25] + quinizarin	$(1.06 \pm 0.08) \times 10^{-3}$
glucose 1%	$(9.32 \pm 0.09) \times 10^{-4}$
glucose 5%	$(8.95 \pm 0.08) \times 10^{-4}$
NaCl 0.5%	$(7.52 \pm 0.10) \times 10^{-4}$
NaCl 0.9%	$(7.02 \pm 0.08) \times 10^{-4}$
urea 0.6%	$(1.02 \pm 0.09) \times 10^{-3}$
urea 1.2%	$(9.93 \pm 0.02) \times 10^{-4}$

drug molecules. These additives are found in the human body and their presence may affect the micellization tendencies of surfactants. The spectral results show that the presence of glucose, NaCl and urea has a pronounced influence on the binding and partitioning process: glucose and NaCl enhance the quinizarin binding and distribution ability into SDS micelles, whereas the addition of urea has an opposite effect. The obtained CMC values of quinizarin/SDS system were found to undergo a decrease in presence of NaCl and glucose, whereas urea has not influence on the micelization process at the concentrations used in the present study.

The results of the present study may provide valuable information in seeking better drug formulation and drug delivery systems taking into account that glucose, NaCl and urea are present in body fluids.

5. References

1. V. Sachithanandam, P. Lalitha, A. Parthiban, J. Muthukumaran, M. Jain, R. Misra, T. Mageswaran, R. Sridhar, R. Purvaja, R. Ramesh, *J. Biomol. Struct. Dyn.* **2022**, *40*, 7218–7229. **DOI:**10.1080/07391102.2021.1894983
2. L. Quinti, N. S. Allen, M. Edge, B. P. Murphy, A. Perotti, *J. Photochem. Photobiol. A* **2003**, *155*, 93–106. **DOI:**10.1016/S1010-6030(02)00395-7
3. R. I. Brinkworth, D. P. Fairle, *Biochim. Biophys. Acta* **1995**, *1253*, 5–8.
4. S. Rossi, C. Tabolacci, A. Lentini, B. Provenzano, F. Carlomosti, S. Frezzotti, S. Beninati, *Anticancer Res.* **2010**, 30, 445–450.
5. G. Zengin, N. S. Degirmenci, L. Alpsoy, A. Aktumsek, *Hum. Exp. Toxicol.* **2016**, 35, 544–553. **DOI:**10.1177/0960327115595687
6. P. Mondal, S. Roy, G. Loganathan, B. Mandal, D. Dharumadurai, M. A. Akbarsha, P. S. Sengupta, S. Chattopadhyay, P. S. Guin, *Biochem. Biophys. Rep.* **2015**, *4*, 312–323. **DOI:**10.1016/j.bbrep.2015.10.008
7. P. S. Guin, S. Das, P. C. Mandal, *J. Solution. Chem.* **2011**, *40*, 492–501. **DOI:**10.1007/s10953-011-9654-x
8. M. B. Gholivand, S. Kashanian, H. Peyman, H. Roshanfekr, *Eur. J. Med. Chem.* **2011**, 46, 2630–2638. **DOI:**10.1016/j.ejmech.2011.03.034
9. V. Verebova, J. Adamcik, P. Danko, D. Podhradsky, P. Miskovsky, J. Stanicova, *Biochem. Biophys. Res. Commun.* **2014**, *444*, 50–55. **DOI:**10.1016/j.bbrc.2014.01.007
10. U. Saha, R. De, B. Das, *J. Mol. Liq.* **2023**, *382*, 121906. **DOI:**10.1016/j.molliq.2023.121906
11. D. Le Garrec, M. Ranger, J.-C. Leroux, *Am. J. Drug Deliv.* **2004**, 2, 15–42. **DOI:**10.2165/00137696-200402010-00002
12. Z. Vinarov, V. Katev, D. Radeva, S. Tcholakova, N. D. Denkov, *Drug Dev. Ind. Pharm.* **2018**, 44, 677–686. **DOI:**10.1080/03639045.2017.1408642
13. N. A. N. Hanafy, M. El-Kemary, S. Leporatti, *Cancers* **2018**, *10*, 238. **DOI:**10.3390/cancers10070238
14. H. Chakraborty, M. Sarkar, *Biophys. Chem.* **2005**, *117*, 79–85. **DOI:**10.1016/j.bpc.2005.04.016
15. W. Caetano, M. Tabak, *Spectrochim. Acta A* **1999**, *55*, 2513–2528. **DOI:**10.1016/S1386-1425(99)00043-8
16. M. Enache, A. M. Toader, V. Neacsu, G. E. Ionita, M. I. Enache, *Molecules* **2017**, *22*, 1079. **DOI:**10.3390/molecules22071079
17. M. Enache, A.M. Toader, *J. Surf. Deterg.* **2018**, *21*, 31–41. **DOI:**10.1002/jsde.12014
18. D. R. Pokhrel, M. K. Sah, B. Gautam, H. K. Basak, A. Bhattarai, A. Chatterjee, *RSC Adv.* **2023**, *13*, 17685–17704. **DOI:**10.1039/D3RA02883F
19. M. Eeman, M. Deleu, *Biotechnol. Agron. Soc. Environ.* **2010**, *14*, 719–736.
20. C. Peetla, A. Stine, V. Labhasetwar, *Mol. Pharm.* **2009**, *6*, 1264–1276. **DOI:**10.1021/mp9000662
21. E. Dutkiewicz, A. Jakubowska, *Colloid Polym. Sci.* **2002**, *280*, 1009–1014. **DOI:**10.1007/s00396-002-0723-y
22. K. R. Acharya, S. C. Bhattacharyya, S. P. Moulik, *J. Photochem. Photobiol. A* **1999**, *122*, 47–52. **DOI:**10.1016/S1010-6030(99)00003-9
23. A. Ali, V. Bhushan, N. A. Malik, K. Behera, *Colloid J.* **2013**, *75*, 357–365. **DOI:**10.1134/S1061933X13040029
24. M. Almgren, S. Swarup, *J. Colloid Interface Sci.* **1983**, *91*, 256–266. **DOI:**10.1016/0021-9797(83)90330-2
25. A. M. Toader, P. Oancea, M. Enache, *Acta Chim. Slov.* **2020**, *67*, 629–637. **DOI:**10.17344/acsi.2019.5641
26. H. A. Benesi, J. H. Hildebrand, *J. Am. Chem. Soc.* **1949**, *71*, 2703–2707. **DOI:**10.1021/ja01176a030
27. Y. Shiraishi, S. Sumiya, Y. Kohno, T. Hirai, *J. Org. Chem.* **2008**, *73*, 8571–8574. **DOI:**10.1021/jo8012447
28. T. S. Banipal, R. Kaur, P. K. Banipal, *J. Mol. Liq.* **2018**, *255*, 113–121. **DOI:**10.1016/j.molliq.2018.01.089
29. S. Chauhan, J. Jyoti, L. Pathania, A. Umar, M.S. Chauhan, *J. Mol. Liq.* **2016**, *218*, 637–648. **DOI:**10.1016/j.molliq.2016.02.078
30. G. S. S. Ferreira, D. M. Perigo, M. J. Politi, S. Schreier, *Photochem. Photobiol.* **1996**, *63*, 755–761. **DOI:**10.1111/j.1751-1097.1996.tb09627.x

31. P. Baglioni, E. Rivara-Minten, L. Dei, E. Ferroni, *J. Phys. Chem.* **1990**, *94*, 8218–8222. **DOI:**10.1021/j100384a044
32. L. Sepulveda, E. Lissi, F. Quina, *Adv. Colloid Int. Sci.* **1986**, 25, 1–57. **DOI:**10.1016/0001-8686(86)80001-X
33. H. Kawamura, M. Manabe, Y. Miyamoto, Y. Fujita, S. Tokunaga, *J. Phys. Chem.* **1989**, *93*, 5536–5540. **DOI:**10.1021/j100351a042
34. A. Cid, J. Morales, J. C. Mejuto, N. Briz-Cid, R. Rial-Otero, J. Simal-Gandara, *Food Chem.* **2014**, *151*, 358–363. **DOI:**10.1016/j.foodchem.2013.11.076
35. V. K. Sharma, O.P. Yadav, J. Singh, *Colloids Surf. A* **1996**, *110*, 23–35. **DOI:**10.1016/0927-7757(95)03409-9
36. A. D. Mudawadkar, T. J. Patil, *Chem. Sci. Trans.* **2016**, 5, 149–162.
37. E. Fuguet, C. Rafols, M. Roses, E. Bosch, *Anal. Chim. Acta* **2005**, *548*, 95–100. **DOI:**10.1016/j.aca.2005.05.069
38. M. Usman, M. A. Rashid, A. Mansha, M. Siddiq, *Thermochim. Acta* **2013**, *573*, 18–24. **DOI:**10.1016/j.tca.2013.08.014
39. M. Usman, M. Siddiq, *Spectrochim. Acta A: Mol. Biomol. Spectrosc.* **2013**, *113*, 182–190. **DOI:**10.1016/j.saa.2013.04.089
40. S. Chauhan, J. Jyoti, K. Sharma, K. Kuma, *Fluid Phase Equilib.* **2014**, *375*, 286–292. **DOI:**10.1016/j.fluid.2014.05.020
41. Md. A. Hoque, Md. M. Alam, M. A. Khan, D. Kumar, J. M. Khan, A. Malik, M. Z. Ahmed, A. Ahamed, *J. Phys. Org. Chem.* **2020**, *34*, e4166. **DOI:**10.1002/poc.4166
42. H. Chakraborty, M. Sarkar, *J. Colloid Interface Sci.* **2005**, *292*, 265–270. **DOI:**10.1016/j.jcis.2005.05.056
43. Md. A. Hoque, Md. M. Alam, M. R.l Molla, S. Rana, M. A. Rub, M. A. Halim, M. A. Khan, F. Akhtar, *Chin. J. Chem. Eng.* **2018**, *26*, 159–167. **DOI:**10.1016/j.cjche.2017.06.016
44. C. C. Ruiz, *Colloid Polym. Sci.* **1995**, *273*, 1033–1040. **DOI:**10.1007/BF00657670
45. S. Kancharla, E. Canales, P. Alexandridis, *Int. J. Mol. Sci.* **2019**, *20*, 5761. **DOI:**10.3390/ijms20225761

Povzetek

Z absorbcijsko spektroskopijo in konduktometričnimi tehnikami smo proučevali tvorbo asociatov med kinizarinom (1,4-dihidroksi-9,10-antrakinonom, Q), analogom kromofora antraciklinskih protirakavih zdravil, in miceli natrijevega dodecil sulfata (SDS) v prisotnosti dodatkov glukoze, NaCl in sečnine. Spektralni rezultati kažejo na povečanje vrednosti vezavne konstante in porazdelitvenega koeficienta v prisotnosti glukoze in NaCl, medtem ko se ob dodatku sečnine vezavna moč in vgrajevanje kinizarina v SDS micelle zmanjša. Povečanje koncentracij NaCl in glukoze je torej ugodno za vgraditev kinizarina v SDS micele. Iz meritev električne prevodnosti smo ugotovili, da se kritična micelna koncentracija (CMC) sistema SDS/kinizarin zmanjša z dodajanjem NaCl in glukoze, medtem ko sečnina nima vpliva na proces micelizacije pri pogojih, uporabljenih v tej študiji. Ker so biološke spojine, kot so glukoza, NaCl in sečnina, prisotne v človeškem telesu, imajo izsledki študije potencialno uporabo pri razvoju učinkovitih sistemov za dostavo zdravil.

DOI: 10.17344/acsi.2023.8576 *Acta Chim. Slov.* **2024,** *71,* 204–214

Scientific paper

Effects of the Extraction Conditions on Functional and Structural Characteristics of Proteins from Fenugreek Seeds

Hilal Isleroglu* and Gamze Nur Olgun

Tokat Gaziosmanpasa University, Faculty of Engineering and Architecture, Food Engineering Dept., 60150, Tokat, Turkey

** Corresponding author: E-mail: hilal.isleroglu@gop.edu.tr*
Phone: +903562521616 (2888); Fax: +903562521729

Received: 12-06-2023

Abstract

The study aims to optimize the extraction process and characterize the proteins found in fenugreek seeds. The water and oil holding capacities, coagulated protein content, foaming, and emulsification properties of the isolated proteins were investigated under all extraction conditions. Also, solubility, molecular weights, structural and thermal properties were determined. In the extraction processes carried out at different pH (pH 6.0–12.0) and solid:solvent ratios (20–60 g/L), it was determined that the highest extraction yield (94.3 ± 0.3%) was achieved when the pH was 11.47 and the solid-solvent ratio was 34.50 g/L. Three distinct bands (46, 59, and 80 kDa) in the range of 22–175 kDa were determined for the fenugreek seed protein isolate obtained under optimum extraction conditions. Protein secondary structures were determined using Fourier Transform Infrared (FT-IR) spectra and it was determined that β-sheet structures were highly present. In addition, denaturation temperature and denaturation enthalpy were calculated as ~119 °C and 28 mJ/g, respectively.

Keywords: Protein isolate, fenugreek seeds, extraction, secondary structure, emulsifying properties

1. Introduction

Proteins are crucial macronutrients in human nutrition, and historically, they have been primarily obtained from animal sources. However, with the increasing population in recent years, the availability of animal protein sources has been decreasing. As a result, there is now an increasing demand for alternative protein sources, such as plant-based proteins. Plant-based proteins are becoming more popular due to their health benefits and their ability to promote physical function.[1,2] Although animal sources contain high-quality proteins, they contain high levels of components such as cholesterol and saturated fatty acids, which cause diseases such as cardiovascular diseases and cancer when consumed frequently. Diets containing plant-based proteins are known to prevent cardiovascular diseases, hypertension, obesity, and some types of cancer.[3] In addition to increasing awareness of healthy nutrition, increasing sustainability concerns regarding food supply also increases consumers' tendency to prefer plant-based proteins. Furthermore, the fact that plant proteins, preferred by special consumer groups such as vegans and vegetarians, are cheaper and have a wide variety of sources, has made plants an alternative protein source for their use in food applications.[4,5]

Although plant-based proteins have many advantages, plant protein sources contain non-nutritive components (tannins, phytic acid, trypsin inhibitors, oligosaccharides, etc.), show weaker amino acid diversity than animal proteins, and their digestibility is not good. In addition, the fact that the functional properties of different protein isolates obtained from a wide variety of plant sources have not been well established limits their use in food formulations.[6] However, knowing the physico-chemical properties that affect the use of plant proteins in food formulations is very important in terms of improving the quality properties of the product. The physico-chemical properties of proteins are defined as the physical and chemical properties that affect the behavior of proteins in foods during production, storage, preparation, and consumption. Solubility, gelling, emulsification, foam formation, water and oil holding capacity, viscosity and film formation are some of the common physico-chemical properties of proteins. In addition to the structural properties of the proteins such as amino acid composition, surface hydrophobicity and hydrophobic/hydrophilic ratio, the extraction meth-

od and the parameters used in their production are also parameters that affect the physico-chemical properties of proteins.[7,8]

Extraction of plant-based proteins, like other proteins, is generally carried out by dissolving the material in a medium far from the isoelectric point and then precipitating the soluble proteins at the isoelectric point.[9] Alkaline extraction, which provides high protein yield, is generally used in the extraction of plant proteins. With the increase in the pH value of the solvent medium, acidic and neutral amino acids become ionized, and thus the solubility of proteins increases. More than 90% protein yield can be obtained with the alkaline extraction method.[10] Although high yields are obtained with alkaline extraction, the digestibility of the protein is affected because the structure of lysine and cysteine is disrupted, which negatively affects the overall quality of the protein.[11] Therefore, it is necessary to determine the alkaline conditions specific to that protein source that will improve or not affect the physicochemical properties of the protein. In addition, alkali concentration as well as other parameters such as solid:-solvent ratio, extraction time, and temperature should be optimized for maximum protein yield and preservation of physicochemical properties.[10] To identify new protein sources and gain application areas, it is necessary to characterize the obtained proteins. For this reason, in recent years, studies on the optimization of alkaline extraction conditions of plant-based proteins in terms of protein yield and physico-chemical properties of isolated proteins have been published in the literature.[2,12–16]

Fenugreek (*Trigonella foenum graecum*), known to have many health benefits, is an annual herbaceous plant in the legume family. Fenugreek, which has a widespread area in the world, differs from other legumes with its appearance and different smell. The protein content of fenugreek seeds has been reported to be in the range of 25–38%. The proteins in fenugreek seeds consist of albumin, globulin, glutelin, and prolamins. In a study where the flour obtained from fenugreek seeds was used in different proportions instead of wheat flour, it was reported that the protein content of products such as bread, biscuits, noodles, and pasta increased significantly, and there was an improvement in their sensory and rheological properties.[17] Therefore, fenugreek seeds, which have high nutritional value, are thought to be a potential protein source.

In this study, the effects of different solid:solvent ratios and pH levels on the extraction yield of the proteins in fenugreek seeds were determined, and the conditions that ensure the highest extraction yield were optimized using response surface methodology. The effects of the extraction conditions on the functional properties namely water holding capacity, oil holding capacity, coagulated protein content, foam capacity, foam stability, emulsion activity, emulsion stability, and emulsion capacity of the isolated proteins were investigated. Additionally, the structural and thermal properties and molecular weight patterns of fenugreek seed protein isolates obtained under optimum extraction conditions were determined.

2. Materials and Methods

2. 1. Material

After removing the foreign substances in the fenugreek seeds purchased from a local market, the seeds were powdered using a household grinder. The powdered seed samples were passed through a 630 μm sieve, and defatting was applied to the under-sieve samples using hexane. To remove the residual hexane, the samples were left to dry at 50 °C for 12 hours and the obtained defatted fenugreek seeds samples were used for protein extraction.

2. 2. Chemicals

H_2SO_4 (CAS#: 7664-93-9), HCl (CAS#: 7647-01-1), NaOH (CAS#: 1310-73-2), Brilliant Blue G-250 (CAS#: 6104-58-1) and Na_2HPO_4 dibasic dihydrate (CAS#: 10028-24-7) were obtained from Sigma-Aldrich, Germany. Boric acid (CAS#: 1043-35-3), methanol (CAS#: 67-56-1) and H_3PO_4 (CAS#: 7664-38-2) were obtained from Merck KGaA, Germany. Hexane (CAS#: 110-54-3) and citric acid monohydrate (CAS#: 5949-29-1) were provided by Tekkim Chemicals, Turkey. Kjeldahl tablets (Kjeltabs ST, AA 09) were obtained from Gerhardt, Germany. Tashiro indicator (CAS#: 64-17-5) was obtained from Riedel-de Haën™, Germany. Biuret Reagent (CB2145) was obtained from ChemBio, Turkey. Sodium phosphate dibasic (CAS#: 151-21-3) was obtained from BioBasic, Canada.

2. 3. Extraction Process and Isolation of the Proteins

Protein extraction from the defatted fenugreek seeds was carried out by mixing (at 750 rpm for 4 hours) the suspensions prepared in different solid:solvent ratios with distilled water as a solvent at different pH values. To optimize the extraction process, pH value (pH 6.0–12.0) and solid-solvent ratio (20–60 g/L) were chosen as independent variables, and a 'Central Composite Design' was carried out (Table 1). The samples were centrifuged at 6000 rpm for 15 minutes at the end of the extraction process. Extraction yield was calculated by proportioning the amount of protein in the supernatant phase (extract) to the protein amount of the initial powdered seed sample (Eq. 1). During the study, the protein contents of the samples were determined by Kjeldahl method[18] in all protein isolates and powder samples, and by Bradford method[19] in supernatant phases.

$$\text{Extraction yield (\%)} = [\text{Protein amount of extract (g)} / \text{Protein amount of fenugreek seeds (g)}] \times 100 \quad (1)$$

In the optimization process, the extraction yield was used as a response and the conditions providing the highest extraction yield were determined with a desirability function approach. The model used for regression analysis is given in Eq. 2.

$$\text{Extraction yield (\%)} = \beta_0 + \sum_{i=1}^{k} \beta_i X_i + \sum_{i=1}^{k} \beta_{ii} X_i^2 + \sum_{i=1}^{k-1} \sum_{j=i+1}^{k} \beta_{ij} X_i X_j \quad (2)$$

(k=1, 2)

where, β_0, β_i, β_{ii} and β_{ij} are the coefficients, X is the independent variable and k is the number of independent variables.

After the extraction process, the pH values of the extracts were adjusted to 4.0 and incubated at room temperature for 6 hours. After the incubation, the samples were centrifuged at 9000 rpm for 60 minutes, the supernatant was removed, and the precipitate was washed three times (5 minutes at 6000 rpm) using distilled water. The washed precipitates were then collected and lyophilized for 72 hours (Christ Alpha 1–4 LSC Plus, Germany). Powder protein isolates obtained as a result of the lyophilization were stored in sealed tubes at –18 °C until the analyses. By determining the amount of protein remaining in the supernatant phase at the end of precipitation, the average recovery in the precipitation process was calculated as 93.75 ± 0.55%.

2. 4. Characterization of the Protein Isolates

2. 4. 1. Coagulated Protein

The percentage of the coagulated protein in the samples was determined using the method described by Kramer and Kwee.[20] For this purpose, 0.2 g protein isolate was dissolved with 10 ml of citrate-phosphate solution (pH 7.0) at a concentration of 0.025 M and centrifuged. Biuret reagent was added to the supernatant phase and the solution was kept in the dark for 30 minutes. The solution was then incubated at 100 °C for 15 minutes and cooled to room temperature. After the cooling, the heating process was applied once again. The coagulated protein (%) was calculated using the absorbances of the samples before heating (A_1) and after heating (A_2) at 540 nm (Eq. 3).

$$\text{Coagulated protein (\%)} = [(A_1 - A_2) / (A_1)] \times 100 \quad (3)$$

2. 4. 2. Water and Oil Holding Capacity

Water holding capacity and oil holding capacity were determined by modifying the method of Vinayashree and Vasu.[10] After vortexing 250 mg of protein isolate with 15 ml of distilled water, it was kept at room temperature for 1 hour. Then, it was centrifuged at 3000 rpm for 20 minutes, the supernatant phase was removed, and the remaining sample was weighed. The water holding capacity is calculated in the g water/g sample. To determine the oil holding capacity, olive oil was used instead of water, and the oil holding capacity was expressed in g oil/g sample.

2. 4. 3. Foaming Capacity and Foam Stability

The foaming capacity and foam stability of the protein isolates were determined by the method proposed by Timilsena *et al.*[21] Aqueous solutions of the protein isolate at a concentration of 20 g/L were homogenized with a homogenizer (Ultra-Turrax IKA T-18 Basic, USA) at 10000 rpm for 5 minutes. Total volumes before homogenization (V_0) and after homogenization (V_1) were measured, and foaming capacity (%) was calculated using Eq. 4.

$$\text{Foaming capacity (\%)} = [(V_1 - V_0) / (V_0)] \times 100 \quad (4)$$

The foam stability was calculated using Eq. 5 by determining the total volume (V_2) of the homogenized sample after it was kept at room temperature for 1 hour.

$$\text{Foam stability (\%)} = [(V_2 - V_0) / (V_1 - V_0)] \times 100 \quad (5)$$

2. 4. 4. Emulsifying Properties

Emulsion activity and emulsion stability of the protein isolates were determined using the turbidity method modified by Feyzi *et al.*[22] First, 22.5 mg of the sample was weighed into a 15 mL tube, 4.5 mL of phosphate buffer solution (pH 7.0) was added, and the sample was vortexed for 1 minute. Sunflower oil (1.5 mL) was added to this mixture and homogenized at 22000 rpm for 2 minutes. To determine the emulsion stability, immediately after the homogenization (t=0), 250 µL emulsion was mixed with 50 mL sodium dodecyl sulfate at a concentration of 1 g/L, and the absorbance of this mixture at 500 nm was recorded (A_0). Similarly, the same process was applied to the initial emulsion that was kept at room temperature for 15 minutes (t=15) and its absorbance was recorded (A_{15}). Emulsion stability (min) was calculated using Eq. 6.

$$\text{Emulsion stability (min)} = [A_0 / (A_0 - A_{15})] \times t \quad (6)$$

Emulsion activity (m^2/g) was determined using Eq. 7.

$$\text{Emulsion activity } (m^2/g) = (2T \times D) / (\Phi \times C) = (2 \times 2.303 \times A_0 \times D) / (\Phi \times C \times L) \quad (7)$$

where, T is the turbidity ($T = 2.303 \times A_0/L$), D is the dilution factor (200), Φ is the emulsion oil volume fraction (g oil/g sample), C is the protein concentration in the solution (0.005 g/ml), L is the cuvette path length (10^{-2} m).

The method given by Neto *et al.*[23] was modified to determine the emulsion capacity. First, an equal volume of sunflower oil was added to the protein isolate solutions

prepared at a concentration of 1.0 % (w/v), and an emulsion was formed by homogenizing with ultra-turrax (7200 rpm, 2 min). These emulsions were then centrifuged at 3250 rpm for 2 minutes. The total height of the emulsion in the tube before centrifugation was expressed as H_0 (cm), the height of the emulsified layer of the centrifuged emulsion was expressed as H_1 (cm), and the emulsion capacity was calculated using Eq. 8.

$$\text{Emulsion capacity (\%)} = [H_1 / H_0] \times 100 \quad (8)$$

2. 4. 5. Protein Solubility

The solubility of the protein isolates (g/L) obtained under optimum extraction conditions was determined by the method reported by Feyzi *et al.*[22] The pH values of the protein isolate solutions prepared with distilled water at a concentration of 15 g/L were adjusted to values in the range of 2.0–12.0 using HCl or NaOH. After agitating the samples for 30 minutes at room temperature, they were centrifuged at 6000 rpm for 15 minutes to determine the protein content in the supernatant phase.

2. 4. 6. Sodium Dodecyl Sulfate-Polyacrylamide Gel Electrophoresis (SDS-PAGE)

The SDS-PAGE method[24] was used to determine the molecular weights of proteins obtained under optimum extraction conditions. In the study, 12% gel was used and 10 μg and 50 μg of samples were loaded. Samples were run under 200 V voltage for 50 min and the gel was stained with Comassie Brillant Blue R-250.

2. 4. 7. Fourier Transform Infrared (FT-IR) Spectroscopy

Structural properties of protein isolates obtained under optimum conditions were determined using a Fourier Transform Infrared (FT-IR) Spectrometer (Perkin Elmer 400, USA). Diamond ATR method was used in the analysis and measurements were made in the spectrum range of 4000–400 cm^{-1}. Considering the Amide I region (1600–1700 cm^{-1}) in the FT-IR spectra, the protein secondary structures of the protein isolates were determined by deconvolution of the peaks and curve fitting using the Peakfit v4.12 package program (Systat Software, USA).

2. 4. 8. Thermal Properties

Denaturation temperature (T_d, °C) and denaturation enthalpy (ΔH_d, mJ/g) of the protein isolates obtained under optimum conditions were determined using a Differential Scanning Calorimetry (DSC) (Perkin Elmer DSC 8000, USA). Analyses were carried out in a nitrogen environment, in the temperature range of 20–200 °C and at a heating rate of 5 °C/minute.

2. 5. Statistical Analysis

The one-sample t-test and 'Univariate Variance Analysis, Duncan post hoc' test were performed using the SPSS 21.0 software package. Regression analysis, contour plots, and optimization processes were performed using Design Expert 7.0 (Stat-Ease, Inc., USA) software to determine the effects of all process variables.

3. Results and Discussion

3. 1. Extraction Process

The experimental design used for the extraction process of the proteins found in fenugreek seeds and the extraction yields are given in Table 1. According to the results, the highest extraction yield (93.13 ± 1.36%) was obtained under the condition that the solid-solvent ratio was 20 g/L and the pH value was 12.0. The lowest extraction yield was determined when the solid-solvent ratio was 60 g/L and the pH value was 6.0 (Table 1). Lower extraction yields were observed at all pHs when the solid-solvent ratio was the highest (60 g/L). The decrease in protein extraction yields when the solid-solvent ratio is high can be explained by the fact that non-protein compounds (gum, mucilage, etc.) in the extraction medium make protein extraction difficult. It is thought that protein extraction yields increase by providing a more effective mixing process at low solid-solvent ratios (20–40 g/L) and increasing the solid-solvent contact surface. It was determined that the pH value chosen as another independent variable in the protein extraction process also affects the extraction yield. The extraction yields increased with increasing pH values in all solid-solvent ratios (Table 1). This situation is associated with the increased solubility of the proteins in fenugreek seeds at high pH values. Similarly, Feyzi *et al.*[25] reported that the solubility of fenugreek seed proteins increased in an alkaline environment (pH 9.25). Jarpa-Parra *et al.*[26] reported that the extraction yield and purity of the obtained proteins increased by using pH values ≥9.0 in protein extraction from lentils. Gao *et al.*[27] carried out protein extraction from yellow peas, which belong to the legume family as fenugreek seeds, and found that the protein extraction yield increased with increasing pH.

To optimize the extraction process, the extraction yield was chosen as the response, and a second-order polynomial model was constructed. According to the ANOVA results given in Table 2, the developed model was found to be statistically significant ($p < 0.05$), and the lack of fit was found to be statistically insignificant ($p > 0.05$). The linear and quadratic effects of the solid-solvent ratio and pH on extraction yield were determined to be statistically significant ($p < 0.05$). On the other hand, it was observed that the solid-solvent ratio-pH interaction did not have a statistically significant effect on the extraction yield ($p >$

Table 1. Experimental design and extraction yields (%)

Experiment no	Solid:solvent ratio (g/L) (X_1)	pH (X_2)	Extraction yield (%)
1	40	9.0	84.72 (± 0.68)
2	20	6.0	58.62 (± 1.36)
3	60	9.0	68.30 (± 0.72)
4	40	9.0	83.76 (± 0.41)
5	40	9.0	85.96 (± 0.27)
6	20	12.0	93.13 (± 1.36)
7	60	12.0	80.12 (± 0.63)
8	40	12.0	91.71 (± 0.54)
9	40	9.0	85.00 (± 0.54)
10	40	9.0	84.43 (± 0.81)
11	40	6.0	54.52 (± 1.08)
12	20	9.0	85.46 (± 1.90)
13	60	6.0	41.14 (± 0.27)

0.05) (Table 2). The model equation, written in terms of the real values of the factors, is given in Eq. 9.

Table 2. ANOVA table and statistical parameters

Source	Degrees of freedom	Sum of squares	Mean square	F Value	p – Value
Model	5	3055.79	611.16	417.80	< 0.0001
X_1	1	378.55	378.55	258.79	< 0.0001
X_2	1	2041.64	2041.64	1395.72	< 0.0001
X_1X_2	1	5.00	5.00	3.42	0.1069
X_1^2	1	114.18	114.18	78.06	< 0.0001
X_2^2	1	286.98	286.98	196.19	< 0.0001
Residual	7	10.24	1.46		
Lack of Fit	3	7.62	2.54	3.88	0.1118
Pure Error	4	2.62	0.66		
Total	12	3066.03			

R^2: 0.9967, adj- R^2: 0.9943, adequate precision: 64.234, *PRESS*: 60.10, *C.V.* (%): 1.58

X_1: solid:solvent ratio (g/L), X_2: pH, adj- R^2: adjusted R^2, *PRESS:* predicted residual error sum of squares, *C.V.* (%): coefficient of variation

$$\text{Extraction yield (\%)} = -65.85+0.72X_1+25.79X_2-0.02X_1^2-1.13X_2^2 \quad (9)$$

The conditions at which maximum protein extraction yield was achieved were determined by the desirability (d) function approach. The scale of the desirability function ranges from the completely unacceptable response (d=0) to the response corresponding to the target value (d=1), and the value of d increases as the desirability of the dependent variable increases. The response surface contour plots of the predicted desirability values and the extraction yields (%) are shown in Fig. 1a and Fig. 1b, respectively. As seen in Fig. 1, the conditions where the maximum desirability value (d=1) was obtained (maximum extraction yield) were selected as the optimum extraction conditions. The solid:solvent ratio was 34.5 g/L and pH was 11.47, and the predicted extraction yield was 94.08% at the optimum conditions (Fig. 1b). For the experimental validation, the extraction process was performed in triplicate under the predicted optimum conditions, and no statistically significant difference (p>0.05) was determined between the experimental extraction yield (94.29 ± 0.26%) and the predicted one.

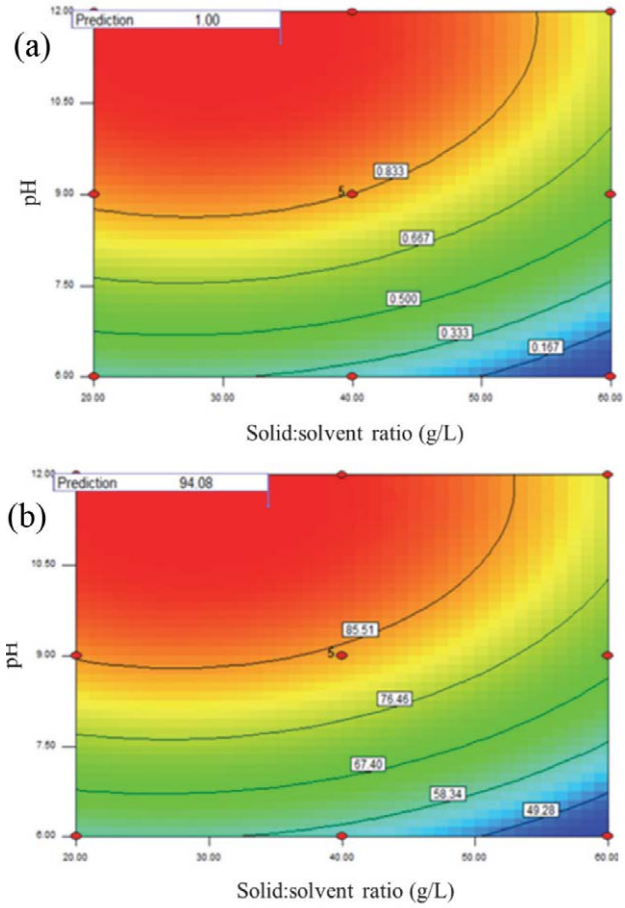

Fig 1. Counter plots of (a) desirability values and (b) predicted extraction yields (%)

3. 2. Characterization of the Protein Isolates

The functional properties of the protein isolates obtained under different extraction conditions are given in Table 3. The foaming properties of the fenugreek seeds protein isolates were determined by measuring the foaming capacity and foam stability. While foaming capacity is defined by the increase in the volume of the solution in the foaming process, foam stability is defined as the ability to keep the air in the foams formed.[28] The foaming capacity of fenugreek seed protein isolates was determined between 10.67 and 18.00%, and the foam stability was determined between 51.92 and 69.67%. As a result of extractions per-

formed at pH 12.0, it was determined that the highest foaming capacity and foam stability values were obtained ($p < 0.05$). Also, it was determined that the highest values were obtained in the extractions performed at a medium level (40 g/L) solid:solvent ratio (Table 3). Differences in the extraction conditions applied when obtaining the protein isolate caused the formation of different protein structures and fractions, affecting the foaming properties.[29] The foaming capacity of the protein isolate obtained under optimum conditions was determined as 19.00 ± 1.00%, and the foam stability was determined as 74.13 ± 2.16%.

The water and oil holding capacities are defined as the amount of water or oil absorbed per unit of protein, and the leakage of substances such as water or oil from the products can be prevented because of these properties of proteins during storage of the food. In addition, the oil holding capacity is important in terms of keeping the oil-soluble flavor substances and the texture of the product. The water and/or oil holding capacity of protein isolates is related to the number of polar or nonpolar amino acids in the structure, surface hydrophobicity and conformation of the proteins.[28] The water holding capacities of fenugreek seed protein isolates varied between 2.04 and 2.73 g/g. It was determined that the highest water holding capacity values belonged to the samples extracted at pH 12.0 (Table 3). In other studies, the water holding capacity value for fenugreek seed protein concentrate was 1.56 g/g[17] and for fenugreek seed protein isolate 2.70 g/g [25]. Liu *et al.*[30] characterized the flaxseed protein isolates and reached water holding capacity values in the range of 0.83–1.05 g/g. Kaur and Ghosal[31] reported the water holding capacity of protein isolate obtained from defatted sunflower meal as 2.00 g/g, and Yancheshmeh *et al.*[32] reported the water retention capacity of the protein isolate obtained from vetch seed as 2.01 g/g. When compared to the studies conducted in the literature, it was observed that the determined water holding capacity value of 2.64 ± 0.04 g/g of fenugreek seed protein isolate obtained under optimum extraction conditions was higher than many plant-derived protein isolates. It was determined that the oil holding capacity values of fenugreek seed protein isolates varied between 1.46 and 2.10 g/g. It was observed that the highest oil holding capacity values were obtained in the protein isolates produced as a result of extractions performed at pH 12.0 ($p<0.05$) (Table 3). The oil holding capacity value obtained under optimum conditions was determined to be 2.00 ± 0.01 g/g. El Nesri and El Tinay[17] determined the oil holding capacity value of fenugreek seed protein concentrate as 1.56 g/g. Feyzi *et al.*[25] determined the oil holding capacity value of fenugreek seed protein isolate as 6.06 ± 0.28 g/g. It is thought that different oil retention capacity values may be related to the extraction conditions of the seeds and the climate in which they are grown.[25]

The coagulated protein (%) refers to the protein percentage of the total soluble protein that will coagulate when heated to 100 °C. Since the uncoagulated protein is in soluble form, it can leak out of the system, which is undesirable. However, non-coagulating proteins are advantageous in forming viscous systems and increasing nutritional value in liquid systems (e.g., in breakfast drinks). It was determined that the coagulated protein values of fenugreek seed protein isolates varied between 3.01 and 4.96%. A decrease in the coagulated protein values was observed at increasing pH values during extraction ($p < 0.05$) (Table 3). Feyzi *et al.*[25] determined the coagulated protein value as 3.17% and emphasized that the proteins can be used in the production of beverages with high nutritional value and protein-added fruit juices due to their low coagulated protein percentages.

Proteins can prevent agglomeration and creaming by forming a layer around oil droplets at the water-oil interface, that are immiscible and thermodynamically unstable due to their amphiphilic structure. The emulsification properties of plant-derived proteins are of great importance for their use in the food industry. Emulsion properties of the proteins are affected by internal factors such as surface charge, hydrophobicity, solubility, molecular size, flexibility of the film formed, and external factors such as presence of other substances in the environment, pH, ionic strength, temperature, protein extraction methods and protein concentration.[33] Emulsion capacity is defined as the maximum amount of oil that can be emulsified by a certain amount of protein and is expressed as a percentage.[22] It was observed

Table 3. Functional properties of the protein isolates

pH	Solid:solvent ratio (g/L)	Foaming capacity (%)	Foam stability (%)	Coagulated protein (%)	Water holding) capacity (g/g	Oil holding capacity (g/g)
6	20	11.50 ± 0.71^{c}	52.80 ± 2.45^{d}	4.81 ± 0.26^{a}	2.13 ± 0.03^{d}	1.57 ± 0.02^{d}
	40	11.50 ± 0.71^{c}	68.06 ± 1.20^{ab}	4.98 ± 0.26^{a}	2.04 ± 0.01^{e}	1.52 ± 0.03^{e}
	60	10.67 ± 0.58^{c}	51.92 ± 2.72^{d}	5.06 ± 0.13^{a}	2.04 ± 0.03^{e}	1.46 ± 0.04^{f}
9	20	14.00 ± 1.00^{b}	60.66 ± 2.60^{c}	3.69 ± 0.13^{c}	2.18 ± 0.02^{c}	1.91 ± 0.02^{c}
	40	15.00 ± 1.00^{b}	63.33 ± 4.71^{bc}	4.02 ± 0.28^{bc}	2.18 ± 0.03^{c}	1.98 ± 0.02^{b}
	60	14.00 ± 0.00^{b}	61.25 ± 1.77^{c}	4.15 ± 0.18^{b}	2.19 ± 0.01^{c}	1.89 ± 0.01^{c}
12	20	17.00 ± 0.00^{a}	64.29 ± 0.00^{abc}	3.07 ± 0.27^{d}	2.66 ± 0.02^{b}	2.07 ± 0.04^{a}
	40	18.00 ± 0.00^{a}	69.67 ± 1.30^{a}	3.08 ± 0.21^{d}	2.65 ± 0.04^{b}	2.09 ± 0.03^{a}
	60	17.00 ± 0.00^{a}	69.44 ± 3.93^{a}	3.16 ± 0.18^{d}	2.73 ± 0.02^{a}	2.10 ± 0.02^{a}

$^{a–g}$ Mean values given different letters in the same column are statistically different from each other ($p < 0.05$).

that the emulsion capacities of the fenugreek seed protein isolates varied between 18.30 and 26.00% (Fig. 2a). It was determined that the emulsion capacities of the obtained fenugreek seed protein isolates were higher when extracted at higher pH values ($p < 0.05$) (Fig. 2a). The emulsion capacity of fenugreek seed protein isolates obtained under optimum conditions was determined as 26.52 ± 0.26%. Emulsion activity is defined as the maximum emulsion surface area per unit protein measured spectrophotometrically based on turbidity.[34] It was determined that the emulsion activities of fenugreek seed protein isolates ranged between 75.82 and 80.95 m^2/g (Fig 2b). Furthermore, the emulsion activity of fenugreek seed protein isolates obtained under optimum conditions was determined as 78.21 ± 0.28 m^2/g. Emulsion stability was determined based on the change in turbidity over time. The emulsion stability of fenugreek seed protein was observed to vary between 23.65 and 28.06 minutes (Fig. 2c). The emulsion stability of fenugreek seed protein isolates obtained under optimum conditions was determined as 28.73 ± 0.35 minutes.

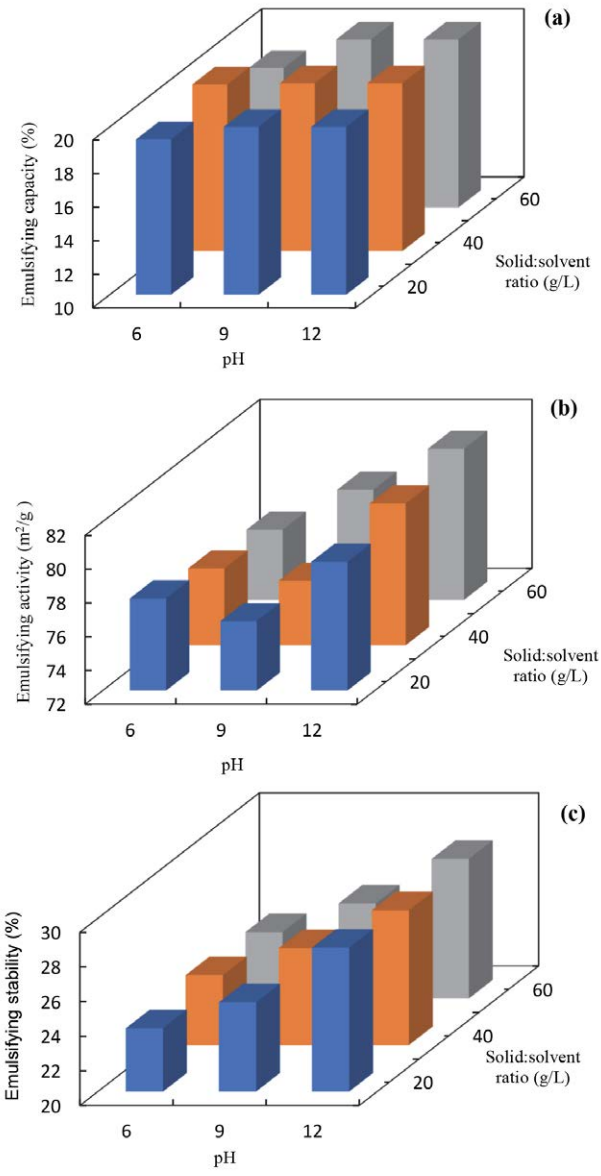

Fig 2. Emulsifying properties of fenugreek protein isolates (a) emulsifying capacity, (b) emulsifying activity, (c) emulsifying stability

Proteins exhibit maximum solubility in highly acidic or basic conditions far from the isoelectric point. The results obtained in the study showed that the solubility properties of the fenugreek seed protein isolate obtained under optimum extraction conditions comply with this phenomenon. As seen in Fig. 3a, solubility values follow a characteristic U-shaped curve in the pH range of 2–12. While the solubility values of the samples ranged between 0.27 and 8.46 g/L, the lowest solubility was observed at pH 4.0. This can be explained by the fact that fenugreek seed proteins have an isoelectric point in the pH range of 4.0–4.5.[22] Since an equilibrium occurs between negatively and positively charged ions at the isoelectric point, the net charge becomes zero. Thus, as the electrostatic repulsion forces decrease, proteins lose their solubility and collapse as a result of the hydrophobic interactions. On the other hand, the electrostatic repulsion force that occurs between the charged ions in acidic and alkaline conditions far from the isoelectric point, which may be different for each protein, ensures the dissolution of the proteins.[35] When the solubilities at high pH values were examined, it was seen that the highest values were obtained at pH 11.0 and pH 12.0 (Fig. 3a). The better solubility of the fenugreek seed proteins at high pH values can be explained by the inhibition of the formation of protein aggregates by the repulsive force of a larger number of negatively charged ions.[25] Similar results for some plant-derived proteins in the literature have been obtained for soy protein isolate, Moringa oleifera seed protein isolate, bitter melon protein isolate, flaxseed protein isolate, and chickpea protein isolate.[36–40] The molecular weight distribution of the fenugreek seed protein isolate was determined to be between ~175 kDa and ~22 kDa, and 10 bands with molecular weights of approximately 175, 159, 80, 59, 46, 38, 31, 27, 23, and 22 kDa were detected. However, 3 distinct bands were observed. These three most prominent bands were detected as ~80, 59, and 46 kDa (Fig. 3b). The bands between 22 and 70 kDa are found to be associated with globulins, specifically legumins and vicilins, which constitute the primary protein constituents in legumes.[41] These proteins were further fractionated into distinct subunits: β-legumin was observed at approximately 22 kDa, while α-legumin was observed at around 40 kDa.[42] Hence, the bands obtained at ~38 and 46 kDa could be associated with α-legumin for the fenugreek seed protein isolate. Moreover, the visible bands at ~22 and 23 kDa could be associated with the presence of β-legumin. The bands ranging from 50 to 80 kDa have been attributed to vicilin and covicilin. Two of the predominant bands observed at ~59 and 80 kDa could be ascribed to the polypeptide constituents of vicilin and convicilin.[43,44]

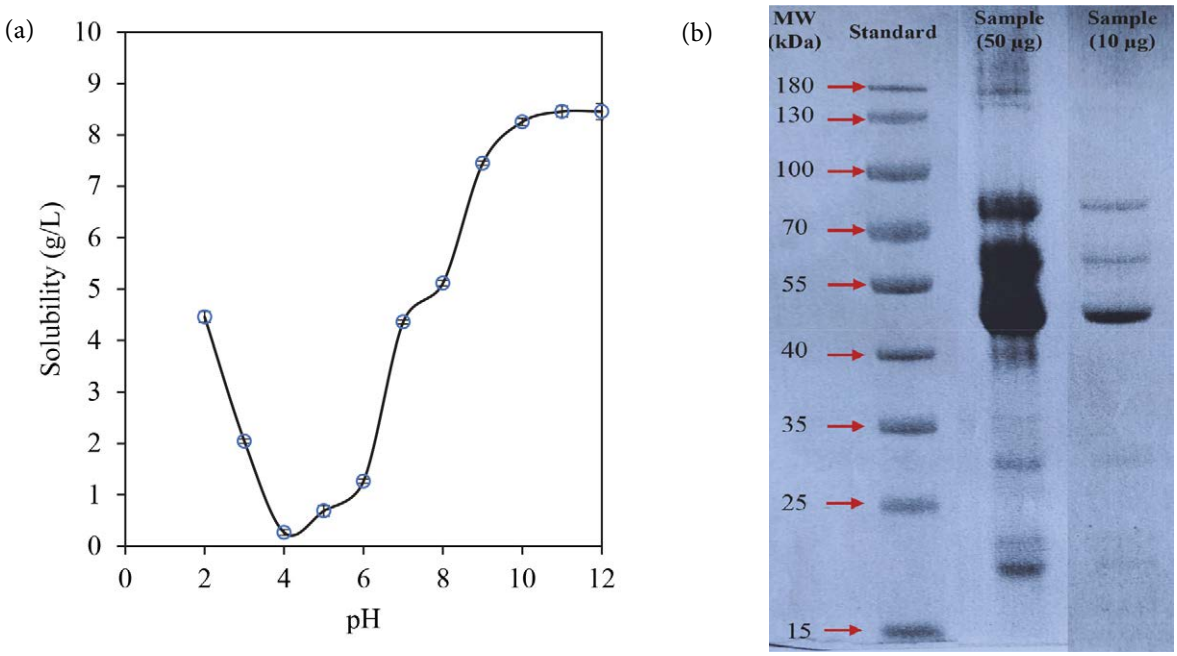

Fig 3. Characteristics of the protein isolates produced at optimum extraction conditions (a) solubility, (b) SDS-PAGE image

Fig. 4 shows the FT-IR spectra of the fenugreek seed protein isolates obtained under optimum conditions. As seen in Fig 4, the Amide I band is observed at the wave number of 1600–1700 cm^{-1}. The region between wave numbers of 1480–1585 cm^{-1} is defined as the Amide II region, and around 40–60% N–H bending vibration and around 18–40% C–N stretching vibration are observed in this region. It was observed that the peaks obtained at the

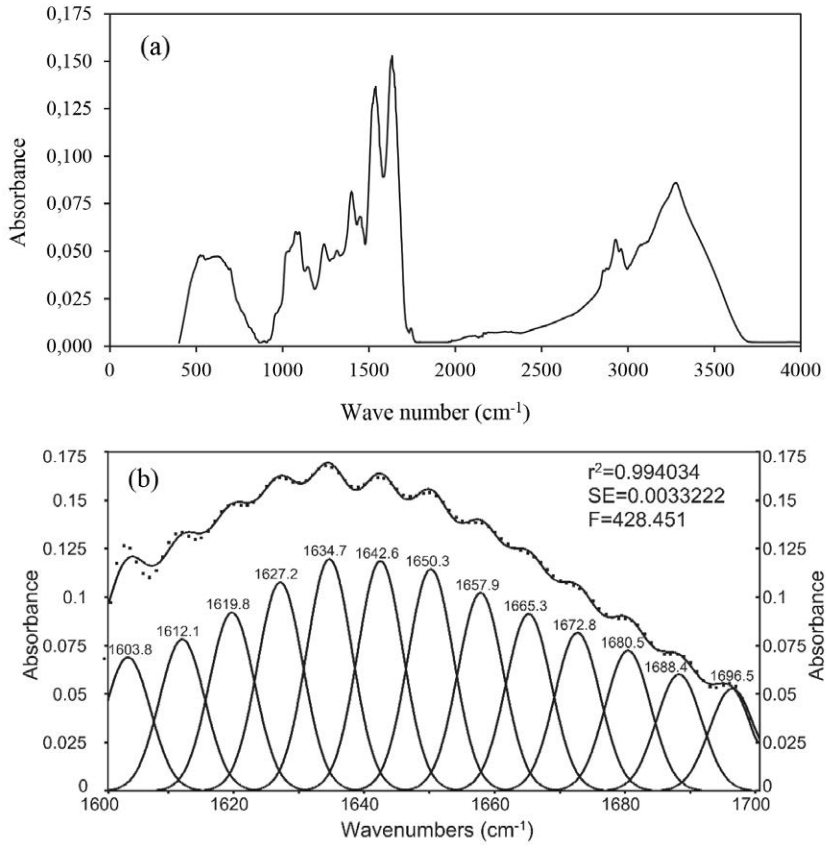

Fig 4. FT-IR spectra of the fenugreek seed protein isolate a) original spectrum, b) deconvolution in the Amide I region

wave numbers of 1447, 1515, and 1532 cm^{-1} for the obtained protein isolate were located in the Amide II region (Fig. 4a). The detection of Amide I and Amide II bands is considered an absolute indicator of the presence of protein structure.[45] The Amide III region is observed at the wave numbers between 1200–1400 cm^{-1} and indicates the existence of interactions between protein and other macromolecules such as carbohydrates. The presence of this region in proteins occurs depending on the side ring structure. C–N stretching vibrations and N–H bending vibrations are observed in this region.[46] It was determined that the peaks obtained at the wave numbers of 1240–1394 cm^{-1} for the fenugreek seed protein isolates were in the Amide III region (Fig. 4a). Secondary structures of the fenugreek seed protein isolates were determined using the peaks in the Amide I region (1600–1700 cm^{-1}) in the FT-IR spectrum. There are α-helix, β-sheet, random coil, or β-turn conformations in the Amide I band of proteins.[47] It has been reported that the β-sheet structure was observed in the wave numbers 1612–1640 cm^{-1} and 1689–1695 cm^{-1}.[48] Furthermore, the α-helix was observed at 1651–1660 cm^{-1} [49,50], the random coil conformation was observed at 1641–1650 cm^{-1} [49] and the β-turn was observed at 1661–1688 cm^{-1} [50]. In the FT-IR spectra, 13 peaks were observed in the Amide I region, and the ratio of the fractions in the protein secondary structure was determined by deconvolution of the peaks in the Amide I region (Fig. 4b). As a result of the analysis, 38.69% of the secondary structure is β-sheet, 18.96% is α-helix, 10.39% is random coil, 26.76% is β-turn and 5.20% is side ring. The high presence of the β-sheet structures indicates that protein isolates have high thermal stability.[50] To determine the thermal properties of the fenugreek seed protein isolates, denaturation temperatures (T_d) and denaturation enthalpies (ΔH_d) were determined using Differential Scanning Calorimetry (DSC). An endothermic peak was observed indicating that energy was required for denaturation to occur, and the denaturation temperature of the fenugreek seed protein isolate was 118.85 °C. In the literature, denaturation temperatures of 91 °C for cowpea protein isolate[51], 95 °C for flaxseed protein isolate[52], 103 °C for quince seed protein isolate[53] and 105 °C for fenugreek seed protein isolate have been reported[25]. The denaturation enthalpy value (ΔH_d) of the obtained protein isolate was also calculated and determined as 28 mJ/g.

4. Conclusion

The study aimed to extract proteins from fenugreek seeds using the alkaline extraction process at different pH values (pH 6.0–12.0) and solid:solvent ratios (20–60 g/L), and to determine the optimum conditions for the highest extraction yield. The optimum extraction conditions were determined as pH 11.47 and solid:solvent ratio 34.5 g/L, and an extraction yield of 94.3% was achieved under these conditions. The protein isolates obtained under different extraction conditions have various properties, including water holding capacity of ~2.0–2.7 g/g, oil holding capacity of ~1.5–2.1 g/g, coagulated protein content of ~3.0–5.0%, foam capacity of ~11.0–18.0%, foam stability of ~%52.0–70.0, emulsion stability of ~24.0–28.0 minutes, emulsion activity of ~76.0–81.0 m^2/g, and emulsion capacity of ~18.3–26.0%. Solubility properties showed that the fenugreek seeds protein isolate was soluble both acidic and basic conditions, which makes it a good candidate for both types of drinks. The study also included secondary structure analysis and thermal property determination, which revealed the thermal stability of the protein isolates. As a result, the extraction process was optimized to achieve the highest extraction yield, which distinguishes it from other studies in the literature. The study also examined how each extraction condition affected the characteristics of protein isolates. In this study, unlike other studies in the literature, the extraction process was optimized to provide the highest extraction efficiency and it was revealed how each extraction condition affected the characteristics of protein isolates. The results showed that the functional properties of protein isolates obtained under different extraction conditions are competitive or even better than other plant-derived proteins in the literature. Based on these findings, fenugreek seed protein isolate, produced under optimum extraction conditions, may be an excellent alternative plant-based protein for several food applications. Its functional, structural, and thermal properties make it suitable for use in different formulations in many food processes.

Acknowledgments

This study was financially supported by Tokat Gaziosmanpasa University Scientific Research Projects Committee (Project No: 2022/114).

5. References

1.. N. Mohan, J. J. Mellem, *LWT-Food Sci. Technol.* **2020**, *129*, 109572. **DOI:**10.1016/j.lwt.2020.109572
2. S. Vinayashree, P. Vasu, *Food Chem*. **2021**, *340*, 128177. **DOI**:10.1016/j.foodchem.2020.128177
3. S. M. Mousavi, A. Jayedi, Y. Jalilpiran, M. Hajishafiee, A. Aminianfar, A. Esmaillzadeh, *Crit. Rev. Food Sci. Nutr*. **2022**, *62*, 1336–1349. **DOI:**10.1080/10408398.2020.1841730
4. S. R. Hertzler, J. C. Lieblein-Boff, M. Weiler, C. Allgeier, *Nutrients*. **2020**, *12*, 3704–3731. **DOI:**10.3390/nu12123704
5. S. Thakur, A. K. Pandey, K. Verma, A. Shrivastava, N. Singh, *Int. J. Food Sci. Technol.* **2023**, *59*, 488–497. **DOI:**10.1111/ijfs.16663
6. F. U. Akharume, R. E. Aluko, A. A. Adedeji, *Compr. Rev. Food Sci. Food Saf.* **2021**, *20*, 198–224. **DOI:**10.1111/1541-4337.12688
7. M. Pojić, A. Mišan, B. K. Tiwari, *Trends Food Sci. Technol.* **2018,** *75*, 93–104. **DOI:**10.1016/j.tifs.2018.03.010

8. M. Kumar, M. Tomar, J. Potkule, Reetu, S. Punia, J. Dhakane-Lad, S. Singh, S. Dhumal, P. C. Pradhan, B. Bhushan, T. Anitha, O. Alajil, A. Alhariri, R. Amarowicz, J. F. Kennedy, *Food Hydrocoll*. **2022**, *123*, 106986. **DOI:**10.1016/j.foodhyd.2021.106986
9. M. Hadnađev, T. Dapčević-Hadnađev, A. Lazaridou, T. Moschakis, A. M. Michaelidou, S. Popović, C. G. Biladeris, *Food Hydrocoll*. **2018**, *79*, 526–533. **DOI:**10.1016/j.foodhyd.2017.12.015
10. K. Kumar, S. Srivastav, V. S. Sharanagat, *Ultrason Sonochem*. **2021**, *70*, 105325. **DOI:**10.1016/j.ultsonch.2020.105325
11. L. J. Deleu, M. A. Lambrecht, J. Van De Vondel, J. A. Delcour, *Curr. Opin. Food Sci*. **2019**, *25*, 98–103. **DOI:**10.1016/j.cofs.2019.02.017
12. M. Du, J. Xie, B. Gong, X. Xu, W. Tang, X. Li, C. Li, M. Xie, *Food Hydrocoll*. **2018**, *76*, 131–140. **DOI:**10.1016/j.foodhyd.2017.01.003
13. D. Garg, S. Chakraborty, J. S. Gokhale, *LWT-Food Sci. Technol*. **2020**, *117*, 108630. **DOI:**10.1016/j.lwt.2019.108630
14. S. Sethi, D. N. Yadav, S. Snigdha, A. Gupta, *LWT-Food Sci. Technol*. **2021**, *137*, 110368. **DOI:**10.1016/j.lwt.2020.110368
15. R. Anusha, S. Deepti, P. Vinita, K. Rajendra, Y. Neelam, *Res. J. Biotech*. **2021**, *16*, 163–172.
16. N. Benzitoune, N. Kadri, M. Adouane, F. Berkani, A. Abbou, F. Dahmoune, H. Remini, S. Bensmail, *J. Food Process. Preserv*. **2022**, *46*, e16471. **DOI:**10.1111/jfpp.16471
17. N. A. El Nasri, A. H. El Tinay, *Food Chem*. **2007**, *103*, 582–589. **DOI:**10.1016/j.foodchem.2006.09.003
18. AOAC, Official methods of analysis of AOAC international. 17th edn. AOAC International, Md., USA, **2000**.
19. M. M. Bradford, *Anal. Biochem*. **1976**, *72*, 248–254. **DOI:**10.1016/0003-2697(76)90527-3
20. A. Kramer, W. H. Kwee, *J. Food Sci*. **1977**, *42*, 207–211. **DOI:**10.1111/j.1365-2621.1977.tb01253.x
21. Y. P. Timilsena, R. Adhikari, C. J. Barrow, B. Adhikari. *Food Chem*. **2016,** *212*, 648–656. **DOI:**10.1016/j.foodchem.2016.06.017
22. S. Feyzi, M. Varidi, F. Zare, M. J. Varidi, *J. Sci. Food Agric*. **2018**, *98*, 1880–1888. **DOI:**10.1002/jsfa.8669
23. V. Q. Neto, N. Narain, J. B. Silva, P. S. Bora, *Food/Nahrung*. **2001**, *45*, 258–262. **DOI:**10.1002/1521-3803(20010801)45:4<258::AID-FOOD258>3.0.CO;2-3
24. U. K. Laemmli, *Nature*. **1970**, *227*, 680–685. **DOI:**10.1038/227680a0
25. S. Feyzi, M. Varidi, F. Zare, M. J. Varidi, *J. Sci. Food Agric*. ***2015***, *95*, 3165–3176. **DOI:**10.1002/jsfa.7056
26. M. Jarpa-Parra, F. Bamdad, Y. Wang, Z. Tian, F. Temelli, J. Han, L. Chen, *LWT-Food Sci. Technol*. **2014,** *57*, 461–469. **DOI:**10.1016/j.lwt.2014.02.035
27. Z. Gao, P. Shen, Y. Lan, L. Cui, J. B. Ohm, B. Chen, J. Rao, *Food Res. Int*. **2020**, *131*, 109045. **DOI:**10.1016/j.foodres.2020.109045
28. V. Kiosseoglou, A. Paraskevopoulou, in: K. B. Tiwari, A. Gowen, B. McKenna (Ed.): Pulse Food: Processing, Quality and Nutraceutical Applications, Elsevier Inc., London, UK, **2011**, pp. 57–90. **DOI:**10.1016/B978-0-12-818184-3.00006-4
29. E. Tsaliki, U. Kechagia, G. Doxastakis, *Food Hydrocoll*. **2002**, *16*, 645–652. **DOI:**10.1016/S0268-005X(02)00030-9
30. M. Liu, J. A. Toth, M. Childs, L. B. Smart, A. Abbaspourrad. *J. Food Sci*. **2023**, *88*, 942–951. **DOI:**10.1111/1750-3841.16467
31. R. Kaur, G. Ghoshal, *Adv. Colloid Interface Sci*. **2022**, *306*, 102725. **DOI:**10.1016/j.cis.2022.102725
32. B. S. Yancheshmeh, L. M. Marvdashti, A. Emadi, A. Abdolshahi, A. Ebrahimi, N. Shariatifar, *Food Anal. Methods*. **2022**, *15*, 1187–1202. **DOI:**10.1007/s12161-021-02185-z
33. A. C. Karaca, N. H. Low, M. T. Nickerson, *Trends Food Sci. Technol*. **2015**, *42*, 5–12. **DOI:**10.1016/j.tifs.2014.11.002
34. Z. Yi-Shen, S. Shuai, R. FitzGerald, *Food Nutr. Res*. **2018**, *60*, 1290. **DOI:**10.29219/fnr.v62.1290
35. N. Singh, M. Kaur, K. S. Sandhu, *Drying Technol*. **2005**, *23*, 975–988. **DOI:**10.1081/DRT-200054253
36. A. A. Heywood, D. J. Myers, T. B. Bailey, L. A. Johnson, *J. Am. Chem. Soc*. **2002**, *79*, 1249–1253. **DOI:**10.1007/s11746-002-0635-y
37. M. Kaur, N. Singh, *Food Chem*. **2007**, *102*, 366–374. **DOI:**10.1016/j.foodchem.2006.05.029
38. R. Horax, N. Hettiarachchy, A. Kannan, P. Chen, *Food Chem*. **2011**, *124*, 545–550. **DOI:**10.1016/j.foodchem.2010.06.068
39. P. Kaushik, K. Dowling, S. McKnight, C. J. Barrow, B. Wang, B. Adhikari, *Food Chem*. **2016**, *197*, 212–220. **DOI:**10.1016/j.foodchem.2015.09.106
40. Y. Cattan, D. Patil, Y. Vaknin, G. Rytwo, C. Lakemond, O. Benjamin. *Innov. Food Sci. Emerg. Technol*. **2022**, *75*, 102903. **DOI:**10.1016/j.ifset.2021.102903
41. M. Felix, M. Cermeño, R.J. FitzGerald, *Food Hydrocoll*. **2019**, *97*, 105220. **DOI:**10.1016/j.foodhyd.2019.105220
42. Z. Nikolić, V. Dordević, A. Torbica, A. Mikić, *J. Food Compos. Anal*. **2012**, *28*, 75–80. **DOI:**10.1016/j.jfca.2012.08.005
43. M. Barać, S. Čabrilo, M. Pešić, S. Stanojević, M. Pavlićević, O. Maćej, N. Ristić, *Int. J. Mol. Sci.* **2011**, *12*, 8372–8387. **DOI:**10.3390/ijms12128372
44. I. Berrazaga, C. Bourlieu-Lacanal, K. Laleg, J. Jardin, V. Briard-Bion, D. Dupont, S. Walrand, V. Micard, *PLoS One*. **2020**, *15*, e0232425. **DOI:**10.1371/journal.pone.0232425
45. T. S. Withana-Gamage, J. P. Wanasundara, Z. Pietrasik, P. J. Shand. *J. Sci. Food Agric*. **2011**, *91*, 1022–1031. **DOI:**10.1002/jsfa.4277
46. Barth, C. Zscherp, *Q. Rev. Biophys*. **2002**, *35*, 369–430. **DOI:**10.1017/S0033583502003815
47. A. Barth, *Biochim. Biophys. Acta Bioenerg*. **2007**, *1767*, 1073–1101. **DOI:**10.1016/j.bbabio.2007.06.004
48. J. Kong, S. Yu, *Acta Biochim. Biophys. Sin*. **2007**, *39*, 549–559. **DOI:**10.1111/j.1745-7270.2007.00320.x
49. I. H. M. Van Stokkum, H. Linsdell, J. M. Hadden, P. I. Haris, D. Chapman, M. Bloemendal, *Biochem*. **1995**, *34*, 10508–10518. **DOI:**10.1021/bi00033a024
50. Y. Wang, Y. Wang, K. Li, Y. Bai, B. Li, W. Xu, *LWT-Food Sci. Technol*. **2020**, *129*, 109563. **DOI:**10.1016/j.lwt.2020.109563
51. K. Shevkani, N. Singh, A. Kaur, J. C. Rana, *Food Hydrocoll*. **2015**, *43*, 679–689. **DOI:**10.1016/j.foodhyd.2014.07.024

52. C. H. Tang, Z. Ten, X. S. Wang, X. Q. Yang, *J. Agric. Food Chem.* **2006**, *54*, 8945–8950. **DOI:**10.1021/jf0619176

53. Y. Deng, L. Huang, C. Zhang, P. Xie, J. Cheng, X. Wang, S. Li. *Food Chem.* **2019**, *283*, 539–548. **DOI:**10.1016/j.foodchem.2019.01.083

Povzetek

Namen študije je optimizacija postopka ekstrakcije in karakterizacija beljakovin, ki jih najdemo v semenih triplata. Zmogljivosti zadrževanja vode in olja, vsebnost koaguliranih proteinov, penjenje in emulgiranje izoliranih proteinov so bile raziskane pri vseh pogojih ekstrakcije. Določene so bile tudi topnost, molekulske mase, strukturne in toplotne lastnosti. Pri ekstrakcijskih postopkih, izvedenih pri različnih pH (pH 6,0–12,0) in razmerjih trdna snov:topilo (20–60 g/L), je bilo ugotovljeno, da je bil največji izkoristek ekstrakcije (94,3 ± 0,3 %) dosežen pri pH 11,47 in razmerju med trdno snovjo in topilom 34,50 g/L. Določeni so bili trije različni pasovi (46, 59 in 80 kDa) v območju 22–175 kDa za proteinski izolat semena triplata, pridobljenega pri optimalnih pogojih ekstrakcije. Sekundarne strukture proteinov so bile določene z uporabo Fourierove transformacijske infrardeče spektroskopije (FT-IR) in ugotovljeno je bilo, da so bile dobro zastopane β-planarne strukture. Poleg tega sta bili izračunani temperatura in entalpija denaturacije kot ~119 °C, oziroma 28 mJ/g.

Scientific paper

1*H*-Indole-2,3-dione 3-thiosemicarbazones Carrying a 4-sulfamoylphenyl Moiety with Selective Antiviral Activity Against Reovirus-1

Füsun Göktaş,[1] Gizem Nur Duran,[2] Mehmet Özbil,[3] Özge Soylu-Eter[1,*] and Nilgün Karalı[1]

[1] *Department of Pharmaceutical Chemistry, Faculty of Pharmacy, Istanbul University, Istanbul, Turkey*

[2] *Department of Chemistry, Institute of Science and Technology, Marmara University, Istanbul, Turkey*

[3] *Department of Biotechnology, Institute of Biotechnology, Gebze Technical University, Kocaeli, Turkey*

** Corresponding author: E-mail: ozge.soylu@istanbul.edu.tr*
Tel.: +902124400000 (Internal 13462)

Received: 12-18-2023

Abstract

1*H*-Indole-2,3-dione 3-[4-(4-sulfamoylphenyl)thiosemicarbazones] **6a**–**j** were evaluated against para-influenza-3, reovirus-1, sindbis, coxsackie B4, and Punto Toro viruses. New 1-methyl-1*H*-indole-2,3-dione 3-[4-(4-sulfamoylphenyl) thiosemicarbazones] **7a**–**c** were synthesized to evaluate the contribution of methyl substitution at position 1 of the indole ring to antiviral activity. The test results showed that 5-trifluoromethoxy substituted compound **6c** (EC_{50} 2–9 μM) and 5-bromo substituted **6f** (EC_{50} 2–3 μM) have non-toxic selective antiviral activity, while not all standards are active against reovirus-1. Molecular docking studies of **6c** and **6f** were carried out to determine the possible binding positions with reovirus-1. Trifluoromethoxy and bromine substitutions at position 5 of the indole ring provided selective antiviral activity, while methyl substitution at position 1 of the indole ring significantly decreased the activity against reovirus-1 and increased toxicity.

Keywords: 1*H*-indole-2,3-dione; thiosemicarbazone; molecular modeling; antiviral activity; reovirus-1.

1. Introduction

Viral pathogenesis examines how a virus interacts with the host at multiple levels when a virus infects a host. Although the pathogenesis of each virus is different, there are many common points shared among all pathogenic viruses in the virus life cycle. When understanding the mechanism according to which the disease develops provides a significant benefit in the development of effective therapies. Virus mediated disease processes can be developed by taking into consideration the common aspects of some general concepts in viral pathogenesis.[1,2]

Reoviruses are useful models to understand the relationship between viral entry and patogenesis.[3,4] Reoviruses are non-enveloped, double-stranded RNA viruses in the family *Reoviridae*. Most mammalian species, including humans, serve as hosts for reovirus infection. Reoviruses attach to host cells via the filamentous attachment protein σ1. The σ1 protein of all reovirus serotypes engages junctional adhesion molecule-A (JAM-A). Reoviruses have 3 major serotypes: reovirus type 1 (strain Lang) (T1L) (mammalian orthovirus 1), type 2 Jones (T2J) and type 3 Dearing (T3D), which differ primarily in σ1 sequence.[5–8] The three serotypes share a common complement fixation antigen but can be distinguished by hemagglutination inhibition and neutralization techniques.[4] The gastrointestinal (GI) tract is a portal of entry for reoviruses. Reovirus serotype 1 strain Lang was shown to specifically infect the epithelial cells of the ileum and disrupt the intestinal immune homeostasis, while sparing the epithelial cells in the duodenum, jejunum, and colon.[9,10] Advanced reovirus studies have provided much information about the mechanisms underlying viral replication and pathogenesis.[11,12] However, *Reoviridae* viruses have limited ability to make specific changes to the genome. Today, a specific treatment or protection measures cannot be recommended because of the lack of a definite relationship in the disease for people with reovirus infections.

1*H*-Indole-2,3-dione (isatin) is a heterocyclic compound which has been known for nearly 150 years and is involved in many pharmacological activities. Isatin is also a highly versatile substrate that can be used in the preparation of a wide variety of heterocyclic compounds for drug synthesis and is a versatile precursor for many biologically active molecules. There are many studies on isatin 3-thiosemicarbazone derivatives with antiviral activity, too.[13–17] Methisazone (1-methylisatin 3-thiosemicarbazone) (**I**) is the first compound approved by Food and Drug Administration (FDA) for treatment of the vaccinia virus causing smallpox.[18,19] It has been determined that 1-methylisatin 3-(4,4'-diethylthiosemicarbazone) (**II**) inhibits the moleney murine leukemia virus.[20] **II** and 1-allylisatin 3-(4,4'-diallylthiosemicarbazone) (**III**) show significantly selective anti-HIV activity.[21] Antiviral activities of isatin 3-thiosemicarbazone derivatives against HSV-1 and HSV-2 viruses were investigated, and SAR studies revealed that the thiourea group in the thiosemicarbazone structure and the nitrogen of the isatin ring play an important role in antiviral activity. As a result of the research, it was determined that derivatives carring various substituents as methyl, ethyl, phenyl and benzyl at position 1 of isatin do not show antiviral activity, and the most effective derivative (IC_{50} 1.54 ± 0.21 μM) against HSV-2 virus was the compound **IV** carrying a diethyl group at the thiosemicarbazone residue. The compound **V** carrying a morpholinyl ring at the thiosemicarbazone residue showed the highest inhibition (IC_{50} 1.30 ± 0.16 and 2.74 ± 0.23 μM) against HSV-1 and HSV-2 viruses, respectively. Moreover, the compound **VI** (IC_{50} 2.20 ± 0.34–5.90 ± 0.26 μM) bearing a 5-methoxy or trifluoromethoxy group as R_1 and a hydrogen, 3-methyl, 3-methoxy, 4-methoxy, 4-chlorine or 4-bromine group as R_2 were found to be selectively effective against HIV-1 virus.[22] The antiviral activities of a series of isatin 3-thiosemicarbazones were examined against vaccinia and cowpox viruses, and their effects were compared with metisazone and cidofovir. Among the tested compounds, the compound **VII** was found to be the strongest inhibitor against vaccinia (EC_{50} 0.6 ± 6.8 μM) and cowpox (EC_{50} 6.0 ± 2.9 μM) viruses and its antiviral activity was stronger than metisazone and cidofovir. Moreover, 5-bromoisatin has been defined as the key pharmacophore for better antiviral activity (Figure 1).[23]

Many studies have been carried out to evaluate the broad-spectrum antiviral activities of 3-imino isatin derivatives carrying the 4-sulfamoylphenyl residue. The inhibitory activities of 4-[(1,2-dihydro-2-oxo-3*H*-indol-3-ylidene) amino]-*N*-(4,6-dimethyl-2-pyrimidinyl)-benzenesulfonamide (**VIII**) and its derivatives against vaccinia and cowpox viruses that cause smallpox were tested *in vitro*. While 5-methylisatin derivative (EC_{50} 18 μM) showed the strongest activity against vaccinia virus, 1-acetylisatin derivative showed strong inhibitory effect against cowpox virus.[24] **VIII** and its derivatives were tested against influenza A and B viruses. Among the compounds tested, **VIII** and its 5-chloro, 5-bromo, 5-methyl and *N*-acetyl derivatives were found to be effective against the H1N1 (EC_{50} 13.8–26.0 μg/mL), H3N2 (EC_{50} 2.7–5.2 μg/mL) and H5N1 (EC_{50} 3.1–6.3 μg/mL) strains of influenza A, and influenza B (EC_{50} 7.7–11.5 μg/mL).[25] **VIII** and its derivatives were also tested against the 2009 pandemic influenza (H1N1) virus and all compounds were found to inhibit the replication of the virus and the most active compound was the 5-bromoisatin derivative (EC_{50} 27 μM).[26] In the study in which some derivatives of **VIII** were tested against HCV and SARS-CoV viruses, it was determined that the 5-fluoroisatin derivative inhibited the HCV RNA synthesis at 6 μg/mL and provided 45% protection against SARS-CoV replication. The results obtained

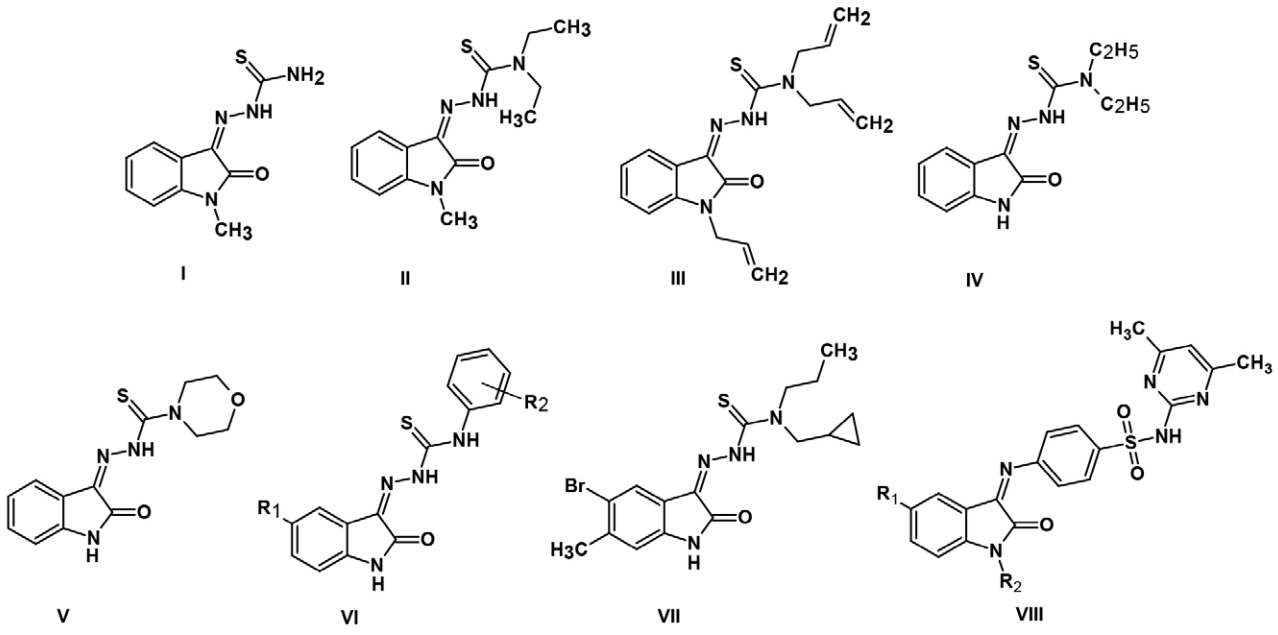

Figure 1. Structures of 2-indolinone derivatives **I**–**VIII** with antiviral activity

showed that sulfonamide side chain was important in **VIII** and its derivatives (Figure 1).[27]

In the present study, 1*H*-indole-2,3-dione 3-thiosemicarbazones **6a–j** carrying a 4-sulfamoylphenyl moiety were evaluated for *in vitro* antiviral activity against para-influenza-3 virus, reovirus-1, sindbis virus, coxsackie virus B4, and Punto Toro virus. To investigate the contribution of methyl substitution at position 1 of the indole ring to antiviral activity, new 5-substituted 1-methyl-1*H*-indole-2,3-dione 3-[4-(4-sulfamoylphenyl)thiosemicarbazones] **7a–c** were synthesized and tested.

2. Results and Discussion

2. 1. Chemistry

5-Substituted 1*H*-indole-2,3-diones **1** were reacted with methyl iodide to yield 1-methyl-5-substituted 1*H*-indole-2,3-diones **2**. (4-Sulfamoylphenyl)isothiocyanate (**4**) was obtained from the treatment of 4-aminobenzenesulfonamide (**3**) with thiophosgene. 4-(4-Sulfamoylphenyl) thiosemicarbazide (**5**) was synthesized by the reaction of **4** and hydrazine hydrate. New 5-substituted 1-methyl-1*H*-indole-2,3-dione 3-[4-(4-sulfamoylphenyl)thiosemicarbazones] **7a–c** were prepared by the condensation of **5** and **2**. The compounds **6a–j** have been previously described in the literature.[28] Analytical and spectral findings proving the analytical purity of the compounds **6a–j** are given in the Supplementary Material. The structures of new compounds **7a–c** were confirmed by elemental analysis and spectral data (IR, ^{1}H NMR, ^{13}C NMR-APT and LCMS-ESI) (Scheme 1, Experimental Section, and Supplementary Material).

IR spectra of **7a–c** showed absorption bands in the 3142–3358 cm^{-1} region for NH stretchings of the thioamide and sulfonamide functions. The bands resulting from

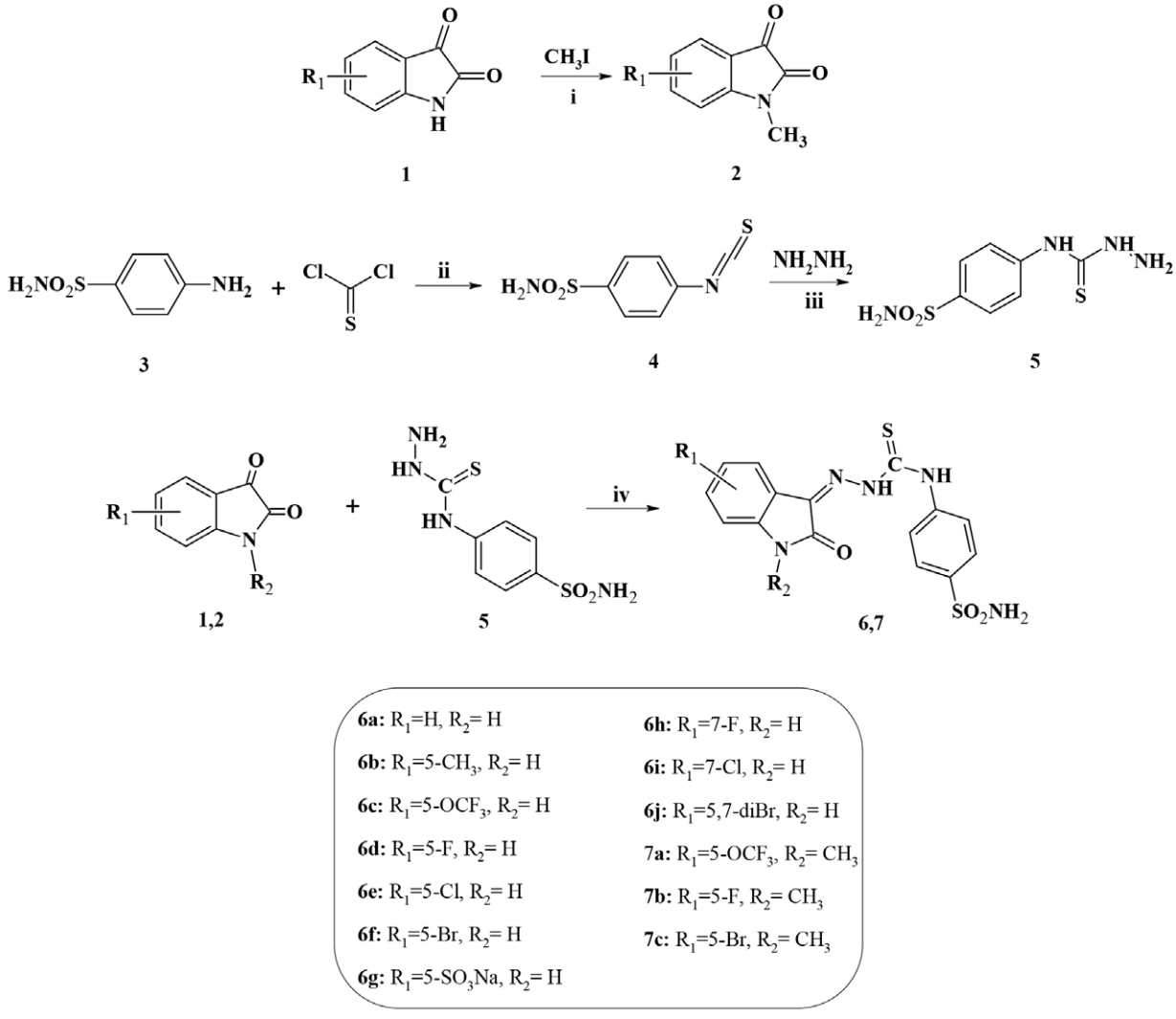

Scheme 1. Synthesis of 1*H*-indole-2,3-dione 3-[(4-sulfamoylphenyl)thiosemicarbazones] **6a–j** and **7a–c**. Reagents and conditions: *i*) DMF, K_2CO_3, KI, stirred, *ii*) H_2O, HCl, stirred, *iii*) EtOH, stirred, cooled, *iv*) EtOH, H_2SO_4, reflux.

lactam C=O and thioamide C=S stretchings appeared at 1680–1691 and 1253–1367 cm^{-1} regions, respectively. S=O stretchings of sulfonamide groups appeared at 1313–1336 and 1151–1166 cm^{-1} regions. ^{1}H NMR spectra of **7a–c** displayed singlets at δ 7.37–7.40, 11.01–11.05 and 12.65–12.71 ppm regions for sulfonamide, thiosemicarbazone N_4 and N_2 protons, respectively. The phenyl protons of 4-sulfamoylphenylthiosemicarbazone moiety which are deshielded by the electron-attracting action of the sulfonamide and thioamide groups, showed as a singlet in the δ 7.37–7.40 ppm area. The N-CH_3 and indole proton resonances of **7a–c** were assigned to the 1-methyl-2-indolinone structure. The indole C_4 and C_6 protons were deshielded by the anisotropic effect of the azomethine group at position 3 of the 2-indolinone ring. The indole C_7 proton was shielded by the mesomeric effect of the anilid NH group in the 2-indolinone ring. The indole C_4, C_6 and C_7 protons of **7a–c** showed at δ 7.67–8.04, 7.33–7.65 and 7.15–7.26 ppm regions, respectively. ^{13}C NMR-APT spectra of **7a–c** displayed signals at δ 176.75–176.86, 160.94–161.41 and 131.00–131.70 ppm regions due to C=S, indole C_2 and C_3 signals, respectively. The phenyl carbon signals were observed in the order of C_3, C_1, C_5, C_6, C_4, and C_2 starting from downfield. Indole C_2 and C_{7a} carbons showed the most downfield shift among the indole carbon signals. The indole C_7 and C_{3a} carbons in the *ortho* position of the lactam group were found to be the most shielded among the indole carbons. In the spectra, shifts were observed in the indole signals based on the nature of the substituents at position 5 of the 2-indolinone ring. The indole C_{3a}, C_4, C_5, C_6 signals in the spectra of the 5-fluorine substituted **7b**, which

Table 1. The MCC and EC_{50} values of the compounds **6** and **7** against different viruses in Vero cells.

Compound	R_1	R_2	MCC (μM)[a]	EC_{50} (μM)[b] Para-influenza-3 virus	Reovirus-1	Sindbis virus	Coxsackie virus B4	Punto Toro virus	
6a	H	H	100	>20	>20	>20	>20	>20	
6b	5-CH_3	H	100	>20	>20	>20	>20	>20	
6c	5-OCF_3	H	>100	>100	**2**	>100	>100	>100	(test1)
			100	>20	**3**	>20	>20	>20	(test2)
			>100	Not tested	**9**	Not tested	Not tested	Not tested	(test3)
6d	5-F	H	>20	>20	>20	>20	>20	>20	
6e	5-Cl	H	100	>20	>20	>20	>20	>20	
6f	5-Br	H	>20	>20	**2**	>20	>20	>20	(test1)
			100	>20	**3**	>20	>20	>20	(test2)
			100	Not tested	**2**	Not tested	Not tested	Not tested	(test3)
6g	5-SO_3Na	H	>100	>100	>100	>100	>100	>100	
6h	7-F	H	100	>100	>100	>100	>100	>100	
6i	7-Cl	H	100	>100	>100	>100	>100	>100	
6j	5,7-diBr	H	100	>20	>20	>20	>20	>20	
7a	5-OCF_3	CH_3	>20	>20	>20	>20	>20	>20	
7b	5-F	CH_3	100	>20	>20	>20	>20	>20	
7c	5-Br	CH_3	20	>4	>4	>4	>4	>4	
	DS-5000*		>100	>100	>100	4	9	9	(test1)
			>100	>100	>100	4	45	20	(test2
			>100	>100	>100	4	20	20	(test3)
	(S)-DHPA		>250	>250	>250	>250	>250	>250	(test1)
			>250	>250	>250	>250	>250	>250	(test2)
			>250	>250	>250	>250	>250	>250	(test3)
	Ribavirin		>250	126	250	>250	>250	112	(test1)
			>250	250	>250	>250	>250	>250	(test2)
			>250	250	>250	>250	>250	>250	(test3)

[a] Minimum cytotoxic concentration: required to cause a microscopically detectable alteration of normal cell morphology.
[b] Required to reduce virus-induced cytopathogenicity by 50%. * Concentration unit is μg/mL.
Note that the SI cannot be exactly calculated when the MCC is higher than the highest concentration tested.

showed that the ^{13}C–^{19}F connections were observed as separate doublets. Electrospray ionization (ESI) mass spectra of **7a–c** were obtained using the positive ionization technique.

2. 2. Antiviral Activity

1*H*-Indole-2,3-dione 3-[4-(4-sulfamoylphenyl)thiosemicarbazones] **6a–j** were evaluated against para-influenza-3 virus, reovirus-1, sindbis virus, coxsackie virus B4, and Punto Toro virus. DS-5000, (*S*)-DHPA and ribavirin were used as standards in the tests (Table 1). Among the compounds tested, the trifluoromethoxy substituted **6c**, and bromine substituted **6f** at position 5 of the indole ring showed selective antiviral activity against reovirus-1. Three independent assays were performed to derive mean fifty percent effective concentration (EC_{50}) values for **6c** and **6f**. The EC_{50} values of **6c** were determined to be 2, 3 and 9 μM and the EC_{50} values of **6f** were determined to be 2, 3 and 2 μM**.** The minimum cytotoxic concentration (MCC) values of **6c** and **6f** were determined as >100 or 100 μM, and 100 or >20 μM in Vero cells, respectively. In Table 1, data indicating antiviral activity are marked in yellow as the selectivity indexs (SI) (ratio of MCC to EC_{50}) are higher than five. The SI values of **6c** and **6f** are in the range of 10–50 in Vero cells. However, in the presence of hydrogen, methyl, chlorine or fluorine substituents at position 5 of the indole ring, the activity against reovirus-1 decreased to >20 μM. In the 5,7-dibromo substitution, the activity decreased to >20 μM, while the 5-sulfonic acid sodium or 7-fluorine and 7-chlorine substituted compounds were found to be inactive. Moreover, none of the compounds used as standard were found to be effective against reovirus-1. The EC_{50} values of DS-5000, (*S*)-DHPA and ribavirin are >100, >250, and 250 or >250 μM, respectively**.**

To investigate the contribution of methyl substitution at position 1 of the indole ring to antiviral activity, the trifluoromethoxy substituted **7a**, the fluorine substituted **7b** and the bromine substituted **7c** at position 5 of the indole ring were also evaluated against para-influenza-3 virus, reovirus-1, sindbis virus, coxsackie virus B4, and Punto Toro virus in Vero cells. The EC_{50} values of **7a–c** against all viruses tested were determined to be >20, >20 and >4 μM, respectively. As seen in the Table 1, the MCC values of **7a–c** are >20, 100 and 20 μM in Vero cells, respectively. In compounds **7a** and **7c**, the introduction of a methyl group at position 1 of indole ring increased the cytotoxicity while decreasing the antiviral activity against reovirus-1.

The antiviral activities of **6c** and **6f**, which are selective and non-toxic against reovirus-1 in Vero cells, have also been investigated in HeLa cells against reovirus-1. Two independent assays were performed to derive mean fifty percent effective concentration (EC_{50}) values for **6c** and **6f**. The EC_{50} values of **6c** were determined to be 45 and 20 M and the EC_{50} values of **6f** were determined to be 45 and 45 M. The MCC values were determined to be >100 M for both **6c** and **6f** in HeLa cells. The SI value of **6c** was calculated as 5, but the SI value of **6f** was determined to be less than 5 (Table 2).

The results obtained show the importance of trifluoromethoxy and bromine substituents at position 5 of the indole ring, as well as the presence of hydrogen at position 1 of the indole ring for the selective and nontoxic effect against reovirus-1. Whereas, with 5-hydrogen, methyl, fluorine, chlorine, sulfonic acid sodium, 5,7-dibromo, 7-fluorine and 7-chlorine substitution at the indole ring, as well as 1-methyl substitution, the activity decreased or inactive derivatives were obtained. The introduction of a methyl group at position 1 of indole ring increased the cytotoxicity while decreasing the antiviral activity against reovirus-1.

Table 2. The MCC and EC_{50} values of the compounds **6c** and **6f** against reovirus-1 in HeLa cells.

Comp.	R_1	R_2	MCC (M)[a]	EC_{50} (M)[b] Reovirus-1	
6c	5-OCF_3	H	>100	**45**	(test1)
			>100	**20**	(test2)
6f	5-Br	H	>100	**45**	(test1)
			>100	**45**	(test 2)
DS-5000*			>100	>100	(test1)
			>100	>100	(test2)
(S)-DHPA			>250	>250	(test1)
			>250	>250	(test2)
Ribarivin			>250	112	(test1)
			>250	>250	(test2)

[a] Minimum cytotoxic concentration: required to cause a microscopically detectable alteration of normal cell morphology. [b] Required to reduce virus-induced cytopathogenicity by 50%. * Concentration unit is g/mL.
Note that the SI can not be exactly calculated when the MCC is higher than the highest concentration tested.

Table 3. List of amino acids and interactions forming binding site of the compounds **6c** and **6f** and binding energies.

Ligand	Binding site residues	Interaction type	Interacting atoms (protein-ligand)	Binding free energy (kcal/mol)
6c	Arg312	H-Bonding	NH1–F1	**–24.1**
	Arg312	H-Bonding	NH2–F2	
	Arg312	H-Bonding	NH2–O3	
	Tyr313	T-shaped π-π Stacking	Phenyl ring–Phenyl ring	
	Val326	Hydrophobic	Side chain carbons–Indole ring	
	Arg329	H-Bonding	NEH–O2	
	Phe330	Hydrophobic	Phenyl ring–Indole ring	
	Gly331	Hydrophobic	Side chain carbons–Phenyl ring	
	Met332	H-Bonding	NH–O2	
	Met332	H-Bonding	O–NH4	
	Lys360	Hydrophobic	Side chain carbons–Aliphatic chain	
	Asp362	Hydrophobic	Side chain carbons–Indole ring	
	Asp363	H-Bonding	OD2–NH	
6f	Trp350	π-π Stacking	Indole ring–Indole ring	**–14.4**
	Arg351	Hydrophobic	Side chain carbons–Indole ring	
	Ala352	Hydrophobic	CB–Aliphatic chain	
	Val354	Hydrophobic	Side chain carbons–Phenyl ring	
	Ser370	H-Bonding	OGH–O2	
	Gln371	Hydrophobic	Side chain carbons	
	Met372	Hydrophobic	Side chain carbons–Phenyl rings	
	Thr373	H-Bonding	NH–N_4	
	Thr374	Hydrophobic	Side chain carbons	
	Asn375	Hydrophobic	Side chain carbons–Phenyl ring	
	Ser376	Hydrophobic	Side chain carbons–Indole ring	

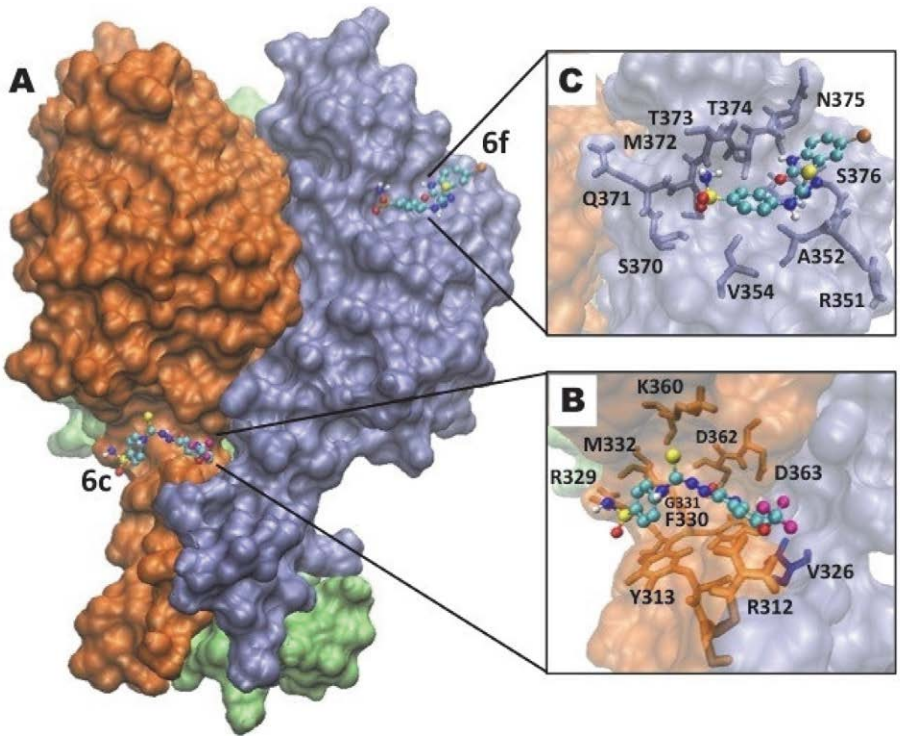

Figure 2. (**A**) The binding sites for **6c** and **6f** are shown (three monomers of T1L are in different colors), (**B**) Detailed view of binding site for **6c**, interacting residues are labelled. (**C**) Detailed view of binding site for **6f**, interacting residues are labelled.

2. 3. Molecular Modeling

The lowest energy structures obtained from molecular dynamics (MD) simulations revealed the most probable binding sites for the compounds **6c** and **6f** (Figure 2A). Moreover, binding free energies from MD simulations revealed that **6c** binds with 9.7 kcal/mol lower free energy than **6f**.

Compound **6c** was buried in between two homodimers in the homotrimer structure of T1L protein (Figure 2A). The binding pocket for **6c** was formed by amino acid residues Arg312, Tyr313, Val326, Arg329, Phe330, Gly331, Met332, Lys360, Asp362 and Asp363 (Figure 2B). It bound to the protein mostly through hydrogen (H-) bondings in addition to few hydrophobic interactions (Table 3). Hydrophobic interactions were mainly governed by its indole ring. Reason for this placement was -OCF_3 group, which interacts with the residue Arg312 of one monomer, which in return interacted with Gln325 residue of the second monomer at the body part of T1L protein. This must be the reason for lower binding energy for compound **6c**.

The binding site of compound **6f** was located in the head domain of one of the monomers in the homotrimer structure of T1L protein (Figure 2A). It bound to the site formed by amino acid residues Trp350, Arg351, Ala352, Val354, Ser370, Gln371, Met372, Thr373, Thr374, Asn375 and Ser376 (Figure 2C). Interactions were mainly hydrophobic, mostly governed by indole and phenyl rings of the ligand (Table 3). The trifluoromethoxy group in **6c**, was replaced by bromine in **6f**, which affects the binding site and nature of the interactions. This binding pocket was very similar to the GM2 glycan binding site.[29] The potent inhibitory activity of this molecule observed in this present study might be due to this critical binding site.

3. Materials and Methods

3. 1. Chemistry

3. 1. 1. General

Melting points of the synthesized derivatives were recorded in open capillaries using a Büchi B-540 Melting Point apparatus and are uncorrected. IR spectra (as KBr discs) were measured with a Shimadzu IR Affinity-1 FTIR spectrophotometer. ^{1}H and ^{13}C NMR spectra were obtained on Varian UNITY INOVA 500 MHz and Bruker Avance NEO 500 MHz spectrophotometers in DMSO-d_6. Mass spectra were recorded on a Thermo Finnigan LCQ Advantage Max spectrometer. Analytical data were obtained on Thermo Finnigan Flash EA 1112 elemental analyzer.

3. 1. 2. Synthesis of 1-methyl-5-substituted 1*H*-indole-2,3-diones 2[30–32]

1*H*-Indole-2,3-diones **1** (5 mmol) and 0.97 g of anhydrous potassium carbonate (K_2CO_3, MW: 138.21, 7 mmol) are stirred in 10 mL of *N*,*N*-dimethylformamide (DMF, MW: 73.09) at room temperature for 1 h. After the addition of methyl iodide (CH_3I, MW: 141.94, 15 mmol) and 0.17 g of anhydrous potassium iodide (KI, MW: 166.00, 1 mmol) as a catalyst, the reaction is heated to 50–60 °C until completed. The reaction mixture was evaporated to dryness under reduced pressure, washed with ice water and recrystallized from ethanol.

3. 1. 3. Synthesis of 4-(isothiocyanato) benzenesulfonamide (4)[33]

4-Aminobenzenesulfonamide (**3**) (MW: 172.20, 3 mmol) was dissolved in 50 mL of water containing 12 mL of concentrated hydrochloric acid (HCl, MW: 36.46). To the solution, thiophosgene ($CSCl_2$, MW: 114.98, 3 mmol) was added in one portion. Stirring was begun immediately and continued until all of the red color of $CSCl_2$ disappeared and the product appeared as a white crystalline precipitate. The precipitate was filtered and washed thoroughly with water.

3. 1. 4. Synthesis of 4-(4-sulfamoylphenyl) thiosemicarbazide (5)[28]

To a solution of hydrazine hydrate ($NH_2NH_2{\cdot}H_2O$, MW: 50.06, 5 mmol) in 10 mL of ethanol, a suspension of 1.07 g of 4-(isothiocyanato)benzenesulfonamide (**4**) (MW: 214.26, 5 mmol) in ethanol (10 mL) was added dropwise with stirring and cooling in an ice bath. The mixture was allowed to stand overnight. The crystals formed were recrystallized from ethanol.

3. 1. 5. Synthesis of 5-(non)substituted 1*H*-indole-2,3-dione 3-[4-(4-sulfamoylphenyl) thiosemicarbazones] 6a–j[28,34,35]

0.86 g of 4-(4-sulfamoylphenyl)thiosemicarbazide (**5**) (MW: 246.3099, 3.5 mmol) was added to the solution of 1*H*-indole-2,3-diones **1a–j** (3.5 mmol) in ethanol (20 mL) containing a catalytic amount of concentrated sulfuric acid (H_2SO_4, MW: 98.08). The mixture was refluxed on a water bath. The product formed after cooling was filtered and washed with ethanol or recrystallized from ethanol. The compounds **6a–j** have been previously described by Karalı *et al.*[33] Experimental information for these molecules is given in the Supplementary Material.

3. 1. 6. Synthesis of 1-methyl-5-substituted 1*H*-indole-2,3-dione 3-[4-(4-sulfamoylphenyl) thiosemicarbazones] 7a–c[28,34,35]

0.86 g of 4-(4-sulfamoylphenyl)thiosemicarbazide (**5**) (MW: 246.3099, 3.5 mmol) was added to the solution of 5-substituted 1-methyl-1*H*-indole-2,3-diones **2** (3.5

mmol) in ethanol (20 mL) containing a catalytic amount of concentrated sulfuric acid (H_2SO_4, MW: 98.08). The mixture was refluxed on a water bath. The product formed after cooling was filtered and washed with ethanol or recrystallized from ethanol.

1-Methyl-5-(trifluoromethoxy)-1*H*-indole-2,3-dione 3-[4-(4-Sulfamoylphenyl)-thiosemicarbazone] (7a). Orange powder (1.16 g, 70%), mp 241–243 °C; IR (KBr): 3358, 3269 (NH), 1681 (C=O), 1616, 1573, 1519, 1479 (C=N, C=C), 1336, 1151 (S=O), 1211 (C=S), 1151 (C-F). ^{1}H NMR (DMSO-d_6, 500 MHz) δ 3.25 (s, 3H, NCH_3), 7.26 (1H, dd, J = 7.8, 1.0 Hz, ind. C_7-H), 7.37 (2H, s, SO_2NH_2), 7.48 (1H, d, J = 7.8 Hz, ind. C_6-H), 7.78 (1H, s, ind. C_4-H), 7.86 (4H, s, phen.), 11.03 (1H, s, N_4-H), 12.69 (1H, s, N_2-H). ^{13}C NMR (^{13}C NMR-APT, DMSO-d_6, 125 MHz) **δ** 26.44 (ind. N-CH_3), 111.63 (ind. C_7), 114.77 (ind. C_4), 120.68 (q, J = 256.1 Hz, OCF_3), 121.08 (ind. C_{3a}), 124.74 (ind. C_6), 126.04 (phen. $C_{2,6}$), 126.54 (phen. $C_{3,5}$), 131.34 (ind. C_3), 141.67 (phen. C_4), 141.85 (phen. C_1), 143.17 (ind. C_{7a}), 144.48 (ind. C_5), 161.41 (ind. C_2), 176.86 (CS). LCMS (ESI (+)) $C_{17}H_{15}F_3N_5O_4S_2$ [M+H]$^+$: 474.456761; found [M+H]$^+$: 474.00. Anal. Calcd for $C_{17}H_{14}F_3N_5O_4S_2.{}^1/_2H_2O$ (482.4570096): C, 42.32; H, 3.13; N, 14.51; found: C, 42.41; H, 2.80; N, 14.85.

1-Methyl-5-fluoro-1*H*-indole-2,3-dione 3-[4-(4-Sulfamoylphenyl)thiosemicarbazone] (7b). Orange powder (1.21 g, 85%), mp 265–268 °C; IR (KBr): 3305, 3228, 3116 (NH), 1680 (C=O), 1618, 1597, 1541, 1475 (C=N, C=C), 1332, 1161 (S=O), 1217 (C=S), 1151 (C-F). ^{1}H NMR (DMSO-d_6, 500 MHz) δ 3.22 (s, 3H, NCH_3), 7.19 (1H, dd, J = 8.4, 4.0 Hz, ind. C_7-H), 7.33 (1H, dt, J = 8.4, 2.8 Hz, ind. C_6-H), 7.39 (2H, s, SO_2NH_2), 7.67 (1H, dd, J = 8.0, 2.4 Hz, ind. C_4-H), 7.87 (4H, s, phen.), 11.01 (1H, s, N_4-H), 12.71 (1H, s, N_2-H). ^{13}C NMR (^{13}C NMR-APT, DMSO-d_6, 125 MHz) **δ** 26.38 (ind. N-CH_3), 108.71 (d, J = 26.1 Hz, ind. C_4), 111.58 (d, J = 7.8 Hz, ind. C_7), 118.03 (d, J = 24.2 Hz, ind. C_6), 121.00 (d, J = 9.3 Hz, ind. C_{3a}), 125.83 (phen. $C_{2,6}$), 126.52 (phen. $C_{3,5}$), 131.70 (ind. C_3), 140.57 (ind. C_{7a}), 141.69 (phen. C_4), 141.73 (phen. C_1), 159.16 (d, J = 238.3 Hz, ind. C_5), 161.29 (ind. C_2), 176.75 (CS). LCMS (ESI (+)) $C_{16}H_{15}FN_5O_3S_2$ [M+H]$^+$: 408.4498546; found [M+H]$^+$: 408.00. Anal. Calcd for $C_{16}H_{14}FN_5O_3S_2.{}^1/_2H_2O$ (416.4501032): C, 46.14; H, 3.63; N, 16.81; found: C, 45.94; H, 3.07; N, 17.25.

1-Methyl-5-bromo-1*H*-indole-2,3-dione 3-[4-(4-Sulfamoylphenyl)thiosemicarbazone] (7c). Orange powder (1.42 g, 87%), mp 275–277 **°C; IR (KBr): 3305, 3236, 3142 (NH), 1680 (C=O), 1595, 1539, 1469 (C=N, C=C),** 1328, 1161 (S=O), 1217 (C=S), 831 (C-Br). ^{1}H NMR (DMSO-d_6, 500 MHz) **δ** 3.21 (s, 3H, NCH_3), 7.15 (1H, d, J = 8.4 Hz, ind. C_7-H), 7.65 (1H, dd, J = 8.4, 2.0 Hz, ind. C_6-H), 7.40 (2H, s, SO_2NH_2), 8.04 (1H, d, J = 2.0 Hz, ind. C_4-H), 7.87 (4H, s, phen.), 11.05 (1H, s, N_4-H), 12.65 (1H, s, N_2-H). ^{13}C NMR (^{13}C NMR-APT, DMSO-d_6, 125 MHz) **δ** 26.38 (ind. N-CH_3), 112.39 (ind. C_7), 115.33 (ind. C_5), 121.73 (ind. C_{3a}), 123.93 (ind. C_4), 125.95 (phen. $C_{2,6}$), 126.51 (phen. $C_{3,5}$), 131.00 (ind. C_3), 133.90 (ind. C_6), 141.68 (phen. C_4), 141.76 (phen. C_1), 143.33 (ind. C_{7a}), 160.94 (ind. C_2), 176.76 (CS). LCMS (ESI-): m/z (%) 466, 468 ([M-H]$^-$, 12, 11), 252, 254 (12, 14), 213 (100), 187 (12), 149 (18), 115, 117 (14, 16). LCMS (ESI (+)) $C_{16}H_{15}BrN_5O_3S_2$ [M+H]$^+$: 469.3554514; found [M+H]$^+$: 469.90. Anal. Calcd for $C_{16}H_{14}BrN_5O_3S_2$ (468.34806): C, 41.03; H, 3.01; N, 14.95; found: C, 40.79; H, 2.60; N, 14.74.

3. . Antiviral Activity

The compounds **6a**–**j** and **7a**–**c** were evaluated for antiviral activity against para-influenza-3, reovirus-1, sindbis virus, coxsackie virus B4, and Punto Toro virus in Vero cells and reovirus-1 in HeLa cells.[36,37] The assays were performed in 96-well plates containing semicon-fluent cell cultures. At the same time with the virus, serial dilutions of the test or reference compounds (DS-5000, (*S*)-DHPA and ribavirin) were added. After the plates were incubated at 37 °C for 3–6 days, the antiviral activities of the compounds [expressed as 50% effective concentration (EC50)] and cytotoxicity [expressed as minimum cytotoxic concentration (MCC)] were determined by microscopy (minimal changes in cell morphology).

3. 3. Molecular Modeling

3. 3. 1. Molecular Dynamics Simulations

Starting structure for reovirus type 1 (strain Lang) (T1L) protein was obtained from RCSB Protein Data Bank, which was obtained by X-ray diffraction with resolution of 2.2 Å (PDB ID: 4xc5).[11] It is a homotrimer structure. Three magnesium ions, which were coordinated to Asn375 and Thr454 residues of each monomer contributing to structural integrity were kept. Crystal water molecules were stripped. Sidechain atoms of some resiudes were missing so they were completed on YASARA Structure software.[38] Protonations states of each titratable residue were calculated on PROPKA server.[39] Upon this calculation the Asp362 residues of each monomer were protonated with pK_a values 12.83, 11.74, and 14.15, respectively. Other titratable residues were calculated to be in their default protonation states, acidic residues were deprotonated and basic residues were protonated.

This T1L protein model was subjected to 20 ns long classical molecular dynamics (MD) simulations, utilizing GROMACS 5.1.4 program[40–42] which was utilized with GROMOS force field GROMOS96 54A7.[43] Protein, with Mg^{2+} ions, was placed in truncated, cubic boxes with dimensions of 10.0 × 10.0 × 10.0 nm. These dimensions ensured that at any point of the simulation the proteins stayed in the simulation box. Single point charge (SPC) water molecules were placed into the box and total of 27 sodium

and chloride ions were added to neutralize the system.[44] Firstly, starting system was subsequently energy-minimized using the steepest descent method for 50,000 steps. Then, energy-minimized structures were taken for the production phase. MD simulation without any constraints was carried out using a constant number of particles (*N*), pressure (*P*), and temperature (*T*), *i.e.* NPT ensemble. The SETTLE algorithm was utilized to constrain the bond length and bond angle of the water molecules while the LINCS algorithm was used to constrain the bond length of the peptide.[45,46] Particle-mesh Ewald (PME) method was utilized to treat long-range electrostatic interactions.[47] A constant pressure of 1 bar was applied with a coupling constant of 1.0 ps and water molecules/ions were coupled separately to a bath at 303 K with a coupling constant of 0.1 ps. The equation of motion was integrated at 2 fs time steps using a leap-frog algorithm.[48] The tools available in the GROMACS and VMD 1.9.1. software were utilized to analyze trajectories.[49] The most representative structure of 20 ns simulation was obtained by clustering tool of GROMACS (g_cluster).

Docking poses, ligand bound structures, with the highest binding affinities, for ligands **6c** and **6f**, were subjected to further 20 ns long classical MD simulations to test the stability of ligands in these binding pockets, utilizing YASARA Structure software, which utilized YASARA2 force field.[50,51] Exactly the same conditions described above for T1L protein MD simulation, including box sizes, were applied. Binding free energies were calculated with the same software, md_analyzebindenergy macro.[38] This module calculates energies without the entropy term.

$$G = E_{bind} + E_{el} + E_{vdW} + G_{polar} + G_{nonpolar}$$

Here, the first three terms represent binding, electrostatic, and van der Waals interactions, respectively. G_{polar} and $G_{nonpolar}$ are polar and nonpolar contributions of solvation free energies, respectively. It is very similar to MM/PBSA for the entropy term, which can be neglected in the context of main goal of these calculations. Then, binding free energy is calculated by the following equation.

$$\text{Binding Energy} = (G_{Receptor} + G_{Ligand}) + (Gsolv_{Receptor} + Gsolv_{Ligand}) - (G_{Complex} + Gsolv_{Complex})$$

The first two terms stand for potential energies of the receptor and ligand, and the next two terms represent solvation energies of the receptor and ligand, and the last terms are potential and solvation energies of the complex.

3. 3. 2. Molecular Docking Simulations

All docking simulations were performed utilizing AutoDock Vina 1.1.2 software.[52] Protein structures were put into a 7.6 × 7.2 × 7.2 nm grid box to occupy the whole ligand-protein systems and the spacing was kept at 1.00 Å, a standard value for AutoDock Vina. Each docking trial produced 20 poses with the exhaustiveness value of 20.

Structures of ligands were optimized by using YASARA software with YAMBER force field.[50,51] Binding poses were grouped according to their binding affinity, high population of hits, and RMSD values. One binding pocket for each ligand, which produced the highest binding affinity, was assessed. AutoDock Vina uses a stochastic optimization algorithm thus, for each ligand docking simulations were repeated twice. Repetition of simulations produced similar binding results with highly similar binding affinities. Ligands in their most probable binding pockets were subjected to 20 ns long classical MD simulations, as described above.

4. Conclusions

These results demonstrate the importance of position 1 of the unsubstituted indole ring for selective activity against reovirus-1 as well as trifluoromethoxy and bromine substitution at position 5 of the indole ring. In compounds substituted with trifluoromethoxy and bromine at position 5 of the indole ring, 1-methyl substitution at position 1 of the indole ring caused a decrease in anti-reovirus-1 activity as well as an increase in cytoxicity. With molecular modeling analyses, the mechanisms of action of selective and non-toxic compounds were determined against reovirus-1.

Supplementary Material

The data that support the findings of this study are available in the Supplementary Material file.

Acknowledgements

This work was supported by The Scientific Research Projects Coordination Unit of Istanbul University (grant number TSG-2018-27798). Also, we want to thank for collaboration to Prof. Lieve Naesens from Department of Microbiology, Immunology and Transplantation, Rega Institute, Leuven, Belgium.

Declarations

Conflict of interest on behalf of all authors, the corresponding author states that there is no conflict of interest.

5. References

1. M. T. Heise, *Reference Module in Biomedical Sciences.* **2014**, B978-0-12-801238-3.00079-9. **DOI:**10.1016/B978-0-12-801238-3.00079-9
2. S. Payne: Viruses from understanding to investigation, USA,

Elsevier, Academic Press E-Publishing, **2017.**
DOI:10.1016/B978-0-12-803109-4.00009-X
3. J. D. Doyle, J. E. Stencel-Baerenwald, C. A. Copeland, J. P. Rhoads, J. J. Brown, K. L. Boyd, J. B. Atkinson, T. S. Dermody, *PLOS Pathog.* **2015**, *11(3)*, e1004693. **DOI:**10.1371/journal.ppat.1004693
4. A. H. Sharpe, B. N. Fields, in: W. K. Joklik (Ed.): Pathogenesis of Reovirus Infection, The Reoviridae, MA: E-Publishing Springer, Boston, **1983**, 229–285. **DOI:**10.1007/978-1-4899-0580-2
5. X. Zhang, H. Wu, C. Liu, J. Tian, L. Qu, *Infect. Genet. Evol.* **2015**, *34*, 415–422. **DOI:**10.1016/j.meegid.2015.06.008
6. T. Hotani, M. Tachibana, H. Mizuguchi, F. Sakurai, *Biochem. Biophys. Res. Commun.* **2015**, *460(4)*, 1041–1046. **DOI:**10.1016/j.bbrc.2015.03.147
7. P. Danthi, G. H. Holm, T. Stehle, T. S. Dermody, *Adv. Exp. Med. Biol.* **2013**, *790*, 42–71. https://dx.doi.org/10.1007%2F978-1-4614-7651-1_3
8. K. W. Boehme, M. Ikizler, T. Kobayashi, T. S. Dermody, *Methods.* **2011**, *55(2)*, 109–113. **DOI:**10.1016/j.ymeth.2011.07.002
9. D. H. Rubin, M. J. Kornstein, A. O. Anderson, *J. Virol.* **1985**, *53(2)*, 391–398. **DOI:**10.1128/jvi.53.2.391-398.1985
10. A. Kapikian, R. E. Shope, in: S. Baron (Ed.): Chapter 63. Rotaviruses, Reoviruses, Coltiviruses and Orbiviruses, Medical Microbiology, TX: University of Texas Medical Branch at Galveston, Galveston, **1996**.
11. E. Stettner, M. H. Dietrich, K. Reiss, T. S. Dermody, T. Stehle, *J. Virol.* **2015**, *89(11)*, 6136–6140. **DOI:**10.1128/JVI.00433-15
12. J. C. Forrest, T. S. Dermody, *J. Virol.* **2003**, *77(17)*, 9109–9115. **DOI:**10.1128/JVI.77.17.9109-9115.2003
13. T. R. Bal, B. Anand, P. Yogeeswari, D. Sririam, *Bioorg. Med. Chem. Lett.* **2005**, *15(20)*, 4451–4455. **DOI:**10.1016/j.bmcl.2005.07.046
14. N. Terzioğlu, N. Karalı, A. Gürsoy, C. Pannecouque, P. Leysen, J. Pashuyse, J. Neyts, E. De Clercq, *ARKIVOC* **2006**, *(i)*, 109–118. **DOI:**10.3998/ark.5550190.0007.113
15. D. Banerjee, P. Yogeeswari, P. Bhat, A. Thomas, M. Srividya, D. Sriram, *Eur. J. Med. Chem.* **2011**, *46(1)*, 106–121. **DOI:**10.1016/j.ejmech.2010.10.020
16. S. Y. Abbas, A. A. Farag, Y. A. Ammar, A. A. Atrees, A. F. Mohamed, A. A. El-Henawy, *Monatsh. Chem.* **2013**, *144*, 1725–1733. **DOI:**10.1007/s00706-013-1034-3
17. Z. Ş. Sevinçli, G. N. Duran, M. Özbil, N. Karalı, *Bioorg. Chem.* **2020**, *104*, 104202. **DOI:**10.1016/j.bioorg.2020.104202
18. D. J. Bauer, P. W. Sadler, *Brit. J. Pharmacol.* **1960**, *15(1)*, 101–110. **DOI:**10.1111/j.1476-5381.1960.tb01216.x
19. P. W. Sadler, *Annals of the New York Academy of Sciences.* **1965**, *130(1)*, 71–79. **DOI:**10.1111/j.1749-6632.1965.tb12541.x
20. L. Sherman, F. Edelstein, G. Shtacher, M. Avramoff, Y. Teitz, *J. Gen. Virol.* **1980**, *46(1)*, 195–203. **DOI:**10.1099/0022-1317-46-1-195
21. Y. Teitz, D. Ronen, A. Vansover, T. Stematsky, J. L. Riggs, *Antiviral Res.* **1994**, *24(4)*, 305–314. **DOI:**10.1016/0166-3542(94)90077-9
22. I-J. Kang, L-W. Wang, T-A. Hsu, A. Yueh, C-C. Lee, Y-C. Lee, C-Y. Lee, Y-S. Chao, S-R. Shih, J-H. Chern, *Bioorg. Med. Chem. Lett.* **2011**, *21(7)*, 1948–1952. **DOI:**10.1016/j.bmcl.2011.02.037
23. M. C. Pirrung, S. V. Pansare, K. Das Sarma, K. A. Keith, E. R. Kern, *J. Med. Chem.* **2005**, *48(8)*, 3045–3050. **DOI:**10.1021/jm049147h
24. P. Selvam, N. Murugesh, M. Chandramohan, K. A. Keith, E. R. Kern, *Antivir. Chem. Chemother.* **2006**, *17(2)*, 107–110. **DOI:**10.1177/095632020601700206
25. P. Selvam, N. Murugesh, M. Chandramohan, R. W. Sidwell, M. K. Wandersee, D. F. Smee, *Antivir. Chem. Chemother.* **2006**, *17(5)*, 269–274. **DOI:**10.1177/095632020601700504
26. P. Selvam, M. Chandramohan, B. L. Hurst, D. F. Smee, *Antivir. Chem. Chemother.* **2010**, *20(3)*, 143–146. **DOI:**10.3851/IMP1471
27. P. Selvam, N. Murugesh, M. Chandramohan, E. De Clercq, E. Keyaerts, L. Vijgen, P. Maes, J. Neyts, M. V. Ranst, *Indian J. Pharm. Sci.* **2008**, *70(1)*, 91–94. **DOI:**10.4103/0250-474X.40339
28. N. Karalı, A. Akdemir, F. Göktaş, P. Eraslan-Elma, A. Angeli, M. Kızılırmak, C. T. Supuran, *Bioorg. Med. Chem.* **2017**, *25(14)*, 3714–3718. **DOI:**10.1016/j.bmc.2017.05.029
29. K. Reiss, J. E. Stencel, Y. Liu, B. S. Blaum, D. M. Reiter, T. Feizi, T. S. Dermody, T. Stehle, *PLOS Pathog.* **2012**, *8(12)*, e1003078. **DOI:**10.1371/journal.ppat.1003078
30. S. J. Garden, J. C. Torres, L. E. DaSilva, A. C. Pinto, *Synth. Commun.* **1998**, *28(9)*, 1679–1689. **DOI:**10.1080/00397919808006872
31. K. L. Vine, J. M. Locke, M. Ranson, S. G. Pyne, J. B. Bremner, *J. Med. Chem.* **2007**, *50(21)*, 5109–5117. **DOI:**10.1021/jm0704189
32. N. Karalı, P. Eraslan-Elma, G. Cihan Üstündağ, F. Göktaş, New 1-substituted 1*H*-indole-2,3-dione compounds ve synthesis methods, *Turk. Pat. Appl.* Patent Number TR 2015 015912 B, date of patent December 11, **2015**.
33. R. L. McKee, R. W. Bost, *J. Am. Chem. Soc.* **1946**, *68(12)*, 2506–2507. **DOI:**10.1021/ja01216a022
34. N. Karalı, P. Eraslan-Elma, F. Göktaş, Process for preparation of N-[(aminosulfonyl)phenyl]-2-(1,2-dihydro-2-oxo-3H-indol-3-ylidene)hydrazinecarbothioamide derivatives, *Turk. Pat. Appl.* Patent Number TR 2015 016135 B, date of patent December 15, **2015**.
35. N. Karalı, F. Göktaş, G. Cihan-Üstündağ, P. Eraslan, N-[(-Aminosulfonyl)phenyl]-2-(1,2-dihydro-2-oxo-3*H*-indol-3-ylidene)hydrazinecarbothioamide derivatives for treating cancer and immunological disorders, *PCT Int. Appl.* Patent Number WO 2017099695 A1, date of patent June 15, **2017**.
36. L. Naesens, E. Vanderlinden, E. Roth, J. Jeko, G. Andrei, R. Snoeck, C. Pannecouque, E. Illyés, G. Batta, P. Herczegh, F. Sztaricskai, *Antiviral Res.* **2009**, *82(1)*, 89–94. **DOI:**10.1016/j.antiviral.2009.01.003
37. C. Pannecouque, D. Daelemans, E. De Clercq, *Nat. Protoc.* **2008**, *3*, 427–434. **DOI:**10.1038/nprot.2007.517
38. E. Krieger, G. Koraimann, G. Vriend, *Proteins.* **2002**, *47(3)*,

393–402. **DOI:**10.1002/prot.10104
39. T. J. Dolinsky, J. E. Nielsen, J. A. McCammon, N. A. Baker, *Nucleic Acids Res.* **2004**, *32 (Web Server issue)*, W665-W667. **DOI:**10.1093/nar/gkh381
40. H. J. C. Berendsen, D. Van der Spoel, D. E. Van Drunen, *Computer Physics Communications.* **1995**, *91(1–3)*, 43–56. **DOI:**10.1016/0010-4655(95)00042-E
41. E. Lindahl, B. Hess, D. Van der Spoel, *J. Mol. Model.* **2001**, *7*, 306–317. **DOI:**10.1007/s008940100045
42. D. Van Der Spoel, E. Lindahl, B. Hess, G. Groenhof, A. E. Mark, H. J. C. Berendsen, *J. Comput. Chem.* **2005**, *26(16)*, 1701–1718. **DOI:**10.1002/jcc.20291
43. N. Schmid, A. P. Eichenberger, A. Choutko, S. Riniker, M. Winger, A. E. Mark, W. F. Van Gunsteren, *Eur. Biophys. J.* **2011**, *40*, 843. **DOI:**10.1007/s00249-011-0700-9
44. P. E. Smith, W. F. Van Gunsteren, *Chemical Physics Letters.* **1993**, *215(4)*, 315–318. **DOI:**10.1016/0009-2614(93)85720-9
45. S. Miyamoto, P. A. Kollman, *J. Comput. Chem.* **1992**, *13(8)*, 952–962. **DOI:**10.1002/jcc.540130805
46. B. Hess, H. Bekker, H. J. C. Berendsen, J. G. E. M. Fraaije, *J. Comput. Chem.* **1997**, *18(12)*, 1463–1472. **DOI:**10.1002/(SICI)1096-987X(199709)18:12<1463::AID-JCC4>3.0.CO;2-H
47. T. A. Darden, D. York, L. Pedersen, *J. Chem. Phys.* **1993**, *98(12)*, 10089–10092. **DOI:**10.1063/1.464397
48. R. W. Hockney, S. P. Goel, J. W. Eastwood, *J. Comput. Phys.* **1974**, *14(2)*, 148–158. **DOI:**10.1016/0021-9991(74)90010-2
49. W. Humphrey, A. Dalke, K. Schulten, *J. Mol. Graph.* **1996**, *14(1)*, 33–38. **DOI:**10.1016/0263-7855(96)00018-5
50. E. Krieger, G. Vriend, *Bioinformatics.* **2002**, *18(2)*, 315–318. **DOI:**10.1093/bioinformatics/18.2.315
51. E. Krieger, T. Darden, S. B. Nabuurs, A. Finkelstein, G. Vriend, *Proteins.* **2004**, *57(4)*, 678–683. **DOI:**10.1002/prot.20251
52. O. Trott, A. J. Olson, *J. Comput. Chem.* **2010**, *31(2)*, 455–461. **DOI:**10.1002/jcc.21334

Povzetek

Preučili smo aktivnost 1*H*-indol-2,3-dion 3-[4-(4-sulfamoilfenil)tiosemikarbazonov] **6a–j** proti naslednjim virusom: para-influenca-3, reovirus-1, sindbis, coxsackie B4 in Punto Toro. Sintetizirali smo nove 1-metil-1*H*-indol-2,3-dion 3-[4-(4-sulfamoilfenil)tiosemikarbazone] **7a–c** in določili vpliv metilnega substituenta na položaju 1 indolnega sistema na antivirusno aktivnost. Rezultati kažejo, da sta 5-trifluorometoksi substituirana spojina **6c** (EC_{50} 2–9 μM) in 5-bromo substituirana **6f** (EC_{50} 2–3 μM) nestrupeni ter da kažeta selektivno antivirusno aktivnost; po drugi strani pa niti vsi standardi niso aktivni proti reovirusu-1. Študije molekulskega sidranja spojin **6c** and **6f** smo izvedli z namenom določanja mesta vezave v reovirusu-1. Trifluorometoksi and bromino substituenta na položaju 5 indolnega sistema zagotavljata selektivno antivirusno aktivnost; metilni substituent na položaju 1 indolnega sistema pa občutno zmanjša aktivnost proti reovirusu-1, hkrati pa ima povečano strupenost.

DOI: 10.17344/acsi.2023.8602 *Acta Chim. Slov.* **2024,** *71,* 226–235

Scientific paper

QSRR Modeling of Lipophilicity of New Spirohydantoin Derivatives Determined with Various TLC Systems

Kristina A. Tot,[1,*] Anita M. Lazić[2] and Tatjana Lj. Djaković Sekulić[1]

[1] *University of Novi Sad, Faculty of Sciences, Department of Chemistry, Biochemistry and Environmental Protection, Trg Dositeja Obradovića 3, 2100 Novi Sad, Republic of Serbia*

[2] *University of Belgrade, Faculty of Technology and Metallurgy, Karnegijeva 4, 11000 Belgrade, Republic of Serbia*

* *Corresponding author: E-mail: kristina.tot@dh.uns.ac.rs*
Fax: +381 21 454 065, Phone: +381 21 485 2743

Received: 12-28-2023

Abstract

A Quantitative structure-retention relationship *(QSRR) analysis has been* performed on the chromatography parameters of lipophilicity of selected spirohydantoins. Multiple linear regression (MLR) was applied to construct the QSRR models. The chromatographic parameters of lipophilicity were determined by reversed-phase thin-layer chromatography. Chromatographic analyses were performed on C-18 modified silica gel with a two-component mobile phase consisting of water and protic organic solvent (ethanol, n-propanol, i-propanol, or t-butanol) in different ratios. QSRR models were also created for additional four aqueous mobile phases: acetone-water, acetonitrile-water, tetrahydrofuran-water, and 1,4-dioxane-water (results published before). In total, chromatographic lipophilicity parameters obtained for two types of organic solvents were subject of the QSRR. The predictive ability of each model was evaluated using internal and external validation. The best QSRR model for predicting the chromatographic parameter of lipophilicity was obtained for tetrahydrofuran as an organic solvent.

Keywords: QSRR modeling, lipophilicity, RP-TLC, spirohydantoins

1. Introduction

Spirohydantoins represent a pharmacologically important class of heterocyclic compounds.[1] These compounds are mostly small and lipophilic molecules, which easily reach the target cells. Derivatives of hydantoin exhibit various pharmacological activities, such as anticonvulsant,[2] antiarrhythmic,[3] antiviral,[4] anti-inflammatory,[5] and anti-HIV activity.[6] Well known hydantoin-based drug is phenytoin (5,5-diphenylhydantoin, Dilantin), which is widely used in treating epilepsy and cardiac arrhythmias.[7] Derivatives of hydantoin can impact cancer metastasis, and for this reason, these derivatives have been recognized as promising therapeutic agents in cancer treatment.[8–14]

The main factor that determines the activity of the compound is chemical structure.[15–17] Some structural parameters are more important for the activity than others. The selection of appropriate parameters that are important for the activity of compound is facilitated by an *in silico* approach. This approach is based on various models, such as QSARs (quantitative structure–activity relationships) or QSPRs (quantitative structure–property relationships).[18] These models allow quantitative assessment of molecular properties or compound activity based on structural characteristics (expressed by various molecular descriptors). Understanding the relationship between the activity, structure and physicochemical properties of various compounds provides an opportunity to identify features that are important for the compound activities, as well as to identify potential bioactive compounds.[19,20]

In recent years the progress in the QSPR approaches has been increasing due to the fast-developing field of chemometrics.[21] QSRR is a specific type of quantitative structure-property relationship. QSRR model is an important approach for assessing and interpreting retention data in relation to the chemical structure of the analyzed substances which is numerically expressed by molecular descriptors.[22] The QSRR model can be used for identifying unknown compounds and understanding the molecular mechanism of separation operating in a specific chromatographic system.[23–29] The logarithm of the partition coefficient, log *P*,

which represents the ratio of equilibrium concentrations of the compound dissolved in the two phase system consisting of two non-soluble solvents (n-octanol and water),[30] is very often included in models as a molecular descriptor. This is not surprising since log *P* is a quantitative expression of lipophilicity, widely used as a structural descriptor. Lipophilicity is one of the key properties associated with the transport and distribution of drugs in organisms, drug–receptor interactions, metabolism, and toxicity, and also plays a role in the onset and duration of the drug's effect.[31]

Reversed-phase thin-layer chromatography (RP-TLC) is often used to determine the lipophilicity due to its simplicity, possibility of examination of a large number of samples in small quantities, reproducibility, and low-cost price.[32–35] Measured values of chromatographic lipophilicity can be used instead of log *P* values as independent variables in the QSAR/QSRR models. The QSRR models allow retention data prediction of the new, not yet synthesized compounds, using their molecular descriptors.[36–38]

The aim of this study was to establish new QSRR models, which will provide insight into which molecular properties are important for the lipophilicity of new spirohydantoins.

2. Experimental

2. 1. Investigated Compounds and Their Solutions

The analyzed compounds were three series of 3-(4-substituted benzyl)-cycloalkylspiro-5-hidantoins, respectively derivatives of 3-(4-substitutedbenzyl)-cyclopentanespiro-5-hydantoin, 3-(4-substituted benzyl)- cyclohexanespiro-5-hydantoin and 3-(4-substituted benzyl)-cycloheptanespiro-5-hydantoin. Chemical structures, substituents and numbering of the investigated spirohydantoins are presented in Figure 1 and Table 1.

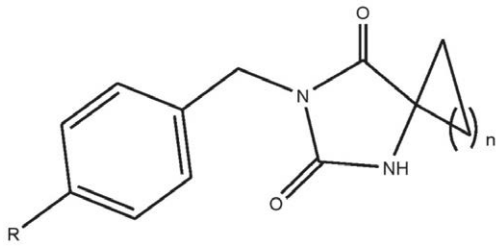

Figure 1: Molecular structure of the investigated 3-(4-substituted benzyl)cycloalkylspiro-5-hydantoins.

The solutions of the investigated compounds were prepared by dissolving 5 mg of each spirohydantoin in 1 ml of ethanol. The 1 ml of each solution was spotted on high-performance thin-layer chromatographic (HPTLC) plates.

2. 2. Reversed-Phase Thin-Layer Chromatography

Thin-layer chromatography was performed on commercially available 10×10 cm high-performance RP-18 modified silica gel (HPTLC plates) with fluorescent indicator F254s (Merck, Darmstadt, Germany). Mobile phases used were mixtures of water and one out of four organic solvents: ethanol (Sigma-Aldrich) (φ(ethanol) = 0.5–0.70 v/v), *n*-propanol (Sigma-Aldrich) (φ(*n*-propanol) = 0.5–0.74 v/v), *i*-propanol (Lachema) (φ(*i*-propanol) = 0.5–0.70 v/v), *t*-butanol (Sigma-Aldrich) (φ(*t*-butanol) = 0.5–0.70 v/v).

Chromatograms were developed by the ascending technique at room temperature (22±2˚C) without previous saturation of the chromatographic chamber (CAMAG, Muttenz, Switzerland) with mobile phase vapor. The developing distance was approximately 45 mm. After development of chromatograms, the plates were dried at room temperature, and individual chromatographic zones were detected under UV light at 254 nm wavelength (CAMAG, Muttenz, Switzerland).

For subsequent calculations, the R_M values were calculated for each investigated compound according to Bate-Smith and Westall's equation:[39]

$$R_M = \log\left(\frac{1}{R_F} - 1\right) \quad (1)$$

In Eq. (1) R_F is the retardation factor, which was calculated as the ratio of the distance of a solute's target zone and the distance of the solvent front.

Table 1: Overview of substituents of the investigated 3-(4-substituted benzyl)cycloalkylspiro-5-hydantoins.

Cyclopentanespiro-5-hydantoins			Cyclohexanespiro-5-hydantoins			Cycloheptanespiro-5-hydantoins		
No.	**n**	**R**	**No.**	**n**	**R**	**No.**	**n**	**R**
CI.1	3	H	**II.1**	4	H	**III.1**	5	H
I.2	3	CH_3	**II.2**	4	CH_3	**III.2**	5	CH_3
I.3	3	OCH_3	**II.3**	4	OCH_3	**III.3**	5	OCH_3
I.4	3	Cl	**II.4**	4	Cl	**III.4**	5	Cl
I.5	3	Br	**II.5**	4	Br	**III.5**	5	Br
I.6	3	CN	**II.6**	4	CN	**III.6**	5	CN
I.7	3	NO_2	**II.7**	4	NO_2	**III.7**	5	NO_2

The R_M values of each compound are determined in the presence of different organic solvent content in the mobile phase. The linear relationship between the R_M values and different mobile phase proportions is established, and the partition coefficient is calculated by extrapolating to a pure water mobile phase:[40]

$$R_M = R_M^0 + S\varphi \quad (2)$$

In Eq. (2), φ is the volume fraction of organic solvent in the mobile phase, R_M^0 is the intercept and S is the slope of Eq. (2). Intercept, R_M^0, correspond to retention extrapolated to 0 % (v/v) of organic solvent and represents the chromatographic lipophilicity parameter.[41]

2. 3. Molecular Descriptors Calculation

Molecular descriptors were calculated by Dragon[42] (40 molecular descriptors in total: MW (molecular weight), Sv (sum of atomic van der Waals volumes), Se (sum of atomic Sanderson electronegativities), Sp (sum of atomic polarizabilities), Si (sum of first ionization potentials), nAT (number of atoms), nBT (number of bonds), RBN (number of rotatable bonds), nH (number of Hydrogen atoms), nC (number of Carbon atoms), nN (number of Nitrogen atoms), nO (number of Oxygen atoms), nCl (number of Chlorine atoms), nHet (number of heteroatoms), nX (number of halogen atoms), ARR (aromatic ratio), nHAcc (number of acceptor atoms for H-bonds), nHDon (number of donor atoms for H-bonds), Hy (hydrophilic factor), AMR (Ghose-Crippen molar refractivity), TPSA(NO) (topological polar surface area using N,O polar contributions), TPSA(Tot) (topological polar surface area using N, O, S, P polar contributions), MLOGP (Moriguchi octanol-water partition coeff. (logP)), MLOGP2 (squared Moriguchi octanol-water partition coeff. (logP^2)), ALOGP (Ghose-Crippen octanol-water partition coeff. (logP)), ALOGP2 (squared Ghose-Crippen octanol-water partition coeff. (logP^2)), Vx (McGowan volume), VvdwMG, (van der Waals volume from McGowan volume), VvdwZaz (van der Waals volume from Zhao-Abraham-Zissimos equation), PDI (packing density index), RBF (rotatable bond fraction), ECC (eccentricity), DBI (Dragon branching index), SAtot (total surface area from P_VSA-like descriptors), SAacc (surface area of acceptor atoms from P_VSA-like descriptors), Uc (unsaturation count), Ui (unsaturation index), Pol (polarity number), IAC (total information index on atomic composition) and ISIZ (information index on molecular size)), ChemDraw Ultra 7.0[43] (for calculation values of ClogP, $\log P_{Crippen}$, $\log P_{Viswanadhan}$ and $\log P_{Brotto}$), Molinspiration[44] (for miLogP), and ADMETlab[45] (for calculation values of log P, log D (distribution coefficient), and log S (water solubility)). The calculated descriptors for each investigated compound are listed in Table S1 (Supplementary Materials).

2. 4. QSRR Modeling

QSRR models were created using chromatographic lipophilicity parameters as dependent variables and calculated molecular descriptors as independent variables. The methodology used for QSRR modeling was multiple linear regressions. All of the calculations were made using data analysis software Statistica v.14.0 (StatSoft (Europe), GmbH, Hamburg).

Before implementing MLR, the number of molecular descriptors was reduced. First, molecular descriptors with the same numerical value for all investigated compounds were excluded. Then, molecular descriptors whose values are not available for all investigated compounds were eliminated. The next step in the elimination of molecular descriptors from the analysis was to exclude descriptors with a high mutual correlation (r>0.800), respectively only one of them was used.[46] The final regression equations were obtained using two methods: the forward stepwise method and the backward stepwise method.

The developed models were validated by cross-validation methodology. The predictivity of each model was measured by the cross-validated regression coefficient (Q^2) defined as (Eq, 3):

$$Q^2 = 1 - \Sigma(Y_{pred} - Y_{exp})^2 / \Sigma(Y_{exp} - Y_{mean})^2 \quad (3)$$

where Y_{pred}, Y_{exp} and Y_{mean} are predicted, experimental, and mean values of the target properties (retention), respectively. For a model to have a high predictive power, it is essential that Q^2 has the high value. The accepted cross-validation of the Q^2 value is considered to be $Q^2 > 0.7$.[47]

3. Results and Discussion

3. 1. Chromatographic Lipophilicity Parameters

The lipophilicity was assessed using reversed-phase thin-layer chromatography (RP-TLC).

The chromatographic lipophilicity parameters of cycloalkylspiro-5-hydantoins were determined using four different mixtures of mobile phase, which differ in organic component, i.e., ethanol, n-propanol, i-propanol, and t-butanol. Calculated chromatographic lipophilicity parameters, intercepts (R_M^0), slopes (S) as well as coefficient of correlations (r), are listed in Table 2.

Relatively high correlation coefficients (r > 0.99) and low standard deviation indicate that calculated equations are statistically significant. Figure 2 shows the impact of the size of cycloalkyl group and the substituent R on R_M^0 values in mobile phase ethanol-water. Graphs showing the size impact of the cycloalkyl group and the substituent R on the values of R_M^0 for other applied solvents are provided in Supplementary material (Figure S1-S3).

Table 2: Intercepts, R_M^0, slopes, S, and correlation coefficients, r, of the equation (2) applied for the various mobile phase.

Investigated compounds	ethanol R_M^0	ethanol −S	ethanol r	n-propanol R_M^0	n-propanol −S	n-propanol r
I.1	1.926(±0.053)	3.312(±0.090)	0.999(±0.016)	1.189(±0.060)	2.732(±0.092)	0.998(±0.017)
I.2	2.528(±0.065)	3.975(±0.110)	0.998(±0.019)	1.441(±0.036)	2.880(±0.056)	0.999(±0.011)
I.3	1.985(±0.126)	3.490(±0.213)	0.993(±0.037)	1.145(±0.044)	2.679(±0.069)	0.999(±0.013)
I.4	2.665(±0.057)	4.056(±0.096)	0.999(±0.017)	1.302(±0.056)	2.740(±0.087)	0.998(±0.016)
I.5	2.783(±0.147)	4.116(±0.248)	0.993(±0.043)	1.329(±0.051)	2.757(±0.079)	0.999(±0.015)
I.6	1.776(±0.094)	3.665(±0.159)	0.996(±0.028)	0.884(±0.047)	2.611(±0.072)	0.999(±0.014)
I.7	2.033(±0.053)	3.449(±0.089)	0.999(±0.015)	1.090(±0.010)	2.609(±0.016)	1.000(±0.003)
II.1	2.523(±0.091)	4.008(±0.154)	0.997(±0.027)	1.416(±0.029)	2.860(±0.045)	1.000(±0.009)
II.2	3.057(±0.057)	4.537(±0.097)	0.999(±0.017)	1.354(±0.034)	2.771(±0.052)	0.999(±0.010)
II.3	2.169(±0.087)	3.551(±0.147)	0.997(±0.026)	1.219(±0.038)	2.757(±0.059)	0.999(±0.011)
II.4	3.046(±0.070)	4.468(±0.118)	0.999(±0.021)	1.408(±0.043)	2.799(±0.067)	0.999(±0.013)
II.5	2.925(±0.070)	4.162(±0.118)	0.998(±0.021)	1.532(±0.022)	2.900(±0.034)	1.000(±0.006)
II.6	2.129(±0.072)	3.934(±0.121)	0.998(±0.021)	1.362(±0.106)	3.285(±0.164)	0.996(±0.031)
II.7	2.513(±0.054)	4.034(±0.092)	0.999(±0.016)	1.095(±0.038)	2.645(±0.060)	0.999(±0.011)
III.1	2.988(±0.045)	4.489(±0.076)	0.999(±0.013)	1.366(±0.065)	2.806(±0.101)	0.998(±0.019)
III.2	3.159(±0.118)	4.526(±0.200)	0.996(±0.035)	1.464(±0.025)	2.843(±0.038)	1.000(±0.007)
III.3	2.729(±0.081)	4.215(±0.136)	0.998(±0.024)	1.267(±0.086)	2.796(±0.134)	0.996(±0.025)
III.4	3.196(±0.115)	4.495(±0.194)	0.996(±0.034)	1.518(±0.039)	2.867(±0.061)	0.999(±0.011)
III.5	3.390(±0.110)	4.715(±0.186)	0.997(±0.032)	1.621(±0.041)	3.000(±0.064)	0.999(±0.012)
III.6	2.466(±0.092)	4.268(±0.155)	0.997(±0.027)	1.189(±0.092)	2.998(±0.142)	0.996(±0.027)
III.7	2.692(±0.103)	4.085(±0.174)	0.996(±0.030)	1.259(±0.045)	2.749(±0.069)	0.999(±0.013)

TABLE 2 Continuation

Investigated compounds	i-propanol R_M^0	i-propanol −S	i-propanol r	t-butanol R_M^0	t-butanol −S	t-butanol r
I.1	1.146(±0.037)	2.420(±0.062)	0.999(±0.010)	1.248(±0.075)	2.697(±0.125)	0.997(±0.021)
I.2	1.334(±0.051)	2.482(±0.084)	0.998(±0.014)	1.574(±0.092)	3.055(±0.152)	0.996(±0.025)
I.3	1.140(±0.047)	2.488(±0.078)	0.999(±0.013)	1.222(±0.049)	2.667(±0.082)	0.999(±0.013)
I.4	1.365(±0.025)	2.517(±0.042)	1.000(±0.007)	1.464(±0.035)	2.843(±0.059)	0.999(±0.010)
I.5	1.510(±0.060)	2.679(±0.100)	0.998(±0.016)	1.626(±0.051)	3.061(±0.084)	0.999(±0.014)
I.6	0.948(±0.043)	2.386(±0.071)	0.999(±0.012)	1.513(±0.084)	3.203(±0.138)	0.997(±0.023)
I.7	1.161(±0.056)	2.518(±0.093)	0.998(±0.015)	1.393(±0.015)	2.952(±0.025)	1.000(±0.004)
II.1	1.430(±0.029)	2.742(±0.049)	1.000(±0.008)	1.423(±0.067)	2.808(±0.112)	0.998(±0.018)
II.2	1.376(±0.093)	2.531(±0.154)	0.995(±0.025)	1.623(±0.066)	3.067(±0.110)	0.998(±0.018)
II.3	1.266(±0.064)	2.573(±0.105)	0.998(±0.017)	1.494(±0.081)	2.976(±0.134)	0.997(±0.022)
II.4	1.664(±0.060)	2.846(±0.100)	0.998(±0.016)	1.603(±0.026)	3.036(±0.043)	1.000(±0.007)
II.5	1.678(±0.080)	2.806(±0.133)	0.997(±0.022)	1.646(±0.045)	3.088(±0.075)	0.999(±0.012)
II.6	1.265(±0.091)	2.799(±0.151)	0.996(±0.025)	1.521(±0.077)	3.264(±0.127)	0.998(±0.021)
II.7	1.399(±0.046)	2.735(±0.076)	0.999(±0.013)	1.404(±0.036)	2.877(±0.060)	0.999(±0.010)
III.1	1.760(±0.087)	3.083(±0.145)	0.997(±0.024)	1.597(±0.043)	3.027(±0.071)	0.999(±0.012)
III.2	2.053(±0.063)	3.309(±0.104)	0.998(±0.017)	1.674(±0.071)	3.098(±0.117)	0.998(±0.019)
III.3	1.646(±0.067)	2.933(±0.110)	0.998(±0.018)	1.663(±0.056)	3.168(±0.093)	0.999(±0.015)
III.4	1.857(±0.094)	3.007(±0.156)	0.996(±0.026)	1.802(±0.075)	3.222(±0.124)	0.998(±0.020)
III.5	1.913(±0.075)	3.033(±0.124)	0.997(±0.020)	1.830(±0.057)	3.281(±0.095)	0.999(±0.016)
III.6	1.582(±0.122)	3.196(±0.201)	0.994(±0.033)	1.578(±0.050)	3.377(±0.082)	0.999(±0.014)
III.7	1.528(±0.027)	2.820(±0.045)	1.000(±0.007)	1.603(±0.037)	3.118(±0.061)	0.999(±0.010)

Compared to the nonsubstituted derivate, the retention of spirohydantoins with nonpolar methyl substituent R in most cases is higher. Higher retention was also observed in the presence of halogens; the highest retention was observed for bromide as a substituent.The type of organic solvent used additionally influence the R_M^0 value. Generally, properties of solvent are described by Hansen's solubility parameters,[48] i.e. dipole interactions (δ_p), dispersion interactions (δ_d), and the ability of the solvent to form hydrogen bonds (δ_h), as well as the dielectric constant (ε).[49]

Based on the values in Table 2 can be noticed that the higher the polarity of the organic solvent (δp and ε) is, the

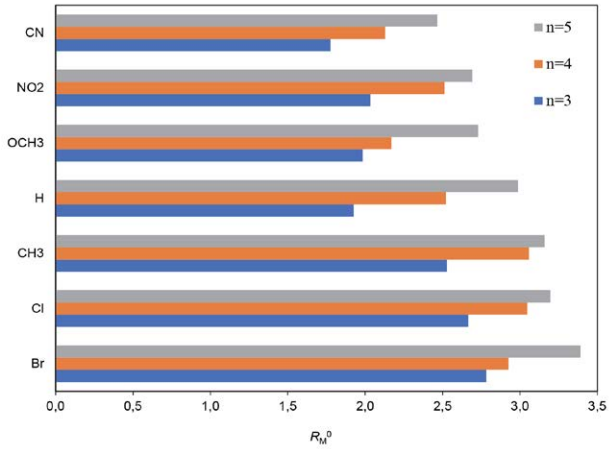

Figure 2: The impact of the size of cycloalkyl group and the substituent R on R_M^0 values in mobile phase ethanol-water.

higher are R_M^0 values. Generally, solvents increase the R_M^0 in the following order:

n-propanol < *t*-butanol < *i*-propanol < ethanol.

The highest R_M^0 values are observed with ethanol and the lowest with *n*-propanol. This can be explained by the fact that ethanol is the most polar of all used solvents, and has the greatest tendency toward polar interactions of all used organic solvents. Compared to other solvents, ethanol has the highest dipole interactions, the ability to form hydrogen bond, as well as the dielectric constant.

3. 2. QSRR

In order to describe the quantitative relationship between chromatographic lipophilicity parameters and molecular descriptors QSRR modeling was performed. QSRR models were also created for additional four aqueous mobile phases: acetone-water, acetonitrile-water, tetrahydrofuran-water, and 1,4-dioxane-water - aprotic organic solvents (results published before).[50] In total, chromatographic lipophilicity parameters obtained for two types of organic solvents: four protic and four aprotic organic solvents were analyzed using QSRR. The obtained models are listed in Tables 3 and 4. The statistical quality of the models was assessed by the coefficient of adjusted determination R^2_{adj}, the standard error of estimate (s), the probability value (p), the Fisher test for significance of the equation (F-value), and the predictive ability of the models (Q^2). The acceptance level for the individual independent variables was set at the 95% significance level.

Table 3: QSRR equations obtained for protic solvents.

Regression equations	Q^2	No. models
$R_M{}^0{}_{ethanol}$ = 0.747(±0.121) + 0.649 (±0.041)ClogP p(intercept) = 0.000; p(ClogP) = 0.000 R^2_{adj} = 0.925; F = 247.928; p = 0.000	0.929	1
$R_M{}^0{}_{ethanol}$ = 0.437(±0.164) + 0.776 (±0.058)miLogP p(intercept) = 0.015; p(miLogP) = 0.000 R^2_{adj} = 0.900; F = 181.297; p = 0.000	0.905	2
$R_M{}^0{}_{n\text{-}propanol}$ = 1.330(±0.274) + 0.244 (±0.030)ClogP – 0.012(±0.005)IAC p(intercept) = 0.000; p(ClogP) = 0.000; p(IAC) = 0.026 R^2_{adj} = 0.760; F = 32.628; p = 0.000	0.784	3
$R_M{}^0{}_{n\text{-}propanol}$ = 0.906 (±0.423) – 0.345 (±0.074)Sv + 0.343(±0.067)Sp p(intercept) = 0.046; p(Sv) = 0.000; p(Sp) = 0.000 R^2_{adj} = 0.565; F = 13.990; p = 0.000	0.609	4
$R_M{}^0{}_{i\text{-}propanol}$ = 0.166(±0.111) + 0.469 (±0.039)miLogP p(intercept) = 0.150; p(miLogP) = 0.000 R^2_{adj} = 0.878; F = 145.597; p = 0.000	0.885	5
$R_M{}^0{}_{i\text{-}propanol}$ = 0.380(±0.101) + 0.384 (±0.035)ClogP p(intercept) = 0.001; p(ClogP) = 0.000 R^2_{adj} = 0.860; F = 123.471; p = 0.000	0.867	6
$R_M{}^0{}_{t\text{-}butanol}$ = 0.832(±0.092) + 0.256 (±0.032)ALOGP p(intercept) = 0.000; p(ALOGP) = 0.000 R^2_{adj} = 0.755; F = 62.655; p = 0.000	0.767	7
$R_M{}^0{}_{t\text{-}butanol}$ = −0.374 (±0.292) – 0.087 (±0.019)Se + 0.209(±0.033)Sp p(intercept) = 0.217; p(Se) = 0.000; p(Sp) = 0.000 R^2_{adj} = 0.721; F = 26.835; p = 0.000	0.749	8

Table 4: QSRR equations obtained for aprotic solvents.

Regression equations	Q^2	No. model
$R_M{}^0{}_{acetonitrile}$ = 1.926(±0,098) + 0.187(±0.019)MLOGP2 p(intercept) = 0.000; p(MLOGP2) = 0.000 R^2_{adj} = 0.825; F = 95.135; p = 0.000	0.834	9
$R_M{}^0{}_{acetonitrile}$ = −1.084 (±0.992) + 0.527 (±0.109)Sp – 0.244 (±0.060)nAT p(intercept) = 0.255; p(Sp) = 0.000; p(nAT) = 0.000 R^2_{adj} = 0.543; F = 12.904; p = 0.000	0.589	10
$R_M{}^0{}_{acetone}$ = 0.301(±0.154) + 0.891(±0.057)logP p(intercept) = 0.066; p(logP) = 0.000 R^2_{adj} = 0.924; F = 242.976; p = 0.000	0.927	11
$R_M{}^0{}_{acetone}$ = −2.842 (±1.005) + 0.615 (±0.119)Sp – 0.261 (±0.065)nAT p(intercept) = 0.011; p(Sp) = 0.000; p(nAT) = 0.000 R^2_{adj} = 0.624; F = 17.609; p = 0.000	0.662	12
$R_M{}^0{}_{THF}$ = −4.185(±0.494) + 0.791(±0.034) miLogP + 1.516(±0.171)Uc – 0.029(±0.006)Pol p(intercept) = 0.000; p(miLogP) = 0.000; p(Uc) = 0.000; p(Pol) = 0.000 R^2_{adj} = 0.980; F = 322.182; p = 0.000	0.985	13
$R_M{}^0{}_{THF}$ = −1.993(±0.422)+0.005(±0.002)V_x−0.555(±0.117)logS+0.072(±0.625)logD p(intercept) = 0.000; p(V_x) = 0.012; p(logS) = 0.000; p(logD) = 0.264 R^2_{adj} = 0.898; F = 59.766; p = 0.000	0.926	14
$R_M{}^0{}_{1,4\text{-dioxane}}$ = −2.477(±0.800) + 0.999(±0.052)logP + 0.748(±0.227)Uc p(intercept) = 0.006; p(logP) = 0.000; p(Uc) = 0.000 R^2_{adj} = 0.952; F = 198.896; p = 0.000	0.957	15
$R_M{}^0{}_{1,4\text{-dioxane}}$ = 1.442(±0.101) + 0.241(±0.020)MLOGP2 p(intercept) = 0.000; p(MLOGP2) = 0.000 R^2_{adj} = 0.879; F = 146.809; p = 0.000	0.885	16

From Tables 3 and 4 can be seen that the calculated logarithm of the partition coefficient, log *P* (ClogP, miLogP, ALOGP, MLOGP2, logP) is the dominant descriptor in the most of the QSRR models. Moreover, half of the models are monoparametric (namely models nos. (1), (2), (5), (6), (7), (9), (11), and (16)) with partition coefficient as a descriptor; the most of them calculated for protic solvents.

The regression coefficients of the descriptor log *P* in monoparamertic as well as multiparametric QSRR models were always positive. As expected the higher the chromatographic lipophilicity, calculated log *P* increases. Besides log *P* in some of the models was present Sp (sum of atomic polarizability) (nos. (4), (8), (10), and (12)). Furthermore, two more descriptors are present in the models namely nAT (number of atoms) (models nos. (10) and (12)) and Uc (number of unsaturated bonds) (models nos. (13) and (15)). In five out of eight QSRR models the partition coefficient (log *P*) was no present. These are models nos. (4), (8), (10), (12), and (14). These five models are obtained for the following organic solvents: n-propanol, t-butanol, acetonitrile, acetone, and THF.

The value of the adjusted coefficient of determination (R^2_{adj}) ranging from 0.755 to 0.980 indicates that in QSRR models (1-3), (5-7), (9), (11), (13), (15) and (16) exist strong dependence between the variables. High F-parameter values indicate good data compatibility. The predictive ability of the QSRR models is described in the validation coefficient Q^2. The calculated models are valid if the value of Q^2 is greater than 0.7, while low values for Q^2 indicate a low predictive ability of the model. The values of the validation coefficient Q^2 (Tables 3 and 4) for these QSRR models range from 0.767 to 0.985. A high value of R^2_{adj}, F, and p indicates that all proposed QSRR models are statistically significant. High values of the validation coefficient Q^2 indicated that the models are reliable for predicting the chromatographic lipophilicity of similar compounds and their chromatographic behavior.

Based on the value of the statistical parameter Q^2 can be concluded that models nos. (4), (10), and (12) are evaluated as models with poor predictive characteristics. The values of the Q^2 parameter indicate that models nos. (8) and (14) have good predictive capabilities. However, in the model no. (8) it is observed that the regression coefficient describing the intercept is not statistically significant ($p > 0.05$), while in the model no. (14), it is noticed that the regression coefficient describing the molecular descriptor logD is not statistically significant ($p>0.05$). Therefore, QSRR models nos. (4), (8), (10), (12), and (14) are less suitable for the prediction of the chromatographic lipophilicity parameter. Accordingly, the mentioned models will be omitted from further consideration.

The multiparametric QSRR model no. (3) for the chromatographic system with n-propanol as an organic solvent include molecular descriptors ClogP (partition coefficient) and IAC (total information index on atomic composition). The negative value of the coefficient for IAC indicates that the dependent variable and molecular descriptor of IAC are negatively correlated. The coefficient value of the molecular descriptor of IAC is very small. However, based on the values of molecular descriptors in Table S1, it can be concluded that the contribution to lipophilicity of a molecular descriptor of IAC is almost identical as it is the contribution of the molecular descriptor of ClogP.

Based on the values of the statistical parameters R^2_{adj} and F, it can be noticed that the QSRR model no. (13) is the best-rated of all the presented models (Tables 3 and 4). The QSRR model no. (13) calculated for tetrahydrofuran as an organic solvent is multiparametric. This model is described with three molecular descriptors (miLogP, Uc, and Pol). The regression coefficient next to the molecular descriptor of Pol is negative and this indicates a negative correlation with dependent variable. The molecular descriptor Uc and miLogP display much higher contribution to lipophilicity than the molecular descriptor of Pol. Besides, Q^2 indicates that this model has the best predictive characteristics suggesting that solvents such as THF, which is seldomly used as a modifier, should be considered more often.

The multiparametric QSRR model no. (15) calculated for the 1,4-dioxane contains molecular descriptors logP (partition coefficient) and Uc (unsaturation count). The regression coefficients of both molecular descriptors are positive. The values of the regression coefficients indicate that both molecular descriptors significantly contribute to lipophilicity.

The experimental and predicted R_M^0 values using QSRR models are compared and presented in Figure 3.

Figure 3 shows linear dependence of the best QSRR model for predicting the chromatographic parameter of lipophilicity.

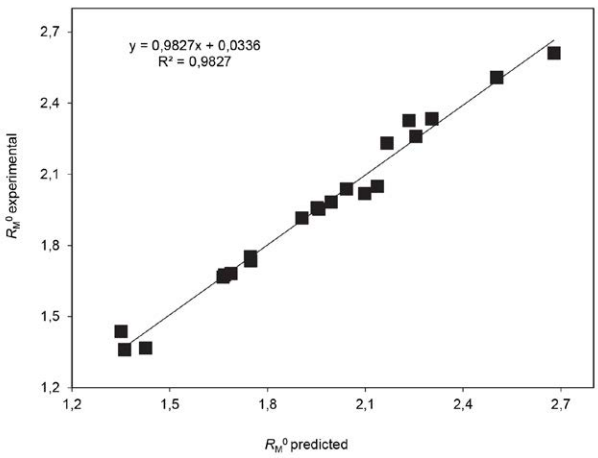

Figure 3: Comparison of experimental and predicted R_M^0 values calculated from the QSRR model no. (13) for the THF-water mobile phase.

3. 3. External Validation of QSRR Models

In order to evaluate the validity of the obtained QSRR models additional external validation was done. The investigated set of 21 compounds was split into the training (76%) and test (24%) sets. The training set is consisted of 16 compounds namely I.2, I.4, I.5, I.6, I.7, II.1, II.2, II.3, II.4, II.7, III.1, III.2, III.3, III.5, III.6, and III.7; the test set includes 5 compounds (I.1, I.3, II.5, II.6, and III.4).

The calculated QSRR equations, using the training set, are listed in Table 5. The statistical quality of the models was assessed by the coefficient of adjusted determination R^2adj, the standard error of estimate (s), the probability value (p), and the Fisher test for significance of the equation (F-value). The acceptance level for the individual independent variables was set at the 95% significance level. Further, the statistical quality of the models was judged using different validation parameters like Q^2 and R^2_{pred}, and also some novel metrics like r_m^2(test). The calculated models are valid if the value of Q^2 is greater than 0.7. The values of R^2_{pred} and r_m^2(test) for an acceptable model should be more than 0.5.[51] The values of validation parameters Q^2, R^2_{pred}, and r_m^2(test) are provided in Table 5.

The Q^2 value (Table 5) range from 0.728 (for acetonitrile) to 0.980 (for THF). Also, the accuracy of models 19-24 was checked using validation parameters R^2_{pred} and r_m^2(test) (Table 5). The R^2_{pred} value for all QSRR models is equal and greater than 0.727, which shows good predictive ability of the model. Values of r_m^2 metrics (r_m^2(test)) more than 0.5 imply the goodness of predictions of these models. In general, high values of the statistical parameters (Q^2, R^2_{pred}, r_m^2(test), R^2_{adj}, F, and p) indicate that the models are statistically significant and convenient for predicting chromatographic lipophilicity.

The QSRR models listed in Tables 5 and 3 are very similar. Both methods (without and with splitting the data) give the models with almost identical molecular descriptors. Also, the calculated QSRR equations do not have significant variations of the statistical parameters. Slightly better statistical data of QSRR equations were obtained using internal validation, compared to external validation. This is due to the larger dataset (21 compounds), which is used for calculating equations in internal validation unlike to 16 compounds in the external validation

4. Conclusion

QSRR modeling is an important tool for processing and evaluation of the experimental chromatographic data in biomedical and chemical research.

Most calculated QSRR models include partition coefficient log *P* as molecular descriptor with the most significant influence on the chromatographic behavior of investigated compounds. Internal validation confirmed that most of the calculated QSRR models have good pre-

Table 5: QSRR equations obtained for all applied solvents.

Regression equations	Q^2	R^2_{pred}	r_m^2(test)	No. models	
$R_M{}^0{}_{ethanol}$ = 0.672(±0.123) + 0.591 (±0.041)ClogP + 0.133(±0.045)logD p(intercept) = 0.000; p(ClogP) = 0.000; p(ClogP) =0.012 R^2_{adj} = 0.949; F = 139.232; p = 0.000	0.955	0.898	0.922	17
$R_M{}^0{}_{n\text{-}propanol}$ = 1.043(±0.161) + 0.238 (±0.028)ClogP – 0.002(±0.001)ECC p(intercept) = 0.000; p(ClogP) = 0.000; p(ECC) = 0.006 R^2_{adj} = 0.849; F = 43.189; p = 0.000	0.969	0.937	0.537	18
$R_M{}^0{}_{i\text{-}propanol}$ = 0.097(±0.160) + 0.496 (±0.056)miLogP p(intercept) = 0.553; p(miLogP) = 0.000 R^2_{adj} = 0.838; F = 78.80; p = 0.000	0.849	0.963	0.843	19
$R_M{}^0{}_{t\text{-}butanol}$ = 1.267(±0.049) + 0.037 (±0.006)ALOGP2 p(intercept) = 0.000; p(ALOGP2) = 0.000 R^2_{adj} = 0.724; F = 40.45; p = 0.000	0.743	0.727	0.623	20
$R_M{}^0{}_{acetonitrile}$ = 2.031 (±0.139) + 0.168 (±0.027) MLOGP2 p(intercept) = 0.000; p(MLOGP2) = 0.000 R^2_{adj} = 0.709; F = 37.55; p = 0.000	0.728	0.931	0.770	21
$R_M{}^0{}_{acetone}$ = 0.508 (±0.158) + 0.826 (±0.058) logP p(intercept) = 0.006; p(logP) = 0.000 R^2_{adj} = 0.929; F = 199.09; p = 0.000	0.934	0.900	0.787	22
$R_M{}^0{}_{THF}$ = −1.419(±0.212)+0.025(±0.003)AMR−0.682(±0.036)MLOGP p(intercept) = 0.000; p(AMR) = 0.000; p(MLOGP) = 0.000 R^2_{adj} = 0.977; F = 325.23; p = 0.000	0.980	0.986	0.959	23
$R_M{}^0{}_{1,4\text{-}dioxane}$ = −2.348(±0.896) + 0.965(±0.068) logP + 0.731(±0.243)Uc p(intercept) = 0.021; p(logP) = 0.000; p(Uc) = 0.010 R^2_{adj} = 0.937; F = 112.739; p = 0.000	0.945	0.964	0.920	24

dictive capabilities and that they potentially provide useful information about lipophilicity. This was additionally confirmed by external validation. The exceptions are models nos. (4), (8), (10), (12), and (14), whose values of statistical parameters indicate their poor predictive properties.

The best QSRR model for prediction of the chromatographic lipophilicity parameter is model where the lipophilicity was determined using THF as an organic solvent. Therefore, solvents such as THF, which are rarely used as a modifier, should be considered more often in these kinds of studies. Since the models have good statistical parameters and high predictive accuracy the possibility of their application to predict the lipophilicity of new structurally similar compounds was confirmed.

Acknowledgments

The authors gratefully acknowledge the financial support of the Ministry of Science, Technological Development and Innovation of the Republic of Serbia (Grants No. 451-03-66/2024-03/200125 & 451-03-65/2024-03/200125.)

Supplementary Materials

The calculated descriptors of investigated compounds are listed in Table S1.

Graphs of the size impact of the cycloalkyl group and the substituent R on the values of $R_M{}^0$ for organic solvents *n*-propanol, *i*-propanol, and *t*-butanol are shown in the Figures S1-S3.

5. References

1. L. Konnert, F. Lamaty, J. Martinez, E. Colacino, *Chem. Rev.* **2017**, *117*, 13757−13809. **DOI:**10.1021/acs.chemrev.7b00067
2. J. H. Block and J. J. M. Beale, (12th ed.): Wilson and Gisvold's Textbook of Organic Medicinal and Pharmaceutical Chemistry, Lippincott Williams and Wilkins, Philadelphia, **2004**.
3. A. Czopek, H. Byrtus, A. Zagorska, A. Siwek, G. Kazek, M. Bednarski, J. Sapa, M. Pawłowski, *Pharmacol. Rep.* **2016**, *68*, 886−893. **DOI:**10.1016/j.pharep.2016.04.018
4. A. Tijsma, H. J. Thibaut, D. Franco, K. Dallmeier, J. Neyts, *Antivir. Res.* **2016**, *133*, 106−109. **DOI:**10.1016/j.antiviral.2016.07.023
5. H. Lu, D. Kong, B. Wu, Y. Wang, *Lett. Drug Des. Discov.* **2012**, *9*, 638−642. **DOI:**10.2174/157018012800673092
6. R. N. Comber, R. C. Reynolds, J. D. Friedrich, R. A. Manguikian, R. W. Buckheit Jr., J. W. Truss, W. M. Shannon, J. A. Secrist III, *J. Med. Chem.* **1992**, *35*, 3567−3572.

DOI:10.1021/jm00097a014
7. T. L. Lemke and D. A. Williams, (6th ed): Foye's Principles of Medicinal Chemistry, Lippincott Williams and Wilkins, Philadelphia, **2008**.
8. G. A. Dijkman, R. A. Janknegt, T. M.de Reijke, F. M. J. Debruyne, *J. Urol.* **1997**, *158*, 160–163. **DOI:**10.1097/00005392-199707000-00051
9. C. Carmi, A. Cavazzoni, V. Zuliani, A. Lodola, F. Bordi, P. V. Plazzi, R. R. Alfieri, P. G., Petronini, M. Mor, *Bioorg. Med. Chem. Lett.* **2006**, *16*, 4021–4025. **DOI:**10.1016/j.bmcl.2006.05.010
10. L. Jiang, B. Zeng, *Adv. Mater. Res.* **2014**, *89*, 512–515. **DOI:**10.1016/j.contraception.2013.12.017
11. C. S. A. Kumar, S. B. B. Prasad, K. Vinaya, S. Chandrappa, N. R. Thimmegowda, K. S. Rangappa, S. Swarup, *Invest. N. Drugs.* **2009**, *27*, 131–139. **DOI:**10.1007/s10637-008-9150-3
12. C. V. Kavitha, M. Nambiar, P. B. Narayanaswamy, E. Thomas, U. Rathore, C. S. A. Kumar, B. Choudhary, K. S. Rangappa, S. C. Raghavan, *PloS One.* **2013**, *8*, 1–10.
13. I. Gomez-Monterrey, G. Santelli, P. Campiglia, D. Califano, F. Falasconi, C. Pisano, L. Vesci, T. Lama, P. Grieco, E. Novellino, *J. Med. Chem.* **2005**, *48*, 1152–1157. **DOI:**10.1021/jm0408565
14. L. H. Ramadani, O. Talhi, N. Taibi, L. Delort, C. Decombat, A. Silva, K. Bachari, M. P. Vasson, F. Caldefie-Chezet, *Anticancer Res.* **2016**, *36*, 6399–6408. **DOI:**10.21873/anticanres.11237
15. A. Atrrog, M. Natić, T. Tosti, D. Milojković-Opsenica, I. Đorđević, V. Tešević, Z. Tešić, *Biomed. Chromatogr.* **2009**, *23*, 250–256. **DOI:**10.1002/bmc.1091
16. A. Czopek, M. Kołaczkowski, A. Bucki, H. Byrtus, M. Pawłowski, G. Kazek, A. Wesołowska, *Bioorg. Med. Chem.* **2015**, *23*, 3436–3447. **DOI:**10.1016/j.bmc.2015.04.026
17. E. H. Rabtti, M. Natić, D. Milojković-Opsenica, J. Trifković, I. Vucković, V. Vajs, Ž. Tešić, *J. Braz. Chem. Soc.* **2012**, *23*, 522–530.
18. A. R. Katritzky, M. Kuanar, S. Slavov, C. D. Hall, M. Karelson, I. Kahn, D. A. Dobchev, *Chem. Rev*. **2010**, *110*, 5714–5789. **DOI:**10.1021/cr900238d
19. R. Kaliszan, *Chem. Rev.* **2007**, *107*, 3212–3246. **DOI:**10.1021/cr068412z
20. K. Heberger, J. Chromatogr. A. **2007**, *1158*, 273–305. **DOI:**10.1016/j.chroma.2007.03.108
21. B. J. Neely, S. V. Madihally, R. L. Robinson, K. A. M. Gasem, *J. Pharm. Sci.* **2009**, *98*, 4069–4084. **DOI:**10.1002/jps.21678
22. R. Kaliszan, T. Baczek, A. Bucinski, B. Buszewski, M. Sztupecka, *J. Sep. Sci.* **2003**, *26*, 271–282. **DOI:**10.1002/jssc.200390033
23. M. Golubović, J. Protić, A. Otašević, B. Zečević, *Talanta* **2016**, *150*, 190–197. **DOI:**10.1016/j.talanta.2015.12.035
24. P. R. Talebi, M. Schuster, G. Shellie, R. A. Szucs, R. Haddad, *J. Chromatogr. A* **2015**, *1424*, 69–76. **DOI:**10.1016/j.chroma.2015.10.099
25. L. T. Qin, S. S. Liu, F. Chen, Q. S. Wu, *J. Sep. Sci.* **2013**, 36, 1553–1560. **DOI:**10.1002/jssc.201300069
26. Y. Bodzioch, K. Durand, A. Kaliszan, R. Baczek, T. Vander Heyden, *Talanta* **2010**, *81*, 1711–1718. **DOI:**10.1016/j.talanta.2010.03.028
27. P. Riahi, S. Pourbasheer, E. Ganjali, M. R. Norouzi, *J. Hazard. Mater.* **2009**, *166*, 853–859. **DOI:**10.1016/j.jhazmat.2008.11.097
28. S. Riahi, M. R. Ganjali, E. Pourbasheer, P. Norouzi, *Chromatographia* **2008**, *67*, 917–922. **DOI:**10.1365/s10337-008-0608-4
29. R. Kaliszan, and T. Baczek, Recent Adv. *QSAR Stud.* **2010**, *8*, 223–259. **DOI:**10.1007/978-1-4020-9783-6_8
30. E. Rutkowska, K. Paja.k, K. Jóźwiak, *Acta Pol. Pharm.* **2013**, *70*, 3–18.
31. J. A. Platts, S. P. Oldfield, M. M. Reif, A. Palmucci, E. Gabano, D. Osella, J. Inorg. Biochem. **2006**, *100*, 1199–1207. **DOI:**10.1016/j.jinorgbio.2006.01.035
32. S. S. P. Wahajuddin, K. S. R. Raju, A. Nafis, G. K. Jain, *J. Pharm. Biomed. Anal.* **2012**, *67–68*, 71–76. **DOI:**10.1016/j.jpba.2012.03.048
33. R. Mannhold, G. I. Poda, C. Ostermann, I. V. Tetko, *J. Pharm. Sci.* **2009**, *98*, 861–893. **DOI:**10.1002/jps.21494
34. L. R. Jevrić, M. Ž. Karadžić, A. I. Mandić, S. O. Podunavac-Kuzmanović, S. Z. Kovačević, A. R. Nikolić, A. M. Oklješa, M. N. Sakač, K. M. Penov Gaši, S. Z. Stojanović, *J. Pharm. Biomed. Anal.* **2017**, *134*, 27–35. **DOI:**10.1016/j.jpba.2016.11.015
35. M. Ž. Karadžić, D. M. Lončar, G. Benedeković, I. Kovačević, V. Popsavin, S. Z. Kovačević, L. R. Jevrić, S. O. Podunavac-Kuzmanović, *Eur. J. Pharm. Sci.* **2017**, *105*, 99–107. **DOI:**10.1016/j.ejps.2017.05.006
36. M. Zapadka, M. Kaczmarek, B. Kupcewicz, P. Dekowski, A. Walkowiak, A. Kokotkiewicz, M. Łuczkiewicz, A. Buciński, *J. Pharm. Biomed. Anal.* **2019**, *164*, 681–689. **DOI:**10.1016/j.jpba.2018.11.024
37. M. A. Fouad, E. H. Tolba, M. A. El-Shal, A. M. El Kerdawy, *J. Chromatogr. A* **2018**, *1549*, 51–62. **DOI:**10.1016/j.chroma.2018.03.042
38. J. Trifunović Ristovski, N. Janković, V. Borčić, S. Jain, Z. Bugarčić, M. Mikov, *J. Pharm. Biomed. Anal.* **2018**, *155*, 42–49. **DOI:**10.1016/j.jpba.2018.03.038
39. E. C. Bate-Smith, R. G. Westall, Biochim. *Biophys. Acta.* **1950**, *4*, 427–440. **DOI:**10.1016/0006-3002(50)90049-7
40. E. Soczewinski, G. Matysik, *J. Chromatogr. A* **1968**, *32*, 458–471. **DOI:**10.1016/S0021-9673(01)80519-7
41. J. Dorsey, M. Khaledi, *J. Chromatogr. A* **1993**, *656*, 485–499. **DOI:**10.1016/0021-9673(93)80815-P
42. DRAGON for windows (Software for molecular descriptor calculation), Version 5.5–Talete srl, http://www.talete.mi.it 2007
43. Chemdraw Ultra 7.0 and Chem3D Ultra, Cambridge Soft Corporation, Cambridge, USA, http://cambridgesoft.com
44. http://www.molinspiration.com (accessed April 3, 2019)
45. J. Dong, N. N. Wang, Z. J. Yao, *J. Cheminform.* **2018**, *10*, 1–11. **DOI:**10.1186/s13321-018-0283-x
46. L.-T. Qin, Y.-H. Chen, X. Zhang, L.-Y. Mo, H.-H. Zeng, Y.-P. Liang, *Chemosphere* **2018**, *198*, 122-129. **DOI:**10.1016/j.chemosphere.2018.01.142

47. A. Golbraikh, J. Tropsha, *J. Mol. Graph. Model.* **2002**, *20,* 269–276. **DOI:**10.1016/S1093-3263(01)00123-1
48. C. M. Hansen, (2nd ed.): Hansen Solubility Parameters, Taylor & Francis Group, New York, **2007**. **DOI:**10.1201/9781420006834
49. C. Reichardt and T. Welton, (4th ed.): Solvents and Solvent Effect in Organic Chemistry, Wiley VCH Verlag GmbH & Co. KGaA, Weinheim, **2011**.
50. K. Tot, A. Lazić, T. Djaković Sekulić, *J. Liq. Chromatogr. Relat. Technol.* **2020**, *43*, 925–933. **DOI:**10.1080/10826076.2020.1856137
51. P. K. Ojha, K. Roy, *Chemom. Intell. Lab. Sys.* **2011**, *109*, 146–161. **DOI:**10.1016/j.chemolab.2011.08.007

Povzetek

Izvedli smo analizo kvantitativnih razmerij med strukturo in retencijo (QSRR) na kromatografskih parametrih lipofilnosti izbranih spirohidantoinov. Uporabili smo tehnike multiple linearne regresije (MLR) za izgradnjo modelov QSRR. Kromatografski parametri lipofilnosti so bili določeni z obratno-fazno tankoslojno kromatografijo. Kromatografske analize smo izvedli na C-18 modificiranem silikagelu z dvokomponentno mobilno fazo, sestavljeno iz vode in protičnega organskega topila (etanol, n-propanol, i-propanol ali t-butanol) v različnih razmerjih. Izdelali smo tudi QSRR modele za dodatne štiri vodne mobilne faze: aceton-voda, acetonitril-voda, tetrahidrofuran-voda in 1,4-dioksan-voda (rezultati so bili objavljeni prej). Skupno smo v tej QSRR študiji proučevali kromatografske parametre lipofilnosti, pridobljene za dve vrsti organskih topil. Napovedno sposobnost vsakega modela smo ocenili z notranjo in zunanjo validacijo. Izmed pridobljenih modelov QSRR za napoved kromatografskega parametra lipofilnosti se je za najboljšega izkazal za tetrahidrofuran kot organsko topilo.

DOI: 10.17344/acsi.2024.8640 *Acta Chim. Slov.* **2024,** *71,* 236–243

Scientific paper

Synthesis, Crystal Structures and Urease Inhibition of Copper(II) and Zinc(II) Complexes Derived from *N,N'*-Bis(4-bromosalicylidene)-1,3-propanediamine

Hai-Ying Chen,[1,2] Rundong Lu,[3] Jinkai Lei,[3] Jiacheng Liu,[3] Chi Liu,[3] Liuxiu Chen[3] and Wu Chen[3,*]

[1] *Engineering Research Center of Clean Production in Textile Printing and Dyeing, Ministry of Education, Wuhan 430073, P. R. China*

[2] *School of Fashion, Wuhan Textile University, Wuhan 430200, P. R. China*

[3] *National Engineering Laboratory for Advanced Yarn and Fabric Formation and Clean Production, Wuhan Textile University, Wuhan 430200, P. R. China*

* *Corresponding author: E-mail: 86082321@qq.com*

Received: 01-23-2024

Abstract

A new tetranuclear copper(II) complex $[Cu_4L_2(N_3)_2(CH_3OH)_2](NO_3)_2{\cdot}4CH_3OH$ (**1**) and a new trinuclear zinc(II) complex $[Zn_3L_2(CH_3COO)_2]$ (**2**) have been prepared from the bis-Schiff base *N,N'*-bis(4-bromosalicylidene)-1,3-propanediamine (H_2L) with copper nitrate and zinc acetate, respectively, in the presence of sodium azide. The complexes were characterized by elemental analysis, IR and UV-Vis spectroscopy. Molecular structures of both complexes were confirmed by single crystal X-ray determination. The Cu(II) atoms in complex **1** are bridged by phenolate oxygen atoms and end-on azide ligands. The Zn(II) atoms in complex **2** are bridged by phenolate oxygen atoms and acetate ligands. The Cu(II) atoms in complex **1** are in square planar and square pyramidal coordination. The Zn(II) atoms in complex **2** are in square pyramidal and octahedral coordination. The Schiff base ligand coordinates to the metal atoms through two phenolate O and two imino N atoms. The biological assay reveals that the copper(II) complex has effective urease inhibition.

Keywords: Schiff base; copper(II) complex; zinc(II) complex; crystal structure; urease inhibition

1. Introduction

Urease, a Ni-containing enzyme, can catalyze the hydrolysis of urea to form ammonia rapidly.[1] The product is harmful for environment, agriculture and animals. In the last few years, a number of compounds have been reported to have urease inhibitory activities.[2] Schiff bases bearing azomethine groups (C=N) have widely biological applications like antibacterial,[3] antioxidant,[4] antitumor,[5] anti-inflammatory[6] and cytotoxic,[7] *etc*. In addition, Schiff bases readily coordinate to transition metal ions to form complexes with versatile structures.[8] Recent research indicated that Schiff bases and their metal complexes have shown urease inhibitory activities.[9] Copper and zinc are biological active trace elements in biological systems. In continuation of our work,[10] and aiming at obtaining new urease inhibitors, a copper(II) complex $[Cu_4L_2(N_3)_2(CH_3OH)_2](NO_3)_2{\cdot}4CH_3OH$ (**1**) and a zinc(II) complex $[Zn_3L_2(CH_3COO)_2]$ (**2**), where L is deprotonated form of *N,N'*-bis(4-bromosalicylidene)-1,3-propanediamine (H_2L) are present.

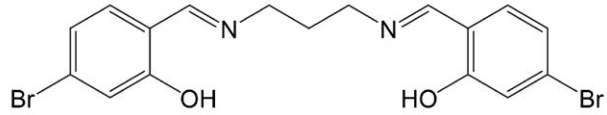

Scheme 1. H_2L

2. Experimental

2. 1. Materials and Methods

4-Bromosalicylaldehyde, propane-1,3-diamine, copper nitrate, zinc acetate and sodium azide were purchased from Aldrich. Solvent and other chemicals were obtained from Xiya Chemical Co. Ltd. CHN elemental analyses were performed on a Perkin-Elmer 240C elemental analyzer. Infrared

spectra were recorded on a Jasco FT/IR–4000 spectrophotometer. Electronic absorption spectra were recorded with a Lambda 35 spectrophotometer. ^{1}H NMR and ^{13}C NMR spectra for H_2L were recorded on a Bruker 500 MHz spectrometer. Single crystal X-ray diffraction was carried out with a Bruker Apex II diffractometer. The molar conductivities were measured at 25 °C with a Synstronics conductivity bridge.

2. 2. Synthesis of *N,N'*-Bis(4-bromosalicylidene)-1,3-propanediamine (H_2L)

4-Bromosalicylaldehyde (4.0 g, 0.020 mol) was dissolved in 50 mL MeOH, to which was added dropwise 40 mL methanolic solution of propane-1,3-diamine (0.74 g, 0.010 mol). The mixture was stirred for 30 min under reflux. The solvent was removed by distillation under reduced pressure. The yellow solid residue was recrystallized from MeOH to give yellowish crystalline product. Yield 3.8 g (86%). Anal. Calcd for $C_{17}H_{16}Br_2N_2O_2$: C, 46.39; H, 3.66; N, 6.36%. Found: C, 46.51; H, 3.73; N, 6.27%. FT–IR data (KBr, cm^{-1}): ν(C=N) 1645, ν(Ar–O) 1296. UV–Vis data [10^{-3} mol L^{-1} in MeOH, λ/nm (ε/L mol^{-1} cm^{-1})]: 225 (17,530), 260 (12,380), 320 (4,535), 406 (2,720). ^{1}H NMR (500 MHz, d_6-DMSO, ppm): δ 11.38 (s, 2H, OH), 8.58 (s, 2H, CH=N), 7.53 (d, 2H, ArH), 7.35 (s, 2H, ArH), 7.15 (d, 2H, ArH), 3.72 (t, 4H, CH_2), 2.07 (m, 2H, CH_2). ^{13}C NMR (126 MHz, d_6–DMSO, ppm) δ 163.23, 156.12, 132.31, 125.02, 123.53, 120.38, 116.71, 59.71, 32.33.

2. 3. Synthesis of $[Cu_4L_2(N_3)_2(CH_3OH)_2](NO_3)_2{\cdot}4CH_3OH$ (1)

The Schiff base H_2L (0.44 g, 1.0 mmol) was dissolved in MeOH (30 mL), to which was added a methanolic solution of copper nitrate trihydrate (0.48 g, 2.0 mmol). The mixture was stirred at room temperature for 10 min. Then, sodium azide (0.13 g, 2.0 mmol) was added to the mixture. The final mixture was further stirred at room temperature for 30 min and filtered. The filtrate was kept still in air for a week to give brown block-shaped single crystals. Yield: 0.43 g (56%). Anal. Calcd for $C_{40}H_{52}Br_4Cu_4N_{12}O_{16}$: C, 31.39; H, 3.42; N, 10.98. Found: C, 31.25; H, 3.50; N, 10.87%. FT–IR data (KBr, cm^{-1}): 2072 ν(N_3), 1628, 1617 ν(C=N), 1584, 1545, 1469, 1386, 1353, 1277, 1213, 1139, 1072, 915, 820, 797, 689, 610, 596, 557, 467. UV-Vis data [10^{-3} mol L^{-1} in methanol, λ/nm (ε/L mol^{-1} cm^{-1})]: 225 (18,270), 250 (13,550), 275 (8,335), 360 (3,127). Λ_M (10^{-3} M in MeOH): 235 Ω^{-1} cm^2 mol^{-1}.

2. 4. Synthesis of $[Zn_3L_2(CH_3COO)_2]$ (2)

The Schiff base H_2L (0.44 g, 1.0 mmol) was dissolved in MeOH (30 mL), to which was added a methanolic solution of zinc acetate dihydrate (0.44 g, 2.0 mmol). The mixture was stirred at room temperature for 30 min and filtered. The filtrate was kept still in air for a week to give colorless block-shaped single crystals. Yield: 0.30 g (51%).

Table 1. Crystal data for the complexes

	1	**2**
Formula	$C_{40}H_{52}Br_4Cu_4N_{12}O_{16}$	$C_{38}H_{34}Br_4N_4O_8Zn_3$
FW	1530.74	1190.44
Crystal shape/colour	block/brown	block/colorless
Crystal size /mm	0.21 × 0.18 × 0.18	0.33 × 0.32 × 0.32
Crystal system	Triclinic	Monoclinic
Space group	*P*Ī	*C*2/*m*
a (Å)	10.838(2)	15.6867(11)
b (Å)	10.836(2)	13.6689(10)
c (Å)	12.548(2)	10.9660(12)
α (°)	75.559(1)	90
β (°)	75.559(1)	107.335(1)
γ (°)	85.902(1)	90
V (Å^3)	1381.9(4)	2244.5(3)
Z	1	2
λ (MoK*α*) (Å)	0.71073	0.71073
T (K)	298(2)	298(2)
μ (Mo*Kα*) (cm^{-1})	4.482	5.202
R_{int}	0.0658	0.0278
Reflections/parameters	5521/351	6057/141
Unique reflections	4041	2193
Observed reflections [$I \geq 2\sigma(I)$]	1348	1787
Restraints	1	0
Goodness of fit on F^2	0.815	1.077
R_1, wR_2 [I ³ 2$s(I)$]	0.0887, 0.2053	0.0275, 0.0616
R_1, wR_2 (all data)	0.2055, 0.2463	0.0367, 0.0639

Anal. Calcd for $C_{38}H_{34}Br_4N_4O_8Zn_3$: C, 38.34; H, 2.88; N, 4.71. Found: C, 38.46; H, 2.81; N, 4.80%. FT-IR data (KBr, cm^{-1}): 1628 ν(C=N), 1580, 1529, 1473, 1453, 1425, 1402, 1386, 1293, 1201, 1137, 1070, 915, 848, 786, 599, 537, 456. UV–Vis data [10^{-3} mol L^{-1} in methanol, λ/nm (ε/L mol^{-1} cm^{-1})]: 240 (14,670), 270 (8,150), 345 (4,030). Λ_M (10^{-3} M in MeOH): 32 Ω^{-1} cm^2 mol^{-1}.

2. 5. X-Ray Crystallography

X-ray diffraction data for the copper(II) and zinc(II) complexes were collected at 298(2) K with graphite–monochromated Mo Kα radiation (0.71073 Å). The collected data were reduced with SAINT.[11] Multi-scan absorption correction was performed with SADABS.[12] Structures of the complexes were solved by direct method with SHELX-TL, and refined against F^2 by full-matrix least-squares method.[13] All non-hydrogen atoms the complexes were refined anisotropically. The H8 atom of complex **1** was located from a difference Fourier map and refined with O–H distance restrained to 0.85(1) Å. The remaining H atoms were placed in calculated positions and constrained to ride on their parent atoms. Crystallographic data for the complexes are summarized in Table 1. Selected bond lengths and angles are given in Table 2.

Table 2. Selected bond lengths (Å) and angles (°) for the complexes

1			
Cu1–N1	1.954(12)	Cu1–N2	1.891(13)
Cu1–O1	1.957(10)	Cu1–O2	1.960(9)
Cu2–N3	1.951(11)	Cu2–O1	1.988(9)
Cu2–O2	1.993(10)	Cu2–N3A	2.003(11)
Cu2–O8	2.273(12)		
N2–Cu1–N1	99.5(5)	N2–Cu1–O1	170.6(5)
N1–Cu1–O1	89.9(5)	N2–Cu1–O2	92.0(5)
N1–Cu1–O2	167.9(5)	O1–Cu1–O2	78.7(4)
N3–Cu2–O1	101.6(4)	N3–Cu2–O2	165.6(5)
O1–Cu2–O2	77.2(4)	N3–Cu2–N3A	79.0(5)
O1–Cu2–N3A	162.5(5)	O2–Cu2–N3A	97.8(4)
N3–Cu2–O8	93.4(5)	O1–Cu2–O8	101.2(4)
O2–Cu2–O8	100.9(4)	N3–Cu2–O8A	96.2(5)

Symmetry code for A: 1 – *x*, 1 – *y*, 1 – *z*

2			
Zn1–O1	2.0634(17)	Zn1–O2	1.998(3)
Zn1–N1	2.058(2)	Zn2–O3	2.069(2)
Zn2–O1	2.1275(17)		
O2–Zn1–N1A	101.74(8)	O2–Zn1–N1	101.74(8)
N1–Zn1–N1A	93.34(13)	O2–Zn1–O1A	99.14(8)
N1–Zn1–O1A	158.21(9)	O2–Zn1–O1	99.15(8)
N1–Zn1–O1	88.42(8)	O1–Zn1–O1A	82.18(10)
O3–Zn2–O3A	180	O3–Zn2–O1B	92.06(7)
O3–Zn2–O1	87.94(7)	O1–Zn2–O1A	79.20(9)
O1–Zn2–O1AA	100.80(9)		

Symmetry codes: A: *x*, 1 – *y*, *z*; B: 1 – *x*, 1 – *y*, 1 – *z*; AA: 1 – *x*, *y*, 1 – *z*.

3. Results and Discussion

3. 1. Synthesis

The Schiff base compound H_2L was prepared by reaction of 2:1 molar ratio of 4-bromosalicylaldehyde and propane-1,3-diamine in MeOH. The copper(II) and zinc(II) complexes were prepared by the self-assembly of H_2L with metal salts in MeOH (Scheme 2). Single crystals of both complexes were generated from their methanolic solution. Molar conductivities of complexes **1** and **2** in methanolic solution at concentration of 1.0×10^{-3} mol L^{-1} are 235 and 32 Ω^{-1} cm^2 mol^{-1}, respectively, indicating the 1:2 electrolytic and non-electrolytic nature.[14]

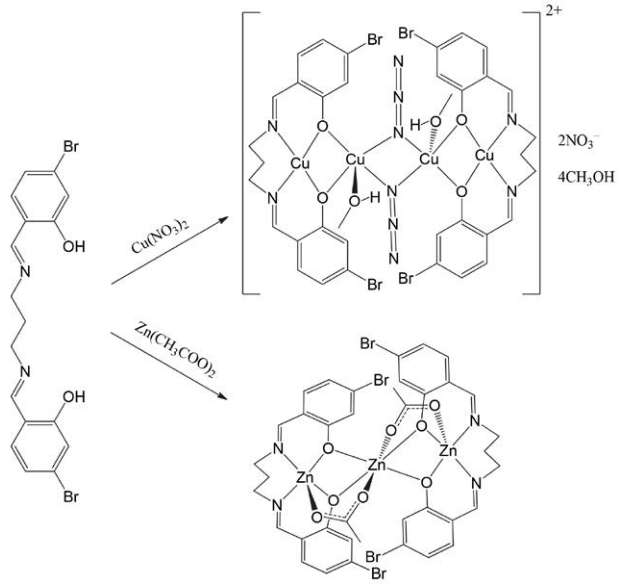

Scheme 2. The synthetic procedure for the complexes

3. 2. Structure Description of Complex 1

Molecular structure of the tetranuclear copper(II) complex is shown in Figure 1. The compound contains a copper(II) complex cation, two nitrate anions and four methanol molecules of crystallization. The Cu···Cu distances are 3.002(2) and 3.051(2) Å, respectively. The compound possesses crystallographic inversion center symmetry. The center is located at the midpoint of the two inner Cu(II) atoms. The Schiff base ligand coordinates to the Cu(II) atoms through the imino N and phenolate O atoms, generating three six-membered chelate rings. The outer Cu1 atom is coordinated by two imino N (N1, N2) and two phenolate O (O1, O2) atoms, forming square planar coordination. The distance between the Cu1 atom and the O4 atom of a methanol molecule is about 2.45 Å. If consider this proximity, the geometry can be considered as square pyramidal. The Cu1 atom deviates from the least-squares plane defined by the four donor atoms by 0.029(2) Å. The inner Cu2 atom is in square pyramidal coordina-

tion, with two phenolate O (O1, O2) of the Schiff base ligand and two N atoms (N3, N3A) from two azide ligands defining the basal plane, and with the methanol O atom (O8) at the apical site. The Cu2 atom deviates from the least-squares plane defined by the four basal donor atoms by 0.273(2) Å. The τ value for Cu2 coordination is 0.05, which suggests a typical square pyramidal geometry.[15] There are three four-membered chelate rings (Cu1–O1–Cu2–O2, Cu2–N3–Cu2A–N3A, Cu1A–O1A–Cu2A–O2A) in the complex molecule, which leads to the deviation of the square planar and square pyramidal geometries. The square pyramidal geometry is distorted, which is demonstrated from the *cis* and *trans* bond angles of 77.2(4)–101.6(4)° and 162.5(5)–165.6(5)°, respectively at the basal plane, and from the angles among the apical and basal donor atoms of 93.4(5)–101.2(4)°. The outer and inner Cu(II) atoms are bridged by two phenolate O atoms, and the two inner Cu(II) atoms are bridged by two end-on azide ligands. The bond lengths around the Cu(II) atoms are within normal values with the Schiff base copper(II) complexes.[16] The dihedral angle between the two benzene rings is 35.5(5)°. The two four-membered chelate rings Cu1–O1–Cu2–O2 and Cu2–N3–Cu2A–N3A form a dihedral angle of 32.3(4)°.

In the crystal structure of the compound, the complex cations are linked by nitrate anions and methanol molecules through O–H···O and O–H···N hydrogen bonds (Table 3), to form one dimensional chain along the *b* axis (Figure 2).

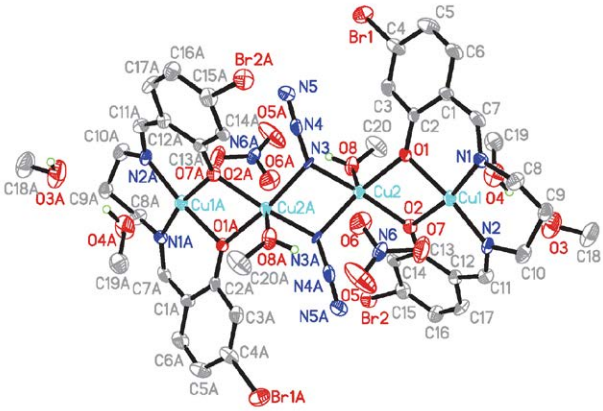

Figure 1. Molecular structure of complex **1**, showing the atom-numbering scheme. Displacement ellipsoids are drawn at 30% probability level. Atoms labeled with the suffix A are related to the symmetry operation 1 – *x*, 1 – *y*, 1 – *z*. Hydrogen atoms except for OH groups are omitted for clarity.

3. 3. Structure Description of Complex 2

Molecular structure of the trinuclear zinc(II) complex is shown in Figure 3. The Zn···Zn distance is 3.0626(5) Å. The compound possesses crystallographic inversion center symmetry. The center is located at Zn2 atom. The Schiff base ligand coordinates to the Zn(II) atoms through the imino N and phenolate O atoms, generating three six-membered chelate rings. The outer Zn1 atom is in square pyramidal coordination, with two phenolate O (O1, O2) and two imino N (N1, N2) atoms of the Schiff base ligand defining the basal plane, and with acetate O (O2) atom at the apical site. The Zn1 atom deviates from the least-squares plane defined by the four basal donor atoms by 0.205(2) Å. The square pyramidal geometry is dis-

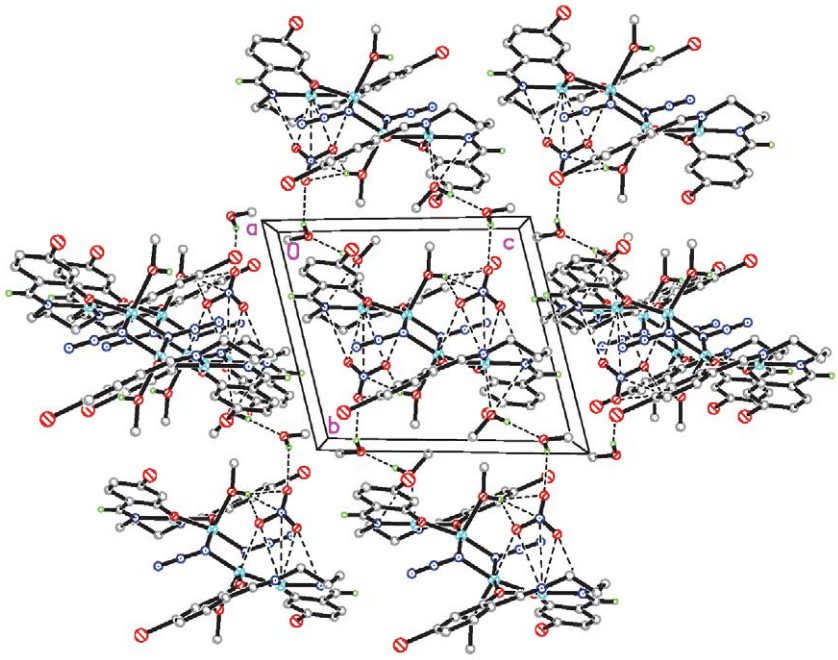

Figure 2. Molecular packing structure of complex **1**, viewed down the *a* axis. Hydrogen bonds are drawn as dotted lines.

torted, which is demonstrated from the *cis* and *trans* bond angles of 82.18(10)–93.34(13)° and 158.21(9), respectively at the basal plane, and from the angles among the apical and basal donor atoms of 99.14(8)–101.74(8)°. The central Zn2 atom is in octahedral coordination, with four phenolate O (O1, O1A, O1B, O1AA) atoms from two Schiff base ligands defining the equatorial plane, and with two acetate O (O3, O3A) atoms at the axial sites. There are two four-membered chelate rings (Zn1–O1–Zn2–O1A, Zn1A–O1AA–Zn2–O1B) in the complex molecule, which leads to the deviation of the square pyramidal and octahedral geometries. The octahedral geometry is distorted, which is demonstrated from the *cis* bond angles of 79.20(9)–100.80(9)° at the equatorial plane, and from the angles among the axial and equatorial donor atoms of 87.94(7)–92.06(7)°. The outer and inner Zn(II) atoms are bridged by two phenolate O atoms and one acetate ligand. The bond lengths around the Zn(II) atoms are within normal values with the Schiff base zinc(II) complexes.[17] The dihedral angle between the two benzene rings is 80.9(4)°. The two four-membered chelate rings Cu1–O1–Cu2–O2 and Cu2–N3–Cu2A–N3A form a dihedral angle of 32.3(4)°.

In the crystal structure of the compound, the complex molecules are stack along the *a* axis (Figure 4).

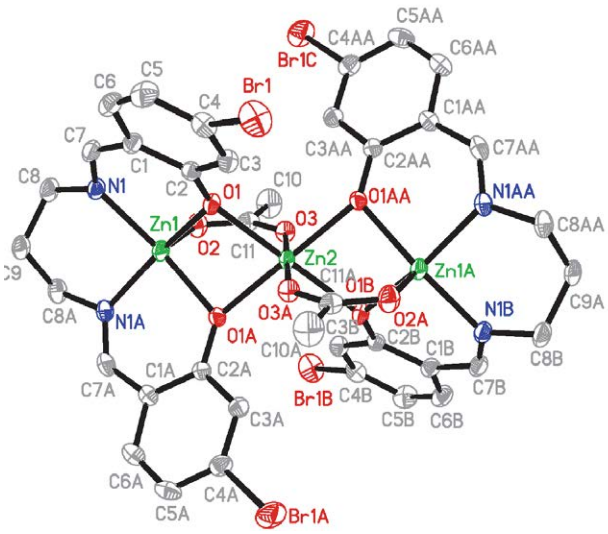

Figure 3. Molecular structure of the complex **2**, showing the atom-numbering scheme. Displacement ellipsoids are drawn at the 30% probability level. Atoms labeled with the suffix A and unlabeled atoms are related to the symmetry operation –*x*, –*y*, 1 – *z*. The methanol molecule is omitted for clarity.

Table 3. Hydrogen bond distances (Å) and bond angles (°) for complex **1**

D*–H···*A	***d*(*D*–H)**	***d*(H···*A*)**	***d*(*D*···*A*)**	**Angle (*D*–H···*A*)**
O3–H3A···O5$^{\#1}$	0.82	2.15	2.84(2)	141(3)
O4–H4···O3	0.82	1.89	2.70(3)	170(3)
O8–H8···N6$^{\#2}$	0.85(1)	2.61(8)	3.41(2)	158(5)
O8–H8···O5$^{\#2}$	0.85(1)	2.42(7)	3.25(3)	165(5)
O8–H8···O6$^{\#2}$	0.85(1)	2.15(7)	2.79(2)	132(5)

Symmetry codes: #1: *x*, –1 + *y*, *z*; #2: 1 – *x*, 1 – *y*, 1 – *z*.

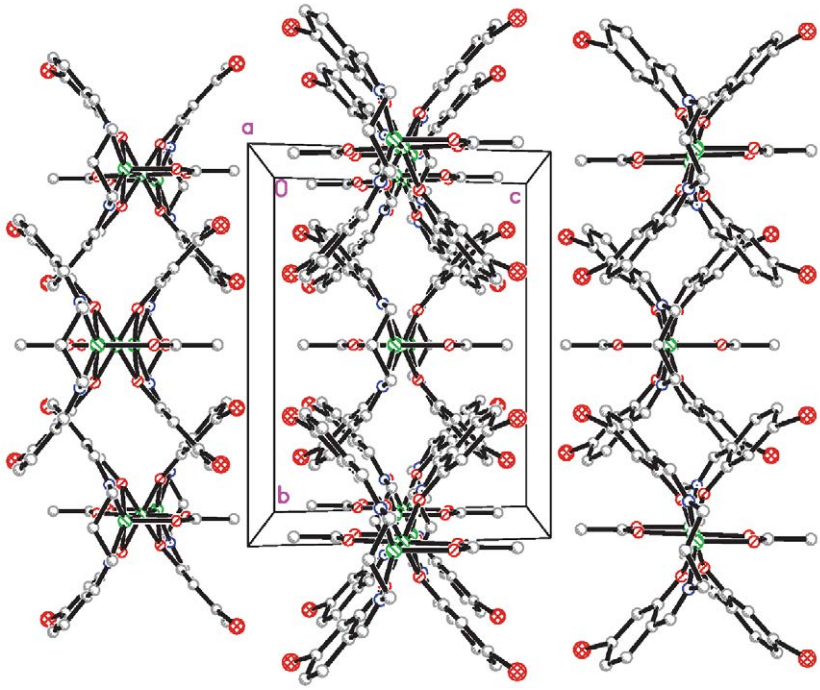

Figure 4. Molecular packing structure of the complex **2**, viewed down the *a* axis. Hydrogen bonds are drawn as dotted lines.

3. 4. IR and UV Spectra

The C=N absorption of the free Schiff base H_2L is observed at 1645 cm^{-1}. However, in the spectra of the complexes, the bands are shifted to lower wavenumbers, *viz.* 1628 and 1617 cm^{-1} for **1**, and 1628 cm^{-1} for **2**.[18] There are two absorptions for C=N bonds, which agree well with that determined by single crystal X-ray determination. In the crystal structure of complex **1**, the bond lengths of the two C=N bonds are 1.26(2) and 1.33(2) Å, which are different from each other. The spectrum of complex **1** shows an intense band at 1386 cm^{-1} characteristic of ionic nitrate.[19] The intense band at 2072 cm^{-1} of complex **1** can be assigned to the azide ligands.[20] In the spectrum of complex **2**, the asymmetric and symmetric stretching vibrations of the acetate groups appear at 1580 and 1425 cm^{-1}, respectively. The difference between $\nu_{asym}(COO)$ and $\nu_{sym}(COO)$ ($\Delta\nu$ = 155 cm^{-1}), which is smaller than 164 cm^{-1} observed in ionic acetate, reflects the bidentate bridging coordination mode.[21] The UV–Vis spectra of the free Schiff base and the complexes display bands in the region 250-320 nm, which are assigned to the n–π^* transitions.[22] The charge transfer LMCT bands of the complexes are located in the region 345–360 nm.[22]

3. 5. Pharmacology Study

The assay for the urease inhibition was carried out with the literature method.[23] The free Schiff base H_2L has weak activity, with low percentage inhibition of 17.1 ± 1.6 at concentration 100 μmol L^{-1}. Interestingly, the copper(II) complex has strong activity than H_2L, with percentage inhibition of 98.7 ± 2.3 at the same concentration, and with IC_{50} value of 0.21 ± 0.7 μmol L^{-1}. The zinc(II) complex has medium activity with percentage inhibition of 33.6 ± 3.1. The copper(II) complex has obviously higher activity than acetohydroxamic acid (IC_{50} = 28.1 μmol L^{-1}), which was used as a reference. As comparison, the copper(II) complex has better activity than copper perchlorate (IC_{50} = 8.8 μmol L^{-1}). Thus, the copper(II) complex may be used as a new urease inhibitor.

4. Conclusion

In summary, a tetranuclear copper(II) complex and a trinuclear zinc(II) complex with the Schiff base ligand *N,N*'-bis(4-bromosalicylidene)-1,3-propanediamine have been prepared and characterized. The Cu(II) atoms in the copper(II) complex are in square planar and square pyramidal coordination. The Zn(II) atoms in the zinc(II) complex are in square pyramidal and octahedral coordination. The Schiff base coordinates to the metal ions through imino nitrogen and phenolate oxygen. The copper(II) complex has effective urease inhibitory activity, with IC_{50} value of 0.21 ± 0.7 μmol L^{-1}.

Supplementary Data

CCDC 2327652 (**1**) and 2327653 (**2**) contain the supplementary crystallographic data for this paper. These data can be obtained free of charge *via* http://www.ccdc.cam.ac.uk/conts/retrieving.html, or from the Cambridge Crystallographic Data Centre, 12 Union Road, Cambridge CB2 1EZ, UK; fax: (+44) 1223-336-033; or e-mail: deposit@ccdc.cam.ac.uk.

5. References

1. (a) K. Shahzadi, S. M. Bukhari, A. Zaidi, T. A. Wani, M. S. Jan, S. Zargar, U. Rashid, U. Farooq, A. Khushal, S. Khan, *Pharmaceuticals* **2023**, *16*, 1552; **DOI:**10.3390/ph16111552
(b) L. Z. Li, C. S. Zhao, X. H. Wang, Y. Tan, X. K. Wang, X. Z. Liu, B.B. Guo, *Environ. Res.* **2023**, *237*, 116781. **DOI:**10.1016/j.envres.2023.116781
2. (a) J. Valentová, L. Lintnerová, B. Sláviková, P. Baran, *Inorg. Chim. Acta* **2023**, *558*, 121707; **DOI:**10.1016/j.ica.2023.121707
(b) S. Ahmad, M. A. Qadir, M. Ahmed, M. Imran, M. Ahmad, N. Yousaf, T. A. Wani, S. Zargar, I. Ali, M. Muddassar, *ACS Omega* **2023**, *8*, 46165–46181; **DOI:**10.1021/acsomega.3c07275
(c) B. Awan, M. A. Khan, I. Ahmad, A. Masood, A. Raza, S. Khaliq, F. Ullah, J. Ahmed, M. R. Khan, *Future Med. Chem.* **2023**, **DOI:**10.4155/fmc-2023-0225
(d) W.-L. Duan, M.-Y. Yan, F. Yan, J. Luan, *CrystEngComm* **2023**, DOI: 10.1039/d3ce01109g; **DOI:**10.1039/D3CE01109G
(e) W. Yang, Z. Y. Peng, G. C. Wang, *J. Enzyme Inhib. Med. Chem.* **2023**, *38*, 361–375; **DOI:**10.1080/14756366.2022.2150182
(f) A. Saeed, A. Ahmed, M. B. Haider, H. Ismail, K. Hayat, G. Shabir, H. R. El-Seedi, *RSC Advances* **2024**, *14*, 1018–1033; **DOI:**10.1039/D3RA06812A
(g) H. Pervez, N. Khan, J. Iqbal, S. Zaib, M. Yaqub, M. M. Naseer, *Acta Chim. Slov.* **2018**, *65*, 108–118. **DOI:**10.17344/acsi.2017.3649
3. (a) M. Patel, T. Kikani, K. Patel, S. Thakore, *J. Mol. Struct.* **2024**, *129*, 136691; **DOI:**10.1016/j.molstruc.2023.136691
(b) S. H. Sumrra, W. Zafar, S. A. Malik, K. Mahmood, S. S. Shafqat, S. Arif, *Acta Chim. Slov.* **2022**, *69*, 200–216;
(c) F. M. Elantabli, R. G. Mohamed, S. M. El-Medani, M. Haukka, R. M. Ramadan, M. A. Afifi, *J. Mol. Struct.* **2024**, *1299*, 137230. **DOI:**10.1016/j.molstruc.2023.137230
4. Y. M. Abdel-Baky, A. M. Omer, E. M. El-Fakharany, Y. A. Ammar, M. S. Abusaif, A. Ragab, *Sci. Rep.* **2023**, *13*, 22792. **DOI:**10.1038/s41598-023-50130-3
5. (a) K. S. Kumar, K. K. Aravindakshan, *Pharm. Chem. J.* **2022**, *55*, 1378–1389; **DOI:**10.1007/s11094-022-02585-3
(b) M. Diz, M. L. Durán-Carril, J. Castro, S. Alvo, L. Bada, D. Viña, J. A. García-Vázquez, *J. Inorg. Biochem.* **2022**, *236*, 111975; **DOI:**10.1016/j.jinorgbio.2022.111975
(c) E. M. Fathalla, M. A. M. Abu-Youssef, M. M. Sharaf, A.

El-Faham, A. Barakat, A. M. A. Badr, S. M. Soliman, A. M. Z. Slawin, J. D. Woollins, *Inorg. Chim. Acta* **2023**, *555*, 121586. **DOI:**10.1016/j.ica.2023.121586

6. (a) Seema, S. Sharma, P. Yadav, S. Kumari, M. Ranka, *Trans. Met. Chem.* **2023**, *48*, 389–400; **DOI:**10.1007/s11243-023-00551-w
(b) Q. U. Sandhu, M. Pervaiz, A. Majid, U. Younas, Z. Saeed, A. Ashraf, R. R. M. Khan, S. Ullah, F. Ali, S. Jelani, *J. Coord. Chem.* **2023**, *76*, 1094–1118. **DOI:**10.1080/00958972.2023.2226794
7. (a) R. N. Gomes, M. L. Silva, K. S. Gomes, J. H. G. Lago, G. Cerchiaro, *J. Inorg. Biochem.* **2024**, *250*, 112401; **DOI:**10.1016/j.jinorgbio.2023.112401
(b) M. Strzelecka, B. Wiatrak, P. Jawien, Z. Czyznikowska, P. Swiatek, *Bioorg. Chem.* **2023**, *139*, 106758. **DOI:**10.1016/j.bioorg.2023.106758
8. (a) L.-W. Xue, X. Fu, G.-Q. Zhao, Q.-B. Li, *Acta Chim. Slov.* **2021**, *68*, 17–24; **DOI:**10.17344/acsi.2020.5817
(b) Y. Yuan, X.-K. Lu, G.-Q. Zhou, X.-Y. Qiu, *Acta Chim. Slov.* **2021**, *68*, 1008–1015; **DOI:**10.17344/acsi.2021.7070
(c) J.-L. Hou, H.-Y. Wu, C.-B. Sun, Y. Bi, W. Chen, *Acta Chim. Slov.* **2020**, *67*, 860–865; **DOI:**10.17344/acsi.2020.5824
(d) P. Middya, Y. Chakravarty, S. Maity, S. Chattopadhyay, *J. Coord. Chem.* **2023**, *76*, 1777–1790; **DOI:**10.1080/00958972.2023.2280514
(e) Q.-U. Sandhu, M. Pervaiz, A. Majid, U. Younas, Z. Saeed, A. Ashraf, R. R. M. Khan, S. Ullah, F. Ali, S. Jelani, *J. Coord. Chem.* **2023**, *76*, 1094–1118; **DOI:**10.1080/00958972.2023.2226794
(f) J. P. Remiya, B. Shyni, T. S. Sikha, U. R. Parvathy, *J. Coord. Chem.* **2023**, *76*, 729–748. **DOI:**10.1080/00958972.2023.2199440
9. (a) S. Han, Y. Wang, *Acta Chim. Slov.* **2021**, *68*, 961–969; **DOI:**10.17344/acsi.2021.6965
(b) H. Zhao, X.-R. Liu, X. Wang, J. Hu, Y.-J. Cai, Q.-A. Peng, *Acta Chim. Slov.* **2021**, *68*, 804–810; **DOI:**10.17344/acsi.2021.6781
(c) B. H. He, Q. Y. Wang, X. Q. Zhang, D. H. Shi, Z. L. You, *Inorg. Chim. Acta* **2023**, *558*, 121738; **DOI:**10.1016/j.ica.2023.121738
(d) Q. Y. Wang, B. H. He, X. Q. Zhang, Y. Cao, A. Li, J. Q. Wang, D. H. Shi, Z. L. You, *J. Coord. Chem.* **2023**, **DOI:**10.1080/00958972.2023.2256935
(e) L. Zhang, Y.-Q. Gu, X.-H. Feng, T. Yang, X. Y. Li, J. Wang, Z. L. You, *Acta Chim. Slov.* **2022**, *69*, 674–680; **DOI:**10.17344/acsi.2022.7578
(f) J. Jiang, P. Liang, H. Y. Yu, Z. L. You, *Acta Chim. Slov.* **2022**, *69*, 629–637. **DOI:**10.17344/acsi.2022.7513
10. (a) W. Chen, Y. G. Li, Y. M. Cui, X. A. Zhang, H. L. Zhu, Q.-F. Zeng, *Eur. J. Med. Chem.* **2010**, *45*, 4473–4478; **DOI:**10.1016/j.ejmech.2010.07.007
(b) Y. M. Cui, Y. G. Li, Y. J. Cai, W. Chen, H. L. Zhu, *J. Coord. Chem.* **2011**, *64*, 610–616; **DOI:**10.1080/00958972.2011.552110
(c) Y. M. Cui, W. T. Liu, Y. Liu, W. Chen, Y. G. Li, *J. Coord. Chem.* **2011**, *64*, 3960–3968; **DOI:**10.1080/00958972.2011.634006
(d) Y.-M. Cui, X.-W. Dong, W. Chen, W.-J. Wang, Y.-G. Li, H.-L. Zhu, *J. Enzyme Inhib. Med. Chem.* **2012**, *27*, 528–532; **DOI:**10.3109/14756366.2011.599065
(e) Y. M. Cui, X. W. Dong, Y. G. Li, Z. W. Li, W. Chen, *Eur. J. Med. Chem.* **2012**, *58*, 323–331. **DOI:**10.1016/j.ejmech.2012.09.037
11. Bruker, SMART (Version 5.628) and SAINT (Version 6.02); Bruker AXS: Madison, Wisconsin, USA, **1998**.
12. G. M. Sheldrick, SADABS Program for Empirical Absorption Correction of Area Detector, University of Göttingen, Germany, **1996**.
13. G. M. Sheldrick, *Acta Crystallogr.* **2008**, *A64*, 112–122. **DOI:**10.1107/S0108767307043930
14. W. J. Geary, *Coord. Chem. Rev.* **1971**, *7*, 81–120. **DOI:**10.1016/S0010-8545(00)80009-0
15. A. W. Addison, T. N. Rao, J. Reedijk, J. van Rijn, G. C. Verschoor, *J. Chem. Soc., Dalton Trans.* **1984**, 1349–1356. **DOI:**10.1039/DT9840001349
16. (a) D. Sadhukhan, A. Ray, R. J. Butcher, C. J. G. Garcia, B. Dede, S. Mitra, *Inorg. Chim. Acta* **2011**, *376*, 245–254; **DOI:**10.1016/j.ica.2011.06.024
(b) S. Bandyopadhyay, J.-M. Lo, H.-H. Yao, F.-L. Liao, P. Chattopadhyay, *J. Coord. Chem.* **2006**, *59*, 2015–2021; **DOI:**10.1080/00958970600717975
(c) S. Hazra, S. Majumder, M. Fleck, N. Aliaga-Alcalde, S. Mohanta, *Polyhedron*, **2009**, *28*, 3707–3714. **DOI:**10.1016/j.poly.2009.08.007
17. (a) X.-X. Zhou, H.-C. Fang, Y.-Y. Ge, Z.-Y. Zhou, Z.-G. Gu, X. Gong, G. Zhao, Q.-G. Zhan, R.-H. Zeng, Y.-P. Cai, *Cryst. Growth Des.* **2010**, *10*, 4014–4022; **DOI:**10.1021/cg100612b
(b) J. Reglinski, S. Morris, D. E. Stevenson, *Polyhedron*, **2002**, *21*, 2175–2182; **DOI:**10.1016/S0277-5387(02)01172-5
(c) B. Dutta, P. Bag, U. Florke, K. Nag, *Inorg. Chem.* **2005**, *44*, 147–157. **DOI:**10.1021/ic049056a
18. K. R. Sangeetha Gowda, H. S. Bhojya Naik, B. Vinay Kumar, C. N. Sudhamani, H. V. Sudeep, T. R. Ravikumar Naik, G. Krishnamurthy, *Spectrochim. Acta A: Mol. Biomol. Spectrosc.* **2013**, *105*, 229–237. **DOI:**10.1016/j.saa.2012.12.011
19. M. F. Iskander, T. E. Khalil, R. Werner, W. Haase, I. Svoboda, H. Fuess, *Polyhedron* **2000**, *19*, 949–958. **DOI:**10.1016/S0277-5387(00)00340-5
20. M. Das, B. K. Shaw, B. N. Ghosh, K. Rissanen, S. K. Saha, S. Chattopadhyay, *J. Coord. Chem.* **2015**, *68*, 1361–1373. **DOI:**10.1080/00958972.2015.1014350
21. U. Kumar, J. Thomas, N. Thirupathi, *Inorg. Chem.* **2010**, *49*, 62–72. **DOI:**10.1021/ic901100z
22. A. Ray, D. Sadhukhan, G. M. Rosair, C. J. Gomez-Garcia, S. Mitra, *Polyhedron* **2009**, *28*, 3542–3550. **DOI:**10.1016/j.poly.2009.07.017
23. T. Tanaka, M. Kawase, S. Tani, *Life Sci.* **2003**, *73*, 2985–2990. **DOI:**10.1016/S0024-3205(03)00708-2

Povzetek

Sintetizirali smo nov štirijedrni bakrov(II) kompleks $[Cu_4L_2(N_3)_2(CH_3OH)_2](NO_3)_2{\cdot}4CH_3OH$ (**1**) in nov trijedrni cinkov(II) kompleks $[Zn_3L_2(CH_3COO)_2]$ (**2**) iz bis-Schiffove baze *N*,*N*'-bis(4-bromosaliciliden)-1,3-propandiamin (H_2L) in bakrovega(II) nitrata oziroma cinkovega(II) acetata v prisotnosti natrijevega azida. Kompleksa smo okarakterizirali z elementno analizo, IR in UV-Vis spektroskopijo. Molekularno strukturo obeh kompleksov smo potrdili z rentgensko monokristalno analizo. V kompleksu **1** so atomi Cu(II) mostovno povezani preko fenolatnih kisikovih atomov in terminalnih azidnih ligandov. V kompleksu **2** so atomi Zn(II) mostovno povezani preko fenolatnih kisikovih atomov in acetatnih ligandov. Cu(II) atomi v kompleksu **1** imajo kvadratno planarno in kvadratno piramidalno koordinacijo. Atomi Zn(II) v kompleksu **2** imajo kvadratno piramidalno in oktaedrično koordinaciji. Ligand Schiffove baze je na kovinske atome koordiniran preko dveh fenolatnih O atomov in dveh imino N atomov. Biološki test je pokazal, da kompleks bakra(II) učinkovito zavira ureazo.

DOI: 10.17344/acsi.2023.8486 *Acta Chim. Slov.* **2024,** *71,* 244–255

Scientific paper

Conformational Stability of 3-aminopropionitrile: DFT and *Ab initio* Calculations

Ashraf M. Al-Msiedeen

Department of Chemistry and Chemical Technology, Faculty of Science, Tafila Technical University, P.O. Box 179, Tafila- 66110, Jordan.

** Corresponding author: E-mail: ashraf_ttu@yahoo.com*
Tel. +962 792269139

Received: 09-30-2023

Abstract

Many conformers of 3-aminopropionitrile are known. Due to the biomedical importance of 3-aminopropionitrile a full investigation of structural, vibrational, and other associated properties of all possible conformers was performed. The geometrical structures, relative stability, and vibrational frequencies of the gauche and trans 3-aminopropionitrile conformers have been studied using *ab initio* (CCSD/6-311+G(d,p)) and DFT (B3LYP and M06 functionals at 6-311+G(d,p) and aug-cc-pVDZ basis set) calculations. The conformational and vibrational studies of 3-aminopropionitrile molecule were presented here are in very good interpretation of the calculated data compared with very poor interpretation in previous studies. The results showed that the gauche 2 conformer is more stable by 0.19 kcal/mol than gauche 1, outlined as enthalpy change ΔH between the conformers, at CCSD/6-311+G(d,p). Additionally, the population analysis shows that the gauche conformers are more prevalent than the trans conformers in the gas phase, present at 72.8%, with gauche 2 being the dominating gauche conformer at 40.1%. These results are in good agreement with earlier experimental and theoretical conclusions. All minima conformers' thermodynamic characteristics have also been studied. The relevant bond lengths, bond angles, and dihedral angles were calculated at a different level of theory for all possible conformers. The geometrical outcomes of the conformers agree very well with the previous experimental results. Electrostatic potential surface (ESP) has been used to interpret the structure-activity relationship. The atomic charges are examined, together with the energy difference between HOMO (Highest Occupied Molecular Orbital) and LUMO (Lowest Unoccupied Molecular Orbital). Additionally, the HOMO-LUMO energy gap and other relevant molecular properties are computed. The most stable conformers' stabilization energy has been determined by the Natural Bond Orbital (NBO) analysis.

Keywords: 3-aminopropionitrile, HOMO-LUMO, ESP, conformer, vibrational frequencies, relative stability.

1. Introduction

Numerous chemical and physical properties of a chemical molecule with various functional groups are influenced by conformational isomerism. Examples include determining the phase of the substances under ambient conditions[1,2] and determining the activity of particular enzymes.[3–5] Nitriles play a significant role in both chemistry and astrochemistry. For instance, succinonitrile is a crucial component of research on solid state batteries[6–9] and is utilized as a solvent of inorganic salts. Additionally, it has been utilized to improve the conductivity of composite polymers as succinonitrile-poly(methyl methacrylate).[10] Interstellar clouds are anticipated to contain some small chain nitriles, which are thought to react with water to create amino acids.[11–13] Numerous organoamines play crucial roles in biomolecules including proteins and amino acids. An organic substance possessing both amine and nitrile functional groups is 3-aminopropionitrile (BAPN), $NH_2CH_2CH_2CN$ (also called 2-cyanoethylamine). It is a colorless liquid. The compound is present naturally and is of interest to the biomedical field.[14] As a result of 3-aminopropionitrile significance in the biomedical field, it can be important for research to estimate its conformational stabilities.

Organoamines play essential roles in biomolecules including proteins and amino acids. As an illustration, β-aminopropionitrile is injected into a tendon that has been wounded 30 to 90 days after the injury in order to bind to the lysyl oxidase enzyme and prevent lysine from

being deaminated. To forecast the result of these binding, one must have a thorough understanding of the β-aminopropionitrile's structure, conformation, reactivity, and interactions. The purpose of this study is to explain the theoretical methods that have been used to interpret the main characteristics of β-aminopropionitrile, particularly its structure.

The results of conformational analysis of 1,2-disubstituted ethane molecules are largely strange to free intra-single-bond rotations. Over time, there have been some intriguing difficulties in determining the conformational stability of 1,2-disubstituted ethane molecules.[15] The 1,2-dihaloethane molecules served as good examples, with 1,2-difluoroethane[16] having a gauche conformer that is (3.35 ± 0.36) kJ mol^{-1} more stable than the trans form and 1,2-dichloroethane having a trans conformer that is (3.87 ± 0.09) kJ mol^{-1} more stable than the gauche from a variable temperature infrared studies of xenon solutions.[17] Trans conformer of butyronitrile ($CH_3CH_2CH_2CN$) is more stable than the gauche, according to a microwave investigation by Hirota,[18] while IR investigation, claimed that the vapor phase of gauche conformer is dominant.[19]

Conformers' relative stabilities can be calculated by vicinal interactions between functional groups revolving around a single free-rotated bond. These interactions can be repulsive (destabilizing), as in the case of the methyl-methyl strain energy in n-butane,[20] or attractive (stabilizing), as in the case of the gauche effect of 1,2-difluoroethane.[21] Based on their relative free energies, which define their relative abundances according to the Boltzmann distribution, the conformers are in equilibrium with one another. The thermodynamic characteristics of the conformers exchange determine its dynamics. Whenever a chemical reaction occurs, the structure and shape of the product are influenced by reactants' thermochemical properties.

Determining the appropriate 3-aminopropionitrile requires investigation, just like the molecules mentioned above, as it has more than one minima conformers (gauche and trans).[22] The conformational study of 3-aminopropionitrile has received little theoretical attention.[15, 22, 23] The most recent one[15] by James et al. employed just two minima for the MP2 (full) *ab initio* and B3LYP density functional theory (DFT) computations. They discovered that the gauche conformer is 0.87 kcal/mol more stable than the trans conformer at their greatest level of theory, MP2 (full)/aug-cc-pVTZ. Enthalpy[15] is the only thermochemical data available for 3-aminopropionitrile.

Due to a lack of information, it is decided to investigate the thermodynamics, structure, and stability of five, three gauche, and two trans minima conformers.[15,22] In this research, the structural details and conformational stabilities of conformers of 3-aminopropionitrile were examined. Additionally, the conformers' thermodynamic data were computed. The results were compared to experimental and theoretical data that had previously been published. The outcomes of this research should aid in elucidating conformational changes.

2. Computational Details

Gaussian09 software was used for all geometry optimization and energy computations.[24] Different theoretical levels, including CCSD,[25] B3LYP and M06,[24] have been employed. These basis sets include 6-311+G(d,p) and aug-cc-pVDZ.[24] Frequency calculations are used to describe the stationary points (minima and transition states; saddle point of first order). Mathematically, the transition states have one imaginary eigenvalue while the minima have none. The vibrational frequency and thermodynamic data were gained using the frequency calculations. The equation described in my earlier work[26] is used to calculate the relative stability between the most stable conformer and the less stable ones or the transition states.

$$\Delta H_{rel} = (E_0 + H_{cor})_{(less)} - (E^0 + H_{cor})_{(most)} \quad (1)$$

$$\Delta G_{rel} = (E_0 + G_{cor})_{(less)} - (E^0 + G_{cor})_{(most)} \quad (2)$$

Where (E_o + H_{corr}) and (E_o + G_{corr}) are, respectively, the corrected electronic energy (E_o + enthalpy correction, H_{corr}), and the corrected electronic energy (E_o + Gibbs correction, G_{corr}), which includes the zero-point energy. Natural bond orbital (NBO) analysis was used to determine the electronic atomic charges.[27] The data collected were utilized to determine the stabilization energy of the conformer that was determined to be the most stable. The Coulomb's potential is used to calculate the electrostatic interaction between the staggered NH_2 group and the point-charged N and C atoms of the nitrile group for this purpose.

$$U_E = k_e \sum_i^N \frac{q_i Q}{r_i} \quad (3)$$

Where r is the distance between the point charges q of the nitrile group and the point charge of the closest H atom on the NH_2 group (Q), $k_e = \frac{1}{4\pi\varepsilon_0} = 8.988\ x\ 10^9 Nm^2C^{-2}$ is Coulomb's constant.

In order to explain the orbital overlaps and the possibility for charge transfer inside the five minima conformers, the energies of the highest occupied molecular orbital (HOMO) and the lowest unoccupied molecular orbital (LUMO) were also calculated using the CCSD/6-311+G(d,p) level of theory.

3. Results and Discussion

3. 1. Geometry

Figure 1 displays the minima's and transition states' optimized structures. Tables 1 and 2 display the relevant

bond lengths, bond angles, and dihedral angles. At a different level of theory, all conformer bond lengths are comparable to one another, with a maximum variation of (0.023 Å). The C≡N bond lengths of the minima and transition states are remarkably similar, with a maximum difference of 0.001 Å, at the same level of theory. With the exception of gauche 1, 2, and TS4, where there is a maximum difference of 0.001 Å, all minima and transition state conformers' C≡N bond lengths are identical at the DFT (B3LYP/aug-cc-pVDZ, M06/aug-cc-pVDZ) and CCSD/6-311+G(d,p) levels of theory. All levels of theory's transition states have C1-C6 bond lengths that are longer than those of minima conformers. At both the B3LYP and M06 levels of theory of DFT, the gauche 2 conformer's C1–C6 bond lengths are the identical. All conformers' C1-C6 bond lengths vary slightly across levels of theory, with the largest differences (0.019 Å) occurring between B3LYP/6-311+G(d,p) and M06/aug-cc-pVDZ in TS3.

All conformers have somewhat varied C1-C4 bond lengths at the same levels of theory, with the M06/aug-cc-pVDZ in TS1 and TS3 having the largest variance (0.011 Å). The lengths of the C1-C4 bonds vary slightly depending on the level of theory, with the greatest difference (0.023 Å) between the M06/6-311+G(d,p) CCSD/6-311+G(d,p) basis fixed for all conformers. The C1-C4 bond's longest length is revealed via a CCSD/6-311+G(d,p) level of theory for all conformers. Out of all the different levels of theory, TS3 has the shortest C1-C4 bond lengths. In Gauche 1, Trans 1, TS1, and TS3 on the one hand, and in Gauche 2, Gauche 3, Trans 2, TS2, TS4, and TS5 on the other, the C6-N9 bond lengths of the various levels of theory are quite closed. All conformers' C6-N9 bond lengths calculated using B3LYP are the ones that come closest to the lengths determined with the CCSD.

Table 2 lists the bond angles as well as the torsional (dihedral) angles. The bond angle C4-C1-C6 is smaller in the minima conformers of the various levels of theory than it is in the conformers of the transition state, particularly in the gauche conformers. The greatest values of the bond angles C1-C6-N9 for minima conformers are found in the gauche 1 and trans 1 conformers. The most conformer has bond angle C1-C4≡N5 approaches 180º of all different levels of theory for minima is trans 1 and for transition states are TS2 and TS5. The differences between the bond angles C1-C4≡N5 are between 0 and 1° for theories at different levels, and between 0 and 1.9° for theories at the same levels. The range of bond angle variances among the various levels of theory is 0 to 1.2°. By comparing the values of the dihedral angle N9-C6-C1-C4 obtained before optimization (gauche = 60°, trans = 180°, TS1, TS2, and TS5 = 120°, TS3 and TS4 = 0°) with those obtained after optimization, we can see that the conformers trans 1 and its interconversion transition state (TS3) had no deformation of any of the different levels of theory, whereas the maximum distortion that occurred on the minima and transition states conformers is in gauche 3 (B3LYP/aug-cc-pVDZ) and TS5 (B3LYP/6-311+G(d,p)) respectively.

In general, all of the bond lengths, bond angles, and dihedral angles of the minimum conformers are compared to the theoretical results,[22] and both the gauche 1 and gauche 2 conformers' parameters agree well with the microwave spectrum results.[23] Given these values, it is obvious that the bond lengths discovered in this study are identical to or extremely close to those observed theoretically or empirically. C1-C6, C1-C4, C4≡N5 and C6-N9 bond lengths of gauche 1 and gauche 2 conformers are 1.548 Å, 1.463 Å, 1.157 Å and 1.475 Å, respectively, are in good agreement with my results. For gauche 1: C1-C6 of CCSD/6-311+G(d,p), C1-C4 of B3LYP/aug-cc-pVDZ, C4≡N5 of B3LYP/6-311+G(d,p) and C6-N9 of CCSD/6-311+G(d,p) with difference 0.001 Å, 0.002 Å, 0.003 Å and 0.018 Å, respectively. For gauche 2: C1-C6 of B3LYP/6-311+G(d,p) and aug-cc-pVDZ, C1-C4 of B3LYP/6-311+G(d,p), C4≡N5 of B3LYP/6-311+G(d,p) and C6-N9 of CCSD/6-311+G(d,p) with difference 0.008 Å, 0.001 Å, 0.003 Å and 0.012 Å, respectively. Unfortunately, to my knowledge, in literature, there are no experimental data about the other minima conformers (gauche 3, trans 1 and trans 2) to compare my theoretical results with. But we can see the significant similarity between the results obtained theoretically [22] with the results of this study. The difference is in the arrange 0 – 0.023 Å.

If the bond angles are considered, the C4-C1-C6 and C1-C6-N9 bond angles in both gauche 1 and gauche 2 obtained by microwave method are near more to the values obtained by M06/aug-cc-pVDZ in this study with difference (0.6°) for C4-C1-C6 and (1.8°) for C1-C6-N9 in each conformer. The C1-C4≡N5 bond angle should be 180°, but there is a small deviations from linearity ranged from 2.1° – 3.0° in gauche 1 and 1.7° – 2.7° in gauche 2. The dihedral angle N9-C6-C1-C4 in both gauche 1 and gauche 2 conformers are closed to that obtained by microwave method especially through M06 and CCSD. For all different levels of theory the difference is in the arrange 0° – 1° for gauche 1 and 3° – 1.7° for gauche 2.

3. 2. The Relative Stability and Thermal Properties

The relative energies of the gauche 1, gauche 3, trans 1, trans 2 and the transition states conformers (relative to the gauche 2 conformer), outlined by their ΔH_{rel} and ΔG_{rel}, are listed in Table 3. 3-aminopropionitrile has five possible minima conformers, three gauche conformers and two trans conformers as shown in Figure 1. Gauche 1 and gauche 2 are more stable than any one of gauche 3, trans 1 and trans 2 by at least 0.23 kcal/mol between gauche 2 and trans 2 and up to 1.49 kcal/mol between gauche 2 and gauche 3 through B3LYP/6-311+G(d,p) and M06/aug-cc-pVDZ, respectively. The enthalpy differences between gauche 2- gauche 1 and gauche 2-trans 1 conformers were determined in the range 0 – 0.19 kcal/mol and 0.23 – 0.70 kcal/mol, respectively, through all different levels of theo-

ry. This values were closed to that given by previous microwave and infrared studies.[15, 23]

Through the highest level of theory used in this study, CCSD/6-311+G(d,p) and M06/aug-cc-pVDZ, the more stable conformer is gauche 2 by 0.19 kcal/mol than gauche 1. This is result is correspond with infrared study, where gauche 2 is more stable than gauche 1 by 75 cm^{-1} (0.21 kcal/mol), outlined as enthalpy change H between the two conformers. Per N. Skancke [22] has studied the same system using *ab initio* with 4-21, 4-31G and 6-31G basis set, his results show that gauche 1 is more stable than gauche 2 by 1.8, 1.2 and 0.8 kJ/mol

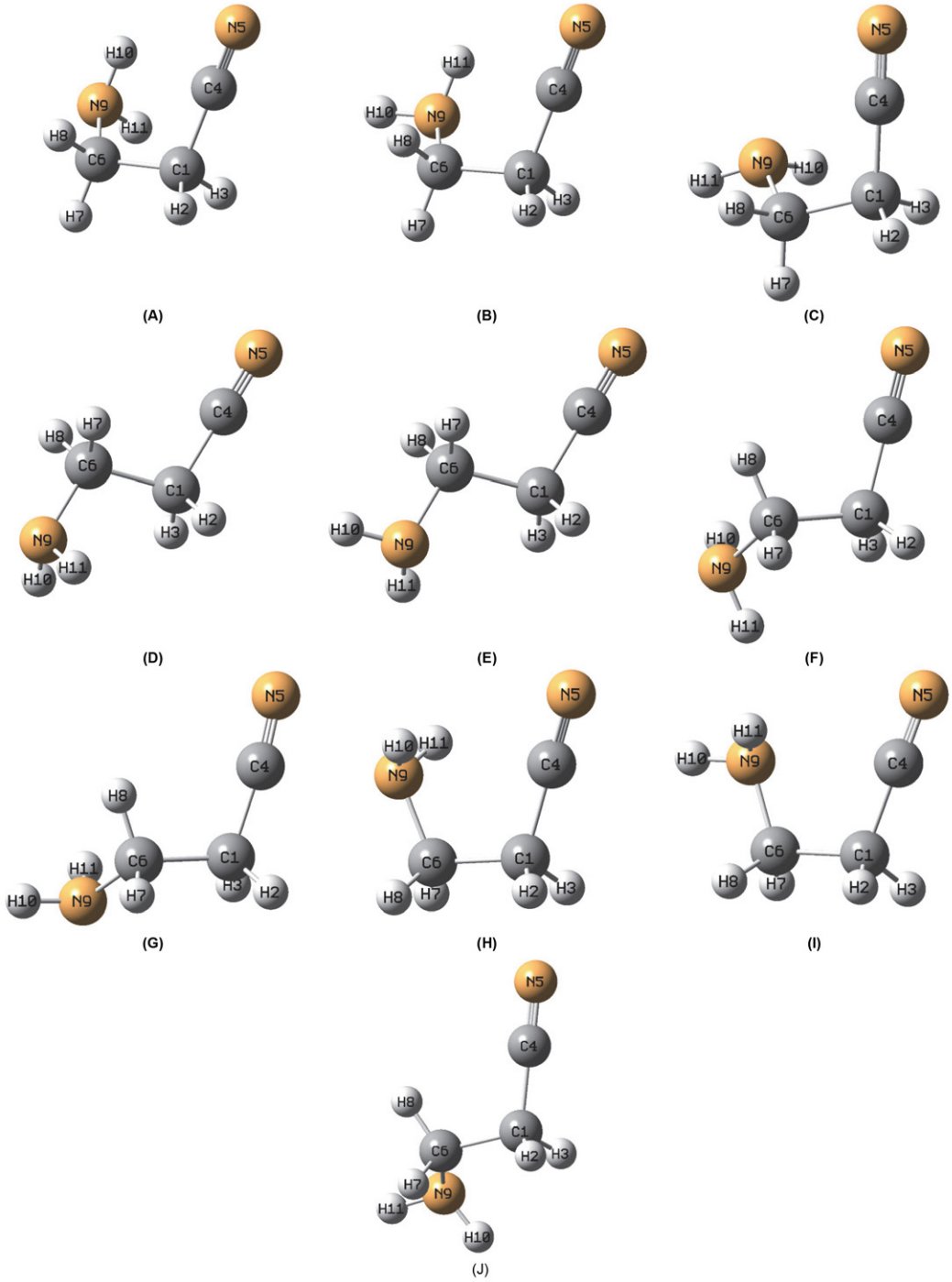

Figure 1. The optimized stationary points of 3-aminopropionitrile conformers. (A) Gauche 1(H8-C6-N9-H11 = –180°), (B) Gauche 2 (H8-C6-N9-H11 = 60°) , (C) Gauche 3 (H8-C6-N9-H11 = –60°), (D)Trans 1(eclipsed H8-C6-N9-H11), (E) Trans 2 (staggered H8-C6-N9-H11), (F) TS1 (eclipsed H8-C6-N9-H11 (-180°), staggered C4-C1-C6-N9), (G) TS2 (staggered H8-C6-N9-H11, staggered C4-C1-C6-N9), (H) TS3 (eclipsed H8-C6-N9-H11, eclipsed C4-C1-C6-N9), (I) TS4 (staggered H8- C6-N9-H11, eclipsed C4-C1-C6-N9), (J) TS5 (eclipsed H8-C6-N9-H11 (0°), staggered C4-C1-C6-N9). The related optimized parameters are shown in Table 1.

(0.43, 0.29 and 0.19 kcal/mol), respectively, which contradicts the infrared and my own results. This may be attributed to the use of low level of theory. Trans 2 conformer is more stable than trans 1 conformer using all different levels of theory as shown in Table 3. The difference between two trances conformer determined by the theoretical side of the infrared study, using B3LYP/6-311+G(d,p), was 67 cm^{-1} (0.19 kcal) which is very closed to that obtained in this study (0.17 kcal/mol) through same level of theory.

Relative populations (N_i) (100%, 70.2%, 11.5%, 21.2% and 46.8%) of the conformers (gauche 2, gauche 1, gauche 3, trans 1 and trans 2), respectively, were calculated using ΔG_{rel} values [$\Delta G_{rel} = -RT \ln(Ni)$]. The population distribution (N_i/N_{total}) at 298.15 K (ambient temperature) were calculated by the Boltzmann distribution.[28]

Table 1. Selected bond lengths (Å) of the optimized gauche, trans and transition states (TS) geometries of 3-aminopropionitrile at the B3LYP, M06, CCSD/6-311+G (d,p), (aug-cc-pVDZ) levels of theory.

Structure		Bond (Å)		B3LYP		M06		CCSD
		Ref[a]	Ref[b]	6-311+G (d,p)	aug-cc-pVDZ	6-311+G (d,p)	aug-cc-pVDZ	6-311+G (d,p)
Gauche 1	C1–C6	1.548	1.560	1.555	1.553	1.539	1.538	1.547
	C1–C4	1.463	1.460	1.460	1.465	1.452	1.456	1.474
	C4≡N5	1.157	1.140	1.154	1.161	1.152	1.161	1.162
	C6–N9	1.475	1.460	1.452	1.454	1.442	1.445	1.457
Gauche 2	C1–C6	1.548	1.540	1.540	1.540	1.527	1.527	1.536
	C1–C4	1.463	1.470	1.462	1.467	1.453	1.458	1.475
	C4≡N5	1.157	1.140	1.154	1.161	1.152	1.161	1.161
	C6–N9	1.475	1.470	1.461	1.462	1.450	1.452	1.463
Gauche 3	C1–C6		1.540	1.541	1.540	1.527	1.526	1.536
	C1–C4		1.460	1.462	1.467	1.453	1.458	1.475
	C4≡N5		1.140	1.153	1.161	1.152	1.160	1.160
	C6–N9		1.460	1.459	1.461	1.447	1.450	1.462
Trans 1	C1–C6		1.560	1.555	1.553	1.538	1.537	1.546
	C1–C4		1.460	1.460	1.466	1.451	1.456	1.474
	C4≡N5		1.140	1.154	1.161	1.152	1.161	1.161
	C6–N9		1.460	1.453	1.455	1.443	1.445	1.458
Trans 2	C1–C6		1.540	1.542	1.541	1.527	1.527	1.537
	C1–C4		1.460	1.460	1.466	1.451	1.456	1.474
	C4≡N5		1.140	1.153	1.161	1.152	1.161	1.161
	C6–N9		1.470	1.462	1.464	1.450	1.453	1.465
TS1	C1–C6			1.574	1.572	1.557	1.572	1.565
	C1–C4			1.459	1.464	1.450	1.464	1.473
	C4≡N5			1.154	1.161	1.153	1.161	1.161
	C6–N9			1.453	1.456	1.442	1.456	1.459
TS2	C1–C6			1.558	1.557	1.543	1.543	1.553
	C1–C4			1.460	1.465	1.451	1.456	1.474
	C4≡N5			1.154	1.161	1.152	1.161	1.161
	C6–N9			1.465	1.467	1.453	1.456	1.467
TS3	C1–C6			1.583	1.581	1.566	1.564	1.573
	C1–C4			1.457	1.463	1.449	1.453	1.472
	C4≡N5			1.154	1.161	1.153	1.161	1.161
	C6–N9			1.450	1.453	1.441	1.444	1.456
TS4	C1–C6			1.562	1.561	1.548	1.546	1.558
	C1–C4			1.461	1.466	1.452	1.457	1.475
	C4≡N5			1.153	1.161	1.152	1.160	1.160
	C6–N9			1.459	1.461	1.447	1.450	1.463
TS5	C1–C6			1.559	1.558	1.543	1.543	1.553
	C1–C4			1.460	1.465	1.451	1.456	1.473
	C4≡N5			1.154	1.161	1.152	1.161	1.161
	C6–N9			1.463	1.466	1.452	1.455	1.467

$$\frac{N_i}{N_{total}} = \frac{e^{-E_i/RT}}{\sum_{k=1}^{M} e^{-E_k/RT}} \quad (4)$$

The population distribution is approximately (40.1%, 28.1%, 4.6%, 8.5% and 18.7%), respectively.

The Gibb's free energies $\Delta G^{\#}$ of the transition states TS1, TS2, TS3, TS4 and TS5 are 4.92, 4.22, 4.84, 6.29 and 4.77 kcal/mol obtained by CCSD/6-311+G(d,p), respectively, relative to the most stable gauche conformer.

The results reveal that TS4 has a higher energy compared to the other transition states through CCSD/6-311+G(d,p) and all other different levels of theory. TS4 Figure 1C has a higher strain than other transition states due to NH_2 and CN eclipsing configuration. The interaction between the electron rich CN region and the N9

Table 2. Selected angles (°) and dihedral angles (torsion angles) (°) of the optimized gauche, trans and transition states (TS) geometries of 3-aminopropionitrile at the B3LYP, M06, CCSD/6-311+G (d,p), (aug-cc-pVDZ) levels of theory.

Structure		Angles (°)		B3LYP		M06		CCSD
		Ref[a]	Ref[b]	6-311+G (d,p)	aug-cc-pVDZ	6-311+G (d,p)	aug-cc-pVDZ	6-311+G (d,p)
Gauche 1	C4–C1–C6	110.5	111.0	112.3	112.2	111.2	111.1	111.5
	C1–C6–N9	114.0±15	114.8	116.7	116.5	115.8	115.8	115.8
	C1–C4≡N5	180.0	178.3	177.9	177.7	177.3	177.0	177.8
	N9–C6–C1–C4	59±3	57.4	60.2	60.0	59.2	58.6	59.0
Gauche 2	C4–C1–C6	110.5	111.3	112.3	112.1	111.2	111.1	111.2
	C1–C6–N9	108.0±15	109.3	110.5	110.4	109.9	109.8	109.8
	C1–C4≡N5	180.0	178.6	178.3	178.2	177.6	177.3	177.9
	N9–C6–C1–C4	63±3	64.2	64.7	64.5	63.4	63.3	62.4
Gauche 3	C4–C1–C6		111.5	111.4	113.4	112.6	112.6	112.4
	C1–C6–N9		109.8	110.9	110.8	110.1	110.1	110.0
	C1–C4≡N5		179.1	178.3	178.3	178.4	178.5	178.2
	N9–C6–C1–C4		61.0	65.1	65.7	63.8	64.3	62.9
Trans 1	C4–C1–C6		112.0	112.5	112.4	112.1	(112.1	111.9
	C1–C6–N9		113.1	115.0	114.9	114.7	114.6	114.6
	C1–C4≡N5		178.7	178.1	178.0	177.9	177.8	178.3
	N9–C6–C–C4		180	180.0	180.0	180.0	180.0	180.0
Trans 2	C4–C–C6		112.0	112.5	112.4	112.2	112.1	111.8
	C1–C6–N9		108.0	109.2	109.1	109.0	108.9	108.9
	C1–C4≡N5		179.1	178.9	178.8	178.6	178.5	178.8
	N9–C6–C1–C4		179.9	179.4	179.4	180.0	179.7	179.9
TS1	C4–C1–C6			113.4	113.3	113.1	113.3	112.6
	C1–C6–N9			116.5	116.4	116.3	116.4	116.0
	C1–C4≡N5			178.4	178.2	178.3	178.2	178.7
	N9–C6–C1–C4			121.1	121.3	121.0	121.3	120.7
TS2	C4–C1–C6			113.6	113.5	113.3	113.2	112.8
	C1–C6–N9			110.2	(110.0	110.0	109.9	109.6
	C1–C4≡N5			179.1	179.0	178.9	178.7	179.1
	N9–C6–C1–C4			123.0	123.2	122.9	123.3	122.2
TS3	C4–C1–C6			113.7	113.6	113.2	113.0	113.0
	C1–C6–N9			118.7	118.5	118.3	118.1	118.2
	C1–C4≡N5			178.8	178.6	178.5	178.0	178.9
	N9–C6–C1–C4			0.0	0.0	0.0	0.0	0.0
TS4	C4–C1–C6			115.1	115.1	114.7	114.6	114.4
	C1–C6–N9			112.7	112.5	112.3	112.1	112.4
	C1–C4≡N5			177.2	177.2	177.4	177.5	177.3
	N9–C6–C1–C4			2.5	2.9	2.8	3.4	2.4
TS5	C4–C1–C6			113.4	113.3	113.1	113.1	112.7
	C1–C6–N9			110.6	110.3	110.3	110.2	109.9
	C1–C4≡N5			179.0	178.9	178.9	(178.7	179.1
	N9–C6–C1–C4			115.9	116.6	116.3	116.8	116.1

[a] Experimental value of gauche conformers are taken from reference [23] [b] Theoretical value of minima conformers are taken from reference [22]

lone-pair is clearly present in TS4, which is inferred by the high energy value. This interaction appears weaker in other transition states. Through all different levels of theory, except M06/aug-cc-pVDZ. TS2 has the lowest strain among all the transition states, indicated by the lower energy value (4.22 kcal/mol). The energies of the transition states are considered to be the energy barriers between gauche and trans conformers or the energy of the rotation around the N9-C6-C1-C4 dihedral angle.

According to more stable gauche conformer through CCSD/6-311+G(d,p), the rate constants *k,* of each rotational step, are ~1.5×10^9 s^{-1}, 5×10^9 s^{-1}, 2×10^9 s^{-1}, 1.5×10^8 s^{-1} and 2×10^9 s^{-1} calculated by using $\Delta G^{\#}_{TS1}$, $\Delta G^{\#}_{TS2}$, $\Delta G^{\#}_{TS3}$, $\Delta G^{\#}_{TS4}$ and $\Delta G^{\#}_{TS5}$ respectively, in following equation.[29]

$$k(T) = \frac{k_B T}{hc^{\circ}} e^{-\frac{\Delta G^{\#}}{RT}} \quad (5) \qquad (5)$$

Where the temperature is T=298.15 K and the concentration is c° = 1. The Boltzmann, Planck, and universal gas constants are denoted as kB, h, and R, respectively. The calculated rate constants indicate that at room temperature, the rotation around the dihedral angle occurs quite quickly.

The point charges of each atom have been determined using the NBO analysis by the CCSD/6-311+G(d,p) level of theory, Figure 2, to look more closely at the cause of the stabilization energy of the gauche 1 and gauche 2 conformers. The contact between the CN group and the eclipsed hydrogen (H10 atom in gauche 1) and (H11 atom in gauche 2) is attractive and has a value of 0.26 and 0.23 kcal/mol, respectively, according to Coulomb's potential in equation (3). This is taken to be the SE of the two gauche conformers' stabilization energy. These findings support the preceding relative energies discovery by demonstrating that the gauche 2 is somewhat more stable than the gauche 1. This is assumed to be the stabilization energy SE of the gauche 2 conformer.

Additionally, the electrostatic potential ESP contours in Figure 3 also depict the alluring contact between the nitrile group on the one hand, and the H10 atom in conformer 1, and the H11 atom in conformer 2. Due to the absence of appealing interactions between functional groups, the SE is missing in gauche 3 and trans conformers.

Additionally, the electrostatic potential ESP contours in Figure 3 demonstrate the attractive interaction between the nitrile group and the H10 (gauche 1) and H11 (gauche 2) atoms. The other conformers lack the SE because there are no alluring interactions between functional units. With

Table 3. The relative energies of each conformer compared with conformer (gauche 2).

Geometry	Method	Basis set	ΔH^a_{rel}	ΔG^a_{rel}	Geometry	Method	Basis set	ΔH^a_{rel}	ΔG^a_{rel}
Gauche 1	CCSD	6-311+G(d,p)	0.19	0.21	TS2[b]	CCSD	6-311+G(d,p)	3.7	4.22
	M06	6-311+G(d,p)	–0.07	–0.16		M06	6-311+G(d,p)	3.71	4.18
		aug-cc-pVDZ	0.07	0.02			aug-cc-pVDZ	3.62	4.08
	B3LYP	6-311+G(d,p)	–0.12	–0.1		B3LYP	6-311+G(d,p)	3.16	3.65
		aug-cc-pVDZ	0	–0.01			aug-cc-pVDZ	3.15	3.66
Gauche 3	CCSD	6-311+G (d,p)	1.35	1.28	TS3[b]	CCSD	6-311+G(d,p)	4.39	4.84
	M06	6-311+G (d,p)	1.38	1.27		M06	6-311+G(d,p)	3.74	4.14
		aug-cc-pVDZ	1.49	1.37			aug-cc-pVDZ	3.57	3.99
	B3LYP	6-311+G (d,p)	1.32	1.22		B3LYP	6-311+G(d,p)	3.66	4.13
		aug-cc-pVDZ	1.33	1.23			aug-cc-pVDZ	3.71	4.17
Trans 1	CCSD	6-311+G(d,p)	0.97	0.92	TS4[b]	CCSD	6-311+G(d,p)	5.87	6.29
	M06	6-311+G (d,p)	1.07	1.02		M06	6-311+G(d,p)	5.5	5.92
		aug-cc-pVDZ	1.01	0.9			aug-cc-pVDZ	5.29	5.76
	B3LYP	6-311+G(d,p)	0.4	0.39		B3LYP	6-311+G(d,p)	5.48	5.91
		aug-cc-pVDZ	0.46	0.44			aug-cc-pVDZ	5.35	5.79
Trans 2	CCSD	6-311+G(d,p)	0.65	0.45	TS5[b]	CCSD	6-311+G(d,p)	4.32	4.77
	M06	6-311+G(d,p)	0.68	0.61		M06	6-311+G(d,p)	4.22	4.58
		aug-cc-pVDZ	0.7	0.61			aug-cc-pVDZ	4.15	4.55
	B3LYP	6-311+G(d,p)	0.23	0.18		B3LYP	6-311+G(d,p)	3.7	4.13
		aug-cc-pVDZ	0.25	0.2			aug-cc-pVDZ	3.63	4.08
TS1[b]	CCSD	6-311+G(d,p)	4.42	4.92					
	M06	6-311+G(d,p)	4.14	4.61					
		aug-cc-pVDZ	4.16	4.66					
	B3LYP	6-311+G(d,p)	3.47	4.01					
		aug-cc-pVDZ	3.5	4.03					

[a] All energies are in kcal/mol. [b] $\Delta H_{rel} \equiv \Delta H^{\#}$ and $\Delta G_{rel} \equiv \Delta G^{\#}$ for transition state.

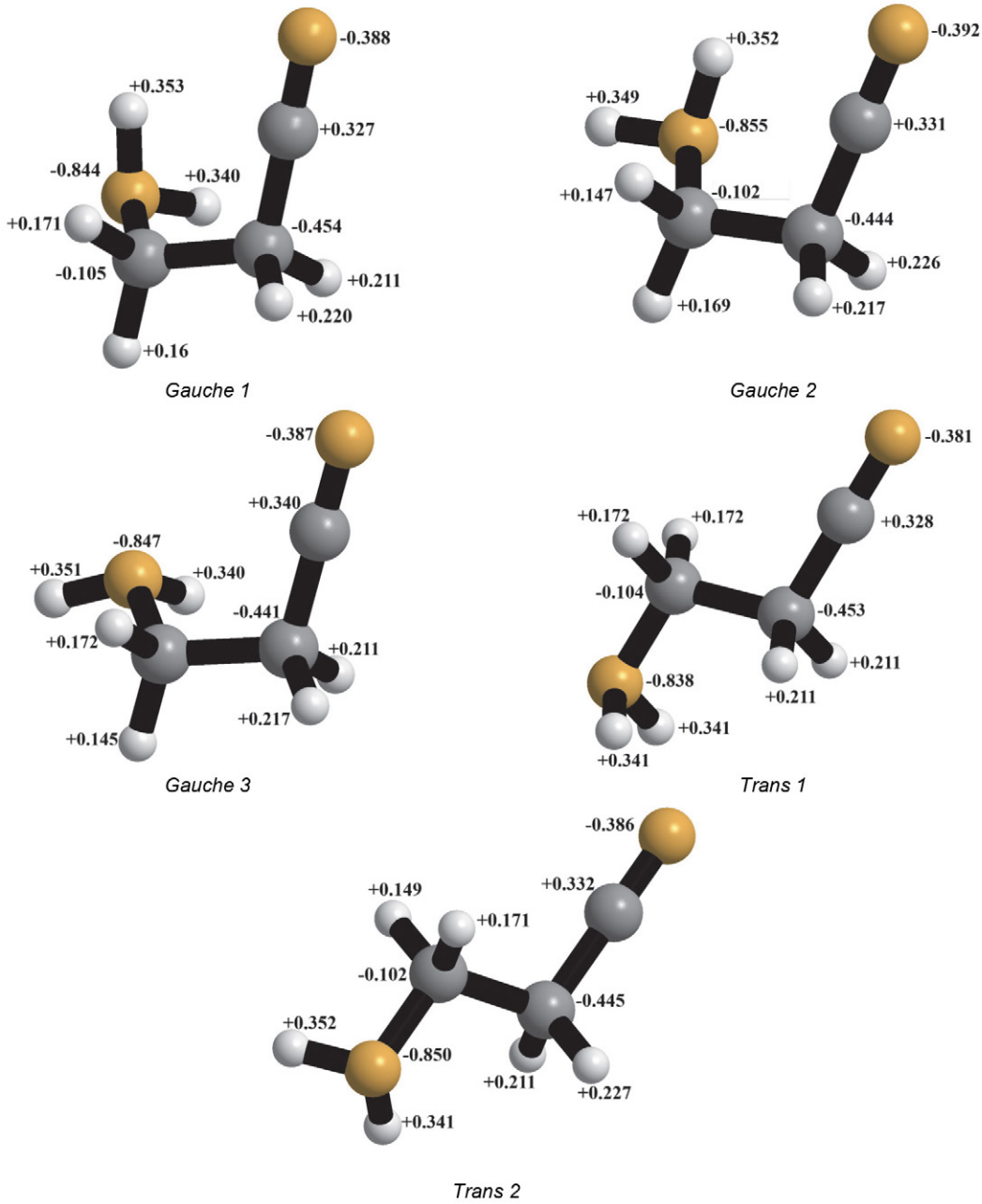

Figure 2. The NBO analysis of atomic charge distributions of the gauche and the trans 3-aminopropionitrile conformers using CCSD/6-311+G(d,p) method.

the help of the CCSD/6-311+G(d,p) method, the SE of gauche 2 was calculated as follows: SE = H_{rel} + ZPE + H_{corr} = 0.12 kcal/mol. This also took into account the addition of the difference between the zero-point energy and the thermal enthalpy correction. This number and the one determined using Coulomb's potential agree rather well.

3. 3. Vibrational Analysis

To show the 3-aminopropionitrile's conformational dynamics at ambient temperature, five minima conformers' vibrational frequencies were calculated using the high accuracy *ab initio* method CCSD with 6-311+G(d,p) basis sets,[30,31] since CCSD demonstrated greater accuracy in the prediction of the geometrical parameters, it is used as the primary computational method in this vibrational analysis. In Table 4, the calculated (CCSD/6-311+G(d,p)) vibrational modes wavenumbers for the five minima conformers (Fig. 2(and an assignment of the observed bands are also presented. The main experimental infrared intensities are also presented. The computed frequencies of more stable conformer are uniformly scaled by 0.934 for a better

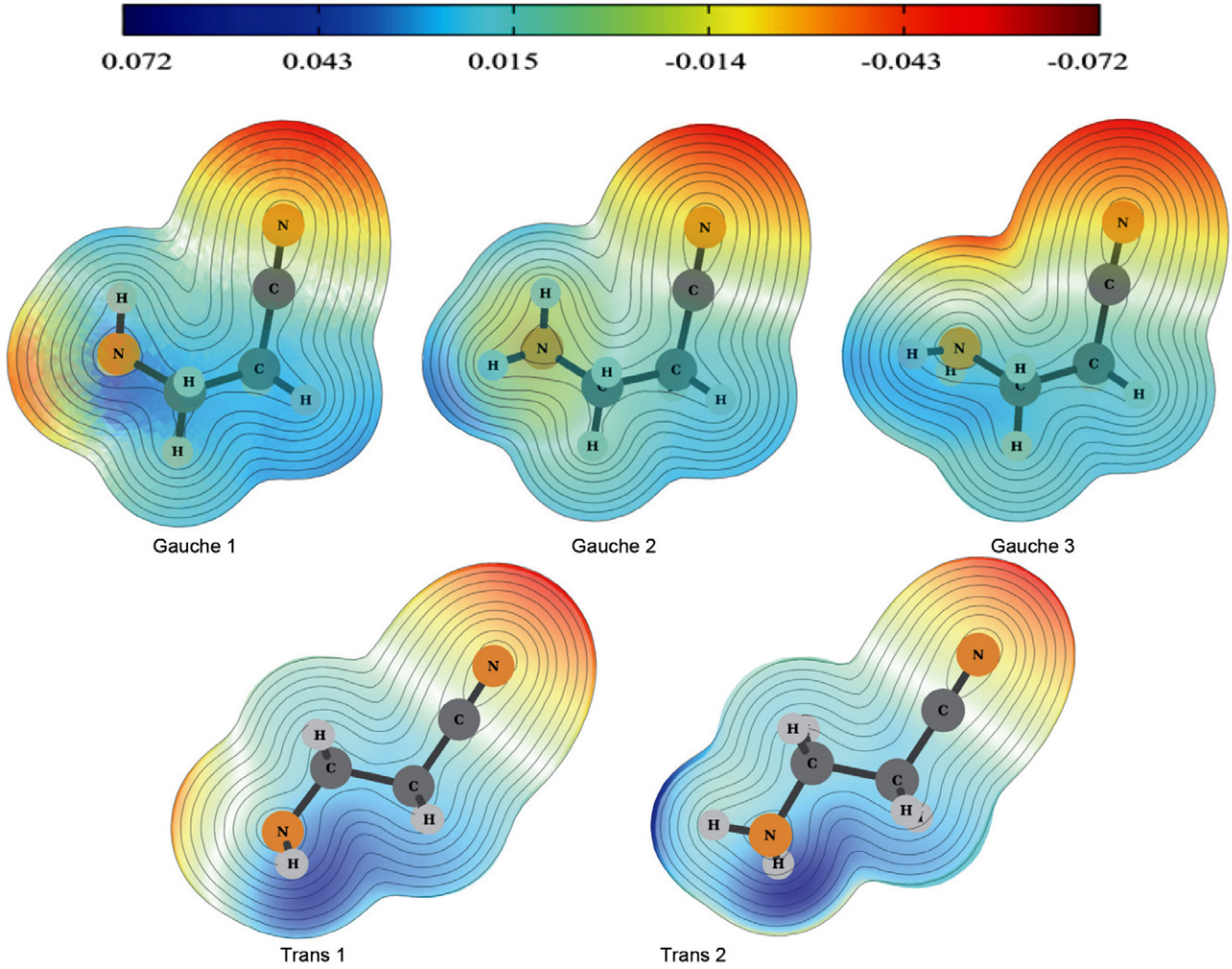

Figure 3. The NBO analysis of the electrostatic potential (ESP) of the gauche and the trans 3-aminopropionitrile conformers using CCSD/6-311+G(d,p) method.

comparison of the calculated frequencies with the observed frequencies.[32]

3-aminopropionitrile molecule has 11 atoms which create 27 internal normal vibrational modes. It has been clearly shown in various earlier research on organic-inorganic and hydrogen-bonded materials that the NH_3 torsion mode is extremely sensitive to changes in hydrogen bonds and conformational states.[33–35] Several conclusions from this study about the NH_3 vibrational modes are important to note: The bands that appear at 1603 cm^{-1} are thought to be the result of the NH_3 groups deforming symmetrically. This vibrational mode occurs at 1572, 1569, and 1565 cm^{-1} for the gauche 1, gauche 2, and gauche 3, respectively, according to the CCSD/6-311+G(d,p) calculations. Modes at 3317 and 3380 cm^{-1} described as symmetric and anti-symmetric deformation modes of the NH_3 groups, respectively. This modes are observed at (3304, 3302, and 3307 cm^{-1}) and (3384, 3382 and 3389 cm^{-1}) for the gauche 1, gauche 2, and gauche 3, respectively, according to this study. The NH_3 rocking and NH_3 twisting modes are at 856 cm^{-1} and 1313cm^{-1} respectively. These modes are observed at 830, 839, and 851 cm^{-1} and 1281, 1273, and 1257 cm^{-1} for the gauche 1, gauche 2, and gauche 3, respectively, according to my CCSD/6-311+G(d,p) calculations.

The more appropriate vibrations of the three conformers with respect to experimental vibrations are that of the conformer 1 as we can see from the difference between the scaled vibrations by CCSD/6-311+G(d,p) and the experimental vibrations (Table 4). Vibrational modes of NH_2 anti-symmetric stretch, α–CH_2 symmetric stretch, deformation, rocking, twisting and wagging, β–CH_2 anti-symmetric stretch, symmetric stretch and wagging, C–N stretch, C–C–C, C –C –N bending and C–C≡N out-of-plane bending of gauche 2 are closer to the experimental vibrations than others conformers.

3. 4. Frontier Molecular Orbitals

The frontier molecular orbitals (FMOs) of the highest occupied molecular orbital (HOMO) and lowest unoc-

Table 4: Calculated vibrational frequencies (cm^{-1}) at the CCSD/6-311+G(d,p) levels of theory.

Approximate description	Vibration (cm^{-1})/ 6-311+G(d,p)								Vibration (cm^{-1})
	Gau 1	Scaled[a]	Gau 2	Scaled[a]	Gau 3	Scaled[a]	Trans 1	Trans 2	Experimental[b]
NH_2 anti-symmetric stretch	3623	3384	3621	3382	3629	3389	3625	3623	3380
NH_2 symmetric stretch	3537	3304	3536	3302	3541	3307	3537	3537	3317
β–CH_2 anti-symmetric stretch	3131	2924	3142	2935	3127	2921	3138	3140	2994
α–CH_2 anti-symmetric stretch	3118	2912	3109	2904	3110	2905	3114	3112	2967
β–CH_2 symmetric stretch	3078	2875	3088	2884	3078	2875	3084	3083	2937
α–CH_2 symmetric stretch	3073	2870	3022	2822	3018	2819	3074	3030	2840
C≡N stretch	2338	2184	2338	2184	2344	2189	2338	2341	2244
NH_2 deformation	1683	1572	1680	1569	1676	1565	1682	1679	1603
α–CH_2 deformation	1513	1413	1535	1434	1534	1433	1519	1539	1474
β–CH_2 deformation	1494	1395	1489	1391	1494	1395	1496	1500	1423
α–CH_2 rock	1418	1324	1454	1358	1452	1356	1430	1461	1386
β–CH_2 rock	1415	1322	1383	1291	1399	1307	1411	1371	1334
NH_2 twist	1372	1281	1363	1273	1346	1257	1329	1343	1313
β–CH_2 twist	1274	1190	1259	1176	1299	1213	1322	1290	1216
α–CH_2 twist	1191	1112	1195	1116	1184	1106	1174	1185	1155
C–C(–N) stretch	1142	1067	1134	1059	1130	1055	1134	1125	1085
C–N stretch	1040	971	1093	1021	1046	977	1054	1089	1044
C–C(≡ N) stretch	977	913	986	921	1001	935	989	1004	973
NH_2 rock	889	830	898	839	911	851	956	948	856
β–CH_2 wag	868	811	876	819	869	812	856	883	850
α–wag	809	756	829	774	819	765	770	793	801
C–C–C bend	574	536	574	536	574	536	519	527	572
C–C–N bend	386	361	401	374	383	358	378	390	419
C–C≡N out-of-plane bend	372	347	371	347	368	344	376	372	375
NH_2 torsion	312	291	268	250	248	232	287	229	–
C–C≡N in-plane bend	190	177	195	182	178	166	164	166	–
C≡C(N) torsion	118	110	118	110	122	114	107	105	–

[a] Scaling coefficient =0.934.[32] [b] Observed vibrations.[15]

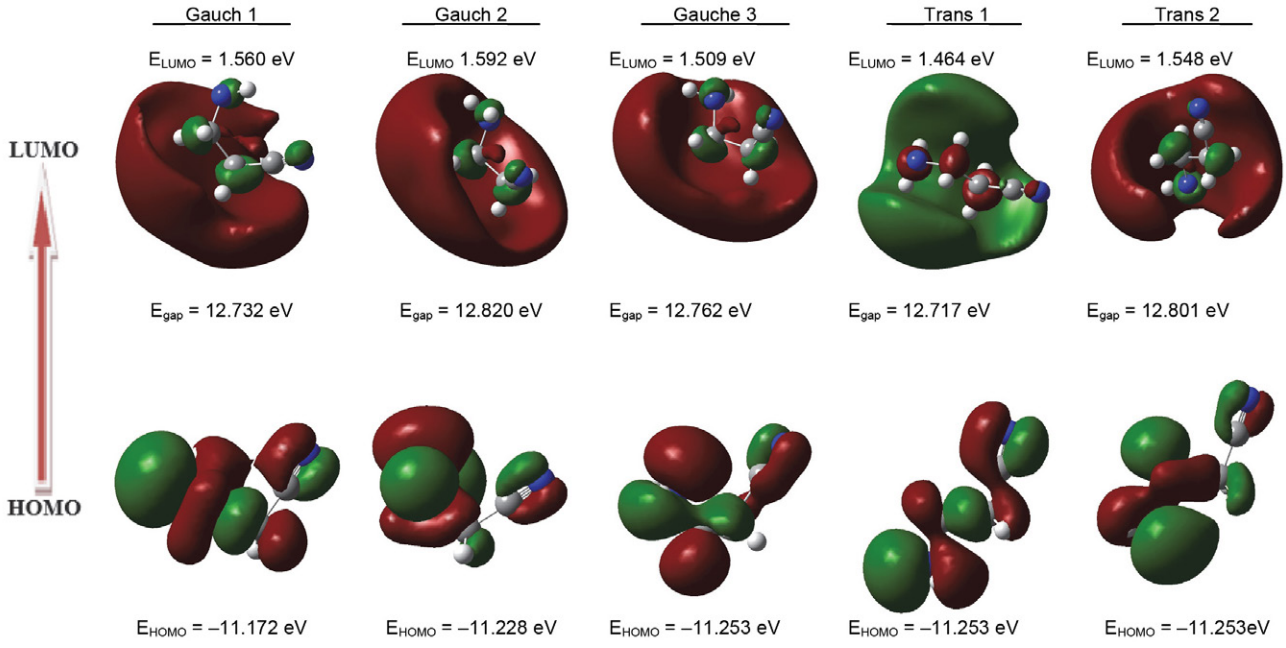

Fig. 4 Frontier molecular orbital of gauche 1, gauche 2, gauche 3, trans 1 and trans 2 conformers.

cupied molecular orbital (LUMO) of chemical species (using CCSD/6-311+G(d,p)) are essential pointers for chemical reactivity together with the stability of conformers (Figure 4). The results revealed that the gauche 2 conformer showed higher energy gap ($E_{LUMO} - E_{HOMO}$ = 1.592 eV – (– 11.228 eV), E_{gap} = 12.820 eV. This implies superior stability and lower chemical reactivity compared to its other conformers. The chemical potential (μ) = 0.5 * (E_{LUMO} + E_{HOMO}); showed negative values for the gauche 1, gauche 2, gauche 3, trans 1 and trans 2: −4.806, −4.818, −4.872, −4.895 and −4.853 eV conformers, respectively.

The phases of the lobes are indicated by the red and green colors. The molecular orbital wave function's positive and negative signs are represented by the colors red and green, respectively. Although there is a minor similarity in the frontier molecular orbitals of the gauche conformers and trans conformers individually, their HOMO and LUMO spatial positions are different. Using HOMO and LUMO orbital energies, the hardness η = 0.5*(E_{LUMO}–E_{HOMO}) is as follows; gauche 1, gauche 2, gauche 3, trans 1 and trans 2: 6.366, 6.41, 6.381, 6.3585 and 6.4005 eV, respectively. The softness S = 1/η; gauche 1, gauche 2, gauche 3, trans 1 and trans 2: 0.1571, 0.1560, 0.1567, 0.1573 and 0.1562 eV, respectively. Chemical hardness is a good indicator of probable chemical stability. A smaller energy gap results in a molecule with a higher softness value. Global electrophilicity index ω = $\mu^2/2\eta$ for gauche 2 is less electrophilic than another conformers with the lowest electrophilicity index of 1.811eV. High softness and low hardness values from the result's electrophilicity index are predictors of a good electrophile.

4. Conclusion

The geometry and relative stability of the 3-aminopropionitrile have been calculated theoretically using *ab initio* (CCSD/6-311+G(d,p)) and DFT (B3LYP and M06 functionals at 6-311+G(d,p) and aug-cc-pVDZ basis sets. The results show that 3-aminopropionitrile has five conformers, three gauche and two trans conformers. The geometrical outcomes of the gauche conformer agree very well with the experimental microwave and infrared results. Also, the thermal properties of the five conformers have been studied in the gas phase. Gauche 2 is the most stable conformer, according to recent study results, which agree with the accumulated experimental results. The results of the geometrical optimizations also closely match previous results that have been described in the literature. The vibrational modes of the five conformers were then computed and compared to past experimental results published in the literature, and the obtained results are in good agreement with the reported data with and without using scaling factor. As HOMO–LUMO gap implies high stability for a molecule, gauche 2 has a high HOMO-LUMO gap (12.820 eV), implies high stability for gauche 2 in the sense of its lower reactivity in chemical reactions. The positive potential sites are found close to the hydrogen atoms, while the negative potential sites are on the nitrile group, according to the ESP map.

Acknowledgements

The author is appreciative to Tafila Technical University (TTU)/Jordan for providing the resources required to perform the current study.

Declaration of Interest Statement

I declare that I do not have any commercial or associative interest that represents a conflict of interest in connection with the work submitted.

5. References

1. T. Endo, T. Kato, K. Tozaki, K. Nishikawa, *J. Phys. Chem. B.* **2010**, 114–407. **DOI:**10.1021/jp909256j
2. M. Maroncelli, S. P. Qi, H. L. Strauss, R. G. Snyder, *J. Am. Chem. Soc.* **1982**, *104*, 6237–6247. **DOI:**10.1021/ja00387a013
3. S. Barbaric, P. L. Luisi, *J. Am. Chem. Soc.* **1981**, *103*, 4239–4244. **DOI:**10.1021/ja00404a044
4. R. Zhang, Y. Liu, X. Huang, M. Xu, R. Liu, W. Zong, *Sci. Total Environ.* **2018**, *622*, 316–315. **DOI:**10.1016/j.scitotenv.2017.11.305
5. L. Zhou, W. Liu, R. Stockmann, N. S. Terefe, *Innov. Food Sci. Emerg. Technol.* **2018**, *45*, 196–207. **DOI:**10.1016/j.ifset.2017.10.012
6. A. Abouimrane, P. S. Whitfield, S. Niketic, I. J. Davidson, *J. Power Sources* **2007**, *174*, 883–888. **DOI:**10.1016/j.jpowsour.2007.06.103
7. P. J. Alarco, Y. Abu-Lebdeh, A. Abouimrane, M. Armand, *Nat. Mater.* **2004**, *3*, 476–481. **DOI:**10.1038/nmat1158
8. L. Carlucci, G. Ciani, D. M. Proserpio, S. Rizzato, *CrystEngComm.* **2002**, *4*, 413–425. **DOI:**10.1039/B202093A
9. S. M. D. R. Long, M. Forsyth, *Solid State Ionics.* **2003**, *161*, 105–112. **DOI:**10.1016/S0167-2738(03)00208-X
10. J. Y. Wang, M. C. Wang, D. J. Jan, *Sol. Energy Mater. Sol. Cells.* **2017**, *160*, 476–483. **DOI:**10.1016/j.solmat.2016.11.009
11. J. E. Elsila, J. P. Dworkin, M. P. Bernstein, M. P. Martin, S. A. Sandford, *Astrophys. J.* **2007**, *660*, 911–918. **DOI:**10.1086/513141
12. P. Ehrenfreund, W. Irvine, L. Becker, J. Blank, J. R. Brucato, L. Colangeli, S. Derenne, D. Despois, A. Dutrey, H. Fraaije, *Reports Prog. Phys.* **2002**, *65*, 1427. **DOI:**10.1088/0034-4885/65/10/202
13. A. Belloche, R. T. Garrod, H. S. P. Muller, K. M. Menten, *Science* **2014**, *345*, 1584–1587. **DOI:**10.1126/science.1256678
14. A "Aminopropionitrile – Compound Summary". PubChem Compound. USA: National Center for Biotechnology Information. 25 March **2005**. Retrieved 7 June **2012**.
15. J. R. Durig, I. D. Darkhalil, J. J. Klaassen, *J. Mol. Struct.* **2012**,

1023, 154–162.
DOI:10.1016/j.molstruc.2012.03.067
16. M. L. Becker, M. R. Nilsson, *J. Chem. Educ.* **2022**, *66*, 1847–1854. **DOI:**10.1021/acs.jchemed.1c00968
17. N. C. Craig, A. Chen, K. H. Suh, S. Klee, G. C. Mellau, B. P. Winnewisser, M. Winnewisser, *J. Am. Chem. Soc.* **1997**, 119, 4789–4790. **DOI:**10.1021/ja963819e
18. E. Hirota, *J. Chem. Phys.* **1962**, *37*, 2918–2920. **DOI:**10.1063/1.1733117
19. J. R. Durig, B. R. Drew, A. Koomer**, S.** Bell**,** *Phys. Chem. Chem. Phys.* **2001**, *3*, 766–775. **DOI:**10.1039/b007856p
20. J. R. Durig, J. Liu, T. S. Little, V. F. Kalasinsky, *J. Phys. Chem.* **1992**, *96*, 8224–8233. **DOI:**10.1021/j100200a006
21. J. J. Turner, M. Poliakoff, S. M. Howdle, S. A. Jackson, J. G. McLaughlin, *Faraday Discuss. Chem. Soc.* **1988**, *86*, 271–284. **DOI:**10.1039/dc9888600271
22. O.-A. Braathen, K.-M. Marstokk, H. Møllendal, *Acta Chem. Scand. A*. **1983**, *37*, 493–501. **DOI:**10.3891/acta.chem.scand.37a-0493
23. P. N. Skancke, *Acta Chem. Scand. A*. **1984**, *38*, 95–99. **DOI:**10.3891/acta.chem.scand.38a-0095
24. M. J. Frisch, G. W. Trucks, H. B. Schlegel, G. E. Scuseria, M. A. Robb, J. R. Cheeseman, G. Scalmani, V. Barone, G. A. Petersson, H. Nakatsuji, et al: Gaussian G09, Revision D. 01, **2013**, Gaussian Inc., Wallingford CT.
25. D. G Purvis, R. J. Bartlett, *J. Chem. Phys.* **1982**, *76*, 1910–1918. **DOI:**10.1063/1.443164
26. A. Al-Msiedeen, *Jordan. J. Eng. Chem. Ind.* **2022**, *5*, 92–101.
27. O. V. Sizova, *J. Mol. Struct.: THEOCHEM* **2006**, *760*, 183–187. **DOI:**10.1016/j.theochem.2005.10.046
28. C. Cercignani, The Boltzmann Equation. In: The Boltzmann Equation and Its Applications. Applied Mathematical Sciences, vol 67. Springer, New York, NY, **1988**, pp. 40–103. **DOI:**10.1007/978-1-4612-1039-9_2
29. D. A. McQuarrie, J. D. Simon, *Chem. Educator* **1999**, *4*, 120–121. **DOI:**10.1007/s00897990307a
30. I. D. Mackie, G. A. Dilabio, *J. Chem. Phys.* **2011**, *135*, 134318–1–10. **DOI:**10.1063/1.3643839
31. K. Remya, C. H. Suresh, *J. Comput. Chem*. **2013**, *34*, 1341–1353. **DOI:**10.1002/jcc.23263
32. R. D. Johnson, NIST 101. Computational chemistry comparison and benchmark database, **1999**, http://cccbdb.nist.gov/.
33. Y. Abid, M. Kamoun, A. Daoud, F. Romain, *J. Raman Spectrosc*. **1990**, *21*, 709–716. **DOI:**10.1002/jrs.1250211103
34. C. Sourisseau, G. Lucazeau, *J. Raman Spectrosc*. **1979**, *8*, 311–319. **DOI:**10.1002/jrs.1250080604
35. H. Feki, M. Bahri, A. Maalej, Y. Abid, N. Jaidane, Z. B. Lakhdar, *Phase Transit.* **2000**, *72*, 331–340. **DOI:**10.1080/01411590008227787

Povzetek

Poznanih je veliko konformer 3-aminopropionitrila. Zaradi biomedicinske pomembnosti smo obširno preiskali strukturne, vibracijske in druge lastnosti možnih konformer. Geometrijske strukture, relativna stabilnost in vibracijske frekvence konformer 3-aminopropionitrila v gauche in trans obliki smo preučili z *ab initio* računi (CCSD/6-311+G(d,p)) in DFT (B3LYP in M06 ter bazna seta 6-311+G(d,p) in aug-cc-pVDZ). Interpretacija predstavlja znatno izboljšanje preteklih študij. Izračun CCSD/6-311+G(d,p) pokaže, da je gauche 2 konformera za 0,19 kcal/mol bolj stabilna od gauche 1 (izraženo v razliki entalpij med konformerama). Analiza verjetnostne porazdelitve kaže, da so v plinski fazi gauche konformere pogostejše kot trans konformere (72,8 % delež) pri čemer je gauche 2 prevladujoča gauche konformera (40,1 % delež). Ti rezultati se dobro ujemajo s prejšnjimi eksperimentalnimi in računskimi študijami. Proučili smo tudi geometrijske značilnosti vseh optimiziranih konformer, ki se zelo dobro ujemajo z prejšnjimi eksperimentalnimi rezultati. Zvezo med strukturo in aktivnostjo smo opisali z izračunom ploskve elektrostatskega potenciala. Analizirali smo tudi atomske naboje ter energijsko vrzel med najvišjo zasedeno in najnižjo nezasedeno molekulsko orbitalo (HOMO-LUMO vrzel). Elektronsko strukturo najbolj stabilnih konformer smo analizirali z metodo naravnih veznih orbital (NBO).

DOI: 10.17344/acsi.2024.8629 *Acta Chim. Slov.* **2024,** *71,* 256–263

Scientific paper

Expression and Purification of Active Human 17β-Hydroxysteroid Dehydrogenase Type 1 from *Escherichia coli*

Sofija S. Bekić,[1,*] Jovana J. Plavša,[2] Miha Pavšič,[3] Brigita Lenarčič,[3] Edward T. Petri[2] and Andjelka S. Ćelić[2]

[1] *University of Novi Sad, Faculty of Sciences, Department of Chemistry, Biochemistry and Environmental Protection, Trg Dositeja Obradovića 3, 21000 Novi Sad, Serbia*

[2] *University of Novi Sad, Faculty of Sciences, Department of Biology and Ecology, Trg Dositeja Obradovića 2, 21000 Novi Sad, Serbia*

[3] *Department of Chemistry and Biochemistry, Faculty of Chemistry and Chemical Technology, University of Ljubljana, SI-1000 Ljubljana, Slovenia.*

** Corresponding author: E-mail: sofija.bekic@dh.uns.ac.rs*
Tel: +381 21 485 2715

Received: 01-19-2024

Abstract

Breast cancer cell growth is often dependent on the presence of steroidal hormones. The 17β-hydroxysteroid dehydrogenase type 1 isoform (17βHSD1) catalyzes NADPH-dependent conversion of estrone to estradiol, a more potent estrogen, and represents potential drug target for breast cancer treatment. To provide active enzyme for inhibitor screening, 17βHSD1 is usually expressed in insect or mammalian cells, or isolated from human placenta. In the present study we describe a simple protocol for expression and purification of active human 17βHSD1 from *Escherichia coli* BL21(DE3) cells. Soluble human 17βHSD1 was expressed using a pET28a(+)-based plasmid, which encodes a hexahistidine tag fused to the N-terminus of the protein, and purified by nickel affinity chromatography. The enzyme activity of purified 17βHSD1 was verified by three methods: thin-layer chromatography, an alkali assay and a spectroscopic assay. These non-radioactive enzyme assays require only standard laboratory equipment, and can be used for screening compounds that modulate 17βHSD1 activity.

Keywords: Steroid hormone; 17β-Hydroxysteroid dehydrogenase; 17βHSD1; breast cancer; alkali assay; TLC

1. Introduction

Endogenous steroid hormones are derived from a cholesterol precursor by a series of successive, coordinated enzymatic reactions in a biosynthetic pathway known as steroidogenesis.[1] Steroidogenic enzymes can be classified into two groups: cytochrome P450 (CYP450) enzymes and steroid dehydrogenases.[2] 17β-Hydroxysteroid dehydrogenases (17HSDs) catalyze the last step in the biosynthesis of the active forms of androgen and estrogen hormones[2], by stereospecific hydrogenation at the C17β position, while in the opposing direction oxidation results in inactivation of these C18 and C19 steroids.[3] In mammalian cells, 17HSDs regulate ligand availability for steroid receptors, acting as a molecular "switch" responsible for catalyzing conversion between the active and inactive forms of steroid hormones.[4] These multifunctional enzymes are characterized by different cofactors (NAD(P)H), substrates (e.g. steroid hormones, bile acids, fatty acids) and tissue expression specificities.[5]

The 17β-Hydroxysteroid dehydrogenase type 1 isoform (17βHSD1) catalyzes: 1) NAD(P)H-dependent reduction of estrone to estradiol, a more potent estrogen, predominantly in the breast, ovaries and placenta[4,5]; 2) conversion of dehydroepiandrosterone (DHEA) to androstenediol; and 3) inactivation of dihydrotestosterone.[6] Mutations and changes in intracellular NAD(P)(H) cofactor abundance and redox state affect the equilibrium ratio

of E2 to E1 catalyzed by 17βHSD1.[7] Imbalances in steroid biosynthesis and signaling are often associated with the development of endocrine disorders, as well as hormone-sensitive cancers.[8] Due to urbanization, changes in lifestyle and increased exposure to endocrine disruptors, the incidence of hormone-dependent malignancies, such as breast and prostate cancer is rising and continues to represent a global health problem.[9] Compared to normal breast tissue, expression of 17βHSD1 is higher in tumor cells[6] and is associated with poor prognosis.[10] Thus, inhibition of this steroid-converting enzyme and reduction of estrogen levels could potentially be a promising treatment strategy. The pentose-phosphate pathway is active in metastatic breast cancers, potentially leading to increased E2 synthesis through the action of 17βHSD1. Therefore, exploring inhibition of interconnected signaling pathways, such as glucose metabolism, could also reduce estrogen levels and become approach for treating estrogen-dependent diseases.[7] Possibly due to its roles in the regulation of intracellular estradiol levels and involvement in breast carcinogenesis and other estrogen-dependent diseases, 17βHSD1 was the first human steroidogenic enzyme to be studied by protein X-ray crystallography. Ghosh et al. reported the X-ray structure of human 17βHSD1 (PDB ID: 1BHS), enabling rational structure-based design of selective 17βHSD1 inhibitors.[11,12] Inhibitors of 17βHSD1 based on steroidal (especially estrone derivatives) [13], nonsteroidal and flavonoid scaffolds have been identified, but have not yet been clinically approved. [10]

Our group is interested in the synthesis and characterization of steroidal inhibitors of steroidogenic enzymes, as well as steroidal ligands of hormone-receptors for use against hormone-dependent cancers or other disorders. As part of this effort, here we report a simple protocol to obtain active human 17βHSD1 for screening steroidal derivatives as potential inhibitors. Previous studies have relied on heterologous expression of 17βHSD1 in insect or mammalian cells[13,14]; or purification of endogenous 17βHSD1 enzyme from the cytosolic fraction of human placenta.[15,16] However, human placenta is difficult to obtain while insect and mammalian expression systems require special equipment and are considerably more challenging and expensive than bacterial expression systems. To date, only one previous study reported the expression and purification of human 17βHSD1 from *E. coli*. [17] In that study, the coding sequence for 17βHSD1 was cloned into a pET28a(+) plasmid and expression in *E. coli* was induced during low temperature (13°C) incubation by addition of 0.25 mM Isopropyl β-d-1-thiogalactopyranoside (IPTG). Unfortunately, the majority of the expressed 17βHSD1 protein was located in the insoluble fraction, and attempts to refold the protein from inclusion bodies yielded inactive, misfolded enzyme.[17] However, recombinant 17βHSD1 isolated from the soluble fraction was demonstrated to be folded by circular dichroism spectroscopy and was shown to be able to catalyze oxidation of estradiol with a pH optimum of 9.3.[17] Mass-spectrometric and radiometric detection are generally used for measuring the enzyme activity of 17βHSDs, with the first method being recommended as more sensitive and accurate.[18] However, this powerful analytical method requires specialized equipment and radioassays are based on the use of tritium-labeled substrates, which limits their application.

In the present study, we optimize the methods originally reported in Chang et al. to obtain soluble 17βHSD1 from this pET28a(+)-17βHSD1 plasmid using induction at 23°C and purification by nickel affinity chromatography. Reduction of estrone to estradiol by recombinant human 17βHSD1 is shown using thin-layer chromatography (TLC). The activity of 17βHSD1 was also measured using an alkali and fluorometric assay, which represent alternative, non-radioactive approaches to measure 17HSD activity that are inexpensive and require only standard laboratory equipment. The methods described in the present study should facilitate production of active human 17βHSD1 from *E. coli* and provide a set of simple *in vitro* screening tools for identification of novel 17βHSD1 inhibitors.

2. Experimental

2. 1. Materials

The plasmid vector pET28a(+)-17bHSD1 was a generous gift from Dr. Chi-Ching Hwang, Department of Biochemistry, Faculty of Medicine, College of Medicine, Kaohsiung Medical University, Taiwan.[17] The host *Escherichia coli* strain BL21(DE3) was obtained from Novagen (Merck KGaA, Germany). All chemicals were of analytical grade and were used without further purification. Components for the preparation of LB media were obtained from Torlak Institute (Belgrade, Serbia). Isopropyl β-D-1-thiogalactopyranoside (IPTG) was obtained from Fisher Scientific (ThermoFisher Scientific). Lysozyme, tris-hydrochloride and mono- and dibasic potassium phosphate were purchased from Sigma-Aldrich. Kanamycin sulfate, imidazole and NADPH were purchased from Carl Roth. All organic solvents used were from Lach-Ner. HisTrap HP columns were obtained from Cytiva and TLC plates (Silica gel 60 F_{254}) from Merck.

2. 2. Expression and Purification of 17βHSD1

A pET28a(+) plasmid containing the coding sequence for human 17b-HSD1 (pET28a-17bHSD1) was used to transform chemically competent *Escherichia coli* BL21(DE3) cells using a calcium chloride heat shock method.[19] Plasmid DNA (pET28a(+)-17bHSD1) was purified according to the manufacturer's instructions using a QIAprep Spin Miniprep Kit (QIAGEN), yielding approximately 80 ng/μl of plasmid. Purified plasmid was verified by restriction digestion using *Eco*RI (40,000 U/μl) according to the manufacturer's instructions (Sigma)

and 1% agarose gel electrophoresis. Chemically competent *Escherichia coli* BL21(DE3) cells that had been stored at –80 °C were thawed on wet ice in 1.5 mL microcentrifuge tubes, and 2 µl of plasmid DNA was gently mixed with 90 µl of thawed cells and incubated on ice for 40 min. Cells were then transferred into a 42 °C water bath (heat-shock) for 45 seconds, followed by recovery on ice for 2 minutes. Afterwards, 900 µl of LB media was added to the transformation mixture, and cells were gently mixed for 1 hour at 37 °C. Cells were then spread onto LB agar plates containing kanamycin (50 µg/mL) and incubated overnight at 37 °C. The following day, a single colony was picked, inoculated into 10 mL of fresh LB media containing kanamycin (50 µg/mL) and incubated at 37 °C overnight in a Biosan orbital shaker-incubator ES-20/60. An aliquot of bacterial cells was then transferred into 1 L of fresh media (1:100) and grown at 37 °C to an optical density at 600 nm (OD_{600}) of approximately 0.4. Protein expression was then induced by addition of IPTG at a final concentration of 0.25 mM and incubation was continued at room temperature (23 °C) for 18 hours. Cells were collected by centrifugation at 5000 × g for 10 minutes at room temperature and the supernatant was discarded. The resulting cell pellet was resuspended in 20 mL of 20 mM TrisHCl pH 7.95, 0.3 M NaCl, 5 mM imidazole. Lysozyme was added at a final concentration of 1 mg/mL and the cell suspension was frozen in an ethanol-dry ice bath and stored at –80 °C. Cell lysis was done using a combination of lysozyme treatment, three freeze-thaw cycles and sonication using a Soniprep 150 sonicator set at 50% amplitude and 30 seconds pulse settings. A single freeze-thaw cycle consists of freezing cells in an ethanol-dry ice bath followed by thawing in a 37 °C water bath. Cells were then sonicated at a frequency of 14 kHz. Seven sonication steps of 30 seconds each were performed, coupled with a recovery interval on ice of 30 seconds between each sonication step. Following sonication, lysed cells were clarified by centrifugation at 12000 × g for 45 minutes at 4 °C, to separate the soluble and insoluble fractions. His-tagged 17βHSD1 was then purified from the soluble fraction by nickel-affinity chromatography using a 1 mL HisTrap HP column (Cytiva) connected to peristaltic pump Pharmacia LKB P-1 following the manufacturer's instructions with slight modifications. A 1 mL HisTrap HP column was equilibrated with 10 column volumes (CV) of binding buffer (20 mM TrisHCl pH 7.95, 0.5 M NaCl) and the soluble fraction was applied. The column was then washed with 10 CVs of binding buffer, and then with 5 CVs of binding buffer plus 20 mM imidazole. 17βHSD1 protein was eluted with 5 CVs of elution buffer (20 mM TrisHCl pH 7.95, 0.5 M NaCl, 400 mM imidazole pH 8.3). Eluted protein was further desalted and excess of residual imidazole was removed by size-exclusion chromatography column packed with Bio-Gel P-10 (Bio-Rad, exclusion limit 20 000 daltons). Protein containing fractions were pooled and buffer was exchanged into 20 mM TrisHCl pH 7.95, 0.1 M NaCl. Samples of fractions from all expression and purification steps were collected and analyzed by SDS-PAGE using a 12% (w/v) polyacrylamide gel. Concentration of total protein was measured by the Bradford method.[20]

2. 3. Enzyme Assay Coupled with TLC Detection

Enzyme activity assays for 17βHSD1 were carried out immediately after purification, because we observed a substantial loss of enzyme activity after storage of the enzyme at –80 °C. Steroid substrates were freshly dissolved in dimethyl sulfoxide (DMSO) at a concentration of 100 mM. Estrone at a final concentration 178 µM was incubated at 37 °C for 90 min in a 560 µl assay mixture containing 50 µl of purified 17βHSD1 enzyme (70 µg), NADPH (final concentration 178 µM) and 100 mM potassium phosphate buffer pH 6.0. In control reactions, 17βHSD1 enzyme was omitted. The reaction was stopped by adding 500 µl of methylene chloride and steroid reaction products were extracted by vortexing for 5 minutes. Phase separation was performed by centrifugation at low speed. The lower organic layer was carefully aspirated and evaporated to dryness at room temperature. Dry residue was then dissolved in 50 µl of methylene chloride and spotted on a 60 F_{254} TLC Silica gel plate. TLC plates were developed using a toluene and ethyl acetate (2:1) solvent system as a mobile phase. After drying, spots were sprayed with 50% H_2SO_4 and heated at ~ 120 °C before images of the plate were captured in Biometra gel imaging system BDAdigital. Concentration of estradiol formed in the reaction was obtained from standard curve after densitometric analysis and specific enzyme activity was expressed as nmol E2 formed min^{-1} mg^{-1}.

2. 4. Alkali Assay

A modified alkali assay that was previously reported for testing the activity of human aromatase[21] was used to evaluate 17βHSD1 activity. This assay is based on the formation of a fluorescence product between a strong alkali and $NADP^+$ produced during NADPH-dependent reduction of substrate. Initially, a reaction mixture containing 70 µg of protein, 40 µM estrone and 200 µM NADPH in up to 500 µl 100 mM potassium phosphate buffer pH 6.0 was incubated at 37 °C for 90 minutes. Upon completion of the reaction, 100 µl of product mixture was transferred to a 96-well microplate (Greiner Bio-One MICROLON) and mixed with 80 µl of 0.3 M HCl at room temperature for 15 minutes in order to eliminate excess unoxidized NADPH. In the next step, 80 µl of this mixture was transferred into a new well and 270 µl of 10 M NaOH was added. Fluorescence intensity was measured at the beginning of the reaction (0 min) using a Fluoroskan Ascent FL with excitation and emission wavelengths of 340 and 460 nm, respectively. To prevent degradation of the resulting fluorescent alkali product, incubation was carried out in the dark at 30 °C for 2 hours. Finally, 10

mM imidazole was added and fluorescence intensity was measured again (120 min) under identical conditions. Parallel control experiments were conducted with 17βHSD1 enzyme that was previously denatured by boiling at 100 °C for 10 min. All experiments were performed in duplicate. Results are expressed as the mean value of the change in fluorescence intensity ($\Delta F = F_{120'} - F_{0'}$). Concentration of NADPH consumed in the reaction was obtained from standard curve and specific enzyme activity was expressed as nmol NADPH consumed min^{-1} mg^{-1}.

2. 5. Fluorimetric NADPH Assay

Because 17βHSD1 is an NADPH-dependent enzyme, reduction of estrone by 17βHSD1 was also assayed indirectly by measuring the decrease in NADPH fluorescence at excitation/emission wavelengths of 340/460 nm using a Fluoroskan Ascent FL fluorimeter. Reaction mixtures contained 67 μM estrone and 167 μM NADPH in 100 mM potassium phosphate buffer pH 6.0. Reactions were initiated with the addition of 50 μl of 17βHSD1 containing fraction (70 μg total protein by Bradford assay). Substrates were freshly dissolved in DMSO and the concentration of DMSO solvent did not exceed 1% in any well. Kinetic measurement of NADPH consumption was performed in a 96-well microplate (Greiner Bio-One MICROLON) at 37 °C and reactions were monitored at 15 seconds-intervals for 20 minutes. A control, blank assay was conducted without 17βHSD1 enzyme to assess non-enzymatic NADPH consumption. Fluorescence *vs*. time data was plotted in Origin Pro8 after slope normalization.

3. Results and Discussion

In humans, the 17βHSD1 isoform is mainly responsible for the final step of estrogen biosynthesis in pre-menopausal women, and is therefore considered to be a potential therapeutic target for estrogen-sensitive cancers and other hormone-dependent disorders.[22] Previous studies have shown that human placental microsomes are rich source of 17βHSD1 for experiments[15], and that Sf9 insect cell expression systems can provide active 17βHSD1 enzyme in high yield.[13,23] However, experiments using human placental tissue require special ethical approval, while heterologous expression of proteins in insect cell systems is technically more challenging and more expensive than use of bacterial expression systems.

Few published reports have described use of human 17βHSD1 expressed from *Escherichia coli*.[10] In the present study we expressed and purified human 17βHSD1 from *Escherichia coli* and optimized three simple non-radioactive assays for *in vitro* measurement of enzyme activity. Expression of 17βHSD1 was induced by addition of 0.25 mM IPTG in mid-logarithmic phase of growth of BL21(DE3) *Escherichia coli* cells transformed with pET28a(+) 17b-HSD1 plasmid. After induction with IPTG and incubation of cells at 23 °C for 18 h, a new band corresponding to ~ 40 kDa was detected by SDS-PAGE gel electrophoresis, consistent with the predicted molecular weight of 39.2 kDa for His-tagged 17βHSD1 (Figure 1, Panel A).

Following induction, cells were lysed by three freeze-thaw cycles and sonication, and the resulting cell lysate was clarified by centrifugation. Comparison of the soluble and insoluble fractions shows that a portion of the expressed 17βHSD1 protein appeared to be localized in the soluble fraction (Figure 1 Panel A). This soluble fraction was applied to a 1 mL HisTrap HP column equilibrated in binding buffer (20 mM TrisHCl pH 7.95, 0.5 M NaCl), washed once in binding buffer, and again in binding buffer plus 20 mM imidazole. Protein was eluted in binding buffer plus 400 mM imidazole (Figure 1 panel B). As measured by Bradford assay, a final yield of 1.4 mg/mL total protein was obtained from 1 L culture of *E. coli* cells, which was sufficient for enzymatic activity studies. Using densitometric analysis of SDS-PAGE gel to quantify protein bands it was determined that 17βHSD1 protein amounts to 10% of the total protein content.

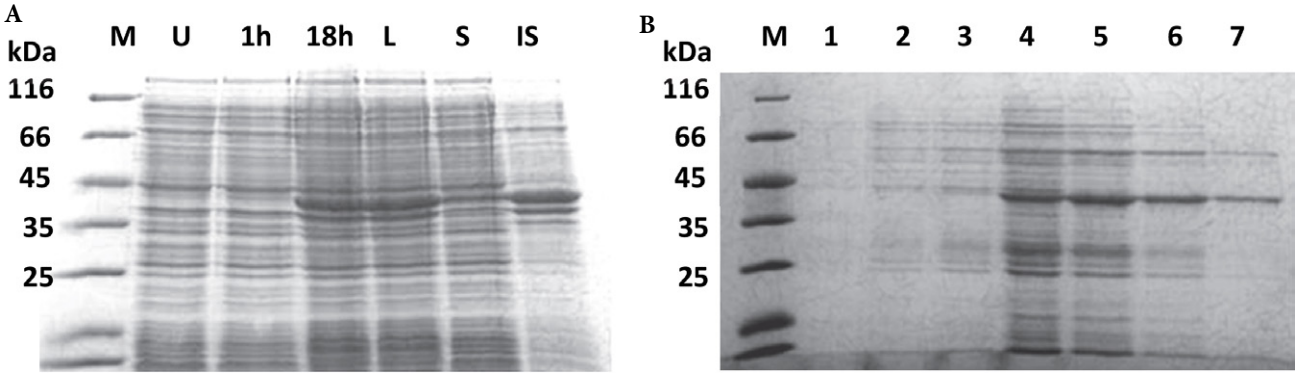

Figure 1. Analysis of the expression and purification of human His-tagged 17βHSD1 by SDS-PAGE electrophoresis. Panel A) Induction of expression of human 17βHSD1 in BL21(DE3) *E. coli* cells with 0.25 mM IPTG followed by 18h incubation at room temperature (23 °C): M-molecular weight marker; U – uninduced cell control; 1h – protein expression 1 hour after IPTG induction at room temperature; 18h – protein expression 18 hours after IPTG induction at room temperature; L – lysate; S – soluble fraction; IS – insoluble fraction. B) M-marker (ROTI®Mark STANDARD); wash fractions (lanes 1, 2) and elution fractions (lanes 3–7) from a 1 mL HisTrap HP nickel column.

In agreement with Chang et al., in our hands the majority of 17βHSD1 was also localized to the insoluble fraction in inclusion bodies. Chang et al were not able to refold and recover functional, catalytically active 17βHSD1 following solubilization of these inclusion bodies using 6 M urea.[17] In addition to refolding, yield of soluble protein can sometimes be improved by use of different host *Escherichia coli* strain and/or plasmid vector combination.[24] Mottinelli et al obtained active human 17βHSD1 from a different plasmid vector (pQE30) and different BL21 *Escherichia coli* host (BL21-CodonPlus DE3 RIL), using a 2 hour induction period at 37 °C and 0.5 mM IPTG.[10] Resulting cells were immediately harvested by centrifugation, resuspended in phosphate buffered saline and lysed by sonication before direct use in enzyme activity assays. Because cell homogenates were not clarified and no further purification steps were employed, the level of 17βHSD1 protein in the soluble fraction following this protocol remains unknown. Interestingly, although not explicitly mentioned by the authors, it appears that in Mottinelli et al. the whole cells and resulting cell homogenate were never frozen before measurement of 17βHSD1 activity. Considering that we observed significant loss of 17βHSD1 activity upon storage of purified protein at –80 °C, consistent with observations also reported by Chang et al[17], it is possible that freezing itself could be detrimental to 17βHSD1 activity. It may be possible to improve upon the results of the present study by optimizing or eliminating freezing steps during expression and purification of human 17βHSD1.

The majority of 17βHSD1 was located in the 3rd elution fraction (lane 5). Pool of fractions 4–6 was immediately applied to a desalting size-exclusion column and new pooled eluates with the highest protein content were used as a source of enzyme for *in vitro* assays. Since we observed loss of 17βHSD1 activity after freezing, all enzyme assays were performed immediately after purification. Cold inactivation of 17HSDs from human placenta was previously reported and protective effects of addition of glycerol, substrate and cofactor were investigated by Jarabak et al.[25] We did not notice that freezing in the presence of glycerol improved enzyme stability after storage at –80 °C.

Published procedures for measuring 17HSD activity usually rely on detection of radioactivity[10,13,16] carrying health risks and requiring use of labeled probes and expensive antibodies[26]. With this in mind, to overcome the hazards of handling radioisotopes, reduce costs and simplify experimental design, we optimized alternative non-radioactive screening assays for the characterization of 17βHSD1 modulators. Although Chang et al reported optimal enzymatic activity at a relatively high pH value of 9.3 in the reaction mixture and a temperature optimum of 25 °C[17]; we performed our activity measurements at pH 6.0 and temperature (37 °C), similarly to Motinelli et al[10] and reflecting physiological conditions.

High performance liquid chromatography (HPLC) is considered to be an analytical procedure of choice for the separation and quantification of steroid products of enzymatic reactions catalyzed by 17HSDs or other steroidogenic enyzmes.[10,13,27] Taking into consideration the relatively high costs of HPLC for preliminary screening, we coupled our enzymatic assay with a more inexpensive and fast TLC detection method. As shown in TLC chromatograms (Figure 2.A and B.) conversion of estrone (E1) to estradiol (E2) was catalyzed by addition of purified 17βHSD1 protein. Confirmation was based on the identical mobility of reaction product (R) and reference standard, estradiol (E2). Moreover, in control reactions in the absence of 17βHSD1 enzyme, no conversion of estrone to estradiol was observed by TLC. Results from TLC also suggest that freezing affects the stability and activity of recombinant 17βHSD1: complete loss of 17βHSD1 activity was observed after storage at –80 °C for several days (Figure 2.C). In order to quantify zones from TLC chromatograms, programs for densitometric image analysis, such as Image J have been used.[28–30] Formation of 17β-hydroxysteroids was previously analyzed by TLC only in the context of biotransformation studies, where steroid molecules undergo metabolic transformations over different time intervals.[31,32] Specific enzyme activity of 17βHSD1 was determined by measuring formation of estradiol. Densitometric analysis of TLC plates and quantification of the amount of product formed was performed using open-source ImageJ software. TLC chromatogram of estradiol at different con-

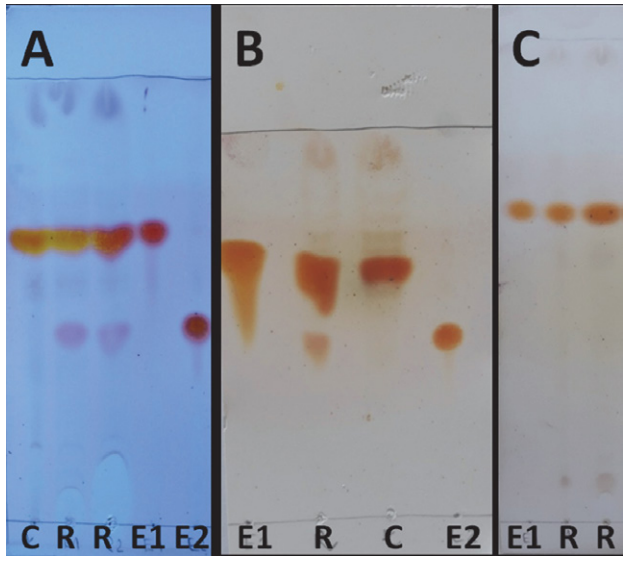

Figure 2. TLC chromatograms of reactions catalyzed by addition of human 17βHSD1 immediately after purification (A and B) or after freezing the enzyme at –80 °C for several days (C). Reaction mixtures consisted of 178 μM estrone, 70 μg of an enzyme, 178 μM NADPH and 100 mM potassium phosphate buffer (pH 6.0). After incubation at 37 °C for 90 minutes steroid metabolites were extracted by vortexing with methylene chloride. Toluene and ethyl acetate (2:1) solvent were used for development and spots were visualized by spraying with 50% H_2SO_4 and heating. Some of the samples were spotted in duplicate. R – Product of enzyme reaction; C – control in the absence of an enzyme; E1 – reference standard estrone; E2 – reference standard estradiol.

centration range and standard curve of peak areas from TLC-densitometry vs. concentrations of estradiol (25, 50, 75, 100 and 125 μM) are provided in Supplemental file 1. (Figure S1 and Figure S2). Specific enzyme activity of 17βHSD1 was 10 nmol min^{-1} mg^{-1}.

Recombinant 17βHSD1 activity was also evaluated by an alkali assay, which was initially developed to test modulators of aromatase activity.[21] This alkali assay is based on fluorimetric detection of an alkali product formed after exposure of $NADP^+$ to a strong alkali, where fluorescence intensity is directly proportional to enzyme activity. NAD(P)H-linked enzymatic activity of 17βHSD1 results in release of $NADP^+$ during reduction of estrone. A potential drawback of this assay appears to be the light sensitivity of the alkali product, which is overcome by adding a stabilizing agent, imidazole.[33] To our knowledge, this is the first report describing use of an optimized alkali assay to study the catalytic properties of purified recombinant 17βHSD1. Tsotsou et al used a similar assay to identify novel CYP450 enzymes substrates in high throughput format using whole *Escherichia coli* cells, confirming that the assay is substrate independent.[34] Using the alkali assay, we detected a 9-fold increase in fluorescence intensity in reactions conducted in the presence of active 17βHSD1 enzyme versus heat-treated, denatured enzyme (Figure 3). Our results are in accordance with previous findings, where the fluorescence intensity measured by the alkali assay in the presence of active aromatase was approximately 10-fold higher than in the presence of heat-inactivated aromatase enzyme.[21] Specific enzyme activity of 17βHSD1 was determined by measuring the consumption of NADPH. Standard curve of fluorescence intensity of alkali product vs. NADPH concentrations (2.5, 25, 62.5, 125, 250 μM) for alkali assay is provided in Supplemental file 1. (Figure S3). Specific enzyme activity of 17βHSD1 was 12 nmol min^{-1} mg^{-1}.

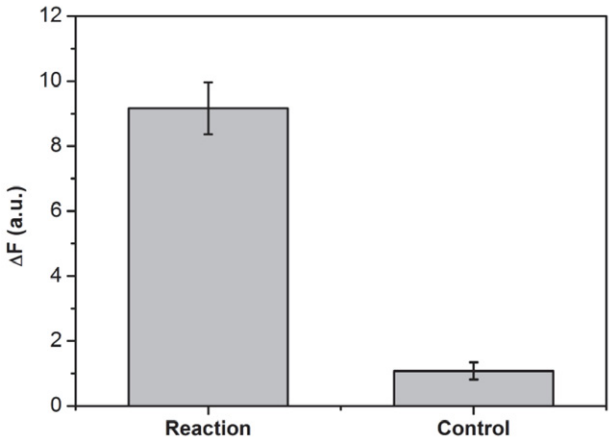

Figure 3. Measurement of the activity of recombinant human 17βHSD1 by alkali assay. A reaction mixture containing 40 μM estrone, 200 μM NADPH and 70 μg of recombinant 17βHSD1 in 100 mM potassium phosphate buffer (pH 6.0) was incubated at 37 °C for 90 min. Formation of $NADP^+$ was monitored by measuring fluorescence of alkali product using an excitation wavelength of 340 nm and emission wavelength of 460 nm. All experiments were performed in duplicate. Results are expressed as the mean difference in fluorescence signal ΔF ($F_{120'} - F_{0'}$) 120 minutes after addition of strong alkali. Control experiments were conducted in the presence of heat-inactivated, denatured enzyme. Histograms were plotted in Origin Pro8 after slope normalization.

The activity of recombinant human 17βHSD1 was also measured by monitoring NADPH consumption using fluorescence spectroscopy. Fluorimetric and spectrophotometric assays for measuring formation or consumption of cofactor in NAD(P)(H)-dependent reactions are routinely used to determine the activity of many oxidoreductases.[35,36] Fluorescence *vs.* time data for reactions catalyzed by 17βHSD1 and control reactions conducted in the absence of enzyme is shown in Figure 4. A decrease in fluorescence intensity over time was observed for reactions conducted in the presence of recombinant human 17βHSD1, corresponding to a loss of NADPH. In contrast, no fluorescence changes were observed in control reactions conducted in the absence of enzyme (Figure 4).

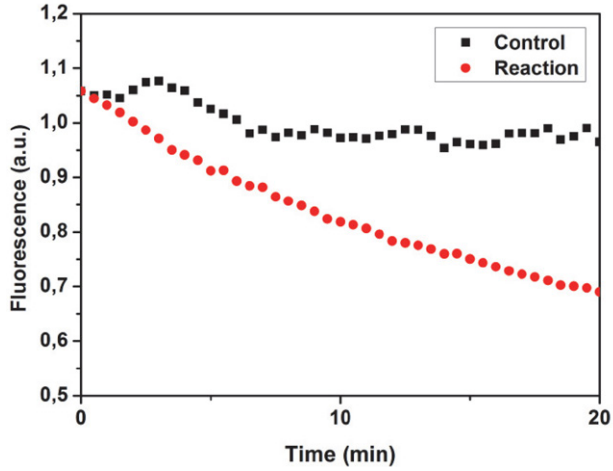

Figure 4. Reaction mixture containing 67 μM estrone, 167 μM NADPH and 70 μg of recombinant 17βHSD1 in 100 mM potassium phosphate buffer (pH 6.0) was incubated at 37 °C for 20 minutes and fluorescence intensity was recorded at 15 seconds-intervals. Reactions were initiated by addition of enzyme fraction and fluorescence was measured over time using an excitation wavelength of 340 nm and emission wavelength of 460 nm. The observed decrease in NADPH fluorescence is consistent with NADPH-dependent conversion of estrone to estradiol catalyzed by recombinant 17βHSD1. In the control reaction, enzyme was omitted. Fluorescence *vs.* time data was plotted in Origin Pro8 after slope normalization.

4. Conclusion

Reduction of estradiol levels in ovaries by inhibition of 17βHSD1 indirectly reduces estrogen-dependent activation of estrogen receptors, and represents a promising prevention or treatment strategy in premenopausal women diagnosed with estrogen-sensitive breast cancer, ovarian cancer or endometriosis. Although inhibitors of 17βHSD1 have been identified, none of these has yet reached clini-

cal trials. Here we provide a simple protocol for expression and purification of human 17βHSD1 from *E. coli*, and for the first time demonstrate 17βHSD1 activity using three independent *in vitro* assays. Catalytic conversion of estrone to estradiol was confirmed directly by detection of product formation or indirectly monitoring consumption of cofactor during reaction. While the current work represents valuable insight into the production of active human 17βHSD1 from *E. coli*, purification requires further improvement and optimization. The present study could be useful for researchers interested in preliminary *in vitro* screening of candidate compounds for 17βHSD1 inhibition using non-radioactive methods.

Acknowledgement

The authors acknowledge financial support of the Ministry of Science, Technological Development and Innovation of the Republic of Serbia (Grants No. 451-03-47/2023-01/200125 and 451-03-47/2023- 01/200113) and the financial support of the Provincial Secretariat for Higher Education and Scientific Research of the Autonomous Province of Vojvodina (Project: New steroid derivatives – potential chemotherapeutics, No. 142-451-3463/2023-01). Graphical abstract was created with BioRender.com, license number FK26NKCZRV. This work was also supported by a joint Serbia-Slovenia Bilateral project (BI-RS/14-15-002 ARRS Slovenian Research Agency; 451-03-3095/2014-09/10 Ministry of Science, Technological Development and Innovation Republic of Serbia).

Author contribution

Sofija S. Bekić: Methodology, Investigation, Software, Visualization, Writing- Original draft. Jovana J. Plavša: Methodology, Investigation, Writing- review & editing. Miha Pavšič: Methodology, Supervision, Writing- review & editing. Brigita Lenarčič: Methodology, Supervision, Writing- review & editing. Edward T. Petri: Conceptualization, Supervision, Writing- review & editing. Andjelka S. Ćelić: Conceptualization, Supervision, Writing- review & editing. All authors have read and approved the final manuscript.

Disclosure statement

The authors declare that they have no known competing financial interests or personal relationships that could have appeared to influence the work reported in this paper.

5. References

1. V. Papadopoulos, W. L. Miller, *Best Pract. Res. Clin. Endocrinol. Metab.* **2012**, *26*, 771–790. **DOI:**10.1016/j.beem.2012.05.002
2. A. H. Payne, D. B. Hales, *Endocr. Rev.* **2004**, *25*, 947–970. **DOI:**10.1210/er.2003-0030
3. V. Luu-The, P. Tremblay, F. Labrie, *Mol. Endocrinol.* **2006**, *20*, 437–443. **DOI:**10.1210/me.2005-0058
4. X. Wu, P. Lukacik, K. L. Kavanagh, U. Oppermann, *Mol. Cell. Endocrinol.* **2007**, *265*, 71–76. **DOI:**10.1016/j.mce.2006.12.006
5. J. M. Day, P. A. Foster, H. J. Tutill, F. Schmidlin, C. M. Sharland, J. D. Hargrave, N. Vicker, B. V. L. Potter, M. J. Reed, A. Purohit, *Endocr. Relat. Cancer.* **2013**, *20*, 53–64. **DOI:**10.1530/ERC-12-0231
6. E. Hilborn, O. Stål, A. Jansson, *Oncotarget.* **2017**, *8*, 30552. **DOI:**10.18632/oncotarget.15547
7. D. P. Sherbet, O. L. Guryev, M. Papari-Zareei, D. Mizrachi, S. Rambally, S. Akbar, R. J. Auchus, *Endocrinol.* **2009**, *150*(9), 4154–4162. **DOI**: 10.1210/en.2008-1817
8. M. L. Auchus, R. J. Auchus, *J. Investig. Med.* **2012**, *60*, 495–503. **DOI:**10.231/JIM.0b013e3182408567
9. V. K. Sali, S. Mani, G. Meenaloshani, A. V. Ilavarasi, H. R. Vasanthi, *Steroids.* **2020**, *159*, 108638. **DOI:**10.1016/j.steroids.2020.108638
10. M. Mottinelli, M. Sinreih, T. L. Rižner, M. P. Leese, B. V. Potter, *Chem Med Chem.* **2021**, *16*, 259–291. **DOI:**10.1002/cmdc.202000762
11. D. Ghosh, V. Z. Pletnev, D. W. Zhu, Z. Wawrzak, W. L. Duax, W. Pangborn, F. Labrie, S. X. Lin, *Structure* **1995**, *3*, 503–513. **DOI:**10.1016/S0969-2126(01)00183-6
12. T. Li, D. Zhu, F. Labrie, S. Lin, *Health.* **2018**, *10*, 1079–1089. **DOI:**10.4236/health.2018.108081
13. J. Messinger, B. Husen, P. Koskimies, L. Hirvelä, L. Kallio, P. Saarenketo, H. Thole, *Mol. Cell. Endocrinol.* **2009**, *301*, 216–224. **DOI:**10.1016/j.mce.2008.10.022
14. M. L. Lu, Y. W. Huang, S. X. Lin, *J. Biol. Chem.* **2002**, *277*, 22123–22130. **DOI:**10.1074/jbc.M111726200
15. J. Jarabak, J. A. Adams, H. G. Williams-Ashman, P. Talalay, *J. Biol. Chem.* **1962**, *237*, 345–357. **DOI:**10.1016/S0021-9258(18)93926-8
16. J. C. Le Bail, C. Pouget, C. Fagnere, J. P. Basly, A. J. Chulia, G. Habrioux, *Life Sci.* **2001**, *68*, 751–761. **DOI:**10.1016/s0024-3205(00)00974-7
17. Y. H. Chang, Y. L. Wang, J. Y. Lin, L. Y. Chuang, C. C. Hwang, *Mol. Biotechnol.* **2010**, *44*, 133–139. **DOI:**10.1007/s12033-009-9221-5
18. M. Sinreih, M. Gjorgoska, G. Möller, J. Adamski, T. L. Rižner, *Methods Enzymol.* **2023**, *689*, 201–234. **DOI:**10.1016/bs.mie.2023.04.015
19. A. Y. Chang, V. Chau, J. A. Landas, Y. Pang, *JEMI Methods.* **2017**, *1*, 22–25.
20. M. M. Bradford, *Anal. Biochem.* **1974**, *72*, 248–254. **DOI:**10.1006/abio.1976.9999
21. R. Baravalle, A. Ciaramella, F. Baj, G. Di Nardo, G. Gilardi, *Biochim. Biophys. Acta – Proteins Proteom.* **2018**, *1866*, 88–96. **DOI:**10.1016/j.bbapap.2017.05.013
22. H. Peltoketo, V. Isomaa, M. Poutanen, R. Vihko, *J. Endocrinol.* **1996**, *150*, 21–30. **DOI:**10.1186/bcr3207
23. P. Nokelainen, T. Puranen, H. Peltoketo, M. Orava, P. Vihko,

R. Vihko, *Eur. J. Biochem.* **1996**, *236*, 482–490. **DOI:**10.1111/j.1432-1033.1996.00482.x
24. W. J. Rhee, E.H. Lee, T. H. Park, *Biotechnol. Bioprocess Eng.* **2009**, *14*, 645–650. **DOI:**10.1007/s12257-009-0081-4
25. J. Jarabak, A. E. Seeds, P. Talalay, *Biochem.* **1966**, *5*, 1269–1279. **DOI:**10.1021/bi00868a021
26. L. Kokko, S. Jaakohuhta, P. Lindroos, T. Soukka, *Assay Drug Dev. Technolog.* **2006**, *4*, 671–678. **DOI:**10.1089/adt.2006.4.671
27. J. F. Thériault, D. Poirier, S. X. Lin, *J. Steroid Biochem. Mol. Biol.* **2021**, *214*, 105963. **DOI:**10.1016/j.jsbmb.2021.105963
28. J. Schindelin, I. Arganda-Carreras, E. Frise, V. Kaynig, M. Longair, T. Pietzsch, S. Preibisch, C. Rueden, S. Saalfeld, B. Schmid, J. Y. Tinevez, D. J. White, V. Hartenstein, K. Eliceiri, P. Tomancak, A. Cardona, *Nat. Methods.* **2012**, *9*, 676–682. **DOI:**10.1038/nmeth.2019
29. J. Schindelin, C. T. Rueden, M. C. Hiner, K. W. Eliceiri, *Mol. Reprod. Dev.* **2015**, *82*, 518–529. **DOI:**10.1002/mrd.22489
30. N. Popovic, J. Sherma, *Trends Chromatogr.* **2014**, *9*, 21–28.
31. H. Suzuki, Y. Ozaki, S. Ijiri, K. Gen, Y. Kazeto, *J. Steroid Biochem. Mol. Biol.* **2020**, *198*, 105550. **DOI:**10.1016/j.jsbmb.2019.105550
32. V. Kollerov, A. Shutov, A. Kazantsev, M. Donova, *Fungal Biol.* **2022**, *126*, 91–100. **DOI:**10.1016/j.funbio.2021.11.002
33. O. H. Lowry, J. G. Carter, *Anal. Biochem.* **1974**, *59*, 639–642. **DOI:**10.1016/0003-2697(74)90319-4
34. G. E. Tsotsou, G. Di Nardo, S. J. Sadeghi, R. Fruttero, L. Lazzarato, M. Bertinaria, G. Gilardi, *J. Biomol. Screen.* **2013**, *18*, 211–218. **DOI:**10.1177/1087057112459351
35. M. P. Savić, J. J. Ajduković, J. J. Plavša, S. S. Bekić, A. S. Ćelić, O. R. Klisurić, D. S. Jakimov, E. T. Petri, E. A. Djurendić, *MedChemComm.* **2018**, *9*, 969–981. **DOI:**10.1039/C8MD00077H
36. M. A. Marinović, E. T. Petri, Lj. M. Grbović, B. R. Vasiljević, S. S. Jovanović-Šanta, S. S. Bekić, A. S. Ćelić, *Mol. Inform.* **2022**, *41*, 2100256. **DOI:**10.1002/minf.202100256

Povzetek

Rast celic raka dojk je pogosto odvisna od prisotnosti steroidnih hormonov. Izoforma 17β-hidroksisteroidne dehidrogenaze tipa 1 (17βHSD1) katalizira od NADPH odvisno pretvorbo estrona v estradiol, ki je močnejši estrogen, in predstavlja potencialno tarčo zdravil za zdravljenje raka dojk. Da bi zagotovili aktivni encim za presejanje inhibitorjev, se 17βHSD1 običajno izrazi v insektnih celicah ali celicah sesalcev ali pa se izolira iz človeške placente. V tej študiji opisujemo preprost protokol za izražanje in čiščenje aktivnega človeškega 17βHSD1 iz celic *Escherichia coli* BL21(DE3). Topen človeški 17βHSD1 je bil izražen z uporabo plazmida na osnovi pET28a(+), ki kodira heksahistidinsko oznako, združeno z N-koncem proteina, in prečiščen z nikljevo afinitetno kromatografijo. Encimsko aktivnost prečiščenega 17βHSD1 smo preverili s tremi metodami: tankoslojno kromatografijo, alkalnim testom in spektroskopskim testom. Ti neradioaktivni encimski testi zahtevajo le standardno laboratorijsko opremo in se lahko uporabljajo za presejanje spojin, ki modulirajo aktivnost 17βHSD1.

DOI: 10.17344/acsi.2024.8726 *Acta Chim. Slov.* **2024,** *71,* 264–287

Scientific paper

In Silico Exploration of Molecular Mechanisms for Inhibiting Inflammatory Responses by 3H-Thiazolo[4,5-*b*]pyridin-2-one Derivatives

Olena Klenina[1,2,*]

[1] *Danylo Halytsky Lviv National Medical University, Faculty of Pharmacy, Department of General, Bioinorganic, Physical and Colloidal Chemistry, 69 Pekarska Str. Lviv, 79010, Ukraine*

[2] *San Pablo CEU University, Faculty of Pharmacy, Department of Chemistry and Biochemistry, Urbanización Montepríncipe, 28668 Boadilla del Monte, Spain*

[*] *Corresponding author: E-mail: olena.klenina@ceu.es; olena_klenina@yahoo.com Phone: +380 98-051-9298; +34 674170236*

Received: 03-01-2024

Abstract

Combined *in silico* strategy for molecular mechanisms exploration of a series 3*H*-thiazolo[4,5-*b*]pyridin-2-ones exhibiting strong anti-exudative action through QSAR analysis, molecular docking and pharmacophore modelling is reported. GA-ML technique was used for QSAR models generation with 2*D* autocorrelation descriptors. One- and two-parameter regressions revealed that certain structural patterns or heteroatoms contribute mutually to the anti-exudative activity potentiation. Possible action mechanisms were discovered through flexible docking simulations with cyclooxygenase pathway enzymes (COX-1, COX-2, mPGES-1). Docking results indicated the possibility of stable complexes formation with the effective docking scores and proper orientation of ligands within the enzymes active sites. Pharmacophore modelling was carried out using protein-ligand interaction fingerprints methodology. Two- and three-centre 3*D* pharmacophore queries were constructed. Their analysis indicated the functionality of bicyclic thiazolopyridine scaffold proved by the steric placement of heteroatoms in the corresponding pharmacophore centres.

Keywords: Thiazolo[4,5-*b*]pyridines, COX inhibitors, mPGES-1 inhibitors, QSAR analysis, docking, pharmacophore modelling

1. Introduction

The development of anti-inflammatory drugs occupies an important role in the field of modern pharmacology. Among the different signalling molecules involved in inflammatory stage arachidonic acid (AA) and its metabolites contribute strongly to the development of inflammatory and related symptoms.[1] Arachidonic acid, formed during the release of phospholipids from cell membranes, can be metabolised by the cyclooxygenase or lipoxygenase pathways. The cyclooxygenase pathway of AA metabolism leads to prostaglandin H2 (PGH2) formation *via* two successive steps both catalysed by COXs. PGH2 serves as a precursor for different PG biosynthesis including PGD2, PGE2, PGI2, and TXA2 depending on the expression of specific terminal synthases. Cyclooxygenases (COX-1 and COX-2) are the key emzymes involved in the arachidonic acid cascade.[2] Classical non-steroidal anti-inflammatory drugs (NSAIDs) are diverse group of compounds used for the treatment of inflammation.[3] The first generation of NSAIDs exert anti-inflammatory, analgesic, and antipyretic effects through the non-selective inhibition of both COX isoforms. Their use is associated with side effects such as gastrointestinal and renal toxicity.[4] Selective COX-2 inhibitors (rofecoxib, celecoxib, valdecoxib etc.) were developed as the second generation of NSAIDs with improved gastric safety profile and therefore more safe. Microsomal prostaglandin E synthase-1 (mPGES-1) is the terminal enzym in PG biosynthesis pathway and catalyses the conversion of PGH2 to PGE2.[5] PGE2 is a well-characterized mediator of inflammation and pain. Therefore mPGES-1 is a novel attractive target with a low risk of side effects. Very few inhibitors of mPGES-1 were identified in experimental screening efforts. Some novel synthetic mPGES-1 inhibitors among different classed of compounds

were identified in the recent decades by using high-throughput screening (HTS) strategy.[6] Thus, it is highly desirable to design and discover novel mPGES-1 inhibitors with different scaffolds in order to develop next-generation therapeutics for anti-inflammatory diseases treatment.

Thiazole-based derivatives are actually a considerable group of heterocyclic compounds possessing a significantly broad spectrum of pharmacological actions and therapeutic effects against many pathological states. In the last years the scaffold consisting of thiazole ring linked to pyridine one and functionalized with different fragments has attracted considerable interest due to diverse activities.[7] A great number of publications have been currently reported thiazolopyridines biological evaluations as potent antihypertensive,[8] antioxidant,[9] antifungal,[10] antimicrobial,[11] antidiabetic,[12] anti-inflammatory,[13] tuberculostatic,[14] herbicidal[15] and anticancer agents.[16] Furthermore, fused thiazolopyridine analogues are also known as H_3 receptor antagonists,[17] phosphoinositide 3-kinase inhibitors[18] and glucokinase activators.[19]

In the past decade fused thiazole-based derivatives became an integral part of new anti-inflammatory agents' discovery. A wide range of synthetic thiazole-bearing derivatives have been studied for their anti-inflammatory properties including COX-1/COX-2 inhibitory action.[20] Mohareb *et al.*[21] reported the synthesis of eleven series of novel fused thiazoles derived from 2-(2-oxo-2*H*-chromen-3-yl)thiazol-4(5*H*)-one and their anti-inflammatory activity evaluation using a carrageenan-induced paw oedema model. All synthesized compounds showed anti-inflammatory activity in the range of 33–96%. Development of novel benzothiazole moiety compounds as promising COX-1/COX-2 inhibitors was reported by El-Kerdawy *et al.*[22] They synthesized a series of new 3-methylbenzo[4,5]imidazo[2,1-*b*]thiazol-2-yl)nicotinoyl)-N-substituted derivatives with the aim to evaluate their anti-inflammatory activity and mechanism of action. The anti-inflammatory activity of this compounds performed by carrageenan-induced mouse paw oedema was in range of 49.0–79.5%. Also, evaluation of COX-1/COX-2 inhibition was performed which revealed non-selective inhibitory activity of benzimidazothiazoles towards both COX isoforms with some compounds being more potent compared to celecoxib and naproxen. Some novel benzyloxybenzo[*d*]thiazole and phenoxylethoxylbenzo[*d*]thiazole analogues were synthesized and evaluated *in vivo* as potential anti-inflammatory and analgesic agents.[23] These derivatives were recognized as promising starting points for the development of COX-2 selective inhibitors.

Thiazole scaffold may be also looked through as an attractive pharmacological profile for the further rational design and discovery of novel mPGES-1 inhibitors as safe and potent NSAIDs. Ongoing efforts are made to identify alternate action modes of thiazole-scaffold bearing compounds which may feasibly lead to reduced PGE_2 level. Smith *et al.*[24] reported the inhibitory activity of 2-aminothiazole derivatives directed to PGE2 production decreasing. A series of 2-aminothiazole congeners was synthesized and tested for the ability to reduce the production of PGE_2 in HCA-7 cells. A total of 36 aminothiazoles were evaluated, and active compounds with limited COX-2 inhibition were identified. One of the derivatives exhibited the most potent cellular PGE_2 reducing activity of the entire series (EC_{50} = 90 nM) with IC_{50} value for COX-2 inhibition of >5 μM *in vitro*. Identification of novel dual LOX/mPGES-1 inhibitors as 2-aminothiazole-featured pirinixic acid derivatives was also reported,[25] one compound among them suppressed mPGES-1 (IC_{50} = 0.4 μM) and 5-LOX (IC_{50} = 0.3 μM) in cell-free assays.

In the present study we propose a combined *in silico* approach, based on efficient multistep virtual screening workflow, which may accelerate and facilitate the identification of novel selective COX-2 and mPGES-1 inhibitors among fused thiazole-scaffold bearing compounds.

2. Materials and Methods

2. 1. QSAR Study

2*D* structures of all molecules were drawn with ACD/ChemSketch chemical drawing software package. Later on, they were converted to 3*D* structures using Hyper-Chem 7.5 software.[26] Energy minimization of all compounds was performed with MM+ force field, and repeated minimization was performed using semi-empirical AM1 quantum-chemical method until the root-mean-square (rms) deviation of 0.01 kcal/mol would be achieved. Conformations of compounds were optimized through semi-empirical AM1 method with the global minimum selection among all energy-minimal conformers. 3*D* globally minimized structures as hin HyperChem output were converted into smi format, SD file was prepared with E-BABEL on-line version and utilized as the input for E-DRAGON software.[27] Molecular descriptors were calculated within 20 subsets, constant and near constant values of descriptors were discarded, and finally over 1666 descriptors were saved and further analyzed. Descriptors with pairwise correlation coefficient exceeding 0.5, determined based on the correlation matrix analysis, were excluded from the descriptor general set. Before starting the construction of the models, the descriptor normalization procedure was carried out, the values of all generated descriptors were scaled as (1):

$$X_{ij}^{n} = \frac{X_{ij} - X_{j,min}}{X_{j,max} - X_{j,min}} \quad (1)$$

where X_{ij} and X_{ij}^{n} are the original and normalized values of the descriptor j (j = 1, 2, … , K) for i^{th} compound (i = 1, 2,…, 32), respectively; $X_{j,min}$ and $X_{j,max}$ are the minimal and the maximal values for the j^{th} descriptor. Thus, for all normalized descriptors the following criteria are true: min (X_{ij}^{n}) = 0 and max (X_{ij}^{n}) = 1. As a result, a set of 482 normalized descriptors for all compounds was prepared.

In order to obtain a validated and predictive QSAR models, we splitted the parent data set into the training and test (validation) ones with the activity ranking algorithm[28] in the ratio 27:9, that is the training set consisted of 27 compounds (75% of all) while the validation set contained 9 compounds (25%).

The training set was used in developing QSAR models with BuildQSAR software application[29] where the biological activity as % protection to inflammation converted to logarithmic value (log %) served as the dependent variable, and the normalized molecular descriptors were independent variables. In this work, the selection of the optimal set of molecular descriptors was carried out using genetic algorithm (GA) for searching the best models and was processed in the terms of the highest correlation coefficient and *F*-test as well as the lowest standard deviation. Variables selection was carried out within each of descriptors` modules namely 0*D*-,1*D*-, 2*D*, 3*D* and module "Other" using previously reported approach.[30] Multiple Linear Regression (MLR) method was applied to perform the statistical processing of the QSAR structure-anti-exudative activity models generation.

The statistical significance of the generated models was determined by examining the coefficient of determination R^2, standard deviation *s*, the value of the Fisher test *F*. Adjusted regression coefficient R^2_{adj} was used to ensure that all independent variables (predictors) contribute with the equal significance to explain dependent (target) variable. R^2_{adj} was defined as (2):[31]

$$R^2_{adj} = 1 - \frac{(1-R^2)(n-1)}{n-p-1} \quad (2)$$

where *n* is the total set size (the total number of observations), *p* is the number of independent variables (the number of descriptors in the model), and *n*-*p*-1 is the residual degree of freedom.

Sum of squares for the regression ($SS_{regression}$ *or SSR*) was estimated as the sum of the differences between the predicted value of the activity $Y_{i\ pred}$ and the mean of the dependent variable for the training set compounds $\bar{Y}_{training}$ (3), while the Mean square for the regression ($MS_{regression}$ or *MSR*) was an estimate of the variance of the regression (4):

$$SSR = \sum_{i=1}^{n}(Y_{i\ pred} - \overline{\overline{Y}_{training}})^2 \quad (3)$$

$$MSR = SSR / DF_{regression} \quad (4)$$

where $DF_{regression}$ is the degree of freedom for the regression: $DF_{regression} = p$.

As the cross-validation coefficients are used as criteria of both robustness and predictive ability of the generated QSAR models, we performed both internal and external cross-validation procedure in the present study. The internal validation of the models was examined using the leave-one-out (LOO) cross-validation method with the training set compounds. In the LOO cross-validation procedure, every compound was eliminated from the training dataset once and its activity was then predicted as a weighted average of the activities of its nearest neighbours using formula 5:[32,33]

$$Q^2_{LOO} = 1 - \frac{\sum(Y_{i\,exp} - Y_{i\,calc})^2}{\sum(Y_{i\,exp} - \bar{Y}_{exp})^2} \quad (5)$$

where $Y_{i\ exp}$ and $Y_{i\ calc}$ are the experimental and calculated values of biological activity for molecule *i* of the training set, respectively; $\bar{Y}_{exp}$ is the mean value of the dependent variable (log %). The summation in this and all the following equations are done over all *n* compounds of the training set.

For the external validation, the group-one-out cross-validation coefficient Q^2_{LGO} with the test set compounds was calculated using formula 6:[34]

$$Q^2_{LGO} = 1 - \frac{\sum(Y_{i\,exp(test)} - Y_{i\,calc\,(test)})^2}{\sum(Y_{i\,exp(test)} - \bar{Y}_{training})^2} \quad (6)$$

where $Y_{i\ exp(test)}$ and $Y_{i\ calc(test)}$ are the activity values for the validation set compounds, observed and predicted with the corresponding model, respectively; and $\bar{Y}_{training}$ is the mean value of the experimantal activity of the training set compounds only.

2. 2. Molecular docking studies

All the computational studies were carried out using Molecular Operating Environment Suite 2012.10 (MOE); Chemical Computing Group Inc. software.[35,36]

Construction and preparation of ligands database

The minimized 3*D* geometries of all compounds obtained using the HyperChem 7.5 software for QSAR analysis were then converted into SD File format with Open Babel version 2.3.2[37] and were used as the input into MOE with a database import function. We firstly generated multiple conformations of each ligand in the database on the systematic search basis. We applied the grid search by rotating each rotatable bond by a fixed angle increment (15° for cyclic, 60° or 120° for acyclic bonds) followed by the conformations` energy minimization with MMFF94x force field and duplicate geometries rejection. The maximum allowed conformations per compound was set to 200 and the energy window (the value used to discard high-energy conformations) was set to 7 kcal/mol. The RMS gradient level was defined as 0.01 kcal/mol/Å^2, RMSD limit was fixed at 0.25 kcal/mol/Å^2 while 200 MM iterations were allowed. A data set of 2545 conformations was prepared in the way of systematic search.

Proteins processing and preparation

The X-ray crystallographic structures of the receptors were retrieved from Protein Data Bank (www.rcsb.

org/pdb): 2.0 Å resolution structure of ovine prostaglandin H_2 synthase-1 (COX-1) in complex with α-methyl-4-biphenylacetic acid (PDB code 1Q4G),[38] 1.73 Å resolution structure of naproxen-COX-2 complex (PDB entry 3NT1), [39] and 1.2 Å resolution structure of human mPGES-1 in complex with glutathione (GSH) (pdb code 4AL0).[40] They were then loaded into MOE working environment.

The enzymes were prepared for docking studies in a few steps. The receptors' structures were prepared in the way of the partial charges calculation, hydrogens were assigned with the "Protonate3D" function at pH 7.4. Thereafter, residues within a radius of 3 Å around the ions were minimized (AMBER99 force field; RMS gradient 0.01 kcal/mol/Å^2). Thus the "Protonate3*D*" application automatically optimized the hydrogen orientations so as to maximize H-bond networks and minimize the overall self-energy. The binding sites of the proteins were defined by using the "Site Finder" tool in MOE. The co-crystalized ligands were removed from protein-ligand complexes and corresponding ligands locations were set as docking site locations. Site Finder tool was applied for the defined pockets, and „dummy atoms" were created.

Docking studying and scoring

The standard MOE Docking protocol was utilized for the docking studies of the ligands database with COX-1 and COX-2. Residues within a radius of 4.5 Å of the generated "dummy atoms" were selected, Alpha Triangle Poses were generated by superposition of ligand atom triplets and triplets of receptor site points. At each iteration a random conformation was selected, a random triplet of ligand atoms and a random triplet of alpha sphere centres were used to determine the pose. The following docking calculations were performed by means of the DOCK tool implemented in MOE, all obtained docking poses were refined using MMFF94x force field as the default for small molecules in MOE. To reduce the number of poses obtained in this way (865 for COX-1 and 880 for COX-2), the pharmacophore queries were generated. For COX-1 the pharmacophore query with projected H-acceptor feature defined on NH_2 group of Arg 120 residue was generated while two pharmacophore queries with projected H-acceptor features defined on NH_2 and NE groups of Arg 120 side chain residue were consequently generated for COX-2. The docking run procedure was repeated with the first rescoring function setting as "London dG", the refinement scoring function fixing to "GBVI/WSA dG". 357 COX-1-ligand complexes and 412 COX-2-ligand complexes were obtained in this way. The molecular docking studies of the ligands database with mPGES-1were utilized by setting "GBVI/WSA dG" function for the first rescoring, followed by the addition of a refinement of the resulting complexes with MMFF94x force field and London dG for a second rescoring. 786 mPGES-1-ligand complexes were obtained in this way.

Thereafter, the minimized complexes were scored by the four scoring functions available in MOE: ***Affinity dG Scoring*** estimated the enthalpic contribution to the free energy of binding, ***Alpha HB Scoring*** evaluated the geometric fit of the ligand to the binding site and hydrogen bonding effects, ***London dG Scoring*** and ***GBVI/WSA dG Scoring*** (forcefield-based) estimated the free energy of binding of the ligand from a given pose. The unit for all scoring functions was kcal/mol. For all scoring functions, lower scores indicated more favourable poses. The docking poses were then expected manually with an eye towards the most proper binding modes verification.

2. 3. Pharmacophore Queries Generation

Protein-ligand interactions fingerprints (PLIF) tool and 3*D* pharmacophore models generation tool implemented in MOE software were used as a post-processing procedure of docking studies for thiazolo[4,5-*b*]pyridin-2-one derivatives as probable COX-1,2 and mPGES-1 inhibitors. Automatized pharmacophore query generation based on the structural data of protein-ligand complexes obtained from docking studies was a two-step procedure. Firstly, the identification of a protein residues interacting with the ligand was fulfilled, and their summarizing was resulted in the barcode diagram construction in which different types of interactions were given as fingerprints bits. Afterwards MOE`s pharmacophore modelling tool determined the most common pharmacophoric feature characteristics that were essential for the binding of ligands to the receptor and their spatial arrangement in 3*D*. On the final step we validated the fingerprint pharmacophore modelling approach by screening the test database as alignments of molecules on high-scoring pharmacophore queries.

3. Results and Discussion

Recently we reported novel N^3 substituted 5,7-dimethyl-6-phenylazo-3*H*-thiazolo[4,5-*b*]pyridin-2-ones synthesis[41] as the integral part of scaffold-based drug-like small molecules design and discovery using traditional organic synthesis protocols and pharmacological screening methodologies.[42] *In vivo* evaluation of novel thiazolo[4,5-*b*]pyridines over the carrageenin induced rat paw oedema revealed strong anti-exudative activity of some compounds which were comparable or exceeded the effects of Diclofenac and Ibuprofen in their effective therapeutic doses which were tested in parallel as an activity references.

As the focus of our systematic research is aimed at developing the molecular pattern based on 3*H*-thiazolo[4,5-*b*]pyridine scaffold for novel drug candidates construction, the objective of the present study was to perform ligan-based and structure-based virtual screening for recently synthesized 3*H*-thiazolo[4,5-*b*]pyridin-2-ones in

order to apprehend the importance of certain structural features, which are critical for their biological activity accentuation. Thus, a three-step virtual screening protocol was proposed in this work, which included QSAR analysis, molecular docking and protein-ligand complex-based pharmacophore search post-processing.

The set of compounds used in the present study comprises a series of 36 N^3 substituted 5,7-dimethyl-6-phenylazo-3*H*-thiazolo[4,5-*b*]pyridin-2-one derivatives evaluated as anti-exudative agents. Their structures are depicted in Figure 1, while the substituent *R* structures are listed in Table 1. The biological activity data as % protection to inflammation were converted to logarithmic value and subsequently used as the response variable for QSAR analysis.

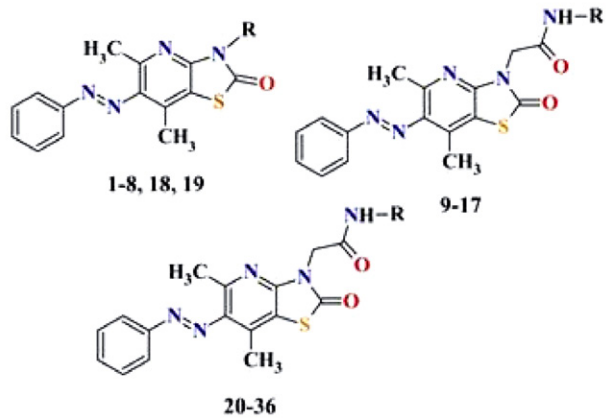

Fig. 1. General structures **of** N^3 substituted 5,7-dimethyl-3*H*-thiazolo[4,5-*b*]pyridine-2-ones

Table 1. Structures of substituents and anti-exudative effect of 5,7-dimethyl-6-phenylazo-3*H*-thiazolo[4,5-*b*]pyridin-2-ones *in vivo* evaluation, given as % and log % protection from inflammation

Compound ID	*R*	% Inhibition	log %	Compound ID	*R*	% Inhibition	log %
1	H	57.2	1.76	**20**	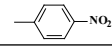	42.0	1.62
2	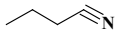	54.2	1.73	**21**		39.2	1.59
3	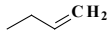	42.1	1.62	**22**	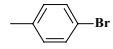	36.1	1.56
4	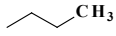	45.1	1.65	**23**	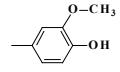	38.4	1.58
5		47.2	1.67	**24**	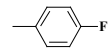	42.0	1.62
6	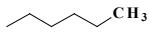	50.2	1.70	**25**		45.1	1.65
7	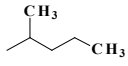	48.1	1.68	**26**	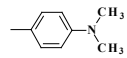	39.3	1.59
8	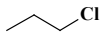	36.5	1.56	**27**	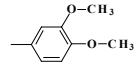	37.1	1.57
9		35.0	1.54	**28**	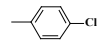	55.3	1.74
10		28.1	1.45	**29**	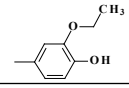	41.1	1.61
11		31.2	1.49	**30**		36.3	1.56
12	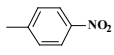	33.2	1.52	**31**		50.5	1.70
13	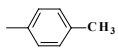	29.0	1.46	**32**	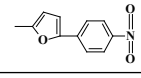	47.2	1.67
14		32.2	1.51	**33**	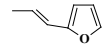	45.1	1.65

Compound ID	*R*	% Inhibition	log %	Compound ID	*R*	% Inhibition	log %
15		39.3	1.59	**34**	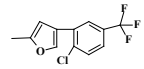	53.0	1.72
16		33.2	1.52	**35**	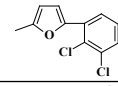	67.5	1.83
17	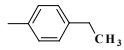	39.3	1.59	**36**	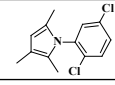	71.2	1.85
18	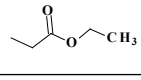	44.1	1.64	**Ibuprofen**		40.2	1.60
19	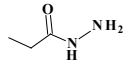	40.2	1.60	**Diclofenac**		52.4	1.72

3. 1. QSAR Analysis of N[3] Substituted 5,7-dimethyl-3*H*-thiazolo[4,5-*b*]pyridin-2-one derivatives

The structures of thiazolo[4,5-*b*]pyridin-2-ones under study were subjected to energy minimization with MM+ force field followed by the repeated minimization with semi-empirical AM1 method. Molecular descriptors for 3*D* optimized structures of the compounds were calculated with E-DRAGON software. Descriptors with the constant and near constant values were discarded. Descriptors with high pairwise correlation, determined based on correlation matrix analysis, were excluded from the multidimensional descriptor space. As a result, the set of 482 descriptors was obtained for both training and test sets compounds. The descriptor normalization procedure was carried out, the values of all generated descriptors were scaled in the range of 0÷1.

Activity sampling method was used for splitting overall dataset into the training and validation (test) sets. The main steps of the technique included sorting compounds by activity. Then the size of a group of compounds was specified by including the specified number of the most active compounds into the first group, the same number of the next most active compounds into the second group, etc. Then the number of compounds in each group, which would be included into the training and test sets, was determined. Thus, all compounds were divided into 6 groups, the numbers of compounds with low, moderate, and high levels of activity in each group were approximately the same. Then a few compounds from each group were assigned to the validation set, and the rest compounds formed the training set. The results of the dataset splitting are given in Table 2.

The selection of the optimal set of molecular descriptors was carried out using genetic algorithm within each of descriptors` modules namely 0*D*-,1*D*-, 2*D*, 3*D* and module "Other" firstly. The most significant descriptors from each dimensionality module were introduced to the final data set. Multiple Linear Regression (MLR) was used to generate QSAR models as a multivariate linear regression within the training set compounds with BuiltQSAR software.

Among the generated models 1 one-parameter and 2 two-parameter QSAR models were selected with the highest statistical characteristics and predictive ability:

log % = –0.3423 GATS7m + 1.8669 (Model **1**);
log % = 0.1315 MATS4e – 0.2781 GATS7m + 1.7706 (Model **2**);
log % = 0.1318 MATS4m – 0.2998 GATS7m + 1.7961 (Model **3**).

Table 2. The number of compounds in training and test sets constructed by the ranking of compounds activities

Group number	Size of a group	Number of compounds assigned to the training set	Compounds ID	
			Training set	Test set
I	6	4	**1**, **28**, **34**, **36**	**2**, **35**
II	5	4	**5**, **6**, **31**, **32**	**7**
III	7	5	**4**, **18**, **20**, **24**, **33**	**25**, **3**
IV	6	5	**17**, **19**, **21**, **26**, **29**	**15**
V	6	5	**8**, **9**, **23**, **27**, **30**	**22**
VI	6	4	**10**, **11**, **12**, **14**	**13**, **16**

Models **1**-**3** were constructed using 2*D* autocorrelation descriptors **GATS7m** (Geary autocorrelation of lag 7 weighted by mass), **MATS4e** and **MATS4m** (Moran autocorrelations of lag 4 weighted by atomic Sanderson electronegativity and by mass, respectively) with low pairwise correlation. The normalized values of molecular descriptors for both training and test sets compounds are listed in Table 1S of the Supplementary materials. To ensure the accuracy in predicting ability of the generated models, the prediction errors and the prediction error standard deviations were calculated (Table 2S of the Supplementary materials).

Based on the validation parameters of the generated models (Table 3), all constructed models satisfied the statistical requirements for their goodness-of-fitting with no current overfitting. Goodness of fitting for QSAR models generated with ***p*** parameters for the training set consisting of 27 compounds was assured by maximizing the correlation coefficient *R* and the determination coefficient R^2, adjusted regression coefficient R^2adj and *F*-test criterion while minimizing $R^2 - R^2_{adj}$ and standard deviation *s*.

Pearson correlation coefficient ***R*** measures the strength of the linear relationship between dependent and independent variables with possible values between -1 and 1. In regression, *R*-squared (***R*²**, or the coefficient of determination) is a statistical measure of how well the regression predictions approximate the real data points providing the relative measure of the percentage of the dependent variable variance that the model explains. The higher values of R^2 indicates the high fitness of the model as R^2 of 1 indicates that the regression predictions perfectly fit the data. Adjusted *R*-squared $\boldsymbol{R^2_{adj}}$ considers and tests different independent variables against the model. Its value may increase or decrease depending on the significance of the independent variable introduced to the regression. So, the higher value of R^2_{adj} ensures the high significance of all variables introduces into the model. The standard deviation (***s***) is a measure of the amount of variation or dispersion of a set of values. A low standard deviation indicates that the values tend to be close to the mean (also called the expected value) of the set. The ***F-test*** reflects the ratio of the variance explained by the model and the variance due to the error in the regression. High values of the *F*-test indicate that the model is statistically significant.

Table 3. Statistical parameters for QSAR models **1** – **3**

No	Statistical parameter	Model 1	Model 2	Model 3
1.	***p***	1	2	2
2.	***R***	0.8117	0.8772	0.8728
3.	$\boldsymbol{R^2}$	0.6589	0.7694	0.7617
4.	$\boldsymbol{R^2_{adj}}$	0.6452	0.7502	0.7419
5.	$\boldsymbol{R^2 - R^2_{adj}}$	0.0137	0.0192	0.0198
6.	***s***	0.0534	0.0448	0.0455
7.	***F***	48.2900	40.0412	38.3644
8.	***p***	0	0	0
9.	$\boldsymbol{DF_{regression}}$	1	2	2
10.	***SSR***	0.1377	0.1608	0.1592
11.	***MSR***	0.1377	0.0804	0.0796

The degree of freedom for the regression equals to the number of independent parameters: $\boldsymbol{DF_{regression} = p}$. It defines the number of values is a dataset having the freedom to vary. $\boldsymbol{SS_{regression}}$ (***SSR***) means the **Sum of squares** for the regression while $\boldsymbol{MS_{regression}}$ (***MSR***) means the **Mean square** for the regression. Regression sum of squares is interpreted as the amount of total variation that is explained by the model. *SSR* is variation in *Y*i associated with the regression line, $\bar{Y}$. It may be referred to as the measure that describes how well our line fits the data. $\boldsymbol{MS_{regression}}$ is

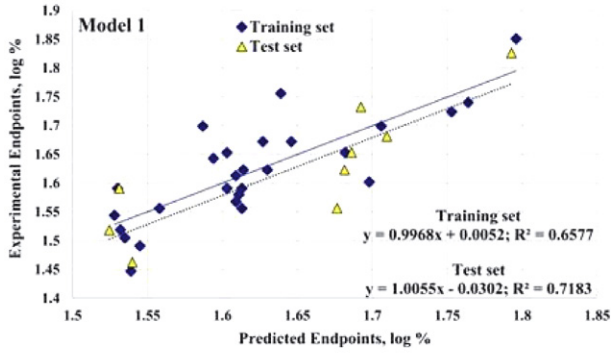

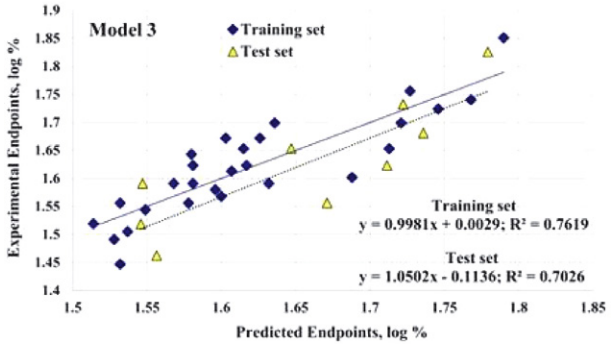

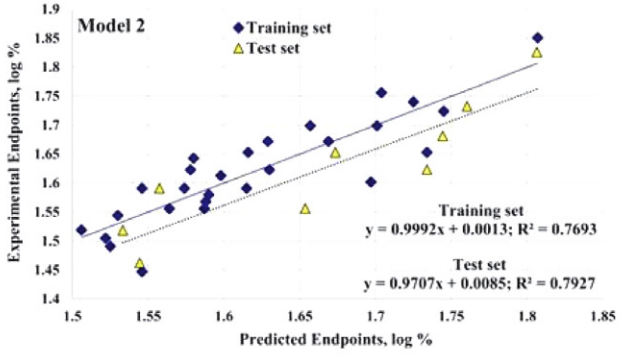

Fig. 2. Correlation between observed activity and activity predicted with Models **1** – **3** together with linear fit statistical parameters

an estimate of the variance of regression, $MS_{regression} = SS_{regression} / DF_{regression}$.

Thus generated QSAR models could approximate the experimental values properly according to their statistical analysis performance parameters.

Predictive ability of the generated models was ensured by using leave-one-out (LOO) cross-validation procedure, when each object is removed from the original training dataset once in turn and the remaining reduced data set is converted into new training set used for a model generation and the response prediction for the excluded compound. The outcome from this procedure is leave-one-out cross-validation coefficient Q^2_{LOO}. The coefficients of determination between observed and predicted activities $R^2_{(observed\ vs.\ predicted)}$ for the training set compounds were also estimated as an internal validation predictivity. Figure 2 shows the regression lines between experimental anti-exudative activity and activity predicted with Models **1**-**3**.

The determination coefficients for observed endpoints versus experimental oner for the derived models were in the range between 0.6577 and 0.7693, so the linear models explained 65.77% – 76.93% of variation in experimental activity. We evaluated the accuracies of QSAR models also using the difference $|R^2 - Q^2_{LOO}|$ absolute value supposing that it tends to minimum for truly predictive model.

The values of Q^2_{LOO} (0.6025 ÷ 0.6995) were reasonable, showing that the models were significant and robust to predict the anti-exudative activity of the compounds under study. We also considered that the values of the difference between R^2 and Q^2_{LOO} ($|R^2 - Q^2_{LOO}|$) were within the suggested limit of $|R^2 - Q^2_{LOO}| < 0.3$,[43] which was the indication that the models had no data overfitting. S_{PRESS} is the predicted residual sums of squares standard deviation, and S_{DEP} is the standard deviation error in prediction. Internal validation parameters are summarized in Table 4.

Table 4. Internal validation parameters for QSAR models **1 – 3**

No	Validation parameter	Model 1	Model 2	Model 3
1.	$R_{2(observed\ vs.\ predicted)}$	0.6577	0.7693	0.7619
2.	Q^2_{LOO}	0.6025	0.6995	0.6908
3.	$\|R^2 - Q^2_{LOO}\|$	0.0552	0.0698	0.0711
4.	S_{Press}	0.0576	0.0512	0.0519
5.	S_{DEP}	0.0565	0.0491	0.0519
7.	DF_{error}	25	24	24
8.	*SSE*	0.0713	0.0482	0.0498
9.	*MSE*	0.0029	0.0020	0.0021

For internal validation we also applied S_{DEP} (standard deviation of error of predictions), which makes a distinguish between 'predictions' for new data points which were not involved into the model construction, and the standard deviation of the predicted residual error sum of squares S_{PRESS}. S_{PRESS} is a form of cross-validation used in regression analysis to provide a summary measure of the fit of a model to a sample of observations that were not themselves used to estimate the model. Both S_{PRESS} and S_{DEP} values display tendency to minimization to ensure that generated models possessed enough predictive power. We also applied *SSE* as the **Sum of squares error** and *MSE* as the **Mean square error**. *MSE* measures error in statistical models by using the average squared difference between observed and predicted values. Highly predictive linear regression should display minimized *SSE*. The degree of freedom for residuals (errors) equals: $DF_{error} = n - p - 1$, where n is the number of observations in the training set. *MSE* is an estimate of the variance of errors: $MSE = SSR / DF_{error}$. If the regression model is "perfect", *SSE* is zero. Thus, *MSE* is a measure of the quality of an estimator. As it is derived from the square of Euclidean distance, it is always a positive value that decreases as the error approaches zero.

To estimate the predictive power of QSAR models, we employed the test set compounds for their external validation. The following statistical characteristics are recommended:[44,45] (i) Q^2_{LGO}; (ii) coefficient of determination R^2_{ext} between the predicted and observed activities; (iii) coefficients of determination (predicted versus observed activities, and observed versus predicted activities) for regressions through the origin; (iv) slopes k and k' of the regression lines through the origin. For acceptable QSAR predictive models, they should satisfy the following conditions:

(**i**) $Q^2_{LGO} > 0.5$; (**ii**) $R^2_{ext} > 0.6$; (**iii**) $(R^2_{ext} - R^2_{0\ ext})/R^2_{ext} < 0.1$ and $0.85 \le k \le 1.15$ or $(R^2_{ext} - R'^2_{0\ ext})/R^2_{ext} < 0.1$ and $0.85 \le k' \le 1.15$; (**iv**) $|R^2 - R'^2_{0\ ext}| < 0.1$.

The values of the external validation criteria are summarized in Table 5.

Table 5. External validation criteria values for Models **1 – 3**

No.	Validation criteria	Models Model 1	Model 2	Model 3
(i)	Q^2_{LGO}	0.6790	0.9860	0.6211
(ii)	R^2_{ext}	0.7183	0.7927	0.7026
(iii)	$R^2_{0\ ext}$	0.9988	0.9991	0.9988
	$(R^2_{ext} - R^2_{0\ ext})/R^2_{ext}$	–0.3905	–0.2604	–0.4216
	k	1.0118	1.0239	1.0172
	k'	0.9872	0.9758	0.9818
(iv)	$\|R^2 - R'^2_{0\ ext}\|$	0.2805	0.2064	0.2962

Based on the statistical evaluation and predictive power of the developed models, it may be concluded that Model 2 is the most reliable with the highest good-

ness-of-fitting assuring, statistical significance, robustness and externally predictivity.

A mechanistic interpretation for a generated QSAR models was then done to make the interpretation of the possible mechanism of activity. All constructed models contain 2*D* autocorrelation descriptors. In particular, all models contain Geary autocorrelation coefficients with lag 7, weighted by atomic masses (**GATS7m**). Models **2** and **3** contain Moran autocorrelations of lag 4 weighted by atomic Sanderson electronegativity and by mass (**MATS4e** and **MATS4m**, respectively). In general, *2D* autocorrelation descriptors represent the topological structure of compounds, describe the mutual correlation of certain properties of atoms in intervals equal to the sums of topological distances in the corresponding structural fragments. They are calculated from molecular graph *G* by summing the products of atom weights of the terminal atoms of all the paths of the considered path length (the lag). 2*D* autocorrelation descriptors are calculated based on the value of the autocorrelation function ATS(d):[46,47]

$$\mathrm{ATS}(d) = \sum_{i=1}^{A}\sum_{j=1}^{A}\delta_{ij}\cdot(\omega_i\cdot\omega_j)_d \qquad (7)$$

where *d* is the corresponding lag, or the number of topological distances in a single fragment of the molecular graph, can have the values between 1 and the maximal topological distance in the molecule; *A* is the number of atoms in the molecule; $\delta_{ij}=\begin{cases}0\,(d_{ij}\neq d)\\1\,(d_{ij}=0)\end{cases}$ – Kronecker's delta; ω_i, ω_j – physicochemical properties of the atoms *i* and *j* (atomic masses *m*, polarizability *p*, electronegativity *e*, van-der-Waals volume *v*).

The Moran autocorrelation descriptors (MATS_{dw}) are given by:

$$I(d) = \frac{\frac{1}{\Delta}\sum_{i=1}^{A}\sum_{j=1}^{A}\delta_{ij}\cdot(\omega_i-\bar{\omega})\cdot(\omega_j-\bar{\omega})}{\frac{1}{A}\sum_{i=1}^{A}(\omega_i-\bar{\omega})^2} \qquad (8)$$

where $\bar{\omega}$ is the average value of the property for the molecule, and $\Delta=\sum\delta_{ij}$ is the number of vertex pairs at distance equal to *d*. The computation of these descriptors involves summing different autocorrelation functions corresponding to different fragment lengths, thereby leading to different autocorrelation vectors according to the lengths of the structural fragments. Also, weighting components in terms of physicochemical properties has been considered, and therefore these descriptors address the topology of the structure or parts of its merged with a selected physicochemical property. Moran autocorrelations usually have values in the interval of [–1, +1] with the positive autocorrelations corresponding to positive values of Moran indices, while the negative autocorrelations correspond to negative values of these indices.

The Geary autocorrelation descriptors (GATS_{dw}) are given by:

$$C(d) = \frac{\frac{1}{2\Delta}\cdot\sum_{i=1}^{A}\sum_{j=1}^{A}\delta_{ij}\cdot(\omega_i-\omega_j)^2}{\frac{1}{(A-1)}\cdot\sum_{i=1}^{A}(\omega_i-\bar{\omega})^2} \qquad (9)$$

2*D* Geary autocorrelation coefficients are the functions of distances and may vary between 0 and ∞. At the same time, strong mutual correlations of atomic properties correspond to low values of the Geary autocorrelation, usually in the range between 0 and 1, while negative mutual correlations correspond to values of the Geary coefficient higher than 1, i.e., the statement "no autocorrelation" corresponds to the equality $C(d) = 1$.

The presence of lags 4 2*D* Autocorrelations in QSAR regressions **2** and **3** may be reviewed as the association of activity information content with structural fragments of such size. It should be noted that mass weighted Moran autocorrelation coefficient **MATS4m** made a positive contribution to the activity. Based on these models' interpretation, it can be stated that the presence of structural fragments with the sum of topological distances (lag) equal to 4 in the molecules of the training set substances, whose terminal atoms have high atomic masses and electronegativities, corresponds to the activity enhancing. All generated regressions also utilize 2*D* Geary autocorrelation **GATS7m** descriptor with the negatively signed regression coefficients. Based on the interpretation and analysis of Geary autocorrelations contribution into anti-exudative activity it can be asserted that the presence of structural fragments with sums of topological distances (lags) equal to 7, whose terminal atoms have high atomic masses, is undesirable. The possible structural fragments with lags 4 and 7 are depicted in Figure 3.

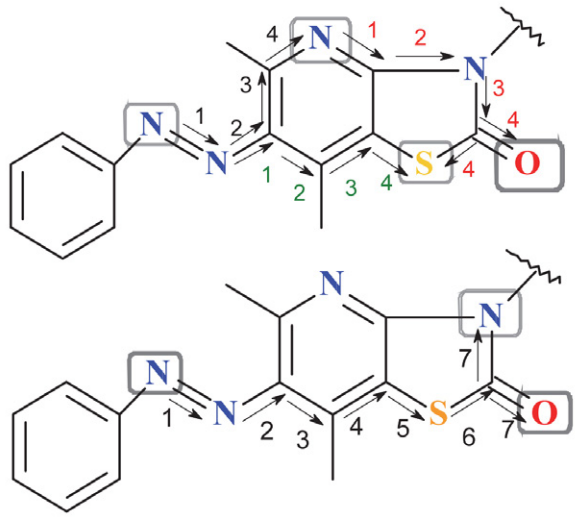

Fig. 3. Possible structural fragments with lags 4 and 7 in the molecules of N^3 substituted 5,7-dimethyl-6-phenylazo-3*H*-thiazolo[4,5-*b*]pyridin-2-one derivatives which may contribute to their anti-exudative action mechanism

It may be concluded that small structural patterns which include heteroatoms of fused thiazole and pyridine

core, and also one of the azo-group nitrogen atoms and closest scaffold heteroatom, may contribute mutually to the anti-exudative action mechanism, while the presence of large motifs started with azo-group nitrogen and ending at oxygen or nitrogen atoms of thiazolidin-2-one, cannot be involved into the activity mechanism realization.

3. 2. Molecular Docking

Suppression of prostaglandin synthesis is associated with inhibition of cyclooxygenase enzyme activity that catalyses the deoxygenation of arachidonic acid (AA) to form prostaglandin G_2 (PGG_2), then prostaglandin H_2 (PGH_2), and finally the resultant prostaglandins and thromboxane A2 (TxA_2).[48] The mechanism of traditional non-steroidal anti-inflammatory drugs (NSAIDs) action is based on non-selective inhibition of both cyclooxygenase isoforms (COX-1 and COX-2) and preventing prostaglandin synthesis. It is supposed that the therapeutic effect of these substances is due to the inhibition of COX-2, but their effect on COX-1 causes damage to the mucous membrane of the gastrointestinal (GI) tract and disorders in regulation of renal and platelet activity.[49] Selective COX-2 inhibitors (coxibs) inhibit the COX-2 isoform while spare COX-1 at clinical doses. This greatly mitigates the adverse effects in the GI tract as well as bleeding secondary to diminished platelet function.[50] Additional importance of COX-2 specific drugs discovering relates to their broader therapeutic applications as the biological role of COX-2 extends beyond inflammation and pain. It is known that COX-2 plays a key role in early female reproductive function, implantation and decidualization are dependent on COX-2.[51] Recent reports suggest that COX-2 may be an effective antitumor therapeutic target as COX-2 overexpression has been reported in several human cancers including lung, colon, prostate, and bladder cancer.[52-54] Selective COX-2 inhibitors, although characterized by a much lower negative effect on the digestive system, also have undesirable side effects, in particular, their effect on the cardiovascular system increases the risk of myocardial infarction, heart failure, stroke, etc.[55] In the light of these complications, it was proposed to identify other drug targets downstream of COX for pain and inflammation therapy. One of the promising new targets for finding bioactive substances that exhibits anti-inflammatory effect is microsomal prostaglandin E synthase-1 (mPGES-1) – the final enzyme in the cascade of arachidonic acid transformations. mPGES-1 is able to convert the cyclooxygenase (COX)-derived unstable prostaglandin H_2 (PGH_2) to the bioactive prostaglandin E_2 (PGE_2).[56] mPGES-1 belongs to a superfamily of Membrane-Associated Proteins (MAPEG family), involved into Eicosanoid and Glutathione metabolism, therefore it is useful for the development of anti-inflammatory and anticancer drugs interfering with prostaglandin and leukotriene biosynthesis.[57] mPGES-1 is regarded as a promising target for selectively suppressing PGE2 production during inflammation and nociceptive processing owing to its preferential coupling with COX-2.[58] But, contrary to the classical non-steroidal anti-inflammatory drugs (NSAIDs), the inhibition of mPGES-1 does not affect the biosynthesis of the other physiologically important PGs.[59] Possible mechanisms of mPGES-1 inhibitors activity are competitive interaction with active centres of cofactor or substrate. Inhibition of mPGES-1 has been shown to result in systemic shunting of PGH2 to PGI2 formation, leading to anti-inflammatory and vasodilatory effects, while preventing platelet activation.[60]

We utilized the standard MOE-Dock architecture for the molecular docking studies of N^3 substituted 5,7-dimethyl-6-phenylazo-3*H*-thiazolo[4,5-*b*]pyridin-2-ones with the selected receptors included the following major components: ligand conformations generation followed by partial charges calculation and energy minimization, receptors preparation, the binding sites definition, the ligand-receptor pose generation with alpha triangle as the placement algorithm, docking and scoring proceeding, receptor-ligand complexes refinement with re-scoring by filtering queries application, the lowest energy complexes extraction with the resulting complexes minimization. A data set of 2545 conformations for 36 compounds under study was prepared in this way. Docking poses were produced from the placement and the minimized receptor-ligand complexes obtained were then scored by the four scoring functions available in MOE: Affinity dG, Alpha HB, London dG, and GBVI/WSA dG Scorings.

3.2.1. Docking Results with COX-1 and COX-2

Both COX-1 and COX-2 isoforms are dimers consisting of 576 and 581 amino acids, respectively, while both iso-enzymes share the same molecular mass of 70 kDa/monomer. Each COX monomer consists of three structural domains:[61] a short N-terminal epidermal growth factor domain, a membrane binding domain, and a large, globular C-terminal catalytic domain. The cyclooxygenase and peroxidase active sites are located on opposite sides of the catalytic domain with inhibitor bound only in the cyclooxygenase active site. COX-1 and COX-2 isoforms present a high degree of homology.[62] The entrance to the COX active site occurs at the base of the membrane binding domain and leads to a long hydrophobic channel that extends deep into the interior of the catalytic domain.[63] The COX channel is composed of three residues (Arg-120, Tyr-355, and Glu-524) that separates the channel from the active site. The hydrophobic catalytic pocket contains catalytic Tyr-385 as well as Ser-530 at the top of the pocket, and also Trp-387, Phe-518, Ala-201, Tyr-248 and Leu-352. The COX-1 and COX-2 active sites are very similar but differ in the presence of a side pocket with larger solvent accessible surface in COX-2 located above the Arg-120/Tyr-355/Glu-524 constriction. This COX-2 side pocket is bordered by Val-523 (Ile-523 in COX-1) and contains His-90 and a

conserved Arg-513 (His-513 in most COX-1) at the base of the side pocket.[64] Most NSAIDs act inhibiting non-selectively both COX-1 and COX-2 iso-enzymes in a competitively reversible noncovalent manner. Aspirin is the only clinically used inhibitor modifies covalently and irreversibly both COX-1 and COX-2 through acetylation of Ser-530.[65] Aspirin analogues, like 2-bromoacetoxybenzoic acid and *o*-acetylsalicylhydroxamic acid, also bind in the COX-1 active site channel, acetylate Ser-530, and hydrogen-bond with Arg-120 at the constriction of the site.[66] In the existing crystal structures of COX with aspirin analogues, a hydrogen bond is formed between the carbonyl oxygen of the acetyl adduct and the phenolic hydrogen of Tyr-385, thus the presence of Tyr-385 across the active site from Ser-530 appears to be a critical determinant of acetylatio.[67] Phenylpropionic and arylacetic acid inhibitors (naproxen, diclofenac, indomethacin, ibuprofen, flurbiprofen, mefenamic acid, and meclofenamic acid) form a two-step binding mode for COX inhibition forming an ion pair and/or hydrogen bond with Arg-120 (this interaction is critical for inhibition) and a hydrogen bond with Tyr-355.[68] The unique binding mode of diclofenac with COX-2 is based on its inverted binding with the carboxylic acid moiety *via* hydrogen-bonded to Ser-530 and Tyr-385. The

Table 6. Calculated docking scores for 36 N^3 substituted 5,7-dimethyl-6-phenylazo-3*H*-thiazolo[4,5-*b*]pyridin-2-one derivatives in complexes with COX-1 and COX-2

Compound ID	COX-1 GBVI/WSA dG	COX-1 London dG	COX-1 Alpha HB	COX-1 Affinity dG	COX-2 GBVI/WSA dG	COX-2 London dG	COX-2 Alpha HB	COX-2 Affinity dG
1	−3.5721	−8.9854	−102.5757	−4.5784	−4.7093	−11.2232	−75.6134	−4.0763
2	−3.4101	−10.2535	−88.3039	−5.6864	−0.5564	−12.4995	−74.2815	−4.9970
3	−3.5094	−10.1962	−86.8319	−5.7342	−2.0131	−12.8897	−78.0022	−6.4081
4	−2.0678	−9.9628	−107.7880	−6.7700	−2.0915	−11.6763	−76.0573	−4.6654
5	−3.6256	−8.1085	−87.9495	−5.4172	−2.4295	−11.9037	−75.1318	−4.7097
6	−2.0591	−10.1058	−108.9735	−7.3861	−5.0659	−12.7828	−90.2685	−7.1683
7	−2.1836	−10.1408	−118.3711	−7.3602	−5.0118	−12.7031	−78.0846	−6.5735
8	−3.5894	−9.0593	−86.7782	−5.7160	−0.5586	−12.0557	−65.6218	−5.1219
9	−3.3979	−9.8344	−135.8003	−7.8005	−5.5785	−13.8054	−83.1410	−6.8872
10	−3.9388	−10.5867	−144.8922	−8.6517	−4.9257	−14.6358	−93.0085	−7.5152
11	−3.8215	−8.9786	−135.7580	−8.4577	−6.2059	−15.1357	−85.5426	−8.2501
12	−3.8334	−9.8577	−129.3662	−8.4110	−5.7290	−14.7253	−86.3963	−7.7120
13	−3.7142	−12.4254	−129.5875	−7.8616	−4.1096	−13.8382	−78.8016	−7.4252
14	−4.3321	−10.3371	−155.4785	−8.1072	−5.7120	−15.0507	−79.7068	−7.9452
15	−2.4523	−11.0348	−136.3768	−7.3664	−5.7441	−14.0444	−80.4431	−7.0865
16	−3.3274	−11.6665	−143.5742	−6.9413	−5.6076	−14.0993	−86.9043	−7.1747
17	−3.9379	−11.9141	−129.8906	−8.0258	−4.7478	−14.1567	−84.6444	−8.3579
18	−2.3838	−10.2205	−124.5617	−6.8422	−3.6734	−11.9241	−78.3305	−4.6454
19	−1.2252	−9.0904	−132.0742	−4.9922	−4.7933	−13.8596	−94.6653	−5.1191
20	−2.6893	−14.1219	−135.4255	−8.8465	−4.6539	−16.0134	−64.9250	−9.7737
21	−2.6710	−13.1721	−132.7236	−8.1597	−5.2945	−17.3721	−98.9472	−8.8459
22	−4.4923	−10.5589	−137.0937	−8.4308	−5.4785	−13.4701	−89.1642	−5.8359
23	−2.3580	−12.8478	−172.6101	−8.5650	−3.9622	−15.0712	−87.9949	−6.0371
24	−2.2812	−10.5789	−137.5367	−8.1755	−4.1854	−16.2461	−87.2868	−8.1194
25	−2.8548	−10.7060	−132.2015	−7.8614	−4.3432	−14.3780	−81.6798	−7.8906
26	−3.7227	−12.1064	−128.3981	−8.0519	−5.2332	−16.7522	−96.1670	−8.7652
27	−3.4848	−8.9993	−144.0276	−7.9182	−4.6807	−18.3361	−97.7554	−8.6181
28	0.1975	−11.4950	−126.1505	−6.7385	−6.0431	−14.7884	−76.8276	−6.6816
29	−6.7684	−12.0197	−140.5306	−5.6753	−7.1984	−16.2490	−84.0470	−8.4898
30	−2.8618	−11.1192	−186.8507	−8.2221	−5.1307	−17.3107	−108.0430	−8.6079
31	−2.8262	−8.7345	−149.1720	−7.4661	−2.2133	−16.3997	−89.4604	−8.0642
32	−7.6292	−11.5782	−151.1346	−9.9868	−5.7125	−18.2977	−93.5176	−10.1135
33	−0.6069	−11.8933	−127.6375	−6.3678	−6.6209	−14.8906	−90.3635	−8.3991
34	1.6951	−12.7936	−177.5706	−9.8437	−7.0093	−16.0785	−107.9989	−10.7538
35	−4.0370	−3.9965	−135.4871	−9.4130	−3.4646	−17.2437	−85.9848	−8.6887
36	−5.0688	−7.1341	−155.8307	−8.3196	−4.0012	−19.3118	−97.8379	−10.0296
Diclofenac	−0.6979	−10.5624	−95.7075	−6.0407	−3.9428	−9.2298	−107.4595	−7.3823
Naproxen	–	–	–	–	−7.2959	−13.9041	−94.5634	−6.0959
α -methyl-4-biphenyl-acetic acid	−7.6663	−13.9861	−102.8187	−7.7516	–	–	–	–

inhibitor also forms extensive van der Waals interactions with several hydrophobic residues within the active site. Indomethacin binds deeply within the COX-2 active site with its *p*-chlorobenzoyl group projects up into the active site channel, and the chlorine atom interacts with Leu-384 at the top of the active site, while the benzoyl oxygen interacts with Ser-530. The benzoyl group itself is stabilized by hydrophobic interactions with Leu-384, Tyr-385, Phe-381, and Trp-387. The carboxylate of indomethacin forms a salt bridge with Arg-120 and makes additional contacts with Tyr-355. The *o*-methoxy group protrudes into a large cavity provided by Ser-353, Tyr-355, and Val-523. The indole ring interacts with Val-349 and the 2'-methyl group projects into a small hydrophobic pocket formed by Val-349, Ala-527, Ser-530, and Leu-531, this interaction is supposed as a key interaction responsible for the time-dependent inhibition of COX enzymes by this inhibitor.[69] When turning to COX-2 selective inhibitors, it was shown, for instance, that lumiracoxib also binds in the COX-2 active site in an inverted orientation: its carboxylate forms hydrogen-bonding interactions with Ser-530 and Tyr-385 at the top of the active site, similar to diclofenac while the methyl group on the phenylacetic acid ring projects into a small groove near Leu-384 in the COX-2 active site. For diaryl heterocycle class of COX-2 selective inhibitors (celecoxib, rofecoxib, valdecoxib, etoricoxib) structure-activity analysis revealed that the fundamental factors responsible for the potent and selective inhibition of COX-2 include (1) two aromatic rings on adjacent positions on a central scaffold and (2) the presence of a sulfonamide or methyl sulfone group on one of the phenyl rings.

Docking calculations for N^3 substituted 5,7-dimethyl-6-phenylazo-3*H*-thiazolo[4,5-*b*]pyridin-2-ones were performed considering the X-ray crystallographic data of oCOX-1 and mCOX-2 with high resolutions downloaded from PDB (PDB entry codes 1Q4G, 3NT1 respectively). The most probable binding sites within the macromolecules were detected by means of MOE Site Finder, the alpha triangle as the placement algorithm was selected, running by superposition of ligand atom triplets and triplets of receptor site points. The receptor site points were represented by alpha sphere centres. At each iteration, a random ligand conformation was selected. A random triplet of ligand atoms and a random triplet of alpha sphere centres were used to determine the pose. The following docking calculations were performed by means of the DOCK tool implemented in MOE with the first rescoring function setting as "London dG", and the obtained poses were refined and rescored based on the refinement scoring function fixing to "GBVI/WSA dG". The values of the calculated docking scores for the compounds under study in their complexes with COX-1,2 are listed in Table 6. Also, co-crystallized ligands (α-methyl-4-biphenylacetic acid in case of COX-1 and naproxen for COX-2) and diclofenac were docked to the receptors as references.

The calculated values of the docking scores for the most energetically favourable receptor-ligand complexes suggest the possible inhibitory activity of 3*H*-thiazolo[4,5-*b*]pyridin-2-ones against both COX iso-forms expressed non-selectively. Alpha HB Scoring as a measure the geometric fit of the ligand to the binding site and hydrogen bonding effects, has significantly higher negative values for ligand-COX-1 complexes in comparison with the ligands complexed with COX-2 including reference drugs. Affinity dG Scoring, which estimated the enthalpic contribution to the free energy of binding, are comparable for both COX-1 and COX-2 complexes with a corresponding ligand.

In case of COX-1 complexes, the values of London dG Scoring, which estimates the free energy of binding of the ligand from a given pose, are close in values to that one for diclofenac while London dG Scoring for α-methyl-4-biphenylacetic acid-COX-1 complex has higher negative value. In case of ligans-COX-2 complexes London dG Scoring is comparable with that one for naproxen-COX-2 complex and has considerably higher negative values as compared with the corresponding ligand-COX-1 and diclofenac-COX-2 complexes, indicating higher thermodynamic probability of inhibitory activity towards COX-2 isoform.

We further analysed the detailed binding modes for COX-1,2 complexes with ligands keeping in mind that the compounds under study starting from **9** contain bulky substituents in their N^3 position and phenyl-azo group in C^6 position while they have no carboxylic group for catalytic Tyr-385 H-binding or Ser-530 acetylation.

It is well known that arylacetic acid inhibitors while binding to COX-1 and COX-2 active sites show two different binding modes with their acidic groups position either coordinating to the catalytic Tyr-385 as well as Ser-530 at the apex of the pocket or to the constriction residues Arg-120 and Tyr-355 at the base of the active site. α-Methyl-4-biphenylacetic acid, the defluorinated analogue of flurbiprofen, binds to COX-1 at the entrance of the long channel which leads into the enzyme active site, forming H-bonding interactions with Arg-120 and Tyr-355. Binding at this site presumably blocks access of substrate to Tyr-385, a residue essential for catalysis.[38] Similarly, the X-ray crystallographic structure of COX-2 in complex with naproxen[39] adopts that naproxen is bound entirely within the main channel of the COX-2 active site in the opposite binding mode: the carboxylate group of naproxen participating in hydrogen-bonding interactions with Arg-120 (2.8 Å) and Tyr-355 (2.5 Å) at the base of the active site while *p*-methoxy group is oriented toward the top of the hydrophobic channel. The remainder of the interactions between the compound and protein are van der Waals contacts.

The inspected binding modes of 5,7-dimethyl-6-phenylazo-3*H*-thiazolo[4,5-*b*]pyridin-2-ones within COX-1,2 active sites revealed that two main ligands orientations are

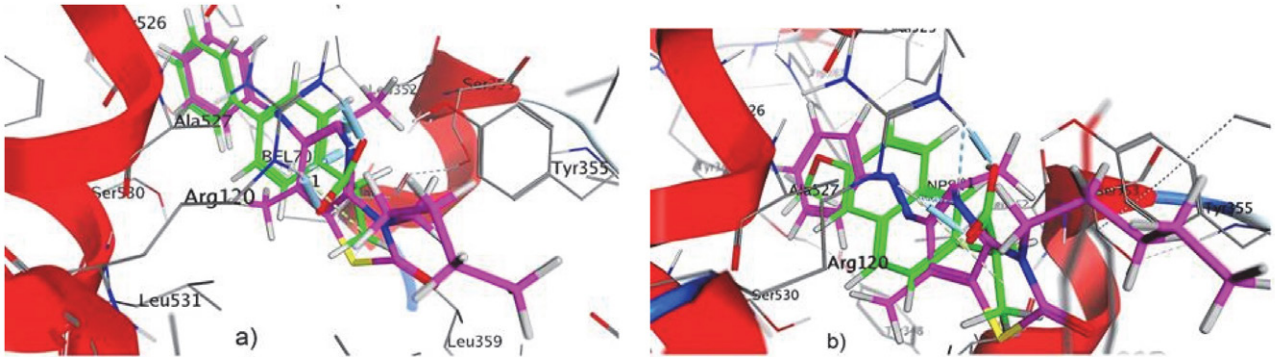

Fig. 4. Three-dimensional binding models of compound **6** in the active sites of COX-1 and COX-2: a) Compound **6** (magenta) overlayed with co-crystallized 2-(1,1'-biphenyl-4-yl)propanoic acid (green) in COX-1 active site; b) Compound **6** (magenta) overlayed with co-crystallized naproxen (green) in COX-2 active site

possible: the N^3 position substituent may be directed both inside and outside of the hydrophobic binding channel of the receptor. Figure 4 shows the binding modes of compound **6** with COX-1 and COX-2.

The binding orientations and interaction mechanisms in ligand-COX-1,2 complexes for the most active compounds are shown in Table 7.

The majority of top ranked poses of N^3 substituted thiazolo[4,5-*b*]pyridin-2-one derivatives docked into COX-1 active site are oriented with their phenylazo group directed inside the hydrophobic pocket with the complex formation maintaining on account of mainly Nitrogen of pyridine core hydrogen-bonding interaction with Arg-120. In some complexes additional stabilization on account of π-cation interaction between thiazole ring and Arg-120 (compounds **4**, **7**, **15**, **16**, **18**, **25**, **26**, **30** and **31**), also H-binding of Oxygen of N^3-substituent acetamide moiety with Arg-120 and Tyr-355 amino acid residues (compounds **14**, **20**). Also compound **20** has been shown to make π-H interaction of phenyl moiety of the substituent with Ile-89 which is thought to be one of the important residues in the lobby region of the protein active site. H-binding between Nitrogen of phenylazo group and Arg-120 is preferable for compounds **1**, **2**, **3**, **5**, **8** and **21** in their complexes with COX-1. In compound **2** - COX-1 complex Nitrogen of nitrile group forms additional binding with Arg-120. Additional hydrogen bond between Oxygen of thiazolidine ring and Arg-83 is forming for compounds **3**, **5**, **8**, **21**. Oxygen of acetamide moiety is forming hydrogen-bonding interactions with both Arg-120 and Tyr-355 for docking poses of compounds **19**, **23**, **24**, **34** in COX-1 active site. The same binding between Oxygen of acetamide moiety with both Arg-120 and Tyr-355 is observed for compound **34** while the ligand in this case has the opposite orientation with the N^3 position substituent orient towards the apex of the catalytic pocket. The same ligand orientation is displayed by compound **36** while the binding with COX-1 in this case is achieved *via* H-bonds between Nitrogen of methylene amino moiety of the substituent and Arg-120, Nitrogen of phenylazo group and Arg-83 and additional π-H interaction between pyridine ring and Ile-89.

Similarly, the majority of top ranking poses of N^3 substituted thiazolo[4,5-*b*]pyridin-2-ones docked into COX-2 active sites show that phenylazo group is directed inside the hydrophobic pocket with the complex formation maintaining on account of mainly Nitrogen of pyridine core hydrogen-bonding interactions with Arg-120 or Tyr-355, located at the base of the active site. Some compounds bind deeply with COX-2 active site forming hydrogen bonds between Oxygen of N^3-substituent acetamide moiety and Arg-120 amino acid residue as a single binding (compounds **20**, **22**, **24**, **26**, **27**, **30**) or in combination with N of pyridine cycle – Tyr-355 H-binding (compounds **10**, **11**, **28**). Additional complexes stabilization may be achieved on account of π-cation interaction between thiazole ring and Arg-120 or π-H interaction between pyridine ring and Tyr-355. While for a few derivatives the opposite orientation in COX-2 active site with the N^3 position substituent orientation towards the apex of the catalytic pocket allowed to form more favourable complexes. For compounds **13** and **19** their opposite orientation still does not prevent the H-bonds formation between pyridine cycle ring and Arg-120. At the same time compound **3** forms hydrogen bonds between Oxygen of thiazolidine ring with catalytic Ser-530 and between Nitrogen of phenylazo group with Arg-120. Compounds **23** and **34** form complexes with COX-2 on account of Nitrogen of phenylazo group and Oxygen of acetamide moiety with Arg-120 and Tyr-355. The complex between compound **34** and receptor is additionally stabilized by π-H interactions between both thiazolidine and pyridine rings with the lobby residue Leu-93. Compound **35** is deeply bonded within COX-2 active site and therefor Oxygen of acetamide moiety is forming hydrogen-bonding interactions with both Arg-120 and Tyr-355. Finally, compound **36** displays H-bonding interactions between acetamide Oxygen with Arg-120 and Chlorine of dichlorophenyl moiety with Glu-524 at the base of the active site.

Table 7. Interaction mechanisms, amino acid residues of the receptors active centers, interactions types and energy for complexes of thiazolo[4,5-*b*] pyridin-2-ones with COX-1 and COX-2

Compound ID	COX-1				COX-2			
	Ligand atoms and groups participating in the interaction with the receptor, and interaction types	**Amino acids residues of the receptor**	**H-bond distance, Å**	**Interaction energy, kcal/mol**	**Ligand atoms and groups participating in the interaction with the receptor, and iuteraction types**	**Amino acids residues of the receptor**	**Bond distance, Å**	**Interaction energy, kcal/mol**
1	=N-*Ph*, H-acceptor	Arg-120: NE	2.67	0.1	N (pyridine core), H-acceptor	Arg-120: NE	3.41	−0.7
	=N-*Ph*, H-acceptor	Arg-120: NH2	2.76	−1.6	Thiazolidine core, π-cation	Arg-120: NE	4.70	0.9
	–	–	–	–	Pyridine core, π-H	Tyr-355: OH	4.43	−0.7
2	=N-*Ph*, H-acceptor	Arg-120: NH1	3.05	−1.2	N (pyridine core),	Arg-120: NE H-acceptor	2.59	0.1
	≡N (nitrile group), H-acceptor	Arg120: NH2	2.68	−1.8	Pyridine core, π-H	Tyr-355: OH	4.14	−1.1
6	N (pyridine core), H-acceptor	Arg-120: NH2	3.38	−2.2	N (pyridine core), H-acceptor	Arg-120: NE	3.28	−1.2
	–	–	–	–	Thiazolidine core, π- cation	Arg-120: NE	4.60	−1.3
28	N (pyridine core), H-acceptor	Arg-120: NH2	3.13	−5.2	N (pyridine core), H-acceptor	Tyr-355: OH	2.72	−1.9
	–	–	–	–	=O acetamide group, H-acceptor	Arg-120: NE	2.39	8.5
	–	–	–	–	Pyridine core, π-cation	Arg-120: NH2	4.84	−1.0
35	N (pyridine core),H-acceptor	Arg-120: NH2	3.54	−1.6	=O acetamide group, H-acceptor	Arg-120: NH2	2.49	2.2
	–	–	–	–	=O acetamide group, H-acceptor	Tyr-355: OH	2.59	−0.9
	–	–	–	–	*Ph* of phenylazo group, π- cation	Lys-83: NZ	3.59	−1.8
36	-N= phenylazo group, H-acceptor	Arg-83 NH1	3.20	−0.7	Cl dichloro-phenylpyrrole fragment, H-donor	Glu-524: OE1	3.00	−2.4
	-N= hydrazide group, H-acceptor	Arg-120 NE	3.05	−3.9	=O acetamide group, H-acceptor	Arg-120: NE	2.67	−5.3
	Pyridine core, π-H	Ile-89: CG2	3.86	−0.8	–	–	–	

3. 2. 2. Docking Results with mPGES-1

mPGES-1 is an inducible and glutathione-dependent enzyme with molecular weight of 15-16 kDa, located on the endoplasmic reticulum. It is a transmembrane homotrimer consisting of 152 amino acid residues long-chain.[70] Each asymmetric monomer is characterized by a four-helix bundle motif. Thus, the quaternary structure of mPGES-1 consists of a homotrimeric protein complex with twelve membrane-spanning alpha helices, and three equivalent active site ~15-Å-deep cavities with an opening measuring 12 × 9 Å within the membrane-spanning region at each monomer interface. The mPGES-1 homotrimer binds three glutathione (GSH) molecules in "U"-shaped geometry due to the strong interactions between its two terminal carboxylic functions and the positively charged residues in the deeper part of the binding site (B:Arg-38, A:Arg-73). The GSH is coordinated by hydrogen bonds involving the side chains of Arg-73, Asn-74,

Glu-77, His-113, Tyr-117, Arg-126, and Ser-127 from helices II and IV, and the side chain of Arg-38 from helix I in a symmetry-related monomer. In addition to the hydrogen bonds, the phenol group of Tyr-130 forms a π-stacking interaction with the gamma peptide linkage between the cysteine and the glutamate side chain of GSH. Several regions in the binding site of mPGES-1 were disclosed which could be targeted by potential ligands. Firstly, it is the binding groove which is located between the GSH binding site and a molecular surface nearby the cytoplasmic part of the protein, mainly composed by aromatic (C:Phe-44, C:His-53) and polar (C:Arg-52) residues. The second binding region is located in a profound cavity corresponding to GSH binding site which is mainly characterized by polar residues. In this area except the side chains residues which coordinate GSH, A:Tyr-130 is a important as its phenol group in the side chain is involved in a π-stacking with the gamma peptide linkage between the cysteine and the glutamate of GSH. This key residue could be targeted by a binder through a π-π interaction and/or polar/H-bond interactions with the phenol hydroxyl moiety in the side chain.[71] Also Arg-126 and Ser-127 of chain A represent another fundamental residues in this binding area since they may play a critical role in catalytical isomerization mechanism from PGH2 to PGE2. Finally, moving from the external part of endoplasmic reticulum membrane to the cytoplasmic part of the protein, a binding groove is identifiable at the intersection between chain B and chain A, with polar (A:Gln-134), aliphatic (B:Val-24) and aromatic (B:Tyr-28) residues, and could be bound by long molecular functions.

In recent years a number of synthetic compounds with the property of mPGFES-1 inhibition were developed. Significant amount of them belong to fused heterocycles-based derivatives. Among them some mPGES-1 inhibitors also possessing anti-inflammatory action were discovered as phenanthrene imidazoles like MF63,[72] benzimidazoles,[73] indole carboxylic acid derivatives like MK886,[74] arylpyrrolizines (Licofelone derivatives),[75] benzoxazoles,[76] aminobenzothiazoles[77] and others.

However, despite the high number of inhibitors identified, to date, only two drug candidates are currently in Phase II clinical trials. GS-248 was initiated by Gesynta Pharma AB for treatment of microvascular diseases in chronic inflammatory conditions and is currently being tested in Phase II trial (https://www.clinicaltrials.gov/search?cond=GS-248) with systemic sclerosis patients. In 2023 GS-248 has been assigned the non-proprietary substance name vipoglanstat and introduced into clinical phase II development as a drug candidate for treatment of endometriosis. GRC 27864 (Glenmark Pharmaceuticals Ltd.) has successfully passed Phase I of clinical trials and has been adopted for Phase II as dose range finding study to evaluate the safety and efficacy in patients with moderate osteoarthritic pain.[78] Figure 5 shows chemical structures of some identified mPGES-1 inhibitors.

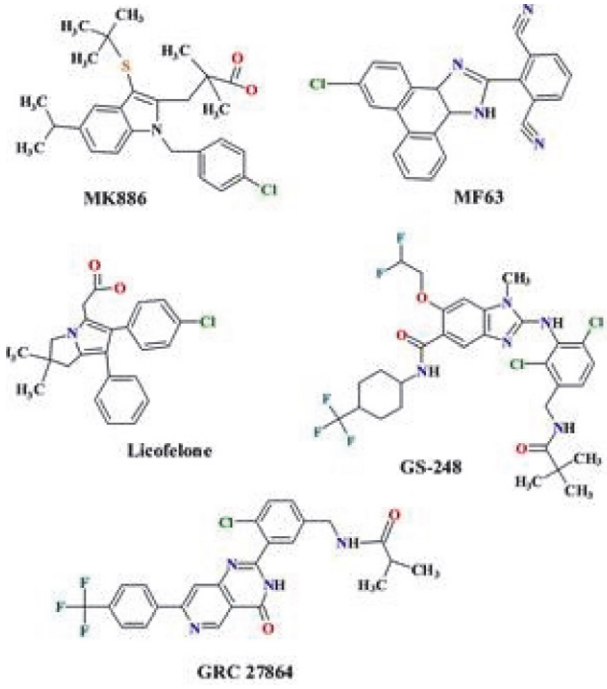

Fig. 5. Chemical structures of some known mPGES-1 inhibitors

In order to identify novel compounds that can inhibit mPGES-1 and to develop a predictive tool for the design of more potent mPGES-1 inhibitors based on thiazolo[4,5-*b*]pyridin-2-one scaffold, we performed docking studies for N^3 substituted 5,7-dimethyl-6-phenylazo-3*H*-thiazolo[4,5-*b*]pyridin-2-one derivatives against mPGES-1 considering the X-ray high-resolution (1.2 Å) crystallographic structure of human mPGES-1 linked to GSH (PDB entry code 4AL0). We utilized molecular structures of three known mPGES-1 inhibitors, MK886 (3-(1-(4-chlorobenzyl)-3-methyl-1*H*-indol-2-yl)-2,2-dimethyl propanoic acid), MF63 ([2-(6-Chloro-1*H*-phenanthro[9,10-dlimidazol-2-yl)-isophthalonitrilel), and Licofelon(2-[2-(4-chlorophenyl)-6,6-dimethyl-1-phenyl-5,7-dihydropyrrolizin-3-yl]acetic acid) as reference ligands. The values of the estimated docking scores for 5,7-dimethyl-6-phenylazo-3*H*-thiazolo[4,5-*b*]pyridin-2-one derivatives and reference drugs in their complexes with mPGES-1 are listed in Table 8.

GBVI/WSA dG, London dG and Alpha HB Scorings for all thiazolo[4,5-*b*]pyridin-2-ones in their complexes with mPGES-1 are comparable with that ones for references, while some compounds exhibit more negative values: compound **21** has more negative values of all three scorings, compounds **25** and **26** are more negative in London dG, compound **35** displays more negative GBVI/WSA dG, and compound **36** has more negative both GBVI/WSA dG and London dG. At the same time Affinity dG Scoring, which estimated the enthalpic contribution to the free energy of binding, has considerably higher negative values

Table 8. The estimated scoring functions for 36 N^3 substituted 5,7-dimethyl-6-phenylazo-3*H*-thiazolo[4,5-*b*]pyridin-2-ones and reference drugs in complexes with mPGES-1

Compound ID	GBVI/ WSA dG	London dG	Alpha HB	Affinity dG	Compound ID	GBVI/ WSA dG	London dG	Alpha HB	Affinity dG
1	−4.813	−4.269	−2.212	−37.696	**21**	−5.309	−8.062	−5.589	−0.361
2	−3.954	−5.206	−1.289	−54.498	**22**	−4.042	−6.481	−1.728	−0.281
3	−3.998	−4.104	−1.438	−23.694	**23**	−4.811	−7.741	−2.422	−24.917
4	−3.376	−4.074	−1.329	−13.094	**24**	−4.114	−6.827	−1.684	−20.803
5	−3.928	−3.301	−1.452	−23.537	**25**	−4.017	−10.518	−1.628	−12.337
6	−4.139	−6.594	−1.582	−19.431	**26**	−4.344	−7.515	−2.389	−24.832
7	−4.068	−6.248	−2.067	−4.959	**27**	−4.942	−9.528	−1.801	−39.510
8	−3.955	−5.837	−1.566	−19.205	**28**	−4.879	−5.241	−2.155	−19.550
9	−3.962	−5.844	−1.987	−25.804	**29**	−5.059	−8.500	−2.345	−15.018
10	−3.656	−6.773	−1.329	−28.648	**30**	−5.023	−7.287	−3.433	−29.696
11	−4.967	−7.646	−2.943	−7.614	**31**	−4.950	−6.732	−2.172	−14.517
12	−5.479	−6.173	−3.163	−14.754	**32**	−4.670	−6.962	−2.199	−42.320
13	−4.432	−6.567	−1.919	−11.702	**33**	−3.500	−7.511	−0.692	0.000
14	−4.375	−6.311	−1.718	−10.856	**34**	−4.474	−8.059	−2.675	−13.970
15	−4.209	−8.831	−2.367	−13.734	**35**	−5.176	−7.469	−3.079	−16.379
16	−4.094	−7.277	−2.611	2.194	**36**	−5.287	−10.276	−2.616	−15.563
17	−4.607	−6.219	−1.972	−12.391	**MK886**	−4.040	−7.472	−2.326	−34.163
18	−3.914	−6.593	−1.588	−1.719	**MF63**	−4.068	−4.599	−1.919	−36.495
19	−4.205	−7.136	−2.109	−31.410	**Licofelon**	−3.996	−7.811	−2.741	−33.234
20	−4.986	−7.152	−3.149	−14.257					

for the complexes of reference drugs with mPGES-1 in comparison with thiazolo[4,5-*b*]pyridin-2-ones complexed, the exceptions are compounds **1**, **2** and **27** with more negative Affinity dG values.

We further analysed the detailed binding modes for mPGES-1 complexes with ligands. The binding orientations and interaction mechanisms in ligand-mPGES-1 complexes for the most active compounds are shown in Table 9.

All ligands fit into the GHS-binding site of mPGES-1, as confirmed by the molecular docking results (Figure 6). Most complexes formation is maintained on account of Arg-126 amino acid residue of mPGES-1 active site interaction with the ligands while ligands` different atoms and functional groups are engaged. For instance, compounds **3**, **5**, **6**, **8**, **23** and **27** form hydrogen bonds between Arg-126 and Oxygen of thiazolidine-2-one ring. Additional complexes stabilization may be achieved on ac-

Table 9. Interaction mechanisms, amino acid residues of the receptors active centers, interactions types and energy for complexes of thiazolo[4,5-*b*] pyridin-2-one derivatives with mPGES-1

Compound ID	Ligand atoms and groups participating in the interaction with the receptor, and interaction types	Amino acids residues of the receptor	Bond distance, Å	Interaction energy, kcal/mol
1	N (pyridine core), H-acceptor	Arg-126: NE	3.53	−0.8
	N (pyridine core), H-acceptor	Arg-126: NH2	3.16	−1.2
	=O of thiazolidine-2-one core, H-acceptor	Arg-73: NH2	2.90	−5.7
	=O of thiazolidine-2-one core, H-acceptor	Tyr-117: OH	2.87	−3.2
	-CH_3 in pyridine core 5^{th} position, H-π	Tyr-130: 6-ring	4.18	−0.6
2	=O of thiazolidine-2-one core, H-acceptor	Arg-126: NE	2.99	−6.6
	=O of thiazolidine-2-one core, H-acceptor	Arg-126: NH2	3.10	−2.3
	≡N (nitrile group), H-acceptor	Arg-73: NH1	3.38	−2.7
	≡N (nitrile group), H-acceptor	Arg-73: NH2	3.11	−5.7
	≡N (nitrile group), H-acceptor	Tyr-117: OH	3.33	−2.0
6	=O of thiazolidine-2-one core, H-acceptor	Arg-126 NH2	3.02	−4,0
28	-NH- of hydrazide moiety, H-donor	Thr-131: OG1	3.10	−2.3
35	Cl dichlorophenyl-furyl fragment, H-donor	Ser-127: OG	3.90	−0.6
	Pyridine core, π-π	Tyr-130: 6-ring	3.93	0.0
36	=N-*Ph,* H-acceptor	Arg-126: NH2	3.36	−1.3
	Thiazolidine core, π-H	Ser-127: CD	3.87	−1.5

count of H-binding between Nitrogen of nitrile group with Arg-127 and Tyr-117 (compound **2**), hydrogen-bonding interaction between nitro group Oxygen of nitrophenyl moiety in N^3 position substituent and Tyr-130 (compound **10**), π-H interaction between pyridine ring and Ser-127 or H-π interaction between Nitrogen in acetamide moiety and Tyr-130 (compounds **4** and **32**, respectively).

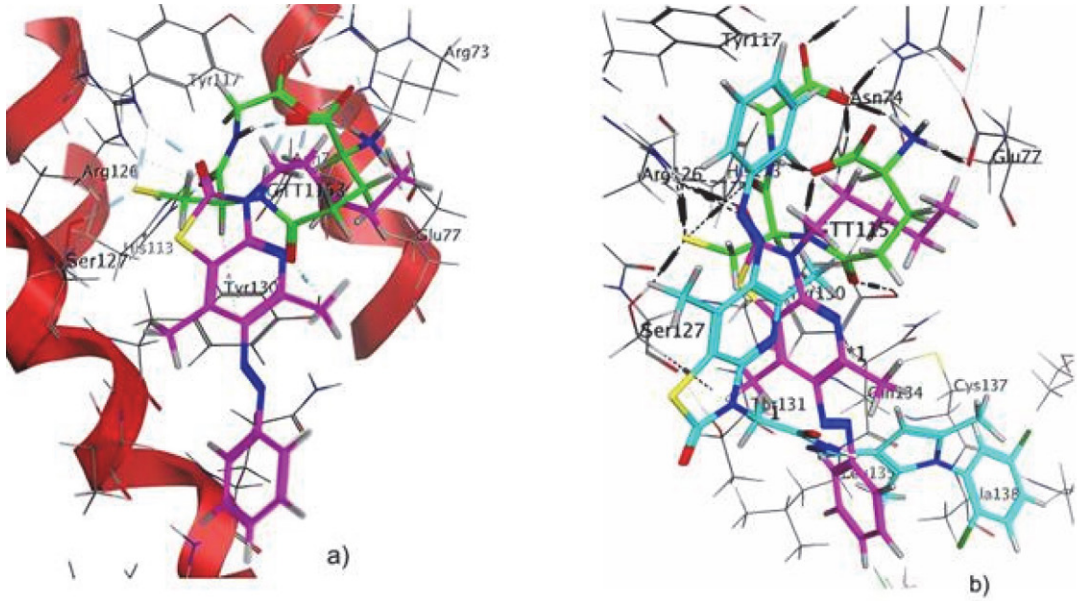

Fig. 6. a) Three-dimensional binding models of compound **6** (magenta) in the GHS-binding site of mPGES-1. The protein is depicted by ribbons (chain A). Glutathione (green) and ligand are represented by sticks; b) Sticks representation of the superposition of GHS (green), compounds **6** (magenta) and **36** (cyan) in mPGES-1 active site

Also, H-bond formation with Arg-126 may be achieved by its interaction with Oxygen of N^3-substituent acetamide moiety like in compound **18** complex with mPGES-1. The same Oxygen atom can form hydrogen bonds with Ser-127 (compounds **9**, **31**). For compound **33**, besides Oxygen of acetamide moiety binding with Arg-126, thiazole ring can form π-cation interaction with Arg-126 while compound **19** can form additional hydrogen bond between Oxygen of thiazolidine-2-one ring with Tyr-130. Some compounds are forming hydrogen bonds between Nitrogen of phenyl-azo moiety and Arg-126 amino acid residue as a single binding (compounds **26**, **34**) or in combination with π-H interaction between thiazolidine-2-one ring and Ser-127 (compounds **25**, **36**) accompanied by H-π interaction between Carbon of methyl group in thiazolo[4,5-*b*]pyridin-2-one fused core C^5 position and Tyr-130 (compounds **13**, **17**, **24**). Arg-126 together with Ser-127 and His-113 may act as H-donors for nitro group Oxygen of nitrophenyl moiety in N^3 position substituent (compounds **11**, **12**, **20**, **21**), while additional complexes stabilizing is maintained on account of π-H interactions between thiazolidine-2-one ring (compound **11**), pyridine ring (compound **12**) or phenyl in phenyl-azo fragment (compound **20**) and Tyr-130. Compound **1** can form H-binding with Arg-126 on account of its Nitrogen of pyridine core. Also hydrogen bonds between Oxygen of acetamide moiety with two amino acids residues – Arg-73 and Tyr-117 exist together with H-π interaction between Carbon of methyl group in thiazolo[4,5-*b*]pyridin-2-one fused core C^5 position and Tyr-130. For compound **35**, its complex with mPGES-1 is formed on account of hydrogen bonding between Arg-126 and carbonyl Oxygen in benzoic acid moiety accompanied by H-binding between Oxygen of acetamide moiety with Tyr-130 and π-H interaction between thiazolidine-2-one ring with Tyr-130. Some compounds can form π-H interaction between phenyl in phenyl-azo fragment and Arg-126 (compounds **7**, **15**, **22**). In complexes of compounds **15** and **28** with mPGES-1 H-bond is formed between Nitrogen of acetamide moiety and Thr-131, while for compounds **7** and **15** additional π-H interaction between pyridine ring and Ser-127 can stabilize corresponding complexes.

In the complex of compound **22** H-bonding with Thr-131 is forming on account of thiazole core Sulfur atom. Similar S-Thr-131 hydrogen bond is formed for compound **29** in its complex with mPGES-1. Thus compounds **28** and **29** have no interactions with Arg-126. Similarly, compounds **14**, **16** and **35** do not form binding with Arg-126. Compound **14** form H-π interaction between Carbon of methyl group in thiazolo[4,5-*b*]pyridin-2-one fused core C^5 position with Tyr-130 in combination with π-H interaction between thiazolidine-2-one ring and Ser-127. Compound **16** can form H-bond between Oxygen of acetamide moiety and Tyr-130 in combination with π-H interaction between thiazolidine-2-one ring and Tyr-130. For compound **35** in its complex with mPGES-1 hydrogen bond between Chlorine of dichlorophenyl-furyl fragment

with Ser-127 is accompanied by pyridine ring – Tyr-130 π-π interaction.

Active dock poses of thiazolo[4,5-*b*]pyridines within the binding pocket of mPGES-1 analysis ensured the acceptor-ligand interaction possibility *via* hydrogen binding between oxygen of thiazole ring, Oxygen of N^3-substituent acetamide moiety, Nitrogen atom of phenyl-azo moiety or Oxygen of nitrophenyl moiety in N^3 position substituent of ligands and key side-chains residues of mPGES-1, confirmed with the effective docking scores.

3. 3. Protein-ligand Interaction Pharmacophore Modelling

A pharmacophore is an abstract description of molecular features that are necessary for molecular recognition of a ligand by a biological macromolecule. The term *pharmacophore* was coined by Paul Ehrlich in 1909 to mean "a molecular framework that carries the essential features responsible for a drug's biological activity".[79] IUPAC defines a pharmacophore to be "an ensemble of steric and electronic features that is necessary to ensure the optimal supramolecular interactions with a specific biological target and to trigger (or block) its biological response".[80] So we may consider a pharmacophore as a 3*D* model describing the type and location of the binding interactions between a ligand and its target receptor. A pharmacophore model explains how structurally diverse ligands can bind to a common receptor site. Furthermore, pharmacophore models can be used to identify through de novo design or virtual screening novel ligands that will bind to the same receptor.

As a predictive tool for the design of more potent inhibitors discovery we performed 3*D* pharmacophore modelling for thiazolo[4,5-*b*]pyridines using protein-ligand interaction fingerprints (PLIF) tool implemented in MOE software. PLIFs may be considered as strings that convert protein–ligand interactions from 3*D* information into 1*D* representations.

There are two categories of interaction in which a residue may participate in a protein-ligand complex: potential (energy-based) contacts and surface (patch) contacts. For potential contacts, the value is that of the strongest interaction between any pair of atoms in the residue and ligand, whereas for surface contacts the value is the total contact area of each type between a residue and the other molecule.

PLIF possesses a composition of seven visible fingerprint bits: side-chain hydrogen bond donor (*D*), side-chain hydrogen bond acceptor (*A*), backbone hydrogen bond donor (*d*), backbone hydrogen bond acceptor (*a*), solvent hydrogen bond (*O*), ionic attraction (*I*) and surface contact (*C*). The hydrogen bond fingerprints are calculated using a method based on protein contact statistics, where-

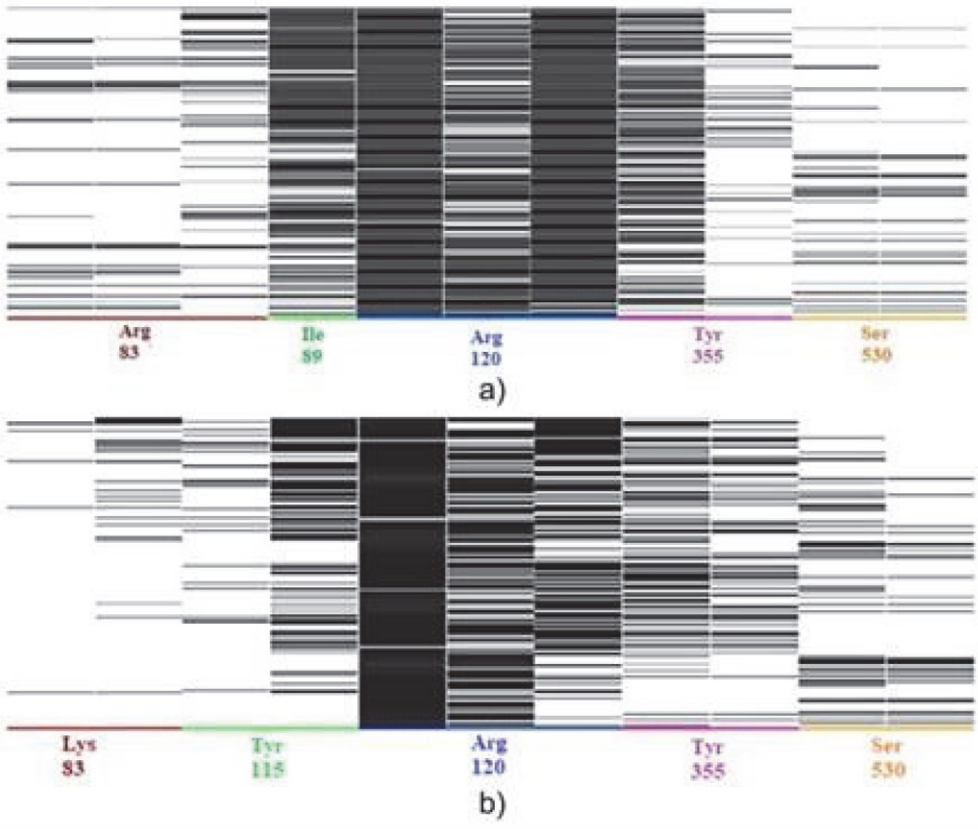

Fig. 7. Barcode representation of the docking interactions between researched compounds and COX-1 (a) and COX-2 (b) isoforms

by a pair of atoms is scored by distance and orientation. Ionic interactions are scored by calculating the inverse square of the distance between atoms with opposite formal charge (e.g. a carboxylate oxygen atom and a protonated amine). Surface contact interactions are determined by calculating the solvent-exposed surface area of the residue, first in the absence of the ligand, then in presence of the ligand.[81,82]

Receptors interaction fingerprints were generated firstly from the docked poses of the virtual screening hits. Affinity dG < −4 was used as a query for active poses. A "barcode" is a matrix image of fingerprints, in which each column corresponds to the formed interaction of a certain type (bit) with the corresponding amino acid residue, amino acid residues are marked on the x-axis. Each line in the "barcode" indicates the active conformational position of the ligand that forms an interaction with the corresponding amino acid residue.

As the interactions summarizing between ligands and both COX isoforms, the barcode diagrams were constructed for the virtual screening hits which depict the most frequent interactions between ligands and the side chains residues of COX-1,2 (Figure 7).

Barcodes for both COX isoforms contain five fingerprints with Arg-83 in COX-1 being changed to Lys-83 in COX-2, also Ile-89 being replaced with Tyr-115. Arg-83 fingerprint in COX-1 barcode consists of 3 bits – AAC, that is it can act as two hydrogen bonds acceptor and may form a surface contact with the ligand. At the same time Lys-83 fingerprint in COX-2 barcode is a two-bits one – AC, acting as hydrogen bond acceptor and forming a surface interaction. Ile-89 fingerprint is one of the most frequently populated in COX-1 barcode while it has just one bit – surface contact. Tyr-115 in COX-2 contains two bits – AC (H-bond acceptor and surface contact). The majority of compounds in the dataset showed interactions with Arg120 residue (99.4% of docking poses for COX-1 and 97.6% of docking poses for COX-2), its fingerprint consists of three bits for both COX isoforms – AAC: it may form two hydrogen bonds with the complexed compound on account of its sidechain nitrogen atoms action as acceptors in the donor-acceptor interactions, and the contact surface interaction is also possible. The most frequently populated interacting residues are also Tyr355 and Ser-530, both are two-bits fingerprints – AA - acting as two hydrogen bonds acceptors.

The pharmacophore query generator option in the PLIF module was used to generate pharmacophore-3*D* models from the fingerprint bits with the input setting of 3 Å maximum radius and feature coverage 50% threshold.

Generated pharmacophore models for both COX isoforms included two features (Figure 8).

Each generated model includes one common pharmacophoric feature, which performs a single function in providing binding between ligands and the protein: feature F1 as hydrogen bond acceptor centre (Acc) with the radius of 1.855 Å for COX-1 and hydrophobic centre feature F1 (HydA) with the radius of 2.986 Å for COX-2. The second pharmacophore centre F2 in both obtained queries can perform a dual function: it is a region with the radius of 1.968 Å (COX-1) or 2.259 Å (COX-2) containing an H-acceptor or a hydrophobic atom (Acc&ML|HydA for COX-1 or HydA|Acc&ML for COX-2). Acc&ML means a combination of hydrogen bond acceptor feature and a metal ligation site. The distances between the pharmacophoric centres are 2.81 Å in the model for COX-1 and 6.28 Å in the model for COX-2.

Constructed pharmacophoric models for COX-1,2 were then validated by screening the test compounds database over them. Compounds overlaying with two-points pharmacophore queries (Figure 9) suggests that H-acceptor feature is commonly overlayed with the steric arrangement of the nitrogen atom of the pyridine heterocycle, nitrogen in hydrazide group, or the oxygen atom of the acetamide fragment in N^3 substituent moiety. Thiazolidine-2-one core, the carbon atom connected to nitrogen in the 3rd position of the thiazolidine ring, or the carbon atoms of the alkyl substituent in N^3 position can act as hydrophobic regions.

Performed pharmacophore search ensured that the pharmacophore queries summary at 357 docking entries obtained for COX-1 are able to describe correctly the absolute hits number of 310 docking conformations (86.83%) with 33 of 36 structures (91.67%) without additional steric

Fig. 8. Two-points pharmacophore queries generated with PLIF tool for thiazolo[4,5-*b*]-pyridin-2-one derivatives in complexes with COX-1 (a) and COX-2 (b)

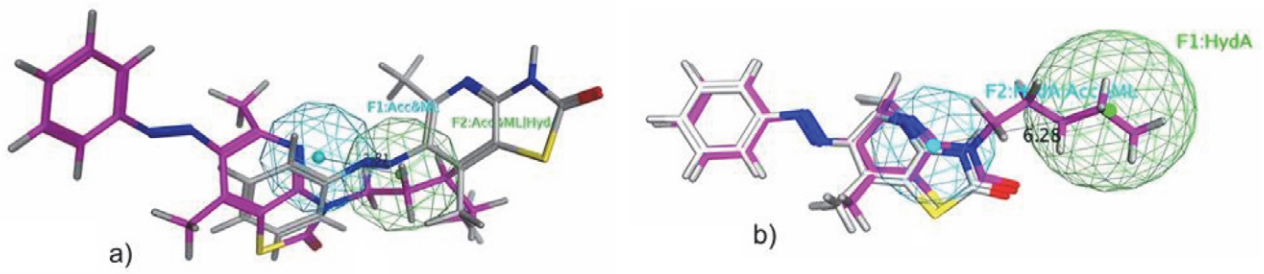

Fig. 9. Two-points pharmacophore queries overlaying with compounds **1** (grey) and **6** (magenta) for COX-1 (a) and COX-2 (b)

modifications of the ligands structure. The correctness of pharmacophore query obtained for COX-2 revealed 23 compounds (63.89%), or 219 conformations (53.16%) out of 412 obtained by docking as the absolute hits. The relative hits number for both COX iso-forms was found 100.00% with the active poses of 36/36 compounds (100.00%).

Receptor interaction fingerprints were generated from the docked poses of the virtual screening hits with mPGES-1 active sites coordinates depicting the interactions between compounds from the dataset and the following receptor amino acids residues: Arg73, His113, Tyr117, Arg126, Ser127, Tyr130, and Thr131 (Figure 10).

Arg-73 fingerprint consists of 2 bits – AC, that is it can act as side-chain hydrogen bond acceptor and may form a surface contact with the ligand. His-113 and Tyr-117 are one-bit fingerprints both acting as hydrogen bond acceptors. The most highly populated Arg-126 amino acid residue and Ser-127 are two-bits fingerprints - AA - both acting as two side-chain hydrogen bonds acceptors. Tyr-130 fingerprint contains 3 bits – AAC, that is it can act as two hydrogen bonds acceptor and may form a surface contact with the ligand. Thr-131 is also a three-bits fingerprint – DDA, while it can act as two side-chain hydrogen bonds donor and may form a surface contact with the ligand.

The generated 3*D* pharmacophoric model obtained as a result of PLIF identification for thiazolo[4,5-*b*]pyridine-2-one derivatives in mPGES-1 active site contains three common features (Figure 11a): hydrogen bond acceptor feature with the radius of 2.915 Å and two hydrophobic center features with the radii of 2.768 Å and 2.893 Å. The distances between the H-acceptor and two hydrophobic centres are 6.18 Å and 4.01 Å, and the distance between the hydrophobic pharmacophoric centres is 6.79 Å. The data set compounds were virtual screened over the developed pharmacophore query in order to validate its correctness (Figure 11b). Compounds overlaying with the constructed pharmacophore query for mPGES-1 suggests that H-acceptor feature is commonly overlayed with the nitrogen atom of the pyridine core or the oxygen atom of the acetamide fragment in N^3 substituent moiety. Thiazolidine core, the part of pyridine core together with methyl substituents in its 5^{th} or 7^{th} positions, or phenyl moiety connected to azo group can act as hydrophobic regions.

The correctness of pharmacophore queries was confirmed in the way of pharmacophore search performing. The summary at 786 entries showed the absolute hits number of 467 docking conformations (59.41%) with 25 of 36 structures (69.44%). The relative hits number for constructed mPGES-1 pharmacophoric model was found as 786 entries (100.00%) for 36/36 compounds (100.00%).

The analysis of all obtained pharmacophore models indicates the functionality of the condensed bicyclic thiazolopyridine scaffold, which is ensured by the steric placement of atoms of at least one of these heterocycles in the corresponding pharmacophore centers. The generated models can be used to screen virtual compound libraries for potentially active molecules.

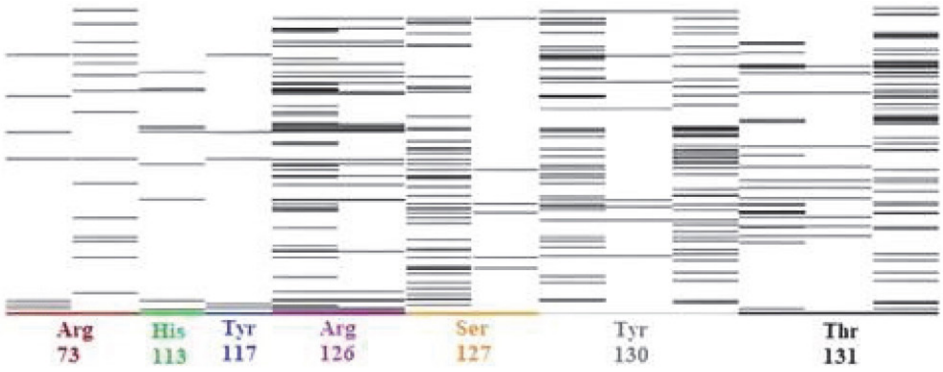

Fig. 10. Barcode representation of the docking interactions between active dock poses of the researched compounds and mPGES-1

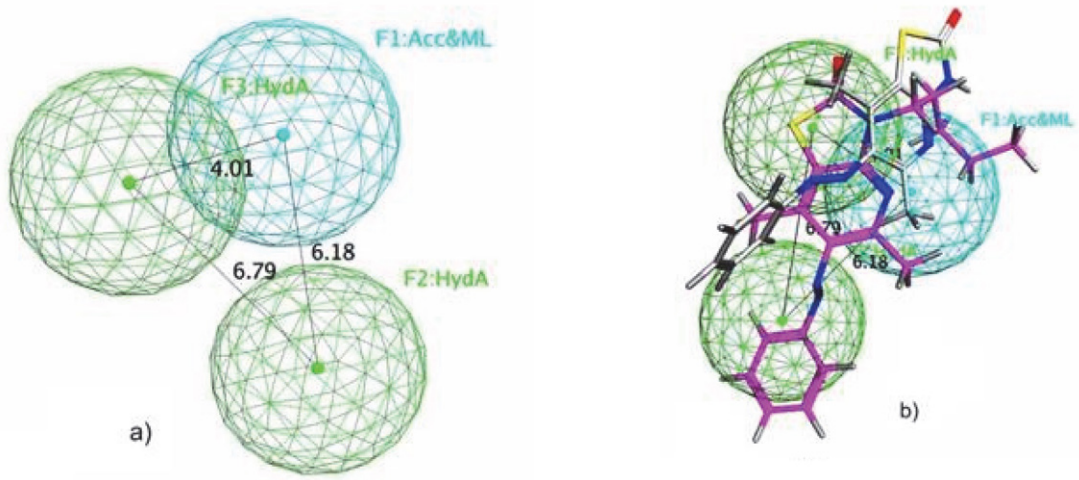

Fig. 11. Three-points pharmacophore query generated with PLIF tool for thiazolo[4,5-*b*]-pyridin-2-ones in complexes with mPGES-1 (a); its overlaying with compounds **1** (grey) and **6** (magenta) (b)

4. Conclusions

Condensed thiazolopyridine heterocyclic system can be considered as a promising scaffold for the combinatorial libraries construction of potential biologically active small molecules. This conclusion is based on the diversity of biological actions possessed by their derivatives and inhibitory properties of this system towards several enzymes, revealed with virtual screening tools, what is typical for privileged structures.

Firstly, the combination of two heterocycles to form a bicyclic condensed system as the scaffold for further functionalization, provides a small number of rotational bonds. Secondly, the affinity of the compounds under study towards several receptors proved by molecular docking results was ensured by the complementarity of the electrostatic and steric surfaces of receptors and ligands in general and the core scaffold in particular, as it was shown that the number of fused bicyclic core heteroatoms were able to form energetically favourable non-covalent interactions with proposed receptors. And, thirdly, the existing possibilities for thiazolopyridine core functionalization, in particular in its 3rd and 6th positions, allow to increase the inhibitory selectivity and specificity of the corresponding derivatives as well as their affinity towards certain receptors by introducing the appropriate substituents into the molecular structure.

The proposed virtual screening results provide an excellent starting point for rational design and *de novo* synthesis of novel thiazolo[4,5-*b*]pyridine-2-one scaffold based potential drug candidates.

Conflict of Interest Statement

The authors confirm that this article content has no conflict of interest.

Acknowledgments

Olena Klenina extends infinite gratitude and appreciation to Authorities of University CEU San Pablo, Madrid, Spain, for opening and funding the position of a researcher within Drug Design and Synthesis research group, School of Pharmacy, she is grateful to the Group Main researcher, Prof. Beatriz de Pascual-Teresa Fernández, and all the Group members, for their solidarity with Ukraine, support, assistance and for the research facilities.

5. References

1. H. Tallima, *ACS Omega* **2021**, *6*, 15559–15563. **DOI:**10.1021/acsomega.1c01952
2. B. Wang, L. Wu, J. Chen, L. Dong, C. Chen, Z. Wen, J. Hu, I. Fleming, D.W. Wang, *Signal Transduct Target Ther.* **2021**, *6*, 94. **DOI:**10.1038/s41392-020-00443-w
3. A. K. Chakraborti, S.K. Garg, R. Kumar, H.F. Motiwala, P.S. Jadhavar, *Curr. Med. Chem.* **2010**, *17*, 1563–1593. **DOI:**10.2174/092986710790979980
4. C. Sostres, C.J. Gargallo, M.T. Arroyo, A. Lanas, *Best Pract. Res. Clin. Gastroenterol.* **2010**, *24*, 121–132. **DOI:**10.1016/j.bpg.2009.11.005
5. J. K. Norberg, E. Sells, H.H. Chang, S.R. Alla, S. Zhang, E.J. Meuillet, *Pharm. Pat. Anal.* **2013**, *2*, 265–288. **DOI:**10.4155/ppa.12.90
6. Q. Wang, Y. Li, M. Wu, S. Huang, A. Zhang, Y. Zhang, Z. Jia, *Am. J. Transl. Res.* **2021**, *13*, 391–419.
7. T. Chaban, O. Klenina, I. Chaban, V. Ogurtsov, S. Harkov, M. Lelyukh, *Pharmacia* **2018**, *65*, 54–70.
8. A. Moran, E. Martin, C. Velasco, M.L. Martin, L. San Roman, E. Caballero, P. Puebla, M. Medarde, A. San Feliciano, *J. Pharm. Pharmacol.* **1997**, *49*, 421–425. **DOI:**10.1111/j.2042-7158.1997.tb06817.x

9. O. Klenina, T. Chaban, T., B. Zimenkovsky, S. Harkov, V. Ogurtsov, T. Chaban, I. Myrko, *Pharmacia* **2017**, *64*, 49–71.
10. I. M. Othman, M. A. Gad-Elkareem, H. A. Radwan, R. Badraoui, K. Aouadi, M. Snoussi, A. Kadri, *ChemistrySelect* **2021**, *6*, 7860–7872. **DOI:**10.1002/slct.202101622
11. H. K. A. El-Mawgoud, *Chem. Pharm. Bull.* **2019**, 67, 1314–1323. **DOI:**10.1248/cpb.c19-00681
12. R. Nurugan, S. Anbazhagan, S. Sriman Narayanan, *Eur. J. Med. Chem*. **2009**, *44*, 3272–3279. **DOI:**10.1016/j.ejmech.2009.03.035
13. V. Kamat, R. Santosh, B. Poojary, S.P. Nayak, B.K. Kumar, M. Sankaranarayanan, Faheem, S. Khanapure, D.A. Barretto, S.K. Vootla, *ACS Omega* **2020**, *5*, 25228–25239. **DOI:**10.1021/acsomega.0c03386
14. T. Chaban, O. Klenina, I. Drapak, V. Ogurtsov, I. Chaban, V. Novikov, *Chem. Chem. Technol.* **2014**, *89*, 287–292. **DOI:**10.23939/chcht08.03.287
15. S. G. Hegde, M.D. Mahoney, *J. Agric. Food Chem.* **1993**, *41*, 2131–2134. **DOI:**10.1021/jf00035a058
16. T. I. Chaban, R. R. Panchuk, O. V. Klenina, N. R. Skorokhyd, V. V. Ogurtsov, I. G. Chaban, *Biopolym. Cell* **2012**, *28*, 389–396. **DOI:**10.7124/bc.000075
17. A. U. Rao, A. Palani, X. Chen, Y. Huang, R. G. Aslanian, R. E. West Jr, S. M. Williams, R.-L. Wu, J. Hwa, C. Sondey, J. Lachowicz, *Bioorganic Med. Chem. Lett.* **2009**, *19*, 6176–6180. **DOI:**10.1016/j.bmcl.2009.09.006
18. L. Xia, Y. Zhang, J. Zhang, S. Lin, K. Zhang, H. Tian, Y. Dong, H. Xu, *Molecules* **2020**, *25*, 4630. **DOI:**10.3390/molecules25204630
19. G. R. Bebernitz, V. Beaulieu, B. A. Dale, R. Deacon, A. Duttaroy, J. Gao, M. S. Grondine, R. C. Gupta, M. Kakmak, M. Kavana, L. C. Kirman, J. Liang, W. M. Maniara, S. Munshi, S. S. Nadkarni, H. F. Schuster, T. Stams, I. St Denny, P. M. Taslimi, B. Vash, S. L. Caplan, *J. Med. Chem.* **2009**, *52*, 6142–6152. **DOI:**10.1021/jm900839k
20. R. Mohareb, F. Al-Omran, M. Abdelaziz, R. Ibrahim, *Acta Chim. Slov.* **2017**, *64*, 349–364. **DOI:**10.17344/acsi.2017.3200
21. M. Ahmadi, S. Bekeschus, K.D. Weltmann, T. von Woedtke, K. Wende, *RSC Med. Chem.* **2022**, *13*, 471–496. **DOI:**10.1039/D1MD00280E
22. M. M. El-Kerdawy, M. A. Ghaly, S. A. Darwish, H. A. Abdel-Aziz, A. R. Elsheakh, R. S. Abdelrahman, G. S. Hassan, *Bioorg. Chem.* **2019**, *83*, 250–261. **DOI:**10.1016/j.bioorg.2018.10.048
23. L. Y. He, S. S. Zhang, D. X. Peng, L. P. Guan, S. H. Wang, *Bioorganic Med. Chem. Lett.* **2020**, *30*, 127376. **DOI:**10.1016/j.bmcl.2020.127376
24. B. Smith, H. H. Chang, F. Medda, V. Gokhale, J. Dietrich, A. Davis, E. J. Meuillet, C. Hulme, *Bioorganic Med. Chem. Lett.* **2012**, *22*, 3567–3570. **DOI:**10.1016/j.bmcl.2012.03.013
25. T. Hanke, F. Dehm, S. Liening, S. D. Popella, J. Maczewsky, M. Pillong, J. Kunze, C. Weinigel, D. Barz, A. Kaiser, M. Wurglics, M. Lämmerhofe, G. Schneider, L. Sautebin, M. Schubert-Zsilavecz, O. Werz, *J. Med. Chem.* **2013**, *56*, 9031–9044. **DOI:**10.1021/jm401557w
26. HyperChem package Release 7.5 for Windows, Hypercube, Inc., 1115 NW 4th Street, Gainesville, Florida 32601, USA. http://www.hyper.com
27. I. V. Tetko, J. Gasteiger, R. Todeschini, A. Mauri, D. Livingstone, P. Ertl, V. A. Palyulin, E. V. Radchenko, N. S. Zefirov, A. S. Makarenko, V. Y. Tanchuk, V. V. Prokopenko, *J. Comput. Aided Mol. Des.* **2005**, *19*, 453–463. **DOI:**10.1007/s10822-005-8694-y
28. A. Golbraikh, M. Shen, Z. Xiao, Y. D. Xiao, K. H. Lee, A. Tropsha, *J. Comput. Aided Mol. Des.* **2003**, *17*, 241–253. **DOI:**10.1023/A:1025386326946
29. D. B. de Oliviera, A. C. Gaudio. *Quant. Struct. Act. Relat.* **2000**, *19*, 599–601. **DOI:**10.1002/1521-3838(200012)19:6<599::AID-QSAR599>3.0.CO;2-B
30. M. M. Suleiman, S. G. Isaev, O. V. Klenina, V. V. Ogurtsov, *J. Chem. Pharm. Res*. **2014**, *6*, 1219–1235.
31. O. Ouattara, T. S. Affi, M. G. - R. Koné, K. Bamba, N. Ziao, *Int. J. Eng. Res. Appl.* **2017**, *7*, 50–56. **DOI:**10.9790/9622-0705015056
32. A. Golbraikh, A. Tropsha, *J. Mol. Graph. Model.* **2002**, *20*, 269–276. **DOI:**10.1016/S1093-3263(01)00123-1
33. N. Chirico, P. Gramatica, *J. Chem. Inf. Model.* **2011**, *51*, 2320–2335. **DOI:**10.1021/ci200211n
34. R. Kiralj, M. Ferreira, *J. Braz. Chem. Soc.* **2009**, *20*, 770–787. **DOI:**10.1590/S0103-50532009000400021
35. Molecular Operating Environment (MOE), 2012.10; Chemical Computing Group Inc., 1010 Sherbooke St. West, Suite #910, Montreal, QC, Canada, H3A 2R7, 2012.
36. S. Vilar, G. Cozza, S. Moro, *Curr. Top. Med. Chem.* **2008**, *8*, 1555–1572. **DOI:**10.2174/156802608786786624
37. N. M. O'Boyle, M. Banck, C. A. James, C. Morley, T. Vandermeersch, G.R. Hutchison, *J. Cheminform.* **2011**, *3*, 1–14. **DOI:**10.1186/1758-2946-3-33
38. K. Gupta, B. S. Selinsky, C. J. Kaub, A. K. Katz, P. J. Loll, *J. Mol. Biol.* **2004**, *335*, 503–518. **DOI:**10.1016/j.jmb.2003.10.073
39. K. C. Duggan, M. J. Walters, J. Musee, J. M. Harp, J. R. Kiefer, J. A. Oates, L. J. Marnett, *J. Biol. Chem.* **2010**, *285*, 34950–34959. **DOI:**10.1074/jbc.M110.162982
40. T. Sjögrena, J. Nordb, M. Eka, P. Johanssona, G. Liub, S. Geschwindnera, *PNAS* **2013**, *110*, 3806–3811. **DOI:**10.1073/pnas.1218504110
41. T. Chaban, O. Klenina, S. Harkov, V. Ogurtsov, I. Chaban, I. Nektegaev, *Pharmacia* **2017**, *64*, 16–30.
42. T. I. Chaban, O. V. Klenina, B. S. Zimenkovsky, I. G. Chaban, V. V. Ogurtsov, L. S. Shelepeten, *Der Pharma Chem.* **2016**, *8*, 534–542.
43. R. Kiralj, M. Ferreira, *J. Braz. Chem. Soc.* **2009**, *20*, 770–787. **DOI:**10.1590/S0103-50532009000400021
44. V. Consonni, D. Ballabio, R. Todeschini, *J. Chemom.* **2010**, *24*, 194–201. **DOI:**10.1002/cem.1290
45. P. Gramatica, *IJQSPR* **2020**, *5*, 61–97. **DOI:**10.4018/IJQSPR.20200701.oa1
46. A. M. Helguera, R. D. Combes, M. P. Gonzalez, M. N. D. S. Cordeiro, *Curr. Top. Med. Chem.* **2008**, *8*, 1628–1655. **DOI:**10.2174/156802608786786598
47. A. Mauri, V. Consonni, R. Todeschini, R. Molecular Descriptors. In: J. Leszczynski, A. Kaczmarek-Kedziera, T. Puzyn, M.

G. Papadopoulos, H. Reis, M. K. Shukla (Eds.): Handbook of Computational Chemistry, Springer, Cham., Switzerland, 2017, pp. 2079–2082. **DOI:**10.1007/978-3-319-27282-5_51
48. T. Grosser, S. Fries, G. A. FitzGerald, *J. Clin. Investig.* **2006**, *116*, 4–15. **DOI:**10.1172/JCI27291
49. T. Brzozowski, P. C. Konturek, S. J. Konturek, Z. Sliwowski, R. Pajdo, D. Drozdowicz, A. Ptak, E. G. Hahn, *Microsc. Res. Tech.* **2001**, *53*, 343–353. **DOI:**10.1002/jemt.1102
50. K. N. Khan, S. K. Paulson, K. M. Verburg, J. B. Lefkowith, T. J. Maziasz, *Kidney Int*. **2002**, *61*, 1210–1219. **DOI:**10.1046/j.1523-1755.2002.00263.x
51. R. D. Puspita, D. M. Rizal, R. A. Syarif, I. P. Sari, *Open Access Maced. J. Med.* Sci. **2023**, *11(F)*, 31–37. **DOI:**10.3889/oamjms.2023.9123
52. T. J. Maier, K. Schilling, R. Schmidt, G. Geisslinger, S. Grösch, *Biochem. Pharmacol.* **2004**, *67*, 1469–1478. **DOI:**10.1016/j.bcp.2003.12.014
53. T. Kamijo, T. Sato, Y. Nagatomi, T. Kitamura, *Int. J. Urol.* **2001**, *8*, S35–S39. **DOI:**10.1046/j.1442-2042.2001.00332.x
54. M. J. Czachorowski, A. F. S. Amaral, S. Montes-Moreno, J. Lloreta, A. Carrato, A. Tardón, M. M. Morente, M. Kogevinas, F. X. Real, N. Malats, *PLOS ONE* **2012**, *7*, e45025. **DOI:**10.1371/journal.pone.0045025
55. L. G. Howes, *Ther Clin Risk Manag.* **2007**, *3*, 831–845.
56. F. Bergqvist, R. Morgenstern, P.–J. Jakobsson, *Prostaglandins Other Lipid Mediat.* **2020**, *147*, 106383. **DOI:**10.1016/j.prostaglandins.2019.106383
57. M. Thulasingam, L. Orellana, E. Nji, S. Ahmad, A. Rinaldo-Matthis, J. Z. Haeggström, *Nat. Commun.* **2021**, *12*, 1728–1739. **DOI:**10.1038/s41467-021-21924-8
58. K. Scholich, G. Geisslinger, *Trends Pharmacol. Sci.* **2006**, *27*, 399–401. **DOI:**10.1016/j.tips.2006.06.001
59. J. Z. Haeggström, C. D. Funk, *Chem. Rev.* **2011**, *111*, 5866–5898. **DOI:**10.1021/cr200246d
60. J. Steinmetz-Späh, P. J. Jakobsson, *Expert Opin. Ther. Targets* **2023**, *27*, 1115–1123. **DOI:**10.1080/14728222.2023.2285785
61. A. L. Blobaum, L. J. Marnett, *J. Med. Chem.* **2007**, *50*, 1425–1441. **DOI:**10.1021/jm0613166
62. U. R. Mbonye, C. Yuan, C. E. Harris, R. S. Sidhu, I. Song, T. Arakawa, W. L. Smith, *Biol. Chem.* **2008**, *283*, 8611–8623. **DOI:**10.1074/jbc.M710137200
63. J. J. Prusakiewicz, K. C. Duggan, C. A. Rouzer, L. J. Marnett, *Biochemistry* **2009**, *48*, 7353–7355. **DOI:**10.1021/bi900999z
64. A. S. Felts, C. Ji, J. B. Stafford, B. C. Crews, P. J. Kingsley, C. A. Rouzer, M. K.Washington, K. Subbaramaiah, B. S. Siegel, S. M. Young, A. J. Dannenberg, L. J. Marnett, *ACS Chem. Biol.* **2007**, *2*, 479–483. **DOI:**10.1021/cb700077z
65. F. J. Van Der Ouderaa, M. Buytenhek, D. H. Nugteren, D. A. Van Dorp, *Eur. J. Biochem.* **1980**, *109*, 1–8. **DOI:**10.1111/j.1432-1033.1980.tb04760.x
66. P. J. Loll, C. T. Sharkey, S. J. O'Connor, C. M. Dooley, E. O'Brien, M. Devocelle, K. B. Nolan, B. S. Selinsky, D. J. Fitzgerald, *Mol. Pharmacol.* **2001**, *60*, 1407–1413. **DOI:**10.1124/mol.60.6.1407
67. S. W. Rowlinson, J. R. Kiefer, J. J. Prusakiewicz, J. L. Pawlitz, K. R. Kozak, A. S. Kalgutkar, W. C. Stallings, R. G. Kurumbail, L. J. Marnett, *J. Biol. Chem.* **2003**, *278*, 45763–45769. **DOI:**10.1074/jbc.M305481200
68. J. A. Mancini, D. Riendeau, J. P. Falgueyret, P. J. Vickers, G. P. O'Neill, *J. Biol. Chem.* **1995**, *270*, 29372–29377. **DOI:**10.1074/jbc.270.49.29372
69. J. J. Prusakiewicz, A. S. Felts, B. S. Mackenzie, L. J. Marnett, *Biochemistry* **2004**, *43*, 15439–15445. **DOI:**10.1021/bi048534q
70. T. Sjögren, J. Nord, M. Ek, P. Johansson, G. Liu, S. Geschwindner, *PNAS* **2013**, *110*, 3806–3811. **DOI:**10.1073/pnas.1218504110
71. G. Lauro, M. Manfra, S. Pedatella, K. Fischer, V. Cantone, S. Terracciano, A. Bertamino, C. Ostacolo, I. Gomez-Monterrey, M. De Nisco, R. Riccio, E. Novellino, O. Werz, P.Campiglia, G. Bifulco, *Eur. J. Med. Chem.* **2017**, *125*, 278–287. **DOI:**10.1016/j.ejmech.2016.09.042
72. D. Xu, S. E. Rowland, P. Clark, A. Giroux, B. Côté, S. Guiral, M. Salem, Y. Ducharme, R. W. Friesen, N. Méthot, J. Mancini, L. Audoly, D. Riendeau, *J. Pharmacol. Exp. Ther.* **2008**, *326*, 754–763. **DOI:**10.1124/jpet.108.138776
73. N. Muthukaman, M. Tambe, S. Deshmukh, D. Pisal, S. Tondlekar, M. Shaikh, N. Sarode, V. G. Kattige, M. Pisat, P. Sawant, S. Honnegowda, V. Karande, A. Kulkarni, D. Behera, S. B. Jadhav, R. R. Sangana, G. S. Gudi, N. Khairatkar-Joshi, L. A. Gharat, *Bioorg. Med. Chem. Lett.* **2017**, *27*, 5131–5138. **DOI:**10.1016/j.bmcl.2017.10.062
74. D. Riendeau, R. Aspiotis, D. Ethier, Y. Gareau, E. L. Grimm, J. Guay, S. Guiral, H. Juteau, J. A. Mancini, N. Méthot, J. Rubin, R. W. Friesen, *Bioorg Med Chem Lett.* **2005**, *15*, 3352–3355. **DOI:**10.1016/j.bmcl.2005.05.027
75. A. Koeberle, U. Siemoneit, U. Bühring, H. Northoff, S. Laufer, W. Albrecht, O. Werz, *J. Pharmacol. Exp. Ther.* **2008**, *326*, 975–982. **DOI:**10.1124/jpet.108.139444
76. N. Kablaoui, S. Patel, J. Shao, D. Demian, K. Hoffmaster, F. Berlioz, M. L. Vazquez, W. M. Moore, R. A. Nugent, *Bioorg. Med. Chem. Lett.* **2013**, *23*, 907–911. **DOI:**10.1016/j.bmcl.2012.10.040
77. M. G. Chini, A. Giordano, M. Potenza, S. Terracciano, K. Fischer, M. C. Vaccaro, E. Colarusso, I. Bruno, R. Riccio, A. Koeberle, O. Werz, G. Bifulco, *ACS Med. Chem. Lett.* **2020**, *1*, 783–789. **DOI:**10.1021/acsmedchemlett.9b00618
78. S. Sant, M. Tandon, V. Menon, N. Khairatkar Joshi, K. Korukonda, O. Levine-Dolberg, *Osteoarthr. Cartil.* **2018**, *26*, S351–S352. **DOI:**10.1016/j.joca.2018.02.698
79. P. Ehrlich, *Ber. Dtsch. Chem. Ges.* **1909**, *42*, 17–47. **DOI:**10.1002/cber.19090420105
80. C. G. Wermuth, C. R. Ganellin, P. Lindberg, L. A. Mitscher, *Pure Appl. Chem.* **1998**, *70*, 1129–1143. **DOI:**10.1351/pac199870051129
81. N. H. N. Moorthy, S. F. Sousa, M. J. Ramos, P. A. Fernandes, *J. Enzyme Inhib. Med. Chem.* **2016**, *31*, 1428–1442. **DOI:**10.3109/14756366.2016.1144593
82. N. H. N. Moorthy, N. M. Cerqueira, M. J. Ramos, P. A. Fernandes, *Chemom. Intell. Lab. Syst.* **2015**, *140*, 102–116. **DOI:**10.1016/j.chemolab.2014.11.009

Povzetek

Poročamo o kombinirani in silico strategiji za raziskovanje molekulskih mehanizmov serije 3H-tiazolo[4,5-b]piridin-2-onov, ki kažejo močno protieksudativno delovanje. Pri raziskavi smo uporabili metode QSAR, molekularnega sidranja in modeliranja farmakoforov. Pri generiranju QSAR modelov z deskriptorji 2D avtokorelacije smo uporabili tehniko GA-ML. Eno- in dvo-parametrska regresija je razkrila, da določeni strukturni vzorci ali heteroatomi vzajemno prispevajo k povečanju protieksudativne aktivnosti. Možne mehanizme delovanja smo določili s fleksibilnimi simulacijami sidranja v encime, ki nastopajo v poti ciklooksigenaze (COX-1, COX-2, mPGES-1). Rezultati kažejo na možnost tvorbe stabilnih kompleksov z dobrimi ocenami sidranja in pravilno orientacijo ligandov znotraj aktivnih mest encimov. Modeliranje farmakoforov je bilo izvedeno z uporabo metodologije prstnih odtisov interakcij med proteinom in ligandom. Napravili smo 3D farmakoforne preiskave z dvema in tremi centri. Njihova analiza je nakazala funkcionalnost bicikličnega tiazolopiridinskega ogrodja, kar dokazuje, da so heteroatimi sterično umeščeni v ustrezne farmakoforne centre.

DOI: 10.17344/acsi.2024.8720 *Acta Chim. Slov.* **2024,** *71,* 288–294

Scientific paper

Synthesis, Crystal Structures and Catalytic Oxidation Property of Two Oxidovanadium(V) Complexes with Schiff bases

Qiwen Yang,[1] Guodong Li,[2] Jun Liu,[2] Wenqiong Xiao,[2] Yan Lei,[2] Xiuchan Xiao[2,*] and Ya Liu[2,*]

[1] *Department of Architectural Engineering, Sichuan Vocational and Technical College of Communications, Chengdu 611730, P. R. China*

[2] *School of Materials and Environmental Engineering, Chengdu Technological University, Chengdu 611730, P. R. China*

* *Corresponding author: E-mail: xiaoxiuchan@126.com*

Received: 02-29-2024

Abstract

Two new oxidovanadium(V) complexes, $[VO_2L^1]$ (**1**) and $[V_2O_2(\mu\text{-}O)_2L^2)]$ (**2**), where L^1 and L^2 are the deprotonated form of 5-bromo-2-(((2-(pyrrolidin-1-yl)ethyl)imino)methyl)phenol (HL^1) and 5-bromo-2-(((2-((2-hydroxyethyl) amino)ethyl)imino)methyl)phenol (HL^2), respectively, have been synthesized and structurally characterized by physico-chemical methods and single crystal X-ray determination. X-ray analysis indicates that the V atom in complex **1** is in square pyramidal coordination, and those in complex **2** are in octahedral coordination. Crystal structures of the complexes are stabilized by hydrogen bonds. The catalytic property for epoxidation of styrene by the complexes was evaluated.

Keywords: Vanadium complex, Schiff base, crystal structure, catalytic property

1. Introduction

Schiff bases bearing typical –CH=N– group represent one of the most attractive series of ligands in coordination chemistry.[1] The compounds can coordinate to various transition and rare earth metal atoms through the imino nitrogen, and/or other oxygen and nitrogen atoms, to form complexes with versatile structures and properties like antibacterial, enzyme inhibition, magnetism, catalytic and photoluminescence.[2] In the past years, a number of complexes with Schiff base ligands have been reported to have fascinating catalytic properties, such as oxidation of sulfides, polymerization and asymmetric epoxidation.[3] Among the complexes those with V centers are of particular interest for their catalytic applications.[4] There are a number of mononuclear and dinuclear vanadium complexes with Schiff base ligands have been reported.[5] However, there is no reasonable explanation on what kind of structures can be obtained. In pursuit of new vanadium

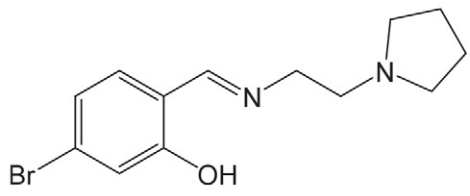

HL^1

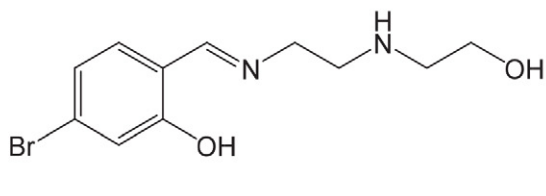

HL^2

Scheme 1. The Schiff bases HL^1 and HL^2.

complexes with Schiff base ligands, and investigating the influence on the formation of mononuclear and dinuclear species, we report herein two new oxidovanadium(V) complexes, $[VO_2L^1]$ (**1**) and $[V_2O_2(\mu\text{-}O)_2L^2)]$ (**2**), where L^1 and L^2 are the deprotonated form of 5-bromo-2-(((2-(pyrrolidin-1-yl)ethyl)imino)methyl)phenol (HL^1) and 5-bromo-2-(((2-((2-hydroxyethyl)amino)ethyl)imino)methyl)phenol (HL^2), respectively (Scheme 1).

2. Experimental

2. 1. Materials

4-Bromosalicylaldehyde, *N*-(2-aminoethyl)pyrrolidine, *N*-hydroxyethyl-1,2-ethylenediamine and $VO(acac)_2$ were purchased from Aldrich. All other reagents with AR grade were used as received. The Schiff bases HL^1 and HL^2 were prepared by reaction of equimolar quantities of 4-bromosalicylaldehyde with *N*-(2-aminoethyl)pyrrolidine and *N*-hydroxyethyl-1,2-ethylenediamine, respectively in methanol according to the literature method.[6]

2. 2. Physical Measurements

Infrared spectra (4000–400 cm^{-1}) were recorded as KBr discs with a FTS-40 BioRad FT-IR spectrophotometer. The electronic spectra were recorded on a Lambda 35 spectrometer. Microanalyses for C, H and N of the complexes were carried out on a Carlo-Erba 1106 elemental analyzer. Solution electrical conductivity was measured at 298K using a DDS-11 conductivity meter. GC analyses were performed on a Shimadzu GC-2010 gas chromatograph.

2. 3. X-ray Crystallography

Crystallographic data of the complexes were collected on a Bruker SMART CCD area diffractometer with graphite monochromated Mo-Kα radiation (λ = 0.71073 Å) at 298(2) K. Absorption corrections were applied by using the multi-scan program.[7] Structures of the complexes were solved by direct methods and successive Fourier difference syntheses, and anisotropic thermal parameters for all nonhydrogen atoms were refined by full-matrix least-squares procedure against F^2.[8] All non-hydrogen atoms were refined anisotropically. The amino and hydroxyl H atoms of complex **2** were located from a difference Fourier map and refined isotropically, with N–H and O–H distances restrained to 0.90(1) and 0.85(1) Å, respectively. The remaining hydrogen atoms were located at calculated positions, and refined isotropically with U_{iso}(H) values constrained to 1.2 U_{iso}(C). The C11 and C12 atoms in complex **1** are slightly disordered and were refined isotropically. The crystallographic data and experimental details for the structural analysis are summarized in Table 1.

Table 1. Crystallographic data for the single crystal of the complexes

	1	**2**
Empirical formula	$C_{13}H_{16}BrN_2O_3V$	$C_{22}H_{28}Br_2N_4O_8V_2$
Formula weight	379.13	738.18
Temperature (K)	298(2)	298(2)
Crystal system	Monoclinic	Triclinic
Space group	$P2_1/c$	P–1
a (Å)	13.2544(16)	6.8311(6)
b (Å)	10.5573(14)	11.6180(10)
c (Å)	10.7724(14)	17.2478(13)
α (°)	90	76.8550(10)
β (°)	102.5040(10)	79.1930(10)
γ (°)	90	89.7430(10)
V (Å^3)	1471.6(3)	1308.30(19)
Z	4	2
F(000)	760	736
μ, mm^{-1}	3.397	3.823
R_{int}	0.0350	0.0540
Collected data	7690	14314
Unique data	2741	4864
Observed data [$I > 2\sigma(I)$]	2045	3680
Restraints	12	4
Parameters	182	355
Goodness-of-fit on F^2	1.050	1.011
R_1, wR_2 indices [$I > 2\sigma(I)$]	0.0563, 0.1643	0.0421, 0.1145
R_1, wR_2 indices (all data)	0.0767, 0.1816	0.0627, 0.1267

2. 4. Synthesis of $[VO_2L^1]$ (1)

HL^1 (1.0 mmol, 0.30 g) and $[VO(acac)_2]$ (1.0 mmol, 0.26 g) were mixed and stirred in methanol (50 mL) for 30 min at 25 °C. The brown solution was evaporated to remove three quarters of the solvents under reduced pressure, yielding deep brown solid of the complex. Yield: 0.22 g (58%). Well-shaped single crystals suitable for X-ray diffraction were obtained by re-crystallization of the solid from methanol. Analysis calculated for $C_{13}H_{16}BrN_2O_3V$: C, 41.18; H, 4.25; N, 7.39%; found: C, 41.07; H, 4.32; N, 7.30%. IR data (KBr, cm^{-1}): 1630 (vs, $\nu_{C=N}$), 943 and 927 (m, $\nu_{V=O}$). UV-Vis data (λ_{max}, nm): 228, 366.

2. 5. Synthesis of $[V_2O_2(\mu\text{-}O)_2L^2)]$ (2)

HL^2 (1.0 mmol, 0.29 g) and $[VO(acac)_2]$ (1.0 mmol, 0.26 g) were mixed and stirred in methanol (50 mL) for 30 min at 25 °C. The brown solution was evaporated to remove three quarters of the solvents under reduced pressure, yielding deep brown solid of the complex. Yield: 0.25 g (68%). Well-shaped single crystals suitable for X-ray diffraction were obtained by re-crystallization of the solid from methanol. Analysis calculated for $C_{22}H_{28}Br_2N_4O_8V_2$:

C, 35.80; H, 3.82; N, 7.59%; found: C, 35.63; H, 3.76; N, 7.51%. IR data (KBr, cm^{-1}): 3372 (w, ν_{OH}), 3206 (w, ν_{NH}), 1632 (vs, $\nu_{C=N}$), 935 and 967 (m, $\nu_{V=O}$). UV-Vis data (λ_{max}, nm): 225, 260, 363.

2. 6. Styrene Epoxidation

The epoxidation reaction was carried out at room temperature in acetonitrile under N_2 atmosphere with constant stirring. The composition of the reaction mixture was 2.00 mmol of styrene, 2.00 mmol of chlorobenzene (internal standard), 0.10 mmol of the complexes (catalyst) and 2.00 mmol iodosylbenzene or sodium hypochlorite (oxidant) in 5.00 mL freshly distilled acetonitrile. When the oxidant was sodium hypochlorite, the solution was buffered to pH 11.2 with NaH_2PO_4 and NaOH. The composition of reaction medium was determined by GC with styrene and styrene epoxide quantified by the internal standard method (chlorobenzene). All other products detected by GC were mentioned as others. The reaction time for maximum epoxide yield was determined by withdrawing periodically 0.1 mL aliquots from the reaction mixture. This time was used to monitor the efficiency of the catalyst on performing at least two independent experiments. Blank experiments with each oxidant and using the same experimental conditions except catalyst were also performed.

3. Results and Discussion

3. 1. Chemistry

Complexes **1** and **2** were prepared by reaction of $VO(acac)_2$ with HL^1 and HL^2, respectively in methanol (Scheme 2). Complex **1** is a mononuclear vanadium compound, while complex **2** is an oxido bridged dinuclear compound. There are two N–H···O hydrogen bonds between the two $[VO_2L^2]$ units in complex **2**, which make the two molecules close to each other. However, in the mononuclear complex **1**, there is no such hydrogen bond. Thus, the formation of mononuclear or dinuclear vanadium complexes depends on whether there are additional interactions like hydrogen bonding between the molecules. The Schiff bases were deprotonated during the coordination. The oxidation of V(IV) in $VO(acac)_2$ to V(V) in both complexes during the reaction in air is not uncommon.[9] The molar conductivities are 35 Ω^{-1} cm^2 mol^{-1} (**1**) and 30 Ω^{-1} cm^2 mol^{-1} (**2**), which are consistent with the values expected for non-electrolyte.[10]

3. 2. Crystal Structure Description of Complex 1

Selected bond lengths and angles for the complex are listed in Table 2. Single crystal X-ray analysis indicates that the complex is a mononuclear oxidovanadium(V) compound. The ORTEP plot of the complex is shown in Fig. 1. The V atom in the complex is in square pyramidal geometry, with the phenolate oxygen (O1), imino nitrogen (N1) and pyrrolidine nitrogen (N2) of the Schiff base ligand and one oxo oxygen (O2) defining the basal plane, and with the other oxo oxygen (O3) locating at the apical position. The V atom displaced towards the apical oxygen by 0.471(1) Å. The geometry can be evidenced by the τ value of 0.44, which indicates it a distorted square pyramidal coordination.[11] The distortion of the coordination can also be observed from the bond angles related to the V atom. The *cis*- and *trans*- angles at the basal plane are 76.75(16)–115.25(18)° and 132.94(19)–159.31(15)°. The deviation from the ideal square pyramidal geometry are mainly origin from the strain created by the five-membered chelate ring V1–N1–C8–C9–N2 and the repulsive force between the two oxo oxygen. The bond lengths of V1–O1 of 1.910(4) Å, V1–N1 of 2.137(4) Å and V1–N2 of 2.170(4) Å are comparable to those observed in Schiff base oxidovanadium(V) complexes.[12] The terminal V1–O2 and V1–O3 are 1.621(4) and 1.615(4) Å, which agree well with the corresponding values reported for related systems.[9]

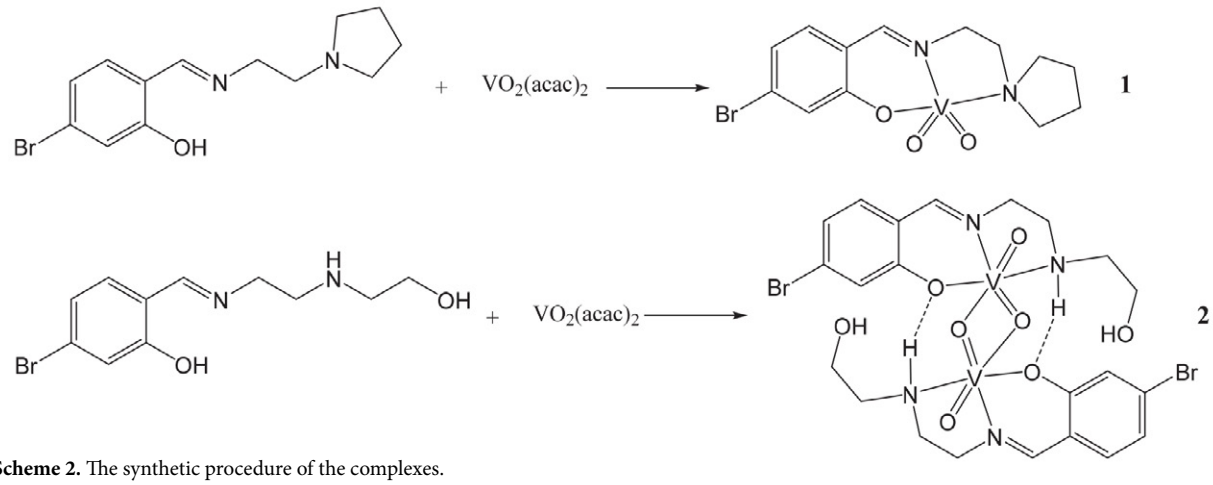

Scheme 2. The synthetic procedure of the complexes.

In the crystal structure of the complex, the molecules are linked by C13–H13B···O3 hydrogen bonds (Table 3), to form one-dimensional chains running along the *c* axis. The chains are further linked through C3–H3···O2 hydrogen bonds at the *b* axis, generate two-dimensional network (Fig. 2).

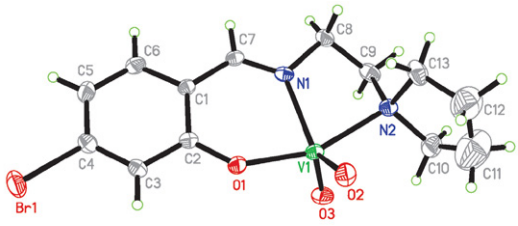

Fig. 1. ORTEP diagram of complex **1** with 30% thermal ellipsoid.

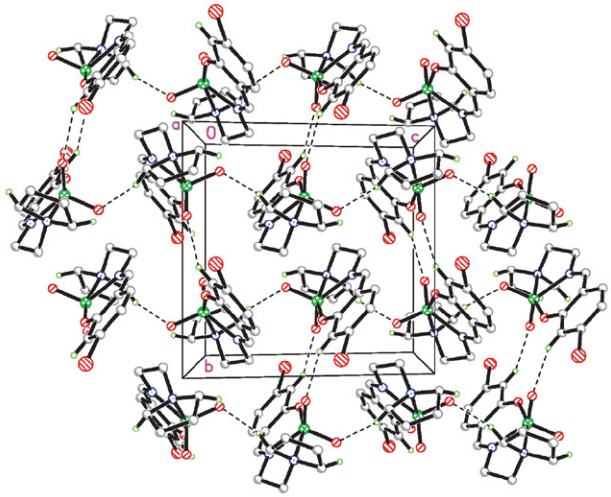

Fig. 2. Molecular packing structure of complex **1** linked by hydrogen bonds (dashed lines).

3. 3. Crystal Structure Description of Complex 2

Selected bond lengths and angles for the complex are listed in Table 2. Single crystal X-ray analysis indicates that the complex is an oxido bridged dinuclear oxidovanadium(V) compound. The molecule possesses crystallographic inversion center symmetry. The ORTEP plot of the complex is shown in Fig. 3. The V atoms in the complex are in octahedral geometry, with the phenolate oxygen (O1), imino nitrogen (N1) and pyrrolidine nitrogen (N2) of the Schiff base ligand and one bridging oxo oxygen (O2) defining the equatorial plane, and with one terminal oxo oxygen (O3) and the other bridging oxo oxygen (O2A) locating at the axial positions. The V atom displaced towards the axial oxygen (O3) by 0.312(1) Å. The distortion of the coordination can be observed from the bond angles related to the V atom. The *cis*- and *trans*- angles at the equatorial plane are 75.86(13)–106.68(14)° and 155.19(13)–173.35(12)°, respectively. The deviation from the ideal octahedral geometry is mainly caused by the five-membered chelate ring V1-N1-C8-C9-N2 and the repulsive force between the two oxo oxygen. The bond lengths of V1–O1 of 1.918(3) Å, V1–N1 of 2.149(3) Å and V1–N2 of 2.182(3) Å are similar to complex **1**, and comparable to those observed in Schiff base oxidovanadium(V) complexes.[13] The bond lengths agree well with the corresponding values reported for related systems.[12,13]

In the crystal structure of the complex, the molecules are linked by N2–H2···O1, O4–H4···O8, N4–H4A···O5, O8–H8···O2, C19–H19A···O6 and C20–H20B···O4 hydrogen bonds, to form two-dimensional network (Fig. 4).

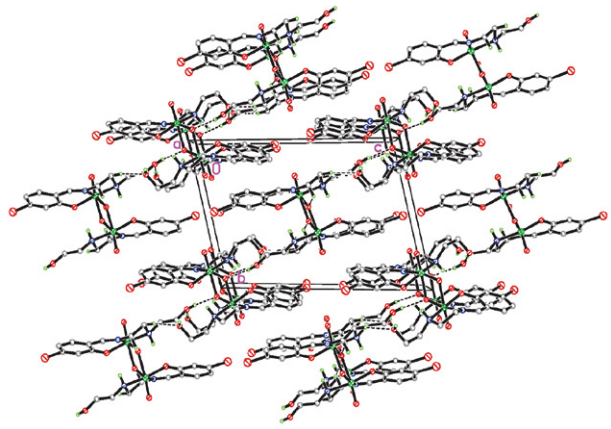

Fig. 4. Molecular packing structure of complex **2** linked by hydrogen bonds (dashed lines).

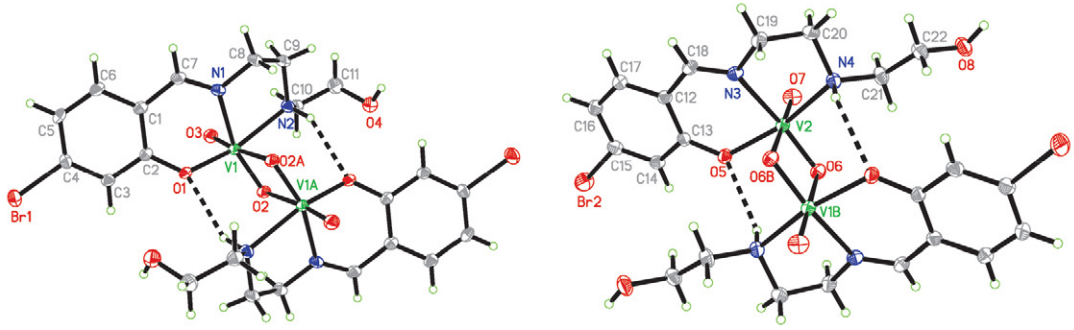

Fig. 3. ORTEP diagram of complex **2** with 30% thermal ellipsoid. Atoms labeled with the suffix A and B are related to the symmetry operations −*x*, −*y*, −*z*, and −*x*, 1 − *y*, 1 − *z*.

Table 2. Selected bond distances (Å) and bond angles (°) for the complexes

1			
V1–O1	1.910(4)	V1–O2	1.621(4)
V1–O3	1.614(4)	V1–N1	2.137(4)
V1–N2	2.169(4)		
O3–V1–O2	110.5(2)	O3–V1–O1	101.28(19)
O2–V1–O1	98.20(18)	O3–V1–N1	115.25(18)
O2–V1–N1	132.95(19)	O1–V1–N1	83.41(15)
O3–V1–N2	92.52(18)	O2–V1–N2	91.16(19)
O1–V1–N2	159.32(15)	N1–V1–N2	76.75(16)
2			
V1–O1	1.918(3)	V1–O2	1.692(3)
V1–O3	1.600(3)	V1–N1	2.149(3)
V1–N2	2.182(3)	V1–O2A	2.328(3)
V2–O5	1.925(3)	V2–O6	1.660(3)
V2–O7	1.615(3)	V2–N3	2.161(3)
V2–N4	2.163(3)	V2–O6A	2.365(3)
O3–V1–O2	106.68(14)	O3–V1–O1	98.29(14)
O2–V1–O1	102.97(13)	O3–V1–N1	95.99(14)
O2–V1–N1	155.19(13)	O1–V1–N1	83.14(12)
O3–V1–N2	94.18(14)	O2–V1–N2	92.26(13)
O1–V1–N2	156.56(13)	N1–V1–N2	75.86(13)
O3–V1–O2A	173.35(12)	O2–V1–O2A	79.22(12)
O1–V1–O2A	83.09(11)	N1–V1–O2A	77.68(11)
N2–V1–O2A	82.38(12)	O7–V2–O6	107.54(15)
O7–V2–O5	101.54(14)	O6–V2–O5	98.45(13)
O7–V2–N3	98.71(15)	O6–V2–N3	152.54(14)
O5–V2–N3	83.76(13)	O7–V2–N4	92.25(15)
O6–V2–N4	93.52(13)	O5–V2–N4	158.02(13)
N3–V2–N4	77.23(13)	O7–V2–O6B	170.70(13)
O6–V2–O6B	77.58(13)	O5–V2–O6B	85.08(12)
N3–V2–O6B	75.34(11)	N4–V2–O6B	79.55(12)

Symmetry operations: A: –*x*, –*y*, –*z*; B: –*x*, 1 – *y*, 1 – *z*.

Table 3. Hydrogen bond distances (Å) and bond angles (°) for the complexes

D*–H···*A **(*D*–H···*A*)**	***d*(*D*–H)**	***d*(H···*A*)**	***d*(*D*···*A*)**	**Angle**
1				
C3–H3···O2$^{\#1}$	0.93	2.49(3)	3.338(5)	151(5)
C13–H13B···O3$^{\#2}$	0.97	2.38(3)	3.314(5)	162(5)
2				
N2–H2···O1$^{\#3}$	0.90(1)	2.34(4)	3.137(4)	148(5)
O4–H4···O8$^{\#4}$	0.85(1)	1.88(1)	2.735(5)	178(7)
N4–H4A···O5$^{\#5}$	0.90(1)	2.38(5)	3.073(5)	134(5)
O8–H8···O2$^{\#6}$	0.85(1)	2.17(1)	3.016(4)	172(6)
C19–H19A···O6$^{\#7}$	0.97	2.54(2)	3.115(4)	118(5)
C20–H20B···O4$^{\#6}$	0.97	2.48(2)	3.442(4)	171(5)

Symmetry codes: #1: 1 – *x*, –*y*, 1 – *z*; #2: *x*, ½ – *y*, –½ + *z*; #3: –*x*, –*y*, –*z*; #4: 1 + *x*, *y*, –1 + *z*; #5: –*x*, 1 – *y*, 1–*z*; #6: *x*, *y*, 1 + *z*; #7: 1 + *x*, *y*, *z*.

3. 4. IR and UV-vis Spectra of the Complexes

The weak absorption at 3372 cm^{-1} and the sharp absorption at 3206 cm^{-1} of complex **2** are attributed to the stretching vibrations of O–H and N–H bonds, respectively. The intense bands at 1630 cm^{-1} for **1** and 1632 cm^{-1} for **2** are assigned to the vibrations of the azomethine groups, ν(C=N).[14] The characteristic of the spectra of both complexes is the exhibition of bands at 943 and 927 cm^{-1} for **1**, and 935 and 967 cm^{-1} for **2**, corresponding to the V=O stretching vibrations.[15] This agrees well with the bond lengths of C=N bonds in the crystal structures determined by single crystal X-ray diffraction. The two bands are close to each other in the spectrum of **1**, while those in complex **2** are not too close. The weak bands in the range 400–650 cm^{-1} are assigned to the vibrations of the V–O and V–N bonds.

In the UV-Vis spectra of the complexes, the bands at 360–370 nm are attributed to the azomethine chromophore π-π* transitions. The bands at higher energy (220–260 nm) are associated with the benzene π-π* transitions.[16]

3. 5. Catalytic Properties of the Complexes

The percentage of conversion of styrene, selectivity for styrene oxide, yield of styrene oxide and reaction time to obtain maximum yield using both the oxidants are given in Table 4. The data reveals that the complexes as catalysts convert styrene most efficiently in the presence of both oxidants. Nevertheless, the catalysts are selective towards the formation of styrene epoxides despite the formation of by-products which have been identified by GC-MS as benzaldehyde, phenylacetaldehyde, styrene epoxides derivative, alcohols *etc.* From the data it is also clear that the complexes exhibit excellent efficiency for styrene epoxide yield. When the reactions are carried out with PhIO and NaOCl, styrene conversions of complexes **1** and **2** were about 88% and 84%, and 83% and 80%, respectively. It is evident that between PhIO and NaOCl, the former acts as a better oxidant with respect to both styrene conversion and styrene epoxide selectivity. The epoxide yields for the complexes **1** and **2** using PhIO and NaOCl as oxidants are 87% and 83%, and 79% and 75%, respectively.

Table 4. Catalytic epoxidation results of complexes **1** and **2***

	1	**1**	**2**	**2**
Oxidant	PhIO	NaOCl	PhIO	NaOCl
Conversion (%)	88	84	83	80
Epoxide yield (%)	87	83	79	75
Selectivity (%)	97	95	89	91

* The time is 2 h for PhIO, and 3 h for NaOCl.

4. Conclusion

A new mononuclear oxidovanadium(V) complex and a new dinuclear oxidovanadium(V) complex derived

from tridentate Schiff bases have been synthesized and characterized. Single crystal X-ray analysis indicates that the V atoms in the mononuclear and dinuclear complexes are in distorted square pyramidal and octahedral coordination, respectively. The complexes have effective catalytic property for the epoxidation of styrene, with conversions over 80% and selectivity over 89%.

Supplementary Material

CCDC 2334633 for **1** and 2334634 for **2** contain the supplementary crystallographic data for this paper. These data can be obtained free of charge *via* http://www.ccdc.cam.ac.uk/conts/retrieving.html, or from the Cambridge Crystallographic Data Centre, 12 Union Road, Cambridge CB2 1EZ, UK; fax: (+44) 1223-336-033; or e-mail: deposit@ccdc.cam.ac.uk.

Acknowledgments

This work was supported by the China-Countries of Central-East Europe Joint Educational Program (2022219) and National College Students Innovation and Entrepreneurship Training Program Project (202311116018).

5. References

1. (a) M. Kumar, A. K. Singh, A. K. Singh, R. K. Yadav, S. Singh, A. P. Singh, A. Chauhan, *Coord. Chem. Rev.* **2023**, *488*, 215176; **DOI:**10.1016/j.ccr.2023.215176
(b) H. R. Sonawane, B. T. Vibhute, B. D. Aghav, J. V. Deore, S. K. Patil, *Eur. J. Med. Chem.* **2023**, *258*, 115549; **DOI:**10.1016/j.ejmech.2023.115549
(c) P. Middya, Y. Chakravarty, S. Maity, S. Chattopadhyay, *J. Coord. Chem.* **2023**, *76*, 1777–1790; **DOI:**10.1080/00958972.2023.2280514
(d) H. Kargar, M. Fallah-Mehrjardi, K. S. Munawar, *Coord. Chem. Rev.* **2023**, *501*, 215587. **DOI:**10.1016/j.ccr.2023.215587
2. (a) P. Middya, D. Chowdhury, S. Chattopadhyay, *Inorg. Chim. Acta* **2023**, *552*, 121489; **DOI:**10.1016/j.ica.2023.121489
(b) S. K. Mandal, P. Seth, *Polyhedron* **2023**, *240*, 116454; **DOI:**10.1016/j.poly.2023.116454
(c) Q. U. Sandhu, M. Pervaiz, A. Majid, U. Younas, Z. Saeed, A. Ashraf, R. R. M. Khan, S. Ullah, F. Ali, S. Jelani, *J. Coord. Chem.* **2023**, *76*, 1094–1118; **DOI:**10.1080/00958972.2023.2226794
(d) R. Kumar, K. Seema, D. K. Singh, P. Jain, N. Manav, B. Gautam, S. N. Kumar, *J. Coord. Chem.* **2023**, *76*, 1065–1093; **DOI:**10.1080/00958972.2023.2231608
(e) M. Zabiszak, J. Frymark, K. Ogawa, M. Skrobanska, M. Nowak, R. Jastrzab, M. T. Kaczmarek, *Coord. Chem. Rev.* **2023**, *493*, 215326. **DOI:**10.1016/j.ccr.2023.215326
3. (a) A. Tyagi, S. Purohit, P. Oswal, S. Rawat, V. Negi, A. K. Singh, A. Kumar, *New J. Chem.* **2023**, *47*, 12511–12535; **DOI:**10.1039/D3NJ01341C
(b) H. Kargar, M. Fallah-Mehrjardi, R. Behjatmanesh-Ardakani, K. S. Munawar, *J. Mol. Struct.* **2021**, *1245*, 131259; **DOI:**10.1016/j.molstruc.2021.131259
(c) Y. Tan, Y. Lei, *Acta Chim. Slov.* **2021**, *68*, 44–50; **DOI:**10.17344/acsi.2020.6044
(c) M. Fallah-Mehrjardi, H. Kargar, K. S. Munawar, *Inorg. Chim. Acta* **2023**, *560*, 121835; **DOI:**10.1016/j.ica.2023.121835
(d) A. A. Sysoeva, A. S. Novikov, V. V. Suslonov, D. S. Bolotin, M. V. Ilin, *Inorg. Chim. Acta* **2024**, *561*, 121867; **DOI:**10.1016/j.ica.2023.121867
(e) Y. Tan, *Acta Chim. Slov.* **2020**, *67*, 1233–1238. **DOI:**10.17344/acsi.2020.6136
4. (a) V. K. Singh, A. Maurya, N. Kesharwani, P. Kachhap, S. Kumari, A. K. Mahato, V. K. Mishra, C. Haldar, *J. Coord. Chem.* **2018**, *71*, 520–541; **DOI:**10.1080/00958972.2018.1434516
(b) G. Romanowski, J. Kira, M. Wera, *Polyhedron* **2014**, *67*, 529–539; **DOI:**10.1016/j.poly.2013.10.008
(c) Y.-J. Cai, Y.-Y. Wu, F. Pan, Q.-A. Peng, Y.-M. Cui, *Acta Chim. Slov.* **2020**, *67*, 896–903; **DOI:**10.17344/acsi.2020.5895
(d) A. Mahdian, M. H. Ardakani, E. Heydari-Bafrooei, S. Saeednia, *Appl. Organomet. Chem.* **2021**, *35*, e6170; **DOI:**10.1002/aoc.6170
(e) P. Mokhtari, G. Mohammadnezhad, *Polyhedron* **2022**, *215*, 115655. **DOI:**10.1016/j.poly.2022.115655
5. (a) K.-H. Yang, *Trans. Met. Chem.* **2014**, *39*, 469–475; **DOI:**10.1007/s11243-014-9821-1
(b) R. N. Patel, Y. P. Singh, Y. Singh, R. J. Butcher, J. P. Jasinski, *Polyhedron* **2017**, *133*, 102–109; **DOI:**10.1016/j.poly.2017.05.028
(c) G.-X. He, L.-W. Xue, Q.-L. Peng, P.-P. Wang, H.-J. Zhang, *Acta Chim. Slov.* **2019**, *66*, 570–575; **DOI:**10.17344/acsi.2018.4868
(d) W. Wang, X. Wang, H. X. Liu, M. Y. Tan, *J. Coord. Chem.* **1995**, *36*, 49–55; **DOI:**10.1080/00958979508022219
(e) M. Tsuchimoto, E. Yasuda, S. Ohba, *Chem. Lett.* **2000**, *5*, 562–563. **DOI:**10.1246/cl.2000.562
6. J. Jiang, Y. Liu, Y. Wang, Z. You, *Acta Chim. Slov.* **2023**, *70*, 139–147. **DOI:**10.17344/acsi.2022.7969
7. G. M. Sheldrick. SAINT (version 6.02), SADABS (version 2.03), Madison (WI, USA): Bruker AXS Inc, **2002**.
8. G. M. Sheldrick. SHELXL-97, A Program for Crystal Structure Solution, Göttingen (Germany): University of Göttingen, **1997**.
9. (a) D.-H. Zou, M. Liang, W. Chen, *Acta Chim. Slov.* **2021**, *68*, 441–446; **DOI:**10.17344/acsi.2020.6553
(b) Q. Yang, P. Wang, Y. Lei, *Acta Chim. Slov.* **2020**, *67*, 957–969; **DOI:**10.17344/acsi.2019.5650
(c) Q.-A. Peng, X.-P. Tan, Y.-D. Wang, S.-H. Wang, Y.-X. Jiang, Y. Cui, *Acta Chim. Slov.* **2020**, *67*, 644–650.
10. W. J. Geary, *Coord. Chem. Rev.* **1971**, *7*, 81–122. **DOI:**10.1016/S0010-8545(00)80009-0
11. A. W. Addison, T. N. Rao, J. Reedijk, J. van Rijn, G. C. Verschoor, *J. Chem. Soc., Dalton Trans.* **1984**, *7*, 1349–1356. **DOI:**10.1039/DT9840001349

12. (a) G. Grivani, V. Tahmasebi, A. D. Khalaji, V. Eigner, M. Dusek, *J. Coord. Chem.* **2014**, *67*, 3664–3677; **DOI:**10.1080/00958972.2014.960405
(b) K.-H. Yang, *Transition Met. Chem.* **2014**, *39*, 469–475; **DOI:**10.1007/s11243-014-9821-1
(c) R. N. Patel, Y. P. Singh, Y. Singh, R. J. Butcher, J. P. Jasinski, *Polyhedron* **2017**, *133*,102–109. **DOI:**10.1016/j.poly.2017.05.028
13. (a) G. X. He, L. W. Xue, G.-Q. Zhao, *Russ. J. Coord. Chem.* **2013**, *39*, 710–715; **DOI:**10.1134/S1070328413100023
(b) X. J. Zhao, Q. Peng, L. W. Xue, *Russ. J. Coord. Chem.* **2014**, *40*, 407–412. **DOI:**10.1134/S1070328414060116
14. N. Mathew, M. Sithambaresan, M. R. Prathapachandra Kurup, *Spectrochim. Acta A* **2011**, *79*, 1154–1161. **DOI:**10.1016/j.saa.2011.04.036
15. (a) M. R. Prathapachandra Kurup, E. B. Seena, M. Kuriakose, *Struct. Chem.* **2010**, *21*, 599–605; **DOI:**10.1007/s11224-010-9589-7
(b) B. Mondal, M. G. B. Drew, T. Ghosh, *Inorg. Chim. Acta* **2009**, *362*, 3303–3308. **DOI:**10.1016/j.ica.2009.02.043
16. S. Mondal, M. Mukherjee, K. Dhara, S. Ghosh, J. Ratha, P. Banerjee, A. K. Mukherjee, *Cryst. Growth Des.* **2007**, *7*, 1716–1721. **DOI:**10.1021/cg060753i

Povzetek

Sintetizirali smo dva nova oksidovanadijeva(V) kompleksa, $[VO_2L^1]$ (**1**) in $[V_2O_2(\mu\text{-}O)_2L^2)]$ (**2**), kjer sta L^1 in L^2 deprotonirani obliki 5-bromo-2-(((2-(pirolidin-1-il)etil)imino)metil)fenola (HL^1) in 5-bromo-2-(((2-((2-hidroksietil)amino) etil)imino)metil)fenola (HL^2), ter ju okarakterizirali s fizikalno-kemijskimi metodami in rentgensko monokristalno analizo. Rentgenska analiza kaže, da je atom vanadija v kompleksu **1** v kvadratno piramidalni koordinaciji, v kompleksu **2** pa v oktaedrični koordinaciji. Kristalni strukturi kompleksov sta stabilizirani z vodikovimi vezmi. Določili smo tudi katalitične lastnosti kompleksov za epoksidacijo stirena.

Scientific paper

A New Multifunctional Phenanthroline-Derived Probe for Colorimetric Sensing of Fe^{2+} and Fluorometric Sensing of Zn^{2+}

Chen-Yu Qi,[†,1] Xue Dong,[†,1] Ying-Cui Fan,[1] Jun-Ru Yuan,[1] Zi-Jie Song,[1] Yong-Han Zhang,[1] Ya-Ping Xie,[1] Feng Yang,[1] Jian-Ping Ma,[2,*] Meng Wang[1,*] and Jie Qin[1,*]

[1] *School of Life Sciences and Medicine, Shandong University of Technology, Zibo 255049, P. R. China*

[2] *College of Chemistry, Chemical Engineering and Materials Science, Key Laboratory of Molecular and Nano Probes, Shandong Normal University, Jinan 250014, P. R. China*

** Corresponding author: E-mail: ddress: xxgk123@163.com; wm902012@163.com; qinjiesdut@163.com Tel.: 0086-533-2786607; Fax: 0086-533-2781329.*

† These authors contributed equally to this work.

Received: 02-22-2024

Abstract

A new phenanthroline derivative bearing imidazole group, (2-(3,5-di(pyridin-4-yl)phenyl)-1-p-tolyl-1*H*-imidazo[4,5-f][1,10]phenanthroline) has been devised. The derivative serves as a multifunctional probe, exhibiting a highly sensitive colorimetric response to Fe^{2+} ion and a selectively ratiometric fluorescent response to Zn^{2+} ion in a buffer-ethanol solution. The colorless-to-red visual color change upon addition of Fe^{2+} accompanied by enhanced absorption makes this derivative a suitable naked-eye sensor for Fe^{2+} ion. Moreover, the derivative displayed a Zn^{2+}-induced red-shift of emission (44 nm), showing a color change from blue to light cyan under a 365-nm UV lamp. Its practical imaging applicability for intracellular Zn^{2+} was confirmed in HeLa cells using a confocal microscope. The improved emission properties and cell imaging capability would provide a new approach to fluorescence sensation for Zn^{2+}.

Keywords: Colorimetric sensor; ratiometric sensor; phenanthroline-imidazole; iron(II) ion; zinc ion

1. Introduction

Metal ions play vital roles in biological and environmental processes. For instance, iron ion (Fe^{2+}/Fe^{3+}), the most abundant transition metal in cellular systems, exists widely in enzymes, proteins, and transcriptional events.[1] Compared to stable Fe^{3+}, the presence of labile Fe^{2+} holds particular significance due to its involvement in oxygen metabolism and intracellular electron transfer processes, which are crucial for various biological functions.[2] Either excess or deficiency of Fe^{2+} can disturb cellular homeostasis and metabolism, leading to severe diseases,[3–5] such as anemia, cardiovascular diseases, and cancer. Zinc ion (Zn^{2+}), the second most abundant metal in the human body, plays a crucial role in modulating brain excitability and is essential for various physiological processes, including immune system function, cell division, wound healing, and synaptic plasticity.[6–8] Moreover, the level abnormality of Zn^{2+} is associated with retarded growth in children, high blood cholesterol, and neurodegenerative disorders such as Alzheimer's and Parkinson's diseases.[6,7] In natural environment, the accumulation of excess Zn^{2+} can reduce the soil microbial activity and result in phytotoxic effects. Therefore, the concentrations of metal ions must be regulated.

At present, a variety of techniques are available for quantitative analysis of metal ions, including atomic absorption/emission spectroscopy, polarography, voltammetry, flow injection, fluorescent probe, etc.[2,3,9–11] Among these detection methods, fluorescent sensors possess several advantages including simplicity, high sensitivity, rapid response to fluorogenic and colorimetric changes and cost-effectiveness. Optical cellular imaging with fluores-

cent probes has been an efficient approach for detecting metal ions in living cells. Therefore, highly selective and sensitive fluorescent sensors that use color and fluorescence intensity or shift are widely used in studies of biological analytes.[12–14] Ratiometric fluorescent probes have garnered increasing attention due to their exceptional properties, including signal read-out independent of instruments and environment, minimal auto-fluorescence, rapid response time, high spatial resolution, and remarkable contrast.[15–18] Additionally, compared to one-to-one chemosensors, using a single chemosensor for detecting multiple targets through differential responses, such as colorimetric or fluorescent spectral changes, offers enhanced efficiency and cost-effectiveness.[19–22] In this context, many of fluorescent probes for Zn^{2+} have been developed.[6–9,23] However, most of them suffer from the interference of Cd^{2+} due to their similar properties as these two metal ions belong to the same group in the periodic table.[6,24,25] Moreover, achieving selective sensing of iron in both oxidation states (Fe^{2+}/Fe^{3+}) using a colorimetric probe that provides distinct signals easily visualized by the naked eye has posed a significant challenge.[10, 26] Therefore, there is an urgent need for the development of a highly selective, facile, simple, and efficient probe capable of detecting Fe^{2+} and Zn^{2+}.

The 1,10-phenanthroline (phen) framework serves as an excellent platform for the construction of chemosensors due to its favorable electro- and photoactive properties.[27–29] Nawaz et al. have previously reported a cellulose-based sensor incorporating phen, enabling selective detection of Fe^{2+} through both visual observation and fluorescent dual modes.[30] Additionally, a polyacrylamide-immobilized phen has been developed as a visual strip sensor to determine Fe^{2+} ion precisely.[31] Moreover, phen derivatives can function as both fluorophores and ionophores for Zn^{2+}, exhibiting discernible changes in fluorescence intensity and specific emission shift upon binding with Zn^{2+} ion.[32–34] Considering these factors, we prepared a hybrid fluorescent sensor derived from the Debus-Radziszewski reaction, namely (2-(3,5-di(pyridin-4-yl)phenyl)-1-p-tolyl-1H-imidazo[4,5-f][1,10]phenanthroline) (**1**) (Scheme 1). The spectroscopic properties and potential application of the compound were systematically investigated. It was observed that compound **1** exhibited a rapid chromogenic response to Fe^{2+} in the EtOH-HEPES buffer, transitioning from a colorless state to red. Additionally, compound **1** demonstrated highly selective and ratiometric fluorescence signals for Zn^{2+} compared to other tested metal ions. The imaging capability of compound **1** for Zn^{2+} was confirmed through microscopic imaging in living cells.

2. Experimental

2. 1. Materials and Apparatus

All chemical reagents were commercially available and of analytical grade. The various metal ions were purchased from Aladdin (Shanghai, China), 1,10-phenanthroline-5,6-dione was purchased from TCI (China). The intermediate 3,5-di(pyridin-4-yl)benzaldehyde was synthesized according to the reported procedure.[35] ^{1}H NMR were measured by a Bruker DRX-400 spectrometer. IR spectra were taken on a Vector22 Bruker spectrophotometer (400–4000 cm^{-1}) with KBr pellets. UV-vis absorption spectra were recorded on Hitachi U-3300 spectrophotometer. Fluorescence emission spectra were determined on Hitachi F-4500. The pH values of sample solutions were monitored by a PHS-3 system. Electrospray mass spectra (ESI-MS) were recorded on a Thermo Fisher LCQ-Fleet mass spectrometer.

2. 2. Synthetic Procedure

1,10-phenanthroline-5,6-dione (2.10 g, 10 mmol), 3,5-di(pyridin-4-yl)benzaldehyde (2.60 g, 10 mmol), *p*-toluidine (1.61 g, 15 mmol), NH_4OAc (3.85 g, 50 mmol) were mixed in a 40 mL glacial acetic acid at room temperature. The mixture was heated at 120 °C for 20 h under stirring. After pouring the mixture into the water (30 mL), the red precipitation was filtered and purified by column chromatography using dichloromethane/methanol (20: 1, v/v) as eluent to afford **1** as gray-white powder with yield of 60%. IR (KBr, cm^{-1}): 3379, 2980, 2923, 1590, 1560, 1551, 1518, 1492, 1452, 1433, 1400, 1379, 1318, 1294, 1223, 1155, 1217, 1087, 1017, 992, 890, 864, 833, 815, 791, 738, 721, 699, 689, 667, 643, 612, 539, 504, 485. ^{1}H NMR (400 MHz, $CDCl_3$) δ: 2.63 (s, 3H), 7.32 (dd, *J* = 4.0, 8.4 Hz, 1H), 7.37 (d, *J* = 6.0 Hz, 4H), 7.51–7.61 (m, 5H), 7.72–7.75 (dd, *J* =

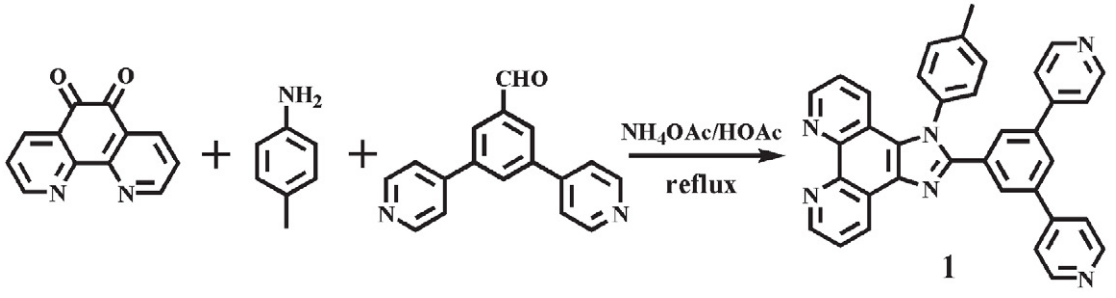

Scheme 1. Synthesis of **1**.

4.4, 8.0 Hz, 1H), 7.81 (s, 1H), 7.92 (d, J = 1.6 Hz, 2H), 8.68 (d, J = 6.0 Hz, 4H), 9.05 (dd, J = 1.6, 4.4 Hz, 1H), 9.13 (dd, J = 1.6, 8.0 Hz, 1H), 9.18 (dd, J = 1.6, 4.4 Hz, 1H). ESI-MS: 541.4200 (M^+). Anal. Calcd for $C_{36}H_{24}N_6$: C, 79.98; H, 4.47, N, 15.55. Found: C, 79.75; H, 4.46, N, 15.61%.

2. 3 Single-Crystal X-Ray Diffraction

Colorless single crystals of **1** were obtained by evaporation of its methanol solution at room temperature. Crystal diffraction data were collected on a Bruker SMART APEX CCD-based diffractometer (Cu-Kα radiation, λ = 1.54184 Å). Multi-scan absorption corrections were applied by SADABS.[36] The structure was solved by direct methods and refined on F^2 by full-matrix least-squares with the Bruker's SHELXS program.[37] All the non-hydrogen atoms were located in the Fourier maps and refined with anisotropic parameters. Hydrogen atoms were placed in their geometrically idealized positions and constrained to ride on their parent atoms. Crystallographic data in CIF format has been deposited in the Cambridge Crystallographic Data Centre (CCDC) under deposition number 2042300. Details of crystallographic data are summarized in Table S1.

2. 4. General Methods for Spectroscopic Analysis

The stock solutions (6 mM) of metal ions ($Mn(NO_3)_2 \cdot 4H_2O$, $Pb(NO_3)_2$, $Co(NO_3)_2 \cdot 6H_2O$, $Zn(NO_3)_2 \cdot 6H_2O$, $Cu(NO_3)_2$ $3H_2O$, $Ni(NO_3)_2 \cdot 6H_2O$, $Cd(NO_3)_2 \cdot 4H_2O$, $HgCl_2$, $FeSO_4 \cdot 7H_2O$, $Fe_2(SO_4)_3$, $CaCl_2 \cdot 2H_2O$, $MgCl_2$, NaCl, and KCl) were prepared in doubly distilled water. **1** was dissolved in spectroscopic pure ethanol to give the stock solution (5 mM). The measurements of both UV-vis absorption and fluorescence spectra were conducted in the solution of HEPES buffer with pH 7.2 containing 50% ethanol (v/v 50 μM) at room temperature. For the metal ions titration, aliquots of 25 μL aqueous metal cation solution were added to the 3 mL diluted **1** solution. The measurements were carried out in 1 min after the addition.

2. 5. Cell Culture and Fluorescence Imaging

HeLa cells were cultured in Dulbecco's Modified Eagle Medium, which was supplemented with 10% fetal bovine serum, penicillin (100 units/mL), streptomycin (100 mg/mL) and 5% CO_2 at 37 °C. After removing the incubation media and rinse with PBS for three times, the cells were treated with **1** (10 μM) for additional 60 min at room temperature. Then the cells were washed three times with PBS before observation. The fluorescence images were captured on Zeiss LSM 710 microscope equipped with a 63×oil-immersion objective. For the imaging of HeLa cells with exogenous Zn^{2+}, the exogenous Zn^{2+} was introduced by incubating the cells with 5μM $ZnSO_4$/ pyrithione solution. After imaging, the cells of exogenous Zn^{2+} were further treated with 50 μM TPEN (N, N, N, N-tetrakis(2-pyridylmethyl)ethylenediamine) solution (prepared by diluting the TPEN stock solution with PBS) to scavenge the intracellular Zn^{2+}. Then the cells were rinsed with PBS and imaged. For all imaging, the samples were excited at 405 nm, and the band pass is 440–520 nm.

3. Results and Discussion

3. 1. Synthesis and Characterization

The probe was constructed by conjugating 3,5-di(pyridin-4-yl)benzene into a fused imidazole/phen system *via* a one-step Debus-Radziszewski reaction. The enlarged conjugated system in **1** and the chelating effect of phenanthroline are expected to report the presence of specific metal cation by triggering the emission change.

The structure of **1** was characterized using FT-IR, ^{1}H NMR, and ESI-MS techniques (Figures. S1-S3). The molecular structure of **1** was also confirmed by single-crystal X-ray diffraction analysis. The crystal structure of **1** with the atom numbering scheme is shown in Figure 1.

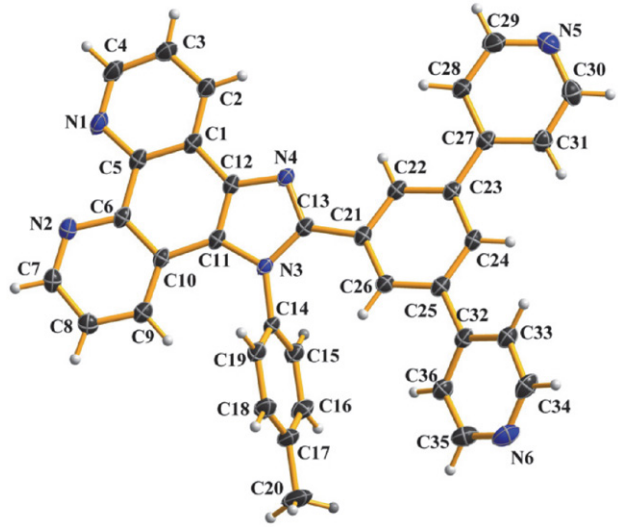

Figure 1. Crystal structure of **1**.

1 was crystallized in the triclinic system with the space group $P\bar{1}$. Each unit cell contains two molecules (Z = 2). **1** features a non-planar structure. The dihedral angle between the para-toluene ring and the imidazole ring is 80.03(1)°; the dihedral angle between the two pyridine rings is 37.52(1)°. The C14–N3 bond length (1.44 Å) is shorter than the standard C–N single bond length (1.47 Å), which may be attributed to the existence of ICT transition between the para-toluene ring and the phen subunit.[38,39]

The intramolecular hydrogen bond is formed *via* C22–H22···N4; meanwhile, the molecules of **1** are connect-

ed by C30–H30···N1^{i} (symmetry code: (i) 1+x, 1+y, z) (Figure S4). As shown in Figure S5, the free methanol molecules are located between these 1D supramolecular chains and serve as hydrogen bonding acceptors and donors, linking these chains into a 2D sheet structure extended in crystallographic *ac* plane. *via* C4–H4···O1^{ii}, C35–H35···O1^{i-ii}, O1–H1···N5^{iv} (symmetry code: (ii) –1+x, y, 1+z; (iii) x, 1+y, z; (iv) x, –1+y, –1+z).

that it was visual by a solution color change from blue to light cyan under a UV lamp only when Zn^{2+} was added into the 1 solution (Figure 2b). The visual detection observation indicated the selectivity towards Fe^{2+} and Zn^{2+} ions, prompting us to conduct further investigations on the metal ion recognition capability using different spectral techniques.

Figure 2. (a) Photograph of **1** test strips wetted by solutions containing 1.0×10^{-2}, 5.0×10^{-3}, 1.0×10^{-3}, 5.0×10^{-4}, 1.0×10^{-4}, 1.0×10^{-5}, 0 M of $FeCl_2$ (from left to right). (b) Photograph of **1** (50 μM) in EtOH-HEPES buffer (1:1, v:v, pH 7.2) solutions containing different metal cations (1 equiv) under visible light (upper row) and UV lamp (lower row).

3. 2. Visual Detection

The selectivity of a fluorescent sensor is a crucial factor for evaluating its performance. The selectivity of a fluorescent sensor is a crucial factor for evaluating its performance. The visual method was employed to investigate the metal ion recognition capability of compound **1**. **1** was treated with 14 kinds of different metal ions (Na^+, K^+, Ca^{2+}, Mg^{2+}, Mn^{2+}, Fe^{2+}, Fe^{3+}, Co^{2+}, Ni^{2+}, Cu^{2+}, Zn^{2+}, Cd^{2+}, Pb^{2+} and Hg^{2+}) to study its sensitivity and selectivity towards particular metal ions. Upon adding an equivalent amount of respective metal ion into compound **1**, only the presence of Fe^{2+} resulted in an instantaneous colorimetric response from colorless to pink under visible light (Figure 2a), which can be easily distinguished by naked-eye. However, no change in color was observed when other cations, including excess amounts of Fe^{3+} ions (5 equiv), were added. Probe **1** was coated on nitrocellulose papers to obtain the test papers. Figure 2a confirms the visual color change phenomena of indicator paper with different concentrations of Fe^{2+}. Consequently, when coating substrate **1**, the resulting materials can be utilized as a qualitative analysis tool for metal ions, serving as a test paper. We also noted

3. 3. Investigations Using UV-VIS Spectrophotometry

The colorimetric sensing performance of sensor **1** was investigated through UV-vis titration with various transition metal cations. A 50 μM solution of the sensor was utilized in the presence of 1 equiv of different metal ions for each experiment. The resulting UV-vis titration spectra are presented in Figure 3. In the HEPES buffer solution, sensor **1** exhibited strong absorption bands below 400 nm, corresponding to the π–π* transitions (245 nm, $\varepsilon = 5.9 \times 10^4$ L mol^{-1} cm^{-1}; 270 nm, $\varepsilon = 6.3 \times 10^4$ L mol^{-1} cm^{-1}; 320 nm, $\varepsilon = 2.1 \times 10^4$ L mol^{-1} cm^{-1}) (Figure 3a). With the addition of Fe^{2+} into **1**, a new band centered at 528 nm appeared in the spectra (Figure 3a) and increased linearly with the $[Fe^{2+}]_{total}$ (Figure 3b). The absorption enhancement reached saturation when the quantity of Fe^{2+} reached 0.5 equiv of sensor **1**, implicating a complexation ratio 2:1 between **1** and Fe^{2+} (Figures. 3b and 3c). Further increments in $[Fe^{2+}]$ did not yield any additional enhancements. Other metal ions did not cause any significant changes at 528 nm under identical conditions (Figure 3a). The distinct color change might be as-

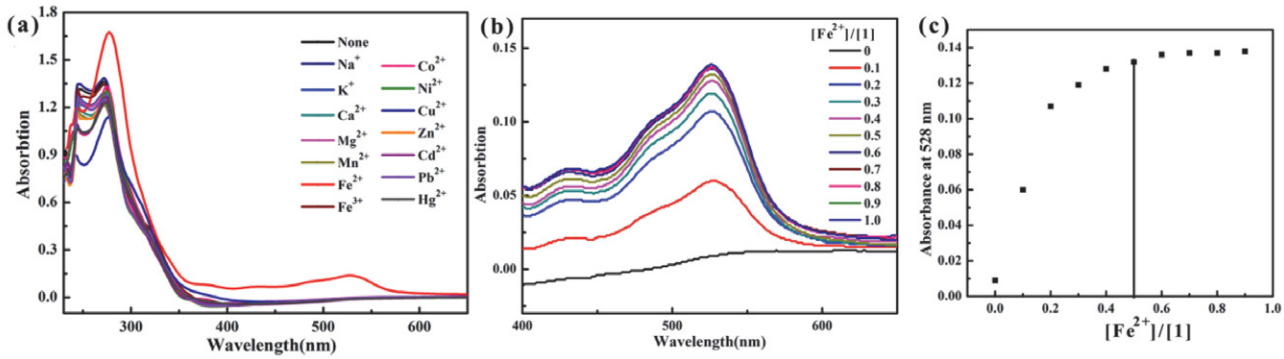

Figure 3. (a) UV-vis titration of **1** (50 μM) with different transition metal cations (1.0 equiv) in EtOH-HEPES buffer (1:1, v:v, pH 7.2) media. (b) UV-vis spectra of **1** (50 μM) upon Fe^{2+} (6 mM) titration in EtOH-HEPES buffer (1:1, v:v, pH 7.2) media. (c) The titration profile of the absorbance at 528 nm.

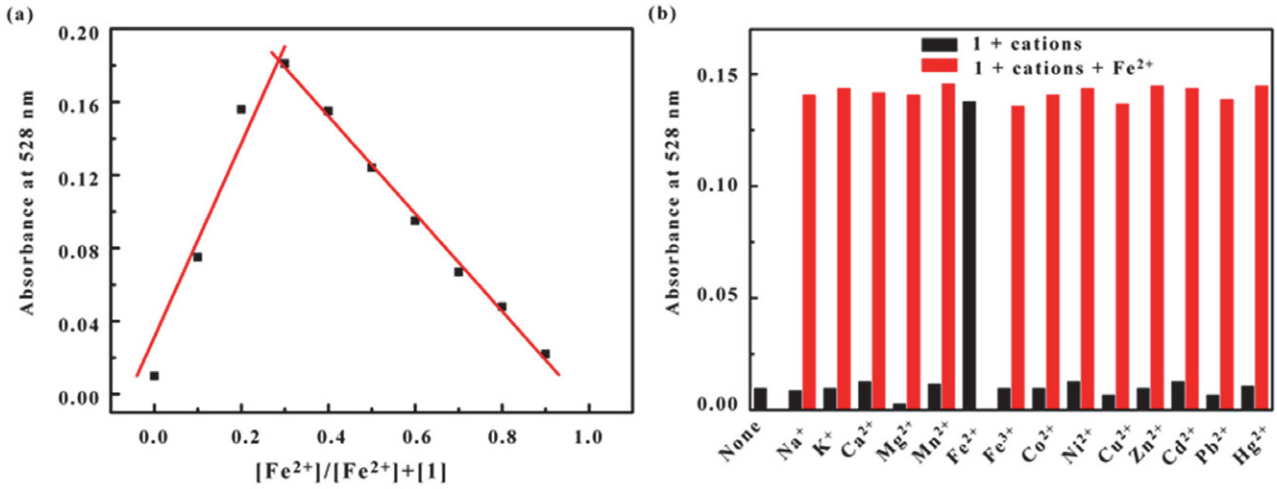

Figure 4. (a) Job's plot for the interaction of **1** with Fe^{2+} ions in EtOH-HEPES buffer (pH = 7.2). The total molar concentration of **1** and Zn^{2+} is 50 μM. (b) Absorbance at 528 nm of **1** (50 μM). Black bars represent the absorbance of free sensor or in the presence of different metal cations. Red bars, the absorbance determined after the addition of 1.0 equiv of competitive metal ions followed by the addition of 1.0 equiv of Fe^{2+}.

cribed to the metal-to-ligand charge-transfer (MLCT) band at 528 nm due to the Fe^{2+} coordination to the phenanthroline moiety.

To better understand the stoichiometry of **1**-Fe^{2+} complex, Job's plot analysis was performed. The total sum of the concentration of 1 and the Fe^{2+} was kept constant, and the Fe^{2+} mole fraction was varied between 0.0 and 0.9. As shown in Figure 4a, the appearance of maximum A_{528} around the 0.3 molar fractions indicates that the stoichiometry of the complex formed between **1** and Fe^{2+} would be 2:1. The proposed coordination mechanism is shown in Scheme S1.

Competitive experiments were also carried out by adding 1.0 equiv of Fe^{2+} to solutions containing 5.0 equiv of other chosen metal ions in EtOH-HEPES buffer (1:1, v:v, pH 7.2). The results shown in Figure 4b indicated that the competitive metal ions had no substantial interference with detecting Fe^{2+}. Therefore, it is clear that **1** can detect Fe^{2+} selectively. The colorimetric limitation of detection (LOD) for Fe^{2+} is determined as 1.0×10^{-6} M (3σ/slope).[24] As stated above, the UV-vis titration spectra characteristics are consistent with the results of visual detection.

3. 4. Fluorescence Spectral Study

To gain insight into the fluorescent sensing capability of **1** towards metal ions, fluorometric titration was conducted in EtOH-HEPES buffer (1:1, v:v, pH 7.2) at room temperature. Free **1** exhibited an emission band centered at 412 nm upon exciting at 350 nm. As shown in Figure 5a, cations such as Na^+, K^+, Ca^{2+} and Mg^{2+} lead to an almost silent fluorescent response, while Fe^{3+}, Cu^{2+}, Mn^{2+} and Co^{2+} triggered emission quenching. Different degrees of fluorescent intensity reduction were observed when Cd^{2+}, Fe^{2+}, Pb^{2+}, Ni^{2+} and Hg^{2+} were added to the system containing sensor **1**. Additionally, the addition of Zn^{2+} resulted in a distinct red-shifted emission from 412 to 456 nm. These observations substantiated the results of the visual detection experiment (Figure 2b) that **1** is highly selective

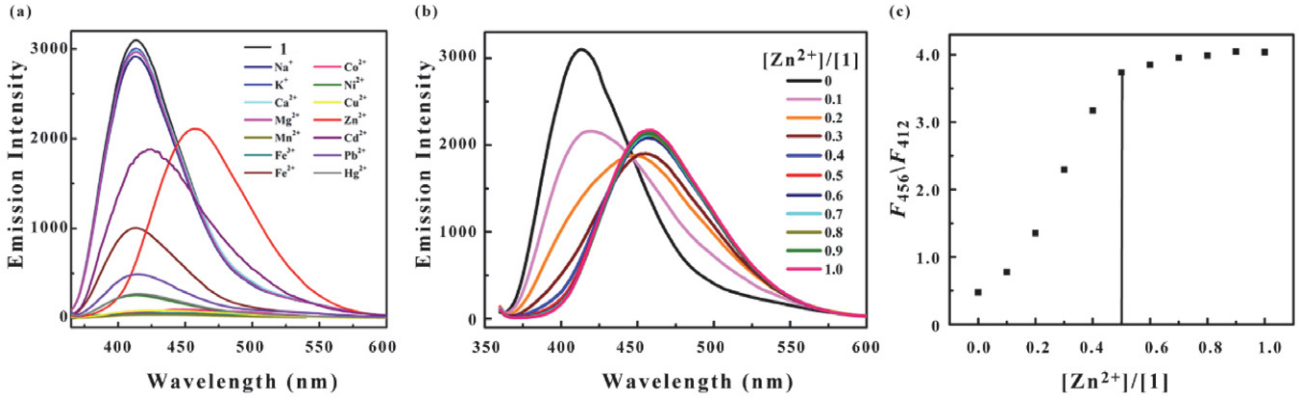

Figure 5. (a) Emission spectra of **1** (50 μM) in presence of various metal ions (1.0 equiv) in EtOH-HEPES buffer (v/v, 1/1, pH 7.2) (b) Emission spectra of **1** (50 μM) obtained upon Zn^{2+} (6 mM) titration. (c) The titration profile based on the emission ratio at 456 and 412 nm, F_{456}/F_{412}.

towards Zn^{2+}. The fluorescence bathochromic shift can be attributed to the intraligand transitions (π–π* transitions).

The dose-dependent fluorescence responses of **1** to Zn^{2+} were also measured. The fluorescence intensity decreased by 30% when 0.1 equiv Zn^{2+} was added into solution **1**. Meanwhile, the maximum peak of the fluorescence red-shifted with an increase of Zn^{2+} dosage. Upon gradually adding of 0.3 equiv Zn^{2+}, the fluorescence emission peak shifted to 456 nm. The fluorescence intensity at 456 nm continued to increase until 0.5 equiv Zn^{2+} was added. The ratio of the emission intensity at 456 and 412 nm (F_{456}/F_{412}) also showed a linear enhancement with the increasing $[Zn^{2+}]_{total}$ until the ratio of $[Zn^{2+}]_{total}/[\mathbf{1}]$ reached 1:2 (Figures. 5b, 5c). After that, the emission spectra of **1** became stable. The remarkable bathochromic shift made **1** a potential ratiometric sensor for Zn^{2+}. In particular, **1** can distinguish Zn^{2+} from the chemically similar Cd^{2+}, whereas the discrimination of Zn^{2+} from Cd^{2+} is well known to be a major obstacle in many cases.[24,25] The atomic radius of Cd^{2+}(0.97 Å) is much larger than that of Zn^{2+}(0.74 Å), and probably does not fit well into the chelate cavity of phenanthroline. The fluorimetric LOD of **1** for Zn^{2+} is 7.1×10^{-7} M.

The stoichiometry between **1** and Zn^{2+} was also determined using Job's continuous variation method. Results demonstrate that the fluorescence intensity F_{456}/F_{412} ratio of the solution reaches the maximum at a mole fraction of approximately 0.34 for Zn^{2+} (Figure 6a), indicating a 2:1 complexation stoichiometry between **1** and Zn^{2+}. The proposed coordination mechanism is also depicted in Scheme S1.

To investigate the applicability of **1** as a Zn^{2+} selective fluorescence sensor, competition experiments were carried out by mixing Zn^{2+} with various common metal ions. The results shown in Figure 6b indicated that no significant alteration in the fluorescence intensity ratio F_{456}/F_{412} was observed in the presence of other selected metal ions. Furthermore, the presence of Na^+, K^+, Ca^{2+}, and Mg^{2+}, abundant in cells, did not interfere with the ratiom-

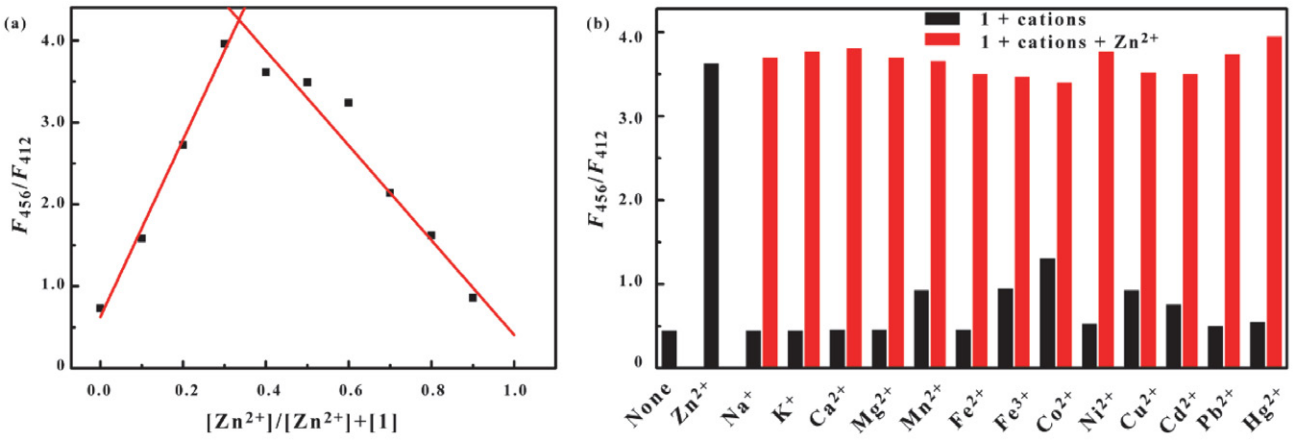

Figure 6. (a) Job's plot of Zn-**1** complex in EtOH-HEPES buffer (1:1, v:v, pH 7.2). The total molar concentration of **1** and Zn^{2+} is 50 μM. (b) Emission ratio at 456 and 412 nm (F_{456}/F_{412}) of **1** (50 μM) in EtOH-HEPES buffer (1:1, v:v, pH 7.2). Black bars represent the F_{456}/F_{412} ratio of the free sensor or in the presence of different metal cations. Red bars represent the F_{456}/F_{412} ratio of **1** determined after the addition of indicated metal ions followed by the addition of 1 equiv of Zn^{2+}. The final concentration is 50 μM for Zn^{2+}, Mn^{2+}, Fe^{2+}, Fe^{3+}, Co^{2+}, Ni^{2+}, Cu^{2+}, Cd^{2+}, Pb^{2+} and Hg^{2+}, for Na^+, K^+, Ca^{2+} and Mg^{2+} is 50 mM.

etric response to Zn^{2+}, even though their concentration was 1000 times higher than [Zn^{2+}]. These results indicated that the recognition of Zn^{2+} by **1** remained unaffected by the coexistence of other metal ions.

The pH value of environment may affect the performance of sensor in the practical application. The pH dependency of **1** toward the detection of Zn^{2+} was investigated (Figure S6). Fluorescent pH titration of **1** and **1**+Zn^{2+} complex showed a relatively stable F_{456}/F_{412} ratio from pH 4.0–8.0, making it suitable for physiological detection applications.

3. 5. Cell Imaging

Zn^{2+} is a crucial metal ion the human body requires in various fundamental biological processes. Therefore, the practical application of **1** in the biological system was further checked with HeLa cells for fluorescence imaging studies. In order to reduce irradiation damage, a 405 nm laser was selected as the excitation source. Because the emission wavelength of **1** (412 nm) is close to 405 nm, only the single green channel (band path 440–520 nm) was employed. The imaging experiment selected TPEN as the fluorescence quenching reagent toward **1**-Zn^{2+}. Before imaging, the cells were incubated with **1** (10 μM) for 60 min. cell. According to the relative fluorescence intensity analyzed by Image Pro-Plus 6.0, the average fluorescence intensity of cells before introducing exogenous Zn^{2+} is 8.25, while that for cells with exogenous Zn^{2+} is 17.15. The result suggests that **1** can bind to intracellular Zn^{2+}, enhancing fluorescence emission. When 50 μM TPEN was introduced into media, a more stable complex was formed between TPEN and Zn^{2+} generating the fluorescence reduction. The average fluorescence intensity of cells recovered to 8.13. Cell imaging experiment results indicate that **1** can be used for fluorescence imaging of Zn^{2+} in living cells.

4. Conclusion

In summary, we successfully synthesized and characterized phenanthroline-modified chemosensor **1**. Our results demonstrate that sensor **1** exhibits remarkable colorimetric sensing ability towards Fe^{2+} ions. Moreover, it is an excellent sensitive and selective ratiometric fluorescence probe for Zn^{2+} in buffer-ethanol solutions. The coordination mode between **1** and Fe^{2+} or Zn^{2+} was confirmed to be 2:1 based on titration profile analysis and Job's plot analysis. Notably, the proposed sensor displays high sensitivity, selectivity for dual-sensing of Fe^{2+} or Zn^{2+}, pH-in-

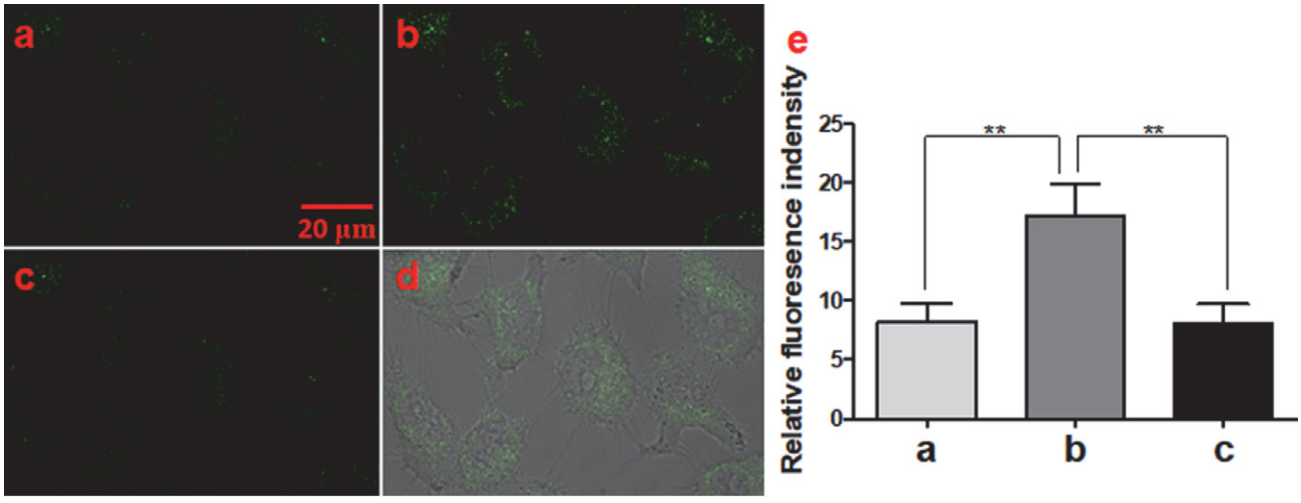

Figure 7. Confocal fluorescence imaging of intracellular Zn^{2+} in HeLa cells stained by **1** solution (10 μM in PBS) at 25 °C for 60 min. (a) HeLa cells preincubated in 10 μM **1** solution at room temperature (25 min). (b) Rinsed HeLa cells (1 × PBS, three times) in (a) were further incubated in 5 μM $ZnSO_4$/ pyrithione (1:1) solution, followed by rinsing with 10 μM **1** solution. (c) HeLa cells in (b) rinsed with 50 μM TPEN solution. (d) overlay between (a) and bright field. (e) Relative fluorescence intensities of (a), (b) and (c) analyzed with Image Pro-Plus 6.0. ** $P < 0.05$, significantly different compared with (b).

The results of fluorescence imaging were presented in Figure 7. After incubation with **1** solution (10 μM in PBS, DMSO/water = 1:99, v/v) at 25 °C for 60 min, the bright fluorescence inside the cells indicated that **1** can be loaded into cells, suggesting the membrane permeability of **1**. When exogenous Zn^{2+} was introduced *via* incubation with 5μM $ZnSO_4$/ pyrithione solution, an image of obvious fluorescence enhancement was observed inside the dependent emission behavior, and cell imaging capability. These findings highlight the potential of our developed sensor in facilitating the advancement of more efficient and practical methods for detecting Fe^{2+} or Zn^{2+} ions. Due to its limited water solubility, the current probe cannot be directly utilized in biological environments. As part of our ongoing research, we are investigating the feasibility of incorporating the probe onto water-soluble nanomaterials.

Supplementary Material

Crystallographic data (excluding structure factors) for the structural analysis have been deposited with the Cambridge Crystallographic Data Center as supplementary publication Nos. CCDC 2042300 (**1**). Copies of the data can be obtained free of charge via www.ccdc.ac.uk/conts/retrieving.html (or from The Director, CCDC, 12 Union Road, Cambridge CB2 1EZ, UK, Fax: +44-1223-336-033. E-mail: deposit@ccdc.cam.ac.uk).

Acknowledgement

We are grateful for financial support from National Natural Science Foundation of China (Nos. 21771120 and 82104112).

5. References

1. P. Li, L. B. Fang, H. Zhou, W. Zhang, X. Wang, N. Li, H. B. Zhong, B. Tang, *Chem.-Eur. J.* **2011**, *17*, 10520–10523. **DOI:**10.1002/chem.201101327
2. A. Parsaei-Khomami, A. Badiei, Z. S. Ghavami, J. B. Ghasemi, *J. Mol. Struct.* **2022**, *1252*, 131978–131988. **DOI:**10.1016/j.molstruc.2021.131978
3. S. Santhoshkumar, K. Velmurugan, J. Prabhu, G. Radhakrishnan, R. Nandhakumar, *Inorg. Chim. Acta* **2016**, *439*, 1–7. **DOI:**10.1016/j.ica.2015.09.030
4. S. Kamali, M. Orojloo, S. Amani, *J. Mol. Struct.* **2021**, *1243*, 130708–130716. **DOI:**10.1016/j.molstruc.2021.130708
5. A. Finelli, V. Chabert, N. Hérault, A. Crochet, C. Kim, K. M. Fromm, *Inorg. Chem.* **2019**, *58*, 13796–13806. **DOI:**10.1021/acs.inorgchem.9b01478
6. H. H. Song, Z. Zhang, *Dyes Pigment.* **2019**, *165*, 172–181. **DOI:**10.1016/j.dyepig.2019.02.011
7. Y. X. Sun, W. M. Ding, J. Li, Y. H. Jia, G. Guo, Z. P. Deng, *J. Mol. Struct.* **2022**, *1252*, 132219–132229. **DOI:**10.1016/j.molstruc.2021.132219
8. J. Y. Koh, S. W. Suh, B. J. Gwag, Y. Y. He, C. Y. Hsu, D. W. Choi, *Science* **1996**, *272*, 1013–1016. **DOI:**10.1126/science.272.5264.1013
9. X. J. He, F. Ding, X. S. Sun, Y. J. Zheng, W. Xu, L. S. Ye, H. Chen, J. L. Shen, *Inorg. Chem.* **2021**, *60*, 5563–5572. **DOI:**10.1021/acs.inorgchem.0c03456
10. X. P. Yang, Y. S. Wang, R. Liu, Y. R. Zhang, J. Tang, E. B. Yang, D. Zhang, Y. F. Zhao, Y. Ye, *Sens. Actuator B-Chem.* **2019**, *288*, 217–224. **DOI:**10.1016/j.snb.2019.02.123
11. N. Dey, *ACS Appl. Bio Mater.* **2021**, *4*, 6893–6902. **DOI:**10.1021/acsabm.1c00600
12. N. Tomer, A. Goel, P. Bhalla, P. Bhagat, R. Malhotra, *J. Photochem. Photobiol. A-Chem.* **2022**, *427*, 113823–113838. **DOI:**10.1016/j.jphotochem.2022.113823
13. A. K. Manna, J. Monda, K. Rout, G. K. Patra, *Sens. Actuator B-Chem.* **2018**, *275*, 350–358. **DOI:**10.1016/j.snb.2018.08.060
14. K. Naik, V. Revankar, *J. Fluoresc.* **2018**, *28*, 1105–1114. **DOI:**10.1007/s10895-018-2273-9
15. Y. Liu, L. Bai, Y. H. Li, Y. Ni, C. Q. Xin, C. W. Zhang, J. H. Liu, Z. P. Liu, L. Li, W. Huang, *Sens. Actuator B-Chem.* **2019**, *279*, 38–43. **DOI:**10.1016/j.snb.2018.09.107
16. G. R. C. Hamilton, S. Kaur, S. Kamila, B. Callan, J. F. Callan, *New J. Chem.* **2018**, *42*, 14986–14993. **DOI:**10.1039/C7NJ04520D
17. A. Mukherjee, P. C. Saha, R. S. Das, T. Bera, S. Guha, *ACS Sens.* **2021**, *6*, 2141–2146. **DOI:**10.1021/acssensors.1c00961
18. R. Azadbakht, M. Koolivand, J. Khanabadi, *Anal. Methods* **2017**, *9*, 4688–4694. **DOI:**10.1039/C7AY01568B
19. S. M. Hwang, M. S. Kim, M. Lee, M. H. Lim, C. Kim, *New J. Chem.* **2017**, *41*, 15590–15600. **DOI:**10.1039/C7NJ03575F
20. A. Mohammadi, J. Jabbari, *Can. J. Chem.* **2016**, *94*, 631–636. **DOI:**10.1139/cjc-2016-0039
21. Y. S. Xie, J. Zhang, L. Yang, Q. X. Chen, Q. Hao, L. Zhang, H. Y. Sun, *Front. Chem. Sci. Eng.* **2022**, *16*, 121–127. **DOI:**10.1007/s11705-021-2051-0
22. D. Singh, D. Rajput, S. Kanvah, *Chem. Commun.* **2022**, *58*, 2413–2429. **DOI:**10.1039/D1CC06944F
23. M. V. Karmegam, S. Karuppannan, D. B. C. Leslee, S. Subramanian, S. Gandhi, *Luminescence* **2020**, *35*, 90–97. **DOI:**10.1002/bio.3701
24. H. He, Z. Cheng, L. Zheng, *J. Mol. Struct.* **2021**, *1227*, 129522–129529. **DOI:**10.1016/j.molstruc.2020.129522
25. S. Mandal, Y. Sikdar, D. K. Malti, R. Sanyal, D. Das, A. Mukherjee, S. K. Mandal, J. K. Biswas, A. Bauzá, A. Frontera, S. Goswami, *J. Photochem. Photobiol. A-Chem.* **2017**, *334*, 86–100. **DOI:**10.1016/j.jphotochem.2016.10.038
26. S. M. Feng, J. R. Zheng, J. Z. Zhang, Z. S. Gui, G. Q. Feng, *Sens. Actuator B-Chem.* **2022**, *371*, 132512–132520. **DOI:**10.1016/j.snb.2022.132512
27. X. Y. Ma, S. Y. Chen, H. Yu, Y. W. Guan, J. J. Li, X. W. Yan, Z. H. Zhang, *Nanoscale Res. Lett.* **2019**, *14*, 318–327. **DOI:**10.1186/s11671-019-3149-x
28. K. Nehra, A. Dalal, A. Hooda, R. K. Saini, D. Singh, S. Kumar, *Polyhedron* **2022**, *217*, 115730–115736. **DOI:**10.1016/j.poly.2022.115730
29. P. Alreja, N. Kaur, *RSC Adv.* **2016**, *6*, 23169–23217. **DOI:**10.1039/C6RA00150E
30. H. Nawaz, W. G. Tian, J. M. Zhang, R. N. Jia, Z. Y. Chen, J. Zhang, *ACS Appl. Mater. Interfaces* **2018**, *10*, 2114–2121. **DOI:**10.1021/acsami.7b17342
31. S. A. Kumar, N. Thakur, H. J. Parab, S. P. Pandey, R. N. Shinde, A. K. Pandey, S. D. Kumar, A. V. R. Reddy, *Anal. Chim. Acta* **2014**, *851*, 87–94. **DOI:**10.1016/j.aca.2014.08.047
32. R. Satheeshkumar, R. Rajamanikandan, M. Ilanchelian, K. Sayin, K. J. R. Prasad, *Spectroc. Acta Pt. A-Molec. Biomolec. Spectr.* **2019**, *221*, 21117196–21117206. **DOI:**10.1016/j.saa.2019.117196
33. B. Zhang, K. S. Cao, Z. A. Xu, Z. Q. Yang, H. W. Chen, W. Huang, G. Yin, X. Z. You, *Eur. J. Inorg. Chem.* **2012**, 3844–3851. **DOI:**10.1002/ejic.201200423
34. S. Karakaya, F. Algi, *Tetrahedron Lett.* **2014**, *55*, 5555–5559. **DOI:**10.1016/j.tetlet.2014.08.059
35. Y. Yu, X. M. Zhang, J. P. Ma, Q. K. Liu, P. Wang, Y. B. Dong,

Chem. Commun. **2014**, *50*, 1444–1446.
DOI:10.1039/C3CC47723A
36. S. G. M. , SADABS, *University of Gottingen* **1996**, *Germany*.
37. G. M. Sheldrick, *Acta Crystallogr. Sect. A* **2008**, *64*, 112–122.
DOI:10.1107/S0108767307043930
38. C. Parthiban, K. P. Elango, *Spectroc. Acta Pt. A-Molec. Biomolec. Spectr.* **2017**, *174*, 147–153.
DOI:10.1016/j.saa.2016.11.022
39. K. Karaoglu, K. Kaya, I. Yilmaz, *Dyes Pigment.* **2020**, *180*, 108445–108454. **DOI:**10.1016/j.dyepig.2020.108445

Povzetek

Sintetizirali smo nov derivat fenantrolina z imidazolno skupino, (2-(3,5-di(piridin-4-il)fenil)-1-p-tolil-1*H*-imidazo[4,5-f][1,10]fenantrolin). Spojina deluje kot multifunkcionalni senzor z visoko občutljivo kolorimetrično reakcijo na Fe^{2+} ione in selektivno fluorescenčno reakcijo na Zn^{2+} v raztopini pufer-etanol. Intenzivna barvna sprememba iz brezbarvne v rdečo ob dodatku Fe^{2+} omogoča zaznavanje že s prostim očesom. Ob dodatku Zn^{2+} opazimo premik emisije (44 nm) proti večjim valovnim dolžinam, kar pod obsevanjem z UV svetlobo valovne dolžine 365 nm povzroči spremembo barve iz modre v modrozeleno. Praktično uporabo za vizualizacijo intracelularnega Zn^{2+} smo preizkusili na HeLa celicah s konfokalnim mikroskopom. Izboljšane emisijske lastnosti in sposobnost opazovanja celic omogočajo nov pristop k fluorescenčnemu zaznavanju Zn^{2+}.

DOI: 10.17344/acsi.2024.8707 *Acta Chim. Slov.* **2024,** *71,* 304–311

Scientific paper

Syntheses, Crystal Structures and Antimicrobial Activity of Copper(II) Complexes with the Ligand *N,N'*-Bis(4-bromosalicylidene)propane-1,2-diamine

Yu-Mei Hao[1,*] and Chang-Chun Sun[2]

[1] *Department of Chemistry, Baicheng Normal University, Baicheng 137000, P.R. China*

[2] *Baicheng Institute of Education, Baicheng 137000, P.R. China*

* *Corresponding author: E-mail: jyxygzb@163.com*

Received: 02-18-2024

Abstract

Three new copper(II) complexes, [CuClL] (**1**), $[CuBrL]_n$ (**2**) and $[CuL(NCS)]_n$ (**3**), derived from the Schiff base 2,4-dichloro-6-((2-pyrrolidin-1-ylethylimino)methyl)phenol (HL) have been prepared and characterized by spectroscopic methods, as well as single crystal X-ray determination. The Cu atom in complex **1** is in square planar coordination, and those in complexes **2** and **3** are in square pyramidal coordination. The Schiff base ligand coordinates to the Cu atoms through phenolate oxygen, imino nitrogen and pyrrolidine nitrogen. The antibacterial activities of the Schiff base and the three copper complexes have been assayed on the bacteria *Staphylococcus aureus* and *Escherichia coli* and the yeast *Candida parapsilosis*.

Keywords: Schiff base; Copper complex; Crystal structure; Antibacterial activity

1. Introduction

Schiff base compounds have been widely used as preferred ligands in the construction of metal complexes with versatile structures due to their easy preparation and good metal-binding ability.[1] The compounds with N, O and S atoms have structure similarities with some natural biological enzymes. Schiff bases and their metal complexes have a broad range of applications in pharmaceutical and biological fields.[2] They have shown remarkable antifungal, antibacterial, anti-proliferative, antimalarial, antiviral, antipyretic, and anti-inflammatory activities.[3] Copper complexes with Schiff base ligands have been extensively studied and are considered as excellent alternatives for classic organic antibacterial agents.[4] Despite the presence of considerable research on the antibacterial activities of Schiff base complexes, it is still necessary to search for new samples to find more effective agents as well as to better understand the biological mechanisms of this type of compounds. With an interest in the chemistry of biologically active compounds, this study aimed to synthesize new Schiff base copper(II) complexes. The newly synthesized complexes, [CuClL] (**1**), $[CuBrL]_n$ (**2**) and $[CuL(NCS)]_n$ (**3**), where L is the deprotonated form of 2,4-dichloro-6-((2-pyrrolidin-1-ylethylimino)methyl)phenol (HL; Scheme 1), are presented and examined for their antimicrobial activities.

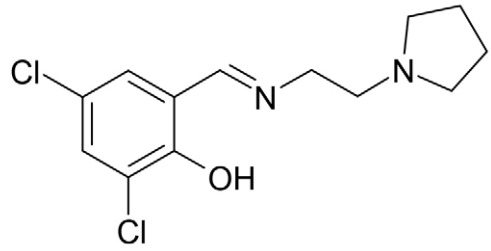

Scheme 1. The Schiff base HL

2. Experimental

2. 1. Materials and Methods

3,5-Dichlorosalicylaldehyde and *N*-(2-aminoethyl) pyrrolidine were purchased from TCI Chemical Reagent Co. Ltd. $CuCl_2{\cdot}2H_2O$, $CuBr_2$, $Cu(CH_3COO)_2$ and NH_4NCS were purchased from Aladdin Chemical Reagent Co. Ltd. The solvent methanol was purchased from Kemiou Chemical Reagent Co. Ltd. The Schiff base HL was prepared by

reaction of 1:1 molar ratio of 3,5-dichlorosalicylaldehyde with *N*-(2-aminoethyl)pyrrolidine in methanol, which was used to prepare the copper complexes without isolation. IR spectra were recorded on a Jasco FT/IR-4000 spectrometer as KBr pellets in the 4000–400 cm^{-1} region. Elemental analyses were performed on a Perkin-Elmer 240C elemental analyzer. UV-Vis spectra were recorded on a Lambda 900 spectrometer. Single crystal X-ray diffraction was carried out on a Bruker SMART 1000 CCD diffractometer.

2. 2. Synthesis of [CuClL] (1)

HL (29 mg, 0.10 mmol) and $CuCl_2{\cdot}2H_2O$ (17 mg, 0.10 mmol) were mixed in methanol (30 mL). The mixture was stirred at room temperature for 30 min to give a brown solution. Single crystals of the complex, suitable for X-ray diffraction, were obtained after a week. Yield: 27 mg (71%). IR data (cm^{-1}): 1638, 1550, 1462, 1396, 1312, 1263, 1187, 1122, 1054, 1038, 985, 963, 870, 823, 751, 580, 530, 513, 455. UV-Vis (MeOH; ε, L mol^{-1} cm^{-1}): 220 (20,330), 240 (18,720), 270 (13,730), 305 (9,890), 380 (3,210). Anal. Calcd. (%) for $C_{13}H_{15}Cl_3CuN_2O$: C, 40.54; H, 3.93; N, 7.27. Found (%): C, 40.38; H, 4.01; N, 7.36. Λ_M (1×10^{-3} mol L^{-1} in methanol): 31 Ω^{-1} cm^2 mol^{-1}.

2. 3. Synthesis of $[CuBrL]_n$ (2)

HL (29 mg, 0.10 mmol) and $CuBr_2$ (23 mg, 0.10 mmol) were mixed in methanol (30 mL). The mixture was stirred at room temperature for 30 min to give a brown solution. Single crystals of the complex, suitable for X-ray diffraction, were obtained after a week. Yield: 33 mg (77%). IR data (cm^{-1}): 1638, 1550, 1461, 1420, 1360, 1313, 1305, 1260, 1187, 1130, 1072, 1045, 980, 867, 831, 750, 715, 580, 535, 517, 496, 445. UV-Vis (MeOH; ε, L mol^{-1} cm^{-1}): 220 (21,150), 240 (17,035), 272 (14,020), 312 (10,720), 385 (4,055). Λ_M (1×10^{-3} mol L^{-1} in methanol): 28 Ω^{-1} cm^2 mol^{-1}.

2. 4. Synthesis of $[CuL(NCS)]_n$ (3)

HL (29 mg, 0.10 mmol), $Cu(CH_3COO)_2{\cdot}H_2O$ (20 mg, 0.10 mmol) and ammonium thiocyanate (7.6 mg, 0.10 mmol) were mixed in methanol (30 mL). The mixture was stirred at room temperature for 30 min to give a brown solution. Single crystals of the complex, suitable for X-ray diffraction, were obtained after a week. Yield: 26 mg (63%). IR data (cm^{-1}): 2120, 1639, 1589, 1510, 1453, 1416, 1321, 1208, 1162, 1079, 1023, 966, 887, 860, 756, 686, 569, 511, 475. UV-Vis (MeOH; ε, L mol^{-1} cm^{-1}): 236 (19,370), 270 (8,935), 297 (5,053), 380 (4,650). Λ_M (1×10^{-3} mol L^{-1} in in methanol): 36 Ω^{-1} cm^2 mol^{-1}.

2. 5. X-ray Crystallography

Single crystal X-ray data for the complexes were collected on a Bruker SMART 1000 CCD diffractometer using the SMART/SAINT software.[5] Intensity data were collected using graphite-monochromatized MoK_α radiation

Table 1. Crystallographic data and refinement parameters for the complexes

	1	**2**	**3**
Chemical Formula	$C_{13}H_{15}Cl_3CuN_2O$	$C_{13}H_{15}BrCl_2CuN_2O$	$C_{14}H_{15}Cl_2CuN_3OS$
Fw	385.16	429.62	407.79
T (K)	298(2)	298(2)	298(2)
Crystal system	Orthorhombic	Orthorhombic	Orthorhombic
Space group	$Pca2_1$	$Pca2_1$	$Pbca$
a (Å)	8.614(2)	8.8300(13)	11.7060(15)
b (Å)	11.068(2)	11.1081(17)	12.3149(15)
c (Å)	15.461(3)	15.322(2)	24.367(2)
α (°)	90	90	90
β (°)	90	90	90
γ (°)	90	90	90
V (Å^3)	1474.0(5)	1502.9(4)	3512.8(7)
Z	4	4	8
μ (Mo Kα) (cm^{-1})	2.020	4.463	1.669
D_c (g cm^{-3})	1.736	1.899	1.542
Reflections collected	16379	19017	40889
Unique reflections	3489	3760	4333
Observed reflections [$I \geq 2\geq(I)$]	3228	3491	2634
Parameters	181	182	199
Restraints	1	1	0
R_{int}	0.0378	0.0273	0.0732
R_1, wR_2 [$I \geq 2\sigma(I)$]	0.0259, 0.0636	0.0206, 0.0534	0.0387, 0.0912
R_1, wR_2 (all data)	0.0300, 0.0659	0.0241, 0.0565	0.0839, 0.1092

(0.71073 Å) at 298(2) K. The structures were solved by direct methods using SHELX.[6] Multi-scan absorption corrections were applied with SADABS.[7] All non-hydrogen atoms were refined with anisotropic displacement coefficients. The hydrogen atoms bonded to carbon were included in geometric positions and given thermal parameters equivalent to 1.2 and 1.5 times those of the atom to which they were attached. Complex **2** has been refined as a twin model. Crystallographic data and refinement parameters are given in Table 1, and important interatomic distances and angles are given in Table 2.

Table 2. Selected bond distances (Å) and angles (°) for the complexes

1			
Cu1–Cl1	2.250(1)	Cu1–O1	1.943(3)
Cu1–N1	1.958(3)	Cu1–N2	2.078(3)
O1–Cu1–Cl1	92.62(7)	O1–Cu1–N1	91.41(11)
O1–Cu1–N2	174.47(9)	N1–Cu1–Cl1	162.19(9)
N1–Cu1–N2	84.29(11)	N2–Cu1–Cl1	92.62(7)
2			
Cu1–Br1	2.3915(6)	Cu1–O1	1.934(2)
Cu1–N1	1.955(3)	Cu1–N2	2.085(3)
Cu1–Br1A	3.051(3)		
O1–Cu1–N1	91.17(11)	O1–Cu1–N2	175.10(11)
N1–Cu1–N2	84.28(11)	O1–Cu1–Br1	92.19(7)
N1–Cu1–Br1	162.73(9)	N2–Cu1–Br1	92.69(8)
N1–Cu1–Br1A	88.85(10)	N2–Cu1–Br1A	85.65(10)
O1–Cu1–Br1A	92.50(10)	Br1–Cu1–Br1A	107.80(10)
Symmetry code for A: ½ + *x*, 1 – *y*, *z*.			
3			
Cu1–O1	1.9188(19)	Cu1–N1	1.937(2)
Cu1–N2	2.063(2)	Cu1–N3	1.952(3)
Cu1–S1A	2.927(3)		
O1–Cu1–N1	92.84(9)	O1–Cu1–N3	89.21(10)
N1–Cu1–N3	165.57(11)	O1–Cu1–N2	177.08(9)
N1–Cu1–N2	84.27(9)	N3–Cu1–N2	93.69(10)
N1–Cu1–S1A	93.41(10)	N2–Cu1–S1A	94.33(10)
N3–Cu1–S1A	100.99(10)	O1–Cu1–S1A	85.43(10)

Symmetry code for A: ½ + *x*, *y*, ½ – *z*.

2. 6. Biological Assay

The antibacterial property of the compounds was evaluated by a macro-dilution method using *Staphylococcus aureus*, *Escherichia coli*, and the yeast *Candida parapsilosis*. The cultures of bacteria and yeasts were incubated under vigorous shaking. The compounds were dissolved in small amount of DMSO. Concentration of the tested compounds ranging from 0.010 to 2.5 mmol L^{-1} for the bacteria and yeasts was used in all experiments. The antibacterial activity was characterized by IC_{50} and MIC values. MIC experiments on subculture dishes were used to assess the minimal microbicidal concentration (MMC). Subcultures were prepared separately in Petri dishes containing competent agar medium and incubated at 30 °C for 48 h. The MMC value was taken as the lowest concentration, which showed no visible growth of microbial colonies in the subculture dishes.

3. Results and Discussion

3. 1. Chemistry

The Schiff base HL was prepared by reaction of 1:1 molar ratio of 3,5-dichlorosalicylaldehyde and *N*-(2-aminoethyl)pyrrolidine in methanol (Scheme 2). The three copper complexes were facile synthesized by reaction of equimolar quantities of the Schiff base HL with copper chloride, copper bromide and copper acetate, respectively in the presence of ammonium thiocyanate in methanol (Scheme 3). Complexes **1** and **2** have no thiocyanate ligands, while complex **3** has one. In fact, complexes **1** and **2** can also be obtained by reaction of HL with copper chloride and copper bromide, respectively. Single crystals of the complexes were formed by slow evaporation of their methanol solution at room temperature.

3.2. Crystal Structure Description of the Complex 1

Molecular structure of complex **1** is shown in Fig. 1. The complex is a mononuclear copper(II) species. The Cu atom in the complex is coordinated by one phenolate oxygen, one imino nitrogen and one pyrrolidine nitrogen of the Schiff base ligand, and one Cl ligand, forming a square planar geometry. The *trans* and *cis* bond angles are 162.19(9)–174.47(9)° and 84.29(11)–92.62(7)°, respectively. Thus, the square planar coordination is slightly distorted, which is mainly caused by the five-membered chelate ring Cu1–N1–C8–C9–N2. The Cu–O and Cu–N bonds in

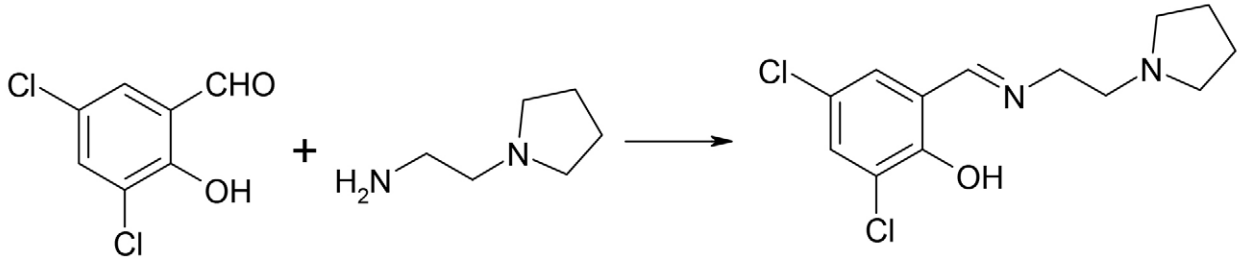

Scheme 2. The synthetic procedure of the Schiff base HL

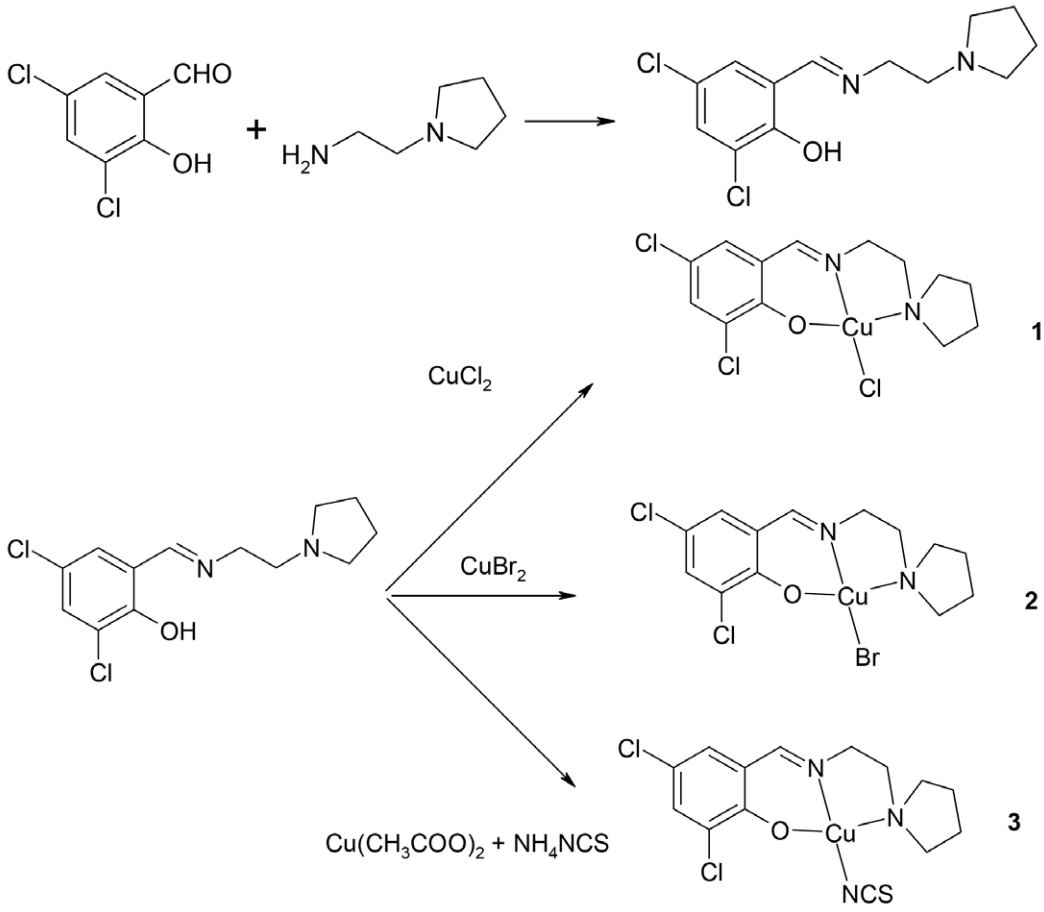

Scheme 3. The synthetic procedure of the complexes

the complex are comparable to those observed in Schiff base copper(II) complexes.[8] In the crystal structure, the molecules are linked through intermolecular hydrogen bonds of C–H···Cl (Table 3), to form two-dimensional sheets parallel to the *ab* plane (Fig. 2).

3. 3. Crystal Structure Description of the Complex 2

Molecular structure of complex **2** is shown in Fig. 3. The complex is a bromide bridged polymeric copper(II)

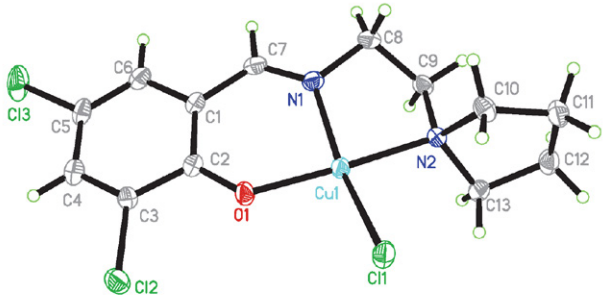

Fig. 1. A perspective view of the molecular structure of complex **1** with the atom labeling scheme. Thermal ellipsoids are drawn at the 30% probability level.

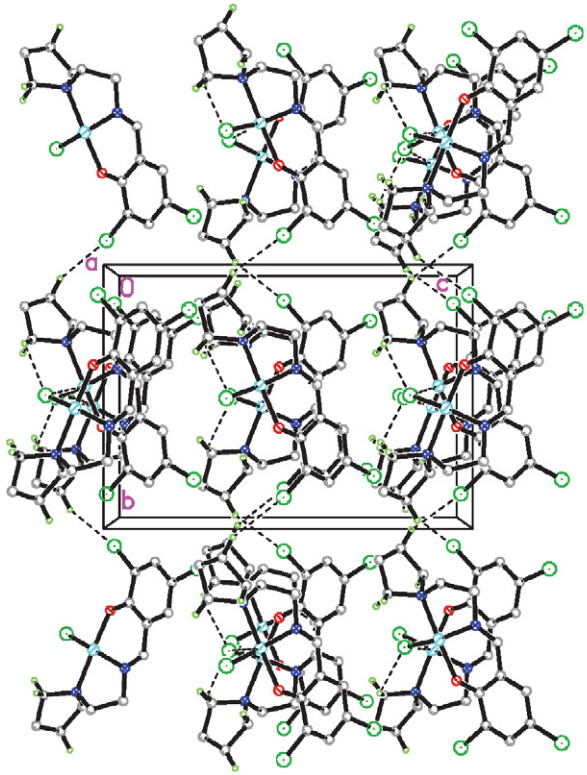

Fig. 2. Molecular packing diagram of complex **1**, viewed along the *a* axis. Hydrogen bonds are shown as dashed lines.

species. The Cu atom in the complex is in a square pyramidal coordination, with the basal plane defined by one phenolate oxygen, one imino nitrogen and one pyrrolidine nitrogen of the Schiff base ligand, and one Br ligand, and with the apical position occupied by one symmetry related Br ligand at the symmetry position ½ + *x*, 1 – *y*, *z*. The *trans* and *cis* bond angles in the basal plane are 162.73(9)–175.10(11)° and 84.28(11)–92.69(8)°, respectively. The bond angles among the apical and basal donor atoms are 107.80(10)°. Thus, the square pyramidal coordination is slightly distorted, which is mainly caused by the five-membered chelate ring Cu1–N1–C8–C9–N2. The Cu–O and Cu–N bonds in the complex are comparable to those observed in Schiff base copper(II) complexes.[9] In the crystal structure, the molecules are liked by Br ligand and intermolecular hydrogen bonds of C-H···Br (Table 3), to form one-dimensional chains running along the *a* axis (Fig. 4).

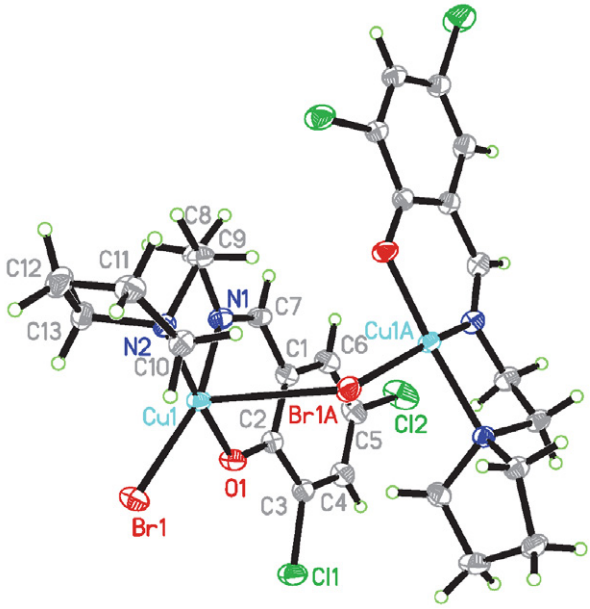

Fig. 3. A perspective view of the polymeric structure of complex **2** with the atom labeling scheme. Thermal ellipsoids are drawn at the 30% probability level. Repeated molecule is related to the symmetry operation ½ + *x*, 1 – *y*, *z*.

3. 4. Crystal Structure Description of the Complex 3

Molecular structure of complex **3** is shown in Fig. 5. The complex is a thiocyanate bridged polymeric copper(II) species. The Cu atom in the complex is in a square pyramidal coordination, with the basal plane defined by one phenolate oxygen, one imino nitrogen and one pyrrolidine nitrogen of the Schiff base ligand, and one N atom of a thiocyanate ligand, and with the apical position occupied by one S atom of a symmetry related thiocyanate ligand. The *trans* and *cis* bond angles in the basal plane are 165.57(11)–177.08(9)° and 84.27(9)–93.69(10)°, respectively. The bond angles among the apical and basal donor atoms are 85.43(10)–100.99(10)°. Thus, the square pyramidal coordination is slightly distorted, which is mainly caused by the five-membered chelate ring Cu1–N1–C8–C9–N2. The Cu–O and Cu–N bonds in the complex are

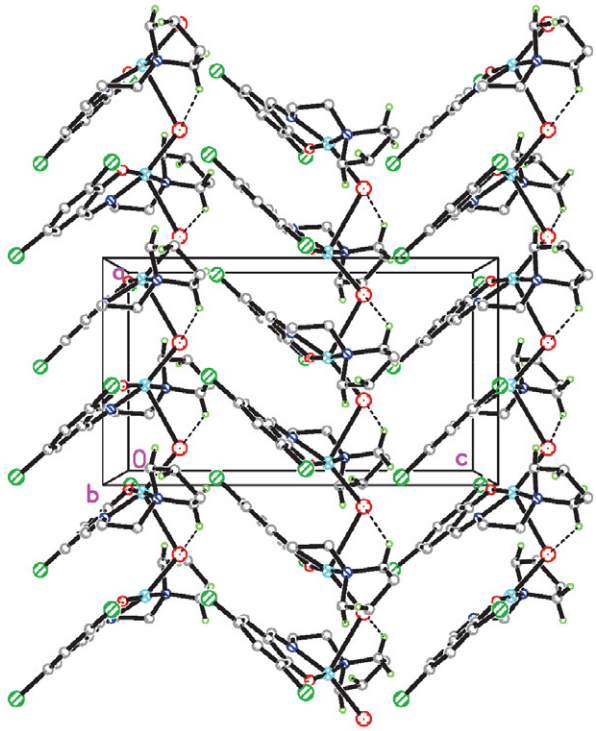

Fig. 4. Molecular packing diagram of complex **2**, viewed along the *b* axis. Hydrogen bonds are shown as dashed lines.

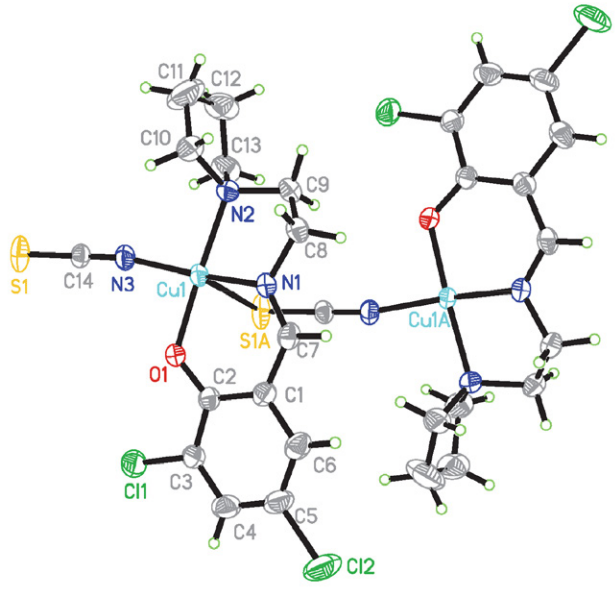

Fig. 5. A perspective view of the polymeric structure of complex **3** with the atom labeling scheme. Thermal ellipsoids are drawn at the 30% probability level. Repeated molecule is related to the symmetry operation ½ + *x*, *y*, ½ – *z*.

comparable to those observed in Schiff base copper(II) complexes.[10] In the crystal structure, the molecules are linked by thiocyanate ligand, to form one-dimensional chains running along the *a* axis. The chains are further linked through intermolecular hydrogen bonds of C-H···S (Table 3) at the *b* axis, to form two-dimensional sheets parallel to the *ab* plane (Fig. 6).

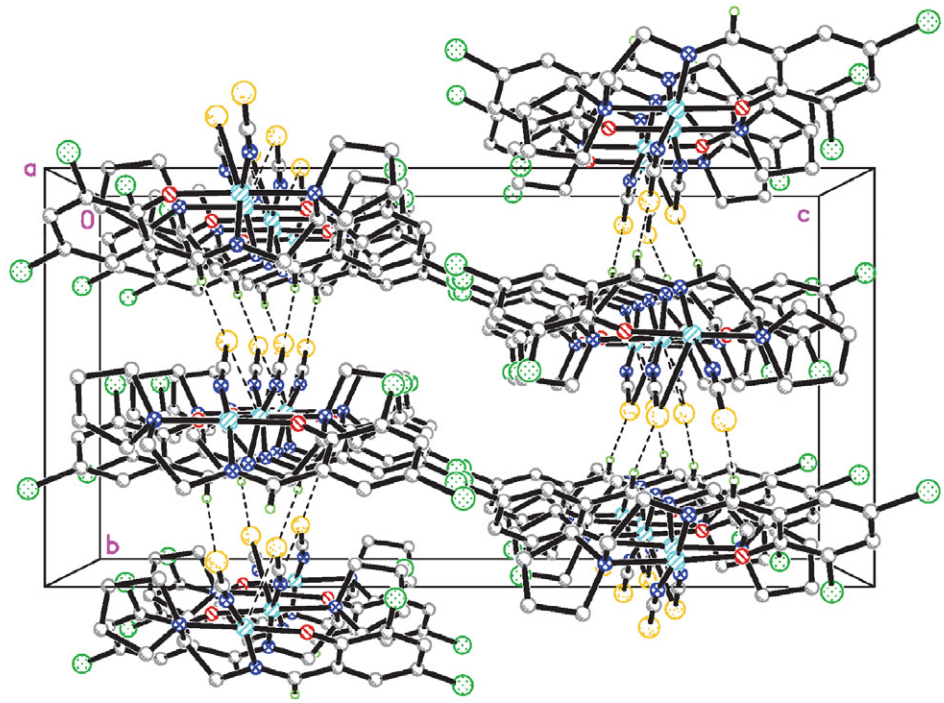

Fig. 6. Molecular packing diagram of complex **3**, viewed along the *a* axis. Hydrogen bonds are shown as dashed lines.

Table 3. Geometrical parameters for hydrogen bonds for the complexes

D–H···A	Distance, Å D–H	H···A	D···A	Angle D–H···A, °
1				
C11–H11B···Cl2^{i}	0.97	2.80(3)	3.715(4)	157(5)
C13–H13A···Cl1^{ii}	0.97	2.79(3)	3.420(4)	123(5)
2				
C10–H10A···Br1^{iii}	0.97	2.88(2)	3.500(4)	122(4)
C12–H12B···Cl1^{iv}	0.97	2.80(2)	3.709(4)	156(4)
3				
C7–H7···S1^{iii}	0.93	2.86(3)	3.785(5)	171(5)

Symmetry transformation used to generate the symmetry related atoms: ^{i} –½ + *x*, 1 – *y*, *z*; ^{ii} *x*, 1 + *y*, *z*; ^{iii} –½ + *x*, 1 – *y*, *z*; ^{iv} *x*, –1 + *y*, *z*; ^{v} ½ – *x*, ½ + *y*, *z*.

3. 5. IR and UV-Vis Spectra

The strong absorption bands at 1638–1639 cm^{-1} for the complexes are assigned to the azomethine groups, *ν*(C=N).[11] The intense band at 2120 cm^{-1} for complex **3** can be assigned to the stretching vibration of thiocyanate ligand.[12] The weak bands in the low wave numbers 440–550 cm^{-1} are due to the vibration of the Cu–O and Cu–N bonds.[13]

In the UV-Vis spectra of the complexes, the intense bands observed at 220–280 nm are assigned to intra-ligand π–π^* transitions. The complexes displayed bands centered at 290–315 nm, which can be assigned to the n–π^* transition.[14] The charge transfer LMCT bands are located at 380–385 nm.[15]

3. 6. Antibacterial Activity

The antimicrobial results are summarized in Table 4. The free Schiff base HL showed medium activity against *E. coli*, while no activity on *S. aureus* and *C. parapsilosis*. Interestingly, the three copper complexes have higher activities than HL. This is caused by the greater lipophilic nature of the complexes than the free ligands. The increased biological activity of the complexes can be explained with the chelating theory.[16] The chloride coordinated mononuclear copper complex **1** and bromide bridged polymeric complex **2** have similar activities, which showed strong activity against *S. aureus* and *E. coli*, and medium activity against *C. parapsilosis*. The thiocyanate bridged polymeric copper complex **3** showed strong activity against *S. aureus* and *E. coli*, while weak activity against *C. parapsilosis*. In general,

Table 4. Antibacterial activity of H_2L and the copper complexes

Compound	*S. aureus*		*E. coli*		*C. parapsilosis*		
	IC_{50}*	MIC*	IC_{50}	MIC	IC_{50}	MIC	
HL	>2.50	>2.50	1.57	1.23	>2.50	>2.50	
1	0.41	0.25	0.26	0.13	1.81	1.53	
2	0.45	0.27	0.28	0.16	1.92	1.60	
3	0.72	0.49	0.55	0.31	2.20	1.87	
Cu-1	0.38	0.23	0.75	0.42	2.03	1.70	[ref. 17]
Cu-2	0.17	0.13	1.16	0.95	2.27	1.89	[ref. 17]
Cu-3	0.27	0.16	0.56	0.32	2.17	1.25	[ref. 18]
Zn-1	1.15	0.62	1.83	1.25	3.39	2.50	[ref. 18]

* mmol L^{-1}

complex **3** has a litter weaker activity against the bacteria and yeast than the other two. Notably, complex **1** has the most activity against *E. coli*, with IC_{50} and MIC values of 0.26 and 0.13 mmol L^{-1}, which deserves further study. The present three complexes have similar antibacterial activities against *S. aureus* and *C. parapsilosis*, while stronger activities against *E. coli* as compared to the copper(II) complexes (Cu-1, Cu-2) with the Schiff base ligand *N,N'*-bis(4-bromosalicylidene)propane-1,2-diamine.[17] The present three complexes have similar antibacterial activities against the bacteria strains with the copper(II) complex (Cu-3) with the Schiff base *N,N'*-bis(4-bromosalicylidene)propane-1,3-diamine, while have stronger activities against the bacteria strains with the zinc(II) complex (Zn-1) with the same ligand.[18]

4. Conclusion

In summary, three new copper(II) complexes derived from 2,4-dichloro-6-((2-pyrrolidin-1-ylethylimino) methyl)phenol with different co-ligands were prepared. The complexes were characterized by physico-chemical methods. Structures of the complexes were confirmed by single crystal X-ray determination. The Schiff base ligand coordinates to the metal atoms through the phenolate oxygen, imino nitrogen and pyrrolidine nitrogen. The complexes have effective antibacterial activities on the bacteria *Staphylococcus aureus* and *Escherichia coli*, and the yeast *Candida parapsilosis*.

Supplementary Material

CCDC 2333475 (**1**), 2333476 (**2**) and 2333477 (**3**) contain the supplementary crystallographic data for this paper. These data can be obtained free of charge at http://www.ccdc.cam.ac.uk/const/retrieving.html or from the Cambridge Crystallographic Data Centre, 12 Union Road, Cambridge CB2 1EZ, UK; fax: +44(0)1223-336033 or email: deposit@ccdc.cam.ac.uk.

5. References

1. (a) H. Kargar, M. Fallah-Mehrjardi, K. S. Munawar, *Coord. Chem. Rev.* **2024**, *501*, 215587; **DOI:**10.1016/j.ccr.2023.215587
(b) J. H. Wu, L. A. Miao, M. M. Yang, A. Li, Y. Cao, Q. Y. Wang, J. H. Zhang, Z. L. You, *Inorg. Chim. Acta* **2023**, *555*, 121573; **DOI:**10.1016/j.ica.2023.121573
(c) C. Maxim, C. D. Ene, I. Nicolau, L. L. Ruta, I. C. Farcasanu, *Dalton Trans.* **2022**, *51*, 18383–18399; **DOI:**10.1039/D2DT02620A
(d) M. Abdi, A. F. Shojaei, M. Ghadermazi, Z. Moradi-Shoeili, *Acta Chim. Slov.* **2020**, *67*, 476–486; **DOI:**10.17344/acsi.2019.5466
(e) L.-W. Xue, Q.-L. Peng, P.-P. Wang, H.-J. Zhang, *Acta Chim. Slov.* **2019**, *66*, 694–700; **DOI:**10.17344/acsi.2019.5151
(f) Z. J. Xu, S. Meng, T. Cao, Y. Xin, M. J. Zhang, X. Y. Duan, Z. Zhou, D. P. Zhang, *Acta Chim. Slov.* **2022**, *69*, 896–904. **DOI:**10.17344/acsi.2022.7680
2. (a) H. Keypour, A. Tafazzoli, S. H. M. Farida, M. Abdollahi-Moghadam, R. W. Gable, *Inorg. Chem. Commun.* **2023**, *155*, 110981; **DOI:**10.1016/j.inoche.2023.110981
(b) M. K. Mahish, E. Zangrando, A. Patra, P. Vojtisek, S. C. Manna, *Polyhedron* **2023**, *243*, 116543; **DOI:**10.1016/j.poly.2023.116543
(c) A. Ali, M. Pervaiz, Z. Saeed, U. Younas, R. Bashir, S. Ullah, S. M. Bukhari, F. Ali, S. Jelani, A. Rashid, A. Adnan, *Inorg. Chem. Commun.* **2022**, *145*, 109903; **DOI:**10.1016/j.inoche.2022.109903
(d) D.-L. Peng, N. Sun, *Acta Chim. Slov.* **2018**, *65*, 895–901; **DOI:**10.17344/acsi.2018.4543
(e) G.-X. He, L.-W. Xue, Q.-L. Peng, P.-P. Wang, H.-J. Zhang, *Acta Chim. Slov.* **2019**, *66*, 570–575; **DOI:**10.17344/acsi.2018.4868
(f) B. H. He, C. E. Dong, X. Q. Wang, Y. Cao, Y. Z. Gao, M. M. Yang, J. H. Zhang, C. L. Jing, D. H. Shi, Z. L. You, *Polyhedron* **2023**, *231*, 116254. **DOI:**10.1016/j.poly.2022.116254
3. (a) X.-Y. Qiu, S.-J. Liu, *Polyhedron* **2023**, *247*, 116708; **DOI:**10.1016/j.poly.2023.116708
(b) X.-X. Liang, X.-Y. Zhao, A. Guo, X.-W. Wang, M. Rong, L. Chang, Z.-Q. Sun, X.-D. Jin, *J. Coord. Chem.* **2023**, *76*, 307–

321; **DOI:**10.1080/00958972.2023.2170795
(c) K.-S. Cao, L.-W. Xue, Q.-R. Liu, *Acta Chim. Slov.* **2023**, *70*, 516–523; **DOI:**10.17344/acsi.2023.8359
(d) M. H. Esfahani, H. Iranmanesh, J. E. Beves, M. Kaur, J. P. Jasinski, M. Behzad, *J. Coord. Chem.* **2019**, *72*, 2326–2336; **DOI:**10.1080/00958972.2019.1643846
(e) Z. M. Jahromi, Z. Asadi, V. Eigner, M. Dusek, B. Rastegari, *Polyhedron* **2022**, *221*, 115891; **DOI:**10.1016/j.poly.2022.115891
(f) L. Ghasemi, M. H. Esfahani, A. Abbasi, M. Behzad, *Polyhedron* **2022**, *220*, 115825. **DOI:**10.1016/j.poly.2022.115825

4. (a) L. Saghatforoush, K. Moeini, S. A. Hosseini-Yazdi, Z. Mardani, A. Bakhtiari, A. Hajabbas-Farshchi, S. Honarvar, M. S. M. Abdelbaky, *Polyhedron* **2019**, *170*, 312–324; **DOI:**10.1016/j.poly.2019.05.057
(b) Y. Yuan, X.-K. Lu, G.-Q. Zhou, X.-Y. Qiu, *Acta Chim. Slov.* **2021**, *68*, 1008–1015; **DOI:**10.17344/acsi.2021.7070
(c) K. Dankhoff, M. Gold, L. Kober, F. Schmitt, L. Pfeifer, A. Durrmann, H. Kostrhunova, M. Rothemund, V. Brabec, R. Schobert, B. Weber, *Dalton Trans.* **2019**, *48*, 15220–15230; **DOI:**10.1039/C9DT02571E
(d) S.-F. Yu, X.-Y. Qiu, S.-J. Liu, *Acta Chim. Slov.* **2020**, *67*, 1301–1308. **DOI:**10.17344/acsi.2020.6321
5. *SMART/SAINT*, Madison (WI, USA): Bruker AXS, Inc., **2004**.
6. G. M. Sheldrick, *Acta Crystallogr.* **2015**, *C71*, 3–11.
7. G. M. Sheldrick, *SADABS*, Göttingen (Germany): Univ. of Göttingen, **1999**.
8. (a) M. R. Maurya, C. Haldar, S. Behl, N. Kamatham, F. Avecilla, *J. Coord. Chem.* **2011**, *64*, 2995–3011; **DOI:**10.1080/00958972.2011.610450
(b) R. Kannappan, S. Tanase, I. Mutikainen, U. Turpeinen, J. Reedijk, *Inorg. Chim. Acta* **2005**, *358*, 383–388; **DOI:**10.1016/j.ica.2004.09.003
(c) N. A. I. Hisham, H. Khaledi, H. M. Ali, H. A. Hadi, *J. Coord. Chem.* **2012**, *65*, 2992–3006. **DOI:**10.1080/00958972.2012.708412
9. D. A. Firmin, E. R. Quilano, R. Cameron, A. K. Pant, E. D. Stevens, O. Kahn, T. Mallah, *Inorg. Chim. Acta* **1990**, *172*, 211–220. **DOI:**10.1016/S0020-1693(00)80858-0
10. (a) D.-M. Xian, Z.-L. You, M. Zhang, P. Hou, X.-H. Li, *J. Coord. Chem.* **2011**, *64*, 3265–3272; **DOI:**10.1080/00958972.2011.619261
(b) S. Banerjee, M. G. B. Drew, C.-Z. Lu, J. Tercero, C. Diaz, A. Ghosh, *Eur. J. Inorg. Chem.* **2005**, 2376–2383; **DOI:**10.1002/ejic.200500080
(c) Z.-L. You, D.-M. Xian, M. Zhang, *CrystEngComm* **2012**, *14*, 7133–7136. **DOI:**10.1039/c2ce26201k
11. (a) K. R. S. Gowda, H. S. B. Naik, B. V. Kumar, C. N. Sudhamani, H. V. Sudeep, T. R. R. Naik, G. Krishnamurthy, *Spectrochim. Acta A* **2013**, *105*, 229–237; **DOI:**10.1016/j.saa.2012.12.011
(b) B. Sarkar, M. G. B. Drew, M. Estrader, C. Diaz, A. Ghosh, *Polyhedron* **2008**, *27*, 2625–2633; **DOI:**10.1016/j.poly.2008.05.004
(c) A. Jayamani, M. Sethrupathi, S. O. Ojwach, N. Sengottuvelan, *Inorg. Chem. Commun.* **2017**, *84*, 144–149. **DOI:**10.1016/j.inoche.2017.08.013
12. (a) A. D. Khalaji, S. Triki, J. M. Clemente-Juan, C. J. Gomez-Garcia, *Polyhedron* **2013**, *50*, 45–50; **DOI:**10.1016/j.poly.2012.10.031
(b) S. Naiya, C. Biswas, M. G. B. Drew, C. J. Gomez-Garcia, J. M. Clemente-Juan, A. Ghosh, *Inorg. Chem.* **2010**, *49*, 6616–6627. **DOI:**10.1021/ic1005456
13. A. Ray, D. Sadhukhan, G. Rosair, C. J. Gomez-Garcia, S. Mitra, *Polyhedron* **2009**, *28*, 3542–3550. **DOI:**10.1016/j.poly.2009.07.017
14. Jayamani, M. Sethupathi, S. O. Ojwach, N. Sengottuvelan, *Inorg. Chem. Commun.* **2017**, *84*, 144–149. **DOI:**10.1016/j.inoche.2017.08.013
15. B. Sarkar, M. G. B. Drew, M. Estrader, C. Diaz, A. Ghosh, *Polyhedron* **2008**, *27*, 2625–2633. **DOI:**10.1016/j.poly.2008.05.004
16. J. W. Searl, R. C. Smith, S. Wyard, *J. Proc. Phys. Soc.* **1961**, *78*, 1174–1181. **DOI:**10.1088/0370-1328/78/6/311
17. Y.-M. Hao, *Acta Chim. Slov.* **2023**, *70*, 327–332. **DOI:**10.17344/acsi.2023.8104
18. Y.-M. Hao, *Acta Chim. Slov.* **2021**, *68*, 102–108. **DOI:**10.17344/acsi.2020.6205

Povzetek

Sintetizirali smo tri nove bakrove(II) komplekse [CuClL] (**1**), $[CuBrL]_n$ (**2**) in $[CuL(NCS)]_n$ (**3**) s Schiffovo bazo 2,4-dikloro-6-((2-pirolidin-1-iletilimino)metil)fenol (HL) in jih okarakterizirali s spektroskopskimi metodami ter z rentgensko monokristalno analizo. Atom Cu v kompleksu **1** je v kvadratno planarni koordinaciji, v kompleksih **2** in **3** pa v kvadratno piramidalni koordinaciji. Ligand Schiffove baze je na Cu centralne atome koordiniran preko fenolatnega kisikovega atoma, imino dušikovega atoma in pirolidinskega dušikovega atoma. Antibakterijske aktivnosti Schiffove baze in treh bakrovih kompleksov smo določili na bakterijah *Staphylococcus aureus* in *Escherichia coli* ter kvasovkah *Candida parapsilosis*.

DOI: 10.17344/acsi.2024.8757 *Acta Chim. Slov.* **2024,** *71,* 312–318

Scientific paper

Synthesis of Bifunctional Amine-Squaramide Organocatalysts Derived from 3-((Dimethylamino) methylene)camphor

Luka Ciber, Helena Brodnik, Franc Požgan, Jurij Svete, Bogdan Štefane and Uroš Grošelj*

University of Ljubljana, Faculty of Chemistry and Chemical Technology, Večna pot 113, SI-1000 Ljubljana,

** Corresponding author: E-mail: uros.groselj@fkkt.uni-lj.si*

Received: 04-07-2024

Abstract

Four bifunctional, noncovalent amine-squaramide organocatalysts were prepared from camphor in five steps. The stereochemistry of the prepared catalysts was thoroughly analyzed using various spectroscopic techniques. Their organocatalytic activity was investigated in the Michael addition of acetylacetone to *trans*-β-nitrostyrene. The addition product was formed in complete conversion and with an enantioselectivity of up to 77% *ee*. In the reactions catalyzed by the 2-*exo*-3-*endo* catalysts, the major (*S*)-enantiomer was formed, whereas in the presence of 2-*endo*-3-*endo* catalysts, the (*R*)-enantiomer was formed as the major product.

Keywords: Camphor, Enaminone, Asymmetric organocatalysis, Bifunctional noncovalent organocatalysts, Squaramide organocatalysts, Michael addition

1. Introduction

The noncovalent bifunctional organocatalyst with thiourea H-bond donor introduced by Takemoto in 2003[1] and the squaramide catalyst developed by Rawal in 2008[2] and their numerous analogs have become the workhorses of noncovalent organocatalysis,[3–7] as they enable the simultaneous activation and coordination of both electrophilic and nucleophilic reactants.[7,8] A typical and most commonly used organocatalyst of this type is a derivative of a chiral 1,2-diamine based on cyclohexane-1,2-diamine[9] or privileged cinchona alkaloids.[10–12] Although several H-bond donors have been described in the literature,[13–15] thiourea and squaramide remain the most common and best H-bond donors.[3–7,16,17] Hydrogen bond donors based on thiourea and squaramide have been very successfully introduced into noncovalent bifunctional quaternary ammonium salt phase-transfer organocatalysts.[18–21]

In the course of our extensive research on camphor-diamine building blocks and their application for the synthesis of noncovalent bifunctional organocatalysts with thiourea or squaramide double H-bond donors,[22–24] we were able to develop highly efficient squaramide organocatalysts based on camphor-derived 1,3-diamine for the addition of 1,3-dicarbonyl nucleophiles and heterocyclic pyrrolone nucleophiles to nitroalkene acceptors.[25,26] In contrast, their thiourea analogs proved to be inferior to the squaramide organocatalysts.[22] While amine-thiourea organocatalysts derived from 3-((dimethylamino)methylene)camphor have already been reported,[23] the corresponding squaramide analogs have not yet been prepared and their organocatalytic activity has not yet been investi-

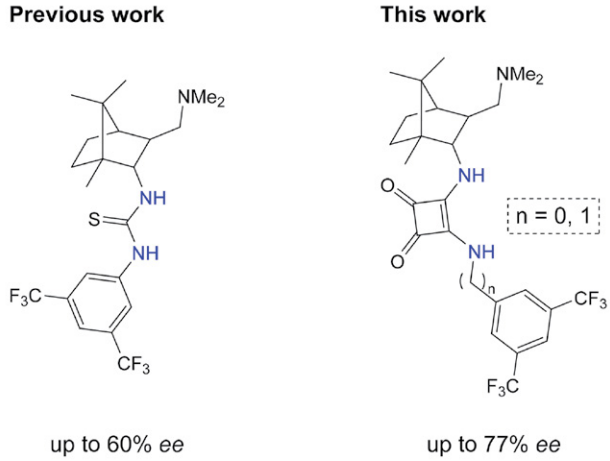

Figure 1. 3-((Dimethylamino)methylene)camphor-derived thiourea and squaramide organocatalysts.

gated (Figure 1). In this work, we present the synthesis of camphor-derived noncovalent bifunctional squaramide organocatalysts **8a**,**b** and **9a**,**b** and their catalytic activity in the addition of acetylacetone to *trans*-β-nitrostyrene.

2. Experimental

2. 1. Materials and Measurements

Solvents for extractions and chromatography were of technical grade and were distilled prior to use. Extracts were dried over technical grade anhydrous Na_2SO_4. Melting points were determined on a Kofler micro hot stage and on SRS OptiMelt MPA100 – Automated Melting Point System (Stanford Research Systems, Sunnyvale, California, USA). The NMR spectra were obtained on a Bruker UltraShield 500 plus (Bruker, Billerica, MA, USA) at 500 MHz for ^{1}H and 126 MHz for ^{13}C nucleus, using $CDCl_3$ and DMSO-d_6 with TMS as the internal standard, as solvents. Mass spectra were recorded on an Agilent 6224 Accurate Mass TOF LC/MS (Agilent Technologies, Santa Clara, CA, USA), IR spectra on a Perkin-Elmer Spectrum BX FTIR spectrophotometer (Perkin-Elmer, Waltham, MA, USA). Column chromatography (CC) was performed on silica gel (silica gel 60, particle size: 0.035–0.070 mm (Sigma-Aldrich, St. Louis, MO, USA)). HPLC analyses were performed on an Agilent 1260 Infinity LC (Agilent Technologies, Santa Clara, CA, USA) using CHIRALPAK AD-H (0.46 cm ø × 25 cm) as chiral column (Chiral Technologies, Inc., West Chester, PA, USA). Catalytic hydrogenation was performed on a Parr Pressure Reaction Hydrogenation Apparatus (Moline, IL, USA). The optical rotation of optical active substances was measured on a Perkin-Elmer 241 MC Polarimeter (Perkin-Elmer, Waltham, MA, USA) equipped with a Na lamp (sodium emission lines at 589.0 nm) at 20 °C. All the commercially available chemicals used were purchased from Sigma-Aldrich (St. Louis, MO, USA).

2. 2. Synthesis of 3-((3,5-Bis(trifluoromethyl) benzyl)amino)-4-(((1*S*,2*S*,3*R*,4*R*)-3-((dimethylamino)methyl)-1,7,7-trimethylbicyclo[2.2.1]heptan-2-yl) amino)cyclobut-3-ene-1,2-dione (8a) and 3-((3,5-Bis(trifluoromethyl)benzyl)amino)-4-(((1*S*,2*S*,3*R*,4*R*)-3-((dimethylamino)methyl)-1,7,7-trimethylbicyclo[2.2.1]heptan-2-yl) amino)cyclobut-3-ene-1,2-dione (8b)

To a solution of diamine **5** (1.21 mmol, 254 mg) in anhydrous CH_2Cl_2 (3 mL) under argon at 25 °C was added 3-((3,5-bis(trifluoromethyl)benzyl)amino)-4-ethoxycyclobut-3-ene-1,2-dione (**6**) (1.1 equiv., 1.331 mmol, 489 mg). The resulting reaction mixture was stirred at 25 °C for 24 h. The volatiles were evaporated *in vacuo* and the residue was purified by column chromatography. First column chromatography: silica gel 60; (i) EtOAc/MeOH/Et_3N = 20:1:0.5 to elute less polar impurities; (ii) EtOAc/MeOH/Et_3N = 10:1:0.5 to elute the combined products **8a** and **8b**. The fractions containing products **8a** and **8b** were combined and the volatiles were evaporated *in vacuo*. The residue was purified by a second column chromatography: silica gel 60; CH_2Cl_2/MeOH/Et_3N = 40:1:1 to separate products **8a** and **8b**. The fractions containing the pure separated products were combined separately and the volatiles were evaporated *in vacuo*.

Compound **8a**. Elutes first from the column. Yield: 296 mg (0.557 mmol, 46%) of white solid; m.p. 248–253 °C. $[\alpha]_D^{r.t.}$ = –149.6 (0.26, $CHCl_3$). EI-HRMS: *m/z* = 532.2390 (MH^+); $C_{26}H_{32}F_6N_3O_2$ requires: *m/z* = 532.2393 (MH^+); IR ν_{max} 3293, 2959, 2770, 1801, 1673, 1580, 1539, 1467, 1379, 1348, 1277, 1167, 1132, 1046, 902, 874, 843, 816, 726, 703, 682 cm^{-1}. ^{1}H NMR (500 MHz, DMSO-d_6): δ 0.71 (s, 3H), 0.83 (s, 3H), 0.95 (s, 3H), 1.00–1.09 (m, 1H), 1.34–1.44 (m, 1H), 1.46–1.57 (m, 2H), 1.69 (s, 1H), 2.12 (s, 6H), 2.16 (s, 1H), 2.21–2.30 (m, 1H), 2.34–2.41 (m, 1H), 3.47–3.57 (m, 1H), 4.88 (dd, *J* = 15.6, 5.9 Hz, 1H), 4.98 (dd, *J* = 15.4, 6.8 Hz, 1H), 7.15 (br s, 1H), 7.85 (br s, 1H), 8.07 (s, 3H). ^{13}C NMR (126 MHz, DMSO-d_6): δ 11.58, 19.60, 19.80, 20.68, 35.32, 45.37, 45.08, 45.68, 46.82, 47.25, 50.08, 60.26, 66.71, 121.29, 123.30 (q, *J* = 272.9 Hz), 128.52, 130.54 (q, *J* = 32.6 Hz), 142.65, 166.82, 168.42, 182.48, 182.62.

Compound **8b**. Elutes second from the column. Yield: 109 mg (0.205 mmol, 17%) of yellowish semisolid. $[\alpha]_D^{r.t.}$ = –27.5 (0.28, $CHCl_3$). EI-HRMS: *m/z* = 532.2391 (MH^+); $C_{26}H_{32}F_6N_3O_2$ requires: *m/z* = 532.2393 (MH^+); IR ν_{max} 3236, 2949, 1797, 1658, 1583, 1534, 1480, 1379, 1346, 1277, 1170, 1130, 902, 843, 813, 704, 682 cm^{-1}. ^{1}H NMR (500 MHz, DMSO-d_6): δ 0.72 (s, 3H), 0.89 (s, 3H), 0.94 (s, 3H), 1.24–1.37 (m, 2H), 1.45–1.56 (m, 1H), 1.59–1.67 (m, 2H), 2.16 (br s, 6H), 2.38–2.46 (m, 3H), 4.44 (t, *J* = 10.5 Hz, 1H), 4.89 (dd, *J* = 15.5, 6.0 Hz, 1H), 4.99 (dd, *J* = 15.6, 7.0 Hz, 1H), 7.82 (br s, 1H), 8.07 (s, 3H), 8.39 (s, 1H). ^{13}C NMR (126 MHz, DMSO-d_6): δ 13.74, 18.15, 19.50, 19.97, 26.29, 36.07, 44.79, 45.67, 46.35, 47.58, 49.95, 56.63, 58.92, 121.19, 123.31 (q, *J* = 272.8 Hz), 128.34, 130.50 (q, *J* = 33.0 Hz), 142.83, 167.25, 169.44, 182.55, 182.61.

2. 3. Synthesis of 3-((3,5-Bis(trifluoromethyl) phenyl)amino)-4-(((1*S*,2*S*,3*R*,4*R*)-3-((dimethylamino)methyl)-1,7,7-trimethylbicyclo[2.2.1]heptan-2-yl) amino)cyclobut-3-ene-1,2-dione (9a) and 3-((3,5-Bis(trifluoromethyl)phenyl)amino)-4-(((1*S*,2*S*,3*R*,4*R*)-3-((dimethylamino)methyl)-1,7,7-trimethylbicyclo[2.2.1]heptan-2-yl) amino)cyclobut-3-ene-1,2-dione (9b)

To a solution of diamine **5** (1.21 mmol, 254 mg) in anhydrous CH_2Cl_2 (3 mL) under argon at 25 °C was added

3-((3,5-bis(trifluoromethyl)phenyl)amino)-4-ethoxycyclobut-3-ene-1,2-dione (**7**) (1.1 equiv., 1.331 mmol, 470 mg). The resulting reaction mixture was stirred at 25 °C for 24 h. The volatiles were evaporated *in vacuo* and the residue was purified by column chromatography. First column chromatography: silica gel 60; (i) Et_2O/MeOH/Et_3N = 20:1:0.5 to elute less polar impurities; (ii) Et_2O/MeOH/Et_3N = 10:2:0.5 to elute the combined products **9a** and **9b**. The fractions containing products **9a** and **9b** were combined and the volatiles were evaporated *in vacuo*. The residue was purified by a second column chromatography: silica gel 60; CH_2Cl_2/MeOH/Et_3N = 40:1:1 to separate products **9a** and **9b**. The fractions containing the pure separated products were combined separately and the volatiles were evaporated *in vacuo*.

Compound **9a**. Elutes first from the column. Yield: 125 mg (0.242 mmol, 20%) of yellowish semisolid. $[\alpha]_D^{r.t.}$ = –88.3 (0.3, $CHCl_3$). EI-HRMS: *m/z* = 518.2237 (MH^+); $C_{25}H_{30}F_6N_3O_2$ requires: *m/z* = 518.2237 (MH^+); IR ν_{max} 2956, 1792, 1690, 1600, 1550, 1436, 1376, 1329, 1276, 1178, 1130, 933, 879, 847, 826, 700, 678, 619 cm^{-1}. ^1H NMR (500 MHz, DMSO-d_6): δ 0.77 (s, 3H), 0.87 (s, 3H), 1.04 (s, 3H), 1.07–1.13 (m, 1H), 1.38–1.45 (m, 1H), 1.49–1.60 (m, 2H), 1.72–1.76 (m, 1H), 2.15 (s, 6H), 2.20–2.34 (m, 2H), 2.35–2.43 (m, 1H), 3.57 (d, *J* = 5.5 Hz, 1H), 7.59 (br s, 1H), 7.66 (s, 1H), 8.11 (s, 2H), 10.37 (br s, 1H). ^{13}C NMR (126 MHz, DMSO-d_6): δ 11.67, 19.82, 19.90, 20.66, 35,46, 44.96, 45.46, 46.83, 47.36, 50.22, 60.23, 67.39, 114.71, 118.14, 123.20 (q, *J* = 272.7 Hz), 131.33 (q, *J* = 32.9 Hz), 141.13, 162.09, 169.84, 180.29, 184.38.

Compound **9b**. Elutes second from the column. Yield: 50 mg (0.0968 mmol, 8%) of yellowish semisolid. $[\alpha]_D^{r.t.}$ = –37.1 (0.07, $CHCl_3$). EI-HRMS: *m/z* = 518.2235 (MH^+); $C_{25}H_{30}F_6N_3O_2$ requires: *m/z* = 518.2237 (MH^+); IR ν_{max} 3355, 2955, 1793, 1685, 1606, 1567, 1505, 1472, 1441, 1375, 1329, 1275, 1173, 1129, 1007, 932, 903, 881, 846, 798, 703, 686, 671 cm^{-1}. ^1H NMR (500 MHz, DMSO-d_6): δ 0.75 (s, 3H), 0.91 (s, 3H), 0.98 (s, 3H), 1.24–1.31 (m, 1H), 1.34–1.43 (m, 1H), 1.49–1.59 (m, 1H), 1.71 (s, 1H), 1.87–1.95 (m, 1H), 2.45 (br s, 6H), 2.52–2.62 (m, 3H), 4.52 (t, *J* = 10.2 Hz, 1H), 7.62 (s, 1H), 8.27 (s, 2H), 8.96 (br s, 1H), 12.05 (br s, 1H). ^{13}C NMR (126 MHz, DMSO-d_6): δ 13.61, 18.24, 19.46, 20.08, 35.52, 44.23, 46.65, 47.64, 50.44, 56.44, 59.86, 114.28, 117.42, 123.23 (q, *J* = 272.8 Hz), 131.38 (q, *J* = 32.9 Hz), 141.79, 162.75, 168.80, 180.23, 184.11 (one signal missing).

2. 4. Organocatalyzed Addition of Acetylacetone to *trans*-β-Nitrostyrene

To a solution of *trans*-β-nitrostyrene (**A**) (14.9 mg, 0.1 mmol) in anhydrous CH_2Cl_2 (1 mL) or anhydrous toluene (1 mL) under argon, a catalyst (10 mol%) was added, followed by the addition of acetylacetone (**B**) (15.4 μL, 0.15 mmol). The resulting reaction mixture was stirred under argon for 24 h at 25 °C. After 24 h, an aliquot of 100 μL of the reaction mixture was withdrawn to determine the reaction conversion by ^1H NMR (in $CDCl_3$). The remainder of the reaction mixture was used to isolate the addition product **C**. The residue was purified by column chromatography (silica gel 60, EtOAc/petroleum ether = 1:2). The reaction mixture was transferred directly to the top of the column without prior evaporation of the volatile components. The fractions containing product **C** were combined and the volatiles were evaporated *in vacuo*. The enantioselectivity was determined by chiral HPLC analysis (chiral column CHIRALPAK AD-H, mobile phase: *n*-hexane/*i*-PrOH = 90:10, flow rate: 1.0 mL/min; λ = 210 nm).

2. 5. X-Ray Crystallography

Single-crystal X-ray diffraction data was collected on Agilent Technologies SuperNova Dual diffractometer with an Atlas detector using monochromated Mo-Kα radiation (λ = 0.71073 Å) at 150 K. The data was processed using CrysAlis PRO.[28] Using Olex2.1.2.,[29] the structures were solved by direct methods implemented in SHELXS[30] or SHELXT[31] and refined by a full-matrix least-squares procedure based on F^2 with SHELXT-2014/7.[32] All nonhydrogen atoms were refined anisotropically. Hydrogen atoms were placed in geometrically calculated positions and were refined using a riding model. The drawings and the analysis of bond lengths, angles and intermolecular interactions were carried out using Mercury[33] and Platon.[34] Structural and other crystallographic details on data collection and refinement for compound **8a** have been deposited with the Cambridge Crystallographic Data Centre as supplementary publication number CCDC Deposition Number **2336641**. These data are available free of charge at https://www.ccdc.cam.ac.uk/structures/, accessed on 04 March 2024 (or from CCDC, 12 Union Road, Cambridge CB2 1EZ, UK; fax: +44 1223 336033; e-mail: deposit@ccdc.cam.ac.uk).

3. Results and Discussion

The starting diamine **5** was prepared as a mixture of diastereomers in four steps (Scheme 1) in 57% yield following the procedures from our previous work.[23] Thus, (1*R*)-(+)-camphor (**1**) was treated with Bredereck's reagent to give enaminone **2**, which was catalytically hydrogenated in the presence of anhydrous hydrochloric acid in ethanol to give amino-ketone hydrochloride **3** as a mixture of two diastereomers in the ratio 76:24. The subsequent reaction with hydroxylamine gave oxime **4** (*dr* = 90:10), while the final reduction with sodium in *n*-propanol gave an inseparable mixture of diastereomeric diamines **5** in the ratio 62:28:10.[23] Treatment of the diastereomeric mixture of amine **5** with squaramate **6**[35] and **7**[36] gave, after extensive purification by column chromatography, diastereomerically pure catalysts **8a** (46% yield)/**8b** (17% yield) and **9a** (20% yield)/**9b** (8% yield), respectively (Scheme 1).

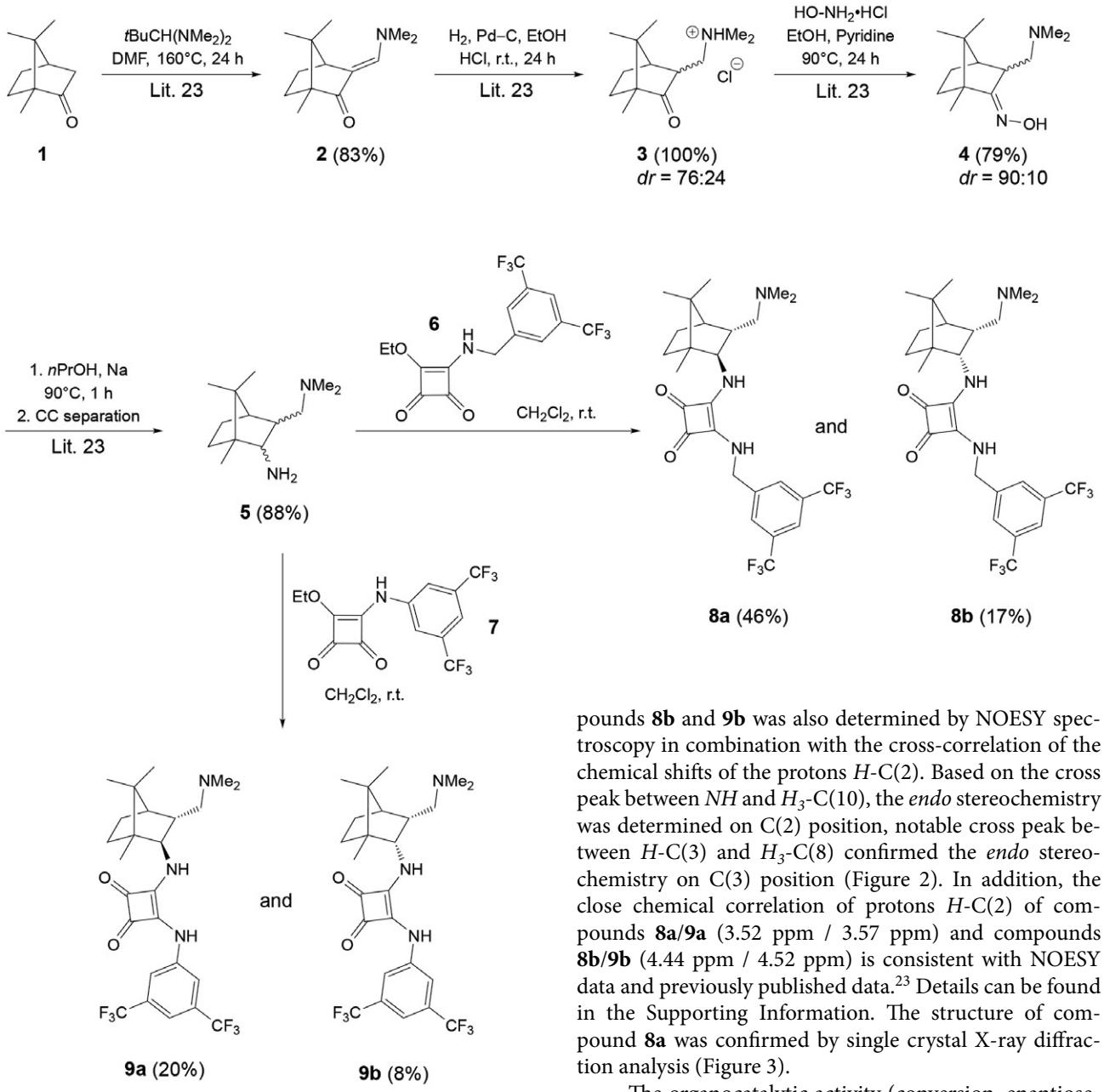

Scheme 1. Synthesis of camphor-derived bifunctional amine-squaramide organocatalysts **8** and **9**.

The structures of compounds **8a**,**b**, and **9a**,**9b** were confirmed by spectroscopic methods (^{1}H and ^{13}C NMR, 2D NMR, IR, and high-resolution mass spectrometry). The 2-*exo*-3-*endo* stereochemistry of compounds **8a** and **9a** was determined by NOESY spectroscopy (Figure 2). Based on cross peaks in NOESY spectra the *exo* stereochemistry on the C(3) position was determined (cross peak between *H*-C(2) and H_3-C(10) as well as *NH* and H_3-C(8)). The *endo* stereochemistry on the C(2) position was determined based on the cross peak between *H*-C(3) and H_3-C(8). The 2-*endo*-3-*endo* stereochemistry of compounds **8b** and **9b** was also determined by NOESY spectroscopy in combination with the cross-correlation of the chemical shifts of the protons *H*-C(2). Based on the cross peak between *NH* and H_3-C(10), the *endo* stereochemistry was determined on C(2) position, notable cross peak between *H*-C(3) and H_3-C(8) confirmed the *endo* stereochemistry on C(3) position (Figure 2). In addition, the close chemical correlation of protons *H*-C(2) of compounds **8a**/**9a** (3.52 ppm / 3.57 ppm) and compounds **8b**/**9b** (4.44 ppm / 4.52 ppm) is consistent with NOESY data and previously published data.[23] Details can be found in the Supporting Information. The structure of compound **8a** was confirmed by single crystal X-ray diffraction analysis (Figure 3).

The organocatalytic activity (conversion, enantioselectivity) of camphor-derived organocatalysts **8a**,**b** and **9a**,**b** was investigated in the 1,4-addition of acetylacetone (**B**) to *trans*-β-nitrostyrene (**A**).[25,27] The reactions were carried out in anhydrous dichloromethane at 25 °C for 24 h with 10 mol% of the catalyst (Scheme 2). The 2-*exo*-3-*endo* catalysts **8a** and **9a** afforded the addition product **C** in complete conversion and with good (*S*)-enantioselectivity, *i.e.* 77% *ee* and 71% *ee*, respectively. In contrast, incomplete conversion (94% and 30%, respectively) with reversed (*R*)-enantioselectivity (62% *ee* and 4% *ee*, respectively) was obtained with the 2-*endo*-3-*endo* catalysts **8b** and **9b**. The catalytic performance of the best catalyst **8a** was additionally carried out in anhydrous toluene, where 40% conversion and 57% *ee* were obtained. The squaramide-based catalysts **8a** and **9a** outperformed the

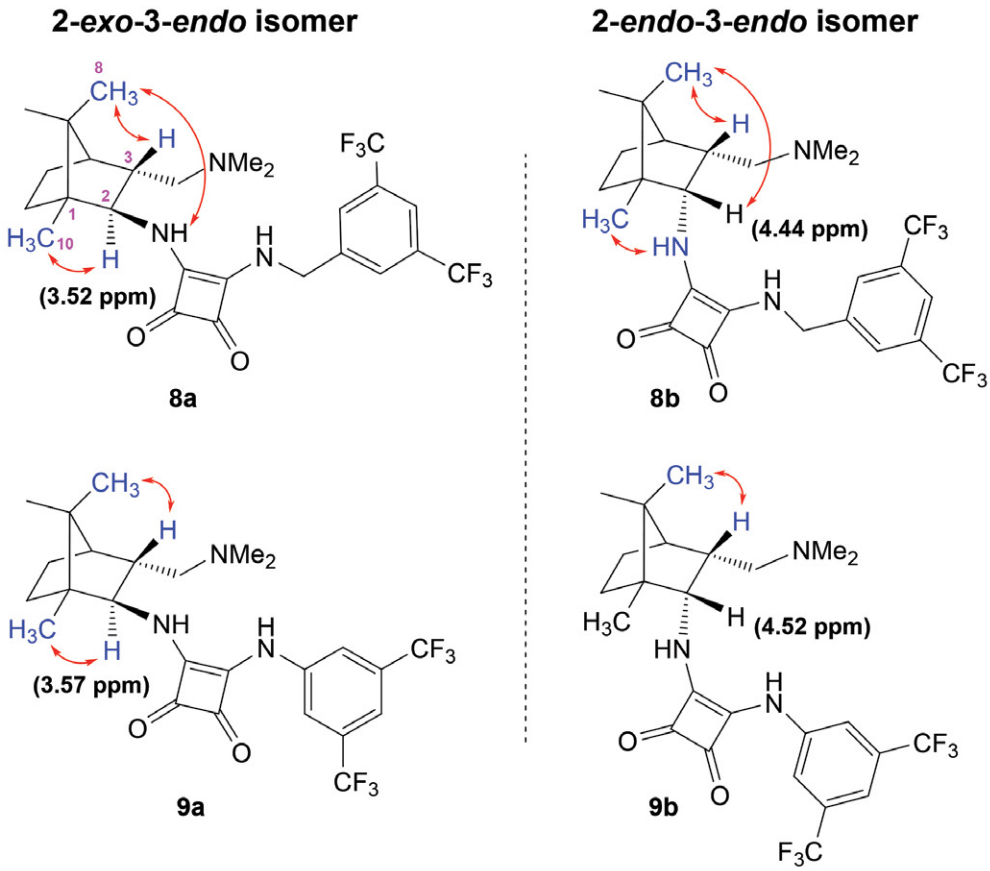

Figure 2. Structure determination by NOESY spectroscopy and cross-correlation of chemical shifts of proton *H*-C(2).

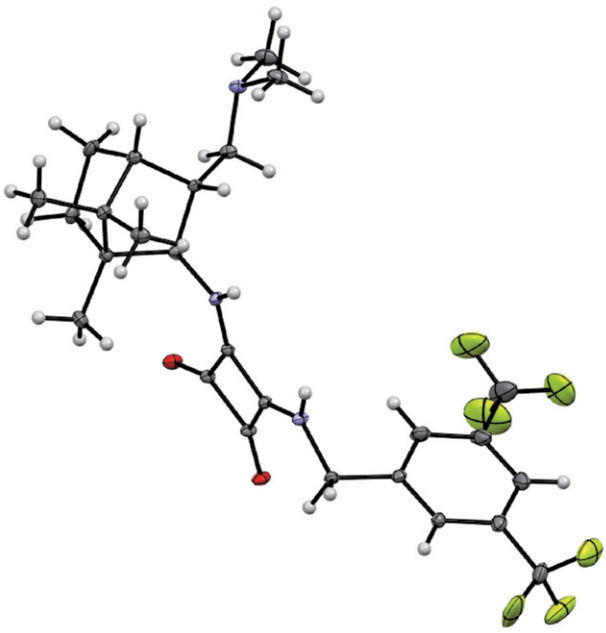

Figure 3. Molecular structure of product **8a** without solvent (2·$CHCl_3$). Thermal ellipsoids are shown at 50% probability.

previously reported thiourea-based catalysts (up to 60% *ee*).[23]

4. Conclusion

The bifunctional noncovalent squaramide organocatalysts **8a**,**b** and **9a**,**b**, prepared from camphor in five steps, were fully characterized and their organocatalytic activity in the addition of acetylacetone to *trans*-β-nitrostyrene was evaluated. The best performing catalyst **8a** gave the addition product **C** in 77% *ee* with (*S*)-enantioselectivity and complete conversion.

Supplementary Material

Crystal data and structure refinement for compound **8a** and copies of IR, HRMS, ^{1}H NMR, ^{13}C NMR and 2D spectra of the products are presented in the supporting information.

Acknowledgement

This research was funded by the Slovenian Research and Innovation Agency (ARIS), Research Core Funding No. P1-0179. The authors acknowledge the support of the

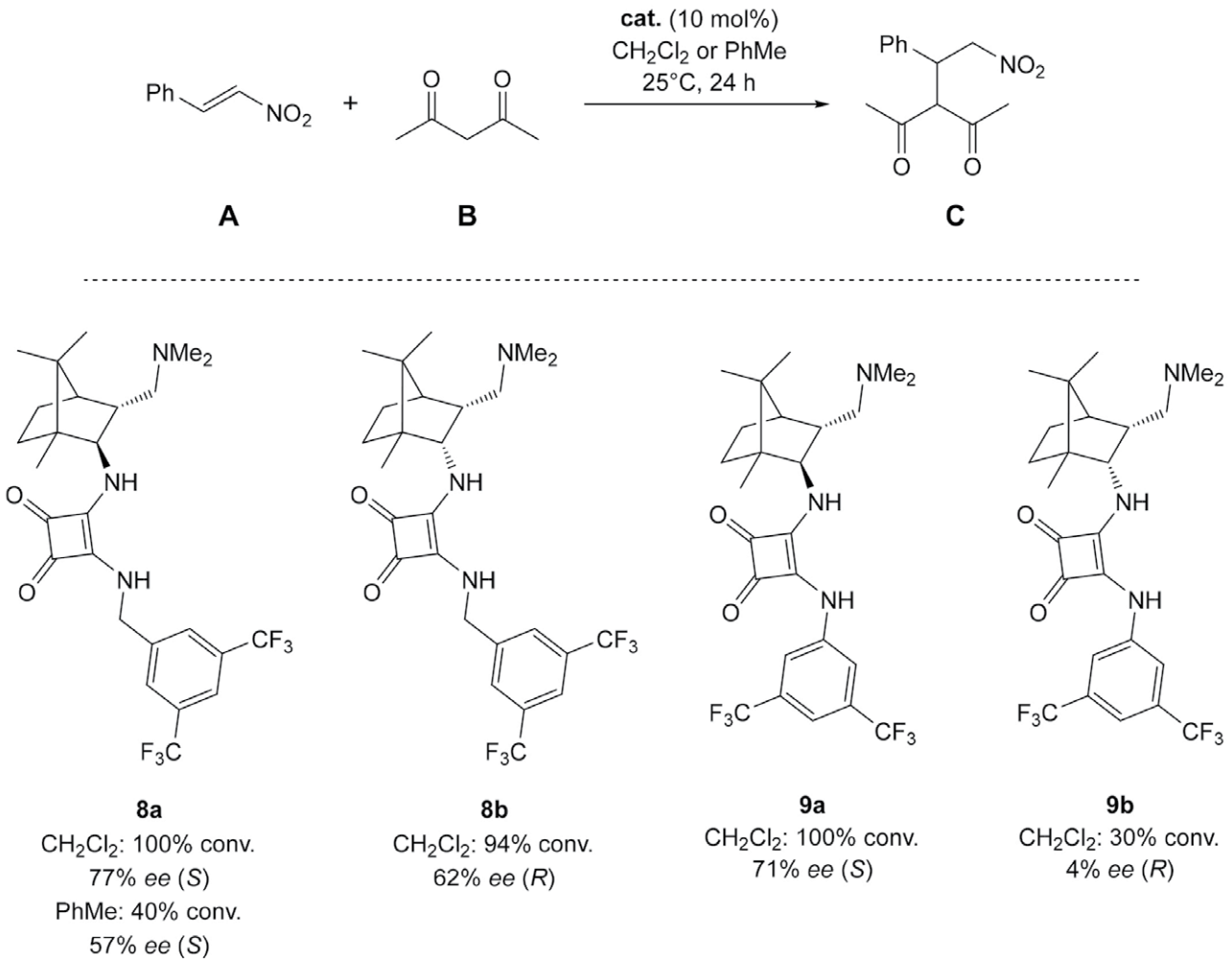

Scheme 2. The organocatalytic activity of organocatalysts **8a**,**b** and **9a**,**b** in the 1,4-addition of acetylacetone (**B**) to *trans*-β-nitrostyrene (**A**).

Centre for Research Infrastructure at the University of Ljubljana, Faculty of Chemistry and Chemical Technology, which is part of the Network of Research and Infrastructural Centres UL (MRIC UL) and is financially supported by the Slovenian Research Agency (Infrastructure programme No. I0-0022).

Conflicts of interest

There are no conflicts to declare.

5. References

1. T. Okino, Y. Hoashi, Y. Takemoto, *J. Am. Chem. Soc.* **2003**, *125*, 12672–12673. **DOI:**10.1021/ja036972z
2. J. P. Malerich, K. Hagihara, V. H. Rawal, *J. Am. Chem. Soc.* **2008**, *130*, 14416–14417. **DOI:**10.1021/ja805693p
3. R. R. Torres (Ed.), Stereoselective Organocatalysis: Bond Formation Methodologies and Activation Modes, 1st ed., John-Wiley & Sons: Hoboken, NJ, USA, **2013**.
4. (a) B. List (vol. Ed.), Asymmetric Organocatalysis 1. Lewis Base and Acid Catalysis. In Science of Synthesis, Georg Thieme Verlag KG: Germany, **2012**.
(b) K. Maruoka (vol. Ed.), Asymmetric Organocatalysis 2. Brønsted Base and Acid Catalysis. In Science of Synthesis, Georg Thieme Verlag KG: Germany, **2012**.
DOI:10.1055/sos-SD-205-00001
5. P. I. Dalko, Comprehensive Enantioselective Organocatalysis: Catalysts, Reactions, and Applications, Wiley-VCH: Weinheim, Germany, **2013**. **DOI:**10.1002/9783527658862
6. K. Etzenbach-Effers, A. Berkessel, Noncovalent Organocatalysis Based on Hydrogen Bonding: Elucidation of Reaction Paths by Computational Methods. In: *Asymmetric Organocatalysis. Topics in Current Chemistry*, B. List, (vol. Ed.), vol. 291, pp 38–69, Springer, Berlin, Heidelberg, **2010**.
DOI:10.1007/978-3-642-02815-1_3
7. A. M. F. Phillips, M. H. G. Prechtl, A. J. L. Pombeiro, *Catalysts* **2021**, *11*, 569. **DOI:**10.3390/catal11050569
8. B. Kótai, G. Kardos, A. Hamza, V. Farkas, I. Pápai, T. Soós, *Chem. Eur. J.* **2014**, *20*, 5631–5639.
DOI:10.1002/chem.201304553

9. M. Kopyt, M. P. Głowacki, P. Kwiatkowski, *trans*-1,2-Diaminocyclohexane and Its Derivatives in Asymmetric Organocatalysis. In *Chiral Building Blocks in Asymmetric Synthesis* (E. Wojaczyńska, J. Wojaczyński, Eds.), **2022**.
10. C. Cassani, R. Martín-Rapún, E. Arceo, F. Bravo, P. Melchiorre, *Nature Protocols*, **2013**, *8*, 325–344. **DOI:**10.1038/nprot.2012.155
11. H. Li, Y. Chen, L. Deng, Cinchona Alkaloids. In *Privileged Chiral Ligands and Catalysts*, Q.-L. Zhou (Ed.), **2011**. **DOI:**10.1016/S1351-4180(11)70298-7
12. Cinchona Alkaloids in Synthesis and Catalysis: Ligands, Immobilization and Organocatalysis. E. S. Choong (Ed.), VCH Verlag GmbH & Co. KGaA **2009**.
13. S.-I. Hirashima, R. Arai, K. Nakashima, N. Kawai, J. Kondo, Y. Koseki, T. Miura, *Adv. Synth. Catal.* **2015**, *357*, 3863–3867. **DOI:**10.1002/adsc.201500816
14. R. Arai, S.-i. Hirashima, J. Kondo, K. Nakashima, V. Koseki, T. Miura, *Org. Lett.* **2018**, *20*, 5569–5572. **DOI:**10.1021/acs.orglett.8b02241
15. Y. Kobayashi, Y. Taniguchi, N. Hayama, T. Inokuma, Y. Takemoto, *Angew. Chem. Int. Ed.* **2013**, *52*, 11114–11118. **DOI:**10.1002/anie.201305492
16. M. Žabka, R. Šebesta, *Molecules* **2015**, *20*, 15500–15524. **DOI:**10.3390/molecules200915500
17. S. Vera, A. García-Urricelqui, A. Mielgo, M. Oiarbide, *Eur. J. Org. Chem.* **2023**, *26*, e202201254. **DOI:**10.1002/ejoc.202201254
18. H.-Y. Wang, Z. Chai, G. Zhao, *Tetrahedron* **2013**, *69*, 5104–5111. **DOI:**10.1016/j.tet.2013.04.079
19. J. Novacek, M. Waser, *Eur. J. Org. Chem.* **2014**, *2014*, 802–809. **DOI:**10.1002/ejoc.201301594
20. H. Wang, *Catalysts* **2019**, *9*, 244. **DOI:**10.3390/catal9030244
21. M. Waser, M. Winter, C. Mairhofer, *Chem. Rec.* **2023**, *23*, e202200198. **DOI:**10.1002/tcr.202200198
22. S. Ričko, F. Požgan, B. Štefane, J. Svete, A. Golobič, U. Grošelj, *Molecules* **2020**, *25*, 2978. **DOI:**10.3390/molecules25132978
23. U. Grošelj, S. Ričko, J. Svete, B. Stanovnik, *Chirality* **2012**, *24*, 412–419. **DOI:**10.1002/chir.22035
24. S. Ričko, A. Golobič, J. Svete, B. Stanovnik, U. Grošelj, *Chirality* **2015**, *27*, 39–52. **DOI:**10.1002/chir.22386
25. S. Ričko, J. Svete, B. Štefane, A. Perdih, A. Golobič, A. Meden, U. Grošelj, *Adv. Synth. Catal.* **2016**, *358*, 3786–3796. **DOI:**10.1002/adsc.201600498
26. S. Ričko, A. Meden, A. Ivančič, A. Perdih, B. Štefane, J. Svete, U. Grošelj, *Adv. Synth. Catal.* **2017**, *359*, 2288–2296. **DOI:**10.1002/adsc.201700539
27. T. Okino, Y. Hoashi, F. Furukawa, X. Xu, Y. Takemoto, *J. Am. Chem. Soc.* **2005**, *127*, 119–125. **DOI:**10.1021/ja044370p
28. CrysAlis PRO, Agilent Technologies UK Ltd.: Yarnton, UK, **2011**.
29. O. V. Dolomanov, L. J. Bourhis, R. J. Gildea, J. A. K. Howard, H. Puschmann, *J. Appl. Cristallogr.* **2009**, *42*, 339–341. **DOI:**10.1107/S0021889808042726
30. G. M. Sheldrick, *Acta Crystallogr. A* **2008**, *64*, 112–122. **DOI:**10.1107/S0108767307043930
31. G. M. Sheldrick, *Acta Crystallogr. Sect. Found. Adv.* **2015**, *71*, 3–8. **DOI:**10.1107/S2053273314026370
32. G. M. Sheldrick, *Acta Crystallogr. Sect. C Struct. Chem.* **2015**, *71*, 3–8. **DOI:**10.1107/S2053229614024218
33. C. F. Macrae, P. R. Edgington, P. McCabe, E. Pidcock, G. P. Shields, R. Taylor, M. Towler, J. van de Streek, *J. Appl. Crystallogr.* **2006**, *39*, 453–457. **DOI:**10.1107/S002188980600731X
34. A. L. Spek, *J. Appl. Crystallogr.* **2003**, *36*, 7–13. **DOI:**10.1107/S0021889802022112
35. S. Sopeña, E. Martin, E. C. Escudero-Adán, A. W. Kleij, *ACS Catalysis* **2017**, *7*, 3532–3539. **DOI:**10.1021/acscatal.7b00475
36. A. E. Aydin, S. Culha, *Chirality* **2021**, *33*, 106–114. **DOI:**10.1002/chir.23295

Povzetek

V petih sinteznih korakih so bili iz kafre pripravljeni štirje bifunkcionalni, nekovalentni amin-skvaramidni organokatalizatorji. Stereokemija pripravljenih katalizatorjev je bila temeljito analizirana z različnimi spektroskopskimi tehnikami. Organokatalitska aktivnost katalizatorjev je bila ovrednotena v modelni reakciji Michaelove adicije acetilacetona na *trans*-β-nitrostiren. Adicijski produkt je nastal s popolno konverzijo in z enantioselektivnostjo do 77 % *ee*. Pri reakciji acetilacetona na *trans*-β-nitrostiren se v prisotnosti 2-*ekso*-3-*endo* katalizatorjev tvori večinski (*S*)-enantiomer, v prisotnosti 2-*endo*-3-*endo* katalizatorjev pa večinski (*R*)-enantiomer.

Scientific paper

Synthesis, Characterization and Biological Activity Evaluation of Novel Quinoline Derivatives as Antibacterial Drug

Maryam Jamaal Kassar[1] and Mohammed Oday Ezzat *,[2]

[1] *Department of Chemistry, College of Education for Pure Sciences, University of Anbar, Ramadi, Anbar, Iraq.*

[2] *Department of Chemistry, College of Education for Women, University of Anbar, Ramadi, Anbar, IRAQ.*

** Corresponding author: E-mail: edw.mohamed_oday@uoanbar.edu.iq.*

Received: 09-27-2023

Abstract

Quinoline and its derivatives are a family with unique medicinal properties, including antibacterial effects. It was assumed that the four quinoline derivatives **1**, **2**, **3** and **4** had significant activity against pathogenic bacteria. These compounds were synthesized and characterized by TLC, IR, ^{1}H NMR, and ^{13}C NMR analyses. The biological activity of compounds was determined as inhibition zone (IZ) in mm. For compound **1** IZ was 19 ± 0.22 against *Klebsiella pneumoniae*, IZ was 18 ± 0.22 against *Bacillus subtilis*, and IZ was 17 ± 0.22 against *Staphylococcus aureus*. **2** displayed IZ of 18 ± 0.22 against both *Klebsiella pneumoniae* and *Bacillus subtilis*. **3** showed IZ of 17 ± 0.22 against *Staphylococcus aureus*. **4** displayed IZ of 21 ± 0.22, thus showing a higher inhibitory activity against *Escherichia coli*, than ciprofloxacin. These results demonstrate the potential of the synthesized compounds to work as antibacterial drugs against these strains by inhibiting or deactivating the target proteins.

Keywords: Quinoline derivatives; drug-resistant; pathogenic bacteria; *Klebsiella pneumoniae*; *Escherichia coli*.

1. Introduction

Bacteria are single-celled micro-organisms that exhibit great morphological diversity with dimensions ranging from 0.5–5 μm. There are only a few types of bacteria that cause disease. These types are called pathogens. Bacteria that inhabit the body naturally and peacefully can sometimes cause disease by producing harmful substances, invading tissues, or both. Among the most important bacterial diseases that may affect some individuals are cholera, diphtheria, dysentery, plague, pneumonia and tuberculosis. The most common and deadly bacterial diseases are respiratory infections and tuberculosis infection, which alone kill two million people each year.[1] Antibacterial drugs are antimicrobial compounds covering a range of effective medications that fight bacterial infections by killing or stopping them from reproducing.

The resistance to antibacterial drugs develops in some types of bacteria due to the acquisition of genes from other bacteria that have become resistant to antibacterial drugs or by mutations in the genes. Genes that enable bacteria to resist antibacterial drugs can be passed on to subsequent generations of the same bacteria, or sometimes to other types.[2] The more an antibacterial drug is used, the greater is the risk of developing resistance to it. For this reason, doctors try not to use antibiotics, unless necessary. Antibiotic-resistant bacteria can also be passed from person to person, becoming widespread globally in a relatively short period. They can also be transmitted from humans to animals, including those on farms.[3]

Among the various medicines, herbs,[4] nanoantibiotics,[5] and heterocyclic organic compounds, quinoline is an important building block in the construction of new medicinal drugs. It is nontoxic to humans by oral absorption and inhalation.[6] Quinolones are one of the most significant groups of antibacterial agents discovered in the last 50 years.[7] The development of quinolones dates back to the 1960s, when George Lesher discovered nalidixic acid by accident during the production of the antimalarial compound chloroquine. Then FDA (Food and Drug Administration) approved this compound for the urinary tract infections and against Gram-negative bacteria.[8] By adding fluorine, the fluoroquinolone family appeared, then FDA documented more than twenty compounds of this family

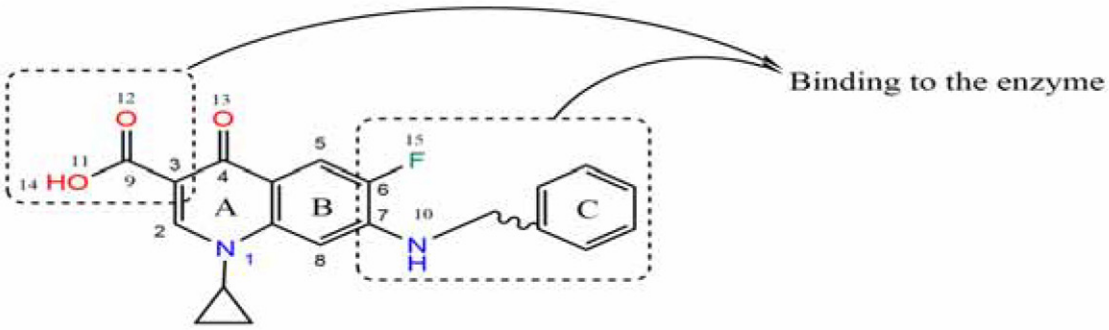

Figure 1. Enzymatic activity center in the fluoroquinolones.

circulating in the market with antimicrobial effects 1000 times stronger than nalidixic acid.[9] Fluorine's key features, at the position 6 (Figure 1), can influence pharmacological, pharmacodynamic and pharmacokinetic effects, as well as biological activity. Due to its electronic, lipophilic, and steric properties, including its strong electronegativity, low polarizability, solubility, hydrogen-bonding, tiny size, and steric effects, the fluorine atom is a significant constituent generally in drug design, particularly in quinolones.[10]

The incorporation of nitrogen into the ring at the position 7, fluoroquinolones have potent activity against Gram-positive respiratory pathogens. The use of a small additional groups at the position 8, such as methoxy and halide, increases the water solubility and anaerobic activity; in some cases it is even possible to switch from intravenous to oral application. When phototoxicity is considered, the methoxy group is preferred over the halide to avoid side effects as well as it is possible that its effectiveness lasts longer, thus reducing the effects of mutations.[11] Finally, the significant effect of the cyclopropyl group cannot be neglected for improve activity of the compounds.[12]

Because of the side effect of antibiotic drugs like quinoline compounds, there is a need for continuous design and development towards the goal of reducing these side effects (emerging of antibacterial resistance) hence the synthesis of novel quinoline derivatives is becoming increasingly essential.

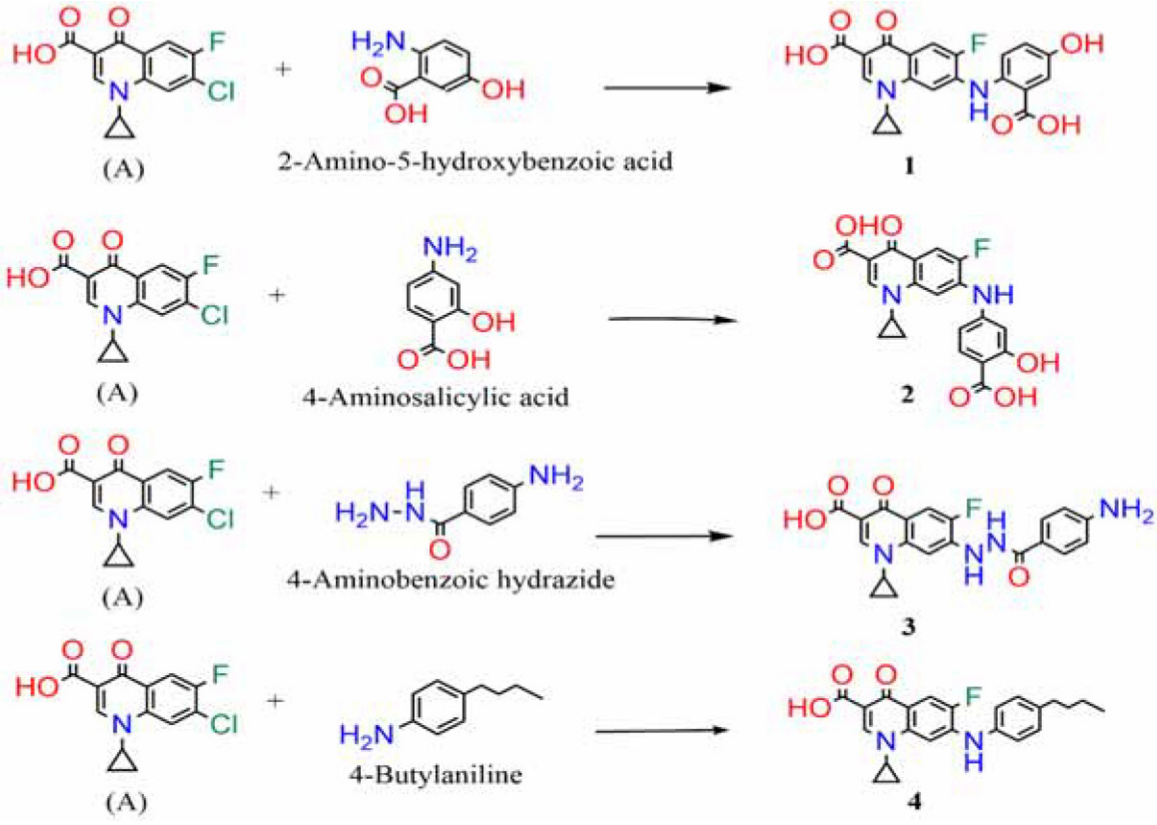

Scheme 1. The synthesis of compounds **1**–**4**.

In this study, four quinoline derivatives: **1**, **2**, **3** and **4** were synthesized, being part of our theoretical study in the research (Kassar and Ezzat, 2023).[13] Characterization of the synthesized compounds was carried out by using melting point determination, pH, TLC, IR, ^{1}H NMR and ^{13}C NMR spectroscopy and then the study of the biological activity was performed.

2. Materials and Methods

All of the chemicals used in this research were of the maximum purity obtainable, and they were used directly from the producers without any further processing.

2. 1. Synthesis

281.67 mg (1 mmol) of 7-chloro-1-cyclopropyl-6-fluoro-1,4-dihydro-4-oxoquinoline-3-carboxylic acid (**A**) were weighed with a sensitive balance, then placed in a round-bottom flask with 10 mL of methanol. To synthesize **1**, 153.14 mg (1 mmol) of 2-amino-5-hydroxybenzoic acid were weight and added to **A**. The solution was heated under reflux while stirring for 2 h. Compound **2** was synthesized by weighting and adding 151.17 mg (1 mmol) of 4-aminobenzoic hydrazide to **A** to yield **2**, followed by the same steps as for the synthesis of **1**. Compound **3** was obtained by adding 153.14 mg (1 mmol) of 4-aminosalicylic acid to **A** followed by the same steps as for the synthesis of **1**. To yield product **4**, 0.17 mL of 4-butylaniline was used, followed by the same steps as for the synthesis of **1** (Scheme 1). After the reaction was finished, the product was placed in a blast drying oven FCD-3000 at 50 °C with a fan for 1 h to allow the methanol to evaporate and the product to dry. The experiment was repeated with dimethyl sulfoxide (DMSO) as the solvent, and the products were allowed to precipitate for 15 days.[14]

2. 2. Characterization

Thin-layer chromatography (TLC). Several solvent systems were tested for TLC on Echo silica gel F254 plates to monitor the reaction. The most suitable were tetrahydrofuran : cyclohexane 7 : 3 (solvent system I), and acetone : cyclohexane 5 : 5 (solvent system II). The spots were detected by using a UV lamp. Retention factors (R_f) and relative lipophilicities (R_m) being log [1 – R_f/R_f]) were determined.

Melting point measurements. The melting points of the products was determined by Electro-thermal Stuart melting point apparatus of finely powdered samples in open capillary tubes with one side closed with a heat source.

Infrared spectroscopy (IR). 2 mg of the products were dried in a blast drying oven at 50 °C. Then, from each compounds, an IR disc was prepared individually with 200 mg of dried KBr. Subsequently, the IR spectrum was recorded within the range of 400 cm^{-1} to 4000 cm^{-1} in the Department of Chemistry's research lab at the University of Anbar's College of Education for Women.

Nuclear Magnetic Resonance (NMR) Spectroscopy. ^{1}H and ^{13}C NMR spectra for the prepared compounds were recorded in DMSO-d_6 using a Bruker 400 MHz and a Jeol Lambda 500 MHz instrument at the research laboratory of the Department of Chemistry at the College of Education for Pure Sciences – University of Basra. Chemical shifts are given in ppm (δ). Multiplet, singlet, doublet, triplet, and quartet are denoted by the letters m, s, d, t, and q, respectively.

2. 3. Biological Activity

Two kinds of bacteria were used, Gram-negative bacteria *Escherichia coli* and *Klebsiella pneumoniae*. As Gram-positive bacteria, *Staphylococcus aureus* and *Bacillus subtilis* were used. These bacteria were diagnosed and cultured on eosin methylene blue (EMB) and nutrient agar medium for use in this experiment, and in measuring the deactivating capacity of the synthesized quinoline derivatives.

The deactivating capacity of the isolated bacteria of the compounds prepared, was tested by using the holes method. In this method the holes were saturated with (10 μL) of 1·10^{-4} M of the compounds **1**, **2**, **3**, **4** and ciprofloxacin, then left for about 15 min in order to spread on the medium. Sequentially, incubated at 25 °C for 24 h. The deactivation diameters were measured by a special ruler designed for this purpose.

3. Results

3. 1. General Characteristics

Compound 1. $C_{20}H_{15}FN_2O_6$: greyish brown powdery product, yield 3.226 g (81%); R_f = 0.85, R_m = –0.75 (solvent system I). R_f = 0.61, R_m = –0.194 (solvent system II). m.p. 228–230 °C. FTIR: ν 2500–3080, 1726, 1610, 1586, 1497, 1250–1400, 3227 cm^{-1}. ^{1}H NMR (400 MHz, DMSO-d_6): δ 14.61 (s, 1H), 8.74 (s, 1H), 8.65–8.60 (m, 2H), 8.50 (d, J = 6.1 Hz, 1H), 8.30 (s, 1H), 8.25 (s, 2H), 8.18 (d, J = 9.0 Hz, 1H), 8.06 (s, 1H), 7.09 (d, J = 2.9 Hz, 2H), 6.77 (dd, J = 8.7, 2.8 Hz, 2H), 6.60 (d, J = 8.8 Hz, 2H), 3.84 (q, J = 5.4 Hz, 1H), 1.32 (t, J = 6.6 Hz, 2H), 1.21 (d, J = 4.2 Hz, 2H). ^{13}C NMR (101 MHz, DMSO-d_6): δ 177.18, 177.15, 169.86, 165.82, 156.82, 154.34, 149.73, 147.02, 145.25, 138.65, 127.67, 127.47, 125.92, 125.85, 123.49, 121.69, 118.13, 115.65, 112.44, 112.21, 110.38, 107.94, 40.54, 40.33, 40.12, 39.91, 39.71, 39.50, 39.29, 36.78, 8.14.

Compound 2. $C_{20}H_{15}FN_2O_6$: yellowish brown powdery product, yield 3.345 g (84%); R_f = 0.97, R_m = –1.50 (solvent system I). R_f = 0.45, R_m = –0.087 (solvent system II). m.p. 193–196 °C. FTIR: ν 3094, 3385, 1726, 3499, 1610

cm^{-1}. ^{1}H NMR (400 MHz, DMSO-d_6) δ (ppm): 14.62 (s, 1H), 11.38 (s, 1H), 8.75 (s, 1H), 8.52 (d, J = 6.1 Hz, 1H), 8.19 (d, J = 9.0 Hz, 1H), 7.41 (d, J = 8.6 Hz, 1H), 6.11–5.89 (m, 3H), 3.86 (tt, J = 7.6, 4.0 Hz, 1H), 1.33 (t, J = 6.5 Hz, 2H), 1.21 (p, J = 5.1 Hz, 2H). ^{13}C NMR (101 MHz, DMSO-d_6) δ (ppm): 177.18, 177.16, 172.56, 165.81, 163.88, 158.51, 156.82, 156.27, 154.34, 150.19, 149.75, 138.67, 131.90, 129.87, 127.67, 127.48, 125.93, 125.86, 121.72, 112.44, 112.22, 107.94, 106.67, 105.89, 103.77, 101.43, 100.54, 98.94, 40.56, 40.35, 40.15, 39.94, 39.73, 39.52, 39.31, 36.80, 8.15.

Compound 3. $C_{20}H_{17}FN_4O_4$: off white powdery product, yield 3.130 g (79%); R_f = 0.81, R_m = –0.62 (solvent system I). R_f = 0.61, R_m = –0.194 (solvent system II). m.p. 208–211 °C. FTIR: ν 3434, 3355, 3306, 3227, 2600–3031, 1734, 1610 cm^{-1}. ^{1}H NMR (400 MHz, DMSO-d_6): δ 9.28 (s, 2H), 8.75 (s, 1H), 8.51 (d, J = 6.1 Hz, 1H), 8.19 (d, J = 9.0 Hz, 1H), 7.53 (d, J = 8.3 Hz, 4H), 6.52 (d, J = 8.4 Hz, 4H), 5.59 (s, 3H), 3.89–3.82 (m, 1H), 1.33 (d, J = 6.7 Hz, 2H), 1.21 (q, J = 4.0, 3.4 Hz, 2H). ^{13}C NMR (101 MHz, DMSO-d_6): δ 177.19, 177.16, 166.92, 165.83, 156.83, 154.35, 151.99, 149.75, 138.68, 128.88, 127.68, 127.48, 125.94, 125.87, 121.71, 120.37, 113.06, 112.45, 112.22, 107.96, 40.57, 40.36, 40.15, 39.94, 39.74, 39.53, 39.32, 36.79, 8.15.

Compound 4. $C_{23}H_{23}FN_2O_3$. light brown powdery product, yield 2.997 g (76%); R_f = 0.93, R_m = –1.12 (solvent system I). R_f = 0.74, R_m = –0.454 (solvent system II). m.p. 235–238 °C. FTIR: ν broad and very strong band 2800–3500, 2967, 2858, 1614, 1561, 1395, 1313, 1211. ^{1}H NMR (400 MHz, DMSO-d_6): δ 8.81 (s, 1H), 8.57 (d, J = 6.1 Hz, 1H), 8.25 (d, J = 8.9 Hz, 1H), 6.87 (d, J = 8.1 Hz, 1H), 6.53 (d, J = 8.1 Hz, 1H), 3.92 (dt, J = 7.2, 3.3 Hz, 1H), 2.57 (d, J = 1.7 Hz, 2H), 2.43 (t, J = 7.6 Hz, 1H), 1.50 (p, J = 7.4 Hz, 1H), 1.44–1.22 (m, 6H), 0.92 (*t*, J = 7.3 Hz, 2H). ^{13}C NMR (101 MHz, DMSO-d_6): δ 177.19, 177.16, 165.86, 156.83, 154.35, 149.76, 146.69, 138.68, 138.66, 129.79, 129.03, 127.69, 127.49, 125.93, 125.86, 121.72, 114.45, 112.44, 112.21, 107.96, 40.52, 40.31, 40.10, 39.89, 39.68, 39.47, 39.26, 36.79, 34.50, 34.10, 22.14, 14.29, 8.14.

4. Discussion

4. 1. Characterization of Compound 4

The synthesis of the selected fluroquinolones was demonstrated by IR analysis, which revealed significant absorption bands. Firstly, a broad and very strong band between 2800–3500 cm^{-1} belongs to the carboxylic group. Medium 2967 cm^{-1} to the stretching vibration of the methyl group, while small 2858 cm^{-1} to the stretching of ethylene group. Medium band at 1614 cm^{-1} corresponds to the α,β-unsaturated ketone, 1561 cm^{-1} is N–H bending, 1395 cm^{-1} O–H bending of carboxylic acid, 1313 cm^{-1} is C–F stretching, medium 1211 cm^{-1} C–N stretching (Figure S1).

The synthesized compounds were characterized using **^{1}H** NMR and **^{13}C** NMR spectroscopy, Characteristic signals for compound **4** in its ^{1}H NMR spectrum are: δ 0.93 to HC29 (t, 2H; H_2C28), 1.25 to H_2C17 (q, 3H; H_2C16, HC15), 1.32 to H_2C28 (m, 5H: H_3C29, H_2C27), 6.53 to HC22,24 (d, 1H; HC21,HC25), 8.24 to HC6 (d, 1F; FC1) 8.8 to HC8 (s). Signals between δ 3.3–3.5 corresponds to water and may indicate sample wetting, as it is known that DMSO is very hygroscopic, while a signal at δ 2.5 is non-deuterated DMSO. In this case, the NH signal either disappears completely or may appear as a broad signal extremely close to the solvent signals (Figure S2).

Characteristic signals for compound **4** in its ^{13}C NMR spectrum are: δ 177.19 and 165.86 to carbonyl C10 and C12, (d, 156.83) to C1, 36.79 to C26, 34.10 to C27, 22.14 to C28, 14.29 to C29, 8.14 to C16 and C17 (Figure S3).

4. 2. Characterization of Compound 1

The absorption bands in IR spectrum of **1** are depicted in Figure S4: the broadened bands at lower frequencies from 2500 to about 3080 cm^{-1} are for the stretching vibration of carboxylic hydroxyl, the C=O bond is weakened by intermolecular hydrogen bonding, lowering the stretching frequency to 1726 cm^{-1}. The band at 1610 cm^{-1} belongs to the cyclic carbonyl, at 1586 cm^{-1} is due to the stretching vibration of the aromatic C=C, and at 1497 cm^{-1} is due to the C–O. The variation in the electronic environment; causes the bond's absorption of C–N shift depending on its location, leading the band to expand from 1250 cm^{-1} to 1400 cm^{-1}. Finally, the characteristic 3227 cm^{-1} band is caused by the stretching vibration of *para*-hydroxyl, with the disappearance of the secondary N–H, often included within the domain of the carboxyl group.

Characteristic signals for compound **1** in its ^{1}H NMR spectrum are: δ 3.88 to HC15 (m, 4H; H_2C16, H_2C17), 7.1 to HC24 (s), 8.19 to HC6 (d, 1F; FC1), 8.50 to HC3 (d, 1H; NH), 8.63 to HO26 (s), 14.6 to HO28 carboxylic proton (Figure S5).

Characteristic signals for compound **1** in its ^{13}C NMR spectrum are: 177.18 to C10, 169.86 to C27, 165.82 to C12, 156.82 to C23, (d,154.34) to C1, 149.73 to C8, 147.02 to C20 (Figure S6).

4. 3. Characterization of Compound 2

Despite having the same functional groups as **1**, IR spectrum of compound **2** revealed considerable variances due to the varied site-substitution on the benzene ring. The intensity of the carboxylic hydroxyl band was reduced by the presence of the hydroxyl close to the carboxyl. The degree of H-bonding determines the position and shape of this band.

The original O–H bond is lengthened during hydrogen bonding. As a result, the bond is weakened, the bond force constant is reduced, as well as the stretching frequency. The *ortho*-carboxylate hydroxyl is detected at 3094

Table 1. Inhibitory activity of the synthesized compounds and comparison with ciprofloxacin.

	Diameter of inhibition zone (in mm) ±0.22 mm			
Compound	***E. coli***	***S. aureus***	***B. subtilis***	***K. pneumoniae***
1	17	17	18	19
2	14	13	18	18
3	16	17	16	13
4	21	13	15	14
Ciprofloxacin	19	16	19	17

cm^{-1}, the secondary N–H (single band) is recorded at 3385 cm^{-1}, the carbonyl is noted at 1726 cm^{-1}, and the overton band for the same group is noted at 3499 cm^{-1}, while 1610 cm^{-1} corresponds to the cyclic carbonyl (Figure S7).

Characteristic signals for compound **2** in its ^{1}H NMR spectrum are: δ 1.20 to H_2C17 (q, 3H; H_2C16, HC15. 6.77 to HO29, 8.51 to HC6 (d, 1F; FC1), 11.38 to HO13 (s) and 14.62 to HO27 of carboxyl (s), 3.40 and 2.51 to water and DMSO, respecitvely (Figure S8).

Characteristic signals for compound **2** in its ^{13}C NMR spectrum are: 177.18, 172.56 and 165.81 to C10, C26 and C12 of carbonyl respectively, (d, 158.51) to C1, 36.80 to C15, 8.15 to C16 and C17 (Figure S9).

4. 4. Characterization of Compound 3

IR spectrum of compound **3** (Figure S10) shows the band at 3434 cm^{-1} belonging to the N–H adjacent to the carbonyl, where the electronic withdrawal of the carbonyl increases the bond strength constant, pushing the band towards a higher frequency. The primary amine on the benzene ring at the *para*-site (dual band) is represented by the 3355 cm^{-1} and 3306 cm^{-1} bands. The 3227 cm^{-1} is for N–H bound to the quinolone ring. The broad band extending from 2600–3031 cm^{-1} is for the quinolone's terminal carboxylate, 1734 cm^{-1} is due to the quinolone ring ketone, 1610 cm^{-1} to the aniline ring-linked ketone.

Characteristic signals for compound **3** in its ^{1}H NMR spectrum are: δ 1.20 to H_2C17 (q, 3H; H_2C16, HC15), 5.59 to HN29 (s), 6.53 to HC25 and HC27 (d, 1H; HC24, HC28), 9.28 to HN20 (s), 3.40 and 2.51 correspond to H_2O and DMSO which cause H-N19 disappearance (Figure S11).

Characteristic signals for compound **3** in its ^{13}C NMR spectrum are: 177.19 to C10, 166.92 to C12, 165.83 to C21, 156.83 to C26, (d,154.35) to C1 (Figure S12).

5. Biological Activity

The antibacterial activity of the synthesized compounds was studied on four previously diagnosed isolates of Gram-positive (*S. aureus* and *B. subtilis*) and Gram-negative (*E. coli* and *K. pneumoniae*) bacteria. Experimental results for the compound **1** showed the following inhibition zones (IZ): 19 ± 0.22 mm against *K. pneumoniae*, 18 ± 0.22 mm against *B. subtilis*, and 17 ± 0.22 mm against *S. aureus*. Compared with ciprofloxacin, the inhibitory activity of the compound **1** was higher against *K. pneumoniae* and *S. aureus*, but lesser against *B. subtilis* as shown in Table 1. In designing drugs with fewer side effects, this means that the compound's influence on non-pathogenic bacteria is lessened, which is an important consideration.

For compound **2**, experimentally, the effect was equal by IZ 18 ± 0.22 mm. Compared with ciprofloxacin, the inhibitory activity of **2** was higher against *K. pneumoniae*, and lesser against *B. subtilis* as shown in Table 1. Compound **3** showed a higher inhibitory activity against *S. aureus* (IZ 17 ± 0.22 mm), than ciprofloxacin (Table 1). Compound **4** showed a higher inhibitory activity against *E. coli* (IZ 21 ± 0.22 mm), than that of ciprofloxacin (Table 1).

These results demonstrate the potential of the synthesized compounds as antibacterial drugs against these strains by inhibiting or activating the target proteins.

6. Conclusions

Four novel quinoline derivatives **1**, **2**, **3** and **4** were successfully synthesized and characterized by TLC, IR, ^{1}H and ^{13}C NMR spectroscopy confirming the success of the synthetic procedures. In comparison to ciprofloxacin, *in vitro* evalution of the synthesized compounds showed that two of them demonstrated good antibacterial activity, suggesting the potential for their future use as an alternative treatment after undertaking the necessary research.

Supporting Information

Scans of IR, ^{1}H and ^{13}C NMR spectra of compounds **1**–**4**.

7. References

1. F. Godoy-Vitorino, *Ann. Transl. Med.* **2019**, *7(14),* 342–342. **DOI:**10.21037/ATM.2019.06.56
2. C. L. Ventola, *Pharm. Ther.* **2015**, *40(4)*, 277. **DOI:**Article.

3. X.-F.Shang, S. L. Morris-Natschke, Y.-Q. Liu, X. Guo, X.-S. Xu, M. Goto, J.-C. Li, G.-Z. Yang, K.-H. Lee, *Med. Res. Rev.* **2018**, *38(3)*, 775. **DOI:**10.1002/MED.21466.
4. A. Alabdali, M. Kzar, S. Chinnappan, R. Mogana, S. I. Khalivulla, H. Rahman, B. M. Abd Razik, *Res. J. Pharm. Technol.* **2021**, *14(12)*, 6741–6746. **DOI:**10.52711/0974-360X.2021.01164.
5. A. Y. M. Alabdali, M. S. Kzar, S. Chinnappan, R. R. Mani, M. Selvaraja, K. J. Wen, L. Sally, F. W. Kuang, *Int. J. App. Pharm.* **2022**, pp 34–39. **DOI:**10.22159/ijap.2022v14i3.43508.
6. M. De Souza, *Mini-Rev. Med. Chem.* **2005**, *5(11)*, 1009–1017. **DOI:**10.2174/138955705774575246.
7. M. G. Ferlin, G. Chiarelotto, F. Antonucci, L. Caparrotta, G. Froldi, *Eur. J. Med. Chem.* **2002**, *37(5)*, 427–434. **DOI:**10.1016/S0223-5234(02)01355-7.
8. T. D. M. Pham, Z. M. Ziora, M. A. T. Blaskovich, *MedChemComm* **2019**, *10*, 1719–1739. **DOI:**10.1039/C9MD00120D.
9. V. T. Andriole. *Clin. Infect. Dis.* **2005**, *41(2)*, S113–S119. https://www.jstor.org/stable/4463376.
10. K. J. Aldred, R. J. Kerns, N. Osheroff, *Biochemistry* **2014**, *53*, 1565–1574. **DOI:**10.1021/BI5000564.
11. J. J. Champoux, *Ann. Rev. Biochem.* **2003**, *70*, 369–413. **DOI:**10.1146/ANNUREV.BIOCHEM.70.1.369.
12. R. Musiol, J. Jampilek, V. Buchta, L. Silva, H. Niedbala, B. Podeszwa, A. Palka, K. Majerz-Maniecka, B. Oleksyn, J. Polanski, *Bioorg. Med. Chem.* **2006**, *14(10)*, 3592–3598. **DOI:**10.1016/j.bmc.2006.01.016
13. M. J. Kassar, M. O. Ezzat, *Egypt. J. Chem.* **2023**, *66(5)*, 119–128. **DOI:**10.21608/EJCHEM.2022.151949.6577.
14. Y. Mirzaie, J. Lari, H. Vahedi, M. Hakimi, *Russ. J. Gen. Chem.* **2016**, *86(12)*, 2865–2869. **DOI:**10.1134/S1070363216120525.

Povzetek

Kinolin in njegovi derivati so družina spojin s posebnimi medicinskimi lastnostmi, vključno s protibakterijskimi učinki. Predvideli smo, da bodo štirje kinolinski derivati (spojine **1**, **2**, **3** in **4**) imeli opazen učinek na patogene bakterije. Spojine smo sintetizirali in jih karakterizirali s TLC, IR, ^{1}H NMR in ^{13}C NMR spektroskopijo. Biološko aktivnost spojin smo določili kot območje inhibicije (IZ) v mm. Za spojino **1** je IZ proti *Klebsiella pneumoniae* znašal 19 ± 0.22, proti *Bacillus subtilis* je bil 18 ± 0.22, proti *Staphylococcus aureus* pa 17 ± 0.22. Spojina **2** je proti *Klebsiella pneumoniae* in proti *Bacillus subtilis* izkazala IZ 18 ± 0.22. Za spojino **3** je IZ proti *Staphylococcus aureus* znašal 17 ± 0.22. Spojina **4** je proti *Echerichia coli* izkazala IZ vrednost 21 ± 0.22, kar predstavlja večjo inhibitorno aktivnost kot ciprofloksacin. Rezultati kažejo, da so sintetizirane spojine potencialno uporabne proti tem vrstam bakterij, saj inhibirajo ali deaktivirajo izbrane proteine.

Scientific paper

Validation of an Isocratic HPLC Method for Simultaneous Estimation of Major Phytosterols in *Prunus spinosa* L. Extracts

Hurija Džudžević-Čančar,[1,*] Alema Dedić-Mahmutović,[1] Amra Alispahić[1] and Ivan Špánik[2]

[1] *Department of Chemistry in Pharmacy, Faculty of Pharmacy, University of Sarajevo, Zmaja od Bosne 8, 71000 Sarajevo, Bosnia and Herzegovina*

[2] *Institute of Analytical Chemistry, Faculty of Chemical and Food Technology, Slovak University of Technology in Bratislava, Radlinského 2101/9, 812 37 Staré Mesto, Bratislava, Slovakia*

* *Corresponding author: E-mail: hurija.dzudzevic-cancar@ffsa.unsa.ba*

Received: 04-17-2023

Abstract

This study aimed to develop a rapid method for the separation of stigmasterol, campesterol and β-sitosterol in *Prunus spinosa* L. (blackthorn) fruit extracts by HPLC system. Samples were prepared by Soxhlet extraction method and separated on a C18 column using acetonitrile-methanol mobile phase and photodiode array detector (PDA). The optimized method resulted in a linear calibration curve ranging from 1.70–130 μg mL^{-1} for all three phytosterols. Analyses of external phytosterol standards showed good linearity (R^2 of 0.998 to 0.999); LOD and LOQ were determined to be 0.32–9.30 μg mL^{-1} and 0.98–28.1 μg mL^{-1}, respectively. Repeatability and reproducibility precision analyses showed acceptable values of %RSD. β-sitosterol was the predominant phytosterol (51.53–81.03% of total) among all samples. Method validation parameters indicated that this analytical method can be applied for accurate and precise determination of campesterol, stigmasterol and β-sitosterol, in selected extracts.

Keywords: phytosterols; *Prunus spinosa* L. ethanolic extracts; HPLC; method validation.

1. Introduction

Prunus spinosa L., called blackthorn or sloe (Fig. 1), is a specie of flowering plant from the Rosaceae family. Blackthorn is a rather bushy tree with dark branches, hence the "black" thorn. In early spring it produces a five-petalled white flower, which is then replaced by deep blue-purple fruits. It blooms from March to April and ripens in October. Blackthorn is native to Europe and western Asia, but can also be found in New Zealand and eastern North America. Traditionally, blackthorn flowers and fruits have been used in various medicines, including tonics and syrups that "purify the blood", aid digestion and relieve rheumatism. Flowers, bark, leaves and fruits are astringent, depurative, diaphoretic, diuretic, laxative and stomachic.[1] Infusion of flowers is used in the treatment of diarrhoea (especially in children), bladder and kidney diseases.[2] Although not specifically mentioned for this species, all members of the genus contain amygdalin and prunasin, substances that break down in water to form hydrocyanic acid (cyanide or prussic acid). In small amounts, this highly toxic compound stimulates breathing, improves digestion and gives a sense of well-being.[3]

Phytosterols are a group of cholesterol-like compounds found naturally in plants. They differ from cholesterol by their carbon side chains and the presence or absence of double bonds. So far, between 200–300 different types of phytosterols have been successfully isolated and identified in botanical sources, where campesterol, stigmasterol and β-sitosterol (Fig. 2) have been found to be dominant and most frequently identified.[4] Phytosterols have attracted much attention due to their nutritional properties and biological effects such as inhibition of intestinal cholesterol absorption, lowering of blood low-density lipoprotein (LDL), anti-inflammatory and anti-cancer effects. Today, they are widely used in pharmaceutical products, nutritional supplements and cosmetics.[3–6]

Fig. 1. *Prunus spinosa* L. leaves, flowers and fruit

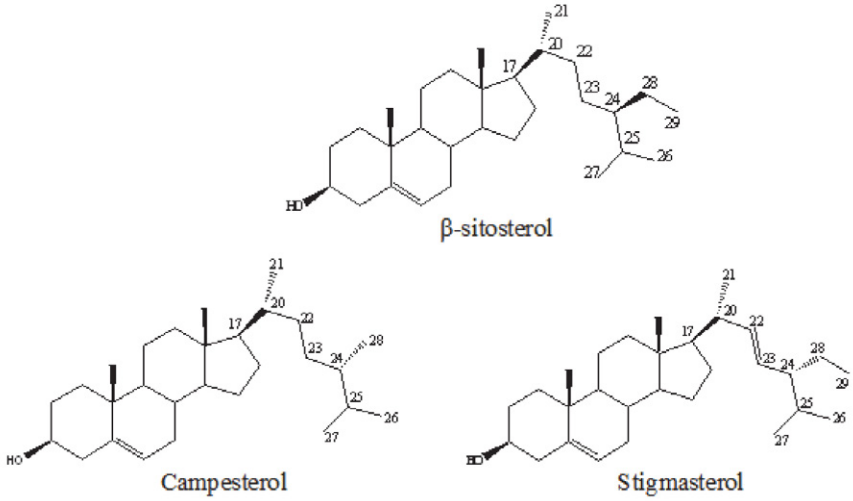

Fig. 2. Structural formulae of *Prunus spinosa* L. major phytosterols

The official methods for the separation and quantitative analysis of phytosterols are conventionally based on gas chromatography (GC). However, it usually requires chemical derivatization for a favourable peak shape, better sensitivity and resolution, and higher stability for labile unsaturated sterols.[7] In general, liquid chromatography (LC) has better operating conditions, including lower temperatures and pressure conditions for column separation, as well as several available detectors and has been widely used for sterol separation.[8–12] Rocco and Fanali[13] developed a nano-LC method for the determination of stigmasterol, campesterol and *β*-sitos-

terol in extra virgin olive oil, with good sensitivity and precision. Zarrouk et al.[14] and Fibigr et al.[15] reported on LC methods successfully applied to direct determination of sterols and lipids.

Until now, no studies on HPLC use for the separation of phytosterols from plant material and plant extracts in Bosnia and Herzegovina have been reported. The present study aimed to develop and validate a simple and rapid method for simultaneous separation of three major phytosterols, campesterol, stigmasterol and β-sitosterol, in plant extracts using HPLC system coupled to PDA detection. Furthermore, it was efficiently validated and used in phytosterol analysis in ethanolic extracts of *Prunus spinosa* L. fruit.

2. Materials and Methods

2. 1. Chemicals and Reagents

All reagents used in this study were of analytical grade. Standard compounds campesterol (99.6%), stigmasterol (98.1%) and β-sitosterol (98.6%) were purchased from Sigma-Aldrich, Chemie GmbH, Germany. Acetonitrile (ACN), ethanol (EtOH) and methanol (MeOH) were of HPLC grade and were obtained from Merck, Darmstadt, Germany. High-purity deionized water was prepared by a Milli-Q ultrapure purification system (Millipore, Billerica, Massachusetts, USA).

2. 2. Plant Material

Prunus spinosa L. plant material was collected from three different locations in Bosnia and Herzegovina (Borije, altitude 892 m, N43°51′16.60″, E18°28′55.33″, Vareš, altitude 739 m, N44°04′40.82″, E18°14′46.41″ and Trnovo, altitude 935 m, N43°41′19.37″ E18°22′34.39″) from March until November. Plant specimen was authenticated at the Department of Biology, Faculty of Science-University of Sarajevo, Sarajevo, Bosnia and Herzegovina.

2. 3. Sample Preparation

Blackthorn fruits were washed well, using tap water and distilled water. Extracts were prepared using Soxhlet extraction with ethanol as a solvent. In a Soxhlet apparatus, 100 g of fresh fruits were extracted at the boiling point of the solvent for 6 h. It was performed 12 extractions in total. The volumes of obtained extracts were reduced in a rotary evaporator (RV-10, IKA, Sigma Aldrich, Deutschland) to approximately 5–7 mL and evaporated to crude extracts in a vacuum concentrator (Thermo Fisher Savant, SPD1010, SpeedVac Concentrator). Extracts in triplicate were stored in glass vials at $T \approx 4.0$ °C and used for the quantification of phytosterols and further determination of biological activities.

2. 4. Standard Solutions and Calibration

The working standard solutions of sterols were prepared by dissolving the respective mass of phytosterols standard compounds in ethanol. A linear regression equation was prepared from seven increasing concentrations by diluting the stock solution in ethanol. A linear relationship between peak area and concentrations (1.70–130 μg mL^{-1}) was obtained, and the linear regression equation for each standard was used for phytosterol quantification in standard solutions during the method validation process and phytosterol quantification in samples.

Tab. 1. Optimization of chromatographic conditions

Mobile phase	Ratio [%, *v/v*]	Mode	Column	Flow rate [mL min^{-1}]	λ [nm]	Temp. [°C]	t_R [min] S	t_R [min] C	t_R [min] B
ACN	100	Isocratic	Symmetry C18 (4.6 mm × 150 mm, 5 μm)	1.00	210	30	16.98	17.9	19.26
MeOH	100	Isocratic	Symmetry C18 (4.6 mm × 150 mm, 5 μm)	1.00	210	30	13.10	13.45	14.00
ACN:MeOH	90:10	Isocratic	Symmetry C18 (4.6 mm × 150 mm, 5 μm)	1.00	210	30	17.32	18.19	19.66
ACN:MeOH*	80:20	Isocratic	Symmetry C18 (4.6 mm × 150 mm, 5 μm)	1.00	210	30	15.46	16.18	17.45
ACN:EtOH	95:5	Isocratic	Symmetry C18 (4.6 mm × 150 mm, 5 μm)	1.00	210	30	16.98	17.6	19.3
ACN:EtOH	60:40	Isocratic	Inertsustain C18 (4.6 mm × 250 mm, 5 μm)	1.00	210	30	11.45	11.51	12.65
ACN:EtOH	40:60	Isocratic	Inertsustain C18 (4.6 mm × 250 mm, 5 μm)	1.00	210	30	11.48	11.51	12.66
ACN:water	95:5	Isocratic	Inertsustain C18 (4.6 mm × 250 mm, 5 μm)	1.00	278	40	15.46	16.11	17.60

* Optimized conditions for chromatographic separation; t_R= Retention time; S-stigmasterol; C-campesterol; B- β-sitosterol.

2. 5. HPLC System and Conditions

Chromatographic conditions were optimized using different columns, flow rates and mobile phase compositions given in Tab. 1. In order to find the most suitable mobile phase and the most appropriate chromatogram for detection and separation of phytosterols in blackthorn extracts, it was necessary to optimize the method regarding the composition of the mobile phase. Several different mobile phases were applied because those used in the study of Kakade and Magdum (2012)[16] were not reproducible for the samples tested in this research. After optimization, the final solvent system ACN:MeOH (80:20, *v/v*) and a flow rate of 1.00 mL min^{-1} in the isocratic mode were selected because these gave good resolution and shape of the chromatographic peaks for the components of interest.

Phytosterols were qualitatively and quantitatively analysed using an Agilent HPLC system series 1200 (Agilent Technologies, USA), equipped with a solvent delivery unit, autosampler and column oven. A PDA detector was used to collect chromatograms and UV spectra. Chromatographic separation was performed using a Symmetry C18 column (Waters, USA) (150 × 4.6 mm, 5 µm) at 30.0 °C and an injection volume of 20 µL. The mobile phase was filtered through a 0.45 µm hydrophilic polypropylene membrane filter and degassed in an ultrasonic bath prior to HPLC injection. Quantification of campesterol, stigmasterol and *β*-sitosterol was performed using a PDA detector set at 210 nm. Identification and quantification of chromatographic peaks were confirmed by comparison of the retention time (t_R) of extracts and phytosterol standards. Calibration curves were constructed by analysing seven concentrations of phytosterol standards ranging from 1.70 to 130 µg mL^{-1}. All analyses were performed at least in triplicate.

2. 6. Validation of the HPLC Analytical Method

Method validation was performed according to the ICH (2013) guidelines.[17] Compound identification was based on retention time matching and co-injection with authentic standards under identical analytical conditions.

Linearity: The linearity range was evaluated by plotting the relative peak area of phytosterol versus the relative concentration. For phytosterol analysis, standard solutions were prepared in ethanol in concentration ranges of 1.70–130 µg mL^{-1} for campesterol, stigmasterol and *β*-sitosterol. Three replicates were made for each of the seven solutions prepared. The correlation coefficient (R^2) was calculated for linearity evaluation. *LOD* and *LOQ* were calculated according to the following equations:

$$\frac{3.3 \times SD}{S} \quad (1)$$

$$LOQ = \frac{10 \times SD}{S} \quad (2)$$

where, S is the slope of the calibration curve and SD is the standard deviation of the response (n = 10). The following method validation criteria were applied: curve equation (y = mx + b), correlation coefficient ($R \geq 0.999$), coefficient of determination ($R^2 \geq 0.980$).[18–21]

Precision: Repeatability and reproducibility, two different levels of precision, were determined. Repeatability (intraday precision) was obtained by analysing standard solutions of phytosterols five times in the same day in triplicate. The same standard solutions were analysed five times in five independent days (once per day in triplicate) to obtain reproducibility (interday precision). Mean values, standard deviation and coefficient of variation were determined. The precision of the phytosterol analysis was assessed by the calculated relative standard deviation-RSD (recommended %RSD ≤ 3.9%).[18–21]

Accuracy: The accuracy of phytosterol analysis was evaluated by performing a recovery test. All phytosterols (campesterol, stigmasterol and β-sitosterol) were added to *P. spinosa* extract samples at three different concentration levels (25, 50, 75 µg mL^{-1}). Spiked samples were then analysed and recovery was calculated by the following equation:

$$Recovery\ (\%) = \frac{S_{total\ phytosterols} - S_{phytosterols\ present}}{S_{spiked\ phytosterol}} \times 100 \quad (3)$$

where, $S_{\text{total phytosterols}}$ = total amount of specific analysed phytosterol in extract sample,
$S_{\text{phytosterols present}}$ = amount of specific phytosterol present in extract sample,
$S_{\text{spiked phytosterol}}$ = spiked amount of specific phytosterol.

2. 7. Quantification of Phytosterols from Ethanolic Extracts of Blackthorn Fruit

The optimized HPLC method was used to estimate the phytosterols content in ethanolic extracts of *P. spinosa* L. fruit collected from three different locations in Bosnia and Herzegovina. The solutions of each crude extract were prepared separately (10 mg mL^{-1}) in ethanol, and sample of 20 µL was subjected to HPLC analysis. The peak area responses were recorded under the optimized and validated chromatographic condition. The phytosterols content expressed as mass concentration was determined from the linear regression equations. The identification of campesterol, stigmasterol and *β*-sitosterol in extracts was carried out by comparison of t_R for phytosterol standard solutions and samples. Samples of standard solutions and extracts were stored in a dark and cold place ($T \approx 4.0$ °C) to avoid oxidative degradation.

3. Results and Discussion

3. 1. Optimization of Chromatographic Conditions – HPLC Method Development and Validation

In this work, a method based on HPLC separation combined with PDA detection has been optimised, vali-

dated and applied for phytosterol analysis in *Prunus spinosa* L. ethanolic extracts. An isocratic elution was chosen since it is simple, requires only one pump and minimizes the variation of baseline and ghost peaks. Various columns are available for HPLC systems, but the Symmetry C18 column (150 × 4.6 mm, 5 μm) was preferred because peak shape, selectivity, and resolution provided the best results using this column. Among the different mobile phases used, acetonitrile:methanol (80:20, *v/v*) was suitable for the analysis of campesterol, stigmasterol and *β*-sitosterol (Tab. 1), due to baseline normalisation and the best separation of the each of three phytosterols (Fig. 3). Furthermore, a flow rate of 1 mL min^{-1} and an injection volume of 20 μL, with UV detection at 210 nm, provided optimal conditions for the analysis of these phytosterols (Tab. 2).

Although various stationary phases and several isocratic programs were tested, at least two phytosterols were not separated using the columns except for Symmetry C18, on which sterol standard solutions were fully separated. Different co-solvents (methanol, ethanol, acetonitrile, and water) and/or ratios were evaluated to enhance the separation of the three phytosterols. The results showed that the best peak shape and resolution were achieved when acetonitrile/methanol, 80:20, *v/v* mixture was applied, with an isocratic elution mode.

Table 2. HPLC system parameters for an optimised analytical method

Column	Symmetry C18, 150×4.6 mm, 5 μm particle size
Flow rate	1 mL min^{-1}
Mobile phase	Acetonitrile:methanol (80:20, *v/v*)
Run time	50 min
Wavelength	210 nm
Temperature	30 °C
Injection volume	20 μL
Sample solvent	Methanol

With optimized method conditions analytes were very good separated, with resolution values between the main peaks ranging from 0.97 to 1.43 (Tab. 3). The flow rate and column temperature were maintained at 1.00 mL min^{-1} and 30.0 °C, respectively.

The other mobile phases showed good results toward detected compounds too, but baseline separation was not reached and resolution was not appropriate.

The linearity of the HPLC method was investigated within the range of 1.70–130 μg mL^{-1} using seven different solutions with increasing concentrations. The calibration curves for investigated phytosterols were linear, with ex-

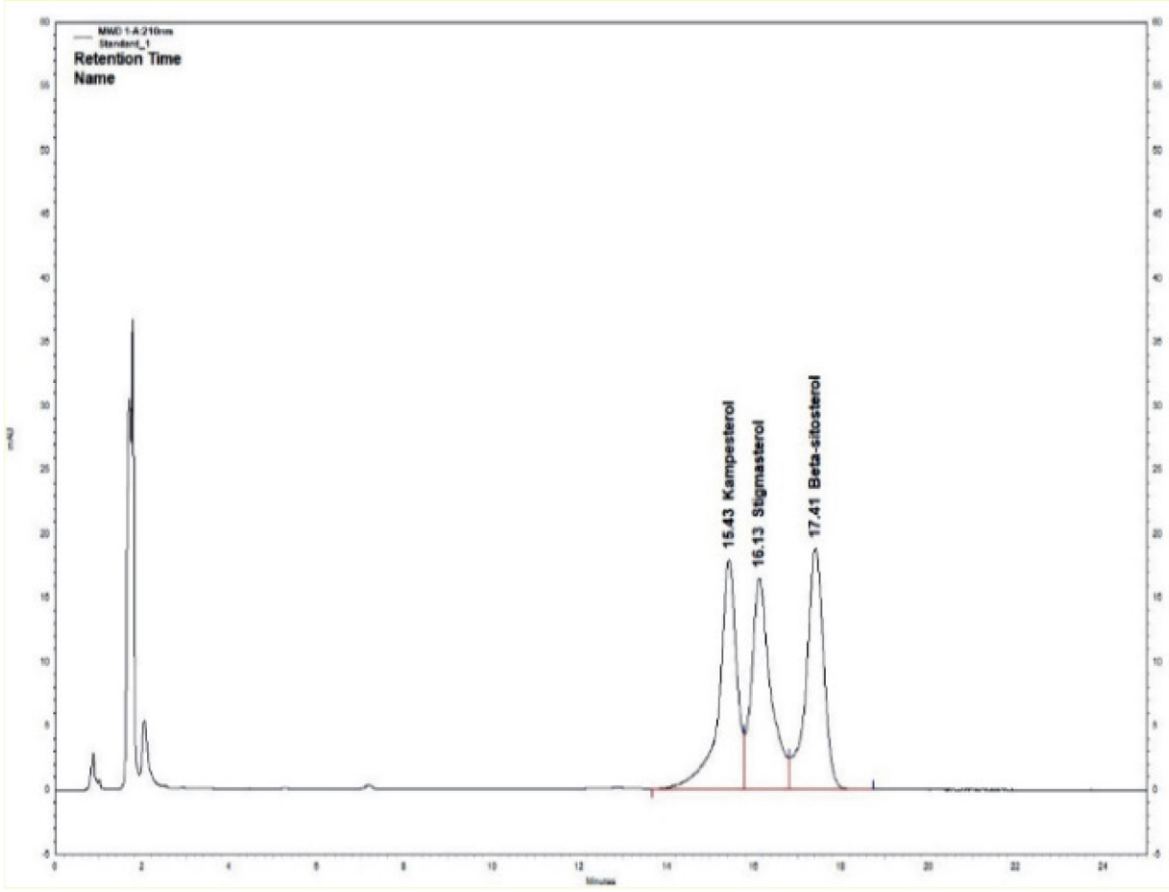

Fig. 3. HPLC chromatogram for phytosterol standards (*β*-sitosterol, campesterol and stigmasterol) on Symmetry C18 column with mobile phase: ACN:MeOH (80:20, *v/v*)

cellent correlation coefficients ranging from 0.998 to 0.999 (Tab. 3). The results further revealed that the minimum concentration levels at which the analyte can be reliably detected (*LOD*) and quantified (*LOQ*) were 0.32 μg mL^{-1} and 0.98 μg mL^{-1} for *β*-sitosterol, 9.30 μg mL^{-1} and 28.1 μg mL^{-1} for campesterol, 0.58 μg mL^{-1} and 1.75 μg mL^{-1} for stigmasterol, respectively, demonstrating good sensitivity of the method.

The system precision results indicated that the %RSD values were within the prescribed limit of %RSD < 2%, with the %RSD values of the peak area being 1.27% for *β*sitosterol, 0.98% for campesterol, and 0.56% for stigmasterol (Tab. 4). Similarly, the results obtained for the system precision showed that the %RSD values of the retention time were 1.15% for *β*sitosterol, 0.97% for campesterol, and 0.99% for stigmasterol (Tab. 4). The method precision results indicate that the %RSD values were also within the prescribed limit of %RSD < 2%, ranging from 1.03% for stigmasterol, 1.15% for campesterol, and 1.44% for *β* sitosterol, as shown in Tab. 4.

The precision of the validated method was expressed as repeatability and reproducibility with %RSD, and accuracy was evaluated by the recovery test. The %RSD values for intra-assay precision (repeatability) were in the range of 1.55% for stigmasterol to 2.50% for *β*-sitosterol (Tab. 5). Whereas the %RSD values for inter-assay (reproducibility) precision were in the range of 0.13% for *β*-sitosterol to 2.56% for campesterol (Tab. 5). These observations suggest that the method provides highly reproducible results, as shown in Tab. 5.

3. 2. Phytosterol Separation, Identification and Quantification in *P. Spinosa* L. Fruit Ethanolic Extracts

To assess the applicability of the validated method to the analysis of *P. spinosa* L. extracts, three ethanolic fruit extracts were obtained and analysed under the above established conditions. One of the goals of the work was to perform a chemical characterization of extracts using the HPLC method in terms of determining the presence of phytosterols, considering their important role in the human body. The presence of *β*-sitosterol was determined and quantified in all extracts of blackthorn fruits, while stigmasterol content was not detected in all samples. Compared to the other two quantified phytosterols, *β*-sitosterol stands out for its content.

Table 3. Calibration curve equations, t_R, R^2, *LOD* and *LOQ* values for phytosterols

Phytosterols	t_R [min]	Equations of Calibration Curves	R^2	*LOD* [μg mL^{-1}]	*LOQ* [μg mL^{-1}]	Resolution
Campesterol	15.43	$y = 8\times10^6x - 2.06\times10^4$	0.9984	9.30	28.1	0.97
Stigmasterol	16.13	$y = 8\times10^6x + 1.39\times10^3$	0.9995	0.58	1.75	1.43
β-sitosterol	17.41	$y = 1\times10^7x + 3.32\times10^3$	0.9996	0.32	0.98	

– In the calibration curve $y = mx + b$, y is the integrated peak area and x is the concentration; t_R – retention time, R – correlation coefficient; *LOD* – limit of detection; *LOQ* – limit of quantification.

Table 4. System and method precision data.

Parameter	System precision						Method precision		
	*β*sitosterol [10.7 μg mL^{-1}]		Campesterol [10.7 μg mL^{-1}]		Stigmasterol [10.7 μg mL^{-1}]		*β*sitosterol [10.7 μg mL^{-1}]	Campesterol [10.7 μg mL^{-1}]	Stigmasterol [10.7 μg mL^{-1}]
	Peak Area	t_R	Peak Area	t_R	Peak Area	t_R	Peak Area	Peak Area	Peak Area
Mean	70068.00	17.41	60251.00	15.43	113558.00	16.13	69180.00	61250.00	112929.00
SD	888.00	0.20	590.00	0.15	638.00	0.16	995.50	707.40	1163.20
%RSD [%]	1.27	1.15	0.98	0.97	0.56	0.99	1.44	1.15	1.03

$n = 6$; SD – standard deviation; RSD – relative standard deviation; t_R – retention time in min.

Tabable 5. Precision of method expressed as repeatability and reproducibility with %RSD

Phytosterols	t_R [min]	Linearity [mg mL^{-1}]	Repeatability %RSD	Reproducibility %RSD	Recovery [%]	%RSD
Campesterol	15.43	0.0017–0.13	2.18	2.56	99.86–100.5	0.05–0.40
Stigmasterol	16.13	0.0017–0.13	1.55	0.38	99.77–100.2	0.02–0.08
β-Sitosterol	17.41	0.0017–0.13	2.50	0.13	99.48–100.2	0.01–0.48

$n = 3$; *RSD* – relative standard deviation.

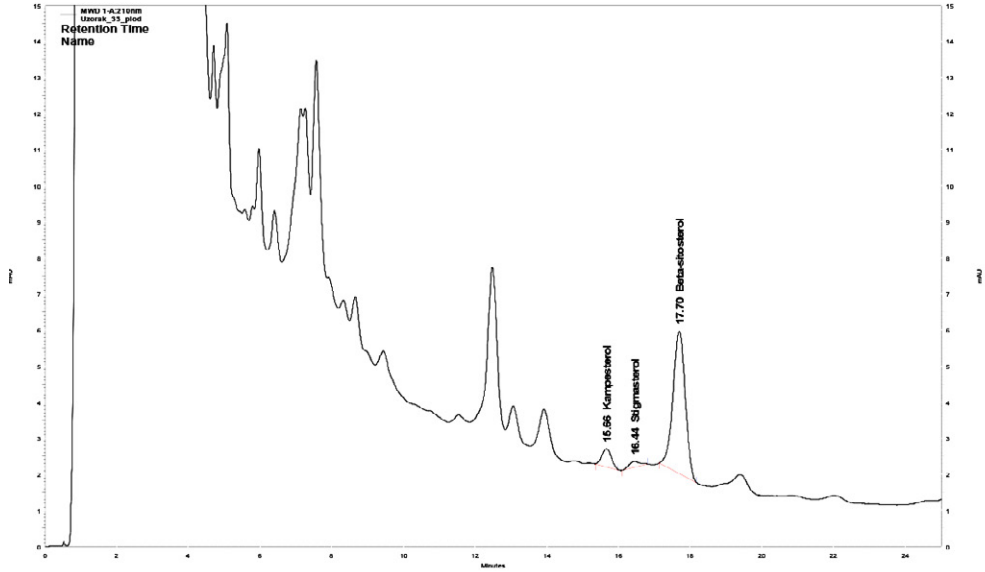

Fig. 4. Chromatogram of the ethanolic extract of fresh blackthorn fruits from the Borije location obtained by Soxhlet extraction

Fig. 4. presents a characteristic chromatogram of the extract mixture where phytosterols of interest were identified by comparison of retention times with standard solutions of phytosterols. HPLC chromatograms of campesterol, stigmasterol and β-sitosterol standard solutions were obtained under optimized chromatographic conditions by injecting 20 μL of solution. Retention times for campesterol, stigmasterol and β-sitosterol were found to be 15.43, 16.13 and 17.41 min, respectively, which were in good agreement with data reported for the standard solutions.

The content of the three main phytosterols in selected samples is summarized in Tab. 6. Fruit extracts from location Borije had the highest content of total sterols (campesterol, stigmasterol, and β-sitosterol) of 18.475 mg g^{-1}, then extracts from Trnovo 8.774 mg g^{-1}, while the extracts from Vareš had the lowest content of 3.82 mg g^{-1}. The content of β-sitosterol in the sample from Borije was 14.765 mg g^{-1}, and the content of campesterol was 3.250 mg g^{-1}. The content of β-sitosterol, campesterol and stigmasterol in the extracts of fresh blackthorn fruit from the location of Trnovo is significantly lower compared to the extracts from the location of Borije. As expected, β-sitosterol was the dominant phytosterol, and campesterol was present at a lower level. Stigmasterol was found in two of three samples at very low levels, which was in accordance with the results presented in previous studies concerning the content of phytosterols in different plant samples.[7,9]

Based on the results shown in Tab. 6, it can be observed that the ethanolic extracts obtained by SE from all three localities had a high content of phytosterols, among which the extract from the Borije location is the leading one. There is no data available in the literature on the specific content of phytosterols (β-sitosterol, campesterol and stigmasterol) in the ethanol extracts of *Prunus spinosa* L., so the obtained values cannot be compared with the results of other studies. The importance of determining phytosterols in plant extracts is related to their biological activities. One of the most important effects of phytoster-

Table 6. Estimation of campesterol, stigmasterol and β-sitosterol in blackthorn fruit ethanolic extracts from three locations in Bosnia and Herzegovina

Sample location	Campesterol		Stigmasterol		β-Sitosterol		Sum of determined phytosterols
	Peak area mean	Content [mg g^{-1}]±SD	Peak area mean	Content [mg g^{-1}]±SD	Peak area mean	Content [mg g^{-1}]±SD	Content [mg g^{-1}]±SD
Borije	18231	3.250±0.000*	6490	0.460±0.012	187753	14.765±0.007	18.475
Vareš	3873	1.850±0.002	–	–	26013	1.970±0.005	3.820
Trnovo	1892	1.641±0.010	1502	0.023±0.004	92164	7.110±0.013	8.774

Values are expressed as the mean of three determinations ± standard deviation.
*All standard deviation values less than 0.001 mg g^{-1}.

ols is antiproliferative activity. Previously published data suggest that the content of phytosterols in the diet is associated with a reduction in common cancers, including colon, breast and prostate cancers.[22,23] Phytosterols affect host systems and potentially enable a stronger antitumor response. This includes the recognition of cancer and strengthening the immune response, influencing the hormonally dependent growth of endocrine cancers and changing the way of sterol biosynthesis. In addition, phytosterols have direct inhibitory effects on cancer growth, including slowing of cell cycle progression, inducing apoptosis and inhibiting cancer metastases.[24] It has been reported that β-sitosterol, the predominant phytosterol in plant foods, can inhibit various cancer cells, such as colon T-29, prostate LNCaP, PC-3, DU145, and MDA-MB-23 breast cancer cells.[23–27] Phytosterols are absorbed from the diet in small but significant amounts. Consumption of 1.5–2.0 g of phytosterols per day reduces LDL cholesterol levels by 10–15% over a period of 3 weeks in hyperlipidaemic populations.[24,28] The recently updated US Code of Federal Regulations also states that foods containing at least 0.65 g per serving of plant sterol esters should be eaten twice daily with meals for a total daily intake of at least 1.3 g, as a diet low in saturated fat and cholesterol can reduce the risk of heart disease.[29]

4. Conclusions

Ethanol extract of blackthorn is generally used in folk medicine in Bosnia and Herzegovina as a natural enhancer of erectile function in men, which is also related to the proper function of the prostate. In order to prove the presence of phytosterols in ethanol extracts, considering their positive effect on prostate function, the goal was to validate a method that can detect phytosterols in *P. spinosa* and clarify its use in folk medicine. A simple, specific, precise, fast and reproducible HPLC method was developed for the quantification of phytosterols, relevant marker compounds, in ethanol extracts of *P. spinosa*. The method showed a good linear relationship between peak area and concentrations, acceptable reproducibility and high accuracy. The validation procedure confirms that this method is suitable for the qualitative and quantitative evaluation of the main phytosterols in ethanol extracts of *P. spinosa*, with a good separation of the components of interest. As for the best of our knowledge, there is no available literature data related to the determination of the presence of phytosterols in crude ethanol extracts of blackthorn by a validated HPLC method, so in our case we cannot rely on literature values specifically for this plant species. The analysis of the content of β-sitosterol and accompanying phytosterols in this plant species provides insight into the proven medicinal properties of this plant, its use in phytotherapy, and confirms its traditional use to alleviate the effects of benign prostatic hyperplasia.

Aknowledgements

The authors warmly thank Prof. Dr. Marin Roje and Dr. Mladenka Jurin from the Ruđer Bošković Institute, Department of Organic Chemistry and Biochemistry, Zagreb, Croatia, for their support and resources provided for the research presented.

5. References

1. E. Launert, Guide to Edible and Medicinal Plants of Britain and Northern Europe. Hamlyn. UK. 1981. ISBN: 0600372162.
2. B.-E. van Wyk, Food Plants of the World: An Illustrated Guide. Timber Press, Portland, USA. 2005. ISBN: 0881927430.
3. A. Dedić, H. Džudžević-Čančar, A. Alispahić, I. Tahirović, E. Muratović, *Int. J. Pharm. Sci. Res.* **2021**, *12*, 3643–3653. **DOI:**10.13040/IJPSR.0975-8232.12(7).3643-53
4. R. A. Moreau, B. D. Whitaker, K. B. Hicks, *J. Lipid Res.* **2002**, *41*, 457–500. **DOI:**10.1016/S0163-7827(02)00006-1
5. P. Fernandes, J. M. S. Cabral, *Bioresour. Technol.* **2007**, *98*, 2335–2350. **DOI:**10.1016/j.biortech.2006.10.006
6. D. M. Tham, C. Gardner, W. L. Haskell, *J. Clin. Endocrinol. Metab.* **1998**, *83*, 2223–2235. **DOI:**10.1210/jcem.83.7.4752
7. M. J. Lagarda, G. García-Llatas, R. Farré, *J. Pharm. Biomed. Anal.* **2006**, *41*, 1486–1496. **DOI:**10.1016/j.jpba.2006.02.052
8. W. R. Sorenson, D. Sullivan, *J. AOAC Int.* **2007**, *90*, 670–678. ISSN: 1060–3271. **DOI:**10.1093/jaoac/90.3.670
9. S. L. Abidi, *J. Chromatogr. A*, **2001**, *935*, 173–201. **DOI:**10.1016/S0021-9673(01)00946-3
10. C. X. Yuan, Y. J. Ju, R. S. Jin, L. L. Ren, X. F. Liu, *Chromatographia*, **2015**, *78*, 273–278. **DOI:**10.1007/s10337-014-2826-2
11. Y. Y. Choo, M. H. Ng, A. N. Ma, C. H. Chuah, M. A. Hashim, *Lipids*, **2005**, *40*, 429–432. **DOI:**10.1007/s11745-006-1400-6
12. N. L. Qi, X. Gong, C. P. Feng, X. X. Wang, Y. W. Xu, L. J. Lin, *Food Chem.* **2016**, *207*, 157–161. **DOI:**10.1016/j.foodchem.2016.03.089
13. A. Rocco, S. Fanali, *J. Chromatogr. A,* **2009**, *1216*, 7173–7178. **DOI:**10.1016/j.chroma.2009.03.081
14. W. Zarrouk, A. Carrasco-Pancorbo, M. Zarrouk, A. Segura-Carretero, A. Fernández-Gutiérrez, *Talanta*, **2009**, *80*, 924–934. **DOI:**10.1016/j.talanta.2009.08.022
15. J. Fibigr, D. Šatínský, P. Solich, *J. Pharm. Biomed. Anal.* **2017**, *140*, 274–280. **DOI:**10.1016/j.jpba.2017.03.057
16. A. N. Kakade, C. S. Magdum, *Int. J. Pharm. Life Sci.* **2012**, *3*, 1666–1669. ISSN: 0976–7126.
17. ICH. 2013. Available from: http://www.ich.org/products/guidelines/quality/article/quality-guidelines.html.
18. USP–The United States Pharmacopeial Convention. Vol. 36. Rockville. MD: Twinbrook Parkway, 2010, pp. 162–165.
19. Guidance for Industry. Analytical Procedures and Methods Validation for Drugs and Biologics Documentation. FDA. U.S. Department of Health and Human Services Food and Drug Administration, Rockville, Maryland. Centre for Drug Evaluation and Research 2001. http://www.chrome-extension://efaidnbmnnnibpcajpcglclefindmkaj/https://www.fda.

gov/files/drugs/published/Analytical-Procedures-and-Methods-Validation-for-Drugs-and-Biologics.pdf
20. D. N. Bliesner, Validating Chromatographic Methods: A Practical Guide. John Wiley & Sons, Inc. Hoboken. New Jersey. USA. **2006**. ISBN: 978-0-471-74147-3.
21. C. C. Chan, H. Lam, Y. C. Lee, X. Zhang, Analytical Method Validation and Instrument Performance. John Wiley & Sons, Inc. Hoboken. New Jersey. USA. **2004**. ISBN: 0-471-25953-5.
22. A. Dedić, H. Džudžević-Čančar, T. Stanojković, M. Roje, A. Damjanović, A. Alispahić, A. Jerković-Mujkić, *Kem. Ind.* **2023**, *72*, 323–330. **DOI:**10.15255/KUI.2022.077
23. M. A. Islam, B. G. Jeong, J. Jung, C. Shin, S. G. Choi, J. Chun, *Food Anal. Methods.* **2017**, *10*, 3225–3234. **DOI:**10.1007/s12161-017-0877-3
24. P. G. Bradford, A. B. Awad, *Mol. Nutr. Food Res.* **2007**, *51,* 161–170. **DOI:**10.1002/mnfr.200600164
25. A. B. Awad, C. S. Fink, *J. Nutr.* **2000**, *130*, 2127–2130. **DOI:**10.1093/jn/130.9.2127
26. A. B. Awad, C. S. Fink, H. Williams, U. Kim, *Eur. J. Cancer Prev.* **2001**, *10,* 507–513. **DOI:**10.1097/00008469-200112000-00005
27. L. Jiang, X. Zhao, J. Xu, C. Li, Y. Yu, W. Wang, L. Zhu, *J. Oncol.* **2019**, *2019,* 1–11. **DOI:**10.1155/2019/7479518
28. R. E. Ostlund, Jr. *Annu. Rev. Nutr.* **2002**, *22*, 533–549. **DOI:**10.1146/annurev.nutr.22.020702.075220
29. CFR 21CFR101.83 (2016) Code of Federal Regulations Title 21, Department of Health and Human Services, United Stated Food and Drug Administration.

Povzetek

Cilj te raziskave je bil razvoj hitre metode za HPLC separacijo stigmasterola, kampesterola in β-sitosterola v ekstraktih sadežev *Prunus spinosa* L. (črni trn). Vzorce smo pripravili s Soxhletovo ekstrakcijo in ločili na C18 koloni z mobilno fazo iz acetonitrila in metanola ter z uporabo detektorja na diodni niz (PDA). Z optimizirano metodo smo pridobili linearno umeritveno krivuljo v območju 1,70–130 μg mL^{-1} za vse tri fitosterole. Analiza eksternih standardov fitosterolov je pokazala dobro linearnost (R^2 od 0,998 do 0,999); LOD pa smo določili kot 0,32–9,30 μg mL^{-1} ter LOQ 0,98–28,1 μg mL^{-1}. Določitev ponovljivosti in obnovljivosti je pokazala sprejemljive vrednosti %RSD. β-sitosterol je bil prevladujoči fitosterol (51,53–81,03 % od skupnega) v vseh vzorcih. Parametri validacije metode so pokazali, da se lahko to analizno metodo uporabi za točno in natančno določitev kampesterola, stigmasterola in β-sitosterola v izbranih ekstraktih.

DOI: 10.17344/acsi.2023.8579 *Acta Chim. Slov.* **2024,** *71,* 334–352

Scientific paper

Synthesis, Characterization and Biological Applications of Substituted Indolo[2,1-*b*]quinazolin-12(6*H*)-one Based Rhenium(I) Organometallic Compounds

Aelvish D. Padariya,[1] Nirbhay K. Savaliya,[1] Milan P. Dhaduk,[1] Ravi A. Dabhi,[1] Bhupesh S. Bhatt,[1] Vaibhav D. Bhatt[2] and Mohan N. Patel[1,*]

[1] *Department of Chemistry, Sardar Patel University, Vallabh Vidyanagar–388 120, Gujarat (India)*

[2] *School of Applied Sciences and Technology, Gujarat Technological University, Ahmedabad, (India)*

* *Corresponding author: E-mail: jeenen@gmail.com*

Received: 07-23-2023

Abstract

The Re(I) organometallic compounds [(Re(CO)$_3$**L**$^{1-6}$)Cl], where ligands **L** are tryptanthrin derivatives, prepared and characterized by various spectroscopic techniques. To assess the binding capacities and binding manner, tests of calf thymus DNA under the impact of organometallic complexes were conducted using absorption titration and viscosity measuring techniques. Data from the research mentioned above point to an intercalation type of binding, which was verified by the docking study. Swiss ADME tools were used to carry out an ADME study. The work focuses on computing the molecular orbital energies for the synthesized compounds using the density functional theory (DFT). The compounds were tested against the MCF-7 cell line to determine their anticancer effects. It was observed that their IC_{50} values were equivalent to those of the standard medication, indicating that they had a similar antiproliferative impact.

Keywords: Re(I) organometallic compounds, DNA and BSA binding, DFT, Molecular docking, ADMET study, Antibacterial activity, Anticancer activity

1. Introduction

Research is heavily focused on creating new, more effective anti-cancer medications because there are drawbacks to present metal-based anticancer drugs like cisplatin.[1] Metal-containing compounds have been investigated recently as prospective possibilities for innovative pharmaceuticals. The finding that apoptosis and the genes that control it considerably impact cancer phenotype has contributed to important improvements in our understanding of cancer biology and genetics.[2] Tryptanthrin, an alkaloid, and antibiotic has been found to have antibacterial, and anti-tumor activity and has been isolated from various sources including *Candida lypolica*, higher plants, and marine micro- and macro-organisms.[3,4] Natural remedies have been used for centuries as sources of treatment and prevention for various illnesses including cancer. The anti-cancer drug paclitaxel was first extracted from *Taxus brevifolia* and approved by the Food and Drug Analysis for the treatment of several types of cancer.[5] Schiff base ligands have been extensively explored in coordination chemistry and are significant in this area because of their stability, chelating properties, and capacity to form complexes with transition metals.[6,7] Tryptanthrin and its derivatives, due to their broad spectrum of activity against various diseases, have become potential biologically active compounds.[8] The quinazoline and indole core structures found in tryptanthrin serve as building blocks.[9] Tryptanthrin's unique indolo[2,1-*b*]quinazoline ring structure has attracted significant attention in chemical research due to its crucial role in the synthesis of natural products, materials, and pharmaceuticals.[10] Many plant species contain tryptanthrin and candidine, phaitanthrins A–E, methylisatoid, and cruciferane (Figure 1).

Nowadays one promising category of synthetic or naturally occurring chemicals that could be used in cancer treatment is quinazoline compounds.[11] Tryptanthrin has been investigated for its potential use in cancer therapy due to its antitumor properties.[12] Chemotherapy is the current standard treatment for cancer in clinical settings.[13,14] However, multidrug resistance affects effectiveness for anticancer medications. One of the most popular

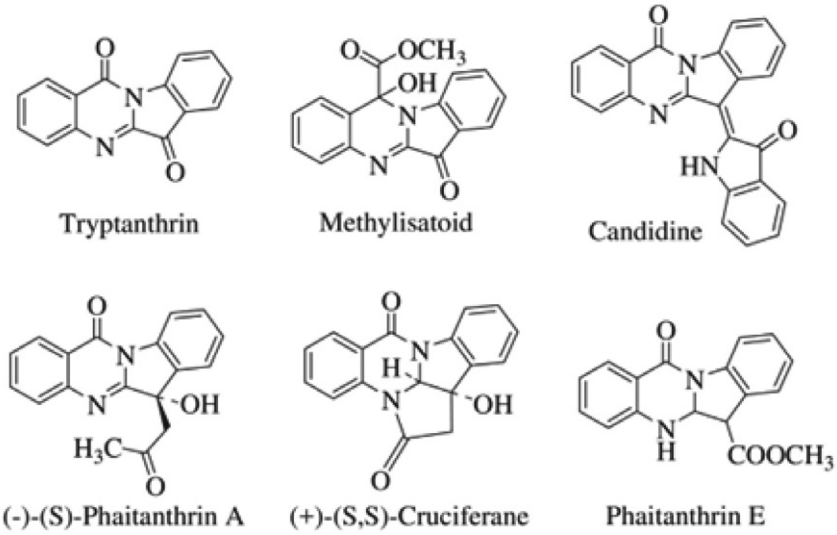

Figure 1. Tryptanthrin and related alkaloids

cytotoxic and antibacterial reagents is a quinazoline alkaloid produced by sublimating natural indigo under reduced pressure.[15]

Density functional theory (DFT) has been increasingly popular in biochemical and medicinal research. DFT is being used more and more in these domains to solve a variety of issues. Dipole moments and global characteristics are one of the main areas of interest in this research since they are essential to understanding the reactivity and bioactivity of compounds, especially those designed for biomedical uses. A useful approach for determining the affinities of candidate compounds to their intended targets is molecular docking studies. This approach is crucial for optimizing potential compounds for medication development and for understanding how ligands interact with their target proteins.[16] Additionally, it is crucial for therapeutic development to estimate the lead compounds ADMET characteristics. These characteristics offer vital information on a drug's absorption, distribution, metabolization, excretion, and potential toxicity.[17,18] Techniques like pharmacokinetic parameter analysis and toxicity evaluation are effective tools in the field of *in silico* drug design. They allow researchers to examine novel chemicals' physical and chemical properties and gauge their potential toxicity. These techniques are essential for swiftly selecting drugs that have potential for additional preclinical and clinical research.[19]

Chemotherapy is a widely used treatment option for cancer, but its lack of specificity towards malignant cells can result in adverse side effects and limit its effectiveness.[20] To overcome this limitation, researchers have been working on developing and synthesizing organometallic compounds with therapeutic potential, particularly those with anticancer properties.[21] Platinum complexes, including *cis*-PtX_2L_2, as well as palladacycles, dimeric, trimeric, tetrameric, and heterobimetallic complexes, have been the focus of much research in the field of anticancer drugs.[22] Recent years have seen the development of a variety of Pt(II) compounds containing nitrogen atom donor ligands like alkyl and aryl type amines and imines. Such as azo, hydrazo, pyridine, and pyrimidine derivatives.[23] Few of these complexes have demonstrated effective anticancer capabilities both *in vivo* and *in vitro*. The tryptanthrin Schiff base and substituted phenyl hydrazine synthesized, characterized, and their interactions within DNA and BSA investigated are presented in this study. In order to ascertain mechanism and type of interaction of organometallic complexes with DNA, the molecular docking technique was also used. These findings could potentially increase the development of the novel and effective anticancer agents with additionally improved specificity toward malignant cells.[24]

2. Experimental Section

2. 1. Materials and Methods

The reagents and solvents employed have high chemical purity and reasonably priced. For spectral measurements, spectroscopic-grade solvents were purchased from Sigma-Aldrich. The following items were acquired from Sigma-Aldrich: isatin, 5-chloroisatin, isatoic anhydride, triethylamine, pentacarbonylchlororhenium(I), dimethyl sulphoxide (DMSO), calf thymus (CT) DNA, and bovine serum albumin (BSA). The SRL was used to purchase the toluene, methanol, and glacial acetic acid. TCI supplied the following: phenylhydrazine hydrochloride, 4-chlorophenylhydrazine hydrochloride, and 2,4-dichlorophenylhydrazine hydrochloride. We purchased Luria broth and ethidium bromide (EtBr) from Hi-media. Using Milli-Q water, all buffers and solutions are created.

Using a deuterated solvent and a Bruker Avance spectrometer the ^{1}H NMR spectra were measured. The ^{13}C NMR spectra were gathered using a Varian Inova spectrometer and a deuterated solvent. Samples were produced as pellets

of potassium bromide (KBr) for the IR spectral analysis, and an Anasys Fourier transform-infrared (FT-IR) spectrophotometer was used to obtain the spectra in the 4000–400 cm^{-1} range. A EURO EA3000 elemental analyzer was used to ascertain the elemental makeup of C, H, and N. Using a UV-160A UV-visible spectrophotometer (Shimadzu, Kyoto, Japan), the absorption titration was carried out. A Horiba spectrofluorometer was used to conduct a study on the quenching of fluorescence. A specialized tool created to monitor and examine fluorescence phenomena is the Horiba spectrofluorometer. A study conducted on five bacterial cultures, including two Gram-positive bacteria, *Staphylococcus aureus* (MTCC-3160) and *Bacillus subtilis* (MTCC-7193), and three Gram-negative bacteria, *Serratia marcescens* (MTCC-7103), *Escherichia coli* (MTCC-433), and *Pseudomonas aeruginosa* (MTCC-1688) was used to evaluate the antimicrobial activity of the synthesized compounds.

2. 2. Synthesis of Ligands and Their Re(I) Organometallic Compounds

2. 1. 1. Synthesis of Substituted Indolo[2,1-*b*] quinazoline-6,12-dione

Substituted isatin (300 mg, 2.04 mmol) was dissolved in toluene (5 mL), and then triethylamine base (0.567 mL, 4.07 mmol) was added. After 10 minutes isatoic anhydride (332 mg, 2.04 mmol) was added to the reaction mixture followed by reflux for 70–80 min. The substituted indolo[2,1-*b*]quinazoline-6,12-dione products were collected, dried, and washed with methanol to remove impurities.

2. 1. 2. Synthesis of Substituted Tryptanthrin Schiff-based Derivatives (L^1–L^6)

Synthesized product (300 mg, 1.21 mmol) was reacted with substituted phenylhydrazine hydrochloride (261 mg, 2.42 mmol) derivatives by Schiff-base reaction in the presence of methanol (3 mL) and drops of glacial acetic acid (2–3 drops) at room temperature for 180–240 min with stirring. The substituted tryptanthrin Schiff base product (L^1–L^6) was obtained and collected using vacuum filtration. The resultant precipitates were then washed with a small amount of methanol followed by drying.

2. 1. 3. Synthesis of Re(I) Organometallic Complexes C^1–C^6

Tryptanthrin Schiff base ligands L^1–L^6 (100 mg, 0.30 mmol) dissolved in toluene and rhenium metal salt (107 mg, 0.30 mmol) were added and refluxed at 95 °C for 8–9 h with vigorous rapid stirring. Then, the reaction mixture was cooled to room temperature. The resulting precipitates were collected, rinsed with a minor amount of toluene and dried. The column chromatography method was used for the purification of these compounds (Scheme 1).

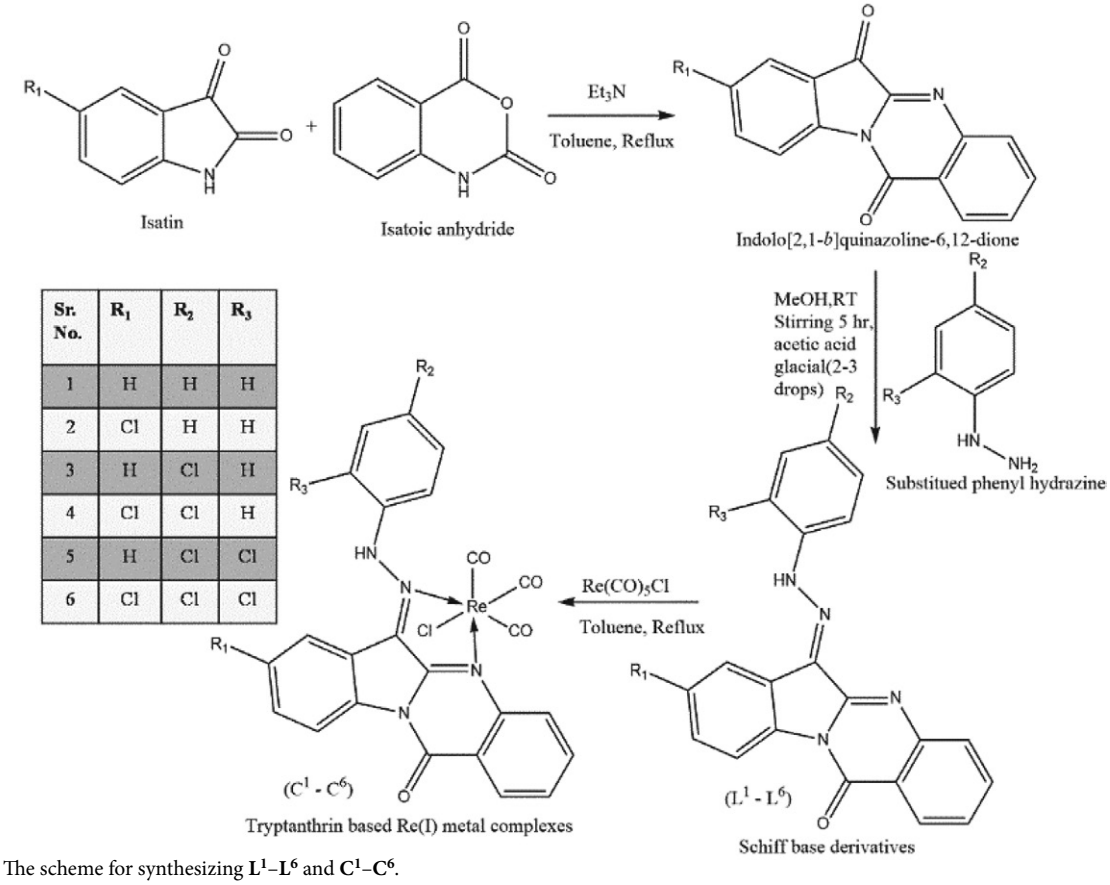

Sr. No.	R_1	R_2	R_3
1	H	H	H
2	Cl	H	H
3	H	Cl	H
4	Cl	Cl	H
5	H	Cl	Cl
6	Cl	Cl	Cl

Scheme 1. The scheme for synthesizing L^1–L^6 and C^1–C^6.

2. 3. Characterization of Ligands and Re(I) Complexes

6-(2-Phenylhydrazono)indolo[2,1-*b*]quinazolin-12(6*H*)-one (L^1)

Yield: 82.56% (247.68 mg) of canary yellow amorphous solid; m.p. 220 °C; mol. wt.: 338.37 g/mol. Anal. calcd. for $C_{21}H_{14}N_4O$: C, 74.54; H, 4.17; N, 16.56. Found: C, 74.41; H, 4.01; N, 14.65. ^{1}H NMR (400 MHz, $CDCl_3$) δ 12.74 (1H, s, $H_{2'}$), 7.98 (1H, d, J = 7.2 Hz, H_5), 7.67 (1H, d, J = 7.6 Hz H_{10}), 7.43–7.36 (4H, m, $H_{3,4,8,9}$), 7.25 (1H, d, J = 7.6 Hz, H_2), 7.22 (1H, d, J = 7.6 Hz, H_7), 7.21–7.01 (3H, m, $H_{5',6',7'}$), 6.97 (1H, d, J = 7.6 Hz, $H_{4'}$), 6.92 (1H, d, J = 8.0 Hz, $H_{8'}$); ^{13}C NMR (125 MHz, $CDCl_3$) δ 159.53 (C_8), 151.38 (C_{16}), 151.02 (C_{17}), 145.47 ($C_{2,3}$), 143.58 (C_{20}), 133.41 (C_4), 131.80 (C_{12}), 129.67 (C_{11}), 129.49 ($C_{22,24}$), 129.39 (C_{14}), 128.99 (C_5), 126.58 (C_3), 126.26 (C_6), 124.29 (C_{13}), 122.25 (C_{23}), 120.48 (C_7), 117.74 (C_{15}), 113.47 ($C_{21,25}$); IR (KBr) v 3047 (=C–H)$_{stretching}$, 1643 (C=O)$_{stretching}$, 1550 (C=N)$_{stretching}$, 1465 (C=C)$_{ar.\ stretching}$, 1164 (C–N)$_{stretching}$, 740 (C–H)$_{bending}$ cm^{-1}; MS *m/z* (%): 338 (100) [M$^+$].

8-Chloro-6-(2-phenylhydrazono)indolo[2,1-*b*]quinazolin-12(6*H*)-one (L^2)

Yield: 85.43% (256.29 mg) of golden yellow amorphous solid; m.p. 260 °C; mol. wt.: 372.81 g/mol. Anal. calcd. for $C_{21}H_{13}ClN_4O$: C, 67.66; H, 3.51; N, 15.03. Found: C, 67.53; H, 3.65; N, 14.89. ^{1}H NMR (400 MHz, $CDCl_3$) δ 12.77 (1H, s, $H_{2'}$), 7.67 (1H, d, J = 7.2 Hz, H_5), 7.56 (1H, s, H_{10}), 7.41–7.40 (4H, m, $H_{4',5',7',8'}$), 7.24 (1H, d, J = 6.8 Hz, H_2), 7.21 (1H, d, J = 7.6 Hz, H_8), 7.14 (1H, t, J = 7.1 Hz, H_3), 7.12 (1H, t, J = 6.8 Hz, H_4), 6.96 (1H, t, J = 7.6 Hz, $H_{6'}$), 6.85 (1H, d, J = 8.4 Hz, H_7); ^{13}C NMR (125 MHz, $CDCl_3$) δ 160.59 (C_8), 151.85 (C_{16}), 151.30 (C_{17}), 145.43 (C_2), 143.79 (C_{10}), 143.18 (C_{20}), 133.47 (C_4), 131.19 (C_{12}), 130.07 (C_{13}), 129.51 (C_{14}), 129.04 ($C_{22,24}$), 127.21 (C_5), 126.79 (C_3), 126.59 (C_6), 124.43 (C_{11}), 122.01 (C_{23}), 120.48 (C_7), 119.13 (C_{15}), 113.43 ($C_{21,25}$); IR (KBr) v 3062 (=C–H)$_{stretching}$, 1635 (C=O)$_{stretching}$, 1550 (C=N)$_{stretching}$, 1465 (C=C)$_{ar.\ stretching}$, 1164 (C–N)$_{stretching}$, 655 (C-Cl)$_{bending}$ cm^{-1}; MS *m/z* (%): 372 (100) [M$^+$], 374 [M^{+2}].

6-(2-(4-Chlorophenyl)hydrazono)indolo[2,1-*b*]quinazolin-12(6*H*)-one (L^3)

Yield: 80.84% (242.52 mg) of bright yellow amorphous solid; m.p. 270 °C; mol. wt.: 372.81 g/mol. Anal. calcd. for $C_{21}H_{13}ClN_4O$: C, 67.66; H, 3.51; N, 15.03. Found: C, 67.79; H, 3.52; N, 14.91. ^{1}H NMR (400 MHz, $CDCl_3$) δ 13.49 (1H, s, $H_{2'}$), 8.53 (1H, d, J = 8.4 Hz, H_5), 8.47 (1H, d, J = 8.0 Hz, H_{10}), 7.87–7.80 (3H, m, $H_{2,7,3}$), 7.61–7.55 (1H, m, H_8), 7.50–7.45 (3H, m, $H_{4,4',5'}$), 7.42 (1H, d, J = 7.6 Hz, $H_{8'}$), 7.40 (1H, d, J = 6.8 Hz, $H_{7'}$), 7.16 (1H, t, J = 7.2 Hz, H_9); ^{13}C NMR (125 MHz, $CDCl_3$) δ 160.24 (C_8), 151.88 (C_{16}), 150.75 (C_{17}), 145.31 ($C_{2,9}$), 141.66 (C_{20}), 133.49 (C_4), 131.17 (C_{12}), 129.71 ($C_{11,24,22}$), 128.98 (C_{14}), 127.45 (C_{23}), 126.99 (C_5), 125.92 (C_3), 125.11 (C_6), 123.81 (C_{13}), 120.57 (C_7), 118.19 ($C_{15,25,21}$); IR (KBr) v 3039 (=C–H)$_{stretching}$, 1674 (C=O)$_{stretching}$, 1558 (C=N)$_{stretching}$, 1512 (C–H)$_{bending}$, 1465 (C=C)$_{ar.\ stretching}$, 1164 (C–N)$_{stretching}$, 655 (C–Cl)$_{bending}$ cm^{-1}; MS *m/z* (%): 372 (100) [M$^+$], 374 [M^{+2}].

8-Chloro-6-(2-(4-chlorophenyl)hydrazono)indolo[2,1-*b*]quinazolin-12(6*H*)-one (L^4)

Yield: 75.62% (226.86 mg) of lemon yellow amorphous solid; m.p. 275 °C; mol. wt.: 407.25 g/mol. Anal. calcd. for $C_{21}H_{12}Cl_2N_4O$: C, 61.39; H, 2.97; N, 13.76. Found: C, 61.76; H, 2.84; N, 13.90. ^{1}H NMR (400 MHz, $CDCl_3$) δ 13.39 (1H, s, $H_{2'}$), 8.54 (1H, d, J = 8.0 Hz, H_5), 8.43 (1H, d, J = 8.0 Hz, H_7), 8.04 (1H, s, H_{10}), 7.82–7.74 (2H, m, $H_{3,4}$), 7.56 (1H, d, J = 7.6 Hz, H_2), 7.51 (1H, d, J = 8.4 Hz, H_8), 7.45–7.29 (4H, m, $H_{4',5',7',8'}$); ^{13}C NMR (125 MHz, $CDCl_3$) δ 162.05 (C_8), 153.95 (C_{16}), 152.83 (C_{17}), 145.87 (C_2), 143.51 (C_{10}), 142.25 (C_{20}), 133.85 (C_4), 131.39 (C_{12}), 130.62 (C_{13}), 129.79 ($C_{24,24}$), 129.20 (C_{14}), 127.64 (C_{23}), 127.04 (C_5), 125.62 (C_3), 124.77 (C_6), 122.51 (C_{11}), 120.59 (C_7), 119.04 ($C_{21,25}$), 117.89 (C_{15}); IR (KBr) v 3055 (=C–H)$_{stretching}$, 1643 (C=O)$_{stretching}$, 1558 (C=N)$_{stretching}$, 1504 (C–H)$_{bending}$, 1465 (C=C)$_{ar.\ stretching}$, 817 (C–Cl)$_{bending}$ cm^{-1}; MS *m/z* (%): 406 (100) [M$^+$], 408 [M^{+2}], 412 [M^{+4}].

6-(2-(2,4-Dichlorophenyl)hydrazono)indolo[2,1-*b*]quinazolin-12(6*H*)-one (L^5)

Yield: 81.44% (244.32 mg) of honey yellow amorphous solid; m.p. 265 °C; mol. wt.: 407.25 g/mol. Anal. calcd. for $C_{21}H_{12}Cl_2N_4O$: C, 61.39; H, 2.97; N, 13.76. Found: C, 62.08; H, 2.86; N, 13.89. ^{1}H NMR (400 MHz, $CDCl_3$) δ 12.99 (1H, s, $H_{2'}$), 7.81 (1H, d, J = 7.2 Hz, H_5), 7.68 (1H, d, J = 7.2 Hz, H_{10}), 7.57 (1H, s, $H_{7'}$), 7.51–7.43 (3H, m, $H_{3,4,8}$), 7.40 (1H, d, J = 7.6 Hz, H_2), 7.32 (1H, d, J = 6.4 Hz, H_7), 7.30 (1H, d, J = 6.8 Hz, $H_{5'}$), 7.14 (1H, t, J = 7.2 Hz, H_9), 6.93 (1H, d, J = 8.0 Hz, $H_{4'}$); ^{13}C NMR (125 MHz, $CDCl_3$) δ 161.42 (C_8), 155.82 (C_{16}), 153.83 (C_{17}), 148.09 ($C_{2,10}$), 147.31 (C_{20}), 133.76 (C_4), 131.98 ($C_{22,12}$), 130.79 (C_{11}), 130.58 (C_{14}), 129.14 (C_{24}), 128.55 (C_5), 126.84 (C_3), 126.14 ($C_{6,21}$), 125.33 (C_{13}), 122.47 (C_{23}), 120.48 (C_{25}), 119.51 (C_{15}), 117.92 (C_7); IR (KBr) v 3055 (=C–H)$_{stretching}$, 1620 (C=O)$_{stretching}$, 1558 (C=N)$_{stretching}$, 1512 (C–H)$_{bending}$, 1465 (C=C)$_{ar.\ stretching}$, 1164 (C–N)$_{stretching}$, 655 (C–Cl)$_{bending}$ cm^{-1}; MS *m/z* (%): 406 (100) [M$^+$], 408 [M^{+2}], 412 [M^{+4}].

8-Chloro-6-(2-(2,4-dichlorophenyl)hydrazono)indolo[2,1-*b*]quinazolin-12(6*H*)-one (L^6)

Yield: 78.38% (235.14 mg) of butter yellow amorphous solid; m.p. 268 °C; mol. wt.: 441.70 g/mol. Anal. calcd. for $C_{21}H_{11}Cl_3N_4O$: C, 57.11; H, 2.51; N, 12.68. Found: C, 57.23; H, 2.38; N, 12.81. ^{1}H NMR (400 MHz, $CDCl_3$) δ 13.47 (1H, s, $H_{2'}$), 8.52 (1H, d, J = 8.0 Hz, H_5), 8.47 (1H, d, J = 8.0 Hz, H_7), 7.99 (1H, s, H_{10}), 7.83 (1H, d, J = 7.6 Hz, H_2), 7.71 (1H, d, J = 7.2 Hz, H_8), 7.58 (1H, t, J = 6.8 Hz, H_3), 7.48 (1H, s, $H_{5'}$), 7.40 (1H, d, J = 8.4 Hz, $H_{8'}$), 7.16 (1H, t, J = 7.2 Hz, H_4), 7.07 (1H, d, J = 7.6 Hz, $H_{7'}$); ^{13}C

NMR (125 MHz, $CDCl_3$) δ 160.35 (C_8), 152.51 (C_{16}), 151.25 (C_{17}), 148.15 (C_2), 147.44 (C_{20}), 143.09 (C_{10}), 139.31 (C_4), 138.25 (C_{12}), 136.92 (C_{22}), 133.77 (C_{13}), 132.90 (C_{14}), 132.14 (C_{24}), 132.04 (C_5), 131.91 (C_3), 131.85 ($C_{6,21}$), 129.18 (C_{23}), 124.85 (C_{11}), 120.52 (C_7), 118.03 ($C_{25,15}$); IR (KBr) v 3078 (=C–H)$_{stretching}$, 1627 (C=O)$_{stretching}$, 1558 (C=N)$_{stretching}$, 1512 (C–H)$_{bending}$, 1450 (C=C)$_{ar. stretching}$, 1172 (C–N)$_{stretching}$, 655 (C–Cl)$_{bending}$ cm^{-1}; MS *m/z* (%): 440 (100) [M$^+$], 442 [M^{+2}], 446 [M^{+4}], 452 [M^{+6}].

[(Re(CO)$_3$L^1)Cl] (C^1)

Yield: 54.32% (54.32 mg) of caramel brown amorphous solid; m.p. >300 °C; mol. wt.: 644.06 g/mol ($C_{24}H_{14}ClN_4O_4Re$); ^{1}H NMR (400 MHz, DMSO-d_6) δ 12.75 (1H, s, $H_{2'}$), 7.56 (1H, d, J = 7.6 Hz, H_2), 7.46–7.33 (5H, m, $H_{3,5,7,8,10}$), 7.30–7.22 (2H, m, $H_{4,9}$), 7.09–6.99 (3H, m, $H_{5';6';7'}$), 6.97–6.81 (2H, m, $H_{4';8'}$); ^{13}C NMR (125 MHz, DMSO-d_6) δ 198.59 (C_{28}, M-CO), 197.36 ($C_{27,29}$, 2M-CO), 163.72 (C_8), 159.53 (C_{17}), 148.11 (C_{20}), 147.43 (C_{10}), 143.58 (C_{16}), 141.41 (C_2), 138.20 (C_4), 131.80 (C_7), 129.67 ($C_{22,24,11}$), 129.49 ($C_{14,12}$), 129.39 (C_5), 129.10 (C_6), 126.26 (C_3), 124.29 (C_{13}), 122.25 (C_{23}), 120.48 (C_{15}), 117.74 ($C_{21,25}$); IR (KBr) v 3078 (=C–H)$_{stretching}$ 2036, 1944, 1920 (Re–CO)$_{stretching}$, 1666 (C=O)$_{stretching}$, 1550 (C=N)$_{stretching}$, 1458 (C=C)$_{ar. stretching}$, 1249 (C–N)$_{stretching}$ cm^{-1}; MS *m/z* (%): 645 (100) [M$^+$], 647 [M^{+2}].

[(Re(CO)$_3$L^2)Cl] (C^2)

Yield: 52.43% (52.43 mg) of tawny brown amorphous solid; m.p. >300 °C; mol. wt.: 678.50 g/mol ($C_{24}H_{13}Cl_2N_4O_4Re$); ^{1}H NMR (400 MHz, DMSO-d_6) δ 12.77 (1H, s, $H_{2'}$), 7.57 (1H, d, J = 7.2 Hz, H_2), 7.49 (1H, d, J = 7.6 Hz, H_5), 7.40–7.37 (2H, m, $H_{3,4}$), 7.28 (1H, d, J = 7.2 Hz, H_7), 7.26 (1H, d, J = 7.6 Hz, H_8), 7.20 (1H, s, H_{10}), 7.13–7.02 (3H, m, $H_{5';6';7'}$), 6.99–6.87 (2H, m, $H_{4';8'}$); ^{13}C NMR (125 MHz, DMSO-d_6) δ 198.31 (C_{28}, M-CO), 197.21 ($C_{27,29}$, 2M-CO), 163.09 (C_8), 161.12 (C_{17}), 152.55 (C_{20}), 148.16 ($C_{10,16}$), 145.43 (C_2), 138.18 (C_4), 131.19 (C_7), 129.51 (C_{13}), 129.04 ($C_{22,24}$), 128.82 (C_{12}), 127.21 (C_{14}), 126.79 (C_5), 126.59 (C_6), 125.48 (C_3), 124.43 (C_{11}), 122.01 (C_{23}), 120.48 (C_{15}), 117.53 ($C_{21,25}$); IR (KBr) v 3062 (=C–H)$_{stretching}$, 2036, 1913, 1874 (Re–CO)$_{stretching}$, 1635 (C=O)$_{stretching}$, 1550 (C=N)$_{stretching}$, 1450 (C=C)$_{ar. stretching}$, 1188 (C–N)$_{stretching}$, 694 (C–Cl)$_{bending}$ cm^{-1}; MS *m/z* (%): 679 (100) [M$^+$], 681 [M^{+2}], 683 [M^{+4}].

[(Re(CO)$_3$L^3)Cl] (C^3)

Yield: 54.23% (54.23 mg) of red amorphous solid; m.p. >300 °C; mol. wt.: 678.50 g/mol ($C_{24}H_{13}Cl_2N_4O_4Re$); ^{1}H NMR (400 MHz, DMSO-d_6) δ 12.71 (1H, s, $H_{2'}$), 7.56 (1H, d, J = 7.2 Hz, H_2), 7.49–7.45 (2H, m, $H_{7,5}$), 7.46 (1H, d, J = 7.6 Hz, H_{10}), 7.34–7.17 (2H, m, $H_{3,8,}$), 7.15–6.98 (2H, m, $H_{4,9}$), 6.95–6.89 (4H, m, $H_{4';5';7';8'}$); ^{13}C NMR (125 MHz, DMSO-d_6) δ 198.66 (C_{28}, M-CO), 197.51 ($C_{27,29}$, 2M-CO), 164.80 (C_8), 160.58 (C_{17}), 150.75 (C_{10}), 147.13 (C_{20}), 145.31 (C_{16}), 141.66 (C_2), 137.17 (C_4), 133.49 (C_7), 131.17 ($C_{22,24}$), 129.71 (C_{11}), 128.98 ($C_{12,14}$), 127.45 (C_5), 126.99 (C_{23}), 125.92 (C_6), 125.11 (C_3), 123.81 (C_{13}), 120.57 (C_{15}), 118.19 ($C_{21,25}$); IR (KBr) v 3047 (=C–H)$_{stretching}$, 2036, 1944, 1920 (Re–CO)$_{stretching}$, 1666 (C=O)$_{stretching}$, 1550 (C=N)$_{stretching}$, 1458 (C=C)$_{ar. stretching}$, 1242 (C–N)$_{stretching}$, 648 (C–Cl)$_{bending}$ cm^{-1}; MS *m/z* (%): 679 (100) [M$^+$], 681 [M^{+2}], 683 [M^{+4}].

[(Re(CO)$_3$L^4)Cl] (C^4)

Yield: 52.96% (52.96 mg) of bright red amorphous solid; m.p. >300 °C; mol. wt.: 712.94 g/mol ($C_{24}H_{12}Cl_3N_4O_4Re$); ^{1}H NMR (400 MHz, DMSO-d_6) δ 12.70 (1H, s, $H_{2'}$), 7.58 (1H, d, J = 7.6 Hz, H_2), 7.56–7.52 (3H, m, $H_{5,7,8}$), 7.45–7.39 (3H, m, $H_{3,4,10}$), 7.32–7.20 (2H, m, $H_{5';7'}$), 6.95–6.86 (2H, m, $H_{3';8'}$); ^{13}C NMR (125 MHz, DMSO-d_6) δ 198.86 (C_{28}, M-CO), 197.34 ($C_{27,29}$, 2M-CO), 162.05 (C_8), 158.73 (C_{17}), 148.13 (C_{20}), 145.87 (C_2), 143.51 ($C_{10,16}$), 138.28 (C_4), 133.85 (C_7), 131.39 (C_{13}), 130.62 ($C_{22,24}$), 129.20 (C_{12}), 127.64 (C_{14}), 127.04 (C_5), 126.56 (C_{23}), 126.09 (C_6), 125.62 (C_3), 124.77 (C_{11}), 122.51 (C_{15}), 117.89 ($C_{21,25}$); IR (KBr) v 3055 (=C–H)$_{stretching}$, 2036, 1944, 1890 (Re–CO)$_{stretching}$, 1658 (C=O)$_{stretching}$, 1550 (C=N)$_{stretching}$, 1450 (C=C)$_{ar. stretching}$, 1211 (C–N)$_{stretching}$, 686 (C–Cl)$_{bending}$ cm^{-1}; MS *m/z* (%): 711 (100) [M$^+$], 713 [M^{+2}], 715 [M^{+4}], 717 [M^{+6}].

[(Re(CO)$_3$L^5)Cl] (C^5)

Yield: 58.66% (58.66 mg) of orange amorphous solid; m.p. >300 °C; mol. wt.: 712.94 g/mol ($C_{24}H_{12}Cl_3N_4O_4Re$); ^{1}H NMR (400 MHz, DMSO-d_6) δ 13.08 (1H, s, $H_{2'}$), 7.80 (1H, d, J = 7.2 Hz, H_2), 7.67 (1H, d, J = 7.6 Hz, H_7), 7.60 (1H, d, J = 7.2 Hz, H_5), 7.49 (1H, d, J = 7.6 Hz H_{10}), 7.48 (1H, s, $H_{7'}$), 7.31 (1H, t, J = 7.6 Hz, H_3), 7.27–7.14 (2H, m, $H_{4,8}$), 7.09 (1H, t, J = 7.6 Hz, H_9), 7.03–6.92 (2H, m, $H_{4';5'}$); ^{13}C NMR (125 MHz, DMSO-d_6) δ 198.70 (C_{28}, M-CO), 197.32 ($C_{27,29}$, 2M-CO), 161.42 (C_8), 159.03 (C_{17}), 153.83 (C_{20}), 148.09 (C_{10}), 147.28 (C_{16}), 141.76 (C_2), 138.33 (C_4), 133.76 (C_7), 131.98 (C_{22}), 130.58 (C_{11}), 129.14 ($C_{12,14}$), 128.55 (C_5), 127.48 (C_{24}), 126.84 (C_6), 126.14 (C_{21}), 125.85 (C_{23}), 125.33 (C_3), 124.24 (C_{13}), 120.48 (C_{15}), 119.51 (C_{25}); IR (KBr) v 3047 (=C–H)$_{stretching}$, 2028, 1920, 1882 (Re–CO)$_{stretching}$, 1643 (C=O)$_{stretching}$, 1550 (C=N)$_{stretching}$, 1450 (C=C)$_{ar. stretching}$, 1180 (C–N)$_{stretching}$, 640 (C–Cl)$_{bending}$ cm^{-1}; MS *m/z* (%): 711 (100) [M$^+$], 713 [M^{+2}], 715 [M^{+4}], 717 [M^{+6}].

[(Re(CO)$_3$L^6)Cl] (C^6)

Yield: 56.62% (56.62 mg) of carrot orange amorphous solid; m.p. >300 °C; mol. wt.: 747.38 g/mol ($C_{24}H_{11}Cl_4N_4O_4Re$); ^{1}H NMR (400 MHz, DMSO-d_6) δ 13.06 (1H, s, $H_{2'}$), 7.87 (1H, d, J = 7.2 Hz, H_2), 7.69 (1H, d, J = 7.6 Hz, H_5), 7.63 (1H, d, J = 8.0 Hz, H_7), 7.61–7.53 (2H, m, $H_{3,4}$), 7.49 (1H, d, J = 8.0 Hz, H_8), 7.48 (1H, s, $H_{5'}$), 7.35 (1H, s, H_{10}), 7.32 (1H, d, J = 6.8 Hz, $H_{8'}$), 6.96 (1H, d, J = 7.2 Hz, $H_{7'}$); ^{13}C NMR (125 MHz, DMSO-d_6) δ 198.90 (C_{28}, M-CO), 197.13 ($C_{27,29}$, 2M-CO), 160.35 (C_8), 158.28

(C_{17}), 148.15 (C_{20}), 147.44 ($C_{10,16}$), 143.09 (C_2), 139.31 (C_4), 138.25 (C_7), 136.92 (C_{22}), 133.77 (C_{13}), 132.90 (C_{12}), 132.14 (C_{14}), 132.04 (C_5), 131.91 (C_{24}), 131.85 (C_6), 129.18 (C_{21}), 126.07 (C_{23}), 124.85 (C_3), 124.06 (C_{11}), 122.39 (C_{15}), 118.03 (C_{25}); IR (KBr) v 3031 $(=C–H)_{stretching}$, 2036, 1974, 1882 $(Re–CO)_{stretching}$, 1643 $(C=O)_{stretching}$, 1550 $(C=N)_{stretching}$, 1458 $(C=C)_{ar.\ stretching}$, 1180 $(C–N)_{stretching}$, 640 $(C–Cl)_{bending}$ cm^{-1}; MS *m/z* (%): 746 (100) $[M^+]$.

2. 4. Computational Study

2. 4. 1. DFT Study

The optimal structural geometry of Re(I) complexes based on tryptanthrin was calculated using the DFT/B3LYP approach with different base sets in Gaussian 09 software.[25] The molecular visualization tool Gauss View is used to display the Gaussian files. Quantum chemical parameters are estimated from the HOMO–LUMO energies based on the numerical pattern shown in the gas-phase view of the compounds. The optimized structures provided information on important bond lengths, excitation energies, and effective charges of coordinating groups. Frontier molecular orbitals (FMOs) energy gap of the ligand and its metal complexes calculated to determine electronic properties related to dynamic stability and chemical reactivity.[26] In the Schiff base ligand, the π–π* electron transfer was facilitated by the HOMO and LUMO orbitals, which were mostly located on the donor site of the ligand. In the L–M complex, these orbitals are found around the metal center.[27]

2. 4. 2. Molecular Docking Study

The process of molecular docking involves the creation of an optimal conformation for a protein and a drug, with their relative orientations optimized to minimize the free energy of the entire system. This process aims to replicate the molecular recognition process that occurs in biological systems.[28] In order to perform this process, various parameters such as interaction mode, connectivity, and connection energy are calculated using software tools such as Auto Dock. In this study, the Auto Dock-1.5.6 program was used in conjunction with DNA and BSA macromolecules to carry out molecular docking investigations on the ligand and rhenium metal complexes. The crystal structures of DNA and BSA were obtained from the Protein Data Bank, a global resource for processing and sharing 3D biological macromolecular structure data. Water molecules were eliminated from the DNA/BSA structures, and the Kollman charges and necessary hydrogen atoms were added to the receptor structure. To study the bonding condition, DNA was examined in a cube box with dimensions of 62 × 72 × 114 $Å^3$ and 112 × 31 × 33 $Å^3$. PDB files for each compound and DNA/BSA translated into PDBQT format using AutoDockTools-1.5.6. The command prompt used Auto Dock Vina to conduct a docking investigation between the substances and DNA/BSA.[29,30] It required one run and produced output files that will be viewed using PyMOL. All compounds with DNA/BSA docked structures were stored in PDB format for further analysis. In summary, molecular docking was used to investigate the interaction between ligands and rhenium metal complexes with DNA and BSA macromolecules. This involved a detailed process of preparing the receptor structures and running the docking simulations using Auto Dock software. The results of this study provide insights into the potential binding modes and energies of these compounds with DNA and BSA, which could have important implications for drug design and development.

2. 4. 3. ADME Study

The field of medicinal chemistry is rapidly expanding, but the development of a new medication is a complex and expensive process that can take more than a decade and costs billions of dollars. With thousands or even millions of compounds to consider, only a small fraction will meet the rigorous requirements necessary to become an approved medication. In order to increase the efficiency and success of drug development, assessments such as ADMET properties are used to predict the likelihood of a compound's success.[31] These assessments focus on the five processes: absorption, distribution, metabolism, excretion, and toxicity (ADMET) to determine how a chemical substance will behave inside the human body. By evaluating a substance's physicochemical properties, ADMET assessments can help identify compounds that are more likely to succeed in clinical trials. The Swiss ADME web server is a valuable tool in this process, as it provides free calculations of physicochemical parameters based on a substance's structure.

2. 5. Biological Study

2. 5. 1. Binding of the DNA Study by Absorption Titration

A popular technique for studying the nucleic acids with nucleic acid interaction of ligands or metal compounds is UV-VIS spectroscopy. The UV-VIS absorbance spectra and DNA-mediated hypochromism of ligands or metal compounds is determined in a series to evaluate metal complex binding to CT-DNA. By calculating the absorbance at 260–280 nm and evaluating ε_a of 6600 $M^{-1}cm^{-1}$ the concentration of the calf thymus DNA will be ascertained. CT-DNA and the method outlined in the pertinent literature are both employed to assess the interaction of binding synthesized ligands with Re(I) metal compounds.[32]

2. 5. 2. Viscosity Measurement

The binding mechanism of the synthesised compounds with calf thymus DNA was assessed using a viscos-

ity measuring method. The viscosity of the DNA solution increases as molecules intercalate between DNA base pairs.[33] On other hand, when compounds bind to the grooves of DNA, the viscosity increases due to the reduction in the double helix length of DNA. A trend for increasing viscosity can distinguish the intercalation-binding mode from the groove-binding mode. In this study, metal complexes showed a higher increase in viscosity compared to the corresponding ligands, indicating stronger binding of the metal complexes to the ligands.[34]

2. 5. 3. Fluorescence Quenching Analysis by DNA Binding

A fluorescence spectrometer is a highly precise, quick, and sensitive tool for analyzing DNA binding activity even at very low concentrations of compounds and DNA. This study uses the fluoromax-4, HORIBA spectrofluorometer to perform fluorescence-quenching analysis, which provides relevant results related to the binding capacity of the synthetic chemicals within DNA. The studies focuses on explaining how chemicals bind with DNA *via* the intercalation, with traditional intercalating agent EtBr used as a fluorescence marker.[35,36]

2. 5. 4. BSA Binding Study by Absorption Spectra

The protein BSA is essential for the movement of both endogenous and foreign materials in plasma. Plasma, though, can be bad for our molecules. Two important things occur when our molecules bind to BSA in the plasma: (1) the toxicity of the drug is decreased, and (2) the bioavailability of the chemical is raised.[37] The absorption spectra of proteins change when our compounds, referred to as quenchers, engage with BSA.[38] This alteration provides information about the binding affinities and modes of all synthetic compounds toward BSA. By understanding this interaction, we can design and develop effective and safe anticancer drugs.[39]

2. 5. 5. Fluorescence Quenching Analysis by BSA Binding

Tryptophan, phenylalanine, and tyrosine are only a few of the particular amino acid residues that give BSA its luminous features. BSA is a good fluorescent marker for analyzing conformational changes brought on by drug interactions thanks to these residues. Tryptophan has the highest fluorescence intensity of these residues and is crucial in suppressing the fluorescence of BSA. Trp-213 and Trp-134, both residues of the tryptophan found in the BSA, are respectively placed on the surface and within the hydrophobic pocket of the molecule.[40] A total 100 μL of BSA and 2400 μL of phosphate buffer were used for the protein binding experiment. The experiment comprised employing varying quantities of ligands $\mathbf{L^1}$–$\mathbf{L^6}$ and complexes $\mathbf{C^1}$–$\mathbf{C^6}$ in a room temperature environment (0, 10, 20, 30, 40, and 50 μL). Utilizing a spectrofluorometer with a 4.5 nm slit width and covering the wavelength range of 280–550 nm, emission spectra were captured. For BSA, 280 nm was chosen as the excitation wavelength.

2. 5. 6. Antibacterial Activity

Broth dilution method was used to evaluate the antibacterial properties of the synthesized compounds. Antibacterial properties of these compounds were tested against two Gram positive bacterial strains, namely *Staphylococcus aureus* (MTCC 7193), and *Bacillus subtilis* (MTCC 3160) and three Gram negative bacterial strains: *Escherichia Coli* (MTCC 433), *Serratia marcescens* (MTCC 7103), and *Pseudomonas aeruginosa* (MTCC P09). An established and standardized approach for assessing a compound's antibacterial activity is the broth dilution method.[41,42] In this procedure, test compounds are serially diluted in a liquid growth medium.[43,44] The effectiveness of a drug in suppressing bacterial growth can be evaluated by measuring the MIC (minimum inhibitory concentration).[45] This method is useful in evaluating the efficacy of antimicrobial compounds against different bacterial strains and in comparing the relative effectiveness of different compounds.[46]

2. 5. 7. Brine Shrimp Lethality Bioassay (BSLB)

To study cytotoxicity for the produced compounds, the most significant BSLB was used as reported by R. A. Dabhi *et al.* (2022).[47] The cytotoxicity assay employed in the study is cost-effective and requires less time compared to other assays, making it advantageous for determining the cytotoxicity of drugs. In accordance with the protocol, the assay involved the preparation of a saline water (2.5%) solution for hatching of *Artemia cysts* type eggs.[48] Further nauplii (10) were added to the test-tube already containing the brine water (5 mL) and additionally freshly made saline water (5 mL) for the assay. The percentage of *Artemia cyst* mortality was seen to grow in step with the increase in chemical concentration (2, 4, 8, 12, 16, and 20 μM).[49] The resulting graph showed a linear relationship, making it possible to calculate the compounds' LC_{50} values.

2. 5. 8. Anticancer Activity

Cancer patients benefit greatly from chemotherapy, and the IC_{50} values of synthesised compounds are used to evaluate their efficacy as chemotherapeutic agents.[50] To determine whether a substance has the potential to be used in the treatment of cancer, its capacity to suppress cell proliferation must be evaluated.[51,52] The cytotoxicity *in vitro* experiment was performed on the breast cancer cell line MCF-7 to assess their anticancer effectiveness.[53]

3. Result and Discussion

3. 1. NMR, IR, Mass, Conductivity Measurements, and Electronic Spectra

It was found that the ligands' aromatic protons resonate between δ 6.85 to 8.54 ppm. The ligands' NH proton signals are visible in the δ 12.77 to 13.49 ppm range. The NH proton signal, notably in the range from δ 12.70 to 13.08 ppm, were shifted into the up-field region in the organometallic complexes. The presence of an aromatic environment is indicated by signals in the range of δ 110–170 ppm that are found in the ^{13}C NMR data for ligands **L^1**–**L^6** and complexes **C^1**–**C^6**. In $Re(CO)_5Cl$ crystal structure the four CO ligands are positioned equatorially, while one CO ligand is positioned axially which is exactly opposite to the Cl atom.[46,54] Re(I) complexes are formed when the heterocyclic bidentate ligand approaches from the equatorial position and then displaces two CO ligands.[55,56] The ^{13}C NMR spectra show that the facial arrangement has two different low-field signals in the regions of δ 195–199 and 196–198 ppm, respectively, which reflect the configuration of the CO ligands in the Re(I) complexes. The facial isomer is responsible for the biological activity.[57] It has a high distribution and polarity as compared to the meridional isomer.[58]

IR spectroscopy was used to further comprehend the Re(I) complexes' characteristics. The stretching bands seen in the spectra, which ranged from 1735–2021 cm^{-1}, confirm the presence of three coordinated carbonyl ligands. This indicates that they are present in the rhenium metal complexes. It is interesting to note that the stretching frequencies of the CO group in complexes are lower than the stretching frequencies of free CO (2143 cm^{-1}). This result is explained by the back-bonding phenomena, in which electrons are given from the metal→CO π back donation into the π* CO orbital. The total bond strength of CO in the complexes decreases because of this interaction, which also increases the Re–CO bonds.

The mass spectra and fragmentation pattern of the ligands based on tryptanthrin are included in the electronic supplementary information. The molecular ion peak $[M]^+$ is represented by the *m/z* 372.0 peak, while the appearance of the *m/z* 374.0 and $[M + 2]^+$ peaks are due to the chlorine substitution in the ligand **L^2**, respectively. The molecular ion peak $[M]^+$ for the ligand **L^6** is found at *m/z* 440.0. Additionally, separate peaks with intensities of 0.9:1:0.3:0.1 are found at $[M + 2]^+$ *m/z* 442.0, $[M + 4]^+$ *m/z* 446.0, and *m/z* $[M + 6]^+$ 452.0, respectively. Three chlorine substitutions are involved, according to these peaks. All synthesized compounds' ^{1}H, ^{13}C NMR, mass, and IR spectra are shown in the electronic supplementary information (ESI 1).

Conductance was used to examine the ionic and electrolytic characteristics of synthesized compounds. At a temperature of 30 ± 5 °C, the complexes' conductance was measured in DMSO solutions. The complexes demonstrate a non-ionic and non-electrolytic character, as evidenced by the conductance values (10.5–18.2 Ω^{-1} cm^2 mol^{-1}). A $\mu_{eff.}$ value zero B. M. indicates that all of the complexes are diamagnetic and have the low spin configuration d^6 (t_2g^6 eg^0). Electronic spectra of the complexes taken in DMSO solution reveal a band in the 250–270 nm region that corresponds to the π–π* transition and a peak in the 300–400 nm region that denotes the MLCT. These results support the hypothesis that the Re(I) metal complexes have a distorted octahedral geometry.

3. 2. DFT Theory

The electron density cloud revealed by surface-mapped charges is consistent with the results of biomolecular docking, which suggests that the most electronegative components form hydrogen bonds with biomolecules and can be used to determine the binding sites. In order to understand biological processes requiring an electron transport channel, the HOMO–LUMO energy difference is essential. Tran-

Table 1. Summary of the HOMO–LUMO energy differences and docking energy of ligands and tryptanthrin-based Re(I) complexes.

Compounds	DFT Study			Docking Energy		
	HOMO (eV)	LUMO (eV)	HOMO–LUMO energy differences	DNA kcal/mol)	BSA kcal/mol)	TOPO II kcal/mol)
L^1	6.0276	3.4060	2.6215	–8.3	–9.9	–11.8
L^2	6.1928	3.5168	2.6760	–8.6	–10.4	–10.7
L^3	6.1724	3.5035	2.6689	–8.5	–9.6	–11.9
L^4	6.3294	3.6107	2.7187	–9.2	–9.6	–11.6
L^5	6.3106	3.4583	2.8523	–8.5	–10.6	–12.6
L^6	6.4744	3.5688	2.9056	–8.7	–9.8	–12.1
C^1	5.6352	3.9559	1.6793	–8.1	–9.9	–9.7
C^2	5.7582	4.1053	1.6529	–8.5	–9.1	–10.0
C^3	5.7633	4.0759	1.6874	–8.2	–8.9	–10.0
C^4	5.8817	4.2332	1.6485	–8.6	–10.1	–9.7
C^5	5.8561	4.2109	1.6452	–8.0	–8.9	–9.9
C^6	5.9704	4.3600	1.6104	–7.9	–9.6	–10.2

sition metal complexes' kinetic stability, chemical reactivity, and biological activity are all predicted using the energy difference between the HOMO–LUMO orbitals (Table 1). The energy gaps for complexes **C¹**–**C⁶** are 1.6793, 1.6529, 1.6874, 1.6485, 1.6452, and 1.6104 eV, respectively (Figures 2 and 3). A smaller energy gap promotes smoother electron transport, which is important for bioactivity through electron transfer. Compound **C_6** has the smallest energy gap and exhibits strong antibacterial and anticancer properties. In Table 2, the Mulliken charges of quinoxaline-based Re(I) complexes **C¹**–**C⁶** and ligands **L¹**–**L⁶** are summarised (the most positive and the most negative five atom charges). The bond length, bond angle, and Mulliken charges for ligands **L¹**–**L⁶** and complexes **C¹**–**C⁶** are shown in electronic supplementary information (ESI 2).

3. 3. Docking Study

The goal of computational docking research using the widely-used software program AutoDock Vina is to forecast the preferred binding mode and interaction locations of small molecules or ligands with target macromolecules like proteins or nucleic acids.[54] In order to determine binding energy of possible receptor-like ligands and compounds, this program combines molecular mechanics with empirical scoring functions. Based on this energy evaluation, it predicts the most stable conformation. Studies have shown that the binding energies of ligands **L¹**–**L⁶** with DNA, as predicted by AutoDock Vina, typically fall in the range between –8.3 to –9.2 kcal/mol. This range of values indicates a strong binding affinity between the ligands and DNA, which is desirable for potential drug candidates. Similarly, Re(I) complexes **C¹**–**C⁶** have also been studied using AutoDock Vina, and their binding energies with DNA all fall within the range of –7.9 to –8.6 kcal/mol. Although binding energies for Re(I) complexes with DNA are slightly lower than those of ligands, they still indicate a strong binding affinity, which could be useful in applications such as imaging or therapeutics. In the context of computational docking studies, a negative binding energy

Table 2. Mulliken charges of ligands **L¹**–**L⁶** and rhenium(I) metal complexes **C¹**–**C⁶**.

	Most negative charge	Most positive charge		Most negative charge	Most positive charge
L¹	24N (–0.35335)	13N (0.07782)	**C¹**	4C (–0.36207)	12C (0.12663)
	27C (–0.32411)	14C (0.14410)		1C (–0.31561)	2C (0.20970)
	30C (–0.31968)	3C (0.16510)		13N (–0.30104)	3C (0.27875)
	5C (–0.29061)	2C (0.22322)		23N (–0.29971)	37Re (0.28489)
	1C (–0.28117)	26C (0.29198)		27C (–0.28049)	38Cl (0.28758)
L²	23N (–0.35247)	12N (0.07935)	**C²**	1C (–0.30591)	11C (0.13612)
	26C (–0.32197)	13C (0.14476)		4C (–0.30586)	2C (0.209034)
	29C (–0.31943)	3C (0.18246)		12N (–0.30256)	37Cl (0.23384)
	1C (–0.26943)	2C (0.21980)		22N (–0.29183)	36Re (0.29485)
	10N (–0.26317)	25C (0.29264)		26C (–0.28169)	3C (0.29771)
L³	23N (–0.35163)	12N (0.07844)	**C³**	4C (–0.35620)	11C (0.13945)
	29C (–0.31503)	13C (0.14441)		1C (–0.31318)	36Cl (0.16812)
	26C (–0.30206)	3C (0.16518)		12N (–0.30220)	2C (0.21322)
	5C (–0.29016)	2C (0.22402)		22N (–0.27595)	3C (0.27825)
	1C (–0.28042)	25C (0.29738)		23N (–0.27324)	35Re (0.30050)
L⁴	23N (–0.35083)	12N (0.07995)	**C⁴**	12N (–0.30723)	11C (0.14675)
	29C (–0.31482)	13C (0.14509)		1C (–0.30386)	25C (0.15633)
	26C (–0.29992)	3C (0.18256)		4C (–0.30263)	2C (0.21277)
	1C (–0.26893)	2C (0.220697)		23N (–0.28844)	3C (0.29942)
	10N (–0.26290)	25C (0.29791)		22N (–0.28706)	35Re (0.30789)
L⁵	23N (–0.34009)	12N (0.07801)	**C⁵**	4C (–0.35094)	37C (0.10036)
	5C (–0.29133)	13C (0.14346)		12N (–0.31432)	11C (0.14383)
	26C (–0.28880)	3C (0.16764)		1C (–0.31239)	2C (0.21318)
	1C (–0.28240)	2C (0.22197)		22N (–0.30076)	3C (0.28067)
	10N (–0.26667)	25C (0.40708)		23N (–0.28999)	34Re (0.31642)
L⁶	23N (–0.33941)	12N (0.07948)	**C⁶**	12N (–0.31386)	11C (0.14926)
	26C (–0.28670)	13C (0.14414)		1C (–0.30514)	2C (0.21142)
	1C (–0.27076)	3C (0.18446)		4C (–0.30112)	34Re (0.30523)
	10N (–0.26241)	2C (0.21886)		22N (–0.29900)	3C (0.30545)
	29C (–0.25226)	25C (0.40823)		23N (–0.28821)	25C (0.32456)

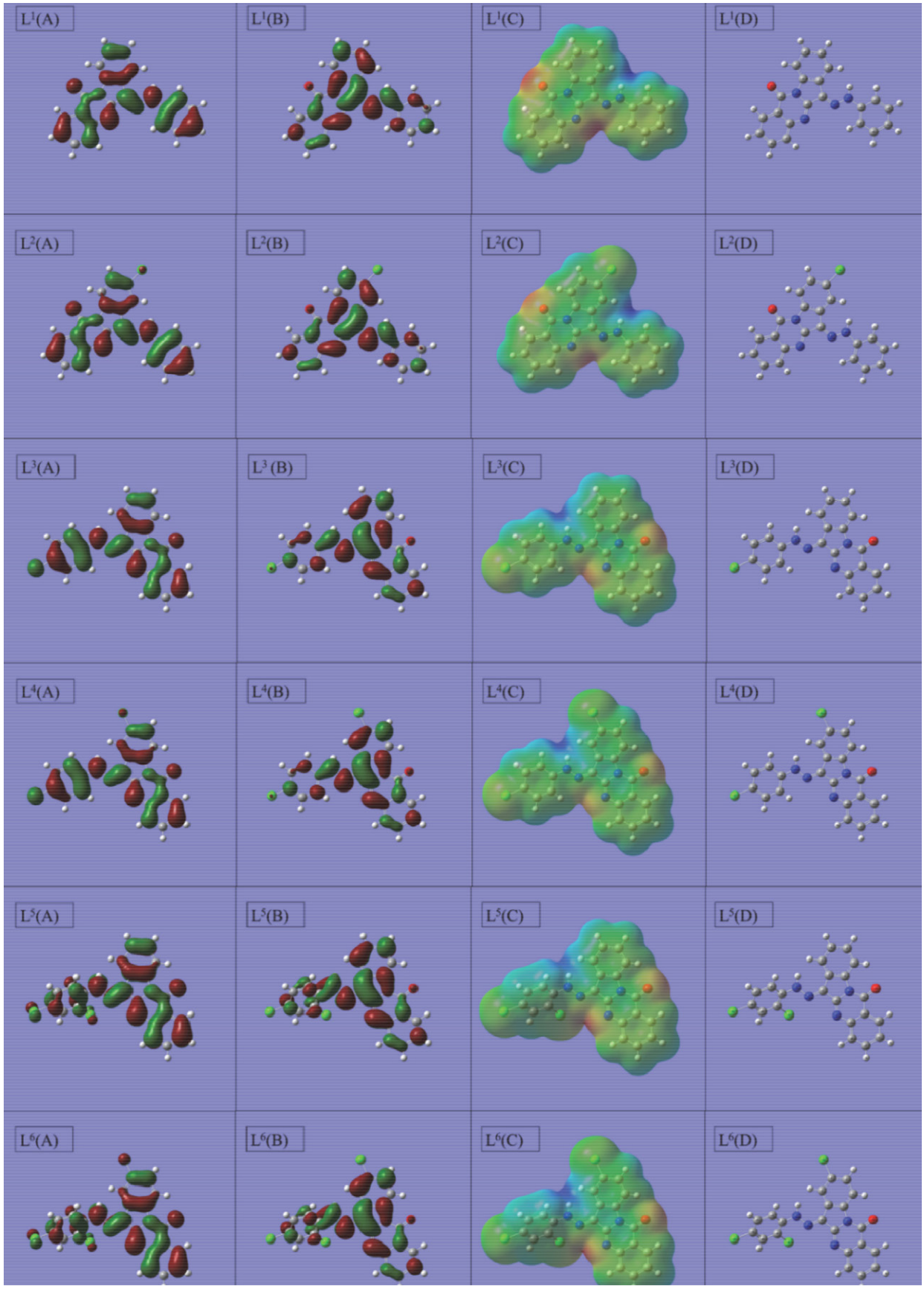

Figure 2. The HOMO (A), LUMO (B), ESP (C) and optimized structures (D) displayed for ligands **L**^{1}–**L**^{6}.

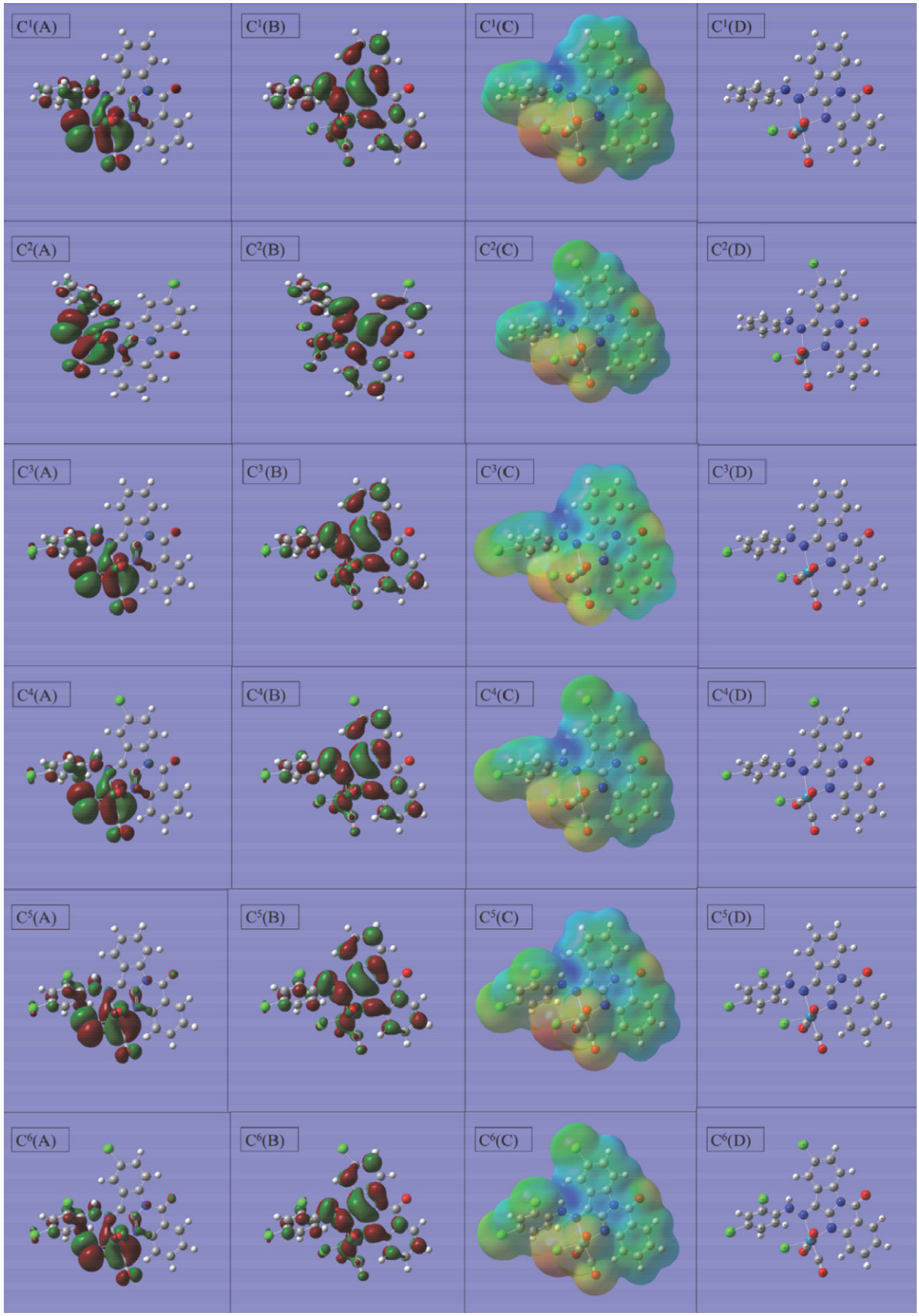

Figure 3. The HOMO (A), LUMO (B), ESP (C) and optimized structures (D) displayed for rhenium(I) metal complexes **C¹**–**C⁶**.

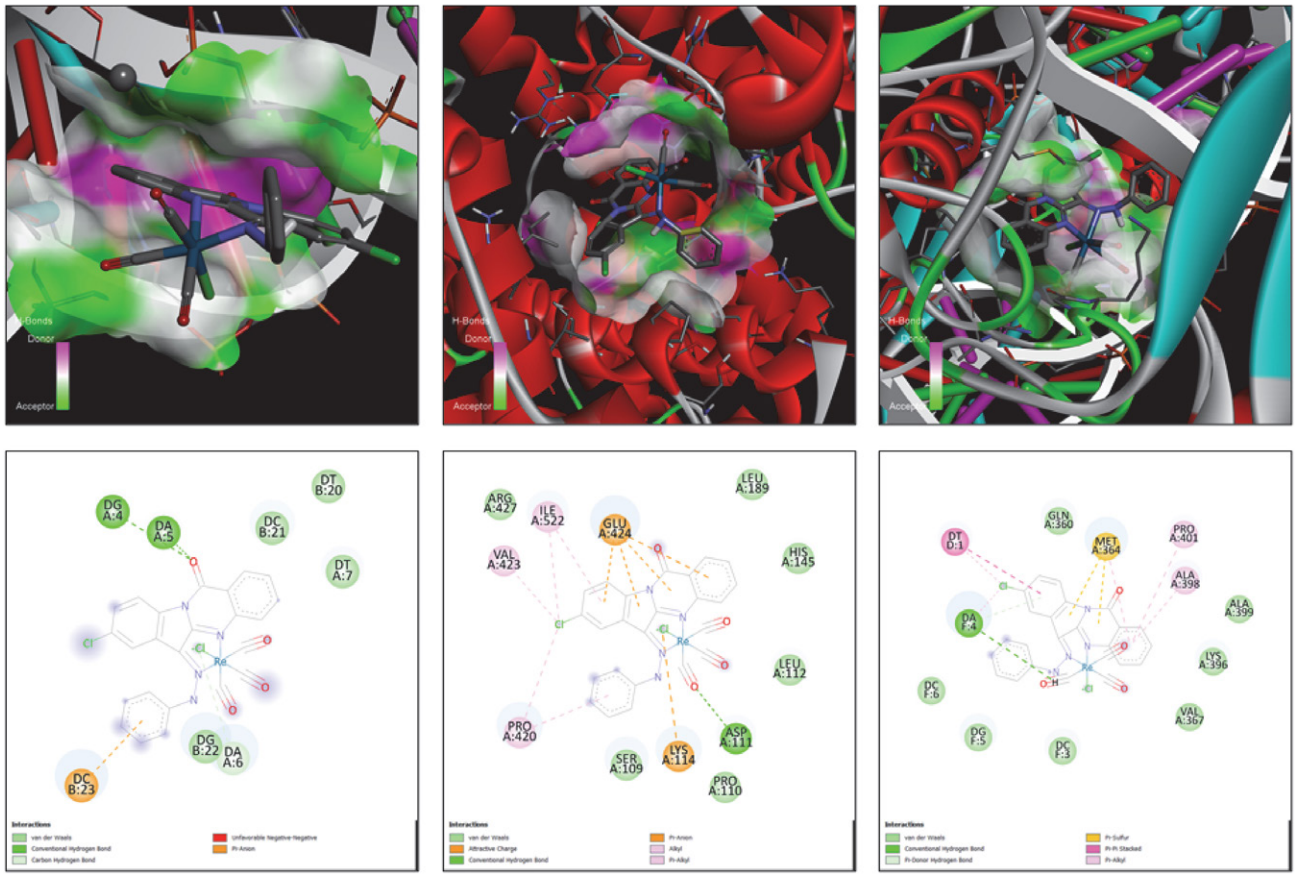

Figure 4. DNA, BSA, and TOPO II binding pose of the complex **C²**.

indicates the most favourable interaction between a small molecule or ligand and a macromolecule such as a protein or nucleic acid. This negative value represents the energy released or gained during the formation of the ligand–macromolecule complex and is an essential factor for determining stability and affinity of the compounds.

Complex **C⁶** has very low binding energy of all the compounds examined, –7.9 kcal/mol, showing a better affinity for binding DNA than the other compounds. Table 1 displays the binding energy information for all synthesized compounds. Using a Discovery studio visualizer, the results of the docking research used to determine. Figure 4 displays the docked structure of complex **C²** with DNA, BSA, and TOPO II. Docking images for each of the synthesized compounds are displayed in the electronic supplementary information (ESI 3).

3. 4. ADME Study

Numerous parameters are provided by Swiss ADME, such as the number of H-bond acceptors, donors and specific atom counts, and molecular refractivity. The partition coefficient between water and *n*-octanol (log $P_{o/w}$), the topological polar surface area (TPSA), blood-brain barrier permeability (BBB), and bioavailability score.[55] On the basis of their examination of the physicochemical characteristics of 2245 drugs in the World Drug Index (WDI) dataset that were authorized for clinical studies in phase II, Lipinski *et al.* proposed a set of five rules in 1997, emphasizing the significance of physicochemical and drug-likeness properties in drug design.[56] TPSA value of 59.28 Å^2 for the ligands **L¹**–**L⁶** indicates a comparatively small polar surface area, smaller than for carboplatin and larger than cisplatin. The ligands **L¹**–**L⁶** have too much smaller values than topotecan, so, this indicates better activities than topotecan. The ligands **L¹**–**L⁶** have higher molar refractivity values than cisplatin and carboplatin, and lower than topotecan, therefore showing higher activity than topotecan.[57,58]

All the ligands have strong permeability and bioavailability because these values are also below 140 Å^2. In other words, these substances are most favourable to be capable to pass *via* biological membranes with ease and have a higher potential of being absorbed into the bloodstream, suggesting favourable traits for their potential as therapeutic candidates.

The log $P_{o/w}$ values, which measure lipophilicity, range between 2.89 and 3.76 for all the ligands. All of the ligands meet the range of values for lipophilicity that is generally accepted because these values are less than 5.

Quantitative classes of solubility in water are defined as insoluble (< –10), poorly (–10 to –6), moderately (–6 to

Table 3. ADME properties of the synthesized compounds.

Ligands	L^1	L^2	L^3	L^4	L^5	L^6	Cisplatin	Carboplatin	Topotecan
Molecular weight	338.37	372.81	372.81	407.25	407.25	441.70	300.05	371.25	457.90
H-Bond acceptors	3	3	3	3	3	3	2	6	7
H-Bond donors	1	1	1	1	1	1	2	2	2
TPSA (Å^2)	59.28	59.28	59.28	59.28	59.3	59.3	6.48	59.08	104.89
log $P_{o/w}$	2.89	2.97	3.15	3.38	3.53	3.76	—	–0.63	1.85
Molar Refractivity	102.86	107.87	107.87	112.88	113	118	21.16	38.49	114.81
log *S*	–5.08	–5.67	–5.67	–6.25	–6.25	–6.84	–0.826	–1.657	–3.02
Rotatable bonds	2	2	2	2	2	2	0	0	2
Lypinski's rule	0	0	0	0	1	1	—	0	0

–4), soluble (–4 to –2), very (–2 to 0), and highly soluble (>0).[55] According to the obtained results, ligand **L^1** demonstrated a solubility rating as "moderately soluble" with a value of –5.1. The solubility ratings for the other ligands, which ranged from –5.1 to –6.8, were within the "soluble" range. It was discovered that there were 3 hydrogen bond donors and one hydrogen bond acceptor in each of the ligands. All of the developed derivatives were found to have molecular weights around 400, suggesting that they could move, diffuse, and absorb easily (Table 3). Good oral bioavailability is influenced by the rotatable bonds and it is essential that this number be lower than 10. There are two rotatable bonds in each of the ligands.

3. 5. UV-visible Absorption Titration Experiment

3. 5. 1. DNA Binding

The efficacy of a target molecule in treating a disease is partially dependent on its ability to bind tightly to DNA. Fortunately, anticancer drugs are designed to target DNA, which can be broken down in multiple ways, including through interactions with specific drug molecules. Moreover, cancer cells typically experience DNA damage first, which can potentially halt cell division and induce cell death.[59]

The literature describes a technique using CT-DNA to evaluate the binding interaction of synthetic compounds. This technique involves using UV-visible spectroscopy experiments to study how tiny medicinal molecules interact with DNA.[60] The resulting UV-visible binding spectra of the compound intercalating in DNA show hypochromicity and bathochromic changes due to the stacking engagement of the ligand to DNA base pairs and aromatic chromophore.[52] The compound's absorption bands display clear hypochromism at 380 nm with a small redshift as the amount of CT-DNA is increased, confirming an intercalation pattern that involves a stacking contact between the quinazoline ring and DNA base pairs.[61]

Tryptanthrin-based ligands **L^1**–**L^6** and the related rhenium(I) complexes **C^1**–**C^6** were studied for their binding mechanisms. The bathochromic and hypochromic shifts noticed, suggest that intercalation, a non-covalent contact, was involved in the binding process. The complexes' binding constants (K_b) ranged from $0.98{\cdot}10^5$ to $1.77{\cdot}10^5$ M^{-1}, whereas the ligands' binding constants (K_b) ranged from $0.8{\cdot}10^5$ to $1.33{\cdot}10^5$ M^{-1}. Examining how the compounds interacted with DNA, it was discovered that adding a DNA solution caused clear spectroscopic changes. The spectra shifted by 3–5 nm as a result of these modifications which included hypochromism and bathochromic effect. The sequence of strength in which the ligands **L^1**–**L^6** and complexes **C^1**–**C^6** attach to CT-DNA was: **C^6** > **C^4** > **C^5** > **C^2** > **C^3** > **C^1** > **L^6** > **L^4** > **L^5** > **L^2** > **L^3** > **L^1**. Equation $\Delta G = -RT\ln K_b$ was used to evaluate the Gibbs free energy (ΔG) at 298 K. Negative ΔG values showed that the compounds and DNA adduct formation were spontaneous. All complexes **C^1**–**C^6** displayed (Figures 5A and B) higher binding constant than the corresponding ligand, which is similar to previously reported Re(I) complexes.[62]

3. 5. 2. Viscosity

The physical characteristics of the interaction can be investigated in order to identify the sort of binding that occurs between DNA and metal complexes. Increased solution viscosity indicates the intercalation-type binding, while decreased solution viscosity suggests the groove binding. Ethidium bromide is commonly used as an intercalator. When synthesized compounds interact with DNA, DNA solutions viscosity changes. Then flow time increases with each addition of the metal complex solution (Figures 5C and D). This demonstrates an interactive mode of binding, as confirmed by related research findings.[63]

3. 5. 3. BSA Binding

It is essential to look into how medication molecules interact with blood plasma proteins in order to assure the targeted distribution of those molecules. Given that HSA (human serum albumin) and BSA (bovine serum albumin) share 78% of their structural similarities, BSA is randomly used as a reference group of amino acids in this research.[64] Here, the binding constant value of ligands **L^1**–**L^6** is obtained in the range of $0.9–1.4{\cdot}10^4$ M^{-1}, and in the case of complexes **C^1**–**C^6** is obtained in the range of $1.43–1.86{\cdot}10^4$

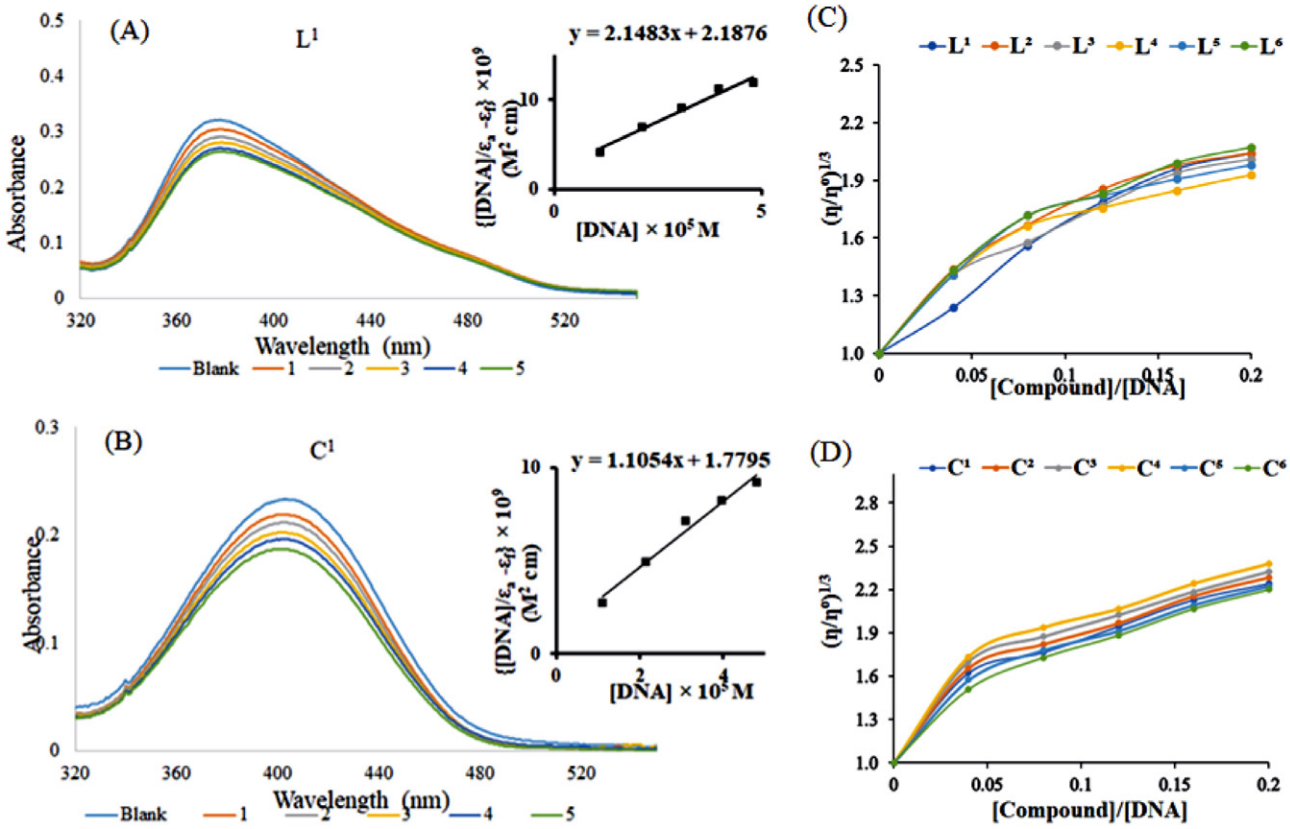

Figure 5. (A) and (B) The K_b value graph and DNA binding spectra of **L¹** and **C¹**. Viscosity (C) of ligands **L¹**–**L⁶** and (D) of complexes **C¹**–**C⁶**.

M^{-1}. For both BSA and DNA interaction, the complexes' **C¹**–**C⁶** binding constants exhibit a consistent pattern. Figure 6 displays a typical spectrum for the BSA binding. The results of the docking investigation also show that the interaction of the substance with BSA has an almost the same pattern in the energy for binding, corroborating the exact binding predicted by theoretical binding predictions.

3. 6. Fluorescence Titration

3. 6. 1. Fluorescence Quenching Studies with DNA

The most efficient and sensitive method for analyzing the interaction between CT-DNA, EtBr (ethidium bromide), and compounds is the use of fluorescence methods.[65] EtBr one of the most delicate fluorescent probes, has a flat shape that intercalates with DNA to bind to it. It is frequently used to investigate DNA structural changes brought on by interactions with proteins or tiny chemicals. When present in an aqueous environment, EtBr typically exhibits modest fluorescence efficiency; however, the presence of DNA significantly increases its fluorescence intensity. Upon excitation at 520 nm, the CT-DNA-EtBr system exhibited a peak emission at 602 nm, indicating the presence of a maximum emission wavelength. As the concentration of the compound increases, the fluorescence intensity of the CT-DNA-EtBr system diminishes, while the wavelength of the emission maximum remains relatively unchanged; there are three possible explanations. Firstly, it

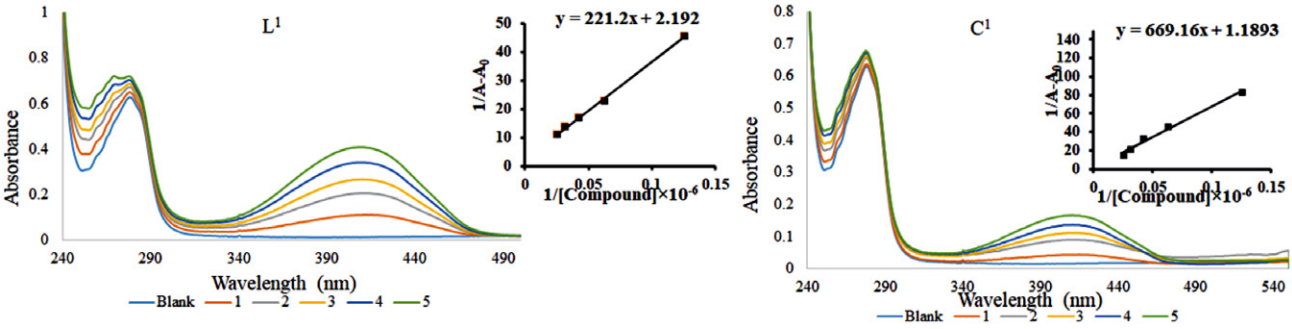

Figure 6. BSA binding spectra, and K_b value graph of **L¹** and **C¹**.

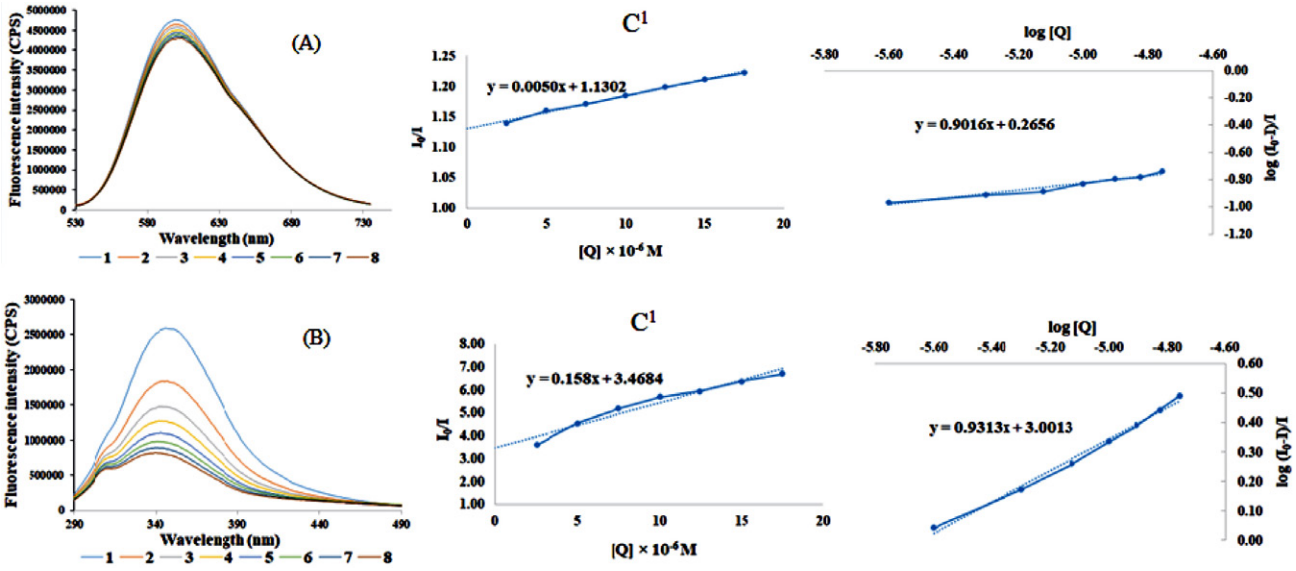

Figure 7. The fluorescence quenching spectra of DNA (A) and BSA (B), I_0/I versus [Q] and log I_0–I/I versus log [Q] plot for complex **C**[1].

could be due to the binding of compounds with EtBr, leading to fluorescence quenching. Secondly, the compounds might compete with EtBr for binding sites on the CT-DNA, thereby displacing intercalated EtBr from the complex and reducing the concentration for EtBr bound to CT-DNA (Figure 7A). Finally, it is possible that a new complex comprising compounds CT-DNA and EtBr will have formed as a result of the interaction between compounds and CT-DNA-EtBr. While the complexes **C**[1]–**C**[6] displayed K_{sv} ranging in between 0.50 to 0.68·10[4] M^{-1}, the ligands **L**[1]–**L**[6] displayed values between 0.35 to 0.54·10[4] M^{-1}.

3. 6. 2. Fluorescence Quenching Study with BSA

Proteins are vital macromolecules widely distributed in cells and essential for maintaining biological processes. Bovine serum albumin (BSA) is a large part of plasma protein and is essential for the body's transportation and metabolization of a variety of substances.[66] This study aims to better understand how the target protein molecule, BSA, interacts with its environment. BSA was chosen because of its crucial attributes for medicine, exceptional binding capabilities, ease of accessibility, and structural resemblance to human serum albumin (HSA).[67,68] The complexes **C**[1]–**C**[6] Stern–Volmer binding constant (K_{sv}) ranged from 1.58 to 1.95·10[4] M^{-1}, while the ligands **L**[1]–**L**[6] showed values between 0.85 to 0.149·10[4] M^{-1}. The representative fluorescence spectra, I_0/I plot, and log I_0–I/I vs. log [Q] graph for complex **C**[1] is shown in Figure 7B.

3. 7. Anticancer Activity

In the MCF-7 cell line, we used a colorimetric technique to evaluate the compounds anticancer potential. Cell viability was variable and increased with sample concentration for both the tryptanthrin-based ligand and Re(I) complexes.[69] After calculating the IC_{50} values and looking at the % viability-concentration graph, we discovered that the ligands had greater IC_{50} values than the equivalent Re(I) complexes. The IC_{50} values for the Re(I) complexes are between 92.62 to 110.04 μg/mL, while those for the tryptanthrin-based ligands are between 142.54 to 175.81 μg/mL. The fact that the complex **C**[6] had the lowest IC_{50} value is noteworthy, and this is because of the presence of chlorine group on the tryptanthrin ring. The complexes show the IC_{50} values that closely resemble that of cisplatin (80.00 μg/mL) and outperform the effectiveness of the widely used medication carboplatin (165.28 μg/mL), indicating that the molecule has a moderate level of cytotoxicity.[70,71] IC_{50} of the ligands **L**[1]–**L**[6] and Re(I) complexes **C**[1]–**C**[6] is shown as a bar plot (Figure 8).

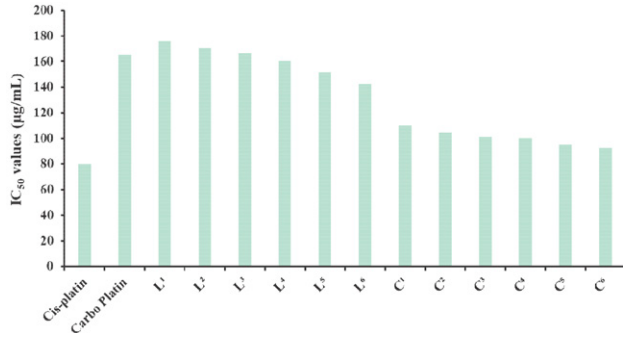

Figure 8. IC_{50} of the ligands **L**[1]–**L**[6] and Re(I) complexes **C**[1]–**C**[6].

3. 8. Antibacterial Activity

To combat infectious diseases, it is crucial to control the growth of microorganisms, and this requires effective

antibacterial agents. The potency of a newly synthesized molecule against various microorganisms can be assessed by measuring its antibacterial activity. Nutrient agar is commonly used to culture bacteria, and DMSO is used to prepare the testing compound's solution.[72] Non-turbid results shows that the specific concentration of the tested compound inhibits the growth of the microorganism.[73]

The antibacterial activity of complexes **C⁵** and **C⁶** is noteworthy and attributed to the presence of 3 and 4 chlorine atoms, respectively, in their aromatic moiety, which may have an electron-donating effect.[74] Moreover, metal complexes tend to exhibit higher antibacterial activity than their ligands, possibly due to the activation of the ligand by the metal ion during complex formation and an increase in lipophilicity; it improves medication molecule penetration across the bacterial membrane.[69,75,76] The compounds' MIC (minimum inhibitory concentration) values are displayed in a bar graph in Figure 9. It is evident that complexes **C⁵** and **C⁶** have lower MIC values than the other compounds, indicating their stronger antibacterial activity.

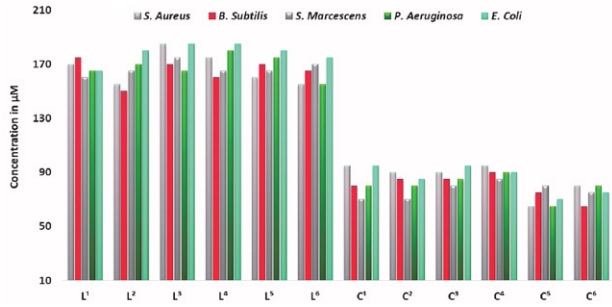

Figure 9. The MIC values for each compound displayed as a bar plot.

3. 9. Cytotoxicity on Brine Shrimp

Brine prawns are an essential component of fish's diet. These small creatures will be studied in a test tube because of their brief seven-day life cycle. They are commonly used to test the cytotoxicity of chemicals on marine species because of their extraordinary ability to thrive in a variety of environmental situations.[77] This research makes use of lab-grown *Artemia cysts*. Analyzing the graph of the mortality percentage versus the logarithm of concentration allows one to determine a substance's lethal concentration (LC_{50}). The minimum concentration necessary to kill 50% of the prawn population under study is known as the lethal concentration.[49,51]

Compound **C⁶** has a lower LC_{50} value because it contains a four-chlorine (-Cl) group, which indicates that it is more cytotoxic than other synthesized compounds. The chlorine substituent, which raises the compounds' lipophilicity and therefore raises its permeability, is to blame for this increased cytotoxicity. All compounds have LC_{50} values that are higher than the widely used anticancer drug, cisplatin (LC_{50} = 3.16 µg/mL). However, compound **C⁶** has an LC_{50} value that is rather closer to cisplatin (Figure 10).

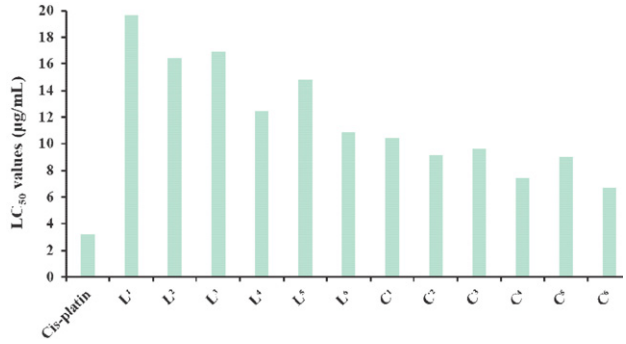

Figure 10. The LC_{50} data of the synthesized compounds on *Artemia cysts*.

4. Conclusion

UV-Vis absorption titration, and docking assays showed that the synthesised compounds had a high affinity for CT-DNA and participated in intercalation-type binding. The IC_{50} values for all the compounds against MCF-7 cells in a cellular investigation range from 90 to 176 µg/mL, indicating substantial anticancer activity. The synthesized rhenium(I) complex **C⁶** shows an IC_{50} value comparable to that of cisplatin and all rhenium complexes exhibit better IC_{50} values than carboplatin. The *in vitro* cytotoxicity tests of synthesized compounds also show how well they work against *Artemia cysts*. The LC_{50} values of complex **C⁶** is closed to the LC_{50} value of cisplatin. The result for the evaluation of the antimicrobial activities on Gram-positive and Gram-negative microorganisms show that all the complexes have better antibacterial activity. According to the ADME analysis all the compounds have an excellent pharmacokinetic profile. DFT simulations reveal that the electronic distribution predominately resides over the metal ion in the HOMO orbital, which is extremely near to the actual results. Notably, the complex **C⁶** has substantial antibacterial and anticancer activity and has the lowest HOMO–LUMO energy gap (1.6104 eV).

Acknowledgement

I am very grateful to the CSIR, New Delhi, for a CSIR-JRF. The authors thank the Sardar Patel University's Department of Chemistry for providing them with access to crucial research resources. We also thank the DST-PURSE at Sardar Patel University for helping with the LC-MS analysis. The authors further acknowledge the support from the CAS Phase-II and UGC-CPEPA programmes as well as the instrumentation and chemical resources made available by Sardar Patel University in India.

5. References

1. I. Yavari, M. Askarian-Amiri, *Synth. Commun.* **2021**, *51*(10), 1602–1608.
2. L. Si, P. Li, X. Liu, L. Luo, *J. Enzyme Inhib. Med. Chem.* **2016**, *31*, 184–196. **DOI:**10.1080/14756366.2016.1178639
3. J. Y. Gao, C. S. Chang, J. C. Lien, T. W. Chen, J. L. Hu, J. R. Weng, *Biomedicines* **2021**, *9*(11), 1527–1539. **DOI:**10.3390/biomedicines9111527
4. M. S. C. Pedras, A. Abdoli, Q. H. To, C. Thapa, *Chem. Biodiversity* **2019**, *16*(3), e1800579–e1800589. **DOI:**10.1002/cbdv.201800579
5. G. M. Shankar, V. V. Alex, A. A. Nisthul, S. V. Bava, S. Sundaram, A. P. Retnakumari, S. Chittalakkottu, R. J. Anto, *Cell Prolif.* **2020**, *53*(1), 1–14. **DOI:**10.1111/cpr.12710
6. M. Maji, D. Panja, I. Borthakur, S. Kundu, *Org. Chem. Front.* **2021**, *8*(11), 2673–2709. **DOI:**10.1039/D0QO01577F
7. C. Teja, K. Ramanathan, K. Naresh, R. Vidya, K. Gomathi, F. R. Nawaz, *Polycycl. Aromat. Comp.* **2023**, *43*(1), 874–894. **DOI:**10.1080/10406638.2021.2021257
8. A. N. M. A. Alaghaz, M. E. Zayed, S. A. Alharbi, R. A. A. Ammar, A. Chinnathambi, *J. Mol. Struct.* **2015**, *1087*, 60–67. **DOI:**10.1016/j.molstruc.2015.01.035
9. A. Popov, A. Klimovich, O. Styshova, T. Moskovkina, A. Shchekotikhin, N. Grammatikova, L. Dezhenkova, D. Kaluzhny, P. Deriabin, A. Gerasimenko, A. Udovenko, V. Stonik, *Int. J. Mol. Med.* **2020**, *46*(4), 1335–1346.
10. M. I. Shahin, D. A. Abou El Ella, N. S. M. Ismail, K. A. M. Abouzid, *Bioorg. Chem.* **2014**, *56*, 16–26. **DOI:**10.1016/j.bioorg.2014.05.010
11. R. Guda, R. Korra, S. Balaji, R. Palabindela, R. Eerla, H. Lingabathula, N. R. Yellu, G. Kumar, M. Kasula, *Bioorg. Med. Chem. Lett.* **2017**, *27*(20), 4741–4748. **DOI:**10.1016/j.bmcl.2017.08.064
12. R. Kaur, S. K. Manjal, R. K. Rawal, K. Kumar, *Biomol. Struct.* 2017, *25*, 4533–4552. **DOI:**10.1016/j.bmc.2017.07.003
13. S. J. S. Franchi, R. A. de Souza, A. E. Mauro, I. Z. Carlos, L. C. de A. Ribeiro, F. V. Rocha, A. V. de Godoy-Netto, *Acta Chim. Slov.* **2018**, *65*(3), 547–553. **DOI:**10.17344/acsi.2017.4112
14. F. V. Rocha, C. V. Barra, S. J. S. Franchi, A. V. G. Netto, A. E. Mauro, R. C. G. Frem, *J. Therm. Anal. Calorim.* **2011**, *106*(2), 385–389. **DOI:**10.1007/s10973-010-1239-1
15. A. Kamal, B. V. S. Reddy, B. Sridevi, A. Ravikumar, A. Venkateswarlu, G. Sravanthi, J. P. Sridevi, P. Yogeeswari, D. Sriram, *Bioorg. Med. Chem. Lett.* **2015**, *25*(18), 3867–3872. **DOI:**10.1016/j.bmcl.2015.07.057
16. D. A. Abdelrheem, A. A. Rahman, K. N. M. Elsayed, H. R. Abd El-Mageed, H. S. Mohamed, S. A. Ahmed, *J. Mol. Struct.* **2021**, *1225*, 129245. **DOI:**10.1016/j.molstruc.2020.129245
17. A. S. El-Tabl, F. A. El-Saied, W. Plass, A. N. Al-Hakimi, *Spectrochim. Acta A Mol. Biomol. Spectrosc.* **2008**, *71*(1), 90–99. **DOI:**10.1016/j.saa.2007.11.011
18. A. S. El-Tabl, F. A. El-Saied, A. N. Al-Hakimi, *Transit. Met. Chem.* **2007**, *32*(6), 689–701. **DOI:**10.1007/s11243-007-0228-0
19. A. S. El-Tabl, M. Mohamed Abd El-Waheed, M. A. Wahba, N. Abd El-Halim Abou El-Fadl, *Bioinorg. Chem. Appl.* **2015**, *2015*, 126023–126036. **DOI:**10.1155/2015/126023
20. Y. Li, S. Zhang, R. Wang, M. Cui, W. Liu, Q. Yang, C. Kuang, *Bioorg. Med. Chem. Lett.* **2020**, *30*(11), 127159. **DOI:**10.1016/j.bmcl.2020.127159
21. E. H. El-Sayed, K. S. Mohamed, *Polycycl. Aromat. Comp.* **2021**, *41*(5), 1077–1093. **DOI:**10.1080/10406638.2019.1653941
22. H. Luo, C. T. Vong, H. Chen, Y. Gao, P. Lyu, L. Qiu, M. Zhao, Q. Liu, Z. Cheng, J. Zou, P. Yao, C. Gao, J. Wei, C. O. L. Ung, S. Wang, Z. Zhong, Y. Wang, *Chin. Med. (United Kingdom)* **2019**, *14*(1), 1–58.
23. A. H. Mane, A. D. Patil, S. R. Kamat, R. S. Salunkhe, *ChemistrySelect* **2018**, *3*(23), 6454–6458. **DOI:**10.1002/slct.201800677
24. Z. Sadeghian, M. Bayat, F. Safari, *Med. Chem. Res.* **2022**, *31*(3), 497–506. **DOI:**10.1007/s00044-022-02856-4
25. M. P. Dhaduk, R. A. Dabhi, B. S. Bhatt, V. D. Bhatt, M. N. Patel, *Mater. Today Proc.* **2022**, *65*, 221–228. **DOI:**10.1016/j.matpr.2022.06.119
26. S. C. Lemos, S. J. S. Franchi, A. V. G. Netto, A. E. Mauro, O. Treu-Filho, R. C. G. Frem, E. T. De Almeida, C. Torres, *J. Therm. Anal. Calorim.* **2011**, *106*(2), 391–397. **DOI:**10.1007/s10973-011-1494-9
27. W. H. Mahmoud, R. G. Deghadi, G. G. Mohamed, *Appl. Organomet. Chem.* **2018**, *32*(4), 1–22. **DOI:**10.1002/aoc.4289
28. W. H. Mahmoud, N. F. Mahmoud, G. G. Mohamed, *J. Organom. Chem.* **2017**, *848*, 288–301. **DOI:**10.1016/j.jorganchem.2017.08.001
29. A. N. M. A. Alaghaz, H. A. Bayoumi, Y. A. Ammar, S. A. Aldhlmani, *J. Mol. Struct.* **2013**, *1035*, 383–399. **DOI:**10.1016/j.molstruc.2012.11.030
30. A. N. M. A. Alaghaz, Y. A. Ammar, H. A. Bayoumi, S. A. Aldhlmani, *J. Mol. Struct.* **2014**, *1074*, 359–375. **DOI:**10.1016/j.molstruc.2014.05.078
31. Y. Kaddouri, B. Bouchal, F. Abrigach, M. El Kodadi, M. Bellaoui, R. Touzani, *J. Chem.,* **2021**, *2021*, 1–11. **DOI:**10.1155/2021/6663245
32. M. N. Patel, P. A. Dosi, B. S. Bhatt, V. R. Thakkar, *Spectrochim. Acta A Mol. Biomol. Spectrosc.* **2011**, *78*(2), 763–770. **DOI:**10.1016/j.saa.2010.11.056
33. M. N. Patel, B. S. Bhatt, P. A. Dosi, *Spectrochim. Acta A Mol. Biomol. Spectrosc.* **2013**, *110*, 20–27. **DOI:**10.1016/j.saa.2013.03.037
34. A. F. Shoair, A. A. El-Bindary, N. A. El-Ghamaz, G. N. Rezk, *J. Mol. Liq.* **2018**, *269*(ii), 619–638. **DOI:**10.1016/j.molliq.2018.08.075
35. P. R. S. Devi, S. T. David, C. Joel, R. B. Bennie, S. D. Abraham, *Ind. J. Chem. A* **2021**, *60*(11), 1416–1426.
36. Y. L. Sang, X. S. Lin, *Acta Chim. Slov.* **2019**, *66*(1), 168–172. **DOI:**10.17344/acsi.2018.4749
37. M. Jayasree, R. S. Aparna, R. R. Anjana, J. S. Anjali Devi, N. John, K. Abha, A. Manikandan, S. George, *Anal. Chim. Acta* **2018**, *1031*(iii), 152–160. **DOI:**10.1016/j.aca.2018.05.026
38. R. R. Varma, J. G. Pandya, F. U. Vaidya, C. Pathak, B. S: Bhatt, M. N. Patel, *Acta Chim. Slov.* **2020**, *67*(3), 957–969.

DOI:10.17344/acsi.2020.6017
39. P. S. Karia, P. A. Vekariya, A. P. Patidar, D. N. Kanthecha, B. S. Bhatt, M. N. Patel, *Acta Chim. Slov.* **2019**, *66*(4), 944–949. **DOI:**10.17344/acsi.2019.5159
40. N. Singh, N. Kumar, G. Rathee, D. Sood, A. Singh, V. Tomar, S. K. Dass, R. Chandra, *ACS Omega* **2020**, *5*(5), 2267–2279. **DOI:**10.1021/acsomega.9b03479
41. J. V. Mehta, S. B. Gajera, M. N. Patel, *Spectrochim. Acta A Mol. Biomol. Spectrosc.* **2015**, *136*, 1881–1892. **DOI:**10.1016/j.saa.2014.10.103
42. E. H. El-Sayed, A. A. Fadda, *J. Heterocycl. Chem.,* **2018**, *55*(10), 2251–2260. **DOI:**10.1002/jhet.3276
43. B. H. Pursuwani, B. S. Bhatt, F. U. Vaidya, C. Pathak, M. N. Patel, *J. Biomol. Struct. Dyn.* **2021**, *39*(8), 2894–2903. **DOI:**10.1080/07391102.2020.1756912
44. D. N. Kanthecha, B. S. Bhatt, M. N. Patel, D. B. Raval, V. R. Thakkar, F. U. Vaidya, C. Pathak, *J. Inorg. Organomet. Polym. Mater.* **2020**, *30*(12), 5085–5099. **DOI:**10.1007/s10904-020-01618-2
45. S. Rishikesan, M. A. M. Basha, *Acta Chim. Slov.* **2020**, *67*(1), 235–245. **DOI:**10.17344/acsi.2019.5379
46. R. R. Varma, B. H. Pursuwani, E. Suresh, B. S. Bhatt, M. N. Patel, *J. Mol. Struct.* **2020**, *1200*, 127068–127079. **DOI:**10.1016/j.molstruc.2019.127068
47. R. A. Dabhi, M. P. Dhaduk, V. D. Bhatt, B. S. Bhatt, *J. Biomol. Struct.Dyn.* **2022**, *41*(12), 5382–5398. **DOI:**10.1080/07391102.2022.2086176
48. E. H. El-Sayed, A. A. Fadda, *Acta Chim. Slov.* **2018**, *65*(4), 853–864. **DOI:**10.17344/acsi.2018.4506
49. R. Lalrempuia, A. Stasch, C. Jones, *Chem. Asian J.* **2015**, *10*(2), 447–454. **DOI:**10.1002/asia.201403089
50. P. Bhattacharjee, T. Ghosh, S. Sarkar, P. Pandya, K. Bhadra, *J. Mol. Recognit.* **2018**, *31*(4), 1–16. **DOI:**10.1002/jmr.2687
51. N. Dey, B. Maji, S. Bhattacharya, *Chem. Asian J.* **2018**, *13*(6), 664–671. **DOI:**10.1002/asia.201701795
52. S. Ghosh, D. Usharani, S. De, E. D. Jemmis, S. Bhattacharya, *Chem. Asian J.* **2008**, *3*(11), 1949–1961. **DOI:**10.1002/asia.200800151
53. M. P. Dhaduk, R. A. Dabhi, B. S. Bhatt, V. D. Bhatt, M. N. Patel, *Chem. Phys. Impact* **2023**, *7*, 100261. **DOI:**10.1016/j.chphi.2023.100261
54. K. Chanawanno, J. T. Engle, K. X. Le, R. S. Herrick, C. J. Ziegler, *Dalton Trans.* **2013**, *42*(37), 13679–13684. **DOI:**10.1039/c3dt50894c
55. G. Balakrishnan, T. Rajendran, K. Senthil Murugan, M. Sathish Kumar, V. K. Sivasubramanian, M. Ganesan, A. Mahesh, T. Thirunalasundari, S. Rajagopal, *Inorg. Chim. Acta* **2015**, *434*(I), 51–59. **DOI:**10.1016/j.ica.2015.04.036
56. A. Núñez-Montenegro, R. Carballo, E. M. Vázquez-López, *J. Inorg. Biochem.* **2014**, *140*, 53–63. **DOI:**10.1016/j.jinorgbio.2014.06.012
57. F. A. Cotton, L. M. Daniels, *Cryst. Struct. Commun.* **1983**, *39*(11), 1495–1496. **DOI:**10.1107/S0108270183009014
58. R. Kia, V. Mirkhani, A. Kálmán, A. Deák, *Polyhedron* **2007**, *26*(8), 1711–1716. **DOI:**10.1016/j.poly.2006.12.025
59. P. Adwin Jose, M. Sankarganesh, J. Dhaveethu Raja, G. S. Senthilkumar, R. Nandini Asha, S. J. Raja, C. D. Sheela, *J. Biomol. Struct. Dyn.* **2022**, *40*(21), 10715–10729. **DOI:**10.1080/07391102.2021.1947382
60. A. Daina, O. Michielin, V. Zoete, *Sci. Rep.* **2017**, *7*, 1–13. **DOI:**10.1038/srep42717
61. S. Debnath, T. Debnath, S. Bhaumik, S. Majumdar, A. M. Kalle, V. Aparna, *Sci. Rep.* **2019**, *9*(1), 1–14. **DOI:**10.1038/s41598-019-53376-y
62. S. Alam, F. Khan, *J. Biomol. Struct. Dyn.* **2018**, *36*(9), 2373–2390. **DOI:**10.1080/07391102.2017.1355846
63. S. Singh, T. Das, M. Awasthi, V. P. Pandey, B. Pandey, U. N. Dwivedi, Bio*technol. Appl. Biochem*. **2016**, *63*(1), 125–137. **DOI:**10.1002/bab.1346
64. L. H. Abdel-Rahman, A. M. Abu-Dief, H. Moustafa, A. A. H. Abdel-Mawgoud, *Arab. J. Chem.* **2020**, *13*(1), 649–670. **DOI:**10.1016/j.arabjc.2017.07.007
65. M. N. Patel, B. S. Bhatt, P. A. Dosi, *Appl. Biotechnol. Appl. Biochem.* **2012**, *166*(8), 1949–1968. **DOI:**10.1007/s12010-012-9623-x
66. J. Zhu, L. Chen, Y. Dong, J. Li, X. Liu, *Spectrochim. Acta A Mol. Biomol. Spectrosc.* **2014**, *124*, 78–83.
67. R. R. Varma, J. G. Pandya, J. Sharma, C. Pathak, M. N. Patel, *Mol. Divers.* **2021**, *25*(2), 687–699. **DOI:**10.1007/s11030-020-10040-2
68. N. Shankaraiah, C. Jadala, S. Nekkanti, K. R. Senwar, N. Nagesh, S. Shrivastava, V. G. M. Naidu, M. Sathish, A. Kamal, *Bioorg. Chem.* **2016**, *64*, 42–50. **DOI:**10.1016/j.bioorg.2015.11.005
69. S. Mukherjee, I. Mitra, C. Fouzder, S. Mukherjee, S. Ghosh, U. Chatterji, S. C. Moi, *J. Mol. Liq.* **2017**, *247*, 126–140. **DOI:**10.1016/j.molliq.2017.09.104
70. A. Jamshidvand, M. Sahihi, V. Mirkhani, M. Moghadam, I. Mohammadpoor-Baltork, S. Tangestaninejad, H. Amiri Rudbari, H. Kargar, R. Keshavarzi, S. Gharaghani, *J. Mol. Liq.* **2018**, *253*, 61–71. **DOI:**10.1016/j.molliq.2018.01.029
71. V. Srinivasan, T. Khamrang, C. Ponraj, D. Saravanan, R. Yamini, S. Bera, M. A. Jhonsi, *J. Mol. Struct.* **2021**, *1225*, 129153. **DOI:**10.1016/j.molstruc.2020.129153
72. D. N. Kanthecha, D. B. Raval, V. R: Thakkar, M. N. Patel, *Acta Chim. Slov.* **2018**, *65*(2), 333–343. **DOI:**10.17344/acsi.2017.4018
73. M. N. Patel, P. A. Dosi, B. S. Bhatt, *Acta Chim. Slov.* **2012**, *59*(3), 622–631.
74. K. Sarkar, P. Dastidar, *Chem. Asian J.* **2019**, *14*(1), 194–204. **DOI:**10.1002/asia.201801462
75. M. A. Khan, M. Zafaryab, S. H. Mehdi, J. Quadri, M. M. A. Rizvi, *Int. J. Biol. Macromol.* **2017**, *97*, 115–122. **DOI:**10.1016/j.ijbiomac.2016.12.090
76. M. Eslami Moghadam, A. Jafari, R. Kiani Khashandaragh, A. Divsalar, M. Ghasemzadeh, *J. Iran. Chem. Soc.* **2021**, *18*(8), 1927–1939. **DOI:**10.1007/s13738-021-02154-7
77. H. M. Parekh, S. R. Mehta, M. N. Patel, *Russ. J. Inorg. Chem.* **2006**, *51*(1), 67–72. **DOI:**10.1134/S003602360601013X
78. B. D. Salih, A. H. Dalaf, M. A. Alheety, W. M. Rashed, I. Q. Abdullah, *Mater. Today Proc.* **2020**, *43*, 869–874. **DOI:**10.1016/j.matpr.2020.07.083

79. L. W. Xue, H. J. Zhang, P. P. Wang, *Acta Chim. Slov.* **2019**, *66*(1), 190–195. :**OI:**10.17344/acsi.2018.4773
80. S. I. Pascu, P. A. Waghorn, B. W. C. Kennedy, R. L. Arrowsmith, S. R. Bayly, J. R. Dilworth, M. Christlieb, R. M. Tyrrell, J. Zhong, R. M. Kowalczyk, D. Collison, P. K. Aley, G. C. Churchill, F. I. Aigbirhio, *Chem. Asian J.* **2010**, *5*(3), 506–519. **DOI:**10.1002/asia.200900446
81. X. Feng, J. Y. Hu, L. Yi, N. Seto, Z. Tao, C. Redshaw, M. R. J. Elsegood, T. Yamato, *Chem. Asian J.* **2012**, *7*(12), 2854–2863. **DOI:**10.1002/asia.201200530
82. F. U. Ohikhena, O. A. Wintola, A. J. Afolayan, *Int. J. Pharmacol.* **2016**, *12*(7), 701–710. **DOI:**10.3923/ijp.2016.701.710

Povzetek

Sintetizirali smo različne Re(I) organokovinske spojine tipa [(Re(CO)$_3$**L**$^{1-6}$)Cl], kjer so ligandi **L** derivati triptantrina, ter jih karakterizirali z različnimi spektroskopskimi tehnikami. Da bi ugotovili jakost in načine vezave, smo v prisotnosti omenjenih organokovinskih kompleksov izvedli test z DNA telečjega timusa z uporabo absorpcijske titracije in merjenja viskoznosti. Zbrani rezultati kažejo, da gre za interkalacijski tip vezave, kar smo dodatno potrdili s študijami molekulskega sidranja. Švicarsko ADME orodje smo uporabili za izvedbo ADME študije. Osredotočili smo se na izračun energij molekulskih orbital sintetiziranih spojin z uporabo teorije gostotnega potenciala (DFT). Da bi ugotovili morebitne protirakave učinke, smo pripravljene spojine testirali na MCF-7 celični liniji. Ugotovili smo, da so IC_{50} vrednosti naših spojin ekvivalentne vrednostim za standardne učinkovine, kar kaže, da imajo naše spojine podobne antiproliferativne učinke.

Scientific paper

Synthesis, Antibacterial and Antibiofilm Activity of New 1,2,3,5-Tetrazine Derivatives from Coupling Reactions of Diazonium Salt of 2-Amino-6-nitrobenzothiazole With Diverse Substituted 2-Aminobenzothiazole Derivatives

Joseph Tsemeugne,[1,*] Yetiny Atuh Bah,[1] Ulrich Joel Tsopmene,[2] Armelle Tontsa Tsamo,[1] Jérôme Ndefo Ndefongang,[1] Pierre Mkounga,[1] Emmanuel Fondjo Sopbué,[3,*] Jean Paul Dzoyem,[2] and Augustin Ephrem Nkengfack[1]

[1] *Laboratory of Natural Products and Applied Organic Synthesis (LANAPOS), Department of Organic Chemistry, Faculty of Science, University of Yaounde I, P.O. Box 812, Yaounde, Republic of Cameroon;*

[2] *Laboratory of Microbiology and Antimicrobial Substances, Department of Biochemistry, Faculty of Science, University of Dschang, P.O. Box 67, Dschang, Republic of Cameroon;*

[3] *Laboratory of Applied Synthetic Organic Chemistry, Department of Chemistry, Faculty of Science, University of Dschang, P.O. Box 67, Dschang, Republic of Cameroon*

** Corresponding author: E-mail: tsemeugne@yahoo.fr, sopbue@yahoo.fr*

Received: 11-12-2023

Abstract

The coupling reaction of diazonium ion of 2-amino-6-nitrobenzothiazole at 0–5 °C with distinctly substituted 2-aminobenzothiazole derivatives produced new 1,2,3,5-tetrazine derivatives. It was found that diazotized 2-amino-6-nitrobenzo[*d*]thiazol reacts with the ring nitrogen atom of variously substituted 2-aminobenzothiazole derivatives to yield tetrazine nucleus. The benzene ring of benzothiazole bearing electron donor group and annulated to the tetrazine was further substituted *in situ* by other (6-nitrobenzo[*d*]thiazol-2-yl)diazinyl to yield the final product. The structure of the prepared compounds was elucidated using their physical data, elemental analyses, and spectroscopic data. The synthesized compounds were tested for their antimicrobial and antibiofilm activities against *Staphylococcus aureus* and *Escherichia coli* bacteria. Two of the synthesis tetrazine derivatives exhibited interesting antibiofilm potential.

Keywords: 1,2,3,5-tetrazine, 2-aminobenzothiazole, azo dye, antibiofilm activity, antibacterial activity

1. Introduction

Tetrazine is one of the most renowned and efficient pharmaceutical class of compounds.[1,2] Tetrazines are frequently labelled in terms of their biological activities, such as possessing antibacterial,[3,4] antifungal,[5,6] anti-cancer[7,8] properties and some of them are currently used in commercially accessible products.[9] The thermal decomposition of tetrazine leads to the opening of the ring, which results in the formation of nitriles and nitrogen molecules. That is why tetrazines are also used in material sciences to make high-density energy compounds.[10–12] A wide range of methods for the synthesis of tetrazines can be found in the literature.[13] Searching for the best synthetic methodology, we decided to use the coupling reaction of diazonium ion of 2-aminobenzothiazole with other 2-aminobenzothiazole derivatives since a similar approach was recently applied successfully in the preparation of analogous systems containing 1,2,3,5-tetrazine framework.[14] A synthetic pathway designed in such a manner would confirm the versatility of the applied methodology. Tetrazine has three isomeric structures: 1,2,3,4-tetrazine, 1,2,3,5-tetrazine and 1,2,4,5-tetrazine, among which, 1,2,3,5-tetrazine and its derivatives are not often reported in the literature.

In medicinal chemistry, benzothiazole derivatives are well-known for their therapeutic applications. An appraisal of the recent literature showed that many effective

antimicrobial drugs contain benzothiazole moiety within their structure.[15,16] The benzothiazole ring system is above all a structural constituent of the marketable benzothiazole drug Riluzole.[17]

Compounds containing the azo functional group have revealed a wide range of medicinal applications including antibacterial, antifungal, antioxidant and anticancer, among others.[18–20] Based on the above considerations, one can assume that hybrid molecular architectures containing 1,2,3,5-tetrazine, benzothiazole and azo moieties would likely combine the interesting features of all the components to exhibit much better biological profiles.[21–23]

2. Results and Discussion

2. 1. Chemistry

The *in situ* generated intermediate diazonium sulphate **2** (Scheme 1) was prepared by reacting 2-amino-6-nitrobenzothiazole (**1**) with nitrosylsulfuric acid at low temperature (0–5 °C).

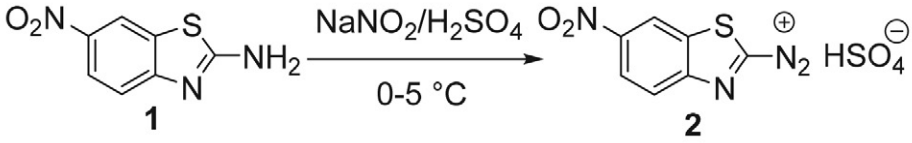

Scheme 1. Synthesis of the diazonium intermediate **2**.

The newly prepared diazonium solution, was then coupled with other 2-aminobenzothiazole derivatives **3**. The subsequent mixture was worked up as usual to yield tetrazine derivatives **4** (Scheme 2). The structure of the newly synthesized compounds **4a–d** was elucidated by IR, UV, and NMR spectroscopy, as well as mass spectral data and elemental analysis data.

The UV–Vis absorption spectra of compound **4** were recorded in the range 270–475 nm, and the results are given in Table 1. All compounds displayed the two usual absorption bands of tetrazines: a weak absorption in the visible range centered around 450 nm due to the combined n→π* transitions of the imine functionalities and a stronger one in the UV around 270 nm corresponding to the π → π* transition of the benzene ring. The broad additional absorption band appearing around 350 nm is also due to an n → π* transition.[24]

In Table 2 are given the important IR data of compounds **4**. One can notice the bands at 883 and 1334 cm^{-1} which are due to the presence of tetrazine skeleton in the structures **4**.[25] The bands at 1118 and 1209 cm^{-1} result from skeletal vibrations of the 1,3-thiazole heterocycle.[26]

Table 2. Assigned IR bands of the compounds **4**

Frequency (cm^{-1})	Type of vibration and bond	Functional group
3065–2920	ν_{CAr-H}	benzyl
1614–1651	$\nu_{C=N}$	1,3-thiazole
1514–1599	$\nu_{C=C}$	benzyl
1441–1487	$\nu_{N=N}$	azo group
1118–1209	ν_{C-S}	1,3-thiazole
883–1334	$\nu_{N-Ntetrazine}$	tetrazine

During the coupling reaction between the diazonium ion of 2-amino-6-nitrobenzothiazole (**2**) with 2-aminobenzothiazole (**3a**), it was established that no substitution reaction occurred between the two components as anticipated. Instead, the condensation product **4a** was isolated from this reaction, probably from the subsequent nucleophilic addition of the heteroaromatic nitrogen atom of the benzothiazole ring as displayed in Scheme 3.

Compound **4a** was obtained as a red powder with a sharp melting point in the range 213–215 °C. The elemental analysis and the HREIMS experiments were used to establish the bruto formula as $C_{14}H_7N_5O_6S_3$, showing that the coupling product crystallized with one sulfate ion SO_4^{2-}. The HRMS showed an ion peak at *m/z* 437 corre-

Table 1: Absorption maxima (λ_{max} in nm) of the compounds **4** in methanol

Solvent	4a		4b		4c		4d	
	λ (nm)	lg ε_{max}	λ (nm)	lg ε_{max}	λ (nm)	lg ε_{max}	λ (nm)	lg ε_{max}
MeOH	277.9	3.85	273.8	4.45	270.4	4.41	277.0	4.15
	296.9	3.74	285.3	4.43	295.2	4.28	295.2	4.04
	343.9	3.86	297.7	4.34	335.6	4.44	300.1	4.04
	400.0	3.67	345.6	4.43	347.1	4.44	341.4	4.20
	470.1	3.98	396.7	4.29	367.4	4.41	364.5	4.20
			475.1	4.64	387.6	4.35	392.6	4.06
					442.9	4.45	465.2	4.24

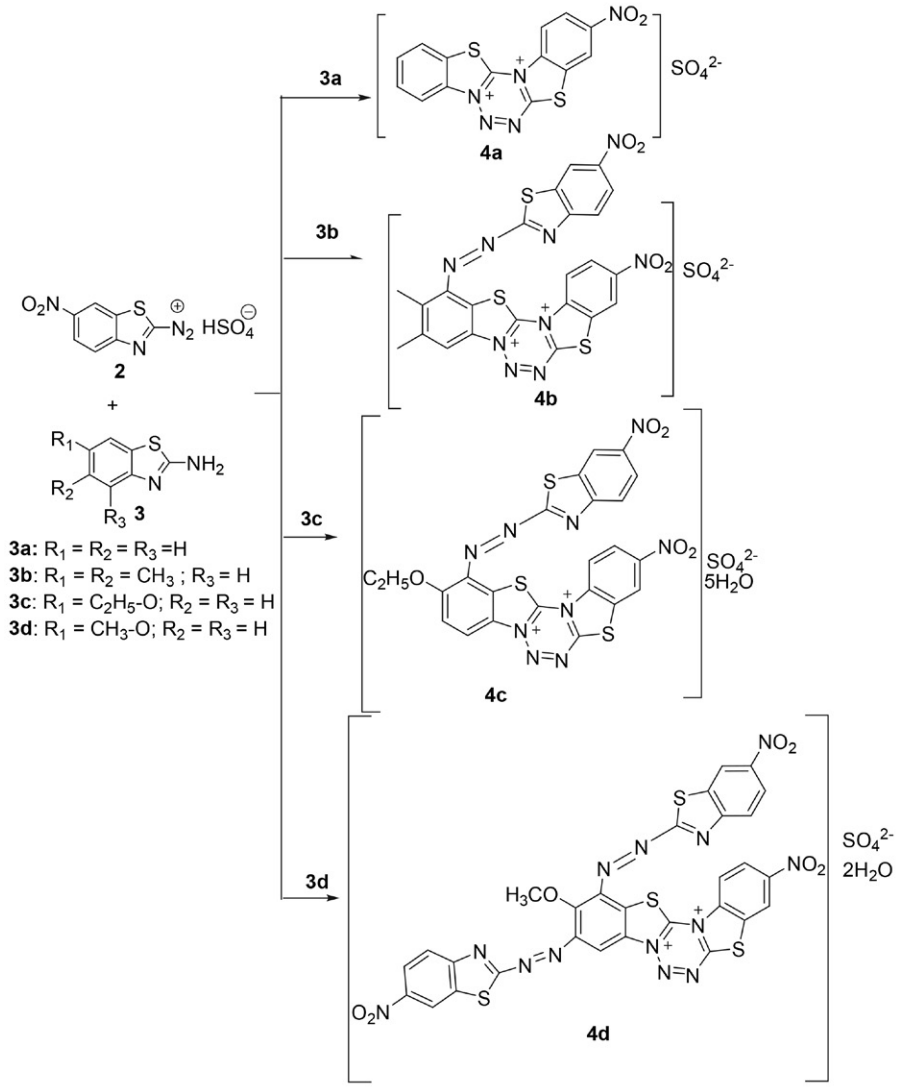

Scheme 2. Reactions' sequences to compounds **4a**–**d**

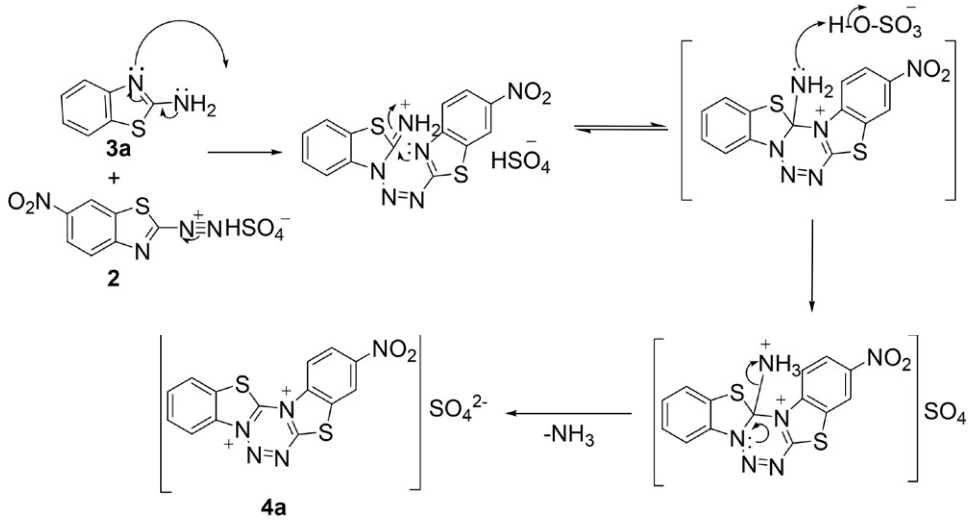

Scheme 3. The plausible mechanism for the formation of compound **4a**.

sponding to [$M^{+\cdot}$ + H] and characteristic fragment ion peaks at *m/z*: 374 ($M^{+\cdot}$ + H – 2S), 329 ($M^{+\cdot}$ + 2H – 2S – NO_2), 313 ($M^{+\cdot}$ + 2H – 2S – NO_2 – O), 285 ($M^{+\cdot}$ + 3H – 2S – NO_2 – O – N_2), 165 ($M^{+\cdot}$ + 2H – 2S – NO_2 – O –C_6H_4 – C_6H_2).

High-resolution mass spectrum reveals the surface SO_4^{2-} exchange of compounds **4a** by methanol used as a model primary alcohol for the analysis.[14] The presence on the HRMS spectrum of peaks at *m/z* 437 ($M^{+\cdot}$ – SO_4^{2-} + $3CH_3OH$), 374 ($M^{+\cdot}$ + H^+ + CH_3OH – SO_4^{2-}), 329 ($M^{+\cdot}$ + $2H^+$ + CH_3OH – SO_4^{2-} – NO_2), 263 ($M^{+\cdot}$ + $2H^+$ + CH_3OH – SO_4^{2-} – NO_2 – H_2S_2) proves that the sulfate of the tetrazinium salt **4a** is completely exchanged by methanol to give numerous peaks, confirming the aforementioned structural hypothesis.

The presence of the tetrazine nucleus in **4a** was further confirmed in the FTIR spectrum by the presence of the characteristic stretching bands at 1332 and 883 cm^{-1}.[25] The ^1H NMR spectrum of compound **4a** gave signals at δ_H 8.90 (d, *J* = 0.7 Hz, 1H, H-7'), 8.20 (d, *J* = 8.6 Hz, 1H, H-5'), 7.85 (d, *J* = 8.5 Hz, 1H, H-4') and 8.26 (d, *J* = 8.7 Hz, 1H, H-4), 8.01 (d, *J* = 8.2 Hz, 1H, H-7), 7.49 (dd, *J* = 7.6 and 7.5 Hz, 1H, H-5) and 7.41 (dd, *J* = 7.4 and 7.6 Hz, 1H, H-6) attributable to one ABX system of nitrobenzothiazole and one ABCD system of benzothiazole **3a**, respectively. These observations confirm the proposed regio-orientation of the nucleophilic addition of the heteroaromatic N of the benzothiazole **3a** on the diazonium ion function of **2** instead of the electrophilic substitution on the benzene ring as initially anticipated.

Table 3. Important HMBC correlations in compound **4a**; ^1H and ^{13}C chemical shifts (δ/ppm) in DMSO-d_6 as the solvent (25 °C).

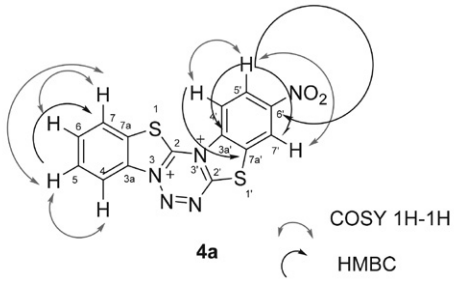

4a

C-atom	$\delta^{13}C$	HMBC (H → C)
7'	119.08	H -5' (8.21)
6'	155.08	H -5' (8.21)
3a'	143.87	H -4' (7.85)
2'	132.56	H -4' (7.85)
3a	127.34	H -6 (7.41)
7	123.2	H -5 (7.49)

The ^{13}C NMR spectrum of compound **4a** shows 14 relevant signals, out of which seven [127.4, 126.0, 123.1, 122.6, 122.4, 120.9, 119.0] were assigned to the tertiary aromatic CH based on the HSQC experiments. The remaining seven signals [170.2 (C-2), 155.0 (C-6'), 144.2 (C-7a'), 143.4 (C-3a'), 132.6 (C-2'), 127.3 (C-3a), 119.6 (C-7a)] were assigned without ambiguity to the seven quaternary C-atoms thanks to the HMBC experiment (Table 3) and the comparison with simulated values.

The powder XRD spectrum of tetrazine **4a** shows many peaks which are well structured due to the good crystalline nature of compound **4a** in which atoms are organized in a regular manner.

Compound **4b** is probably formed through two-step reaction, *via* the hypothetical non isolated intermediate **4b'** over a mechanism similar to that of the formation of **4a** (Scheme 3). Favorable electronic and steric factors enable further addition of another diazonium electrophile **2** at position 7 on the electron rich benzene ring of **4b'** bearing the methyl groups (Scheme 6).

The structure of compound **4b** was elucidated by means of various spectroscopic techniques such as ^1H and ^{13}C NMR spectra and elemental analysis.

Compound **4b** was obtained as a brown powder with a sharp melting point in the range 216–218 °C. The elemental analysis and the HREIMS experiments were used to establish the bruto formula as $C_{23}H_{13}N_9O_8S_4$ showing that the coupling product crystallized with one sulfate ion SO_4^{2-}.

The structure of compound **4b** is further strongly supported by its HRMS (ESI+ mode), which shows the pseudo-molecular ion peak at *m/z* 717 (1%) corresponding to [M^+ + $2Na^+$] and characteristic fragment ion peaks

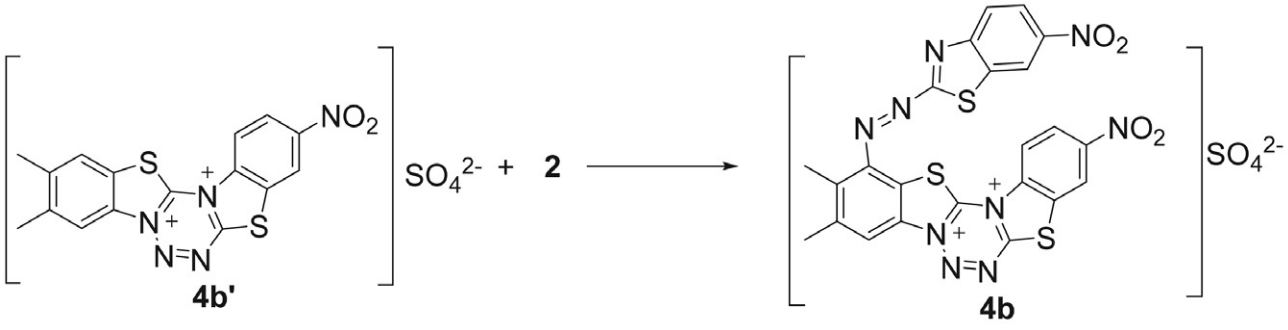

4b' **4b**

Scheme 6. Synthesis of compounds **4b**.

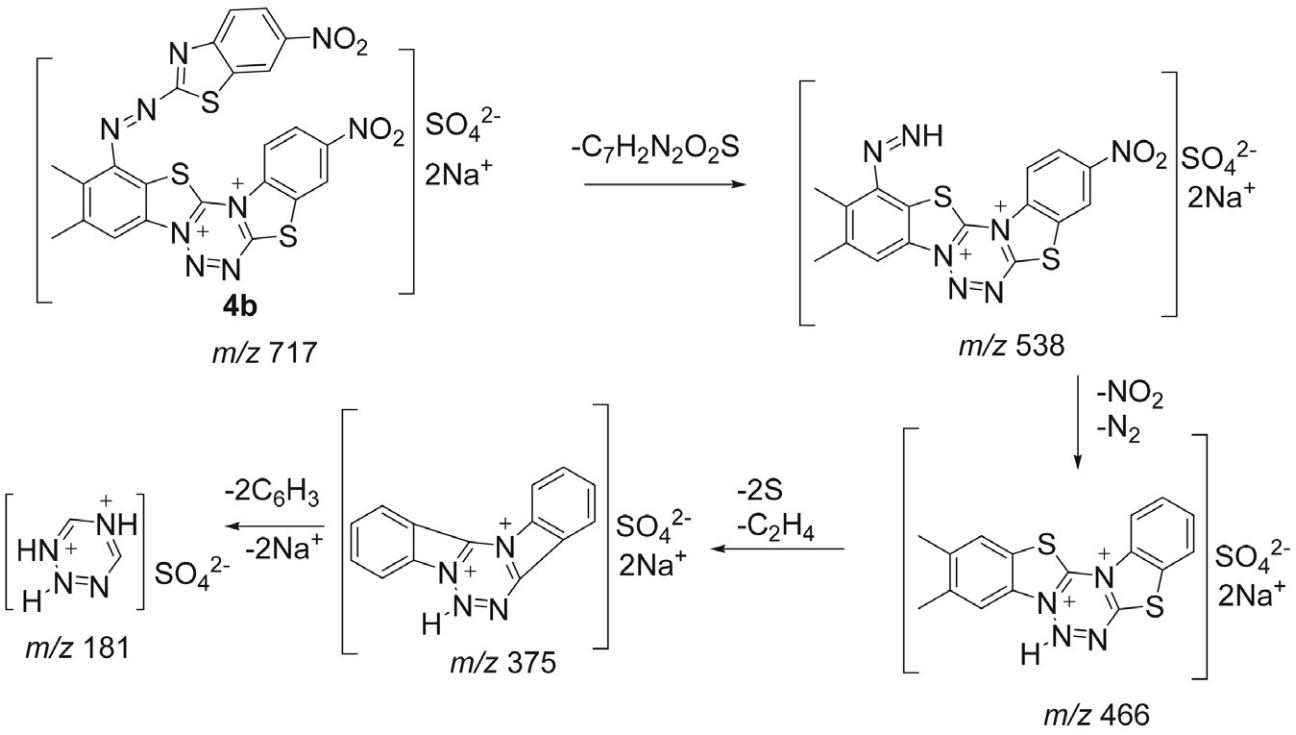

Scheme 7. Some important ESI+ mode fragments of compound **4b**.

at *m/z* 538 (1%, $[M^+ + 2Na^+ - C_7H_3N_2O_2S]$), 466 (3%, $[M^+ + 2Na^+ + 2H - C_7H_3N_2O_2S - NO_2 - N_2]$), 375 (2%, $[M^+ + 2Na^+ + 2H - C_7H_3N_2O_2S - NO_2 - N_2 - 2S - C_2H_4]$) and 181 (1%, $[M^+ + 2Na^+ + 2H - C_7H_3N_2O_2S - NO_2 - N_2 - 2S - C_2H_4 - 2Na^+ - 2C_6H_3]$) and were assigned as shown in Scheme 7, confirming the above structural hypothesis.

The infrared spectrum of compound **4b** showed absorption bands due to the stretching vibrations of the aromatic C–H at 2920 cm^{-1}, while those of N=N appeared at 1444 cm^{-1}. Two other bands belonging to the tetrazine group appear at 1334 and 881 cm^{-1}.[25] The structure of synthesized tetrazine was determined based on the ^1H and ^{13}C NMR chemical shifts and on the proton–proton coupling constants. On the ^1H NMR spectrum, the methyl protons on the benzothiazole ring resonated at δ_H 2.53 and 2.32 ppm, respectively as singlets.[14] In the aromatic region, two ABX proton systems are exhibited at 8.88 (poorly resolved d, 1H, H-7''), 8.21 (dd, *J* = 8.8 and 2.2 Hz, 1H, H-5''), 7.84 (d, *J* = 8.8 Hz, 1H, H-4'') and 8.42 (dd, *J* = 8.4 and 2.3 Hz, 1H, H-5'), 8.28 (d, *J* = 9.0 Hz, 1H, H-4'), 7.96 (poorly resolved d, 1H, H-7') and a singlet at 7.76 (s, 1H, H-4) confirming the proposed regio-orientation of the electrophilic substitution of the benzothiazole diazonium ion at position 7 in the 2-amino-5,6-dimethylbenzothiazole reagent.

The ^{13}C NMR spectrum of the tetrazine **4b** shows 23 signals attributable to the 23 carbon atoms of the molecule. In addition, the characteristic signals of two methyl groups (CH_3) appearing at δ 20.2 and 20.1 ppm, are in agreement with the presence of a 5,6-dimethylbenzothiazole unit in the assigned structure of **4b**.

The structures of compounds **4c** and **4d** were assigned based on their analytical and spectral data by following similar reasoning as above.

The investigation into the thermal stability of tetrazine derivatives reveals that, in most instances, their stability primarily hinges on the decomposition of the substituent they carry, rather than the tetrazine ring itself.[27] Consequently, a subsequent examination will delve into the impact of various substituents present in compounds **4** on their stability. It is worth noting that combining two heterocyclic systems, such as benzothiazole and tetrazine as observed in compounds **4**, may lead to enhanced molecular stability.[28] Conversely, the literature suggests that tetrazine energetic materials with limited or no oxygen content tend to yield high enthalpy species during combustion, thereby impeding the complete release of stored energy.[27] To address this, active oxygen can be introduced into the molecule by synthesizing tetrazine salts using inorganic oxidizing acids.[29] Compounds **4**, crystallizing in salt form with sulphate ions as counter ions and featuring the oxygen-rich nitro function in the cationic component, could play a pivotal role in achieving complete energy release from the material. Furthermore, optimal energy performance could be attained by bringing together the endothermic cycle of tetrazine and active oxygen within the cationic segment of compounds **4**.[27]

2. 2 Antibacterial and Antibiofilm Activity

S. aureus and *E. coli* are among the most frequent causes of biofilm-associated infections. With the emer-

Table 4. MIC and MBC values of the synthesized compounds and the reference antibiotic against Staphylococcus aureus and *Escherichia coli* strains.

Compounds	*S. aureus* ATCC1026			*E. coli* ATCC 10536		
	MIC	MBC	MBC/MIC	MIC	MBC	MBC/MIC
1	512	1024	2	512	>1024	—
3a	512	1024	2	1024	>1024	—
3b	1024	1024	1	1024	>1024	—
3c	1024	1024	1	1024	>1024	—
3d	512	1024	2	1024	>1024	—
4a	512	512	1	512	1024	2
4b	256	1024	2	512	>1024	—
4c	512	512	1	256	1024	4
4d	512	512	1	256	1024	4
Gentamicin 2	**2**	**4**	**2**	**4**	**8**	

—: not determined.

gence of antibiotic-resistancy, there is an urgent need to discover novel inhibitory compounds against these clinically important pathogens. In this study, newly synthesized 1,2,3,5-tetrazine were tested for antibacterial and antibiofilm activity against *S. aureus* and *E. coli* strains.

The antibacterial effect of the synthesized compounds and reference antibiotic gentamicin against the two bacterial strains tested, is presented in Table 4. The MIC values range from 256 μg/mL to 1024 μg/mL for tested compounds and were 2 μg/mL and 4 μg/mL for gentamicin, respectively, against *S. aureus* and *E. coli*. The results indicate that the tested compounds had moderate to weak antibacterial activity. Even though previous studies reported the activity of some tetrazine derivatives against bacterial strains, this was not the case in this study.[30] A plausible explanation to our findings is that the antibacterial activity of compounds might result from the basic skeleton of the molecules as well as from their nature, the number of nitrogen and sulfur atoms, and the presence of NO_2 substituents.[31] Similarly to the bactericidal nature of the reference antibiotic gentamicin, all the tested compounds showed also bactericidal activity with MBC/MBIC ratio ≤4.

Table 5. Percentage of the inhibition of biofilm formation (%) and the minimum biofilm inhibitory concentration ($MBIC_{50}$) values of the synthesized compounds against *S. aureus* and *E. coli* strains.

Compounds	*S. aureus*		*E. coli*	
	Inhibition (%)	$MBIC_{50}$	Inhibition (%)	$MBIC_{50}$
1	34.87	—	51.68	256
3a	41.09	—	48.18	—
3b	11.54	—	14.47	—
3c	20.12	—	29.22	—
3d	71.76	128	62.45	256
4a	32.87	—	52.78	256
4b	85.53	64	64.34	128
4c	31.22	—	71.14	128
4d	34.56	—	74.83	64
Gentamicin	**83.66**	**8**	**79.21**	**16**

—: not determined.

The result of the antibiofilm activity of the synthesized compounds and reference antibiotic gentamicin against *S. aureus* and *E. coli* strains is presented in Table 5, revealing that all the compounds showed the ability to inhibit biofilm formation to various extents. The percentage of biofilm formation inhibition varied from 11.54% to 85.53% in *S. aureus* and from 14.47% to 74.83% in *E. coli*. Compounds **1**, **3d**, **4a**, **4b**, **4c**, and **4d** showed more than 50% of inhibition against *E. coli* and two compounds (**3d** and **4b**) against *S. aureus*. Compound **4b** had the highest percentage of inhibition (85.53%) and $MBIC_{50}$ value of 64 μg/mL against *S. aureus*, while compound **4d** showed the highest percentage of inhibition against *S. aureus* (74.83%) and $MBIC_{50}$ value of 128 μg/mL. Compounds **4b** and **4d** showed the lowest $MBIC_{50}$ value (64 μg/mL) for *S. aureus* and *E. coli*, respectively. Although several works have reported the ability of tetrazine derivatives to inhibit the growth of bacterial pathogens, studies focusing on their capacity to interfere with the formation of biofilm in bacteria are very scarce. To the best of our knowledge, this is the first study reporting the antibiofilm potential of synthesized tetrazine derivatives.

Although no rational structure-activity correlation could be established from this study, some structural features that might have predisposed the antibacterial activity of these azo compounds can be drawn from the comparison of the chemical structures of compounds with different activity. The 2-aminobenzothiazole derivatives **3c** and **3d** are differ only in position 6 with ethoxy group in compound **3c** and methoxy group in compound **3d**. Compounds **3c** and **3d** show moderate antibacterial activity in *S. aureus* and weak antibacterial activity in *E. coli* (Table 4). This difference could be linked to the different mechanisms of action of these two compounds con-

sidering that, the main difference between the two tested bacteria is the structure of their cell wall which might change their susceptibility to the compounds. In contrast, the two reaction products obtained from these two reagents, namely compounds **4c** and **4d**, show both moderate antibacterial activity on the two microorganisms tested. The improvement in the activity of compounds **4c** and **4d** on the microorganism *E. coli* could be enlightened by the improved antibacterial profiles of the hybrid compounds due to the synergetic interactions of the primary potent pharmacophores combined in the single molecular platform.

3. Experimental Section

3. 1. Chemistry

3. 1. 1. General

A Büchi melting point apparatus was used to measure uncorrected melting points. Progress of the reaction was monitored by thin-layer chromatography and the purity of compounds was checked by TLC on Eastman Chromatogram Silica Gel Sheets (13181; 6060) with fluorescent indicators. A mixture of hexane (Hex) and ethyl acetate (EA) (4:6) was used as the mobile phase and spots were visualized by iodine vapors or irradiation with UV light (254 nm). IR spectra (KBr, cm^{-1}) were recorded with a Fourier Transform Infrared spectrometer JASCO FT/IR-4100 and a Perkin-Elmer FT-IR 2000 spectrometer. The absorption spectra of the compounds were recorded with a Beckman U-640 Spectrophotometer, using samples' solutions of concentration $5{\cdot}10^{-5}$ $mol{\cdot}L^{-1}$. Elemental analyses were determined using a Euro EA CHNSO analyser from Hekatech company, and the results were found to be in good agreement (±0.3%) with the calculated values. Positive ion electrospray mass spectra were recorded on a 6200 series TOF/6500 series Q-TOF (11.0.221.1) mass spectrometry system running in ESI_pos_ACN_below1000_CD.m, 1 minute of acquired spectra were combined and centroided. ^{1}H NMR spectra were recorded in DMSO-d_6 with a 400 and 600 MHz spectrometer NMR Bruker Avance-III. ^{13}C NMR spectra were recorded in DMSO-d_6 with a 100 and 150 MHz spectrometer NMR Bruker Avance-III. Tetramethylsilane (TMS) was used as the internal reference. Simulated ^{1}H and ^{13}C(^{1}H) NMR spectra were performed using http://www.nmrdb.org/ spectral simulation software.

3. 1. 2. Preparation of the Reagents and Starting Materials

All chemicals mentioned in this work were purchased from commercial sources and were used without further purification.

3. 1. 3. Preparation of Diazonium Salt Solution

Diazonium solution **2** was prepared according to the reported procedure.[14]

3. 1. 4. General Procedure for the Preparation of the Coupling Products 4

To a solution of 2-aminobenzothiazole derivatives **3a**–**d** (10 mmol) in DMSO (10 mL) in a 500 mL conical flask cooled in an ice-bath at 0–5 °C was added drop wise over 1 h the previously prepared diazonium solution of **2** maintained at 0–5 °C. After stirring for 30 min, 15 mL of sodium acetate solution (10%) was added to the mixture. The pH of the mixtures was kept in the range 9–11. The crystals obtained were filtered on a Büchner funnel. The product was crystallized from methanol.

3-Nitrobenzo[4,5]thiazolo[3,2-*c*]benzo[4,5]thiazolo[3,2-*e*][1,2,3,5]tetrazine-8,14-diium Sulfate (**4a**). Obtained in 48% yield (1.74 g) as a red powder; m.p. 213–215 °C. UV/Vis (MeOH) λ_{max} (lg ε_{max}) see Table 1. IR (KBr) ν_{max} /cm^{-1} see Table 2. ^{1}H NMR (600 MHz, DMSO-d_6, 25 °C, TMS) δ 8.90 (d, *J* = 0.7 Hz, 1H, H-7'), 8.26 (d, *J* = 8.7 Hz, 1H, H-4), 8.20 (d, *J* = 8.6 Hz, 1H, H-5'), 8.01 (d, *J* = 8.2 Hz,1H, H-4), 7.85 (d, *J* = 8.5 Hz, 1H, H-4'), 7.49 (dd, *J* = 7.6 and 7.5 Hz, 1H, H-5), 7.41 (dd, *J* = 7.4 and 7.6 Hz, 1H, H-6). ^{13}C NMR (150 MHz, DMSO-d_6) δ 170.2 (C-2), 155.0 (C-6'), 144.2 (C-7a'), 143.4 (C-3a'), 132.6 (C-2'), 127.5 (C-5), 127.2 (C-3a), 125.9 (C-6), 123.2 (C-7), 122.6 (C-4), 122.4 (C-5'), 120.9 (C-4'), 119.6 (C-7a), 119.2 (C-7'). HRMS ((+)-ESI) *m/z* (%) 437 (2), 374 (1), 329 (3), 314 (10), 285 (1), 263 (1), 200 (1), 162 (12). Anal. calcd. for $C_{14}H_7N_5O_6S_3$: C, 38.44; H, 1.61; N, 16.01; S, 21.99. Found: C, 38.43; H, 1.59; N, 16.00; S, 22.01. R_f 0.48 (Hex/EA 4:6).

10,11-Dimethyl-3-nitro-12-((6-nitrobenzo[*d*]thiazol-2-yl)diazenyl)benzo[4,5]thiazolo[3,2-*c*]benzo[4,5]thiazolo[3,2-*e*][1,2,3,5]tetrazine-8,14-diium Sulfate (**4b**). Obtained in 41% yield (2.75 g) as a brown powder; m.p. 216–218 °C. UV/Vis (MeOH) λ_{max} (lg ε_{max}) see Table 1. IR (KBr) ν_{max} /cm^{-1} see Table 2. ^{1}H NMR (600 MHz, DMSO-d_6, 25 °C, TMS) δ 8.88 (poorly resolved d, 1H, H-7''), 8.42 (dd, *J* = 8.4 and 2.3 Hz,1H, H-5'), 8.28 (d, *J* = 9.0 Hz, 1H, H-4'), 8.21 (dd, *J* = 8.8 and 2.2 Hz, 1H, H-5''); 7.96 (poorly resolved d, 1H, H-7'), 7.84 (d, *J* = 8.8 Hz, 1H, H-4''), 7.76 (s, 1H, H-4), 2.52, 2.33 (2×s, 6H, CH_3). ^{13}C NMR (150 MHz, DMSO-d_6) δ 172.2 (C-2), 157.0 (C-2'), 147.5 (C-4), 145.1 (C-2''), 144.08 (C-6''), 143.7 (C-6'), 126.9 (C-6), 139.7 (C-7a'), 136.5 (C-7a''), 136.1 (C-3a'), 133.1 (C-5), 132.9 (C-3a''), 123.6 (C-3a), 123.1 (C-7'), 122.6 (C-7''), 122.2 (C-5'), 122.1 (C-5''), 120.9 (C-4'), 120.1 (C-4''), 119.5 (C-7), 118.8 (C-7a), 20.2 (CH_3), 20.1 (CH_3). HRMS ((+)-ESI) *m/z* (%) 717 (1), 538 (1), 456 (1), 410 (1), 374 (2), 360 (3), 269 (1), 144 (3). Anal. Calcd. for: $C_{23}H_{13}N_9O_8S_4$: C, 41.13; H, 1.95; N, 18.77; S, 19.09.

Found: C, 41.11; H, 1.94; N, 18.78; S, 19.10. R_f 0.30 (Hex/EA 4:6).

11-Ethoxy-3-nitro-12-((6-nitrobenzo[*d*]thiazol-2-yl)diazenyl)benzo[4,5]thiazolo[3,2-*c*]benzo[4,5]thiazolo[3,2-*e*][1,2,3,5]tetrazine-8,14-diium Sulfate (**4c**). Obtained in 43% yield (3.31 g) as a red powder; m.p. 205–207 °C. UV/Vis (MeOH) λ_{max} (lg ε_{max}) see Table 1. IR (KBr) ν_{max} /cm^{-1} see Table 2. ^{1}H NMR (600 MHz, DMSO-d_6, 25 °C, TMS) δ 8.87 (poorly resolved d, 1H, H-7''), 8.20 (dd, *J* = 8.7 and 1.0 Hz, 1H, H-5'), 7.90 (d, *J* = 8.7 Hz, 1H, H-7'), 7.84 (d, *J* = 8.8 Hz, 1H, H-4'), 7.74 (dd, *J* = 6.7 and 1.6 Hz, 1H, H-5''), 7.55 (d, *J* = 8.8 Hz, 1H, H-5), 7.16 (d, *J* = 9.1 Hz, 1H, H-4), 7.08 (d, *J* = 8.8 Hz, 1H, H-4''), 4.10 (s, 2H, CH_2), 1.59 (s, 3H, CH_3). ^{13}C NMR (150 MHz, DMSO-d_6) δ 174.0 (C-2), 157.2 (C-2'), 156.7 (C-2''), 146.2 (C-6), 145.2 (C-6''), 143.8 (C-7a), 143.3 (C-6'), 137.1 (C-7a'), 133.1 (C-7a''), 123.1 (C-7'), 122.8 (C-4), 122.1 (C-5'), 120.9 (C-4'), 119.4 (C-3a''), 118.7 (C-7''), 117.1 (C-3a'), 116.5 (C-3a), 116.2 (C-4''), 112.8 (C-7), 106.7 (C-5), 105.1 (C-5''), 64.13 (O-CH_2), 15.25 (CH_3). HRMS ((+)-ESI) *m/z* (%) 854 (4), 438 (3), 423 (11), 402 (17), 374 (11), 371 (7), 289 (1), 191 (10), 167 (3). Anal. Calcd. for $C_{23}H_{23}N_9O_{14}S_4$: C, 35.52; H, 2.98; N, 16.21; S, 16.49. Found: C, 35.49; H, 2.99; N, 16.18; S, 16.53. R_f 0.41 (Hex/EA 4:6).

11-Methoxy-3-nitro-10,12-bis((6-nitrobenzo[*d*]thiazol-2-yl)diazenyl)benzo[4,5]thiazolo[3,2-*c*]benzo[4,5]thiazolo[3,2-*e*][1,2,3,5]tetrazine-8,14-diium Sulfate (**4d**). Obtained in 54% yield (4.94 g) as a brown powder; m.p. 218–220 °C. UV/Vis (MeOH) λ_{max} (lg ε_{max}) see Table 1. IR (KBr) ν_{max} /cm^{-1} see Table 2. ^{1}H NMR (600 MHz, DMSO-d_6, 25 °C, TMS) δ 8.87 (d, *J* = 1.7 Hz, 1H, H-7'), 8.28 (s, 1H, H-4), 8.21 (dd, *J* = 8.8 and 2.2 Hz, 1H, H-5'), 7.94 (d, *J* = 8.8 Hz, 1H, H-4''), 7.75 (d, *J* = 2.5 Hz, 1H, H-7'''), 7.64 (d, *J* = 2.4 Hz, 1H, H-7''), 7.58 (d, *J* = 8.8 Hz, 1H, H-4'), 7.38 (d, *J* = 8.9 Hz, 1H, H-4'''), 7.20 (dd, *J* = 8.8 and 2.5 Hz, 1H, H-5''), 7.10 (dd, *J* = 8.8 and 2.3 Hz, 1H, H-5'''), 4.11 (s, 3H, OCH_3). ^{13}C NMR (150 MHz, DMSO-d_6) δ 170.1 (C-2), 158.3 (C-3'''), 158.2 (C-6), 157.9 (C-2''), 157.5 (C-2'), 156.8 (C-3a'), 154.7 (C-3a''), 153.6 (C-3a'''), 150.8 (C-7a), 146.4 (C-6'), 145.4 (C-6'''), 143.8 (C-6''), 143.4 (C-7), 137.4 (C-7a'''), 137.1 (C-7a''), 133.0 (C-7a'), 123.2 (C-4''), 122.8 (C-4), 122.1 (C-5'), 120.9 (C-5), 119.3 (C-3a), 118.8 (C-7'), 118.3 (C-4'), 116.8 (C-5''), 116.0 (C-5'''), 112.2 (C-4'''), 106.2 (C-7''), 104.7 (C-7'''), 56.3 (O-CH_3). HRMS ((+)-ESI) *m/z* (%) 827 (10), 717 (4), 522 (5), 452 (5), 410 (6), 408 (25), 387 (82), 196 (100), 152 (37). Anal. Calcd. for $C_{29}H_{17}N_{13}O_{13}S_5$: C, 38.03; H, 1.87; N, 19.88; S, 17.50. Found: C, 37.99; H, 1.85; N, 19.87; S, 17.48. R_f 0.32 (Hex/EA, 4:6).

3. 2. Antimicrobial Activity

3. 2. 1. Microorganisms and Culture Conditions

Two bacteria strains obtained from the American Type Culture Collection were used: *Staphylococcus aureus* ATCC1026 and *Escherichia coli* ATCC 10536. They were maintained on Mueller Hinton agar slant at 4 °C and subcultured on fresh appropriate agar plates 24 h before antibacterial assay.

3. 2. 2. Minimum Inhibitory Concentration (MIC) and the Minimum Bactericidal Concentration (MBC) Determination

The minimum inhibitory concentration (MIC) and the minimum bactericidal concentration (MBC) of the synthesized compounds were determined by the broth microdilution method, as described by Bisso *et al.*[32] Briefly, samples were prepared at 4096 μg/mL and serially diluted two-fold with Mueller Hinton agar (MHB) in a 96-well microplate at a volume of 100 μL. The concentration of the reference antibiotic and compounds ranged from 1024 to 8 μg/mL. Then, wells were filled with 100 μL of inoculum (1.5·106 CFU/mL) and the microplate was incubated at 37 °C. Wells containing only bacteria inoculum were used as the negative control, while those containing microorganisms and standard drugs (gentamicin) were used as a positive control. After 24 h, 40 μL of iodonitrotetrazolium chloride (INT) solution (0.2 mg/mL) was added to each well and the microplate was further incubated for 30 min. Viable bacteria cells turned the yellow dye of INT to a pink colour. The lowest concentration of compound preventing the colour change medium was considered as the MIC. The MBC was determined by adding 50 μL from the wells that did not show growth after incubation for the MIC test to 150 μL of MHB. Then, the microplate was incubated at 37 °C for 48 h. The MBC was defined as the lowest concentration of compound that killed all bacteria. The MBC/MIC ratio was then calculated to determine the bactericidal (MBC/MIC ≤ 4) or bacteriostatic (MBC/MIC > 4).[33]

3. 2. 3. Biofilm Formation Inhibition Assay

The capacity of the synthesized compounds to inhibit the biofilm formation was determined using the microtiter plate method as previously described.[34] Briefly, 100 μL of compounds at half MIC concentration and reference antibiotic at 25 μg/mL were added in the wells of 96-well microtitre plates. Then 100 μL aliquots of bacterial cultures (1.5·106 CFU/mL) in Mueller Hinton broth supplemented with 2% glucose were added and incubated at 37 °C for 24 h. Following incubation, plates were washed with phosphate-buffered saline (PBS, pH 7.2) to remove the planktonic cells. The remaining cells in biofilms were fixed with methanol, then stained with 150 μL of safranin (1%), incubated for 15 min. After that, the excess safranin was removed, the dye bound to the cells was solubilized with 150 μL of ethanol (95%), and the optical density (OD) was measured at 570 nm using a microplate reader (Spectramax 190, Molecular Devices). The wells containing only

MHB broth supplemented with 2% glucose without bacteria were used as blank while the untreated wells were the positive control. The percentage of biofilm inhibition was determined using the following formula:

$$\% \text{ Inhibition } = [\frac{(ODControl - ODBlank) - (ODSample - ODBlank)}{(ODControl - ODBlank)}] \cdot 100$$

Compounds showing more than 50% inhibition were further two-fold serially diluted in MHB. The minimum biofilm inhibitory concentration ($MBIC_{50}$) was determined as the lowest concentration of compounds that reduces the biofilm biomass by 50%. All experiments were performed in triplicate.

4. Conclusion

An efficient procedure for the synthesis of new 1,2,3,5-tetrazine derivatives linker with a 1,3-benzothiazole ring has been presented. The diazotized title 2-amino-6-nitrobenzothiazole derivative **2** is a powerful electrophilic reagent as initially anticipated which is first attacked by the ring nitrogen atom of benzothiazoles used as couplers. Benzothiazole couplers with donor groups **3b**–**d** further participate in an *in situ* electrophilic substitution reaction at its favourable non-substituted ring positions with another diazonium ion **2** to yield the corresponding 1,2,3,5-tetrazine hybrid compounds **4b**–**d**. Their structural assignment was done based on the obtained analytic and spectroscopic data. This study revealed that compounds **4b** and **4d** exhibited interesting antibiofilm potential and could be considered promising drug candidates for the development of therapeutic molecules to overcome biofilm-associated infections caused by *S. aureus* and *E. coli*.

Supplementary Information

UV spectra for compounds **4a**–**d**, ^{1}H and ^{13}C NMR spectra for compounds **4a**–**d**, IR spectra for compounds **4a**–**d**, HRMS ESI+ mode of compounds **4a**–**d** and powder XRD patterns of compound **4a** are provided.

Acknowledgements

J. T. is grateful to Till Opatz and Paul Eckhardt for running the NMR and MS spectra. Additional financial supports for the work were obtained from the Cameroonian Ministry of Higher Education special research allocation.

5. References

1. R. N. Butler: The structure, reactions, synthesis and uses of heterocyclic compounds. In Comprehensive Heterocyclic Chemistry; K. T. Potts (Ed.), Pregamon Press, Oxford, 1984, (5), pp. 791–838. **DOI:**10.1016/B978-008096519-2.00081-3
2. R. N. Butler: The structure, reactions, synthesis and uses of heterocyclic compounds. In Comprehensive Heterocyclic Chemistry II; R. C. Storr (Ed.), Pregamon Press, Oxford, 1996, (4), pp. 621–678. **DOI:**10.1016/B978-008096518-5.00095-2
3. Y. Méndez, G. De Armas, I. Pérez, T. Rojas, M. E. Valdés-Tresanco, M. Izquierdo, M. A. del Rivero, Y. M. Álvarez-Ginarte, P. A. Valiente, C. Soto, L. de León, A. V. Vasco, W. L. Scott, B. Westermann, J. González-Bacerio, D. G. Rivera, *Eur. J. Med. Chem.* **2019**, *163*, 481–499. **DOI:**10.1016/j.ejmech.2018.11.074
4. B. A. Hassan, H. N. Naser, M. Abdulridha, *Int. J. Res. Pharm. Sci.* **2019**, *10*, 1254–1258.
5. P. A. Cano, A. Islas-Jácome, J. González-Marrero, L. Yépez-Mulia, F. Calzada, R. Gámez-Montaño, *Bioorg. Med. Chem.* **2014**, *22*, 1370–1376. **DOI:**10.1016/j.bmc.2013.12.069
6. P. A. Cano, A. Islas-Jácome, Á. Rangel-Serrano, F. Anaya-Velázquez, F. Padilla-Vaca, E. Trujillo-Esquivel, P. Ponce-Noyola, A. Martínez-Richa, R. Gámez-Montaño, *Molecules,* **2015**, *20*, 12436–12449. **DOI:**10.3390/molecules200712436
7. L. V. Myznikov, A. Hrabalek, G. I. Koldobskii, *Chem. Heterocycl. Comp.* **2007**, *43*, 1–9. **DOI:**10.1007/s10593-007-0001-5
8. J. Zhang, S. Wang, Y. Ba, Z. Xu, *Eur. J. Med. Chem.* **2019**, *178*, 341–351. **DOI:**10.1016/j.ejmech.2019.05.071
9. S. Q. Wang, Y. F. Wang, Z. Xu, *Eur. J. Med. Chem.* **2019**, *170*, 225–234. **DOI:**10.1016/j.ejmech.2019.03.023
10. T. Wang, C. Zheng, J. Yang, X. Zhang, X. Gong, M. Xia, *J. Mol. Model.* **2014**, *20*, 2261–2271.
11. N. Saracoglu, *Tetrahedron,* **2007**, *63*, 4199–4235. **DOI:**10.1016/j.tet.2007.02.051
12. V. Sinditskii, V. Y. Egorshev, G. F. Rudakov, S. A. Filatov, A. V. Burzhava: High-Nitrogen Energetic Materials of 1,2,4,5-Tetrazine Family: Thermal and Combustion Behaviors. In Chemical Rocket Propulsion a Comprehensive Survey of Energetic Materials; L. T. de Luca, T. Shimada, V. P. Sinditskii, M. Calabro (Eds.), Springer International Publishing, Cham, Switzerland, 2017, Vol. 45, pp. 89–125. **DOI:**10.1007/978-3-319-27748-6_3
13. G. Clavier, P. Audeber, *Chem. Rev.* **2010**, *110*, 3299–3314. **DOI:**10.1021/cr900357e
14. J. Tsemeugne, A. Y. Bah, J. P. Dzoyem, N. J. Ndefongang, I. M. Famuyide, J. Lyndy L. J. McGaw, P. K. Nangmo, B. M. W. Ouahouo, P. Mkounga, G. Edwards, P. F. W. Simon, A. Tsopmo, E. F. Sopbué, A. E. Nkengfack, *Arkivoc* **2022**, *(ix)*, 73–89. **DOI:**10.24820/ark.5550190.p011.866
15. I. Argyropoulou, A. Geronikaki, P. Vicini, F. Zani, *Arkivoc* **2009**, *(vi)*, 89–102. **DOI:**10.3998/ark.5550190.0010.611
16. N. Naira, D. Gladsy, *Pharm. Chem.* **2012**, *4*, 1277–1282.
17. S. K. Rangappa, R. P. Mahadeo, A. P. Siddappa, B. A. Srinivasa, *Eur. J. Med. Chem.* **2015**, *89*, 207–251.
18. H. E. Gaffer, M. M. G. Fouda, M. E. Khalifa, *Molecules* **2016**, *21*, 122. **DOI:**10.3390/molecules21010122
19. J. D. D. Tamokou, J. Tsemeugne, E. F. Sopbué, S. Prodipta, J. R. Kuiate, A. N. Djintchui, B. L. Sondengam, P. B. Kumar, *Pharmacologia* **2016**, *7*, 182–192.

DOI:10.5567/pharmacologia.2016.182.192
20. K. S. D. Djeukoua, F. E. Sopbué, J. D. D. Tamokou, J. Tsemeugne, P. F. W. Simon, A. Tsopmo, F. M. Tchieno, S. E. Ekom, C. N. Pecheu, I. K. Tonle, J.-R. Kuiate, *Arkivoc* **2019**, (*vi*), 416–430. **DOI:**10.24820/ark.5550190.p010.994
21. H. M. S. Kumar, L. Herrmann, S. B. Tsogoeva, *Bioorg. Med. Chem. Lett.* **2020**, *30*, 127514. **DOI:**10.1016/j.bmcl.2020.127514
22. V. Ivasiv, C. Albertini, A. E. Gonçalves, M. Rossi, M. L. Bolognesi, *Curr. Top. Med. Chem.* **2019**, *19*, 1694–1711. **DOI:**10.2174/1568026619666190619115735
23. S. Sahil, S. Mishra, P. Singh, *Eur. J. Med. Chem.* **2016**, *124*, 500–536. **DOI:**10.1016/j.ejmech.2016.08.039
24. S. F. Mason, *J. Chem. Soc.* **1959**, 1240–1246. **DOI:**10.1039/JR9590001240
25. R. H. Wiley Jr., C. H. Jarboe, F. N. Hayes, *J. Org. Chem.* **1957**, *22*, 835–836. **DOI:**10.1021/jo01358a609
26. A. Tupys, J. Kalembkiewicz, Y. Yurii Ostapiuk, V. Matiichuk, O. Tymoshuk, E. Woźnicka, Ł. Byczyński, *J. Therm. Anal. Calorim.* **2017**, *127*, 2233–2242. **DOI:**10.1007/s10973-016-5784-0
27. V. P. Sinditskii, V. Y. Egorshev, G. F. Rudakov, S. A. Filatov, A. V. Burzhava: High-Nitrogen Energetic Materials of 1,2,4,5-Tetrazine Family: Thermal and Combustion Behaviors. In: Chemical Rocket Propulsion; L. De Luca, T. Shimada, V. Sinditskii, M. Calabro (Eds.), Springer Aerospace Technology, Springer, Cham, Switzerland, 2017. **DOI:**10.1007/978-3-319-27748-6_3
28. A. I. Lesnikovich, O. A. Ivachkevich, S. V. Levchik, A. I. Balabanovich, P. N. Gaponik, A. A. Kulak, *Thermochim. Acta* **2002**, *388*, 233–251. **DOI:**10.1016/S0040-6031(02)00027-8
29. J. H. Yi, F. Q. Zhao, B. Z. Wang, Q. Liu, C. Zhou, R. Z. Hu, Y. H. Ren, S. Y. Xu, K. Z. Xu, X. N. Ren, *J. Hazard. Mater.* **2010**, *181(1–3)*, 432–443. **DOI:**10.1016/j.jhazmat.2010.05.029
30. A. A. M. El-Reedy, N. K. Soliman, *Sci. Rep.* **2020**, *10(1)*, 6137.
31. M. A. Al-Omair, A. R. Sayed, M. M. Youssef, *Molecules* **2015**, *20(2)*, 2591–2610. **DOI:**10.3390/molecules20022591
32. B. N. Bisso, R. N. E. Nkwele, T. R. Tchuenguem, J. P. Dzoyem, *Adv. Pharmacol. Pharm. Sci.* **2022**, 1–8. **DOI:**10.1155/2022/1998808
33. G. A. Pankey, L. D. Sabath, *Clin. Infect. Dis.* **2004**, *38*, 864–870. **DOI:**10.1086/381972
34. B. N. Bisso, T. C. R. Kuaté, J. P. Dzoyem, *Can. J. Infect. Dis. Med. Microbiol.* **2021**, 7029944.

Povzetek

Z reakcijo pripajanja diazonijevega iona 2-amino-6-nitrobenzotiazola pri 0–5 °C na substituirane derivate 2-aminobenzotiazola smo pripravili nove 1,2,3,5-tetrazinske derivate. Ugotovili smo, da diazotirani 2-amino-6-nitrobenzo[*d*]tiazol reagira z obročnim dušikovim atomom različno substituiranih 2-aminobenzotiazolnih derivatov; ob tem nastane tetrazinski obroč. Benzenski obroč benzotiazolov, ki vsebuje elektron donorsko skupino in je pripojen k tetrazinskemu, smo dodatno *in situ* substituirali z drugimi (6-nitrobenzo[*d*]tiazol-2-il)diazinili, da smo dobili končni produkt. Strukture pripravljenih spojin smo določili glede na njihove fizikalne lastnosti, elementno analizo in spektroskopske podatke. Pripravljenim spojinam smo določili antimikrobno aktivnost ter aktivnost proti tvorbi biofilma z bakterijama *Staphylococcus aureus* in *Escherichia coli*. Dva izmed pripravljenih tetrazinskih derivatov sta pokazala zanimiv potencial pri preprečevanju tvorbe biofilmov.

Scientific paper

Graphene Oxide/Polyamidoamine G4 as a High Efficient and Eco-Friendly Adsorbent for Dichromate Ions

Razieh Shekari Moghadam,[1] Babak Samiey[1,*] and Jiang Ning Wu[2]

[1] *Department of Chemistry, Faculty of Science, Lorestan University, Khoramabad 68137-17133, Lorestan, Iran*

[2] *Department of Chemical Engineering, Toronto Metropolitan University, Toronto, Ontario, M5B 2K3, Canada*

* *Corresponding author: E-mail: babsamiey@yahoo.com, samiey.b@lu.ac.ir*

Received: 08-04-2023

Abstract

In this study, graphene oxide/polyamidoamine G4 was used as a biocompatible nanocomposite adsorbent to adsorb dichromate ions. In alkaline solutions, dichromate ions changed to chromate ions which were not adsorbed on the surface of adsorbent. Thus, experiments were carried out in acidic and neutral water solution. Under these conditions, adsorption sites of adsorbent were protonated by primary and ternary amine groups of adsorbent shown as $-NH_3^+$ and $-NHR_2^+$ respectively that adsorbed dichromate ions through electrostatic interactions. Adsorption isotherms of dichromate on graphene oxide/polyamidoamine G4 were obtained under various ionic strengths, pHs and temperatures. Isotherms were analyzed by the adsorption isotherm regional analysis (ARIAN) model. The highest observed adsorption capacity of this process was 246.7 mg g^{-1} at pH = 0 and 318 K. Tests at pH = 2 showed that this process was endothermic. Adsorption kinetic experiments were carried out under various initial dichromate concentrations, pHs, temperatures, shaking rates and ionic strengths and were analyzed by the kinetics of adsorption study in the regions with constant adsorption acceleration (KASRA) model and intraparticle diffusion, ideal-second-order (ISO) and non-ideal process of adsorption kinetics (NIPPON) equations. The four-region ARIAN and KASRA models using a series of equations can interpret thermodynamics and kinetics of interactions of adsorbent and adsorbate under different conditions, respectively. Pb^{2+}, Cd^{2+}, Cr^{3+} and tannic acid were separated by graphene oxide/polyamidoamine G4 from dichromate ions and the graphene oxide/polyamidoamine G4 was recycled by using an alkaline solution.

Keywords Graphene oxide/PAMAM4, ARIAN model, KASRA model, Separation

1. Introduction

The wastewater produced by industries like cosmetics, tannery, petrochemistry, paper and food factories are dangerous for life and pollution of water sources by them is considered as one of most important threats for environment. There are different chemical, physical and biological techniques for wastewater treatment and some of them are filtration,[1] adsorption,[2] precipitation,[3] coagulation,[4] ion exchange,[5] ozonisation,[6] aerobic[7] and reverse osmosis[8] which most of them are not economic and have a complex nature. Among them, adsorbents used in adsorption method are high efficient, mostly recyclable and low cost compared with other treatment methods.

Polyamidoamine (PAMAM) compounds are environment friendly dendrimers[9,10] and some application of them are using them as drug delivery vehicles,[11] dendrimer-drug conjugates,[12] dendrimer/gene complexation,[13] size adaptive dendrimer clustered nanoparticles,[14] cancer gene therapy,[15] as an anti-atrophic agent,[16] anti-inflammatory and anti-thrombotic agent,[17] pulmonary drug delivery agents.[18] PAMAM compounds are generally synthesized from ethylenediamine and methyl acrylamide through a divergent method.[19–22] These dendrimer structures grow outward by alternating between Michael addition reaction of the methyl acrylate molecule to amino-terminated surface of a core initiator molecule (ethylenediamine) that leads to an ester-terminated outer layer (called half-generation) and then coupling of this compound with ethylenediamine to produce an amino-terminated surface (called full-generation). In this work, the products of the subsequent syntheses were called G –0.5, G 0, G 0.5, G 1, G 1.5, G 2, G 2.5, G 3, G 3.5 and G 4 which G is an abbreviation for generation. PAMAM generation 4 (PAMAM4) like other integer or full generations is an amino-terminated PAMAM dendrimer,[23] Fig. 1.

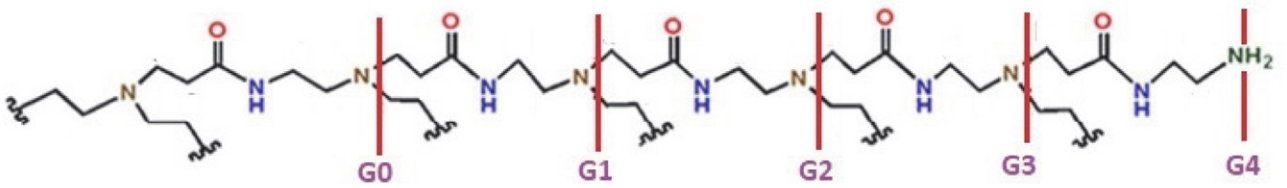

Fig. 1 A PAMAM4 dendrimer fragment

Graphene oxide (GO) films are two-dimensional structures which are composed from ultra-thin layers and have large surface areas. They were produced through the modified Hummer method.[24,25] To produce GO, strong oxidizing agents, like permanganate, make oxygenated functionalities in the graphite structure and produce graphite oxide. Graphite oxide is a hydrophilic compound and can be exfoliated in water and some organic solvents by sonication[26] and monolayer or few-layer oxygen-functionalized flakes of GO are produced in its dispersion. In this work, GO was produced from sonication of graphite oxide in DMF and in spite of graphite oxide, GO is not toxic.[27] GO has applications in catalysis,[28] nanocompounds,[29] energy storage,[30] biomedical usages[31] and polymer composite materials.[32]

PAMAM compounds are soluble in water and organic solvents like DMF and ethanol. Thus, in this research, for using them as adsorbent, they should be immobilized on an insoluble compound like GO. In this work, a GO suspension in DMF and a solution of PAMAM4 (an amino-terminated polyamidoamine) in DMF were mixed and interactions like electrostatic and dipole-dipole interactions between amine groups of PAMAM4 and carboxyl groups of GO,[23] and hydrophobic and Van der Waals interactions between their functional groups and physical entrapment of GO nanosheets in PAMAM4 dendrimers produced graphene oxide/polyamidoamine G4 nanocomposite (abbreviated as GO/PAMAM4) which was a stable precipitate in the used temperature and pH range.

Potassium dichromate that produces dichromate (DC) ions and in this work was considered as a pollutant, is an anionic dye used as an oxidizing agent and analytical reagent in different laboratory applications, an etching material and for cleaning glassware, tannery,[33] photography and printing.[34]

As-synthesized GO/PAMAM4 was characterized by FTIR, XRD, BET, SEM and EDS techniques Authors analyzed effects of different parameters like pH, temperature, ionic strength, shaking rate, DC concentration and time on adsorption capacity of GO/PAMAM4 for DC. Kinetics and thermodynamics of adsorption of DC on GO/PAMAM4 were studied by the KASRA and ARIAN models and ISO and NIPPON equations. Hereafter, in this work, neutral water is called water.

2. Materials and Methods

2. 1. Chemicals

Potassium dichromate ($K_2Cr_2O_7$) (>99.9%), sodium nitrate (≥99%), potassium permanganate (>99%), sodium chloride (>99.5%), sodium hydroxide (>98%), hydrochloric acid (37%), concentrated sulfuric acid (98%), hydrogen peroxide (30%), methanol (≥99.9%), ethanol (≥99.9%), ethylenediamine (≥99%), methyl acrylate (≥99%), N,N-dimethylformamide (DMF) (≥99.8%), lead nitrate ($Pb(NO_3)_2$) (99%), chromium nitrate ($Cr(NO_3)_2.9H_2O$) (99%) and cadmium nitrate ($Cd(NO_3)_2.4H_2O$) (98%) were purchased from Merck. Graphite powder (<20 μm) and tannic acid was purchased from Sigma-Aldrich. All chemicals were used without further purification.

2. 2. Instruments

Pore Size Micrometrics-tristar 3020 equipment (to obtain BET isotherms), Malvern Zetasizer instrument (to obtain zeta potential), PerkinElmer Frontier FTIR spectrophotometer, Rigaku D-max C III X-ray diffractometer (XRD) using Ni-filtered Cu-Kα radiation (λ = 1.5406 Å), MIRA3 TESCAN instrument at 15 keV used to take FESEM (field emission scanning electron micrograph) and EDS (energy dispersive X-ray spectroscopy) spectra.

2. 3. GO Synthesis

By following the published procedure,[35,36] graphite oxide was prepared through a modified Hummer's method.[23,24] Then, GO was made by sonication of graphite oxide for 30 min in DMF and at room temperature.

2. 4. PAMAM4 Dendrimer Synthesis

PAMAM4 dendrimer was synthesized using methyl acrylate and ethylenediamine, based on published methods.[19–22] Similar to our earlier works with generation 2 of PAMAM,[35,36] the first synthesized PAMAM generation was named G –0.5 and after that G 0, G 0.5, G 1, G 1.5, G 2, G 2.5, G 3, G 3.5 and G 4 compounds were prepared.

2. 5. GO/PAMAM4 Synthesis

The GO/PAMAM4 was synthesized based on the procedure used for GO/PAMAM2 synthesis.[35–37] 5 g of

PAMAM4 was dissolved in 20 ml of methanol and then was poured dropwise to a round-bottomed flask including a solution of 1 g GO in 120 ml of DMF (formerly dissolved in DMF by 25 min sonication) stirred in 600 rpm. Then, the solution was refluxed at 80 °C for 24 h. After this step, GO/PAMAM4 was separated from solution by centrifuging its solution in 6000 for 10 min. Then, 50 ml ethanol was added to GO/PAMAM4 and was centrifuged in 6000 rpm for 15 min. This step was carried out for four times.

2. 6. The XTT Cell Viability Assay of GO/PAMAM4

The XTT cell viability assay offers a straightforward technique for assessing cellular metabolic activity as a sign of cytotoxicity of GO/PAMAM4. The succinate-tetrazolium reductase system, which is exclusive to metabolically active living cells, reduces XTT (2,3-Bis-(2-Methoxy-4-Nitro-5-Sulfophenyl)-2*H*-Tetrazolium-5-Carboxanilide), a tetrazolium derivative, into a water-soluble orange product. The quantity of live cells in the sample determines how much orange product is produced. The total amount of mitochondrial dehydrogenases in the sample decreases as the number of live cells decreases. The absorbance, which measures the quantity of orange formazan generated, directly coincides with this drop. Tumor cell lines used were Hep2, Vero cells and human hepatoma G2 (HepG2) cells.[38,39] Details of this test were explained in Supporting Information, Fig. S1.

2. 7. Adsorption Isotherms and Kinetic Tests

Adsorption experiments were carried out by adding 10 mL of DC solutions with different initial concentrations to 0.0015 g of GO/PAMAM4. The solutions were shaken at 100 rpm in a temperature-controlled water bath shaker (Fater electronic Co., Persian Gulf model) at 308, 318 and 328 K within ±0.1 K for 6 h to reach equilibrium. The initial concentration ranges of DC were 1×10^{-5}–2×10^{-4} M. After completion of adsorption, DC concentrations were measured by a UV mini 1240V Shimadzu spectrophotometer at its maximum wavelength values. The λ_{max} value of DC at pHs of 0–6 (neutral water), was 350 nm. In alkaline pHs, DC ion changed to chromate ion and its λ_{max} value was 375 nm. DC adsorption capacity on the GO/PAMAM4, q_e (mg g^{-1}), was calculated using the following relation

$$q_e = \frac{(c_0 - c_e)Mv}{1000\, w} \quad (1)$$

where c_0 and c_e are the initial and equilibrium concentrations of adsorbate in each solution (M) respectively, M is the molecular weight of adsorbate (mg mole^{-1}), v is the volume of solution (mL) and w is the weight of the used adsorbent (g).

To carry out adsorption kinetic experiments, 0.0015 g GO/PAMAM4 samples were added to 10 mL of DC solutions. In this series of experiments, initial concentrations of used DC solutions were 5×10^{-5}, 1×10^{-4} and 2×10^{-4} M. These solutions were shaken at 40, 70 and 100 rpm in a temperature- controlled water bath shaker (Fater electronic Co., Persian Gulf model) at 308, 318 and 328 K and different ionic strengths and pHs. The DC residual concentrations in the solutions were measured at various contact times during the adsorption process, by a UV mini 1240V Shimadzu spectrophotometer at their values. To calculate adsorption capacity of DC on on GO/PAMAM4, q_t (mg g^{-1}), the following relation was used

$$q_t = \frac{(c_0 - c_t)Mv}{1000\, w} \quad (2)$$

where c_t and q_t are adsorbate concentration (M) at time t and the adsorption capacity at time t (mg g^{-1}), respectively.

2. 8. Adsorption Isotherms and Models

Thermodynamics of adsorption was analyzed using adsorption isotherms. Adsorption isotherms were studied by the ARIAN model which is an abbreviation for "*adsorption isotherm regional analysis model*".[40,41] This model was introduced by Samiey[40] and is used for analysis of adsorption isotherms up to four regions (I to IV). In this work, isotherms included regions I, II and IV, and we explained about them. A comprehensive explanation about the ARIAN model was written in Supplementary Information. The region I of the ARIAN model is studied by the Henry's law:

$$q_e = Kc_e \quad (3)$$

where there is a linear relation between adsorbate concentration and adsorption capacity and K is the binding constant of adsorbate on the adsorbent surface. This equation studies the most active adsorption sites. In this model, region II starts from the *starting second region concentration* (abbreviated as *ssc*) point. In region II, monolayer adsorption happens and is analyzed by an appropriate isotherm such as the Temkin equation, etc. The Temkin equation[42] is written as

$$q_e = c_1 \ln(c_2 c_e) \quad (4)$$

where c_1 is a constant and c_2 is adsorption equilibrium constant.

The region IV of this model begins where the adsorption capacity reaches the maximum, showing a plateau on the isotherm, or where the isotherm starts to go down.[40] Here, region IV showed the maximum. Depending upon the features of adsorbate and adsorption sites, two or more sub-regions may be observed in each of regions II or III or IV of an adsorption isotherm. Each of these sub-regions are called a section and are characterized as IIA, IIB,… for the purpose of differentiation.

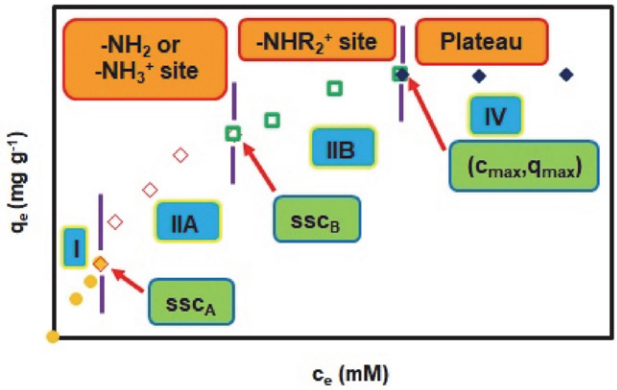

Fig. 2. Typical adsorption isotherms of DC on mesoporous adsorption sites of GO/PAMAM4 in different regions according to the ARIAN model

Typical adsorption isotherm of DC on GO/PAMAM4 based on the ARIAN model was shown in Fig. 2.

2. 9. Adsorption Kinetic Models and Equations

There are several equations for study of adsorption kinetics. The intraparticle diffusion equation[43] is written as

$$q_t = k_{dif} t^{0.5} + I \tag{9}$$

where k_{dif} is the rate constant for intraparticle diffusion and I is the boundary layer thickness.

The KASRA model and KASRA equation[44–46] were used for analysis of the adsorption kinetics, too. KASRA is an abbreviation for "*kinetics of adsorption study in the regions with constant adsorption acceleration*". The KASRA model is based on the three assumptions for adsorption of an adsorbate species on an adsorption site: (1) each time range that adsorption acceleration in it is constant, is called a *"region"*, (2) there are two regions before reaching the plateau region, and (3) the boundary between the first and second regions is named *starting second region* (abbreviated as *ssr*) point and that of between the second and third (plateau) regions is named *kinetics of adsorption termination* (abbreviated as *kat*) point. *ssr* and *kat* points are determined by the KASRA equation[44,45] which is given as follows:

$$q_t = \frac{1}{2} a_i t^2 + (v_{0i} - a_i t_{0i}) t + q_{0i} - \frac{1}{2} a_i t_{0i}^2 - (v_{0i} - a_i t_{0i}) t_{0i} \tag{10}$$

where q_0, v_{0i} and t_{0i} are q_t, velocity and time at the beginning of the *ith* region, respectively and a_i is the acceleration of adsorption kinetics in the *ith* region whereas i = 1–3. Each a_i is a negative value because during adsorption process the adsorbate concentration decreases. In the first region, t_{01} and q_{01} are equal to zero. The second region begins from *ssr* point which is assigned with the coordinates t_{02} and q_{02}. Finally, plateau (third) region starts at the equilibrium time, t_e, and equilibrium adsorption capacity, q_e which are coordinates of *kat* point. In this region, $v_{03} = a_3 = 0$, $t_{03} = t_e$ and $q_{03} = q_e$ and Eq. (10) is simplified to $q_t = q_e$. Due to different features of the first and second regions, parameters obtained for these two regions like rate constants are different from each other.

In this work, to avoid confusion in relation to the regions in isotherms and kinetic curves, kinetic regions are shown using numbers like region 1, etc. Typical adsorption kinetic curves of DC on GO/PAMAM4 based on the KASRA model were shown in Fig. 3.

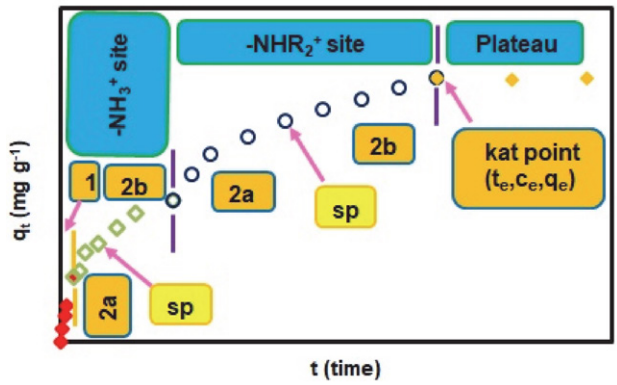

Fig. 3. Typical adsorption kinetic diagrams of DC on mesoporous adsorption sites of GO/PAMAM4 at pH = 2 based on the KASRA model

The *ideal-second-order* (or abbreviated as ISO) equation[45] is given as

$$\ln\left(\frac{q_e - q_t}{a c_t}\right) = -\frac{k_I c_e}{q_e} t + A' \tag{11}$$

where $k_I = k_I^2 q$.[27] k_I and k_I^2 are the first- and second-order adsorption rate constants of the ISO equation in each region and are in M^{-1} mg g^{-1} min^{-1} and M^{-1} min^{-1}, respectively and $A' = \ln\left(\frac{q_e}{a c_0}\right)$ (where $a = \frac{Mv}{1000\, w}$), v is the volume of solution (ml), w is the weight of the used adsorbent (g) and M is the molecular weight of adsorbate (mg $mole^{-1}$).

As referred before, based on the KASRA model, there are two regions in adsorption kinetic curves before reaching the plateau which result from non-ideality in adsorption process. In the first one, completely ideal adsorption happens on the bare surface of adsorbent. The progressively changes occurred on the surface of adsorbent in region 1 finally result in emerging another ideal region (region 2) in which adsorption carries out on a partly adsorbate-covered surface. Using the ISO equation shows that region 2 is composed from two another ideal parts that are named 2a and 2b. The first part of the second region, 2a, begins after *ssr* point and the second one, 2b, starts after *starting second part* (or abbreviated as *sp*) point

and ends at the *kat* point.[44] Detailed explanation of the ARIAN model equation was written in Supporting Information.

If the ISO rate constant of a step obeys Arrhenius equation, that step is adsorption- or reaction-controlled and otherwise it is called diffusion-controlled. As referred above, in some adsorbents, there are two or more different adsorption sites which lead to observing two or more successive adsorption kinetic curves in an adsorption kinetic diagram. In these cases, region 1, (completely ideal) is only observed in the first adsorption kinetic curve,[35] Fig. 3. Detailed explanation of the ISO equation was written in Supporting Information.

The NIPPON equation is used to determine the exact nature of the boundary of adjacent regions obtained from the KASRA equation.[47] The NIPPON equation is written as

$$q_t^N = k\,ln(1 + t) + cte \tag{12}$$

where $cte = q_{ts}^N + k\,ln(1 + t_s)$. q_{ts}^N, k and t_s are adsorption capacity, rate constant and time in the starting point of the assumed time range, respectively. When $t << 1$ we have $ln(1 + t) \approx t$ and then

$$q_t^N = kt \tag{13}$$

Dimension of natural logarithm argument, $1 + t$, is in $\frac{time}{1\,unit\ of\ time}$. Equation (12) was derived and introduced by Samiey,[47] and was called "*non-ideal process of adsorption kinetics equation*" or abbreviated as the NIPPON equation. NIPPON is a Japanese name of Japan and means the origin of sun. By taking the first and second derivatives of the NIPPON equation, non-ideal velocity and non-ideal acceleration adsorption kinetic equations, Eqs. (14) and (15), were obtained respectively. These equations are as follows

$$v_t^N = \frac{k}{1+t} \tag{14}$$

$$a_t^N = -\frac{k}{(1+t)^2} \tag{15}$$

where v_t^N and a_t^N were non-ideal velocity and acceleration of adsorption of adsorbate, respectively. On the other hand, at $t = 0$, $v_0^N = k$ and $a_0^N = -k$ and at $t = t_e$ we have

$$v_e^N = \lim_{t\to\infty} \frac{k}{1+t} = 0 \tag{16}$$

$$a_e^N = -\lim_{t\to\infty} \frac{k}{(1+t)^2} = 0 \tag{17}$$

where v_e^N and a_e^N were non-ideal velocity and acceleration of adsorption of adsorbate at $t = t_e$, respectively. In initial time ranges of adsorption process, adsorption is ideal and may comply with the KASRA equation. Detailed explanation of the NIPPON equation was written in Supporting Information.

3. Results and Discussion

3. 1. Characterization of GO/PAMAM4

BET nitrogen adsorption- based isotherms were used to calculate the surface area of as-synthesized GO/PAMAM4 and DC-adsorbed GO/PAMAM4 BET samples obtained at pH = 2, Fig. S1. BET isotherms on these tests, were Type IV and based on them, GO/PAMAM4 was a porous material, Fig. S2.

Based on the BET isotherms, the BET surface area, adsorption average pore diameter (by BET) and pore volume were 17.41 $m^2\ g^{-1}$, 5.52 nm, 0.033 $cm^3\ g^{-1}$ for as-synthesized GO/PAMAM4 and 13.33 $m^2\ g^{-1}$, 5.47 nm and 0.029 $cm^3\ g^{-1}$ for DC-adsorbed GO/PAMAM4 at pH = 2, respectively. As reported before,[48] the surface area of GO is 9.10 $m^2\ g^{-1}$ and doubling the surface area in GO/PAMAM4 verified more exfoliation of GO layers during synthesis of GO/PAMAM4.

Data obtained from BET surface area measurements of GO/PAMAM4 showed that its pores were mesopore which involved in adsorption process. The obtained hysteresis loops of these BET isotherms were H3 which were ascribed to aggregates (loose assemblages) of platelike particles (GO layers) forming slit-like pores.[49]

IR spectra of as-synthesized GO, PAMAM4 and GO/PAMAM4 compounds and GO/PAMAM4 samples were taken under various experimental conditions by using KBr pellet technique, Figs. 4(a)–4(h). In the IR spectrum of GO, peaks at 3090.0, 1727.3, 1653.8 and 1097.8 cm^{-1} were assigned to the vibration modes of –OH, –COOH, C=O and C–O groups,[50] respectively, Fig. 4(a).

In FTIR spectrum of PAMAM4, Fig. 4(b), the peak at 3621.7 cm^{-1} was assigned to stretching vibration modes of –OH groups of methanol impurity and 3336.5 cm^{-1} was attributed to $–NH_2$ group and the peak at 1564.2 cm^{-1} was assigned to the amide C=O group stretching vibration modes, respectively.[23,51,52] The peaks at 2867.0 and 1488.9 cm^{-1} were assigned to the stretching and bending vibration modes of aliphatic CH_2 group and peak at 1186.9 cm^{-1} was attributed to ternary amine stretching vibration modes respectively.[51] Lack of peak at 1740.0 cm^{-1} assigned to carboxyl C=O group proposed formation of PAMAM4 from its 3.5 half generation.

FTIR spectrum of GO/PAMAM4 showed peaks at 1560.0 cm^{-1} (assigned to –CONH– of PAMAM4), 2839 cm^{-1} (attributed to aliphatic CH_2 group of PAMAM4)[53] and 3209.5 cm^{-1} (assigned to –OH group of GO) confirmed that the PAMAM4 was grafted onto the flakes of GO, Fig. 4(c). This information showed that GO/PAMAM4 was synthesized successfully.

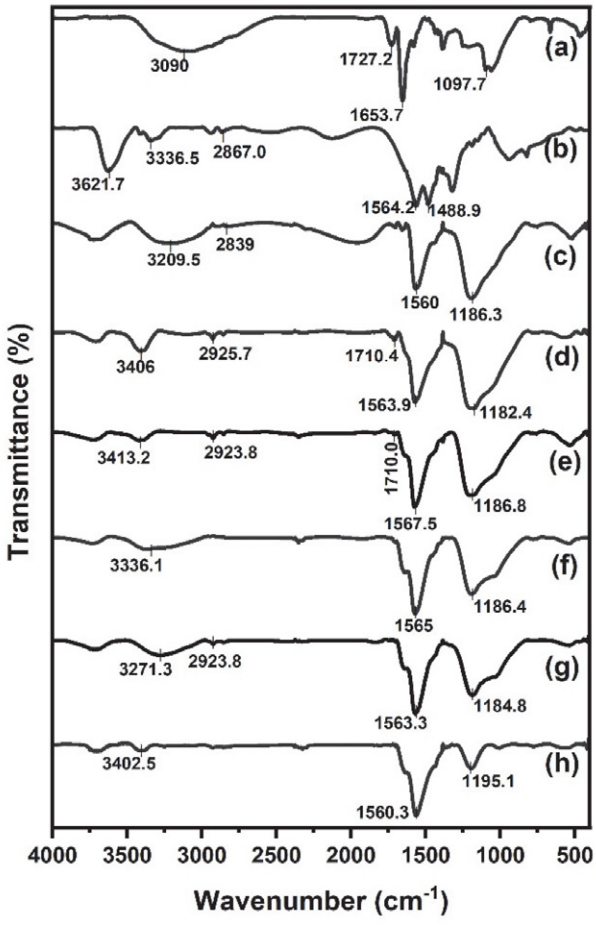

Fig. 4. IR spectra of (a) as-synthesized GO, (b) PAMAM4, (c) GO/PAMAM4 and DC-adsorbed GO/PAMAM4 samples at pHs of (d) 1, (e) 2, (f) 3, (g) 6 (water) and (h) 11

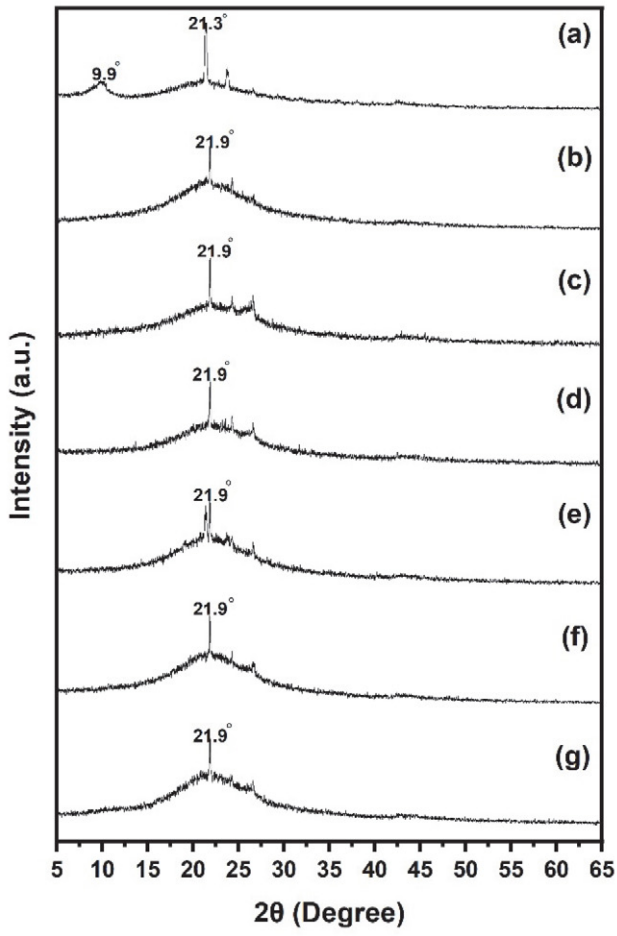

Fig. 5. XRD spectra of (a) as-synthesized GO, (b) as-synthesized GO/PAMAM4 and DC-adsorbed GO/PAMAM4 samples at pHs of (c) 1, (d) 2, (e) 3, (f) 6 (water) and (g) 11

Peaks of –NH– part of amide groups in FTIR spectra of DC-adsorbed GO/PAMAM4 at pHs of 1, 2, 3, water and 11 appeared at 1563.9, 1567.5, 1565.0, 1563.3 and 1560.3 cm^{-1} were approximately similar to those of as-synthesized GO/PAMAM4 that confirmed that –NH– part of their amide groups didn't interact with DC ions, Figs.

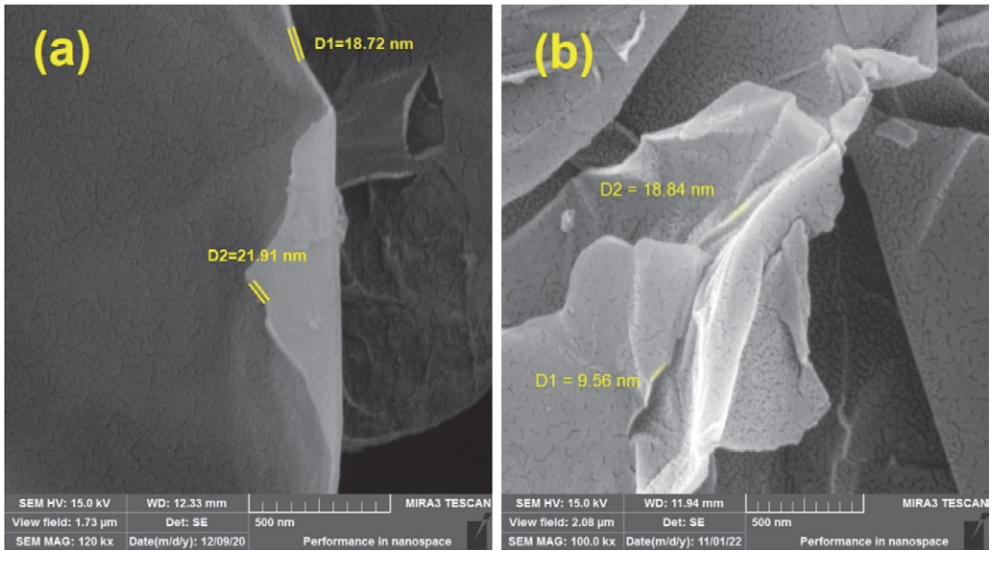

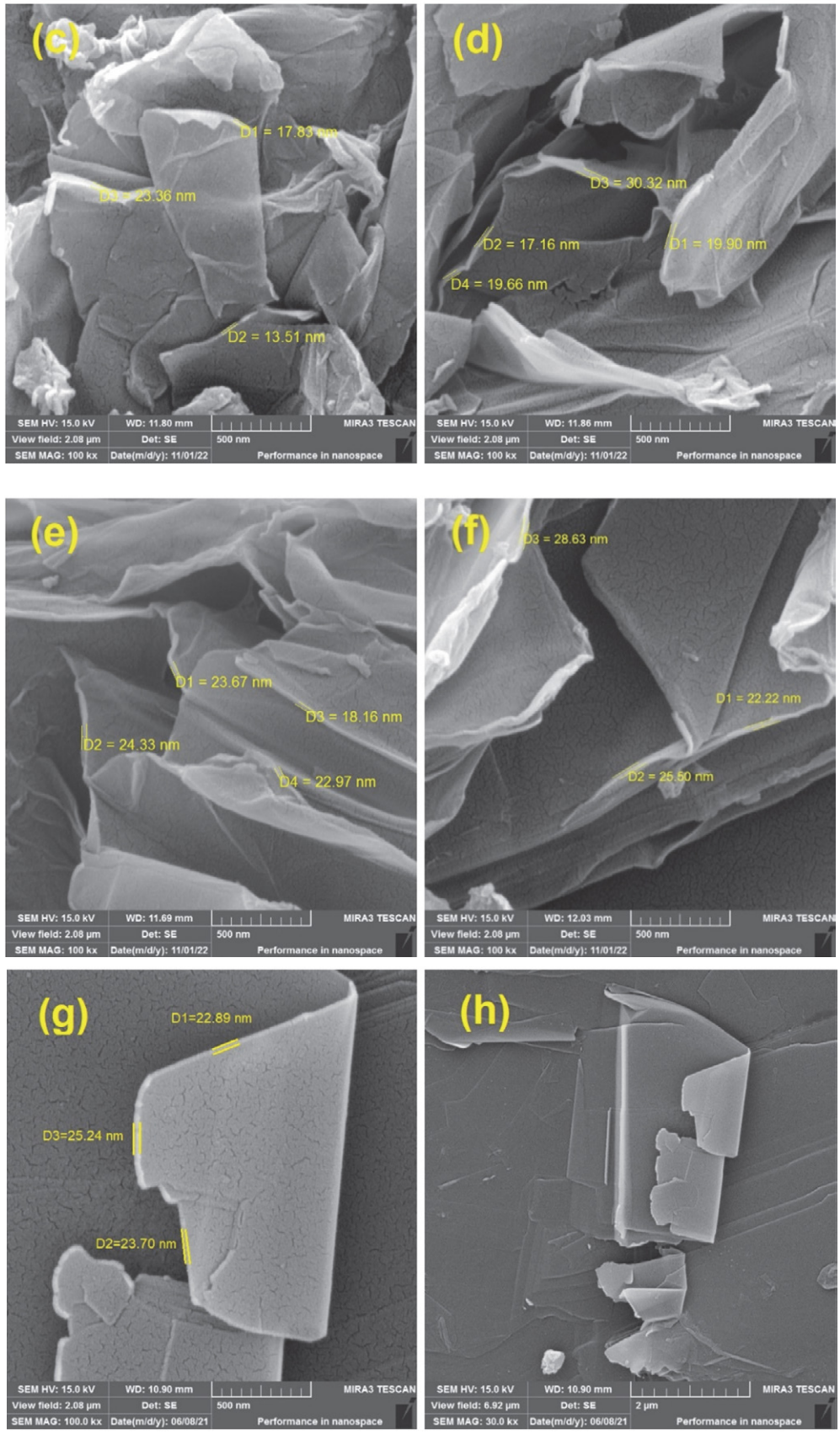

Fig. 6. FESEM images of (a) pristine GO/PAMAM4 and DC-adsorbed GO/PAMAM4 at pHs of (b) 1, (c) 2, (d) 3, (e) 6 (water), (f) 11, (g) and (h) GO. The magnification of the SEM images from (a) to (g) is 100,000 x and that of (h) is 30,000 x

4(d)–4(g) which was due to their involvement in resonance forms of amide group. Also, as seen in Figs. 4(c)-4(g), the IR spectra of the adsorbent in the pH range of 1–11 were very similar to each other that confirmed that the GO/PAMAM4 was stable in the pH range of 1–11 in the presence of DC.

Crystalline structure of as-synthesized GO, GO/PAMAM4 and GO/PAMAM4 and several DC-adsorbed GO/PAMAM4 samples were obtained under different experimental conditions, Figs. 5(a)–5(g). The weak peak of as-synthesized GO at 2θ of 9.9° was attributed to (002) crystal planes[54] and broad peak appeared at 2θ of 21.3° was attributed to amorphous GO,[53] Fig. 5(a). Broad peak of pristine GO/PAMAM4 and DC-adsorbed GO/PAMAM4 samples at 2θ of 21.9° was assigned again to the amorphous exfoliated structure of graphitic layers of its GO part and peak observed at 2θ of 9.9° of its GO part disappeared due to its exfoliation after interaction with PAMAM4 dendrimer, Figs. 5(b)-5(g). Peaks of XRD spectra of DC-adsorbed GO/PAMAM4 at pHs of 1, 2, 3, water and 11 appeared at 2θs of 21.9° and were similar to each other which confirmed that GO/PAMAM4 structure was stable under used conditions, Figs. 5(b)–5(g).

Images of as-synthesized GO/PAMAM4 and its samples were taken at various pHs, Figs. 6(a)–6(h) and Fig. S3. It was shown that average thickness of GO was 23.94 nm, Fig. 6(h) and that of PAMAM4-covered GO layers in pristine GO/PAMAM4 was 20.32 nm which confirmed that GO/PAMAM4 was a two-dimensional nanocompound, Fig. 6(a). Decrease in thickness of GO layers of GO/PAMAM4 and change in morphology and decrease in glossiness of GO/PAMAM4 layers, Fig. 6(a), compared to those of GO, Fig. 6(h), verified formation of GO/PAMAM4. It was observed that PAMAM4 dendrimers surrounded GO nanosheets surface and GO/PAMAM4 was formed through electrostatic, dipole-dipole and Van der Waals interactions between their functional groups.[23] Also, as seen in Figs. 6(a)–6(f), morphologies of GO/PAMAM4 in the pH range of 1–11 were similar to each other.

EDS (energy dispersive X-ray spectroscopy) spectra of pristine GO, pristine GO/PAMAM4 and DC-adsorbed GO/PAMAM4 samples were taken under different experimental pHs and confirmed that DC ions did not adsorb on GO/PAMAM at pHs upper than 6, Table 1.

Also, it was observed that treatment of Hep2, HepG2 and Vero cells with GO/PAMAM4 in XTT assay had no toxic effect on the cells compared to the control group and showed that GO/PAMAM4 was an eco-friendly compound, Supporting Information, Fig. S1.

Information obtained from IR, XRD, SEM, EDS and BET techniques verified synthesis of GO/PAMAM4 nanocompound.

3. 2. Adsorption Isotherms of DC on GO/PAMAM4

As seen in Fig. 7, DC ions were changed to chromate ions in pHs higher than 6 (water) and our investigation showed that adsorption on the surface of GO/PAMAM4 happened till pH of 6. It confirmed that only DC ions were adsorbed on the surface of GO/PAMAM4. Adsorption isotherms of this process were studied by the ARIAN model at 308–328 K, various ionic strengths and pHs, Tables 2 and 3 and Fig. 8.

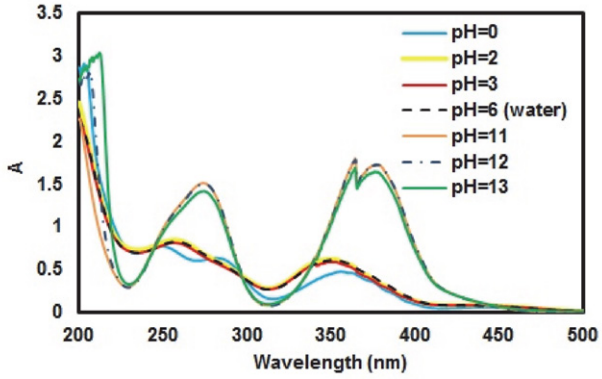

Fig. 7. UV-Vis spectra of DC at pHs of 0, 2, 3 and 6 and those of chromate ions at pHs of 11, 12 and 13 at room temperature. All tests were carried out using 0.2 mM solutions of

As referred before, Figs. 3(c)–3(g), amide groups of GO/PAMAM4, due to formation of resonance forms and involvement of their –NH– part in these forms did not interact with DC ions at pH range of 1–6.

In neutral aqueous (pH ≈ 6) and pH = 3 solutions of DC ions, only acidic form of primary amine groups of GO/

Table 1. Elements weight percentage (W%) of as-synthesized GO/PAMAM4 and DC-adsorbed GO/PAMAM4 samples under various pH conditions obtained from their EDS spectra

Element	GO	As-synthesized GO/PAMAM4	DC-adsorbed GO/PAMAM4 at pH = 1	pH = 2	pH = 3	water	pH = 11	pH = 12	pH = 13
C	82.3	61.2	54.5	62.5	55.3	64.4	64.2	62.9	60.1
N	–	14.3	21.4	16.9	22.1	17.9	20.6	21.2	22.1
O	17.7	24.5	19.5	18.5	21.2	17.3	14.7	15.1	16.6
Cl	–	–	4.1	1.4	0.9	–	–	–	–
Cr	–	–	0.5	0.7	0.5	0.4	–	–	–
Na	–	–	–	–	–	–	0.5	0.8	1.2

Table 2. Parameters obtained from the Henry and Temkin isotherms of different regions (I and II) and ssc_A, q_{sscA}, ssc_B and q_{sscB} values for adsorption of DC on GO/PAMAM4 in water, acidic and alkaline solutions at 308–328 K

Solvent	T (K)	Henry (region I)			Temkin (section IIA)			Temkin (section IIB)		
		K	ssc_A	q_{sscA}	c_2	ssc_B	q_{sscB}	c_2	c_{max}	$q_{e,max}$
		DC on $-NH_3^+$ site			DC on $-NH_3^+$ site			DC on $-NHR_2^+$ site		
pH = 0	318	2.06×10^6	0.016	46.8	1.02×10^5	0.029	100.1	5.66×10^4	0.074	246.7
pH = 1	318	5.58×10^6	0.010	58.6	2.36×10^5	0.039	159.1	2.07×10^5	0.075	206.2
pH = 2	308	4.09×10^6	0.010	39.8	2.66×10^5	0.034	89.7	1.05×10^5	0.095	165.2
	318	6.95×10^6	0.006	46.0	3.44×10^5	0.021	114.7	2.22×10^5	0.086	222.6
	328	2.44×10^7	0.003	72.5	1.91×10^6	0.013	131.6	3.69×10^5	0.056	242.7
0.1 M NaCl	318	1.20×10^6	0.037	45.1	5.26×10^4	0.073	92.9	2.87×10^4	0.121	154.9
pH = 3	318	3.43×10^6	0.015	50.1	9.87×10^5	0.028	119.8	–	–	–
Water	318	6.55×10^5	0.066	45.0	2.14×10^4	0.014	141.1	–	–	–

Units of K and c_2 are in mg g^{-1} M^{-1} and M^{-1}, respectively. Units of ssc_A, ssc_B and c_{max} are in mM. Units of q_{sscA}, q_{sscB} and $q_{e,max}$ are in mg g^{-1}. At pHs of 2 (in 0.1 M NaCl), 3 and water, due to lack of section IIB, section IIA is region II and $q_{sscB} = q_{e,max}$ and $ssc_B = c_{max}$.

Table 3. Equilibrium constants (K) and thermodynamic parameters for adsorption of DC on GO/PAMAM4 in water and at pH = 2 solutions at 308–328 K

pH	308 K		318 K		328 K		ΔH	ΔS
	K	ΔG	K	ΔG	K	ΔG		
2 (region I)	4.09×10^6	–39.0	6.95×10^6	–40.3	2.44×10^7	–43.6	74.7	367.9
2 (section IIA)	2.66×10^5	–32.0	3.44×10^5	–32.6	1.91×10^6	–37.0	82.1	368.4
2 (section IIB)	1.05×10^5	–29.6	2.22×10^5	–31.5	3.69×10^5	–32.8	52.9	268.0

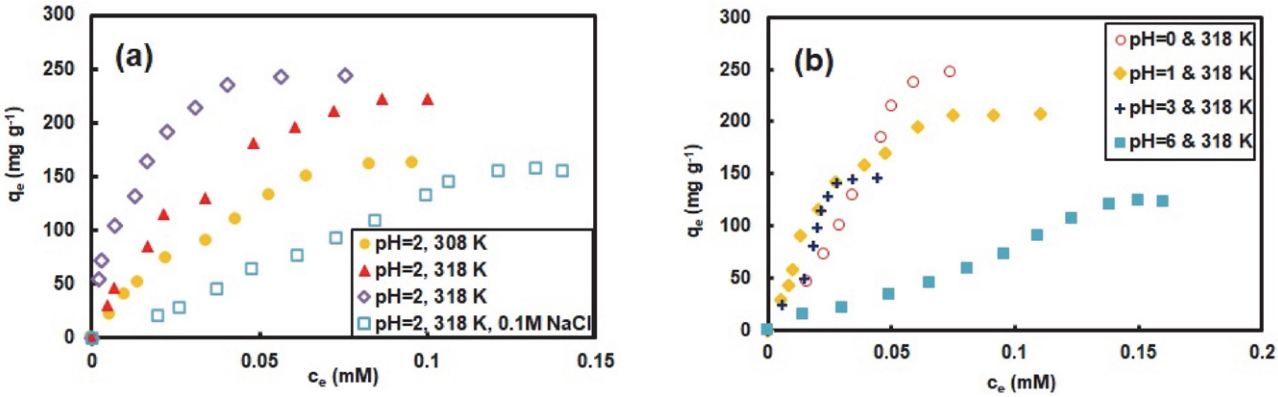

Fig. 8. Adsorption isotherms of DC on GOPAMAM4 (a) at pH = 2 and at ● 308 K, ▲ 318 K, ◇ 328 K and □ in 0.1 M NaCl at 318 K and (b) at pHs of ○ 0, ◆ 1, + 3 and ■ 6 (water) at 318 K. All tests were carried out at 100 rpm

PAMAM4, $-NH_3^+$ groups, are its adsorption sites for DC ions. Hydrogen atom of these groups interact with oxygen atom of DC ions. Analysis of adsorption isotherms at these pHs by the ARIAN model showed that they were formed from regions I and II which were studied by the Henry and Temkin isotherms, respectively, Table 2.

At each pH value, due to steric hindrance of adsorbed molecules and an increase in negative charge of adsorbent surface, adsorption equilibrium constants decreased from region I to region II. As reported before, PAMAM generations are positively charged at water[55] and adsorbent surface potential became more positive with a decrease in pH of solutions.[56] As measured at this work, pH of point of zero charge (pH_{PZC}) of GO/PAMAM4 was 3.9 and a decrease in pHs of DC solutions from pH of 6 (water) to 3 made more positive the surface potential of GO/PAMAM4, Fig. 9 and resulted in an increase in adsorption equilibrium constants in regions I and II of process at pH of 3 compared to that at pH of 6. On the other hand, this caused stronger interactions between these protonated ternary amine and amide groups of PAMAM4 dendrimers which made its structure more compact and decreased adsorbent capacity.[36,57,58]

At pH = 2, due to the repulsion between primary and tertiary amines of PAMAM4 dendrimer, its structure was opened[59] and as observed, $-NR_2H^+$ groups could adsorb

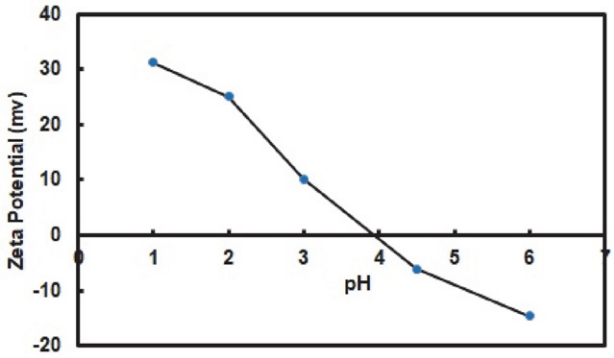

Fig. 9. Zeta potential vs. pH for GO/PAMAM4

DC ions. Due to steric hindrance of big R groups of $-NR_2H^+$ groups, lower tendency for attachment to proton and more hydrophobicity character of ternary amines compared to primary amines, electrostatic interactions of DC ions with $-NR_2H^+$ groups (region I) were weaker than that with $-NH_3^+$ groups (region II) of adsorbent, Table 2.

At this pH, isotherms were composed from regions I and section IIA for adsorption of DC ions on $-NH_3^+$ and section IIB for adsorption of DC ions on $-NR_2H^+$ adsorption sites, respectively. The adsorption processes in all these three regions were endothermic that was due to hydrophobic interactions of DC ions with opened adsorbent structure and their entropy changes were large positive numbers which was due to disorder in the adsorbent structure and detaching water molecules from adsorption sites during adsorption process, Table 3. In 0.1 M NaCl solutions of DC at pH = 2 and 318 K, the equilibrium adsorption constants and adsorption capacity of this adsorption process decreased compared to their values at pH = 2 and 318 K which was due to surrounding effect of Na^+ ions on DC ions.

Like pH = 2, at pHs of 0 and 1, DC ions interacted with $-NH_3^+$ (analyzed by the Henry and Temkin isotherms) and $-NR_2H^+$ (analyzed by the Temkin isotherm) groups of adsorbent and adsorption capacities of DC ions on GO/PAMAM4 decreased with a decrease in pH from 2 to 1, due to formation of $HCr_2O_7^-$ from a number of DC ions (pKa = 1.18)[60] and increased with a decrease in pH from 1 to 0 which was due to a highly increase in positive charge of adsorbent surface[59], Fig. 9. Mechanism of adsorption of DC on GO/PAMAM4 in different pH ranges was shown in Fig. 10.

As seen from XRD and IR spectra and SEM images of pristine GO/PAMAM4 and DC-adsorbed GO/PAMAM4 at different pHs, structure of adsorbent is stable under different conditions in these series of tests, Figs. 4–6.

At the end, adsorption capacities of a number of adsorbents for potassium dichromate were shown in Table 4 and as it is evident, adsorption capacity of GO/PAMAM4 for DC is higher than most of other adsorbents used for this purpose.[61–67]

Table 4. Maximum adsorption capacity ($q_{e,max}$) of DC on a number of compounds

Adsorbent	pH	T (K)	$q_{e,max}$ (mg g^{-1})	Reference
Graphene oxide-magnetic	2	298	3.2	61
Carboxyl-rich carbon nanocomposite	1	298	142.9	62
Zr^{4+} cross-linked magnetic chitosan/polyaniline composite	2	298	491.4	63
MCM-41–AEAPTMS–Fe(III)Cl	3	298	84.9	64
Meidum black clay and pomegranate peel extract	2	323	78.1	65
Mag@LDH-ER	7	298	54.7	66
Chitosan	5	298	7.4	67
GO/PAMAM4	0	318	246.7	This work

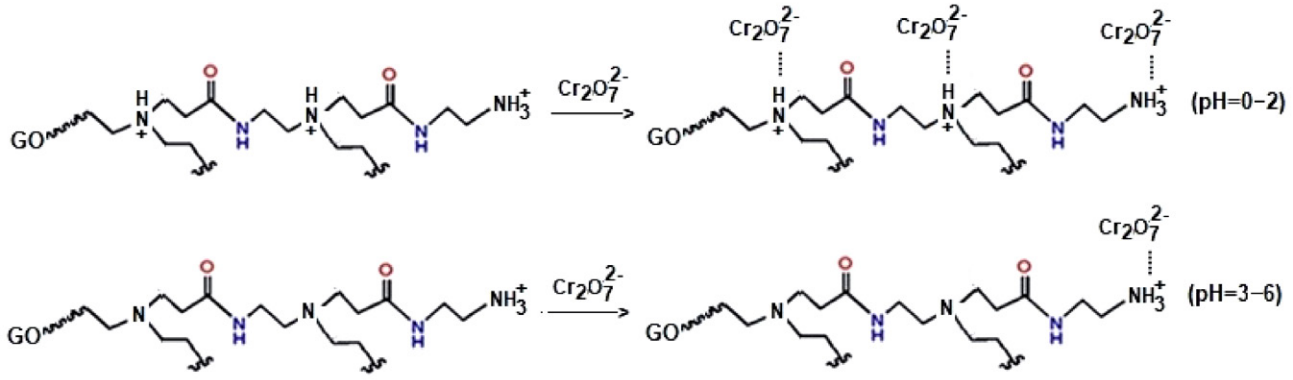

Fig. 10. Schematic representation of adsorption of DC on GO/PAMAM4 in different pH ranges

3. 3. Adsorption Kinetics of DC on GO/PAMAM4

Kinetics of DC adsorption on GO/PAMAM4 surface was studied in different initial DC concentrations, temperatures, ionic strengths, shaking rates and pHs. Kinetic curves were analyzed by the KASRA model and ISO, intraparticle diffusion and NIPPON equations, as given in Figs. 11 and 12 and Tables 5–7**.** Analysis of the kinetic curves by the KASRA model and intraparticle diffusion equation showed that they were composed from one or two curves and in each curve there were two regions (1 and 2) and their accelerations and velocities of adsorption and k_{dif} values decreased from region 1 to region 2. This is due to a decrease in DC concentration and an increase in negative charge of adsorbent surface and spatial hindrance on adsorption sites due to adsorbed DC ions.

As referred before, at pH = 6 (neutral aqueous solutions) and pH = 3 DC solutions, $-NH_3^+$ groups of GO/PAMAM4 adsorbed DC ions. In each of these cases, the initial DC concentration was 0.2 mM which was on the plateau of their isotherm and was involved all interactions between

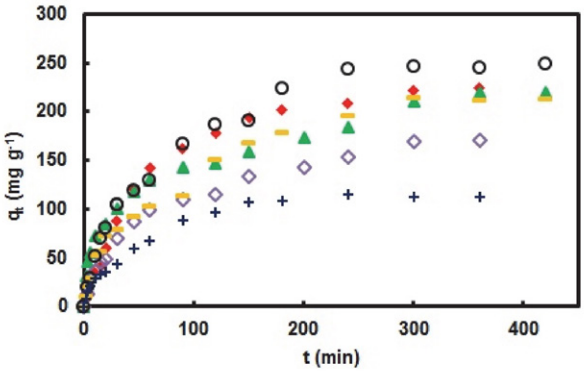

Fig. 11. Adsorption kinetic curves of DC on GOPAMAM4 at pHs of ◆ 0, ▲ 1 and + 3 at 318 K and at pH = 2 at ◇ 308, – 318 and ○ 328 K. All tests were carried out at 100 rpm and in $[DC]_0$ = 0.2 mM

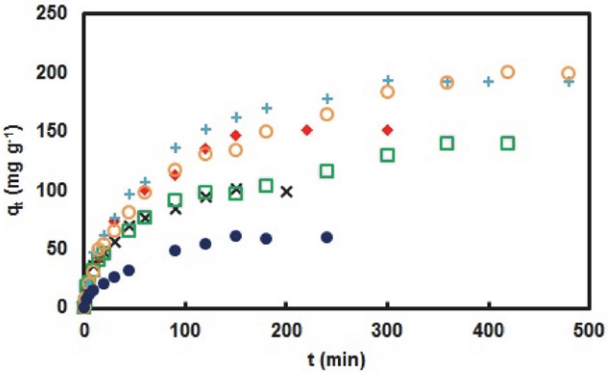

Fig. 12. Adsorption kinetic curves of DC on GOPAMAM4 ◆ at pH = 6 and in $[DC]_0$ = 0.2 mM and 100 rpm and □ pH = 2 in 0.1 M NaCl and $[DC]_0$ = 0.2 mM and 100 rpm and + at pH = 2, 70 rpm and in $[DC]_0$ = 0.2 mM and ○ at pH = 2, 40 rpm and in $[DC]_0$ = 0.2 mM and ● at pH = 2, in $[DC]_0$ = 0.05 mM and 100 rpm and × at pH = 2, in $[DC]_0$ = 0.1 mM and 100 rpm

Table 5. Experimental t_e, q_e, t_{02}, q_{02}, t_{03} and q_{03} values and coefficients obtained from the KASRA equation and k_{dif} values of intraparticle diffusion equation for kinetics of DC adsorption on GO/PAMAM4 at different temperatures and in various shaking rates and initial DC concentrations

Solvent	T (K)	$[DC]_0$ (mM)	rpm	KASRA region 1 (1st curve)			KASRA region 2 (1st curve)			KASRA region 2 (2nd curve)				(t_e, q_e)
				a_1	v_{01}	k_{dif}	(t_{02}, q_{02})	a_2	v_{02}	k_{dif}	(t_{03}, q_{03})	a_3	v_{03}	k_{dif}	
Corresponding to:				**ARIAN region I ($-NH_3^+$ site)**			**ARIAN section IIA ($-NH_3^+$ site)**				**RIAN section IIB ($-NHR_2^+$ site)**				
pH = 0	318	0.20	100	–0.290	5.00	13.3	(5,41.9)	–0.054	3.42	26.2	(60,142.6)	–0.002	0.84	8.6	(360,224.7)
pH = 1	318	0.20	100	–5.110	23.60	5.1	(5,55.0)	–0.018	1.80	31.4	(120,146.6)	–0.001	0.43	65.8	(480,228.7)
pH = 2	318	0.05	100	–0.100	2.54	8.1	(5,11.0)	–0.004	0.60	5.2	–	–	–	–	(150,60.4)
	318	0.10	100	–0.252	4.80	12.5	(20,47.1)	–0.005	0.73	6.8	(150,101.4)	–0.001	0.34	6.0	(420,142.7)
	308	0.20	100	–0.296	5.31	12.1	(20,48.6)	–0.086	3.44	17.0	(45,86.9)	–0.001	0.45	6.8	(420,177.6)
	318	0.20	100	–0.314	6.71	21.3	(10,52.4)	–0.018	1.46	10.1	(90,114.4)	–0.004	0.79	9.5	(360,210.8)
	328	0.20	100	–0.920	7.98	17.1	(5,28.4)	–0.074	3.05	18.7	(60,130.3)	–0.003	0.91	14.4	(240,244.0)
	318	0.20	70	–0.240	5.82	19.8	(10,47.2)	–0.010	1.47	13.8	(90,136.1)	–0.001	0.40	6.9	(300,193.6)
	318	0.20	40	–0.124	3.93	14.7	(20,54.0)	–0.009	1.23	10.9	(150,134.2)	–0.001	0.39	8.0	(420,200.6)
0.1 M NaCl	318	0.20	100	–0.200	4.24	12.4	(15,40.2)	–0.008	0.99	11.1	(150,97.4)	–0.001	0.28	11.1	(480,141.8)
pH = 3	318	0.20	100	–0.65	5.97	9.69	(15,9.69)	–0.006	1.05	9.13	–	–	–	–	(240,114.5)
Water	318	0.20	100	–0.438	6.12	10.6	(15,42.5)	–0.007	1.22	12.2	–	–	–	–	(150,147.5)

Units of a_1, a_2 and a_3 are in mg g^{-1} min^{-2} and those of v_{01}, v_{02} and v_{03} are in mg g^{-1} min^{-1}. Units of t_e, t_{02} and t_{03} are in min and those of q_e, q_{02} and q_{03} are in mg g^{-1}. In region 1, t_{01} and q_{01} are equal to zero. t_e and q_e are the *kat* point coordinates. k_{dif} is in mg g^{-1} min$^{-0.5}$.

Table 6 Coefficients of region 1 and region 2 (parts *2a* and *2b*) of the first kinetic curve and region 2 (parts *2a* and *2b*) of the second kinetic curve of the ISO equation for kinetics of DC adsorption on different sites of GO/PAMAM4 at different temperatures and in various shaking rates and initial DC concentrations

				KASRA region 1 (1st curve)			KASRA region 2 (1st curve)				KASRA region 2 (2nd curve)			
Solvent	**T (K)**	**$[DC]_0$ (mM)**	**rpm**	**k_{I1}**	**(t_{ssr}, q_{ssr}) (min,mg g^{-1})**	**k_{I2a}**	**(t_{sp}, q_{sp}) (min,mg g^{-1})**	**k_{I2b}**	**($[DC]^1_{t,max}$, t^1, $q^1_{t,max}$) (mM,min,mg g^{-1})**	**k_{I2a}**	**(t_{sp}, q_{sp}) (min,mg g^{-1})**	**k_{I2b}**	**($[DC]_e$, t_e, q_e) (mM,min,mg g^{-1})**
	Corresponding to:			**ARIAN region I and section IIA (–NH_3^+ site)**							**ARIAN section IIB (–NHR_2^+ site)**			
pH = 0	318	0.20	100	2.28×10^4	(5,41.9)	–	–	4.86×10^4	(0.127,60,142.6)	2.08×10^4	–	–	(0.090,360,224.7)
pH = 1	318	0.20	100	2.14×10^4	(60,130.3)	–	–	4.46×10^4	(0.125,120,146.6)	1.04×10^4	(240,184.6)	2.26×10^4	(0.083,480,228.7)
pH = 2	318	0.05	100	1.10×10^5	(5,11.0)	2.17×10^4	–	–	(0.034,45,31.6)	3.87×10^4	–	–	(0.192,150,60.4)
	318	0.10	100	4.26×10^4	(20,47.1)	3.19×10^4	(60,77.1)	3.67×10^4	(0.048,150,101.4)	5.35×10^4	–	–	(0.029,360,140.9)
	308	0.20	100	2.25×10^4	(15,48.6)	–	–	3.17×10^4	(0.160,30,70.3)	9.04×10^3	(240,154.0)	2.63×10^4	(0.110,420,177.6)
	318	0.20	100	3.48×10^4	(10,52.4)	2.56×10^4	–	–	(0.142,90,114.4)	1.98×10^4	(180,178.2)	2.38×10^4	(0.091,300,214.0)
	328	0.20	100	3.83×10^4	(5,28.4)	–	–	4.49×10^4	(0.134,60,130.3)	1.97×10^4	(150,191.0)	1.01×10^5	(0.076,240,244.0)
	318	0.20	70	3.18×10^4	(10,47.2)	1.88×10^4	–	–	(0.131,90,136.1)	1.44×10^4	–	–	(0.010,300,193.6)
	318	0.20	40	1.90×10^4	(20,54.0)	1.67×10^4	(60,98.4)	3.58×10^4	(0.132,150,134.2)	1.70×10^4	–	–	(0.098,420,200.6)
0.1 M NaCl	318	0.20	100	1.85×10^4	(20,45.9)	1.32×10^4	(60,76.9)	2.68×10^4	(0.150,150,97.4)	6.09×10^3	(240,116.4)	2.22×10^4	(0.128,480,141.8)
pH = 3	318	0.20	100	6.69×10^4	(5,21.4)	1.51×10^4	(45,59.6)	3.91×10^4	–	–	–	–	(0.042,240,114.5)
Water	318	0.20	100	1.70×10^4	(15,42.5)	1.37×10^4	(90,112.7)	3.98×10^4	–	–	–	–	(0.125,150,147.5)

$[DC]^1_{t,max}$, t^1 and $q^1_{t,max}$ are DC concentration, time and adsorption capacity at the end of the adsorption on –NH_3^+ sites (in the first curve), respectively and due to lack of region 2 at pHs of 3 and water, are considered as the *kat* point coordinates. $[DC]_e$, t_e and q_e are DC concentration, time and adsorption capacity at the beginning of the plateau for adsorption on –NHR_2^+ sites (in the second curve), respectively and are the *kat* point coordinates, too. Units of k_{I1}, k_{I2a}, and k_{I2b} are in mg g^{-1} M^{-1} min^{-1}.

surface of adsorbent and DC ions. As referred before, with a decrease in pH from 6 (in water) to less than 4, tertiary amine groups of PAMAM4 started to be protonated and this made adsorbent surface more positive that increased ISO kinetic parameters in regions 1 and 2 (including k_{I1}, k_{I2a} and k_{I2b}). ISO kinetic parameters are related to interaction of adsorbent surface and DC ions in the Stern layer. On the other hand, this caused stronger interactions between these protonated ternary amine groups with amide groups of PAMAM4 dendrimers which made its structure more compact and increased the time of reaching to equilibrium.

Due to surrounding effect of H^+ ions on DC ions at pH = 3, adsorption accelerations, velocities and k_{dif}, related to moving DC ions toward the Gouy layer, at this pH were less than those at pH = 6.

As referred before, due to opening the structure of PAMAM4 part of adsorbent at pHs of 0, 1 and 2, in addition to –NH_3^+ groups of PAMAM4 as regions 1 and 2a and/or 2b in the first kinetic curve, internal –NHR_2^+ groups of PAMAM4 as region 2a and/or 2b in the second kinetic curve involved in adsorption process. As seen from Tables 5–7, adsorption acceleration and velocities, k_{dif} and k_{I1} of region 1 increased with an increase in temperature from 308 to 328 K at 100 rpm and increasing shaking rate from 40 to 100 rpm at 318 K at 0.2 mM of DC and an increase in DC concentration from 0.05 to 0.2 mM of DC at 100 rpm and 318 K.

It was observed that only k_{I1} parameters of 0.2 mM of DC solution at 318–328 K and 100 rpm and pH of 2 obey from Arrhenius equation and their activation energy of adsorption was 22.5 kJ mol^{-1}. It showed that adsorption of DC ions on GO/PAMAM4 under these conditions was adsorption-controlled in region 1 and thus in other regions of the first and second curves was diffusion-controlled.

At pH = 1, the time of reaching to equilibrium was much greater than that observed for pHs of 0 and 2 which was due to changing some of DC ions to of $HCr_2O_7^-$ ions.[60] At pH = 0 compared to pH = 1, in region 1, adsorption accelerations and velocities decreased and ISO equation k_{I1} rate constant of adsorption increased due to an increase in positively charged adsorbent surface.

At pH = 2 and 0.1 M of NaCl, adsorption accelerations and velocities and ISO equation k_{I1} rate constant of adsorption of region 1 decreased compared to those at pHs of 1 (0.1 M of HCl) and 2 (0.01 M of HCl) at 318 K and 100 rpm which confirmed that surrounding DC ions by Na^+ ions was responsible for these observations.

Finally, kinetic data were analyzed with the NIPPON equation and compared to regions obtained from the KASRA model. As seen from Table 7, there are at most three curves which can be considered correspondence to regions obtained from the KASRA model in Table 5. As seen from Table 7, based on the NIPPON equation, the boundaries of different regions of kinetic curve(s) at pHs of 1, 3 and 6 (water) and also cases at pH of 2 and 0.2 mM of DC at 318 and 328 K at 100 rpm and 318 K at 40 rpm were ideal and similar to those obtained from the KASRA model.

Table 7. Non-ideal adsorption acceleration and velocity parameters for the NIPPON curves from analysis of adsorption of DC on GO/PAMAM4 at different temperatures, various pHs, shaking rates and in various initial DC concentration

Solvent	T	$[DC]_0$	rpm	First NIPPON curve				Second NIPPON curve			Third NIPPON curve		
	(K)	(mM)		a^N_{fc}	v^N_{fc}	t_{sc}	q_{sc}	a^N_{sc}	v^N_{sc}	t_{tc}	q_{tc}	a^N_{tc}	v^N_{tc}
pH = 0	318	0.20	100	−15.65	15.65	15	41.9	−0.03	4.67	45	121.2	−0.03	1.15
pH = 1	318	0.20	100	−30.04	30.04	10	72.6	−0.28	3.07	120	146.6	−0.004	0.51
pH = 2	318	0.05	100	−6.64	6.64	20	20.1	−0.05	0.98	–	–	–	–
	318	0.10	100	−12.39	12.39	5	21.3	−0.62	3.96	90	85.0	−0.005	0.48
	308	0.20	100	−16.81	16.81	20	48.6	−0.09	1.83	120	115.6	−0.003	0.41
	318	0.20	100	−16.04	16.04	5	28.7	−0.86	5.18	90	114.4	−0.01	0.86
	328	0.20	100	−21.20	21.20	5	28.4	−0.04	1.26	60	130.3	−0.02	1.33
	318	0.20	70	−13.87	13.87	6	24.6	−0.98	5.85	60	106.7	−0.01	0.84
	318	0.20	40	−12.87	12.87	10	30.7	−0.33	3.68	150	134.2	−0.003	0.43
0.1 M NaCl	318	0.20	100	−15.67	15.67	20	45.9	−0.07	1.50	–	–	–	–
pH = 3	318	0.20	100	−12.84	12.84	30	43.4	−0.04	1.17	–	–	–	–
Water	318	0.20	100	−15.17	15.17	15	42.5	−0.18	2.83	–	–	–	–

Units of a^N_{fc}, a^N_{sc} and a^N_{tc} were in mg g^{-1} hour^{-2}, v^N_{fc}, v^N_{sc} and v^N_{tc} were in mg g^{-1} hour^{-1} and t_{sc} and t_{tc} were in min and q_{sc} and q_{tc} were in mg g^{-1}, respectively. Subscripts *fc, sc* and *tc* are abbreviations for starting first, second and third curves, respectively.

At pH = 0, a small movement was observed in boundaries of regions 1 and 2 in first curve and between the first and second curves obtained from the KASRA model.

Boundary between regions 1 and 2 of the only curve in 0.05 mM of DC at pH = 2 and 318 K and boundary between the first and second curves in 0.2 mM of DC at pH = 2 and 328 K obtained from the KASRA model disappeared which showed that in average the adsorption character of these regions were similar to each other. Also, boundary between regions of 1 and 2 of the first curve in 0.1 mM of DC at pH = 2 and 318 K (obtained from the KASRA model) disappeared and the boundary of the first and second curves moved toward smaller time which showed the character of these two curves was similar to the second curve. In these three recent cases, boundaries disappeared and characters of those regions became similar to each other due to a decrease in DC concentration and an increase in temperature.

In 0.1 M NaCl of 0.2 mM of DC at pH = 2, inconsistent with ideal results obtained from the KASRA model, there were no boundaries between the first and second curves which showed these regions were similar to each other.

At pH=2 at 70 rpm, boundaries of the first and second curves moved to smaller times compared to those obtained from the KASRA model which showed that properties of their boundaries were more similar to region 2a than region 2b.

3. 4. Using GO/PAMAM4 for Selective Separation of Metal Ions and Tannic Acid

In a series of tests, it was observed that some metal ions, including Pb^{2+}, Cr^{3+} and Cd^{2+} and also tannic acid (TA) were not adsorbed by GO/PAMAM4 and was used for separation of them from DC ions. These tests were carried out at pH = 2 which resulted in a highly positively charged surface of GO/PAMAM4 that adsorbed severely DC ions and repelled the positively charged metal ions. Concentrations of Pb^{2+}, Cr^{3+} or Cd^{2+} ions in mixed solutions of these ions with DC before and after adding adsorbent to the solutions were measured by the Agilent 200 series AA atomic absorption spectrophotometer and it was observed that only DC ions were adsorbed on GO/PAMAM4. We used mixed solutions of 0.025 mM of DC and 0.01 mM of each of above-mentioned ions and 0.006 g of adsorbent at pH = 2. For example, the UV spectra of this process for selective separation of Cr^{3+} from its mixture with DC were shown in Fig. 13. Also, GO/PAMAM4 was used to separate DC from tannic acid (TA), Fig. 14. pK_a of TA[68] is nearly 6 and at pH = 2, its phenolic hydroxyl groups did not dissociate and thus was not negatively-charged and did not have affinity to be adsorbed on GO/PAMAM4. As seen from Fig. 15, due to adsorption of DC on GO/

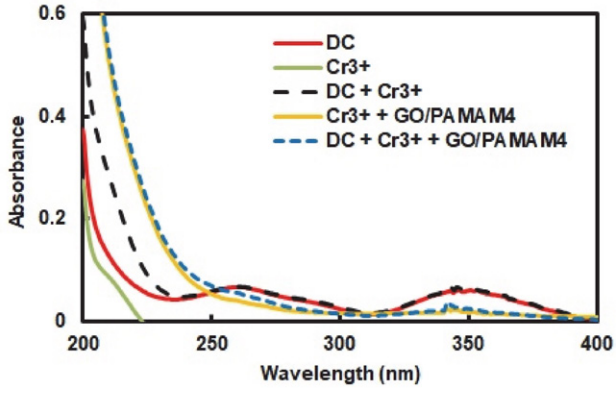

Fig. 13. UV-Vis spectra of (1) 0.025 mM DC, (2) 0.01 mM Cr^{3+}, (3) 0.025 mM DC + 0.01 mM Cr^{3+}, (4) 0.01 mM Cr^{3+} + 0.006 g GO/PAMAM4 and (5) 0.025 mM DC + 0.01 mM Cr^3 + 0.006 g GO/PAMAM4. The volume of solution in each bottle was 10 mL. In all solutions pH was 2 and tests were carried out at room temperature and during one hour

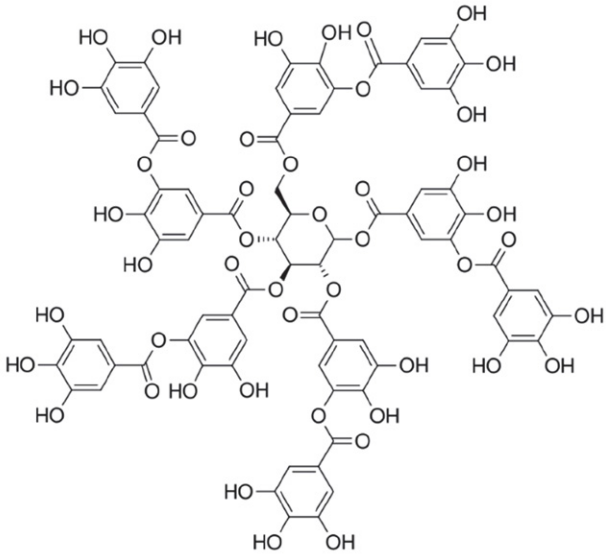

Fig. 14. Tannic acid structure

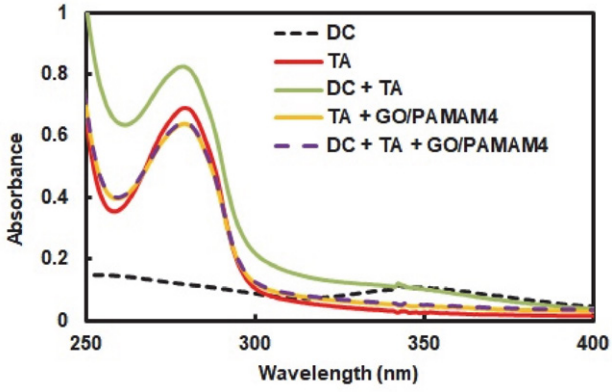

Fig. 15. UV spectra of (1) 0.025 mM DC, (2) 0.05 mM TA, (3) 0.025 mM DC + 0.05 mM TA, (4) 0.05 mM TA + 0.006 g GO/PAMAM4 and (5) 0.025 mM DC + 0.05 mM TA + 0.006 g GO/PAMAM4. pH of all solutions was 2 and tests were carried out at room temperature and during one hour. The volume of solution in each bottle was 10 mL

PAMAM4, TA was separated completely from DC ions. Some practical applications of separation of metal ions and TA[69] were explained in supporting information.

3. 5. Recycling the Used GO/PAMAM4

According to results of our experiments, in alkaline pHs, DC ions changed to chromate ions and as was observed in the adsorption tests, chromate ions were not adsorbed on GO/PAMAM4, Eq. (18). Thus, for recycling the used GO/PAMAM4, in a series of experiments at room temperature, 15 mL of 0.1 M NaOH solution was added to 0.005 g used GO/PAMAM4 and after about half an hour, adsorbent was washed with distilled water and the solution turned in yellow. It was observed that after three times recycling, the adsorption capacities of the recycled GO/PAMAM4 were about 92–95% of the as-synthesized GO/PAMAM4. Details of this process were explained in supporting information.

$$Cr_2O_7^{2-}..GO/PAMAM4_{(S)} + 2OH^- \rightarrow 2CrO_4^{2-} + H_2O + GO/PAMAM4_{(S)} \quad (18)$$

where $Cr_2O_7^{2-}$ . ..GO/PAMAM4$_{(S)}$ and GO/PAMAM4$_{(S)}$ were the used and recycled adsorbents, respectively.

4. Conclusions

In this research, mesoporous GO/PAMAM4 nanocompound was prepared from GO and PAMAM4 dendrimer and was used as an eco-friendly adsorbent for dichromate (DC) ions. GO/PAMAM4 had two different types of various adsorption sites which at pHs of 0, and 2 were protonated forms of primary and tertiary amine groups of GO/PAMAM4 which were shown as $-NH_3^+$ and $-NHR_2^+$, and at pHs of 3 and 6 were $-NH_3^+$ groups. DC ions interacted with these adsorption sites through electrostatic interaction. It was observed that in alkaline solutions DC ions changed to chromate ions and chromate ions were not adsorbed on the GO/PAMAM4 surface.

Due to stronger interaction of $-NH_3^+$ groups and their location on the end of PAMAM4 branches of adsorbent, at pHs of 3 and 6 DC ions interacted with them and analysis of their isotherms by the ARIAN model showed that they were composed from regions I and IIA and at pHs of 0, 1 and 2 interacted first with $-NH_3^+$ (composed from regions I and IIA) and then with $-NHR_2^+$ groups (region IIB) which was due to opening the structure of PAMAM4 at pHs of 0–2. Study of DC adsorption on this adsorbent at pH = 2 showed that adsorption capacity for DC ions increased with an increase in temperature and the process was endothermic. Maximum capacity for adsorption of DC ions was 246.7 mg g^{-1} at pH = 0 and 318 K.

Adsorption kinetics of DC on GO/PAMAM4 was studied by the KASRA model and intraparticle diffusion, ISO and NIPPON equations. At pHs of 3 and 6, kinetic curve was composed from regions 1 and 2 (due to adsorption on $-NH_3^+$ sites) and at pHs of 0, 1 and 2 they were formed from regions 1, 2a and/or 2b (for adsorption on $-NH_3^+$ sites) and 2a and/or 2b (for adsorption on $-NHR_2^+$ sites). At pH = 2, adsorption accelerations and velocities of regions 1 and 2a and/or 2b of the first curve (obtained from the KASRA model) and the value of k_{I1} rate constants of region 1 (obtained from ISO equation) for adsorption of DC on $-NH_3^+$ sites increased with an increase in temperature, shaking rate and decreased with increasing ionic strength.

k_{I1} rate constants in the range of 308–328 K obeyed from Arrhenius equation and thus adsorption in region 1 was adsorption-controlled. Analysis of kinetic data by using the NIPPON equation showed that boundaries of dif-

ferent regions of kinetic curve(s), obtained from the KASRA model, at pHs of 1, 3 and 6 (water) and also cases at pH of 2 and 0.2 mM of DC at 318 and 328 K at 100 rpm and 318 K at 40 rpm were ideal and similar to those obtained from the KASRA model. By using data of this research, we can find the optimum condition for separating of DC from wastewater produced in labs and also removing DC stains from surfaces and clothes by this recyclable adsorbent. Thus, during a series of tests some metal ions like Pb^{2+}, Cd^{2+} and Cr^{3+} and tannic acid (TA) were separated successfully from their mixtures with DC ions. Finally, the DC-adsorbed GO/PAMAM4 was regenerated by using an alkaline solution.

Acknowledgement

The authors would like to extend their gratitude to Prof. Nahid Rahimi Fard and her team at Sarv Saadat Medical Laboratory for their collaboration on the cytotoxicity tests.

5. Reference

1. M. Che Razali, N. Abdul Wahab, N. Sunar, N. Hazahsha Shamsudin, *Membranes* **2023,** *13*, 285. **DOI:**10.3390/membranes13030285
2. T. S. Algarni, A. M. Al-Mohaimeed, *J. King Saud Univ. Sci.* **2022,** *34*, Article ID: 102339. **DOI:**10.1016/j.jksus.2022.102339
3. M. Maurer, D. Abramovich, H. Siegrist, W. Gujer, *Water Research* **1999,** *33*, 484–493. **DOI:**10.1016/S0043-1354(98)00221-8
4. M. Sillanpää, M. Chaker Ncibi, A. Matilainen, M. Vepsäläinen, *Chemosphere* **2018,** *190*, 54–71. **DOI:**10.1016/j.chemosphere.2017.09.113
5. H. Al Abdulgader, V. Kochkodan, N. Hilal, *Sep. Pur. Technol.* **2013,** *116*, 253–264. **DOI:**10.1016/j.seppur.2013.05.052
6. J. Wang, H. Chen, *Sci. Total Environ.* **2020,** *704*, Article ID: 135249. **DOI:**10.1016/j.scitotenv.2019.135249
7. Q. Zhang, X. Chen, Z. Zhang, W. Luo, H. Wu, L. Zhang, X. Z hang, T. Zhao, *Bioresour. Technol.* **2020,** *315*, Article ID: 123813. **DOI:**10.1016/j.biortech.2020.123813
8. A. Srivastava, R. Singh, V. D. Rajput, T. Minkina, S. Agarwal, M. C. Garg, *Chemosphere* **2022**, Article ID: 135230. **DOI:**10.1016/j.chemosphere.2022.135230
9. D. Luo, K. Haverstick, N. Belcheva, E. Han, W. M. Saltzman, *Macromolecules* **2002**, *35*, 3456–3462. **DOI:**10.1021/ma0106346
10. M. Florendo, A. Figacz, B. Srinageshwar, A. Sharma, D. Swanson, G.L. Dunbar, J. Rossignol, *Molecules* **2018**, *23*, Article ID: 2238. **DOI:**10.3390/molecules23092238
11. H. He, Q. Yuan, J. Bie, R.L. Wallace, P. J. Yannie, J. Wang, M. G. Lancina, O. Y. Zolotarskaya, W. Korzun, H. Yang, S. Ghosh, *Transl. Res.* **2018**, *193*, 13–30. **DOI:**10.1016/j.trsl.2017.10.008
12. V. Gupta, S. Nayak, *J. Appl. Pharm. Sci.* **2015**, *5*, 117–22. **DOI:**10.7324/JAPS.2015.50321
13. C. Dufès, I. F. Uchegbu, A.G. Schätzlein, *Adv. Drug Delivery Rev.* **2005**, *57*, 2177–202. **DOI:**10.1016/j.addr.2005.09.017
14. Y. Gao, J. Wang, M. Chai, X. Li, Y. Deng, Q. Jin, J. Ji., *ACS Nano* **2020**, *14*, 5686–5699. **DOI:**10.1021/acsnano.0c00269
15. P. Tarach, A. Janaszewska, *Int. J. Mol. Sci.* **2021**, *22*, Article ID: 2912. **DOI:**10.3390/ijms22062912
16. V. Márquez-Miranda, J. Abrigo, J. C. Rivera, I. Araya-Duran, J. Aravena, F. Simon, N. Pacheco, F. D. Gonzalez-Nilo, C. Cabello-Verrugio, *Int. J. Nanomed.* **2017**, *12*, 1985–1999. **DOI:**10.2147/IJN.S125521
17. J. Lee, J.G. Jackman, J. Kwun, M. Manook, A. Moreno, E. A. Elster, A. D. Kirk, K. W. Leong, B. A. Sullenger, *Biomaterials* **2017**, *120*, 94–102. **DOI:**10.1016/j.biomaterials.2016.12.024
18. Q. Zhong, O.M. Merkel, J. J. Reineke, S. R. P. Da Rocha, *Mol. Pharm.* **2016**, *13*, 1866–1878. **DOI:**10.1021/acs.molpharmaceut.6b00036
19. D. A. Tomalia, H. Baker, J. Dewald, M. Hall, G. Kallos, S. Martin, J. Roeck, J. Ryder, P. Smith, *Polym. J.* **1985**, *17*, 117–132. **DOI:**10.1295/polymj.17.117
20. D. A. Tomalia, *Macromolecules* **1986**, 19, 2466–2468. **DOI:**10.1021/ma00163a029
21. J. Peterson, A. Ebber, V. Allikmaa, M, Lopp, *Proc. Estonian Acad. Sci. Chem.* **2001**, *50*, 156–166. **DOI:**10.3176/chem.2001.3.05
22. M. Ficker, V. Paolucci, J. B. Christensen, *Can. J. Chem.* **2017**, *95*, 954–964. **DOI:**10.1139/cjc-2017-0108
23. Y. Piao, T. Wu, B. Chen, *Ind. Eng. Chem. Res.* **2016**, *55*, 6113–6121. **DOI:**10.1021/acs.iecr.6b00947
24. W. S. Hummers, R. E. Offeman, *J. Am. Chem. Soc.* **1958**, *80*, 1339. **DOI:**10.1021/ja01539a017
25. S. Movahedi, M. Adeli, A. KakanejadiFard, M. Maleki, M. Sadeghizadeh, F. Bani, *Polymer* **2013**, *54*, 2917–2925. **DOI:**10.1016/j.polymer.2013.04.014
26. J. I. Paredes, S. Villar-Rodil, A. Martínez-Alonso, J. M. D. Tascón, *Langmuir* **2008**, *24*, 10560–10564. **DOI:**10.1021/la801744a
27. A. M. L. Oliveira, M. Machado, G. A. Silva, D. B. Bitoque, J. T. Ferreira, L. A. Pinto, Q. Ferreira, *Nanomaterials* **2022**, *12*, Article ID 1149 **DOI:**10.3390/nano12071149
28. H. Sachdeva, *Green Process. Synth.* **2020**, *9*, 515–537. **DOI:**10.1515/gps-2020-0055
29. M. Kowalska-Góralska,K. Czyż,Z. Dobrzański, B. Patkowska-sokoła, Z. Kowalski, *Przemysl Chemiczny* **2010**, *89*, 430–433.
30. Y. Tian, Z. Yu, L. Cao, X. Li Zhang, C. Sun, D-W Wang, *J. Energy Chem.* **2021**, *55*, 323–344. **DOI:**10.1016/j.jechem.2020.07.006
31. S. Priyadarsini, S. Mohanty, S. Mukherjee, S. Basu, M. Mishra, *JNC* **2018**, *8*, 123–137. **DOI:**10.1007/s40097-018-0265-6
32. X. Fu, J. Lin, Z. Liang, R. Yao, W. Wu, Z. Fang, W. Zou, Z. W u, H. Ning, J. Peng, *Surf. Interfaces* 2023, *37*, 102747. **DOI:**10.1016/j.surfin.2023.102747
33. M. Saha, C.R. Srinivas, S.D. Shenoy, C. Balachandran, *Contact Dermatitis* **1993**, *28*, 260–264. **DOI:**10.1111/j.1600-0536.1993.tb03428.x

34. P. Roto, H. Sainio, T. Reunala, P. Laippala, *Contact Dermatitis*. **1996**, *34*, 43–50 **DOI:**10.1111/j.1600-0536.1996.tb02111.x
35. M. Rafi, B. Samiey, CH Cheng, *Materials* **2018**, *11*, Article ID 496. **DOI:**10.3390/ma11040496
36. M. Rafi, B. Samiey, C-H Cheng, *Acta Chim. Slov.* **2020**, *67*, 1124–1138. **DOI:**10.17344/acsi.2020.5963
37. O. C. Compton, D. A. Dikin, K. W. Putz, L. C. Brinson, S. B. T. Nguyen, *Adv. Mater.* **2010**, *22*, 892–896. **DOI:**10.1002/adma.200902069
38. L. Huyck, C. Ampe, M. Van Troys, *Assay and drug development technologies* **2012**, *10*, 382–392. **DOI:**10.1089/adt.2011.391
39. H. S. Huang, J. F. Chiou, H. F. Chiu, *Archive der pharmazie* **2002**, *335*, 33–38. **DOI:**10.1002/1521-4184(200201)335:1<33::AID-ARDP33>3.0.CO;2-G
40. B. Samiey, S. Golestan, *Cent. Eur. J. Chem.* **2010**, *8*, 361–369. **DOI:**10.2478/s11532-009-0135-7
41. B. Samiey, S. Abdollahi Jonaghani. *J. Pollut. Eff. Con.* **2015**, *3*, Article ID 2.
42. M. I. Themkin, *Zh. Fit. Khim.* **1941**, *15*, 296–332.
43. M. Ozacar, I.A. Şengil, *Colloids Surf. A* **2004**, *242*, 105–113. **DOI:**10.1016/j.colsurfa.2004.03.029
44. B. Samiey, S. Farhadi, *Acta Chim. Slov.* **2013**, *60*, 763–773.
45. B. Samiey, A. Dadkhah Tehrani, *J. Chin. Chem. Soc.* **2015**, *62*, 149–162. **DOI:**10.1002/jccs.201400093
46. N. Safar Beyranvand, B. Samiey, A. Dadkhah Tehrani, K. Soleimani K, *J. Chem. Eng. Data* **2019**, *64*, 5558–5570. **DOI:**10.1021/acs.jced.9b00655
47. S. Ghobadi, B. Samiey, E. Esmaili, C-H Cheng, *Acta Chim. Slov.* **2023**, 70, 44–58. **DOI:**10.17344/acsi.2022.7777
48. N. Jahan, H. Roy, A. H. Reaz, S. Arshi, E. Rahman, S. H. Firoz, Md. S. Islam, CSCEE, **2022**, *6*, 100239. **DOI:**10.1016/j.cscee.2022.100239
49. K. S. W. Sing, D.H. Everett, R. A. W. Haul, L. Moscou, R. A. Pierotti, J. Rouquerol, T. Siemieniewska, *Pure Appl. Chem.* **1985**, *57*, 603–619.
50. J. Song, X. Wang, C-T Chang C-T, *J. Nanomater.* **2014**, Article ID 276143.
51. X. Zheng, T. Wang, H. Jiang, Y. Li, T. Jiang, J. Zhang, S. Wang, *Asian journal of pharmaceutical sciences* **2013**, *8*, 278–286. **DOI:**10.1016/j.ajps.2013.09.001
52. D. M. Shadrack, E. B. Mubofu, S. S. Nyandoro, *Int. J. Mol. Sci.* **2015**, *16*, 26363–26377. **DOI:**10.3390/ijms161125956
53. A. Ramezanpour, K. Karami, M. Kharaziha, C. Silvestru, P. Bayat, *Appl. Organomet. Chem.* **2021**, Article ID 6329.
54. X. Jiao, Y. Qiu, L. Zhang, X. Zhang, *RSC Adv.*, **2017**, *7*, 52337–52344. **DOI:**10.1039/C7RA10809E
55. Y. Zeng, Y. Kurokawa, T-T Win-Shwe, Q. Zeng, S. Hirano, Z. Zhang, H. Sone, *J. Toxicol. Sci.* **2016**, *41*, 351–370. **DOI:**10.2131/jts.41.351
56. M. A. Dobrovolskaia, A. K. Patri, J. Simak, J.B. Hall, J. Semberova, S.H. De Paoli Lacerda, S.E. McNeil, Mol Pharm. 2012 Mar 5; 9(3): 382–393. **DOI:**10.1021/mp200463e
57. W. Xiao, B. Yan, H. Zeng, Q. Liu, *Carbon* **2016**, *105*, 655–664. **DOI:**10.1016/j.carbon.2016.04.057
58. P. K. Maiti, T. Çağin, S-T Lin, W. A. Goddard, *Macromolecules* **2005**, *38*, 979–991. **DOI:**10.1021/ma049168l
59. Y. Liu, V. S. Bryantsev, M. S. Diallo, W. A. Goddard, *J. Am. Chem. Soc.* **2009**, *131*, 2798–2799. **DOI:**10.1021/ja8100227
60. F. Brito, J. Ascanioa, S. Mateoa, C. Hernandeza, L. Araujoa, P. Gili, P. Martin-Zarzab, S. Dominguez, A. Mederos, *Polyhedron*, **1997**, *16*, 3835–3846. **DOI:**10.1016/S0277-5387(97)00128-9
61. Y. A. B. Neolaka, Y. Lawa, J. A. Naat, A. A. P. Riwu, M. Iqbal, H. Darmokoesoemo, H. S. Kusuma, *JMR&T*, **2020**, *9*, 6544–6556. **DOI:**10.1016/j.jmrt.2020.04.040
62. Z. Sun, B. Liu, M. Li, C. Li, S. Zheng, *JMR&T*, **2020**, *9*, 948–959. **DOI:**10.1016/j.jmrt.2019.11.034
63. C. Zu, D. Zhong, H. Chang, J. Mou, H. Wang, H. Shen, *J. Environ. Chem. Eng.*, **2022**, *10*, Article ID108977.
64. R. K. Madri, D. Tiwari, I. Sinha, *RSC Adv.*, **2021**, *11*, 11204–11214. **DOI:**10.1039/D0RA07425J
65. H. S. Ramadan, M. Mobarak, E. C. Lima, A. Bonilla-Petriciolet, Z. Li, M. K. Seliem, *J. Environ. Chem. Eng.*, **2021**, *9*, Article ID 105352. **DOI:**10.1016/j.jece.2021.105352
66. G-H Gwak, M-K Kim, J-M Oh, *J. Nanomater.* **2016**, *37*, 1–10. **DOI:**10.1155/2016/8032615
67. A. Al Shra'ah, *JJC*, **2020**, *15*, 13–22.
68. W. Yan, M. Shi, C. Dong, L. Liu, C. Gao, *Adv. Colloid Interface Sci.* **2020**, *284*, 102267. **DOI:**10.1016/j.cis.2020.102267
69. Z. Su-fang, Y. Yong, S. Shao-min, D. Chuan, *Food Science* **2009**, *30*, 218–220.

Povzetek

V študiji smo uporabili grafen oksid/poliamidoamin G4 kot biokompatibilen nanokompozitni adsorbent za adsorbcijo dikromatnih ionov. V alkalnih raztopinah so se dikromat ioni spremenili v kromatne ione, ki niso bili adsorbirani na površini adsorbenta. Tako so bili eksperimenti izvedeni v kisli in nevtralni vodni raztopini. Pri teh pogojih so bila adsorpcijska mesta adsorbenta protonirana s primarnimi in ternarnimi amino skupinami adsorbenta, prikazanimi kot $–NH_3^+$ in $–NHR_2^+$, ki so adsorbirali dikromatne ione z elektrostatsko interakcijo. Adsorpcijske izoterme dikromata na grafen oksidu/poliamidoaminu G4 so bile pridobljene pri različnih ionskih močeh, pH in temperaturah. Izoterme smo analizirali z modelom regionalne analize adsorpcijske izoterme (ARIAN). Najvišja opažena adsorpcijska kapaciteta tega procesa je bila 246,7 mg g^{-1} pri pH = 0 in 318 K. Testi pri pH = 2 so pokazali, da je ta proces endotermen. Adsorpcijski kinetični eksperimenti so bili izvedeni pri različnih začetnih koncentracijah dikromata, pH, temperaturah, hitrostih stresanja in ionskih močeh ter analizirani s kinetiko študije adsorpcije v regijah s konstantnim adsorpcijskim pospeševalnim modelom (KASRA) in difuzijo delcev, z enačbo idealno-sekundarnega reda (ISO) in neidealnim procesom adsorpcijske kinetike (NIPPON). Štiriregijska modela ARIAN in KASRA z uporabo serije enačb lahko interpretirata termodinamiko in kinetiko interakcij adsorbenta in adsorbata pri različnih pogojih. Pb^{2+}, Cd^{2+}, Cr^{3+} in taninske kisline smo ločili z grafen oksidom/poliamidoaminom G4 iz dikromatnih ionov in reciklirali grafen oksid/poliamidoamin G4 z alkalno raztopino.

DOI: 10.17344/acsi.2024.8661 *Acta Chim. Slov.* **2024,** *71,* 380–387

Scientific paper

Preparation, Structures, Photoluminescence and Semiconductive Properties of Two New Lanthanide Mercury Materials with a 3-D Framework Structure

Hao-Dong Liu,[1] Xi-Yu Shao,[1] Yu-Yue Xu,[1] Wen-Tong Chen,*[,1,2] Cheng Liu,*[,1] Sheng-Ping Dai[1] and Chang-Wang Pan[1]

[1] *Institute of Applied Chemistry, School of Chemistry and Chemical Engineering, Ji'an Key Laboratory of Photoelectric Crystal Materials and Device, Humic Acid Utilization Engineering Research Center of Jiangxi Province, Jiangxi Province Key Laboratory of Coordination Chemistry, Jinggangshan University, 343009, Ji'an, Jiangxi, China*

[2] *Department of Ecological and Resources Engineering, Fujian Key Laboratory of Eco-Industrial Green Technology, Wuyi University, 354300, Wuyishan, Fujian, China*

** Corresponding author: E-mail: wtchen_2000@aliyun.com (W.-T. Chen); 234871279@qq.com (C. Liu) +86(796)8100490; fax +86(796)8100490*

Received: 02-05-2024

Abstract

Two new lanthanide mercury materials, $[Gd(IA)_3(H_3O)_2Hg_3Br_6]_nCl_{2n}$ (**1**) and $[La(IA)_3(H_3O)_2Hg_3Br_6]_nCl_{2n}$ (**2**) (IA = isonicotinic anion), have been prepared under solvothermal conditions and characterized by single-crystal X-ray diffraction techniques. They are isomorphic and characterized by a three-dimensional (3-D) framework structure. The lanthanide ions are bound by eight oxygen atoms to exhibit a square antiprismatic geometry. The solid-state photoluminescence experiment discovers that compound **1** shows a strong emission in the red region. Compound **1** possesses CIE (Commission Internationale de l'Éclairage) chromaticity coordinates of 0.7347 and 0.2653. Its CCT (correlated color temperature) is 6514 K. Compound **2** displays yellow photoluminescence and it has CIE chromaticity coordinates of 0.4411 and 0.5151. The CCT of compound **2** is 3633 K. Solid-state UV/Vis diffuse reflectance spectra revealed that their semiconductor band gaps are 2.16 eV and 2.85 eV, respectively.

Keywords: Lanthanide; mercury; photoluminescence; band gap; semiconductor

1. Introduction

For several decades, lanthanide coordination compounds have received more and more attention from chemical and material researchers, because lanthanide coordination compounds generally exhibit useful physicochemical properties such as photoluminiscence, catalyst, magnet and biochemical sensors, which makes them attractive in display, catalysis, medical and other applications fields.[1–6] The interesting physicochemical properties of lanthanide coordination compounds dominantly rise from the rich 4*f* electron of the lanthanide ion. Among these attractive physicochemical properties, photoluminiscence is especially interesting. Lanthanide coordination compounds generally show strong photoluminescence emission if the 4*f* electron transition can efficiently occur. People have so far completed a lot of exploration about lanthanide coordination compounds, in order to find out their potential use in the areas of electrochemical displays, luminescent sensors, medicine, magnetic material, light-emitting diode, and so on.[7–12]

Zinc, cadmium and mercury are group 12 (IIB) elements and they have also attracted a lot of attention because of the following reasons: vital roles played by zinc in biological systems, various coordination motifs, attractive photoelectric and photoluminescence behavior, and so forth.[13–16] Moreove, the IIB elements can also be applied for synthesizing semiconductor materials and, to this day, many semiconductor materials containing IIB elements have been documented.[17–20]

Organic molecules with different functional groups are very useful in the construction of metal coordination

compounds. N-containing heterocyclic molecules (for instance, isonicotic acid, nicotic acid, 4,4'-bipy, 2,2'-bipy, etc.) have been widely applied for the preparation of metal coordination compounds because of their rich coordination sites and various coordination modes.[21–23] To our knowledge, isonicotinic acid is an useful building molecule because it possesses two carboxylic oxygen atoms at one side and one nitrogen atom at the other side. As a result, isonicotinic acid molecules can bind to different metal ions to form new compounds. Isonicotic acid molecules are deemed to be a nice chelating and bridging ligand to form metal coordination compounds with high dimensional extended structures. Furthermore, the pyridyl ring of isonicotic acid molecule possesses delocalized π-electrons which endow isonicotic acid molecules to be a good candidate to prepare luminescent materials in the fields of organic light emitting diode (OLED), chemical sensor, solar energy conversion, and so forth.[24–26]

During these years, our group keeps exploring the photoluminescence, magnetism and semiconductor materials. We recently become interested in the crystal engineering of lanthanide IIB materials. For the sake of investigating new lanthanide IIB materials with new structural motifs and attractive performance, we focus on the design and preparation of new lanthanide IIB materials with various organic molecules by means of solvothermal reactions. In this research, we report the preparation, crystal structures, photoluminescence, CIE, CCT, FT-IR, PXRD (powder X-ray diffraction) and semiconductive investigation of two new lanthanide mercury compounds with a 3-D framework structure, namely, $[Gd(IA)_3(H_3O)_2Hg_3Br_6]_nCl_{2n}$ (**1**) and $[La(IA)_3(H_3O)_2Hg_3Br_6]_nCl_{2n}$ (**2**) (IA = isonicotinic anion) which were prepared through solvothermal reactions.

2. Experimental

2. 1. Instruments and Chemicals

All of the chemicals used for the reactions were commercially bought and directly applied for the syntheses of the title compounds. The C, H and N elemental analyses were performed on an Elementar Vario EL elemental analyzer. The FT-IR spectroscopy were conducted on a PE Spectrum-One FT-IR spectrophotometer with a KBr pellet and the wavenumber is in the span of 400 cm^{-1} ~ 4000 cm^{-1}. The PXRD pattern was obtained on a AL-Y3000 powder diffractometer with Cu-K (λ = 1.54056 Å), 10° ≤ 2θ ≤ 50°, 0.1° step size, and one second of exposure time. The theoretical powder curve was obtained from the X-ray single-crystal diffraction data set and processed using the free version of Mercury v1.4 program software offered by the Cambridge Crystallographic Data Centre.The photoluminescence spectra were carried out on a F97XP photoluminescence spectrometer with the wavelength in the range of 200 nm ~ 900 nm. The solid-state UV/Vis diffuse reflectance spectra were measured on a TU1901 UV /Vis spectrometer with the wavelength in the range of 190 nm ~ 900 nm.

2. 2. Synthesis of $[Gd(IA)_3(H_3O)_2Hg_3Br_6]_nCl_{2n}$ (1)

The $Gd(NO_3)_3{\cdot}6H_2O$ (0.5 mmol, 452 mg; Sigma-Aldrich company, analytical reagent, CAS # 19598-90-4), $HgBr_2$(1.5 mmol, 540 mg; Sigma-Aldrich company, analytical reagent, CAS # 7789-47-1), isonicotinic acid (1.5 mmol, 185 mg; Sigma-Aldrich company, analytical reagent, CAS # 55-22-1), concentrated hydrochloric acid (0.1 mL; Sigma-Aldrich company, analytical reagent, CAS # 7647-01-0) and distilled water (10 mL) were mixed into a 25 mL Teflon-lined stainless steel autoclave. The autoclave was heated at 433 K for ten days and powered off. After naturally cooling down to room temperature, yellow crystals suitable for the single-crystal X-ray diffraction measurement were collected, washed with distilled water and dried in air. The yield was 41% (based on $Gd(NO_3)_3{\cdot}6H_2O$). $C_{18}H_{18}Br_6Cl_2GdHg_3N_3O_8$: calc. C, 12.62; H, 1.06; N, 2.45; Found C,

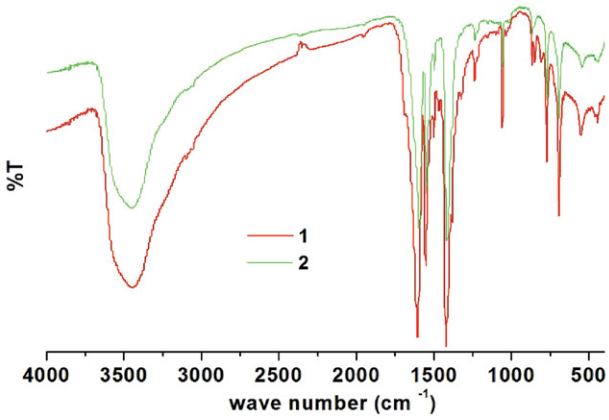

Fig. 1: FT-IR spectroscopy of **1** and **2**.

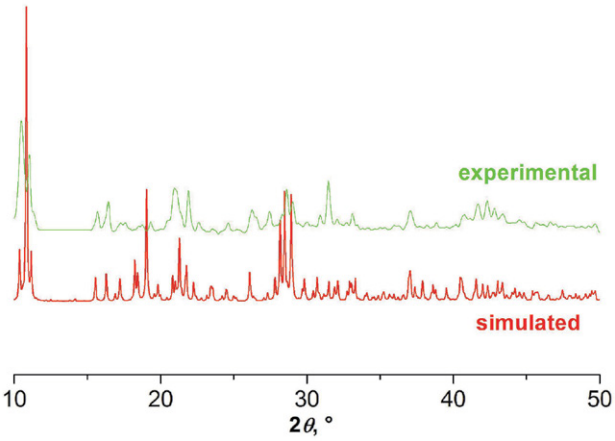

Fig. 2: PXRD of **1**.

12.69; H, 1.09; N, 2.51. FT-IR peaks (KBr, cm^{-1}): 3440(vs), 1950(w), 1607(vs), 1551(s), 1500(w), 1420(vs), 1233(m), 1062(s), 864(w), 809(w), 768(s), 693(s), 552(m) and 440(w), as shown in Fig. 1. The purity is confirmed by PXRD, as shown in Fig. 2.

2. 3. Synthesis of $[La(IA)_3(H_3O)_2Hg_3Br_6]_nCl_{2n}$ (2)

The $La(NO_3)_3{\cdot}6H_2O$ (0.5 mmol, 217 mg; Sigma-Aldrich company, analytical reagent, CAS # 10277-43-7), $HgBr_2$(1.5 mmol, 540 mg; Sigma-Aldrich company, analytical reagent, CAS # 7789-47-1), isonicotinic acid (1.5 mmol, 185 mg; Sigma-Aldrich company, analytical reagent, CAS # 55-22-1), concentrated hydrochloric acid (0.1 mL; Sigma-Aldrich company, analytical reagent, CAS # 7647-01-0) and distilled water (10 mL) were mixed into a 25 mL Teflon-lined stainless steel autoclave. The autoclave was heated at 433 K for ten days and powered off. After naturally cooling down to room temperature, colorless crystals suitable for the single-crystal X-ray diffraction measurement were collected, washed with distilled water and dried in air. The yield was 34% (based on $La(NO_3)_3{\cdot}6H_2O$). $C_{18}H_{18}Br_6Cl_2Hg_3LaN_3O_8$: calc. C, 12.75; H, 1.07; N, 2.48; Found C, 12.80; H, 1.11; N, 2.52. FT-IR peaks (KBr, cm^{-1}): 3444(vs), 1950(w), 1596(vs), 1551(s), 1501(w), 1415(vs), 1234(m), 1056(s), 865(w), 769(s), 688(s), 547(m) and 438(w), as shown in Fig. 1. The purity is confirmed by PXRD, as shown in Fig. 3.

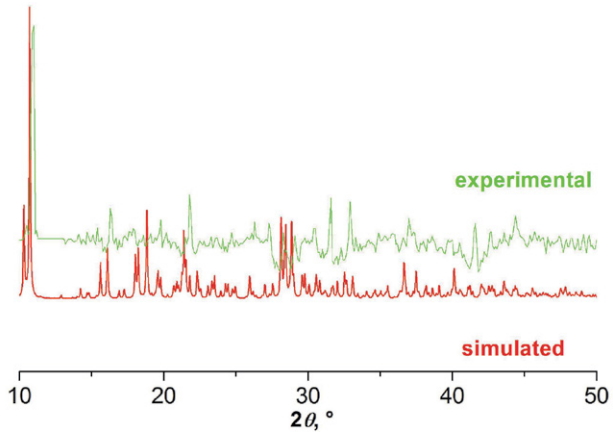

Fig. 3: PXRD of **2**.

2. 4. X-ray structure determination

The crystal data sets of the title compounds were measured using a Rigaku Mercury CCD X-ray diffractometer equipped with graphite monochromated Mo-Kα radiation source with a wavelength being of 0.71073 Å. The measurements were conducted with the use of an ω scan mode. The data reduction and empirical absorption corrections were performed by using the CrystalClear software. The crystal structures were solved by means of the direct methods. The Siemens SHELXTLTM Version 5 software packages were used to solve the structures. All of the non-hydrogen atoms were found based on the subsequent difference electron density maps and refined anisotropi-

Table 1: Crystallographic data and structural analyses for the title compounds

Compound	1	2
Formula	$C_{18}H_{18}Br_6Cl_2GdHg_3N_3O_8$	$C_{18}H_{18}Br_6Cl_2Hg_3LaN_3O_8$
M_r	1713.73	1695.39
Color	yellow	colorless
Crystal size/mm	0.14 0.11 0.09	0.19 0.04 0.03
Crystal system	Monoclinic	Monoclinic
Space group	$P2_1/n$	$P2_1/n$
a (Å)	12.5309(6)	12.4632(4)
b (Å)	9.7214(3)	9.8237(3)
c (Å)	32.7114(8)	33.0857(8)
β (°)	94.253(3)	94.448(3)
V (Å^3)	3973.9(2)	4038.6(2)
Z	4	4
$2\theta_{max}$/°	50	50
Reflections collected	16417	21697
Independent, observed reflections (R_{int})	5307, 4087 (0.0569)	6926, 5180 (0.0435)
$d_{calcd.}$ (g/cm^3)	2.864	2.788
μ/mm^{-1}	19.406	18.510
T/K	293(2)	293(2)
F(000)	3036	3008
R_1, wR_2	0.0787, 0.1746	0.0629, 0.1447
S	1.027	1.072
Largest and mean Δ/σ	0.002, 0.000	0.002, 0.000
$\Delta\rho$(max, min) (e/Å^3)	1.731, –1.407	2.574, –1.785

cally, while all hydrogen atoms were theoretically located. The final structures were refined by using the full-matrix least-squares refinement on F^2. Crystallographic data and structural analyses for the title compounds are listed in Table 1. Selected bond lengths and bond angles are presented in Table S1.

3. Result and Discussions

The FT-IR spectroscopy of the title compounds were conducted at room temperature. The FT-IR peaks of the title compounds are mainly found in the frequency range of 500 cm^{-1} ~ 1600 cm^{-1}, as shown in Fig. 1. The FT-IR spectroscopy of the title compounds are very similar, because they are isomorphic. The very strong intensity peaks at 3440 cm^{-1} and 3444 cm^{-1} can be assigned to the O–H asymmetric vibration of the water molecules. The very strong peaks at 1607 cm^{-1} and 1596 cm^{-1} should be ascribed to the stretching vibrations of the C=O bonds. The peaks at 1551 cm^{-1}, 1420 cm^{-1}, 1415 cm^{-1}, 1233 cm^{-1} and 1234 cm^{-1} can be ascribed to the stretching vibrations of the pyridyl ring of the isonicotinic ligands. The peaks locating in the range of 864 cm^{-1} ~ 1062 cm^{-1} can be assigned to the bending vibration of the pyridyl ring of the isonicotinic ligands. The peaks at 438 cm^{-1} ~ 769 cm^{-1} can be ascribed to the stretching vibrations of the Hg–Br bonds.

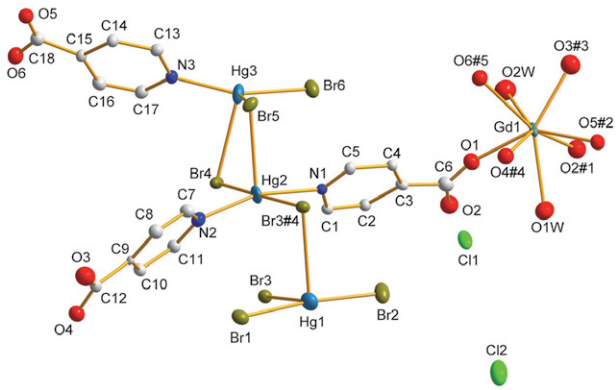

Fig. 4: An ORTEP figure of **1** with 25% thermal ellipsoids. Hydrogen atoms were omitted for clarity.

As discovered by the single-crystal X-ray diffraction measurements, compounds **1** and **2** are isomorphic. They crystallize in the space group $P2_1/n$ of the monoclinic system with four formula units in one cell. In this section only the crystal structure of compound **1** is described herein as an example. The crystallographically asymmetric unit is comprised of one Gd^{3+} cation, three Hg^{2+} cations, six Br^- anions, two isolated Cl^- anions, three isonicotinic acid anions and two water molecules, as presented in Fig. 4. All of the crystallographic independent atoms are resided at general positions. The Gd^{3+} cation is coordinated by eight oxygen atoms, of which two come from two coordination water molecules and six are offered by six isonicotinic acid ligands, to yield a square antiprismatic GdO_8 motif. All water molecules are bound to the Gd^{3+} cation. The Gd–O bond length locates in the span of 2.304(7) Å ~ 2.538(9) Å with an average value of 2.392(10) Å, as listed in Table S1. The Gd–O bond lengths are in the normal range and comparable with the values documented in the references.[27,28] The O–Gd–O bond angle is in the span of 69.2(3)° ~ 144.2(3)°. All of the isonicotinic acid molecule act as a μ_3-bridging ligand with two oxygen atoms coordinating to two Gd^{3+} cations and one nitrogen atom binding to one Hg^{2+} cation (Fig. 4). The Gd^{3+} cations are linked by two or four isonicotinic acid ligands to form a one-dimensional (1-D) $[Gd(IA)_3(H_3O)_2]_n$ chain running along the *b* axis, as presented in Fig. 5.

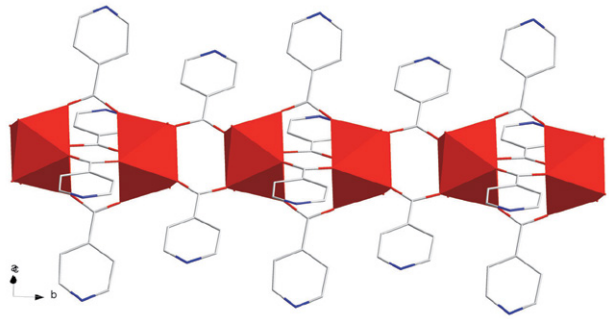

Fig. 5: A 1-D $[Gd(IA)_3(H_3O)_2]_n$ chain of **1** in polyhedral and wires representation. The polyhedron is GdO_8.

The three mercury ions are grouped into three types. The Hg1 is surrounded by four Br^- anions to give a distorted $HgBr_4$ tetrahedron. The Hg3 is coordinated by three Br^- anions and one nitrogen atom to form a distorted $HgBr_3N$ tetrahedron. Differently, the Hg2 is coordinated by three Br^- anions and two nitrogen atoms to yield a distorted $HgBr_3N_2$ pyramid. The bond lengths of Hg–Br are in the range of 2.4128(11) Å ~ 3.1143(10) Å with an average value of 2.8202(12) Å, as listed in Table S1. The Hg–Br bond lengths are in the normal range and comparable with the values documented in the references.[29,30] The Br–Hg–Br bond angle is in the span of 89.23(3)° ~ 175.15(3)°. The Hg–Br–Hg bond angles are in the range of 82.11(3)° ~ 178.45(3)°. The bond lengths of Hg–N are in the span of 2.136(7) Å ~ 2.230(6) Å with an average value of 2.171(8) Å. The Hg–N bond lengths are in the normal range and comparable with the values documented in the references.[31,32] The N–Hg–Br bond angle is in the span of 85.89(16)° ~ 156.81(19)°. The N(2)-Hg(2)-N(1) bond angle is 162.7(3)° which is almost linear, as shown in Fig. 4. The mercury ions are connected by the Br^- anions to yield a 1-D $[Hg_3Br_6]_n$ chain running along the *b* direction, as presented in Fig. 6. The 1-D $[Hg_3Br_6]_n$ chains and the above mentioned 1-D $[Gd(IA)_3(H_3O)_2]_n$ chains are interlinked by the isonicotinic acid ligands to yield a two-dimensional (2-D) layer extending along the *bc* plane, as

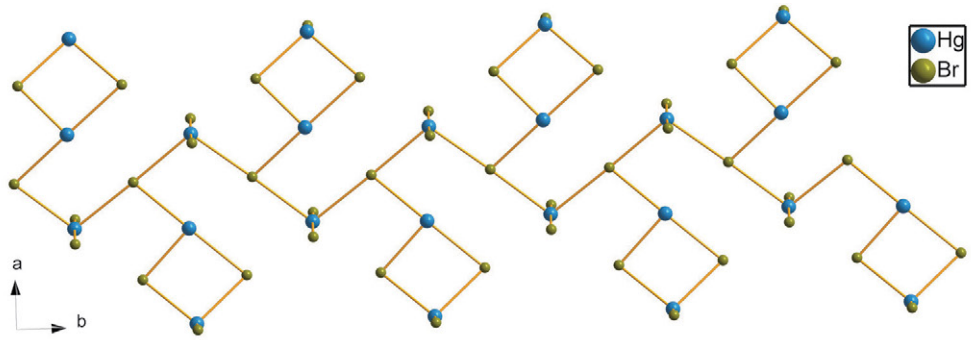

Fig. 6: A 1-D $[Hg_3Br_6]_n$ chain in **1**.

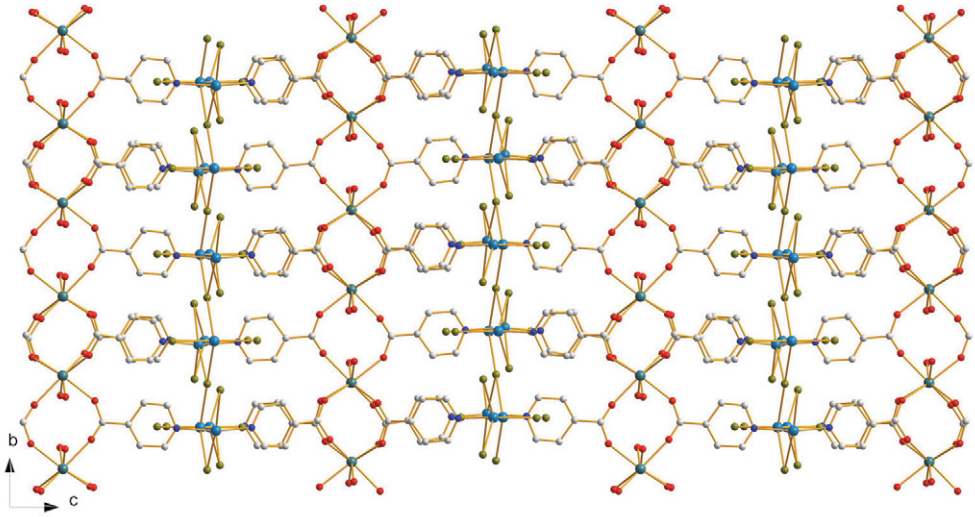

Fig. 7: A 2-D layer in **1**.

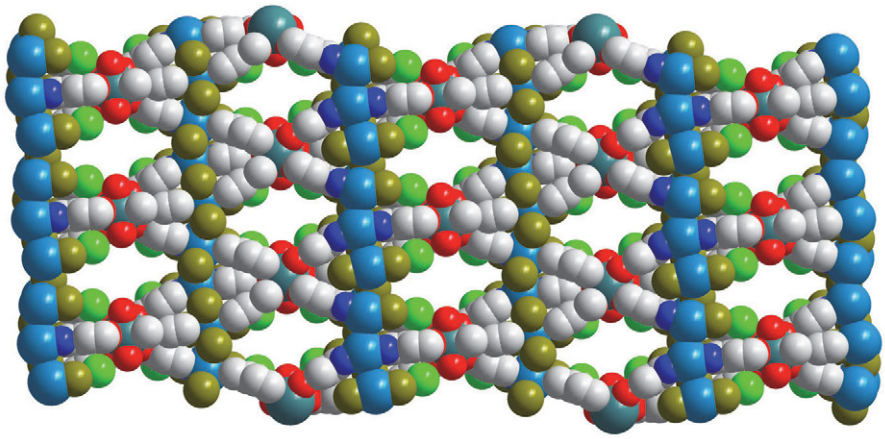

Fig. 8: The 3-D framework structure of **1** in space-filling representation with the channel window size being of 8.057 Å × 14.879 Å.

displayed in Fig. 7. The 2-D layers are further interconnected together to construct a three-dimensional (3-D) framework structure with the channel window size being of 8.057 Å × 14.879 Å, as shown in Fig. 8.

It is well-known that many lanthanide coordination compounds can exhibit photoluminescence emissions. Therefore, both of the title compounds are possible to display photoluminescence performance because they have lanthanide ions. Based on such a thought, the powder samples of compounds **1** and **2** were adopted to carry out their photoluminescence measurements under room temperature. The results of the photoluminescence measurements are shown in Fig. 9 and Fig. 11. With regard to compound **1**, when it was excited by the 284 nm light, it

displayed red photoluminescence with an emission band locating at 740 nm, as presented in Fig. 9. Compound **1** possesses CIE (Commission Internationale de l'Éclairage) chromaticity coordinates of 0.7347 and 0.2653, as shown in Fig. 10. Its CCT (correlated color temperature) is 6514 K. As a result, compound **1** is expected to be a potential red light photoluminescent material. As for compound **2**, when it was excited by the 322 nm UV light, it shows yellow photoluminescence with the emission band locating at 561 nm, as presented in Fig. 11. Compound **2** possesses remarkable CIE chromaticity coordinates of 0.4411 and 0.5151, as displayed in Fig. 12. The CCT for compound **2** is 3633 K. As a result, compound **2** is expected to be a potential yellow light photoluminescent material. The photoluminescence features of compounds **1** and **2** are clearly different, although they have isomorphic crystal structures. This suggests that the lanthanide ions plays important role for their photoluminescence performances.

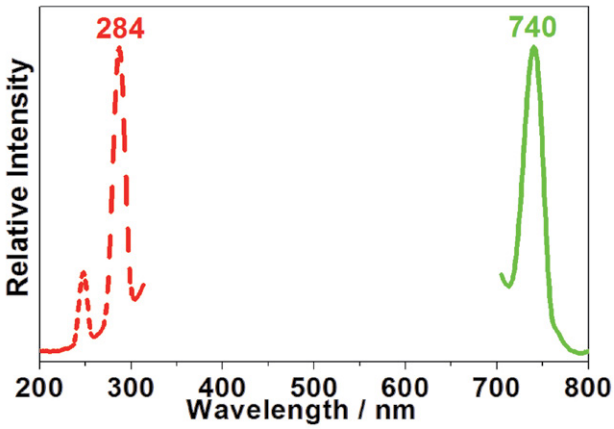

Fig. 9: Solid state photoluminescence spectra of **1** with the red and green lines representing excitation and emission spectra, respectiely.

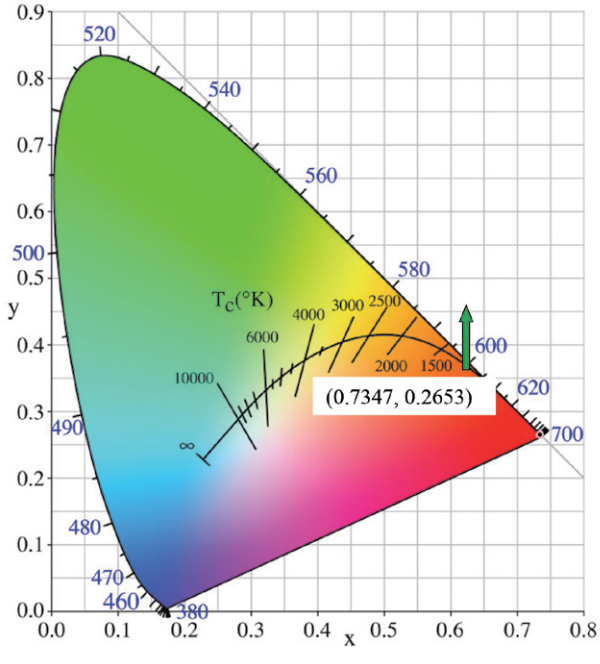

Fig. 10: CIE diagram of **1**.

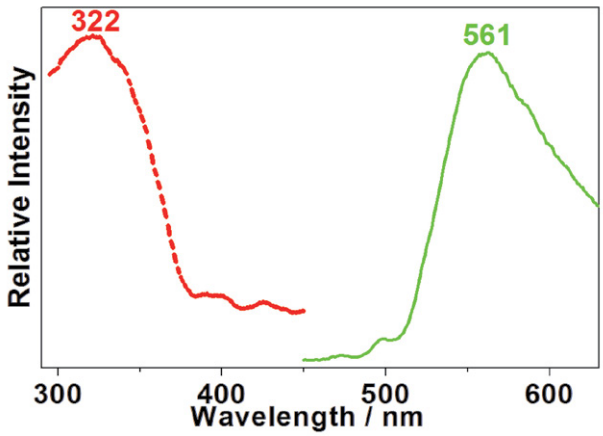

Fig. 11: Solid state photoluminescence spectra of **2** with the red and green lines representing excitation and emission spectra, respectively.

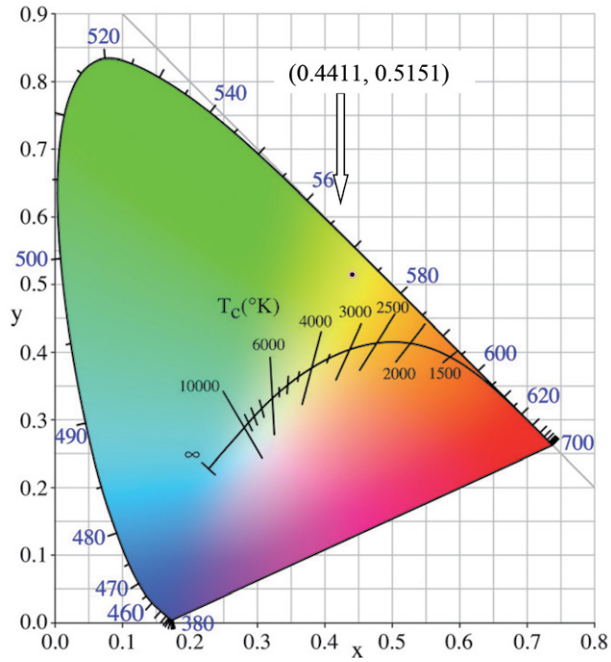

Fig. 12: CIE diagram of **2**.

The photoluminescence performances, catalytic properties and magnetic behavior of lanthanide coordination compounds have thus far been broadly investigated, however, their semiconductor performances have been rarely studied. Because of such a reason and in order to more deeply investigate the physicochemical properties of both title compounds, the solid state UV/Vis diffuse reflection experiments were conducted with finely ground powder samples under room termperature. The solid state UV/Vis diffuse reflectance spectrum data sets for both title compounds were processed by means of the well-known

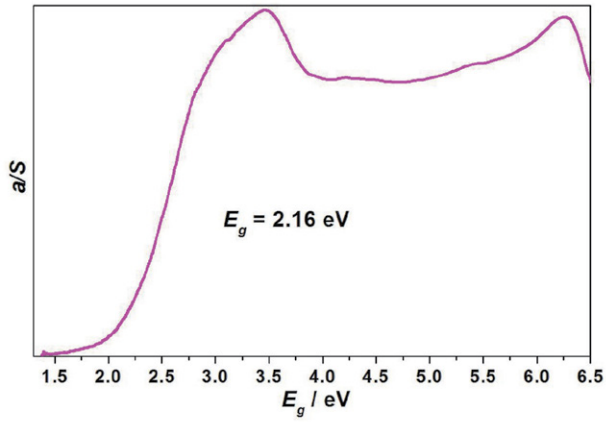

Fig 13: The UV-vis diffuse reflectance curve measured with solid state samples of **1**.

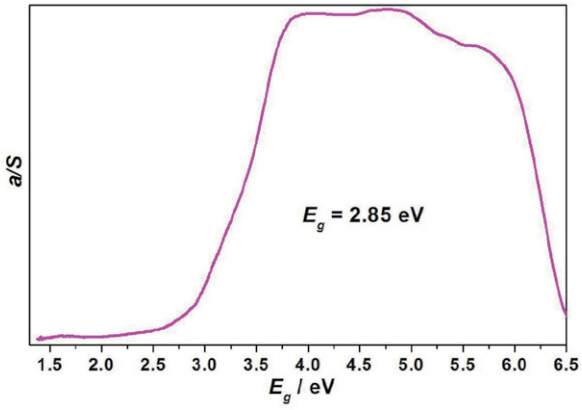

Fig 14: The UV-vis diffuse reflectance curve measured with solid state samples of **2**.

Kubelka-Munk formula $\alpha/S = (1-R)^2/2R$, of which the α is the absorption coefficient, S means the scattering coefficient, while R refers to the reflection coefficient. The transferred solid state UV/Vis diffuse reflectance spectra are shown in Fig. 13 and Fig. 14 for compounds **1** and **2**, respectively. The semiconductor band gap for both title compounds were determined by means of the straight line epitaxy method from the maximum absorption edge of the α/S versus energy curve. Based on such a method, the semiconductor band gaps for compounds **1** and **2** can be determined as 2.16 eV and 2.85 eV, respectively. Moreover, the solid state UV/Vis diffuse reflectance diagrams of both title compounds discover that their absorption edges are not steep. This suggests that both title compounds have gone through an indirect transition process.[33] Therefore, the title compounds are probably candidates for wide band gap semiconductive materials.

4. Conclusions

In conclusion, we have prepared two new lanthanide mercury materials via a solvothermal reaction. They are isomorphic and characterized by a 3-D framework structure. They exhibit red or yellow photoluminescent emissions with different CIE and CCT values. This suggests that they are a potential red or yellow light photoluminescent material in display and other imaging fields. The solid state UV/Vis diffuse reflectance spectrum reveals that they are probably candidates for wide band gap semiconductive materials. Both of the photoluminescence features and semiconductor performances for compounds **1** and **2** are obviously different, although they show isomorphic crystal structures and only metal ions are different. This indicates that the lanthanide ions play a very vital role for their photoluminescence features and semiconductor performances. Therefore, using other lanthanide ions, similar compounds with new properties may be obtained. More explorations on the relationship between the crystal structure and the physicochemical performance in this field are in progress in our group.

Acknowledgements

This work was supported by the National Natural Science of Foundation of China (22265014), the Science and Technology Project of Jiangxi Provincial Department of Education (GJJ2201602), and the Science and Technology Planning Project of Nan Ping, Fujian, China (N2020Z008).

Supplementary Material

Crystallographic data for the structure reported in this paper have been deposited with the Cambridge Crystallographic Data Centre as supplementary publication no. CCDC 2330402 and 2330403 for compounds **1** and **2**, respectively. Copies of the data can be obtained free of charge on application to CCDC, 12 Union Road, Cambridge CB2 1EZ, UK (fax: (44) 1223 336-033; e-mail: deposit@ccdc.cam.ac.uk

7. References

1. P. Ivanchenko, G. Escolano-Casado, L. Mino, L. Dassi, J. F. Fernandez-Sánchez, G. Martra, J. Gómez-Morales, *Colloid. Surface. B* **2022**, *217*, 112620. **DOI:**10.1016/j.colsurfb.2022.112620
2. Z. Z. Weng, C. L. Chen, L. W. Ye, L. S. Long, L. S. Zheng, X. J. Kong, *Sci. China Chem*. **2023**, *66*, 443–448. **DOI:**10.1007/s11426-022-1493-y
3. W. M. Wang, N. Qiao, J. L. Wang, Y. Chen, J. C. Yan, C. Y. Xu, C. S. Cao, *Catal. Today* **2024**, *425*, 114359. **DOI:**10.1016/j.cattod.2023.114359
4. Q. Fan, C. Sun, B. L. Hu, Q. Wang, *Mater. Today Bio*. **2023**, *20*, 100646. **DOI:**10.1016/j.mtbio.2023.100646
5. H. Jia, N. Li, H. Y. He, X. C. Zhang, Y. Y. Teng, W. P. Qin, *Adv. Opt. Mater.* **2024**, DOI10.1002/adom.202302583.

6. F. Pointillart, K. Bernot, B. Le Guennic, O. Cador, *Chem. Commun*. **2023**, *59*, 8520–8531. **DOI:**10.1039/D3CC01722B
7. X. T. Dong, M. Q. Yu, Y. B. Peng, G. X. Zhou, G. Peng, X. M. Ren, *Dalton Trans*. **2023**, *52*, 12686–12694. **DOI:**10.1039/D3DT02106H
8. J. R. Thomas, M. J. Giansiracusa, R. A. Mole, S. A. Sulway, *Cryst. Growth Des.* **2023**, *24*, 573–583. **DOI:**10.1021/acs.cgd.3c01380
9. K. Nehra, A. Dalal, A. Hooda, P. Kumar, D. Singh, S. Kumar, R. S. Malik, P. Kumar, *J. Lumin.* **2023**, *249*. **DOI:***10.1016/j.jlumin.2022.119032*
10. A. Dalal, K. Nehra, A. Hooda, D. Singh, P. Kumar, S. Kumar, R. S. Malik, B. Rathi, *Inorg. Chim. Acta* **2023**, *550*, 121406. **DOI:**10.1016/j.ica.2023.121406
11. Y. J. Chen, C. X. Dou, P. P. Yin, J. T. Chen, X. G. Yang, B. Li, L. F. Ma, L. Y. Wang, *Dalton Trans*. **2023**, *52*, 13872–13877. **DOI:**10.1039/D3DT01869E
12. K. M. Zhu, H. Y. Xu, Z. Y. Wang, Z. L. Fu, *Inorg. Chem. Front*. **2023**, *10*, 3383–3395. **DOI:**10.1039/D3QI00529A
13. M. Arici, *Cryst. Growth Des.* **2017**, *17*, 5499–5505. **DOI:**10.1021/acs.cgd.7b01024
14. B. Mohapatra, S. Verma, *Cryst. Growth Des.* **2013**, *13*, 2716–2721. **DOI:**10.1021/cg4006168
15. L. N. Wang, L. Fu, J. W. Zhu, Y. Xu, M. Zhang, Q. You, P. Wang, J. Qin, *Acta Chim. Slov*. **2017**, *64*, 202–207. **DOI:**10.17344/acsi.2016.3109
16. P. Wang, Y. S. Wu, X. M. Han, S. S. Zhao, J. Qin, *Acta Chim. Slov*. **2017**, *64*, 431–437. **DOI:**10.17344/acsi.2017.3268
17. Y. Yoshida, H. Ito, Y. Nakamura, M. Ishikawa, A. Otsuka, H. Hayama, M. Maesato, H. Yamochi, H. Kishida, G. Saito, *Cryst. Growth Des.* **2016**, *16*, 6613–6630. **DOI:**10.1021/acs.cgd.6b01294
18. L. Zhang, H. Lin, Y. Wu, S. Zhuo, *Chem. Phys. Lett.* **2016**, *661*, 224–227. **DOI:**10.1016/j.cplett.2016.08.079
19. Y. Zeng, D. F. Kelley, *J. Phys. Chem. C* **2016**, *120*, 17853–17862. **DOI:**10.1021/acs.jpcc.6b06282
20. T. Uematsu, E. Shimomura, T. Torimoto, S. Kuwabata, *J. Phys. Chem. C* **2016**, *120*, 16012–16023. **DOI:**10.1021/acs.jpcc.5b12698
21. E. E. Moushi, A. Kourtellaris, I. Spanopoulos, M. J. Manos, G. S. Papaefstathiou, P. N. Trikalitis, A. J. Tasiopoulos, *Cryst. Growth Des.* **2015**, *15*, 185–193. **DOI:**10.1021/cg501141m
22. L. B. Zhu, F. Li, M. L. Sun, Y. Y. Qin, Y. G. Yao, *Chinese J. Struct. Chem*. **2021**, *40*, 1031–1038.
23. Y. L. Liu, Y. X. Zhao, J. H. Zhang, Y. Ye, Q. Q. Sun, *J. Solid State Chem.* **2022**, *313*, 123332. **DOI:**10.1016/j.jssc.2022.123332
24. F. E. Özbek, M. Sertçelik, M. Yüksek, G. Ugurlu, A. M. Tonbul, H. Necefoglu, T. Hökelek, *J. Fluoresc*. **2019**, *29*, 1265–1275. **DOI:**10.1007/s10895-019-02440-x
25. J. F. Zhang, J. J. Wu, G. D. Tang, J. Y. Feng, F. M. Luo, B. Xu, C. Zhang, *Sensor Actuat. B-Chem.* **2018**, *272*, 166–174. **DOI:**10.1016/j.snb.2018.05.121
26. N. N. Pang, D. X. Lin, Z. Y. Zhan, X. D. Ding, T. T. Shi, Q. X. Meng, P. Y. Liu, W. G. Xie, *Mat. Sci. Semicon. Proc.* **2022**, *145*, 106639. **DOI:**10.1016/j.mssp.2022.106639
27. A. Hernandez, J. Jenkins, H. Maslen, M. Zeller, G. Horner, C. Dempsey, J. Urteaga, C. Dunlap, R. A. Zehnder, *Inorg. Chim. Acta* **2018**, *471*, 104–112. **DOI:**10.1016/j.ica.2017.10.001
28. T. Jiang, J. Zhou, R. Li, H.-H. Zou, L. Fu, *Inorg. Chim. Acta* **2018**, *471*, 377–383. **DOI:**10.1016/j.ica.2017.11.032
29. L. K. Rana, S. Sharma, G. Hundal, *J. Mol. Struct*. **2018**, *1153*, 324–332. **DOI:**10.1016/j.molstruc.2017.10.015
30. S. J. Sabounchei, M. Ahmadianpoor, A. Hashemi, F. Mohsenzadeh, R. W. Gable, *Inorg. Chim. Acta* **2017**, *458*, 77–83. **DOI:**10.1016/j.ica.2016.12.023
31. V. Amani, R. Alizadeh, H. S. Alavije, S. F. Heydari, M. Abafat, *J. Mol. Struct.* **2017**, *1142*, 92–101. **DOI:**10.1016/j.molstruc.2017.04.034
32. M. Khanpour, A. Naghipour, A. A. Tehrani, A. Morsali, D. Morales-Morales, S. Hernandez-Ortega, *J. Mol. Struct.* **2017**, *1135*, 26–31. **DOI:**10.1016/j.molstruc.2017.01.024
33. S. F. M. Schmidt, C. Koo, V. Mereacre, J. Park, D. W. Heermann, V. Kataev, C. E. Anson, D. Prodius, G. Novitchi, R. Klingeler, A. K. Powell, *Inorg. Chem*. **2017**, *56*, 4796–4806. **DOI:**10.1021/acs.inorgchem.6b02682

Povzetek

Pod solvotermalnimi pogoji smo sintetizirali dve novi koordinacijski spojini živega srebra z lantanoidi, $[Gd(IA)_3(H_3O)_2Hg_3Br_6]_nCl_{2n}$ (**1**) in $[La(IA)_3(H_3O)_2Hg_3Br_6]_nCl_{2n}$ (**2**) (IA = izonikotinatni anion). Produkta smo karakterizirali z monokristalno rentgensko analizo. Spojini sta izomorfni in tvorita tridimenzionalno (3-D) ogrodje. Lantanoidni ioni so osemštevno koordinirani s kisikovimi atomi v obliki kvadratne antiprizme. Fotoluminiscenčne meritve v trdnem stanju kažejo, da ima spojina **1** močno emisijo v rdečem območju. Spojina **1** ima barvne koordinate CIE (Commission Internationale de l'Éclairage) 0.7347 in 0.2653. Njena vrednost korelirane barvne temperature (CCT) je 6514 K. Spojina **2** kaže rumeno fotoluminiscenco ter barvne koordinate CIE 0.4411 in 0.5151. Vrednost CCT za spojino **2** znaša 3633 K. Z meritvami UV/Vis v trdnem stanju smo določili širini prepovedanega pasu za obe spojini, ki znašata 2.16 eV in 2.85 eV.

DOI: 10.17344/acsi.2024.8714 *Acta Chim. Slov.* **2024,** *71,* 388–397

Scientific paper

The Reusage of Different Wastes by Using the Multiple's Effect Technique for Sustainable Gasoline Production

Anita Kovač Kralj

Faculty of Chemistry and Chemical Engineering, University of Maribor, Smetanova 17, Maribor, Slovenia

** Corresponding author: E-mail: anita.kovac@um.si*
+386 02 2294454 Fax: +386 02 2527 774

Received: 02-12-2024

Abstract

The unused garbage which is accumulating the landfills, such as raw materials, could be reused for synthetic gasoline production. This study presents the multiple's effect technique, which is based on the reusage of different non, party and sorted municipal solid wastes (MSW), or biogas for syngas, converted into synthetic gasoline. The novelties of this technique include a basic multiple's effect parameter (MU_W), which present a level of waste sorting, an effect of oxygen inhibition into different wastes, a simplified mathematical model and simulation with an Aspen Plus® simulator using the retrofitted methanol plan converted into the synthetic gasoline production. This technique includes a circular economy by using a circulated purified flue gas as raw material, co-products of hydrogen and water.

This technique was tested on an existing methanol process, replacing natural gas with different alternatives of wastes or biogas for the synthetic gasoline production. The best alternative was the sorted MSW, which could generate an additional profit of 4.8 MEUR/a, including the garbage and CO_2 emission reductions of $0.106 \cdot 10^6$ t/a and of $0.084 \cdot 10^6$ t/a.

Keywords: Waste; biogas; gasoline production; multiple's effect; circular economy

1. Introduction

Non-renewable petroleum resources could be replaced with gasification of sustainable resources, such as waste, intermediate raw materials, bio-waste, for gasoline or other synthetic fuels` production, using different catalytic converters of Fischer-Tropsch (FT) synthesis, fixed-bed reactors, plasma etc.

The Introduction includes in detail the literatures of the research of different synthetic production, such as gasoline and fuels, including the gasification technique. Lu et al. contributed the new research of the selective conversion of CO and H_2 to gasoline products (iso-paraffin and olefin), including the demonstrated effective H-USY zeolite supported nano-cobalt bifunctional catalysts for this catalytic reaction, which are prepared by the novel physical sputtering process. Compared with H-Mor, H-Beta and other zeolite supported catalysts, the H-USY zeolite supported cobalt catalyst shows the clearest promotional effect on the activity of Fischer-Tropsch synthesis.[1] Javed et al. presented new research of the high CO_2 selectivity of Fe-based Fischer-Tropsch microcapsule catalysts for gasoline production. The novelties of this research were the included Silicalite-1 shell turned the Fe/ZSM-5 core's surface hydrophilicity to hydrophobicity, the hydrophobic nature of the silicalite-1 layer`s decreased water-gas shift reaction's kinetics, including $CO_2$ selectivity, was decreased by suppressing the water-gas shift reaction activity. All zeolite supported Fe-based catalysts showed significantly high gasoline range hydrocarbons` selectivity (about 60%).[2]

Li et al. presented the novelties of the HZSM-5/MnAPO-11 composite and the catalytic synthesis of high-octane gasoline from syngas in flow-type fixed-bed reactors, including the highest gasoline yield. The HZSM-5/MnAPO-11 composite was prepared via hydrothermal synthesis, and the catalytic synthesis of high-octane gasoline from syngas was studied in flow-type fixed-bed reactors. The HZSM-5/MnAPO-11 composite showed the highest gasoline yield and iso-paraffin selectivity, due to the presence of more mesopores and moderate acid sites.[3] Lu and co-workers stated the study of the production of gasoline-range hydrocarbons from nitrogen-rich syngas over an Mo/HZSM-5 bi-functional catalyst in a bench-scale continuous stainless steel fixed-bed reactor with different reaction conditions. The reaction conditions, i.e., temperature, pressure and gas hourly space velocity, affected the hydrocarbon selectivity significantly.

The novelties included that the nitrogen-rich syngas can be converted into gasoline-range hydrocarbon over Mo/HZSM-5 in one step, and high nitrogen content in syngas was found to affect liquid hydrocarbon distribution.[4]

Zhang et al. developed the upgrade of the Ni/ASA catalysts with various Ni contents, which were prepared successfully through a wet impregnation method for the gasoline-range hydrocarbons` production from the oligomerization of olefins-rich bio-syngas. The studies of this research, which contained the catalytic performance, may be relevant to the balance between acid and nickel ion sites and fuels, and the high Ni loading amount of Ni/ASA may enhance the hydrogenation reaction of olefins.[5] Liu and co-workers presented the novelties of the catalytic performance with cobalt nanoparticles embedded into zeolite crystals for the direct synthesis of gasoline from syngas. The highlights of the research were series CoZ-xN catalysts with a novel cobalt-embedded zeolite structure, the coincidence of the rate of silica dissolving and zeolite growth was important, and the formation mechanism was proposed of the catalyst.[6]

Martin and Cirujano contributed the new research of the multifunctional heterogeneous catalysts for the tandem CO_2 hydrogenation Fischer-Tropsch synthesis of gasoline, including several iron-containing multifunctional catalysts based on metal oxides, carbon or zeolite materials. The novelties of this research were the included advantages of metal oxides, carbons or zeolites as support of the active Fe-catalyst, including Fe-support interactions, and the electronic and geometric properties of the active sites.[7] Li et al. presented the new research of the conversion of dimethyl ether to gasoline, using a series of nanocrystal H[Fe,Al]ZSM-5 zeolite samples with different SiO_2/Al_2O_3 ratios with a hydrothermal method. The highlights contained zeolite acidity, which was related with the synergistic effect of Al- and Fe-based acid sites, and a catalyst with an SiO_2/Al_2O_3 ratio of 45 exhibited the best catalytic performance for a dimethyl ether to gasoline reaction.[8] Su et al. developed the upgrade of the catalysts for dimethyl ether conversion to iso-paraffin-rich gasoline, including nanosized ZSM-5 (NZ5) and zinc isomorphously substituted ZSM-5 ([Zenial]NZ5) zeolites with different Si/Me ratios in initial gels (Me = Al or Al and Zn). The novelties contained iso-paraffin selectivity in gasoline hydrocarbons, which was enhanced by Zn incorporation, and $ZnOH^+$ species showed the excellent hydrogenation activity for a dimethyl ether to gasoline reaction.[9]

Magomedova et al. proposed the upgrade of the syngas-to-gasoline technology for the synthesis of liquid hydrocarbons through oxygenates (methanol and dimethyl ether), giving a light synthetic oil with a low concentration of aromatic compounds (8–16 wt %). The study contained dimensionless criteria for heat and mass transfer, which were used for plant scaling, and the operation was carried out of a pilot plant for syngas to low-aromatic gasoline via DME.[10] Szczygieł and Kułażyński contributed the research of the gasoline production from dimethyl ether and methanol, including thermodynamic limitations of synthetic fuel production. Thermodynamic analysis of the classic methanol-to-gasoline process that employs CO as a raw material allowed a comparison with the modified version of the process, assessment of their effectiveness, and deductions concerning the possible benefits and losses resulting from replacing CO with carbon dioxide. The use of CO as a raw material was clearly more favourable in terms of the tendency towards a spontaneous reaction.[11]

Rabah presented the upgrade of syngas production from biomass gasification as a potential energy source for power generation and manufacturing synthetic gasoline and diesel via Fischer-Tropsch synthesis. The operating conditions under which the objective function and the constraint were satisfied were the steam to biomass ratio, equivalent ratio, and gasification temperature.[12] Shiying et al. contributed the upgrade of the dual-stage entrained flow gasification and CO_2 cycling in biomass-to-gasoline/diesel, including design and techno-economic analysis. The dual-stage entrained flow gasification avoided separate torrefaction of biomass feedstock and provided higher cold gas efficiency, which made the addition of steam as a gasification agent feasible. The high efficiency of Fe-based slurry-phase Fischer-Tropsch synthesis reactors also enhanced the gasoline production.[13] Borugadda et al. explored the new research of the techno-economic and life-cycle assessment of the integrated Fischer-Tropsch process in the ethanol industry for bio-diesel and bio-gasoline production, using syngas obtained from the gasification of dry distillers' grain. The lab-scale experiment using pelletised promoted iron supported on Carbon Nano Tubes (Fe/CNT) was used to simulate a plant for the production of 1000 kg of syncrude/h.[14]

Mascal and Dutta presented the study of the synthesis of highly-branched alkanes, such as iso-alkanes and cycloalkanes, for renewable gasoline production from bio-oil and raw biomass using chemo-catalytic methods. Gasoline can be made from biomass pyrolysis gas via the Fischer-Tropsch or methanol-to-gasoline processes, as well as the refining of bio-oil, raw biomass, etc.[15] Hnich et al. investigated the study of the life cycle sustainability performance of synthetic diesel and gasoline from Tunisian date palm waste, and compared it with that of conventional fossil fuels. The potential environmental impacts of the biomass-to-liquid system were concluded to be associated mainly with direct emissions and the system's demand for electricity and oxygen.[16] Wang et al. designed the upgrade of the pilot plant for biomass converted to liquid fuels, including gasification, direct synthesis of dimethyl ether (DME) and DME to gasoline. The operating results showed that both the pressure and gas hourly space velocity (GHSV) not only influenced the CO conversion and the DME yield, but also had a significant effect on the manipulation of the reaction heat in the adiabatic reactor. High pressure and low GHSV favoured the high CO conversion

and the DME yield.[17] Navas-Anguita et al. presented the study of the simulation and life cycle assessment of a biogas-to-liquid plant for the coproduction of synthetic fuels (diesel and gasoline) and electricity. The system comprised a biogas dry reforming process to produce syngas, Fischer-Tropsch synthesis, and a combined-cycle process. In particular, the life-cycle environmental profile of synthetic biodiesel as the main product of the biogas-to-liquid plant was calculated, and compared with that of conventional diesel.[18]

Bahri et al. presented the novelties of the synergistic effect of a bifunctional mesoporous ZSM-5 supported Fe-Co catalyst for selective conversion of syngas with a low riblet ratio into synthetic fuel. The Fe-Co bimetallic active metals were loaded on mesoHZSM-5 with varying Fe-Co ratios, with a constant total metal loading of 30%, using the sonication process to increase active metal dispersion. The catalytic activity was tested in the laboratory scale fixed bed reactor.[19] Aluha and Abatzoglou contributed the study of the synthetic fuels from 3-φ Fischer-Tropsch synthesis using syngas feed and novel nanometric catalysts. The research presented the novel carbon-supported Co-Fe bimetallic catalysts which were synthesised through plasma. All the catalysts reduced in CO or H_2 showed equal activity of about 40% CO conversion.[20] Ali et al. defined the new research of the direct synthesis of liquid fuels and aromatics from syngas using the Fischer-Tropsch synthesis reaction on hybrid catalysts containing a highly ordered mesoporous FeZrOx bimetal oxide mixed physically with Mo-modified ferrierite (Mo/HFER). The hybride FeZrOx-Mo/HFER catalyst showed synergistic effects with a higher CO conversion to liquid fuels and aromatics. Optimal hydrophobicity and acidic sites on the Mo/HFER were responsible for the enhanced catalytic stability.[21]

Selvatico et al. obtained the upgrade of the kinetic model, based on Langmuir–Hinshelwood–Hougen–Watson for the Fischer-Tropsch synthesis of fuel, converting it into a well-established industrial process simulator. A low temperature Fischer-Tropsch process was modelled for the middle distillate production.[22] Wu et al. reported the novelties of the reformation of n-pentane (C_5H_{12}) using methane (CH_4) or carbon dioxide (CO_2) in a temperature-controlled dielectric barrier discharge reactor to produce hydrogen and clean carbon-based fuels, by using low-temperature plasma. A mechanistic study suggested that electron-induced chemistry dominates C_5H_{12} and the added gas conversion, whereas the thermochemistry controls the product distribution.[23] Liu and Larson described the study of two routes to produce liquid hydrocarbon fuels from solids via synthesis gas, Fischer-Tropsch (FT) synthesis and methanol-to-gasoline (MTG). This study compared the performance and cost of the Fischer-Tropsch and MTG processes on a self-consistent basis. In particular, FT and MTG production from coal and coal/biomass cofeeds were compared, including detailed mass, energy and carbon balances.[24] Dutta et al. provided the new research of an overview of producing fuel precursors from biomass components, and their catalytic transformation into aviation-, diesel-, and gasoline-range hydrocarbon fuels (HCFs), including strategic applications of various organic transformations for the molecular design. Emphasis was also given to the process conditions and details of the catalysts employed in these processes. The synthesis of HCFs was warranted to ensure the high quality and homogeneity of the properties, including minimizing the energy input.[25]

Santos and Alencar presented the upgrade of the syngas production from biomass gasification and its subsequent conversion into fuels through the Fischer-Tropsch synthesis. This study included a debate on the main catalysts, industrial process requirements, and chemical reaction kinetics and mechanisms of Fischer-Tropsch synthesis. Lignocellulosic material of biomass would be considered a low-cost feedstock to the liquid biofuel production on a large scale.[26] Campanario and Ortiz contributed the upgrade of the Fischer-Tropsch biofuels` production from syngas obtained by supercritical water reforming of the bio-oil aqueous phase, including the produced maximum biofuels and electrical power. The highlights of this research contained the upgraded production of syngas by using water-gas-shift, dry reforming and Fischer-Tropsch (FT) reactors, and followed the optimal conditions in the FT reactor: 220 °C, 40 bar and H_2/CO ratio of 1.70.[27]

Gharibi et al. contributed the study of the metaheuristic particle swarm optimization for enhancing energetic and exergetic performances of hydrogen energy production from plastic waste gasification. The novelties contained were multi-objective particle swarm optimization for plastic gasification, using grey relational analysis, and achieving lower heating for the polypropylene gasification and higher efficiency of cold gas.[28] Gharibi et al. prepared a few novel studies to predict polyethylene waste performance in gasification using multilayer perceptron (MLP) machine learning algorithms and interpreting them using multi-criteria decision-making methods. The main aims of this study were to develop MLP artificial neural networks and regression models to predict polyethylene gasification performance with high accuracy.[29] Mojaver et al. prepared the novel thermodynamic assessment of an integrated solid oxide fuel cell with a steam biomass gasification and high-temperature sodium heat pipes for combined heating and power production. The modelling and analysis of the system were performed using mass and energy conservation laws and equilibrium constants. The results of the extended model were confirmed by the experimental results.[30] Mojaver et al. defined the multi-objective optimization using response surface methodology and exergy analysis of a novel integrated biomass gasification, solid oxide fuel cell and high-temperature sodium heat pipe system. Response surface methodology was utilised to investigate the effect of the decision variables on the responses, i.e., the electrical power and the exergy effi-

ciency.[31] Hasanzadeh and Azdast defined the novel machine learning utilisation on air gasification of polyethylene terephthalate waste. The machine learning algorithms had good performance in predicting the performance. The models for lower heating values and cold gas efficiency showed excellent accuracy.[32] Doniavi et al. improved the efficiency of polyethylene gasification. This research was focused on the energy, exergy, and environmental impact in relation to the material conditions. These models were then optimised using a general algebraic modelling system. The results indicated that the ideal conditions consist of 84.40 % carbon content, 15 % hydrogen content, and no oxygen or nitrogen content.[33]

Hasanzadeh and Abdalrahman defined a novel research, in which it was recognised that the processing parameters have a crucial impact on the assessment of polyvinyl chloride waste gasification. The study used data collected through a validated thermodynamic model, and three different regression models were tested and compared in detail. Cold gas efficiency and normalised carbon dioxide emission were predicted using linear, quadratic, and quadratic with interaction algorithms.[34] Khalilarya et al. contributed a new research, which combined a heat and power system which consisted of a gasifier, a micro gas turbine, an organic Rankine cycle, a heat exchanger and domestic heat recovery. Air, steam, and oxygen were considered as different gasification mediums. The Taguchi approach was employed to optimise the generated power in the air, steam and oxygen medium cases.[35] Mojaver et al. researched the novel system of a fluidised bed gasifier with steam as the gasifying agent. The synthesis of gas composition and efficiencies of the system were investigated with respect to different biomasses considered as gasification fuels. The results indicated that the molar fractions of hydrogen and carbon dioxide were increased, and the molar fraction of carbon monoxide was reduced with the steam to biomass ratio.[36]

Hasanzadeh et al. improved the gasification model of polyethylene waste, by using the Gibbs free energy minimisation and Lagrange method of undetermined multipliers. A central composite design was employed, to assess and optimise the polyethylene waste gasification. The findings revealed that hydrogen production was improved significantly by 48% by raising the steam to polyethylene waste ratio according to the water–gas shift and reforming reactions.[37] Mojaver et al. compared the performances between biomass and plastic waste gasification. The important novelty and contribution of this study was the analytical hierarchy process/technique for order performance by similarity to the ideal solution coupled method that was employed in gasification of conventional biomass and plastic waste, to prioritise the considered criteria and to select the best feedstock for gasification.[38] Mojaver et al. presented a new study, in which the steam gasification was modelled of polyethylene, polypropylene, polycarbonate and polyethylene terephthalate waste. The effects of key features, including the steam to plastic waste ratio, temperature, moisture content and pressure, were assessed on hydrogen-rich syngas compositions, and the exergy destruction rate. The Taguchi approach was utilised to investigate and optimise the process. The findings revealed that the gasification of polypropylene waste led to the highest hydrogen production at all the processing conditions.[39]

In this study, the gaps in the literature were covered about the usage of the different wastes for syngas, and further into sustainable synthetic gasoline productions. The novelties of this study present the multiple's effect technique, which uses the basic multiple's effect parameter (MU_W) for the different level of waste sorting, including the effect of oxygen inhibition into different wastes. The contributions of this research include the circular economy by using a simple mathematical model for different municipal solid wastes (MSW) from non-sorted to sorted, or biogas. The objectives of this study contain the applied composition data of different wastes and the simulation model by using the Aspen Plus® simulator.

2. The Multiple's Effect Technique

The nature source, such as petroleum, would be replaced by the non-sorted (WNS), partially sorted (WPS), or sorted (WS) wastes from landfill or biogas for the sustainable synthetic gasoline production, by using the multiple's effect technique. This study presents the multiple's effect technique, which is based on the reusage of different MSW or biogas, supported by a mathematical model and the Aspen Plus® simulator for syngas converted into synthetic gasoline. This technique adapts the replacement of the existing methanol process to synthetic gasoline production, by using the same process units. The simple mathematical model uses the basic multiple's effect parameter (MU_W), which presents the level of waste sorting (MU_W; $MU_{WNS} = 0$; $MU_{WPS} = 1$; $MU_{WS} = 2$). The sorted wastes include the highest value of the multiple's effect parameter. The multiple's effect parameter allows easy calculation of the product's production and other important amounts from different wastes, including the sustainable co-produced raw materials, such as water, hydrogen and flue gas.

The synthetic gasoline would be produced from the different MSW by using the basic process units (Fig.1), which are very similar to methanol production, such as gasification of MSW (G-MSW), reforming (Ref), cooling (Coo), the first water removing (Rem1-H_2O), compressing (Com), preheating to the reaction's temperature (PreH-R), reacting (R), the first crude product cooling (Coo1-SG), the second water removing (Rem2-H_2O), the second crude product cooling (Coo2-SG), the liquid product's purification (P-SG), and hydrogen separation from nonreacted gas with a pressure swing adsorption column (PSA-H_2). The adapted process units include the optimal parameters,

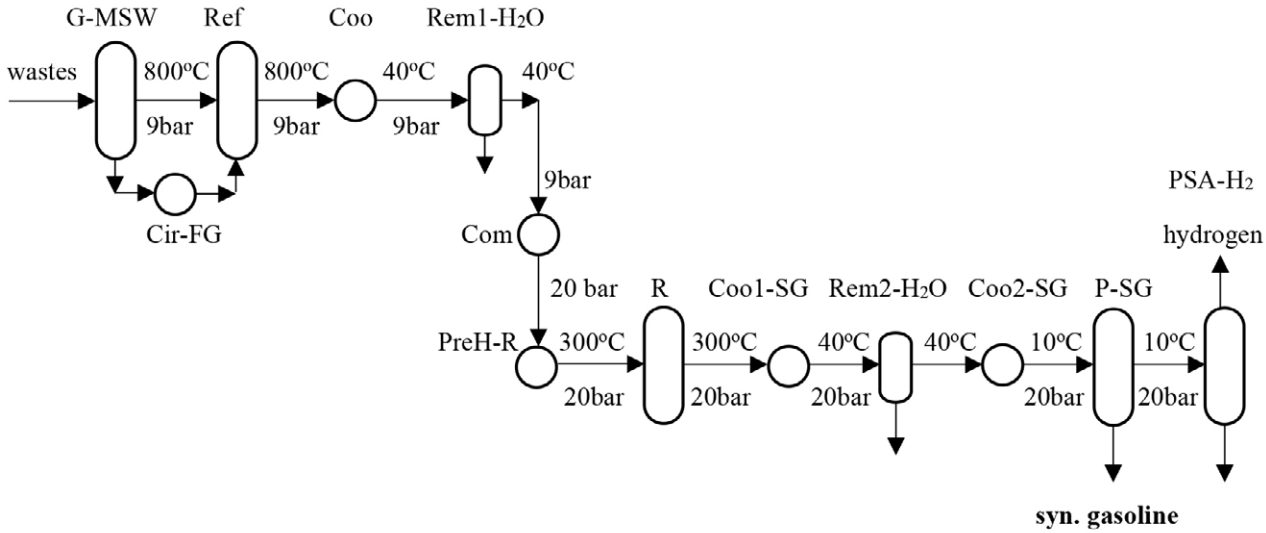

Figure 1: The process flow-diagram of the synthetic gasoline production for the different wastes including the parameters.

effects and characteristics (Fig. 1). MSW should be gassed before reforming (G-MSW). The flue gas of gasification, such as raw material, would be purified and circulated into reforming (Cir-FG).

Different municipal solid wastes (MSW) would be converted into syngas by using combustion, gasification and reforming. The purified flue gas of combustion (without particles, NO_x, SO_x, oxygen and nitrogen), including steam and carbon dioxide, is transported circularly into the gasification-reforming part, without releasing the outlet exhaust into the atmosphere. The purified flue gas is used as sustainable raw material, which would reduce the emissions and amount of clean steam. The different MSW are presented with the basic components of C, H_2, O_2 and N_2. The non-sorted MSW include lower plastics and woods (as components of C and H_2), because of a higher content of rubbers, leathers, textiles, papers, etc (as components of O_2 and N_2, too). The sorted MSW includes more plastics and woods because of the lower content of rubbers, leathers, textiles, paper, etc. The carbon and hydrogen ($F_{C,W}$, $F_{H2,W}$) are affected mostly by the reactions. The amount of oxygen is reducing the production of the synthetic gasoline and the neutral nitrogen is filling the process flows. The purified and circulated flue gas contains the components of CO_2 and H_2O, representing a circular economy system.

The basic simplified endothermic reaction of Re1 takes place into the reformer (Ref), which is producing syngas with a yield of carbon monoxide ($Y_{CO,Re1}$ = 0.999) mostly from the waste's carbon. The circulated carbon dioxide from the flue gas (FG) is converted to carbon monoxide with 80% conversion of Re2 reaction ($X_{FG,CO,Re2}$ = 0.8), and the remaining 20% (or (1 – $X_{FG,CO,Re2}$)) flows into the product's reactor (R).

$$C + H_2 + H_2O \leftrightarrows CO + H_2 + H_2O \quad \text{(Re1)}$$

$$CO_2 + H_2 \leftrightarrows CO + H_2O \quad \text{(Re2)}$$

The syngas converts to the synthetic gasoline (SG) from wastes into the reactor (R) by using two basic exothermic reactions (Re3, Re4) with the conversions of CO and CO_2 ($X_{CO,Re3}$ = 0.996, $X_{CO2,Re4}$ = 0.56).

$$8\ CO + 17\ H_2 \leftrightarrows C_8H_{18} + 8\ H_2O \quad \text{(Re3)}$$

$$8\ CO_2 + 25\ H_2 \leftrightarrows C_8H_{18} + 16\ H_2O \quad \text{(Re4)}$$

The carbon molar flow rates ($F_{C,W}$) of different wastes (non-sorted, WNS or partially-sorted, WPS, or sorted, WS; W = WNS,WPS,WS) are dependent on the lowest inlet ($F_{C,WNS}$ = 600 kmol/h) and the difference in carbon amounts (ΔF_C = 100 kmol/h), including the multi-

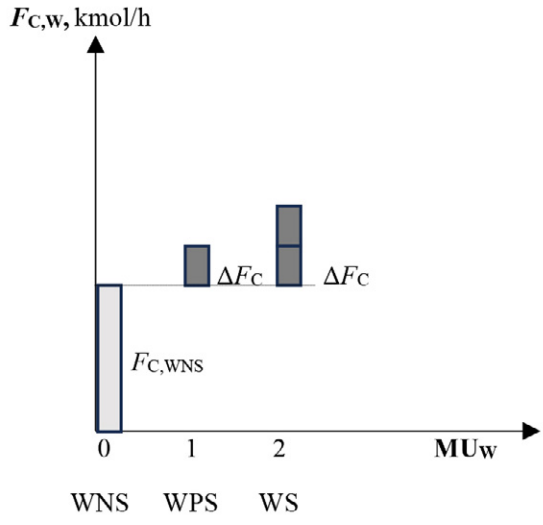

Figure 2: Flow-diagram of the graphical presentation the carbon molar flow rates ($F_{C,W}$) for different wastes by using the multiple's effect technique.

ple's effect parameter (MU_W; MU_{WNS} = 0; MU_{WPS} = 1; MU_{WS} = 2; Eq. 1).

$$F_{C,W} = F_{C,WNS} + \Delta F_C \cdot MU_W \quad W = WNS, WPS, WS \tag{1}$$

The carbon molar flow rates ($F_{C,W}$) of different wastes can be presented graphically by using the multiple's effect technique (Fig. 2).

The reacted synthesised gasoline molar flow rate ($_rF_{SG,W}$; Eq. 4) into reactor (R) from different wastes is dependent on the reactions (Re1 and Re3) of CO reacting ($_rF_{SG,Re3,W}$; Eq. 2) and the circulated CO_2 molar flow rate from the flue gas ($F_{FG,CO2}$ = 240 kmol/h), which takes place at the reactions (Re2 and Re3) of CO and CO_2, reacting for using the reaction of Re4 ($_rF_{SG,FG}$; Eq. 3), including eight gasoline's molecules (M = 8).

$$_rF_{SG,Re3,W} = (F_{C,W} \cdot Y_{CO,Re1} \cdot X_{CO,Re3})/M \quad W = WNS, WPS, WS \tag{2}$$

$$_rF_{SG,FG} = [(F_{FG,CO2} \cdot X_{FG,CO,Re2} \cdot X_{CO,Re3}) + (F_{FG,CO2} \cdot (1 - X_{FG,CO,Re2}) \cdot X_{CO2,Re4})]/M \tag{3}$$

$$_rF_{SG,W} = (_rF_{SG,Re3,W} + _rF_{SG,FG}) \quad W = WNS, WPS, WS \tag{4}$$

The reacted synthesised gasoline ($_rF_{SG,W}$) is lost because of the oxygen in the non-sorted waste and the product's cleaning (P-SG) by 4% (Eq. 5; $L_{P\text{-}SG,W}$ = 0.04). The oxygen in the non-sorted waste acts as an inhibitor, with the different losses dependent on the sorting levels ($L_{O2,WNS}$ = 0.1, $L_{O2,WPS}$ = 0.05, $L_{O2,WS}$ = 0.0). The total produced synthesised gasoline ($F_{SG,W}$) can be calculated by using Equation 5.

$$F_{SG,W} = _rF_{SG,W} \cdot (1 - L_{P\text{-}SG,W}) \cdot (1 - L_{O2,W}) \quad W = WNS, WPS, WS \tag{5}$$

The hydrogen molar flow rate ($F_{H2,W}$; Eq. 6) of different wastes, such as coproduct, separates from nonreacted gas using the pressure swing adsorption column (PSA-H_2), which is calculated dependent on the lowest inlet ($F_{H2,WNS}$ = 1600 kmol/h), the difference of the inlet ($\Delta F_{H2,W}$ = 100 kmol/h), the lowest reacted amount ($_rF_{H2,WNS}$ = 1334 kmol/h) and the reacted difference of the hydrogen amount (Δ_rF_{H2} = 87 kmol/h), including the multiple's effect parameter (MU_W; MU_{WNS} = 0; MU_{WPS} = 1; MU_{WS} = 2).

$$F_{H2,W} = (F_{H2,WNS} + \Delta F_{H2} \cdot MU_W) - (_rF_{H2,WNS} + \Delta_rF_{H2} \cdot MU_W) \quad W = WNS, WPS, WS \tag{6}$$

The produced water molar flow rate ($F_{H2O,W}$; Eq. 7) through the plant is determined with the lowest produced ($F_{H2O,WNS}$ = 815 kmol/h) and difference (ΔF_{H2O} = 97 kmol/h) amounts, including the multiple's effect parameter (MU_W; MU_{WNS} = 0; MU_{WPS} = 1; MU_{WS} = 2).

$$F_{H2O,W} = F_{H2O,WNS} + \Delta F_{H2O} \cdot MU_W \quad W = WNS, WPS, WS \tag{7}$$

The Re1 reaction needs the inlet steam molar flow rate ($F_{H2O,Re1,W}$; Eq. 8) deriving from the flue gas, which is dependent on the lowest ($F_{H2O,re1,WNS}$ = 350 kmol/h) and difference ($\Delta F_{H2O,Re1}$ = 100 kmol/h) amounts, including the multiple's effect parameter (MU_W; MU_{WNS} = 0; MU_{WPS} = 1; MU_{WS} = 2).

$$F_{H2O,Re1,W} = F_{H2O,Re1,WNS} + \Delta F_{H2O,Re1} \cdot MU_W \quad W = WNS, WPS, WS \tag{8}$$

The simplified energy analysis includes the needed energy of gasification (ϕ_G = 25 MW), which is the same for all wastes, and reforming ($\phi_{ref,W}$; Eq. 9), including the available energy of the product's reactor ($\phi_{R,W}$; Eq. 10). The endothermal heat flow rate of the reformer ($\phi_{ref,W}$; Eq. 9) expresses with the lowest ($\phi_{ref,WNS}$ = 24 MW) and difference ($\Delta\phi_{ref}$ = 3.7 MW) of the heat flow rates, including the multiple's effect parameter (MU_W; MU_{WNS} = 0; MU_{WPS} = 1; MU_{WS} = 2).

$$\phi_{ref,W} = \phi_{ref,WNS} + \Delta\phi_{ref} \cdot MU_W \quad W = WNS, WPS, WS \tag{9}$$

The exothermal heat flow rate of the product's reactor ($\phi_{R,W}$; Eq. 10) is dependent on the lowest ($\phi_{R,WNS}$ = 37 MW) and difference ($\Delta\phi_R$ = 4.3 MW) of the heat flow rates, including the multiple's effect parameter (MU_W; MU_{WNS} = 0; MU_{WPS} = 1; MU_{WS} = 2).

$$\Phi_{R,W} = \phi_{R,WNS} + \Delta\phi_R \cdot MU_W \quad W = WNS, WPS, WS \tag{10}$$

The objective function of the retrofit using different MSW (OBF_W; Eq 11) maximises the additional profit. The additional income accounts for the product (*In*SG; with price of Co_{SG} = 10 EUR/kmol) and co-product purchases (*In*H2; with price of Co_{H2} = 3 EUR/kmol). The same applied costs, independent of the wastes, include the cost of the retrofit (Cret = 5 MEUR/a, including a new catalyst), the cost of gasification (Cgas = 3 MEUR/a), and the cost of the circulated flue gas (CFG = 1 MEUR/a). The applied costs, dependent on the wastes, contain the cost of sorting (Csor,W; Eq. 12) and the cost of energy analysis (Cen,W; Eq. 13), using 8,000 operating hours (O) per year.

$$OBF_{W = In}SG + InH2 - (Cret + Cgas + CFG) - (Csor,W + Cen,W) = F_{SG,W} \cdot Co_{SG} \cdot O + F_{H2,W} \cdot Co_{H2} \cdot O - (C_{ret} + C_{gas} + C_{FG}) - (C_{sor,W} + C_{en,W}) \quad W = WNS, WPS, WS \tag{11}$$

The cost of sorting includes the constant (C_{sor} = 1 MEUR/a) and variable parts, which is dependent on the difference (ΔC_{sor} = 0.4 MEUR/a) cost, including the multiple's effect parameter (MU_W; MU_{WNS} = 0; MU_{WPS} = 1; MU_{WS} = 2).

$$C_{sor,W} = C_{sor} + \Delta C_{sor} \cdot MU_W \quad W = WNS, WPS, WS \tag{12}$$

The cost of energy analysis determines the difference between endothermal ($\phi_{ref,W}$) and exothermal ($\Phi_{R,W}$) heat flow rates, temperatures into both units (T_{ref} = 800 °C and T_R = 300 °C) and the energy cost (Co_{en} = 100 EUR/(MW °C a).

$$C_{en,W} = \phi_{ref,W} \cdot T_{ref} \cdot Co_{en} - \phi_{R,W} \cdot T_R \cdot Co_{en} \quad W = WNS, WPS, WS \tag{13}$$

2. 1. The Multiple's Effect Technique of Biogas

The simple mathematical model of biogas (BG) is even more simplified because of its not so different composition as the MSW, therefore, is not necessary use the multiple's effect parameter. The biogas contents are mostly components of methane and carbon dioxide ($F_{CH4,BG}$, $F_{CO2,BG}$). The flow-diagram of synthetic gasoline production from biogas is very similar to the flow-diagram from different wastes, only without the circulated flue gas and gasification, which is replaced with preheating biogas (preH-BG; Fig. 3). The basic reaction of Re5, producing syngas from biogas (as molar flow rates of $F_{CH4,BG}$ and $F_{CO2,BG}$) takes place during the reformer (Ref), with yields of the carbon monoxide from methane ($Y_{CO,Re5,BG}$ = 0.7).

$$CH_4 + H_2O \leftrightarrows CO + 3H_2 \tag{Re5}$$

The syngas converts to synthetic gasoline from biogas into the reactor (R) by using two basic exothermic reactions (Re3, Re4), with the conversions of CO and CO_2 ($X_{CO,Re3,BG}$ = 0.996, $X_{CO2,Re4,BG}$ = 0.56) .

The reacted synthesised gasoline molar flow rate ($_rF_{SG,BG}$; Eq. 16) from biogas ($F_{CH4,BG}$ = 650 kmol/h and $F_{CO2,BG}$ = 350 kmol/h) takes place during the reactions of Re3 (Eq. 14) and Re4 (Eq. 15).

$$_rF_{SG,Re3,BG} = (F_{CH4,BG} \cdot Y_{CO,Re5,BG} \cdot X_{CO,Re3,BG})/M \tag{14}$$

$$_rF_{SG,Re4,BG} = (F_{CO2,BG} \cdot X_{CO2,Re4,BG})/M \tag{15}$$

$$_rF_{SG,BG} = {}_rF_{SG,Re3,BG} + {}_rF_{SG,Re4,BG} \tag{16}$$

The reacted synthesised gasoline ($_rF_{SG,BG}$) from biogas is lost into the product's purification unit (P-SG) by 4% ($L_{P\text{-}SG,BG}$ = 0.04), therefore, the amount of produced synthesised gasoline ($F_{SG,BG}$) is lower (Eq. 17).

$$F_{SG,BG} = {}_rF_{SG,BG} \cdot (1 - L_{P\text{-}SG,BG}) \tag{17}$$

The other processed and energetic parameters are not so variable, mostly because of the constant composition of the biogas.

3. Case Study of The Multiple's Effect Technique for the Different Wastes

The synthetic gasoline production of different municipal solid wastes (MSW) has been tested by using the multiple's effect technique, which was adapted from the existing methanol process for synthetic gasoline production, because of very similar process units. The case study

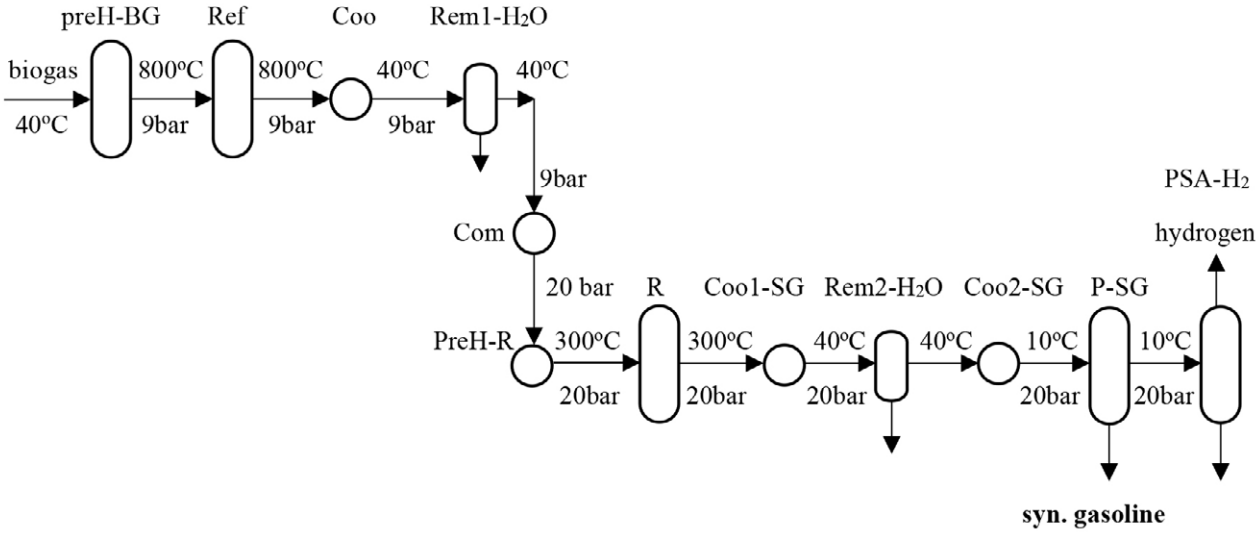

Figure 3: The process flow-diagram of the synthetic gasoline production for biogas including the parameters.

of simulated synthetic gasoline production was undertaken using the optimal parameters, effects and characteristics from Figure 1, by using the Aspen Plus® simulation. The synthetic gasoline production[3] from waste was simulated by using the verified real thermodynamic method and rector model, such as Grayson and Requil from the Aspen Plus® simulator. The economic analyses were included the applied purchase and operation costs for the retrofit.

The total produced synthesised gasolines from non-sorted to sorted wastes were determined as the amounts of 87, 104 and 121 kmol/h ($F_{SG,WNS}$, $F_{SG,WPS}$, $F_{SG,WS}$; Eqs 1–5). The coproduct of hydrogen molar flow rates were estimated as the amounts of 266, 279 and 292 kmol/h ($F_{H2,WNS}$, $F_{H2,WPS}$, $F_{H2,WS}$; Eq. 6).

The produced water molar flow rates were assessed as the amounts of 815, 912 and 1009 kmol/h ($F_{H2O,WNS}$, $F_{H2O,WPS}$, $F_{H2O,WS}$; Eq. 7). The inlet steam molar flow rates were calculated as the amounts of 350, 450 and 550 kmol/h ($F_{H2O,Re1,WNS}$, $F_{H2O,Re1,WPS}$, $F_{H2O,Re1,WS}$; Eq. 8).

The reformer endothermal heat flow rates were expressed as energies of 24, 27.7 and 31.4 MW ($\phi_{ref,WNS}$, $\phi_{ref,WPS}$, $\phi_{ref,WS}$; Eq. 9). The reactor exothermal heat flows were estimated as energies of 37, 41.3 and 45.6 MW ($\phi_{R,WNS}$, $\phi_{R,WPS}$, $\phi_{R,WS}$; Eq. 10).

The objective function of the retrofit generated profits of 2.2, 3.6, and 4.8 MEUR/a using the non, partially and sorted MSW for synthesised gasoline productions (Eqs 11-13). The best alternative was the synthesised gasoline production of $0.127 \cdot 10^6$ t/a from sorted MSW, because of the highest profit of 4.8 MEUR/a and the garbage reduction of $0.106 \cdot 10^6$ t/a into the landfill, including the flue gas and CO_2 emission reductions of $0.164 \cdot 10^6$ and $0.084 \cdot 10^6$ t/a. The hydrogen and processed water coproducts of $4.6 \cdot 10^3$ t/a and $0.145 \cdot 10^6$ t/a could justify the execution too. This alternative could be used to reduce the Russian natural gas and petroleum inflows into the industries and transports.

3. 1. Case Study of the Multiple's Effect Technique for the Biogas

The simple mathematical model of biogas (BG) was simulated by using the parameters from Figure 3, which were contained mostly in the methane and carbon dioxide ($F_{CH4,BG}$ = 650 kmol/h and $F_{CO2,BG}$ = 350 kmol/h). The synthesised gasoline ($F_{SG,BG}$) produced was the amount of 78 kmol/h (Eqs. 14-17). The coproducts of hydrogen and processed water produced amounts of 120 and 780 kmol/h ($F_{H2,BG}$, $F_{H2O,BG}$). The Re5 reaction needed the amount of 950 kmol/h ($F_{H2O,Re5,BG}$). The preheating, endothermal and exothermal heat flow rates were the energies of 11, 37 and 27 MW ($\phi_{preH\text{-}BG}$, $\phi_{ref,BG}$, $\phi_{R,BG}$).

The objective function of the retrofit generated a profit of 1.0 MEUR/a for synthesised gasoline production of $0.08 \cdot 10^6$ t/a from biogas using Equation 11, without the costs of gasification, circulated gas and sorted waste, with those replacing with cost of biogas (C_{BG} = 1 MUR/a).

The comparisons between all alternatives of different raw materials were collected into Table 1, which included the data of the synthetic gasoline production. The distinctions between production and energetic molar and heat flow rates were fairly linear, because of using the multiple's effect parameter (MU_W), which was also the best approximation of the simulated data.

4. Conclusion

The study of synthetic gasoline production from different wastes, such as non, or partially, or sorted wastes, or biogas, would be one of the alternatives of petroleum compensation and reductions of the CO_2 emission and the wastes into landfill, by using the multiple's effect technique. This technique bases on the multiple's effect parameter (MU_W), which presents the level of waste sorting (MU_W; MU_{WNS} = 0; MU_{WPS} = 1; MU_{WS} = 2), and the sorted waste represents the highest value of the multiple's effect parameter. The multiple's effect parameter could simplify the amount calculations of the product and co-product productions, including the energies into process units and the effect of oxygen inhibition into different wastes. The sustainable synthetic gasoline production would be worked according to the principle of the circular economy, including that the purified flue gas of gasification would be circulated back into the process.

The calculations of all the presented alternatives were performed by using the presented technique, and confirmed that the waste should be separated, because of the environmental reasons and more profitable synthetic gasoline production. The sustainable synthesised gasoline production from sorted waste generated the highest additional profit of 4.8 MEUR/a, synthesising the amount of 0.127 10^6 t/a of synthetic gasoline. The garbage from landfill was reduced by 0.106 10^6 t/a by using sustainable

Table 1: The important results comparisons between all alternatives.

Raw. material	F_{SG}, kmol/h	F_{H2}, kmol/h	F_{H2O}, kmol/h	ϕ_{ref}, MW	ϕ_R, MW	Incomes, MEUR/a	Costs, MEUR/a	Profit, MEUR/a
WNS	87	266	815	24.0	37.0	13.3	11.1	2.2
WPS	104	279	912	27.7	41.3	15.0	11.4	3.6
WS	121	292	1009	31.4	45.6	16.7	11.9	**4.8**
BG	78	120	788	37.0	27.0	9.1	8.1	1.0

synthetic production. The outlet exhausts of the flue gas and CO_2 emission have been lowered into the atmosphere by 0.164 10^6 and 0.084 10^6 t/a. The hydrogen and processed water coproduced the amounts of 4.6 10^3 t/a and 0.145 10^6 t/a.

This study could be ensured as environmentally sustainable for the commercial synthetic gasoline production, because the raw materials will be coming from the garbage as useless MSW and flue gas. The feasibility of this project could be made more feasible because of the usage of the existing available process units. The existing methanol process could be replaced with the synthetic gasoline production, because of increasing market demand. In this case the synthetic gasoline production would be a potential challenge for replacing the non-renewable petroleum. The long-term realisation view of the synthetic gasoline production is justified by using the multiple's effect technique because of the environmental and economic aspects. The potential operation and environmental uncertainties of the synthetic gasoline production were low because of the usage real model. The multiple's effect technique has simplified the calculation greatly and defined the optimal production of biogas from sorted MSW quickly. New research aims to clean the flue gases after gasification and return them to the process by using the pressure swing adsorption (PSA) columns with zeolites.

5. References

1. P. Lu, J. Sun, P. Zhu, T. Abe, R. Yang, A. Taguchi, T. Vitidsant, N. Tsubaki, *J. Energy Chem.* **2015**, *24*, 637–641. **DOI:**10.1016/j.jechem.2015.08.004
2. M. Javed, G. Zhang, W. Gao, Y. Cao, P. Dai, X. Ji, C. Lu, R. Yan g, C. Xing, J. Sun, *Catal. Today* **2019**, *330*, 39–45. **DOI:**10.1016/j.cattod.2018.08.010
3. J. Li , Y. Tan, Q. Zhang, Y. Han, *Fuel* **2010**, *89*, 3510–3516. **DOI:**10.1016/j.fuel.2010.06.001
4. Y. Lu, J. Hu, J. Han, F. Yu, *J. Energy Inst.* **2016**, *89*, 782–792. **DOI:**10.1016/j.joei.2015.03.010
5. Q. Zhang, T. Wang, Y. Li, R. Xiao, T. Vitidsant, P. Reubroycharoen, C. Wang, Q. Zhang, L. Ma, *Fuel Process. Technol.* **2017**, 702–710. **DOI:**10.1016/j.fuproc.2017.07.035
6. J. Liu, D. Wang, J. F. Chen, Y. Zhang, *Int. J. Hydrogen Energy* **2016**, *41, 47,* 21965–21978. **DOI:**10.1016/j.ijhydene.2016.10.004
7. N. Martín, F. G. Cirujano, *J. CO_2 Utilization* **2022**, *65*, 102176. **DOI:**10.1016/j.jcou.2022.102176
8. J. Li, D. Han, T. He, G. Liu, Z. Zi, Z. Wang, J. Wu, J. Wu, *Fuel Process. Technol.* **2019**, *191*, 104–110. **DOI:**10.1016/j.fuproc.2019.03.029
9. X. Su, K. Zhang, Y. Snatenkova, Z. Matieva, X. Bai, N. Kolesnichenko, W. Wu, *Fuel Process. Technol.* 2020, *198*, 10624. **DOI:**10.1016/j.fuproc.2019.106242
10. M. V. Magomedova, E. G. Galanova, M. I. Afokin, M. A. Kipnis, Z. M. Matieva, A. L. Maksimov, *J. Nat. Gas Sci. Eng.* **2020**, *78*, 103288. **DOI:**10.1016/j.jngse.2020.103288
11. J. Szczygieł, M. Kułażyński, *J. Clean. Prod.* **2020**, *276*, 122790. **DOI:**10.1016/j.jclepro.2020.122790
12. A. A. Rabah, *Energy* **2022**, *59*, 124980. **DOI:**10.1016/j.energy.2022.124980
13. Y. Shiying, Y. Yucheng, L. Yongjun, *Comp. Chem. Eng.* **2019**, *128*, 106–116. **DOI:**10.1016/j.compchemeng.2019.05.031
14. V. B. Borugadda, G. Kamath, A. K. Dalai, *Energy* **2020**, *195*, 116985. **DOI:**10.1016/j.energy.2020.116985
15. M. Mascal, S. Dutta, *Fuel Process. Technol.* **2020**, *197*, 106192. **DOI:**10.1016/j.fuproc.2019.106192
16. K. B. Hnich, M. Martín-Gamboa, Z. Khila, N. Hajjaji, J. Dufour, D. Iribarren, *Sci. Total Environ.* **2020**, *796*, 148961. **DOI:**10.1016/j.scitotenv.2021.148961
17. Z. Wang, T. He, J. Li, J. Wu, J. Qin, G. Liu, D. Han, Z. Zi, Z. Li, J. Wu, *Fuel* **2016**, *186*, 587–596. **DOI:**10.1016/j.fuel.2016.08.108
18. Z. Navas-Anguita, P. L. Cruz, M. Martín-Gamboa, D. Iribarren, J. Dufour, *Fuel* **2019**, *235*, 1492–1500. **DOI:**10.1016/j.fuel.2018.08.147
19. S. Bahri, T. Patra, Sonal, S. Upadhyayula, *Microporous Mesoporous Mater*. **2019**, *275*, 1–13. **DOI:**10.1016/j.micromeso.2018.08.004
20. J. Aluha, N. Abatzoglou, *Biomass Bioenergy* **2016**, *95*, 330–339. **DOI:**10.1016/j.biombioe.2016.05.010
21. M. Ali, H.M. Koo, S. Kasipandi, G. Y. Han, J. W. Bae, *Fuel* **2020**, *264*, 116851. **DOI:**10.1016/j.fuel.2019.116851
22. D. Selvatico, A. Lanzini, M. Santarelli, *Fuel* **2016**, *186*, 544–560. **DOI:**10.1016/j.fuel.2016.08.093
23. Z. Wu, W. Zhou, X. Hao, X. Zhang, *Energy* **2019**, *189*, 116265. **DOI:**10.1016/j.energy.2019.116265
24. G. Liu, E. D. Larson, *Energy Proc.* **2014**, *63*, 7315–7329. **DOI:**10.1016/j.egypro.2014.11.768
25. S. Dutta, V. Madav, G. Joshi, N. Naik, S. Kumar, *Fuel* **2023**, *347*, 128437. **DOI:**10.1016/j.fuel.2023.128437
26. R. G. Santos, A. C. Alencar, *Int. J. Hydrogen Energy* **2020**, *45*, *36*, 18114–18132. **DOI:**10.1016/j.ijhydene.2019.07.133
27. F. J. Campanario, F. J. G. Ortiz, *Energy Convers. Manag.* **2017**, *150*, 599–613. **DOI:**10.1016/j.enconman.2017.08.053
28. A. Gharibi, E. Doniavi, R. Hasanzadeh, *Energy Convers. Manag.* **2024**, *308*, 118392. **DOI:**10.1016/j.enconman.2024.118392
29. A. Gharibi, R. Babazadeh, R. Hasanzadeh, *Process Saf. Environ. Prot.* **2024**, *183*, 46–58. **DOI:**10.1016/j.psep.2023.12.069
30. P. Mojaver, S. Khalilarya, A. Chitsaz, *Energy Convers. Manag.* 2018, *171*, 287–297 **DOI:**10.1016/j.enconman.2018.05.096
31. P. Mojaver, S. Khalilarya, A. Chitsaz, *Appl. Therm. Eng.* 2019, *156*, 627–639. **DOI:**10.1016/j.applthermaleng.2019.04.104
32. R. Hasanzadeh, T. Azdast, *Waste Manag. Bull.* 2024, *2*, 75–82. **DOI:**10.1016/j.wmb.2023.12.011
33. E. Doniavi, R. Babazadeh, R. Hasanzadeh, *Process Saf. Environ. Prot.* **2024**, *182*, 86–97 **DOI:**10.1016/j.psep.2023.11.068
34. R. Hasanzadeh, R. Abdalrahman, *Polymers* **2023**, *15*, 2767 **DOI:**10.3390/polym15132767
35. S. Khalilarya, A. Chitsaz, P. Mojaver, *Int. J. Hydrogen Energy* **2021**,*46*, 1815–1827 **DOI:**10.1016/j.ijhydene.2020.10.020

36. P. Mojaver, S. Jafarmadar, S. Khalilarya, A. Chitsaz, *Int. J. Hydrogen Energy* **2019**, *44*, 27726–27740 **DOI:**10.1016/j.ijhydene.2019.08.240
37. R. Hasanzadeh, M. Mojaver, T. Azdast, C. B. Park, *Energy Convers. Manag***. 2021**, *247*, 114713. **DOI:**10.1016/j.enconman.2021.114713
38. M. Mojaver, R. Hasanzadeh, T. Azdast, C. B. Park, *Chemosphere* **2022**, *286*, 131867 **DOI:**10.1016/j.chemosphere.2021.131867
39. M. Mojaver, T. Azdast, R. Hasanzadeh, *Int. J. Hydrogen Energy* **2021**, 46, 29846–29857 **DOI:**10.1016/j.ijhydene.2021.06.161

Povzetek

Predstavljena je metoda večkratnega učinka, ki temelji na uplinjanju in ponovni uporabi trdnih komunalnih odpadkov (TKO) ter vključuje osnovni parameter večkratnega učinka (MU_W; $MU_{WNS} = 0$; $MU_{WPS} = 1$; $MU_{WS} = 2$), ki predstavlja stopnjo sortiranja od ne sortiranih do sortiranih TKO. Zaradi tega parametra in uporabe simulatorja Aspen Plus® se matematični model poenostavi za iskanje optimalne trajnostne surovine za proizvodnjo sinteznega plina, ki nadomešča netrajnosti zemeljski plin za nadaljnjo proizvodnjo metanola. Metodo smo testirali na obstoječem procesu in najboljša alternativa so sortirani TKO, s katerimi tudi proizvedemo največ metanola.

DOI: 10.17344/acsi.2023.8501 *Acta Chim. Slov.* **2024,** *71,* 398–408

Scientific paper

Modification of PVA Nanofiber by Simple Hot Water Treatment and Application on the Removal of Malachite Green Dye From Aqueous Solutions

Banaz A. Abdulghafar,[1] Suhad A. Yasin[1] and Nawzat S. Saadi[2]

[1] *University of Duhok, College of Science, Department of Chemistry, Duhok City, Kurdistan Region, Iraq 42001*

[2] *University of Duhok, College of Science Department of Physics, Duhok City, Kurdistan Region, Iraq 42001*

** Corresponding author: E-mail: banaz.abdulghafar@uod.ac suhad.yasin@uod.ac; nawzat@uod.ac*

Received: 10-11-2023

Abstract

In this study, the crosslinking of PVA nanofiber was increased using solvent vapor treatment. Then, Fe_3O_4 nanoparticles were synthesized by a simple hot water technique and composited with the nanofiber. The study focuses on applying the modified PVA nanofibers to remove malachite green (MG) from water using different pH, contact times, and dye initial concentrations. The surface morphology of the nanofiber was determined using SEM, FTIR, and XRD techniques. SEM showed that the crosslinking was increased, and Fe_3O_4 nanoparticles appeared as agglomerates on the surface of the nanofiber. The removal percentages at optimal pH and contact time were 99.76%, and 99.5%, respectively. Thereafter, kinetics was studied by the linear pseudo-first order, pseudo-second order, Elovich equation, and Intraparticle diffusion models. Results demonstrated that the adsorption kinetics follow the pseudo-second order. Moreover, the adsorption isotherm was discussed using Langmuir and Freundlich equations. The Langmuir equation best described the adsorption with R^2 value of 0.9771, and the maximum removal was 128.205 mg/g. As a result, the MG dye molecules covered the PVA nanofiber/Fe_3O_4 nanoparticles in a monolayer and homogenous coverage. The results of this study are significant for industries' wastewater treatment as they provide a potential solution for the removal of MG dye from textile, paper, cosmetics, food, and aquaculture industries' wastewater.

Keywords: Iron oxide nanoparticles, modification of nanofibers, adsorption, malachite green, hot water treatment.

1. Introduction

Population growth and industrial development have resulted in water pollution, which is one of the most serious problems nowadays. Many types of pollutants may cause water pollution, but toxic organic pollutants have become a severe problem to the human environment and cause serious health issues due to their hazardous effects, chemical stability, and difficulty to remove.[1] One type of these organic contaminators is water-soluble organic dyes that show extensive applications in industries like paints, textiles, plastic products, and so on. Organic dyes can change the color and properties of water even at low concentrations because of the existence of aromatic compounds and heavy metals in their structures.[2,3] Also, they can reduce the transmission of light in aquatic systems, eventually decreasing the efficiency of the photosynthesis process of aquatic plants.[4,5] In addition, the accumulation of dyes in animals and plants can result in skin irritation, allergic dermatitis, mutations, and cancer, thus being harmful to the brain, kidneys, liver, central nervous system, and reproductive system in living organisms. Therefore, dyeing wastewaters are the riskiest wastewaters and are hard to purify.[6,7] Moreover, malachite green (MG) dye, which is the chemical structure seen in Figure 1: (a), is a tri-phenyl methane cationic dye that has been widely employed in industries for dyeing purposes. On the other hand, oral consumption of MG is harmful due to the presence of nitrogen in its chemical structure and would be carcinogenic for both humans and animals.[8] Various physical, chemical, and biological techniques may be used for MG dye removal from wastewater, for instance, advanced oxidation processes, nanophotocatalysis, ceramic membrane separation,[9] electrochemical techniques,[10] and aerobic granular sludge.[11] Also, adsorption is widely used among these techniques and could be a predominant

method, since it's simple, economical, flexible, and easily implemented. The high efficiency of adsorption and the development of practical processes require the complete and fast adsorption of coloring materials by adsorbents. For that reason, chemical or physical modifications in adsorbents are beneficial to increase the kinetics and capacity of adsorption. In addition, the nanofiber's structural morphology has attracted considerable attention in various applications and fields. Electrospinning is a widely used technique to generate nanofibers with a broad range of characteristics and advantages. Porous webs of nanofibers with different sizes and shapes can result from this technique, which modifies and promotes the nanofiber's properties and applications.[12–14] For instance, porous structures have high specific surface area and can be used in oil clean up, and catalysis, grooved structures have surfaces with parallel lines and can be used in tissue engineering,[12] branched structures have large porosity, tiny diameters, excellent biological properties, and thermal insulation and can be utilized in air filtrations, energy storage and harvesting, photocatalysis, and oil cleanup.[13] Also, crimped fibers that have spring-like behavior, notable surface area, and remarkable biological and piezoelectric properties are applied in tissue engineering, energy harvesting, wound dressing, drug delivery, and textile.[14] One of these modifications is the use of nanoparticles to increase the process of adsorption.[15,16] In general, nanoparticles have attracted wide interest recently because of their high efficiency, low consumption of energy, large surface area, catalytic potential, and high reversibility.[17] Specifically, iron nanoparticles have acquired massive scientific and technological attention as they have shown an outstanding capacity for the remediation of the environment.[18] For example, iron nanoparticles have been utilized for the removal of chlorinated organic materials,[19–21] dyes,[22–24] heavy metals from water,[25] and nuclear contaminants degradation.[26] Furthermore, numerous ways have been applied for the synthesis of nanoparticles, such as gas condensation which was the first method to prepare nanoalloys and crystals, vacuum deposition, chemical precipitation, and electrodeposition.[27] Each of these methods may include many drawbacks like being specific to a few numbers of metals, being expensive, or requiring elevated temperatures that minimize their application. However, recently a simple process of using only hot water has been demonstrated as an alternative and novel method to produce iron nanoparticles. Unlike the previous methods, hot water treatment (HWT) can be applied to plentiful materials and requires depressed temperatures and low-cost equipment. It is catalyst-free, has a high yield of production, as well as is environment-friendly because it uses water as the main material that is non-toxic and safe to use.[28] In this study, polyvinyl alcohol (PVA) nanofiber, Figure 1: (b), was used as a membrane for the adsorption of MG dye in aqueous solutions after it was modified by two steps. Firstly, improving the mechanical properties, specifically increasing the crosslinking of the nanofiber through solvent vapor treatment (SVT). Secondly, synthesizing Fe_3O_4 nanoparticles from Fe metal powder by hot water treatment (HWT) and composite these nanoparticles to the previously crosslinked PVA nanofiber to ensure efficient dye isolation from water. Recent studies have shown that the mechanical strength of nanofiber mats can be enhanced by the solvent vapor technique without changing the dimension or the membrane morphology of the mats. Also, it is less aggressive for fiber welding. In this technique, nanofiber mats are exposed to solvent vapors at a particular temperature according to the solvent used, thus, the solvent vapor will facilitate fusion between fibers at their junction points and increase the crosslinking. In this instance, better adhesion between fibers can be achieved by utilizing solvents with high boiling points. Moreover, the crosslinking of the modified nanofibers will increase in a short time, and the porous structure of the alleged membranes can be controlled easily.[29–33]

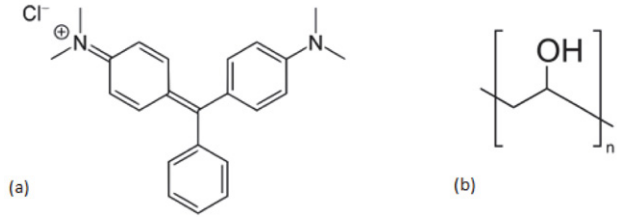

Figure 1: (a) chemical structure of malachite green (MG), (b) polyvinyl alcohol (PVA)

2. Materials and Methods

2. 1. Chemicals and Reagents

PVA nanofiber was purchased from Inovenso, N, N-Dimethylformamide (DMF), iron (Fe) powder, and Malachite green were from BDH Chemicals, NaOH from Sigma-Aldrich, and HCl was supplied by Ricca Chemical Company.

2. 2. Solvent Vapor Ttreatment (SVT)

Small coupons (approximately 9 cm × 3 cm) of PVA nanofiber mats were prepared and placed on the top of a petri dish (D = 9 cm). DMF (3 mL) was used as a solvent and placed in a beaker sealed properly with the petri dish that contains the nanofiber coupon. The solvent was then evaporated on a hot plate stirrer at a temperature of 40 °C for 3 hours. After treatment, that sample was air dried for 24 hours to remove all solvent residual before further treatment.[29]

2. 3. Hot Water Treatment (HWT)

At first, Fe metal powder was prepared for hot water treatment by removing native iron oxides that act as impu-

rities and other organic contaminants using sanding paper polishing process. Then, the Fe powder was cleaned with acetone and deionized water (DI). The pre-washed Fe powder, along with the thermally treated PVA nanofiber membrane, was added to a glass beaker containing ultrapure DI water and then placed on the hot plate at a temperature of 75 °C for 1.5 hours with stirring. This temperature was selected as the standard temperature for water in this experiment, according to Nawzat. Saadi *et al.*[25] Also, one hour was defined as the critical time for the complete formation of Fe_3O_4 nanoparticles, but we increased the time to 90 min. At last, the composited nanofiber membrane was rinsed with DI water several times and air dried overnight, then delivered for SEM (Thermo Fisher Phenom Pro G6) and XRD (Bruker D8-Discover) to study the morphological, crystallographic, and chemical composition, respectively. On the other hand, Fourier transform infrared spectroscopy (FTIR) was performed for the water samples of the HWT as well as from the modified membrane for the study of the presence of Fe_3O_4 nanoparticles in both.

2. 4. MG Adsorption Studies

The batch operations of adsorption were studied for MG by taking the experimental conditions: pH, contact time, and effect of concentration. Firstly, the influence of pH was tested in the range (5.0–9.0) that was adjusted using 0.1 M NaOH and 0.1 M HCl solutions. A pH meter (JENWAY 3505) was also used for the measurements of the pH. The study of the pH effect was carried out using the adsorbent 0.003g and MG dye solution 5 ml of 10 mg/L concentration. The solutions were then stirred for 1 hour at room temperature. The MG absorbance was measured by using a UV-visible spectrophotometer (JANEWAY 7315) at 618 nm, which is the maximum absorbance wavelength of MG.[34] The experiment of contact time for adsorption of MG was investigated, and the kinetic studies were performed at optimal circumstances: pH 8.0, adsorbent weight 0.003g, and 5 ml of MG solution 10 mg/L concentration. The batch tests were accomplished at room temperature with various time contacts (5, 10, 15, 20, 25, 30, 35, 40, 45, and 50) min.

Moreover, the impact of initial concentrations on MG adsorption was carried out by mixing and stirring 5 ml of different MG initial concentrations (10, 20, 30, 40, and 50) mg/L with pH 8 and 0.003 g of adsorbent for 20 minutes at room temperature until reached equilibrium.[6]

The following equation is used for calculating the (q_e) value, which is the equilibrium adsorption capacity and the removal percentage (R%) of MG.[35]

$$q_e = \frac{(C_i - C_e) * V}{W} \quad (1)$$

$$R\% = \frac{C_i - C_e}{C_i} \times 100 \quad (2)$$

where; C_i= Initial concentration of MG (mg/L)
C_e= equilibrium concentration of MG (mg/L) in the solution.
V = Volume of dye solution (L)
W = adsorbent mass (g).

3. Results and Discussion

3. 1. Characterization of PVA Nanofiber/ Fe_3O_4 Nanoparticles

3. 1. 1. SEM

In this study, the morphology of the modified PVA nanofiber before and after both treatments, SVT and HWT, was investigated by scanning electron microscopy (SEM). Figure 2: (a), shows the PVA mats before treatments, while, Figure 2: (b), represents the morphological and conformational changes that happened on the matt

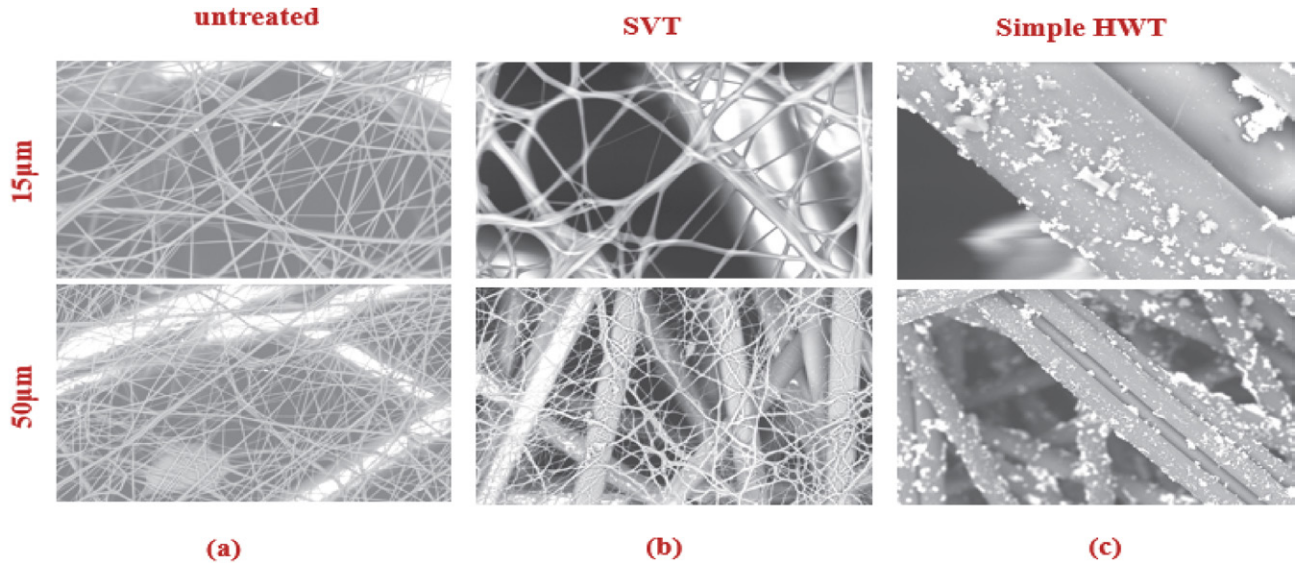

Figure 2: SEM of (a) untreated PVA nanofiber, (b) PVA nanofiber after SVT, (c) formation of PVA nanofiber/ Fe_3O_4 nanoparticles by HWT

after SVT when the mats were exposed to DMF vapor for 3 hours. It is obvious from the figures that in both 15μm and 50μm the crosslinking among the nanofibers has increased. Furthermore, a significant swelling has appeared on nanofibers, that may occur as a result of the absorbance of an amount of solvent vapor by nanofibers as there is an affinity of nanofibers to solvent. Also, Figure 2: (c), indicates the presence of iron oxide Fe_3O_4 nanoparticles on the PVA nanofiber surface that have irregular shapes that adsorb like aggregates on the nanofiber surface. The formation of different particle sizes may be a result of the agglomeration of nanoparticles on different sides of nanofiber during the sample preparation.[36] The mechanism by which Fe_3O_4 nanoparticles are present on the nanofiber's surface can be explained by a combination of the Fe_3O_4 nanoparticle's growth and deposition processes. In the first process, iron oxide ions can form on the Fe powder surface during HWT, release into the water, and then grow on the nanofiber, forming nanoparticles. This process, which is called plugging, is explained in more detail in the previous study.[25] In the deposition process, Fe_3O_4 nanoparticles grown on Fe metal powder can be detached from the powder surface and re-deposited on nanofibers.

3. 1. 2. Characterization of Fe_3O_4 Nanoparticles by (FTIR)

Fourier transform infrared spectroscopy (FTIR) gives information on nanoparticle structures from the Fe_3O_4 nanoparticle's bond vibrational modes. Although it is incapable of quantifying the generated nanoparticles precisely in the samples, it provides a qualitative identification of the proportion of the produced nanoparticles. Figures 3 (a), and (b), show the infrared spectra of Fe_3O_4 nanoparticles presented in water samples after HWT and PVA nanofiber/Fe_3O_4 nanoparticles, respectively. To indicate the presence of Fe_3O_4 nanoparticles, the range of 800–400 cm^{-1} was a characteristic of the Fe–O bond. In Figure 3: (a), Fe_3O_4 showed characteristic peaks at 469 cm^{-1} and a maximum peak at 569 cm^{-1} with a shoulder at 745 cm^{-1} which was attributed to surface oxidation.[37–39] Besides, Figure 3: (b), represents the formation of Fe_3O_4 on PVA nanofiber and shows additional peaks in the spectral range 501–575 cm^{-1} with a broad spectrum at 723 cm^{-1} while no peaks appeared around the 400 cm^{-1} region. Moreover, the two peaks observed at 616 cm^{-1} and 636 cm^{-1} identify Fe_{Th}–O–Fe_{Oh} stretching vibrations on PVA nanofiber, where, Fe_{Th} is iron tetrahedral and Fe_{Oh} is iron octahedral. The appearance of the broadband at 3397 cm^{-1} corresponded to the O–H group stretching vibrations, 2966 cm^{-1} was the peak for the C–H bond, and the 1088 cm^{-1} peak referred to the Fe–O–C bond.[40] The decrease in peak intensity in PVA nanofiber/Fe_3O_4 nanoparticles suggests the interaction between (C–H) and (O–H) groups of the nanofiber with Fe_3O_4 nanoparticles and indicates the well dispersion of the nanoparticles on the surface of the PVA nanofiber. [41]

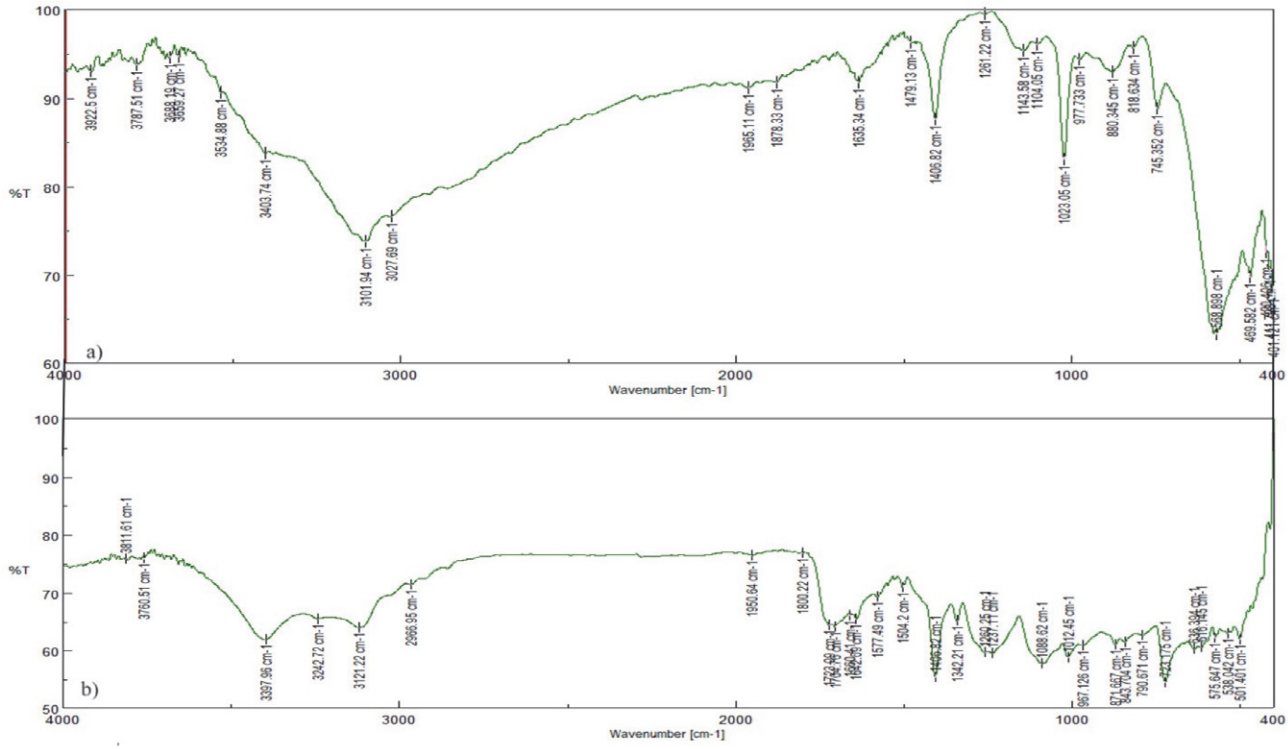

Figure 3: (a) FTIR spectrum of Fe_3O_4 nanoparticles in water samples synthesized by simple HWT, (b) FTIR spectrum of PVA nanofiber/ Fe_3O_4 nanoparticles synthesized by simple HWT

3.1.3 Characterization of Fe_3O_4 Nanoparticles by X-ray Diffraction (XRD)

The XRD charts of the Fe_3O_4 nanoparticles and composite with PVA nanofiber were compared and shown in Figure 4. The spectra of XRD of the nanoparticles showed three diffraction peaks of 11.46, 15.85, and 149.15. Also, the XRD pattern of PVA nanofiber/Fe_3O_4 nanoparticles showed four peaks of 14.26, 54.10, 43.99, and 347.66. These peaks confirm the formation of Fe_3O_4 nanoparticles in both samples as related to (JCPD98-026-3010).[42] The two XRD spectra show two sharp peaks that appeared with 2θ of 72.565 and 72.515, which are identical to those of reference and indicate the presence of Fe_3O_4 nanoparticles. These data also detected that the nanoparticles have crystalline and spinel structures.

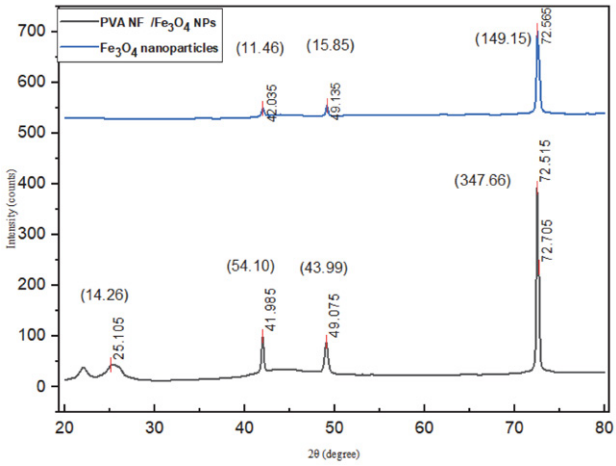

Figure 4: XRD diffraction of Fe_3O_4 nanoparticles compared to PVA nanofiber /Fe_3O4 nanoparticles

3.2 Effect of pH

It is substantial to examine the impact of pH on the adsorption of MG because pH has an essential role in adsorption capacity. It has an influence on the surface charge of the adsorbent, the tendency of the existent compounds in the solution to ionize, the adsorbent's active sites functional groups dissociation, and also the solution dye chemistry.[43] MG has pK_a of 10.3 which protonates under acidic conditions and deprotonates at higher pH values and a high positive charge is detected on the dye molecule at lower pH due to its protonation.[44,45] Also, it was perceived in this study that the adsorption is strongly dependent on pH and the superior adsorption was on pH 8 with a top removal rate of 99.76% which means that the electrostatic interactions between MG dye and the adsorbent are strong on this pH value that result in a high adsorption capacity. On the other hand, under acidic conditions low adsorption rates are observed and that is due to the excess availability and high concentrations of positive charge resulting from H^+ protons and cationic dye molecules in the solution. Furthermore, the surface of the membrane may be positively charged, causing repulsions with the cationic dye molecules and decreasing the removal rates. The pH effect on the adsorption capacity of MG on PVA nanofiber/ Fe_3O_4 nanoparticles was examined over pH values (5.0, 6.0, 7.0, 8.0, and 9.0) using 0.1N NaOH, and 0.1N HCl solutions to adjust pH. Figure 5 explains the amount of removal of MG as a function of pH for the adsorbent initial concentration of 10 mg/L. The adsorption capacity was high at pH 8, but at lower pH values (4–7) the adsorption was low, and at pH 9 it decreased again.

3. 2. Effect of Contact Time

Figure 6 exhibits the time effect on the removal of the MG dye process. It's shown that the percentage of the removal of MG kept increasing with time until the maximum removal of color was seen at 20 min, with a maximum removal of 99.5%. The process of adsorption was fast from the beginning to 20 minutes when the removal of dye was achieved, which resulted from the attraction of charges on the adsorbent surface to MG dye. After that, the ad-

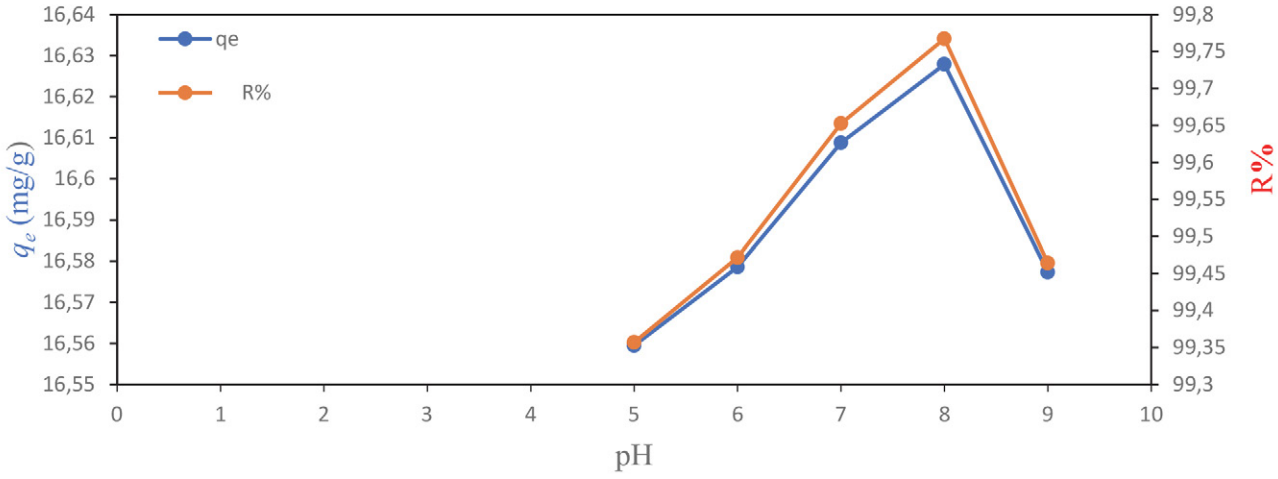

Figure 5: The effect of pH on MG adsorption on PVA nanofiber/ Fe_3O_4 nanoparticles

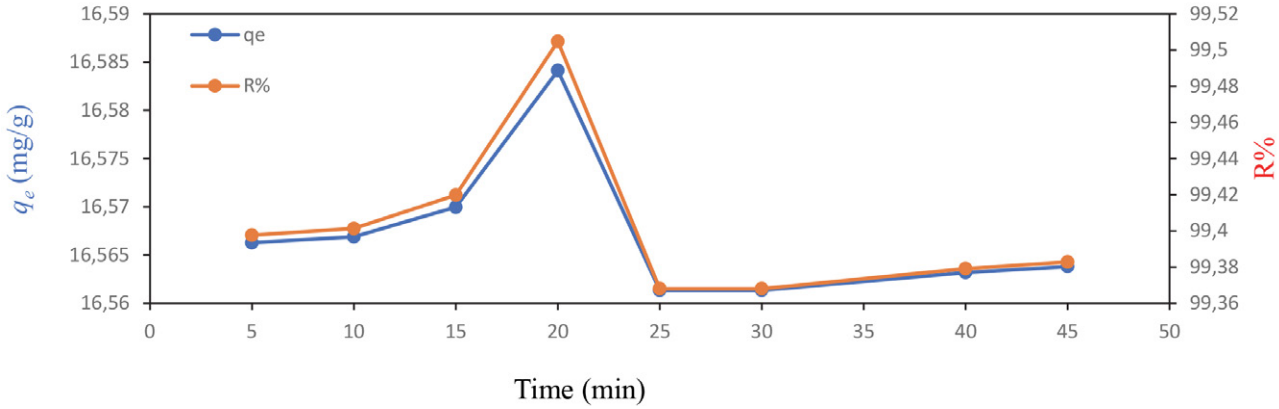

Figure 6: The effect of contact time on MG adsorption on PVA nanofiber/ Fe_3O_4 nanoparticles

sorption capacity dropped significantly at 25 min, became steady, and reached equilibrium at 45 min, when no more dye removal was noted. Therefore, 20 minutes was chosen as the maximum time for MG adsorption on PVA nanofiber/ Fe_3O_4 nanoparticles.

3. 3. Adsorption Kinetic Studies

Four kinetic models evaluate the process of adsorption and interpret the kinetic results to examine the kinetics of the mechanism of adsorption and select the optimum conditions of the operation. Pseudo-first-order, Pseudo-second-order equations, as well as, Elovich, and Intraparticle diffusion equations, were applied and represented as the following equations respectively.[46–49]

3. 4. 1. Pseudo-first-order Model

$$log\,(q_e - q_t) = log\,q_e - \left(\frac{k_1}{2.303}\right)t \qquad (3)$$

Where; q_e represents the adsorption capacity at equilibrium (mg/g), q_t represents the adsorption capacity at time (t) (mg/g), t means time (min), and k_1 is defined as the Lageragren rate constant of adsorption (min^{-1}). The q_e and k_1 values were determined from the intercept and the slope of the linear equation of ln $(q_e - q_t)$ against t as shown in Figure 7, and found to be 0.018, and 0.005, respectively. Also, the correlation coefficient for this kinetic model which represents the R^2 value was 0.4147.

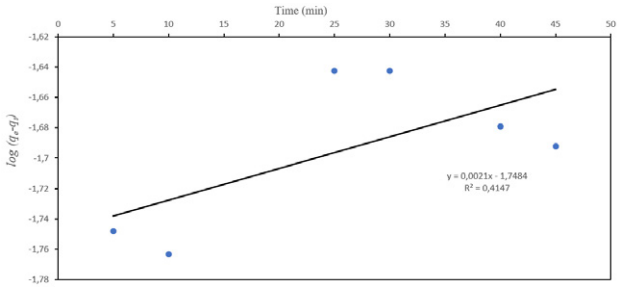

Figure 7: The pseudo-first-order kinetic model of adsorption of MG on PVA nanofiber/Fe_3O_4 nanoparticles

3. 4. 2. Pseudo-second-order Model

The pseudo-second-order model was then analyzed and given by the following equation:

$$\frac{t}{q_t} = \frac{1}{k_2\ q_e^2} + \frac{1}{q_e}(t) \qquad (4)$$

Here, k_2 is known as the rate constant of adsorption (g/mg min) for pseudo-second-order. Also, for this model, k_2 and q_e were found from the slope and the intercept of the linear plot of (t/q_t) against t, as shown in Figure 8, and found to be 9.12, and 16.55, respectively, while the R^2 value for pseudo-second-order was 1.00. These results refer to the fact that the MG dye adsorption onto the modified membrane follows the pseudo-second-order model. This denotes that the chemical adsorption (chemisorption) of Fe_3O_4 nanoparticles on PVA nanofiber is the rate determining step, and the total rate of the adsorption process of MG may be controlled by the chemical attraction between the adsorbent and adsorbate.[50]

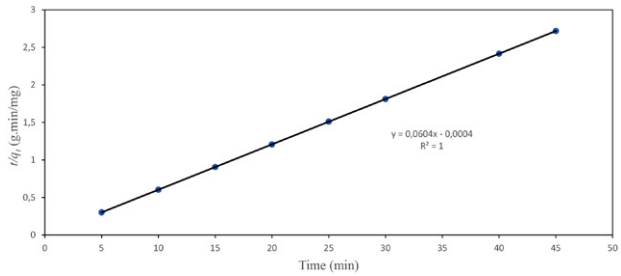

Figure 8: Pseudo-second-order kinetic model of adsorption of MG on PVA nanofiber/Fe_3O_4 nanoparticles

3. 4. 2. Elovich Kinetic Model

Elovich kinetic model for the adsorption of MG was also studied, which usually can be expressed as in equation 5 and is dependent on the adsorption capacity q_t plot versus ln t (Figure 9). This equation was first used in studying the kinetics of chemical adsorption of gasses on the surface of solids, however, it has also been successfully applied

for the solute adsorption from liquid solutions.[51]

$$q_t = \frac{1}{\beta} ln\,(\alpha\beta) + \frac{1}{\beta} ln\ (t) \quad (5)$$

Where; the parameter a (mg/g min) is the initial sorption rate, and b (g/mg) is the extent of surface coverage and activation energy for chemical adsorption. The values are determined and displayed in Table 1.

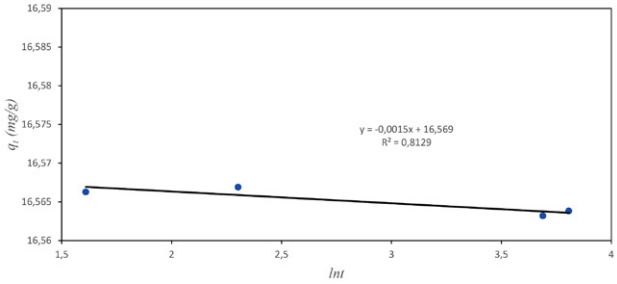

Figure 9: Elovich kinetic for the adsorption of MG on PVA nanofiber/Fe_3O_4 nanoparticles

3. 4. 4. Intraparticle Diffusion

The intraparticle diffusion study is the most widely applied model for the identification mechanism in the process of adsorption, which is indicated as follows: [52]

$$q_t = K_{dif} t^{\frac{1}{2}} + B_L \quad (6)$$

Where; K_{dif} refers to the rate constant of the intraparticle diffusion (mg/g min), B_L is the intercept that points to the boundary layer thickness (mg/g). The q_t plot against $t^{1/2}$ is represented in Figure 10. The value of K_{dif} =0.0008 mg/g min, B_L =16.569 mg/g, while the R^2 values for the intraparticle diffusion is 0.866. The intercept value is directly proportional to the effect of the boundary layer, the higher the intercept value, the greater the effect the boundary layer has. By other means, the amount of the adsorbate on the boundary layer rises.[53]

3. 5. Effect of Initial Concentration of MG

Adsorption studies with different initial concentrations of 10 to 50 mg/L were carried out to calculate PVA nanofiber/Fe_3O_4 nanoparticles adsorption capacity towards MG dye. The initial concentration of the dye plays an influential role in the adsorption capacity of the adsorbent. In this experiment, it was clear from the results that the adsorption capacity of the adsorbent increased with the increase of the initial concentration of dye from 10 to 50 mg/L. The relationship of the adsorption coefficient (q_e) against initial concentrations is given in Figure 11. Adsorption isotherms, on the other hand, are graphical representations that indicate the interaction of adsorbate molecules with adsorbent and provide information on proceeding with the adsorption system.[54]

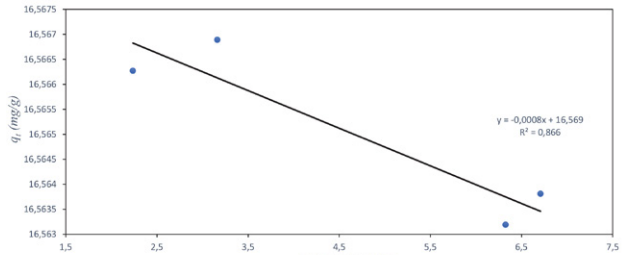

Figure 10: Intraparticle diffusion for the adsorption of MG on PVA nanofiber/Fe_3O_4 nanoparticles

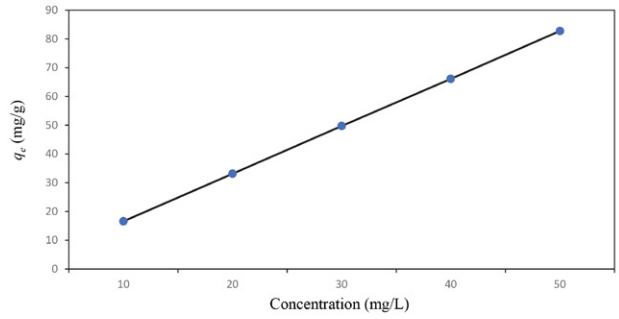

Figure 11: The effect of concentration on MG on PVA nanofiber/Fe_3O_4 nanoparticles

Two well-known adsorption mathematical equations were used to interpret the equilibrium adsorption data. The first one was the Langmuir model, and the second was the Freundlich model, which is widely utilized to describe adsorption behavior. The Langmuir equation is:

Table 1: kinetic parameters of adsorption of MG on PVA nanofiber/Fe_3O_4 nanoparticles

Pseudo-first-order			**Pseudo-second-order**			
R^2	K_1	q_e (calc.)	R^2	K_2	h	q_e (calc.)
0.4147	0.005	0.018	1	9.12	2500	16.55
Elovich model			**Intraparticle diffusion**			
R^2	α	β	R^2	K_{dif}	B_L	
0.8129	2.7182	666.6	0.866	0.0008	16.569	

$$\frac{1}{q_e} = \left(\frac{1}{b\ q_m}\right)\frac{1}{C_e} + \frac{1}{q_m} \quad (7)$$

Here, q_e is the equilibrium adsorption capacity of the adsorbent (mg/g), b is the Langmuir adsorption constant (L/mg), q_m is the maximum capacity of the adsorbent (mg/g) and C_e is the equilibrium MG concentration in solution (mg/L). Moreover, heterogeneous adsorption systems can be described by the linear form of the Freundlich equation, which is represented as the following equation:

$$lnq_e = ln\ ln\ k_f + \frac{1}{n} ln\ C_e \quad (8)$$

Table 2: Adsorption isotherm constants for PVA nanofiber/Fe_3O_4 nanoparticles

Langmuir			Freundlich		
R^2	b (L/mg)	q_m (mg/g)	R^2	k_f (mg/g)	n
0.9771	3.39	128.205	0.9692	169.76	1.3460

Table 3: Maximum adsorption capacity (q_m) of MG dye onto different reported adsorbents.

Adsorbent	q_m (mg/g)	Adsorbent dose/ dye volume (g/ml)	Reference
Alg-Fe_3O_4 NPs	47.84	0.03 g/ 50 ml	6
PVA NF/Fe_3O_4 NPs	128.205	0.003g/ 5 ml	This study
Coal fly ash / $CoFe_2O_4$	90.9	0.6 g/ 150 ml	58
Wood apple shell	35.84	0.15 g/ 1000 ml	59
Zein/Graphene oxide	86.95	0.01 g/ 10 ml	60
CNF-Ag NPs	142.8	0.01 g/ 20 ml	61
Au-NP-AC	140.85	0.015 g/ 50 ml	62
Fe-Zn-PVA NCs	92.59	0.02 g/ 50 ml	63
Fe_3O_4/ Sawdust Carbon	41.66	0.2–1 g/100ml	64

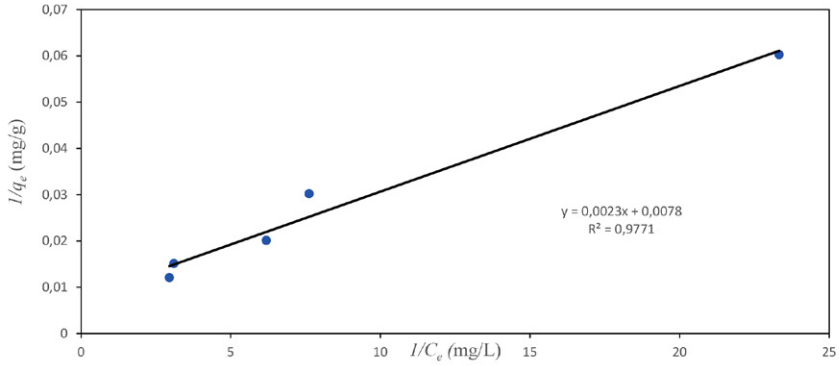

Figure 12: (a) Langmuir plot indicates the linear change of $1/q_e$ with $1/C_e$

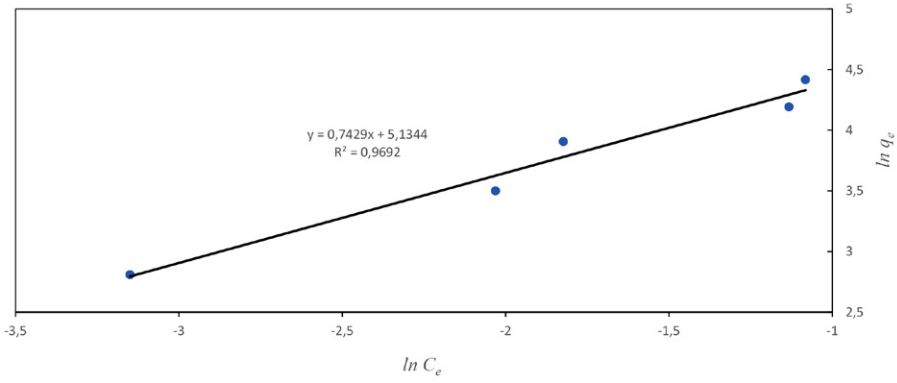

Figure 12: (b) Freundlich plot indicating the linear change of ln q_e on ln C_e.

Where; K_f is the Freundlich constant (mg/g), n is the heterogeneity factor, and q_e and C_e are described above. [55,56] The values of q_m and b were acquired from the intercept and slope of the linear plot of $1/q_e$ against $1/C_e$ (Figure 12: a), while k_f and n values were calculated from the intercept and slope of the linear plot of ln q_e versus ln C_e (Figure 12: b), respectively. Table 2 lists the constants and coefficients of Langmuir and Freundlich adsorption isotherms. The results show that the data of equilibrium adsorption isotherms fit well in both Langmuir and Freundlich linear equations. The R^2 value in Langmuir was 0.9771, and in Freundlich was 0.9692. These two values are close, but they are more fitted to Langmuir, and according to the Langmuir equation, the MG molecules adsorption happens on the surface of the homogeneous adsorbent as monolayer coverage.[57] According to the Langmuir equation, the maximum adsorption capacity of PVA nanofiber/ Fe_3O_4 nanoparticle towards MG dye was calculated to be 128.205 mg/g, which indicates a higher capacity than the previously stated adsorbents (Table 3). Moreover, the n value of 1.3460 means that the adsorption of MG on PVA nanofiber/Fe_3O_4 nanoparticle is a favorable process.

4. Conclusions

To conclude, the significance of this study is to composite PVA nanofiber with iron oxide nanoparticles by simple hot water treatment, which is a simple and efficient technique. This study proves that the PVA nanofiber/ Fe_3O_4 nanoparticles membrane is very efficient, and the preparation process is highly economical. This newly synthesized material can be used as an adsorbent to remove MG dye from contaminated water. The study shows that the quantity of the adsorbed dye depends on the pH, adsorbent contact time, and initial dye concentration. Furthermore, the removal of dye is rapid, and the maximum removal is at 20 minutes then dropped to be steady and reach equilibrium. The adsorption rate follows pseudo-second-order kinetics and the Langmuir model of adsorption isotherm. Thus, the main advantage of PVA nanofiber/ Fe_3O_4 nanoparticles is that the maximum adsorption capacity is in progress compared with other studies and the adsorption rate is fast. Also, the method of preparation is very appropriate and practical. Our results showed that utilizing the HWT to integrate PVA nanofiber with Fe_3O_4 nanoparticles modified and improved the crosslinking of nanofiber. Also, the enhanced removal percentage of MG dye is promising for an effective, low-cost, eco-friendly alternative method for the removal of MG dye from several industries wastewater.

Acknowledgments

The authors thank the UoD PEER laboratory for supporting this work at the University of Duhok.

Conflicts of Interest

The authors declare that there are no competing financial interests.

5. Reference

1 J. O. Tijani, O. O. Fatoba, G. Madzivire and L. F. Petrik, *Water, Air, Soil Pollut.*, **2014**, *225,* 2102. **DOI:**10.1007/s11270-014-2102-y
2 H. Zangeneh, A. A. L. Zinatizadeh, M. Habibi, M. Akia and M. Hasnain Isa, *J. Ind. Eng. Chem.*, **2015**, *26,* 1–36. **DOI:**10.1016/j.jiec.2014.10.043
3 H. Sun, J. Jiang, Y. Xiao and J. Du, *ACS Appl. Mater. Interfaces*, **2018**, *10,* 713–722. **DOI:**10.1021/acsami.7b15242
4 B. M. Thamer, A. Aldalbahi, M. Moydeen A, M. Rahaman and M. H. El-Newehy, *Polymers (Basel).*, **2020**, *13,* 20. **DOI:**10.3390/polym13010020
5 W. Zhang, L. Wang, E. Mäkilä, S. Willför and C. Xu, *Ind. Crops Prod.*, **2022**, *177,* 114513. **DOI:**10.1016/j.indcrop.2021.114513
6 A. Mohammadi, H. Daemi and M. Barikani, *Int. J. Biol. Macromol.*, **2014**, *69,* 447–455. **DOI:**10.1016/j.ijbiomac.2014.05.042
7 R. K. Gautam, V. Rawat, S. Banerjee, M. A. Sanroman, S. Soni, S. K. Singh and M. C. Chattopadhyaya, *J. Mol. Liq.*, **2015**, *212,* 227–236. **DOI:**10.1016/j.molliq.2015.09.006
8 P. Arabkhani and A. Asfaram, *J. Hazard. Mater.*, **2020**, *384,* 121394. **DOI:**10.1016/j.jhazmat.2019.121394
9 N. Y. Donkadokula, A. K. Kola, I. Naz and D. Saroj, *Rev. Environ. Sci. Bio/Technology*, **2020**, *19,* 543–560. **DOI:**10.1007/s11157-020-09543-z
10 L. Qiu, Y. Peng, B. Liu, B. Lin, Y. Peng, M. J. Malik and F. Yan, *Appl. Catal. A Gen.*, **2012**, *413–414,* 230–237. **DOI:**10.1016/j.apcata.2011.11.013
11 G. Yang, N. Zhang, J. Yang, Q. Fu, Y. Wang, D. Wang, L. Tang, J. Xia, X. Liu, X. Li, Q. Yang, Y. Liu, Q. Wang and B.-J. Ni, *Water Res.*, **2020**, *169,* 115249. **DOI:**10.1016/j.watres.2019.115249
12 B. Zaarour, L. Zhu and X. Jin, *ChemistrySelect*, **2020**, *5,* 1335–1348. **DOI:**10.1002/slct.201903981
13 B. Zaarour and M. F. Alhinnawi, *J. Ind. Text.*, **2022**, *51,* 1S–35S. **DOI:**10.1177/15280837221083031
14 B. Zaarour, L. Zhu, C. Huang and X. Jin, *Polym. Adv. Technol.*, **2020**, *31,* 1449–1462. **DOI:**10.1002/pat.4876
15 M. El-Kammah, E. Elkhatib, S. Gouveia, C. Cameselle and E. Aboukila, *Sustain. Chem. Pharm.*, **2022**, *29,* 100753. **DOI:**10.1016/j.scp.2022.100753
16 O. A. Shabaan, H. S. Jahin and G. G. Mohamed, *Arab. J. Chem.*, **2020**, *13,* 4797–4810. **DOI:**10.1016/j.arabjc.2020.01.010
17 N. Torasso, A. Vergara-Rubio, P. Rivas-Rojas, C. Huck-Iriart, A. Larrañaga, A. Fernández-Cirelli, S. Cerveny and S. Goyanes, *J. Environ. Chem. Eng.*, **2021**, *9,* 104664. **DOI:**10.1016/j.jece.2020.104664
18 S. Xiao, M. Shen, R. Guo, S. Wang and X. Shi, *J. Phys. Chem. C*, **2009**, *113,* 18062–18068. **DOI:**10.1021/jp905542g
19 F. He and D. Zhao, *Environ. Sci. Technol.*, **2005**, *39,* 3314–20.

DOI:10.1021/es048743y
20 X. Wang, M. Zhu, H. Liu, J. Ma and F. Li, *Sci. Total Environ.*, **2013**, *449,* 157–67. **DOI:**10.1016/j.scitotenv.2013.01.008
21 L. M. Kustov, E. D. Finashina, E. V. Shuvalova, O. P. Tkachenko and O. A. Kirichenko, *Environ. Int.*, **2011**, *37,* 1044–1052. **DOI:**10.1016/j.envint.2011.05.003
22 T. Shahwan, M. Anjass and R. Naser, *J. Mater. Environ. Sci.*,**2021**, vol. 12.
23 J. Liu, N. Wang, H. Zhang and J. Baeyens, *J. Environ. Manage.*, **2019**, *238,* 473–483. **DOI:**10.1016/j.jenvman.2019.03.009
24 D. Talbot, J. Queiros Campos, B. L. Checa-Fernandez, J. A. Marins, C. Lomenech, C. Hurel, G. D. Godeau, M. Raboisson-Michel, G. Verger-Dubois, L. Obeid, P. Kuzhir and A. Bee, *ACS Omega*, **2021**, *6,* 19086–19098. **DOI:**10.1021/acsomega.1c02401
25 V. K. Yadav, D. Ali, S. H. Khan, G. Gnanamoorthy, N. Choudhary, K. K. Yadav, V. N. Thai, S. A. Hussain and S. Manhrdas, *Nanomaterials*, **2020**, *10,* 1551. **DOI:**10.3390/nano10081551
26 J. G. Darab, A. B. Amonette, D. S. D. Burke, R. D. Orr, S. M. Ponder, B. Schrick, T. E. Mallouk, W. W. Lukens, D. L. Caulder and D. K. Shuh, *Chem. Mater.*, **2007**, *19,* 5703–5713. **DOI:**10.1021/cm0607379
27 N. Rajput, *Int. J. Adv. Eng. Technol.*, **2015**, *7,* 1806–1811.
28 N. S. Saadi, L. B. Hassan and T. Karabacak, *Sci. Rep.*, **2017**, *7,* 7158. **DOI:**10.1038/s41598-017-07783-8
29 A. Rianjanu, A. Kusumaatmaja, E. A. Suyono and K. Tryana, *Heliyon,* **2018,** *4,* 2405-8440. **DOI:**10.1016/j.heliyon.2018.e00592
30 T.-M. Huang, F. Pang, I.-F. Hsieh and M. Cakmak, *Synth. Met.*, **2016**, *221*, 309–318. **DOI:**10.1088/1757-899X/429/1/012019
31 N. S. A. Halim, M. D. H. Wirzal, M. R. Bilad, A. R. M. Yusoff, N. A. H. M. Nordin, Z. A. Putra and J. Jaafar, *IOP Conf. Ser. Mater. Sci. Eng.*, **2018**, *429,* 012019. **DOI:**10.1016/j.memsci.2012.12.037
32 L. Huang, S. S. Manickam and J. R. McCutcheon, *J. Memb. Sci.*, **2013**, *436,* 213–220. **DOI:**10.1016/j.memsci.2016.03.062
33 C. Liu, X. Li, T. Liu, Z. Liu, N. Li, Y. Zhang, C. Xiao and X. Feng, *J. Memb. Sci.*, **2016**, *512,* 1–12. **DOI:**10.1016/j.synthmet.2016.09.009
34 Q. Ren, C. Kong, Z. Chen, J. Zhou, W. Li, D. Li, Z. Cui, Y. Xue and Y. Lu, *Microchem. J.*, **2021**, *164,* 106059. **DOI:**10.1016/j.microc.2021.106059
35 W. Qu, T. Yuan, G. Yin, S. Xu, Q. Zhang and H. Su, *Fuel*, **2019**, *249,* 45–53. **DOI:**10.1016/j.fuel.2019.03.058
36 S. Mohanraj, S. Kodhaiyolii, M. Rengasamy and V. Pugalenthi, *Appl. Biochem. Biotechnol.*, **2014**, *173*, 318–331. **DOI:**10.1007/s12010-014-0843-0
37 J. A. A. Abdullah, L. Salah Eddine, B. Abderrhmane, M. Alonso-González, A. Guerrero andA.Romero, *Sustain. Chem. Pharm.*, **2020**, 17, 100280. **DOI:**10.1016/j.scp.2020.100280
38 M. Srivastava, J. Singh, M. Yashpal, D. K. Gupta, R. K. Mishra, S. Tripathi and A. K. Ojha, *Carbohydr. Polym.*, **2012**, *89,* 821–829. **DOI:**10.1016/j.carbpol.2012.04.016
39 A. Moharana, D. Kumar and A. Kumar, *J. Phys. Conf. Ser.*, **2020**, *1531,* 012113. **DOI:**10.1088/1742-6596/1531/1/012113
40 S. Kayal and R. V. Ramanujan, *Mater. Sci. Eng. C*, **2010**, *30,* 484–490. **DOI:**10.1016/j.msec.2010.01.006
41 P. Bahmani, A. Maleki, H. Daraei, R. Rezaee, M. Khamforoush, S. Dehestani Athar, F. Gharibi, A. H. Ziaee and G. McKay, *Environ. Sci. Pollut. Res.*, **2019**, *26,* 21993–22009. **DOI:**10.1007/s11356-019-05228-5
42 S. Ju, T.-Y. Cai, H.-S. Lu and C.-D. Gong, *J. Am. Chem. Soc.*, **2012**, *134,* 13780–13786. **DOI:**10.1021/ja305167h
43 E. Bulut, M. Özacar and İ. A. Şengil, *Microporous Mesoporous Mater.*, **2008**, *115,* 234–246. **DOI:**10.1016/j.micromeso.2008.01.039
44 G. Crini, H. Peindy, F. Gimbert and C. Robert, *Sep. Purif. Technol.*, **2007**, *53,* 97–110. **DOI:**10.1016/j.seppur.2006.06.018
45 S. Arellano-Cárdenas, S. López-Cortez, M. Cornejo-Mazón and J. C. Mares-Gutiérrez, *Appl. Surf. Sci.*, **2013**, *280,* 74–78. **DOI:**10.1016/j.apsusc.2013.04.097
46 Uma, S. Banerjee and Y. C. Sharma, *J. Ind. Eng. Chem.*, **2013**, *19,* 1099–1105. **DOI:**10.1016/j.jiec.2012.11.030
47 B. H. Hameed and M. I. El-Khaiary, *J. Hazard. Mater.*, **2008**, *153,* 701–708. **DOI:**10.1016/j.jhazmat.2007.09.019
48 F. Othman, M. S. Sadeghian, F. Ebrahimi and M. Heydari, *Int. Proc. Chem. Biol. Environ. Eng.*, **2013**, *51,* 6. **DOI:**10.7763/ipcbee
49 T. Shean, Y. Choong, K. L. Lau, M. Abdullah and S. N. A. MD Jamil, *Materials (Basel).*, **2019**, *12,* 1–17. **DOI:**10.3390/ma12111734
50 H. Sun, L. Cao and L. Lu, *Nano Res.*, **2011**, *4,* 550–562. **DOI:**10.1007/s12274-011-0111-3
51 C. Gerente, V. K. C. Lee, P. Le Cloirec and G. McKay, *Crit. Rev. Environ. Sci. Technol.*, **2007**, *37,* 41–127. **DOI:**10.1080/10643380600729089
52 G. Vijayakumar, C. K. Yoo, K. G. P. Elango and M. Dharmendirakumar, *Clean - Soil, Air, Water*, **2010**, *38,* 202–209. **DOI:**10.1002/clen.200900125
53 T. S. Najim and S. A. Yassin, *E-Journal Chem.*, **2009**, *6,* S153–S158. **DOI:**10.1155/2009/804256
54 C. Ng, J. N. Losso, W. E. Marshall and R. M. Rao, *Bioresour. Technol.*, **2002**, *85,* 131–5. **DOI:**10.1016/S0960-8524(02)00093-7
55 E. Lorencgrabowska and G. Gryglewicz, *Dye. Pigment.*, **2007**, *74,* 34–40. **DOI:**10.1016/j.dyepig.2006.01.027
56 H. A. Ahmed, P. H. Saleem, S. A. Yasin and I. A. Saeed, in *Journal of Physics: Conference Series*, **2021**,*1853,* 012006. **DOI:**10.1088/1742-6596/1853/1/012006
57 X. Guo and J. Wang, *J. Mol. Liq.*, **2019**, *296,* 111850. **DOI:**10.1016/j.molliq.2019.111850
58 M. Zhang, Y. Mao, W. Wang, S. Yang, Z. Song and X. Zhao, *RSC Adv.*, **2016**, *6,* 93564–93574. **DOI:**10.1039/C6RA08939A
59 A. S. Sartape, A. M. Mandhare, V. V. Jadhav, P. D. Raut, M. A. Anuse and S. S. Kolekar, *Arab. J. Chem.*, **2017**, *10,* S3229–S3238. **DOI:**10.1016/j.arabjc.2013.12.019
60 A. S. Keshtiban, S. M. Seyedahmadian, B. Habibi and K. Farhadi, *Prog. Color. Color. Coatings*, **2021**, *14,* 55–65. **DOI**: 10.30509/pccc.2021.81679
61 N. Chinthalapudi, V. V. D. Kommaraju, M. K. Kannan, C. B. Nalluri and S. Varanasi, *Carbohydr. Polym. Technol. Appl.*, **2021**, *2,* 100098. **DOI:**10.1016/j.carpta.2021.100098

62 M. Roosta, M. Ghaedi, N. Shokri, A. Daneshfar, R. Sahraei and A. Asghari, *Spectrochim. Acta. A. Mol. Biomol. Spectrosc.*, **2014**, *118,* 55–65. **DOI:**10.1016/j.saa.2013.08.082
63 M. Saad, H. Tahir, S. Mustafa, O. A. Attala, W. A. El-Saoud, K. A. Attia, W. M. Filfilan and J. Zeb, *Nanomaterials*, **2023**, *13,* 1747. **DOI:**10.3390/nano13111747
64 Z. Bonyadi, F. S. Khatibi and F. Alipour, *Appl. Water Sci.*, **2022**, *12,* 221. **DOI:**10.1007/s13201-022-01745-w

Povzetek

Študija opisuje uporabo hlapov topil za obdelavo in povečano zamreženje PVA nanovlaken. S preprosto tehniko vroče vode so bili sintetizirani nanodelci Fe_3O_4 v kompozitu z nanovlakni. Študija se osredotoča na uporabo modificiranih PVA nanovlaken za odstranjevanje malahitno zelene (MG) iz vode pri različnih pH, kontaktnih časih in začetnih koncentracijah barvila. Površinska morfologija nanovlaken je bila določena s tehnikami SEM, FTIR in XRD. SEM je pokazal, da se je zamreženje povečalo, Fe_3O_4 nanodelci pa so se pojavili kot aglomerati na površini nanovlaken. Odstotek odstranjevanja pri optimalnem pH in kontaktnem času je bil 99,76 % oziroma 99,5 %. Nato smo proučevali kinetiko z linearnimi modeli psevdo-prvega reda, psevdo-drugega reda, Elovicheve enačbe in modela notranje difuzije. Rezultati so pokazali, da kinetika adsorpcije sledi psevdo-drugemu redu. Poleg tega smo adsorpcijsko izotermo potrjevali z uporabo Langmuirjeve in Freundlichove enačbe. Langmuirjeva enačba je najbolje opisala adsorpcijo z vrednostjo R^2 0,9771, največja odstranitev pa je bila 128,205 mg/g. Posledično so molekule barvila MG prekrile nanovlakna PVA/nanodelci Fe_3O_4 v enoslojni in homogeni plasti. Rezultati študije so pomembni za čiščenje odpadne vode v industriji, saj zagotavljajo možno rešitev za odstranitev barvila MG iz odpadne vode v tekstilni, papirni, kozmetični, živilski in ribogojni industriji.

Scientific paper

A Mat Based on PVA Doped with TiO_2 Nanoparticles for Removal of Methylene Blue Dye from Aqueous Solution and Improving the Carbon Footprint

Salah M. Abdullah,[1,*] Aseel F. Alwan,[1] Atheer M. Majeed[2] and Suhad A.Yasin[3]

[1] *Polymer Research Unit, College of Science, Mustansiriyah University, Baghdad, Iraq*

[2] *College of Arts, Mustansiriyah University, Baghdad, Iraq*

[3] *Chemistry of Department, College of Science, University of Duhok, Kurdistan Region, Iraq*

* *Corresponding author: E-mail: salah_md@uomustansiriyah.edu.iq*

Received: 08-24-2023

Abstract

Water supply is the great challenge for climate change and overpopulation. A nanofiber mat consisting of polyvinyl alcohol (PVA), nanoTiO_2, and citric acid (PTC) was prepared using an electrospinning technique at a constant flow rate (0.5 ml/h). The morphology of the mat was detected using (FESEM) technique and image J software. The results show that the mat has a nanofiber morphology with an average diameter of 170 nm. This mat was used to remove methylene blue (MB) from water in two ways, the adsorption process and by photodegradation using UV light. The kinetic study of the adsorption of methylene blue MB on a PTC mat was carried out. Results show that the pseudo-second order is the best to describe the adsorption, of MB, and the intraparticle diffusion is the rate determining step. Seven isotherm models; four of two-parameters and three of three-parameters were used to examine the adsorption experimental data by applying linear and non-linear regression methods using six error functions. The results showed comparable data between linear and non-linear regression methods for two parameters isotherms, and the best isotherm fitting with the data were Freundlich and Temkin models. On the contrary, three parameters isotherms showed distracted data between linear and non-linear regression methods. In addition, the results appear that the best predictive error function was Chi-square.

Keywords: Electrospinning, Nanofibers, Adsorption, Photodegradation, Methylene blue, Carbon footprint

1. Introduction

Nanotechnology is one of the versatile fields which can be defined as the ability to control and manipulate nanomaterials and apply them in different fields of industry such as, the biomedical, and food industries.[1,2] The international standardization organization (ISO) defines the nanomaterials as a material that any one of the dimensions must be on a nanometric scale, either the surface or internal structure.[3] The huge expansion in nanotechnology in the last decades contribute to the development of nanofibers with wide applications, especially in medical, agricultural, and environmental fields[4,5,6] Many different methods are used to produce nanofibers such as melt-blown technology, centrifugal spinning, and template synthesis but the most used technique is electrospinning[7]which is a designed process for manufacturing fibers with thin diameters and large surface area[8,9]. This process is proper for polymers (natural and synthetic)[5], inorganic materials, and composites.[10] The electrospinning method is based on the use of electrostatic forces to produce very fine continuous fibers with diameters ranging from nano to micrometers under room temperature and atmospheric conditions.[11,12] The process begins when a high voltage is applied to the polymeric solution that exists in the tip of the metallic needle which induces electrical charges in the polymer droplet leading to the form of a conical droplet which is known as the Tylor cone.[13] When the electric forces overcome the surface tension of the solution, one or more jets are generated and travels towards the collector, the solvent evaporates and nanofibers consequently can be collected.[14,15] The nanofibers resulting from the electrospinning process has a large surface area and the overlapping between these nanofibers leads to the form of a pore structure which makes this fiber an ideal material to be used in a huge number of applica-

tions such as in the biomedical field, tissue engineering, and textiles.[16] Poly (vinyl alcohol) is a well-known polymer with remarkable properties; it is a highly hydrophilic polymer[17] with a high content of hydroxyl groups obtained from hydrolysis of poly (vinyl acetate).[18] It has good chemical, thermal stability[19]and good water solubility,[20,21] PVA is also known as a biocompatible and biodegradable[22,23] polymer, these enthusiastic properties made the PVA one of the most favorable and widely used in the biodegradable materials industry like tissue engineering, drug delivery, and wrapping membrane used in the medical field. Dyes or pigments represent a major challenging problem in the environmental field, especially in developing countries because of their hazardous and toxic effect on living creatures.[24] In the industrial sector, these materials are indispensable due to their wide use in many vital industrial processing like textile, plastic, paper, and cosmetics.[25] The increasing amounts of dyes waste have a bad impact on the ecosystem since dyes are mostly stable compounds against heat and light which means that they degraded slowly in the environment[26,27] and that double the risk of their existence in the waste water. The traditional treatment systems include some techniques like ozonation, filtration, membrane separation, and precipitation.[28,29,30]

The aim is to study the global warming performance or carbon footprint of water production for the residential sector for chemicals as polyvinyl alcohol used in water treatment.

However, some of these methods were highly cost and hard to use on an industrial scale, for example, electrochemical oxidation and coagulation.[31] While the use of the adsorption method in water treatment has superior advantages are beginning from its simplicity, effectiveness low costs, and the possibility of the adsorbent being regenerated.[32] Methylene blue (MB) $C_{16}H_{18}N_3SCl\text{-}3H_2O$ is a cationic dye and the most commonly used dye in the textile industry, when this dye is found in waste water or sewage system it can cause health problems to animals and humans sometimes by inhalation, ingestion, or can cause eye burns by direct contact.[33,34]

In this study, the electrospinning technique used to prepare the PVA mat adopted with TiO_2 nanoparticles and citric acid to enhance the ability of PVA to remove MB dye in two ways by the adsorption process and by photolytic of MB using UV light.

2. Experimental Section

2. 1. Materials

Both of PVA with code no. 63018, and Methylene blue supplied by (Rediel De Haen AG, Seelze, Germany), Titanium dioxide nanoparticles (TiO_2 (with particle size (30 ∓ 5) nm supplied by Changsha S and tech, Citric acid (CA) Chem- supply. Both NaOH granules and HCl with 37% concentration were supplied by (Fluka).

2. 2. Equipment

A double nozzle syringe pump voltage 110-230AC, power frequency 50–60 Hz, (fig. s1), field emission scanning electron microscope (FESEM) supplied by (Hitachi S-570), power sonic410 supplied by Daihan lab tech Co. Ltd (Korea),

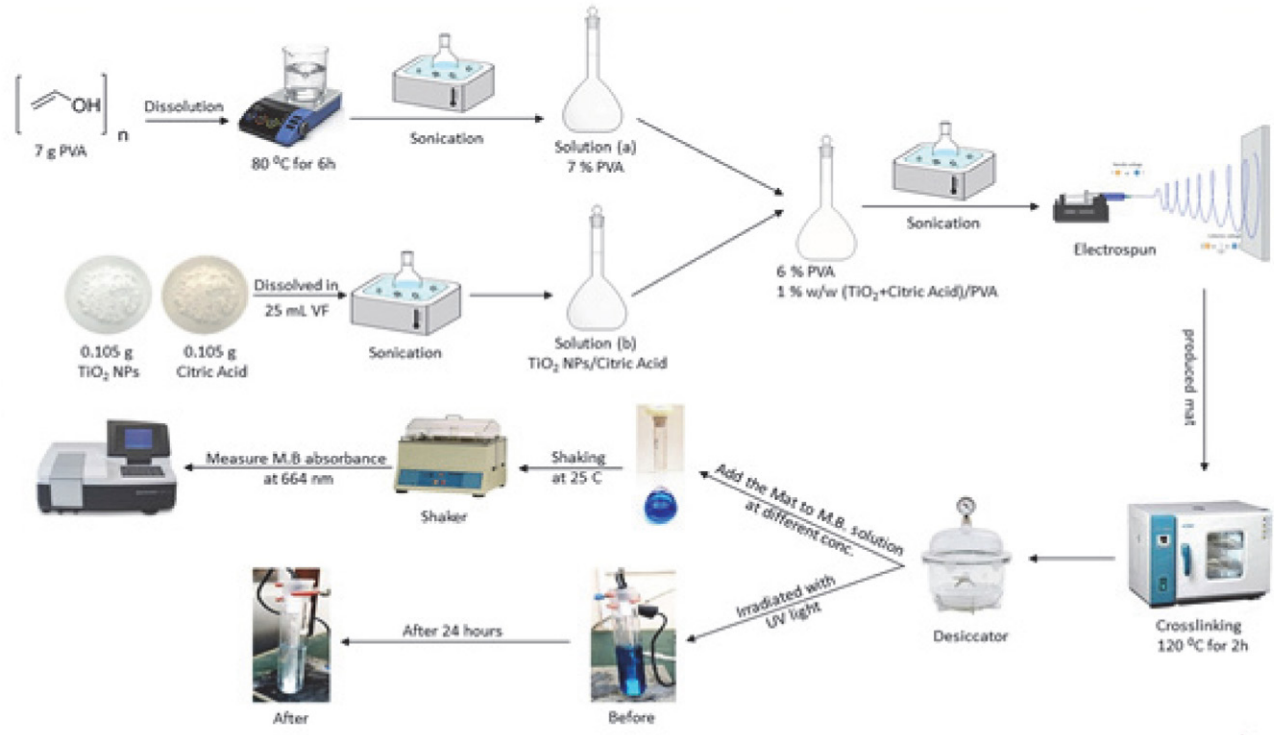

Scheme 1: Synthesis of electrospun PTC mat

UV /visible spectrometer lambda 25 Perkin Elmer. A commercial type UV lamp (made in China) is usually used in reverse osmosis (RO) sterilized water purchased from the Al-Sinak region in Baghdad City, FTIR spectra were recorded on 4200 (JASCO) with a frequency range of (400–4000) cm^{-1}. The pH was measured using a DZS-706A multi-meter (INESA Scientific Instrument Co., Ltd. Shanghai, China).

2.3 Preparation of PTC solution

7 g of PVA was dissolved in 100 ml of hot distilled water at 80 °C to prepare a 7% PVA solution. Equal amounts (0.105g) of both nano TiO_2 and citric acid (CA) were dissolved in 25 ml of distilled water. (6:1) v/v of PVA to CA+TiO_2 solutions were mixed using a sonicator to prepare the (PTC) solution. This solution; consists of 6% w/v of PVA and 1% w/w (TiO_2 and CA) to PVA was used to prepare a PTC mat by electrospinning device.

2. 4. Preparation of PTC Mat Nanofiber

PTC solution was placed into a 5 ml plastic syringe (0.5mm internal diameter needle). The flow rate was 0.5 ml h^{-1}. The distance between the collector and the pump was 10 cm, the electrospinning device was set at 100rpm for the cylinder collector which was wrapped by aluminum foil (see fig. S2), and the applied voltage was adjusted to 25 kV using DC high voltage power source. After that, the produced mat was cured at 120 °C for 2 hours in an oven for crosslinking (See scheme 1 and fig. S3). The morphology of the (PTC) mat was examined by FESEM.

2. 5. Batch Adsorption Study

The adsorption capacity of MB on the electrospun PTC mat was accomplished in a batch adsorption experiment by studying the effect of two different experimental variables, the pH, and the initial MB concentration with a stable weight (0.03 g) of the PTC mat.

2. 5. 1. Study of pH Effect

The initial pH of the MB solutions was adjusted with 0.1 M hydrochloric acid (HCl) and sodium hydroxide (NaOH) to (3, 4.0, 5.8, 6.7, 9.0, 9.8) using a pH meter. A 0.03 g of the PTC electrospun mat was added to each of 10 ml volumetric flasks containing 5 mL of MB solution at certain concentrations. All the solutions were agitating overnight at 25 °C, and 60 rpm. After the adsorption process, the solutions were analyzed by UV spectrometer at 664 nm to estimate the adsorption process.

2. 5. 2. Effect of MB initial concentration

The MB initial concentration (5, 8, 11, 13, 16, 21, 26, and 32 mg l^{-1}) was used to study their effect on the adsorption process with fixed other parameters: the temperature at 25 °C, weight of PTC mat 0.03 g, and the MB solution volume is 10 ml. The amount of dye adsorbed on adsorbent (q_e) and the removal percentage of dye were calculated, respectively, as follows[35]:

$$q_e = \frac{C_i - C_e}{W} V \quad (1)$$

Where *qe* is the amount of dye adsorbed on adsorbent at equilibrium (mg g^{-1}), C_i and *Ce* (mg ml^{-1}) are the liquid-phase concentrations of dye at the initial and equilibrium, respectively. V (L) is the volume of the solution, and W (g) is the mass of the dry adsorbent used.

$$\%\, Adsorption(\%R) = \frac{C_i - C_e}{C_i} \times 100 \quad (2)$$

2. 6. Kinetic Study

The kinetic studies were achieved at the pH of distilled water without any adjustment by immersing 0.03 g of the mat in 10 ml of 15 mg l^{-1} MB solution in a volumetric flask at room temperature with shaking in the shaker and the samples were collected at different time intervals. The decanted solutions were analyzed using a UV-visible spectrophotometer at 664 nm. The aqueous samples were taken at preset time intervals, and the concentrations of dye were similarly measured.

To find the adsorption mechanism, the kinetic models; Elovich model, intra-particle

diffusion, pseudo-first order and pseudo-second-order; were used under optimum conditions : the temperature degree is 25 °C, 10 ml of 15 mg l^{-1} MB solution, pH = 6.5–7, and 0.03 g of absorbent.

$$q_t = \frac{1}{\beta}\ln(\alpha\beta) + \frac{1}{\beta}\ln(t) \quad (3)$$

linear Elovich model[35]

$$q_t = K_{dif} t^{\frac{1}{2}} + B_L \quad (4)$$

intra- particle diffusion[35]

$$\log(q_e - q_t) = \log q_e - \left(\frac{k_1}{2.303}\right) t \quad (5)$$

linear pseudo-first-order[35]

$$\frac{t}{q_t} = \frac{1}{k_2\, q_e^2} + \frac{1}{q_e}(t) \quad (6)$$

linear pseudo-second-order[35]

Where K_{dif} (mg g^{-1} $min^{-1/2}$), K_1 (min^{-1}), and K_2 (g mg^{-1} min^{-1}) are the rates constant for the intra particle diffusion, first-order and second-order respectively, α regarded as the initial adsorption rate (mg g^{-1} min^{-1}), β is the desorption constant (g mg^{-1}), B_L corresponding to the thickness of the boundary layer[35].

2. 7. Error Functions

The set of error functions is used to find non-linear equation parameters of adsorption isotherms models. These function errors are:

Chi- square test (χ^2)[36,37]

$$\chi 2 = \sum_{i=1}^{p} \left[\frac{(q_{e,meas} - q_{e,calc})^2}{q_{e,meas}} \right]_i \quad (7)$$

Sum of squares of the errors (SSE)[38]

$$SSE = \sum_{i=1}^{p} (q_{e,meas} - q_{e,calc})_i^2 \quad (8)$$

A Derivative of Marquard's Percent Standard Deviation(MPSD)[39] :

$$MPSD = \sum_{i=1}^{p} \left(\frac{q_{e,meas} - q_{e,calc}}{q_{e,meas}} \right)_i^2 \quad (9)$$

The Average Relative Error (ARE)[40]:

$$ARE = \sum_{i=1}^{p} \left| \frac{q_{e,meas} - q_{e,calc}}{q_{e,meas}} \right|_i \quad (10)$$

Sum of Absolute Error (EABS)[41]:

$$EABS = \sum_{i=1}^{p} |q_{e,meas} - q_{e,calc}|_i \quad (11)$$

Coefficient of determination (R^2)[39]:

$$R^2 = \frac{\sum (q_{e,meas} - \bar{q}_{e,calc})^2}{\sum (q_{e,meas} - \bar{q}_{e,calc})^2 + \sum (q_{e,meas} - q_{e,calc})^2} \quad (12)$$

Where ($q_{e,meas}$), ($q_{e,calc}$), and ($\bar{q}_{e,calc}$) are the amount in (mg) of MB absorbed at one gram of absorbent experimentally, theoretically, and as average respectively. Try and error method was applied to find the parameters values for three isotherms parameters and also for the non-linear of two parameters isotherm's equations using the Microsoft Excel solver Add-Ins. To solve the non-linear equations, one of the error functions was chosen (except R^2) and fined the parameters of the selected isotherm which gives the minimum value of the choosing error function. Then the other corresponding error functions were calculated depending on the chosen error function. So we get a set of error functions' values. The above process was repeated for other error functions, so each time we get a set of error functions and parameters values for the selected isotherm. To avoid the bias for which the values of parameters are dependent, we divided all the values of error functions to its corresponding maximum value, and this set of resulting values for the error functions was summited. So we get a set of summited values and the one that gives the minimum value was dependent, this method is called the Sum of Normalized Error (SNE).

2. 8. Carbon Footprint

The climate change initiating the drought and the rapid growth of the population with the estimation around 3.5 million people by the middle of the century.[42] It is predicted that by 2030, there will be an imbalance between water supply and public demand if nothing is done to reduce water demand or improve water supply efficiency[41]. To meet future water demand, the demand for electricity and chemicals used to operate these treatment plants will rise. As a result of increased water treatment, GHG (Greenhouse gases) emissions associated with increased energy and chemical consumption will rise.

3. Results and Discussion

3. 1. Characterization

The prepared mat was characterized by FESEM to provide a description of the morphology of the mats and to investigate the nanostructure. The FESEM images in Fig.1 shows that the mat has nanofibers with smooth and fine surface structure. The Image J software reveals that the average diameter of the produced fiber was 170 nm.

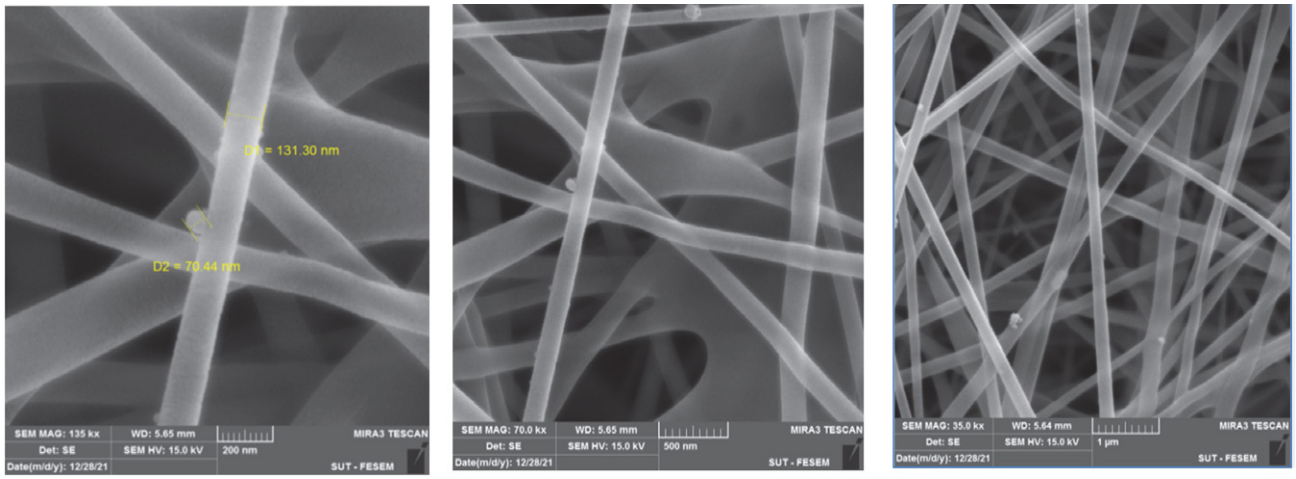

Fig. 1: FESEM images of the prepared (PTC) mat at different resolutions (135 KX), (70 KX) and (35 KX)

FTIR spectra of the PTC mat before and after curing and pure PVA are exhibited in Fig.2 this figure shows the same peaks for all spectra at the studied range (500–4000cm^{-1}) because they have the same functional groups. Whereas the main peaks were observed at 3180–3400 cm^{-1} this peak is related to O–H stretching vibration of the hydroxyl group, peaks 2926 cm^{-1}, 2854 cm$^{-1,}$ assigned to CH_2 asymmetric and symmetric stretching vibration respectively, peak observed at1642 cm^{-1}, peak at 1425 cm^{-1} peak at 1172 cm^{-1}, 1026 cm^{-1} related to C–O stretching of acetyl groups and C-C stretching vibration respectively,[43] A weak peak corresponding to Ti-O stretching appears at 620 cm^{-1} in PTC mat before and after curing.[44]

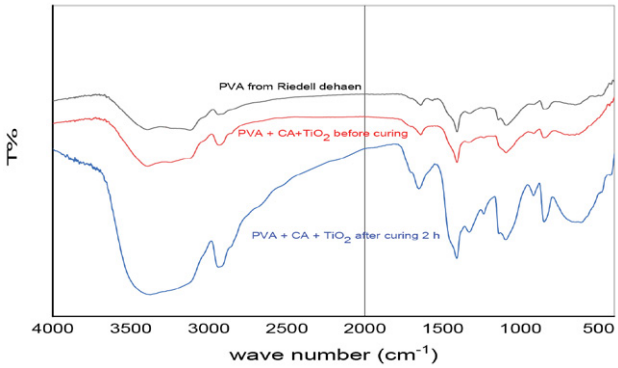

Fig. 2: FTIR spectra of (PTC) nanofibers mat before and after curing and pure PVA

3. 2. Effect of pH

The pH of the dye solution is an essential factor that plays an important role in controlling the whole adsorption process, especially in adsorption capacity.[45] Fig.3 illustrates the effect of pH on the adsorption of MB onto the PTC mat. The effect of the initial pH of the dye solution on the quantity of the dye absorbed was studied by using different pH values under other constant parameters.

When the pH increased from 4 to 6.4, the adsorption capacity increased from 0.3 to 0.77 mg g^{-1}. The adsorption system contains three functional groups, amines from the methylene blue, hydroxyl, and carboxyl group from the PTC mat. In the acidic medium, the amine group in MB will interact with the H^+ in the solution so there is a low chance to interact with the –COOH group in the PTC mat leads to low adsorption of MB, while, In the basic solution, there are free amine groups so it can interact very easy with $–COO^-$ group so the adsorption of MB will increase. When the pH gradually increased towards more basicity the adsorption of MB stays almost constant with a little decrease in the adsorption, this may refer to the bonding of amine groups in MB with OH groups in the solution due to decreasing MB adsorption.

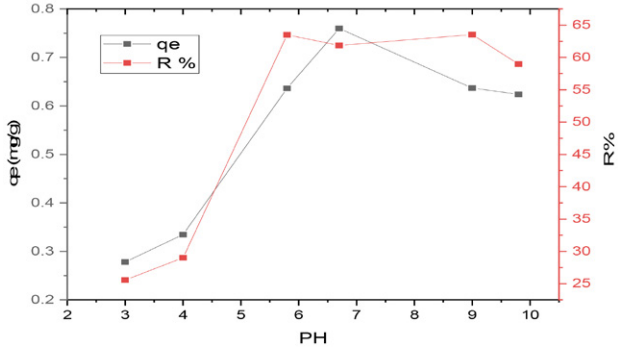

Fig 3: The pH effect of the MB amount adsorbed onto (PTC) mat

3. 3. Effect of Initial MB Concentration

The initial concentration effect of the MB dye adsorbing onto the (PTC) mat was studied between (5 to 32 mg l^{-1}). The adsorption capacity (q_e) of the (PTC) mat increased with the increase the initial MB, while the percent of adsorption (%R) increased with the increasing of the initial MB concentration and reached the maximum point at 15.75 ppm and after that R% gradually decreased with the increasing of MB concentration, as shown in fig. 4.The explanation of this behavior is with increasing of the MB concentration, the adsorption of the dye on the free sites of the mat increased leading to increasing the value of q_e and %R (eqn.1and 2). Until reaching the sites fully saturated. The continuous increasing in MB concentration did not produce any other adsorption of the dye that conduct to decrease in %R value and continuous increasing of q_e values (eqn. 1 and 2).

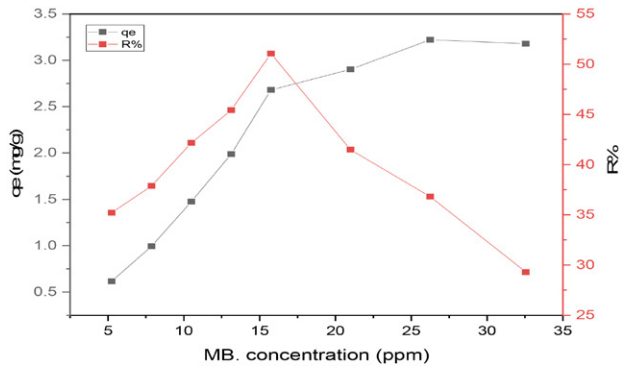

Fig.4: The relationship between MB concentration with (q_e) and R%

3. 4. Effect of Contact Time

Contact time is also one of the important factors that deal with the removal of the dye from the waste water. Fig. 5 shows the relationship between time with adsorption amount (q_e) and the percent of adsorption (%R). In the beginning, the rate of the MB adsorption is very fast due to there being a lot of free sites on the mat until reaches 120 min. after that, the number of free sites will decrease so the

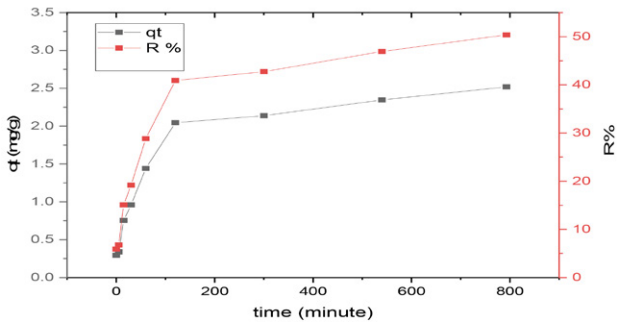

Fig. 5: The time effect for the MB adsorption onto PTC mat

rate decreased until reaching the equilibrium point at 800 min. which represents the best color removal, this behavior is the most common in adsorption studies[46].

3. 5. Find the Location of Adsorption Sites

To find out the sites that MB adsorb onto PTC mat, three types of mats were prepared which are: (A) PVA with TiO_2 mat, (B) PTC mat without curing, and (C) PTC mat with curing at 120 °C for 2 hours. The adsorption process was carried out at optimum conditions (0.03 g of mat, 15 ppm of MB concentration, and pH = 7 at ambient temperature) using these mats, the results showed that the PTC mat with curing gave the highest amount of MB adsorption while the other mats barely gave adsorption that indicates without any doubts, the adsorption of MB was carried out on the site of –COOH groups on the mat which earned from CA. Moreover, to improve the crosslinking was achieved, two pieces of (B) and (C) PTC mats were immersed in distilled water at 80 °C for two hours, and it was found that the (B) mat was completely dissolved while the (C) mat did not.

3. 6. Photolytic study

The photolytic study was carried out using a UV lamp in a quartz tube. A strip of PTC mat collected on an aluminum foil was immersed in a Pyrex tube containing 100 ml of 15 mg l^{-1} of MB dye solution. The color of the MB solution (deep blue) disappeared gradually with irradiation time until reached a colorless solution after 24 hours (see Figs S4, S5, and S6). This result agrees with many studies of TiO_2/UV system for decolourization of (MB) from an aqueous solution.[47]

3. 7. Kinetic Study:

3. 7. 1 Pseudo-first Order and Pseudo- Second Order

Table 2, figures S7 and S8 illustrate the obtained results of pseudo-first order and pseudo- second order for adsorptions of MB on (PCT) mat at optimization condition.

The pseudo-second order has a higher value of correlation coefficient R^2 (0.995) than for pseudo first-order is (0.961), also the value of $q_e$cal. for pseudo-second order is (2.65 mg g^{-1}), these values are very close to the $q_{e\ meas}$. (2.66 mg g^{-1}) while the value of $q_e$cal. for pseudo-first order (1.99 mg g^{-1}) is too far from the $q_{e\cdot\ meas}$ value so the system obeys without any doubt the pseudo second order.

3. 7. 2. Elovich Equation

The first one who proposed the Elovich equation was Roginsky and Zeldovich[61]. It is used satisfactorily for chemisorption kinetic and heterogeneous surface.[62]

In this, model when we plot (q_t) against, ln(t) we get a straight line with intercept (–0.7213), slope equal to (0.4578), and the R^2 value is 0.9697 (see figure S9). The desorption constant value (β) is 2.1841 g mg^{-1} and the initial adsorption rate (α) is 0.0947 mg g^{-1} min^{-1}. (see table 2), these results showed a good match with the Elovich equation which that indicates to the adsorption is a chemical process and heterogeneous surface of the mat.

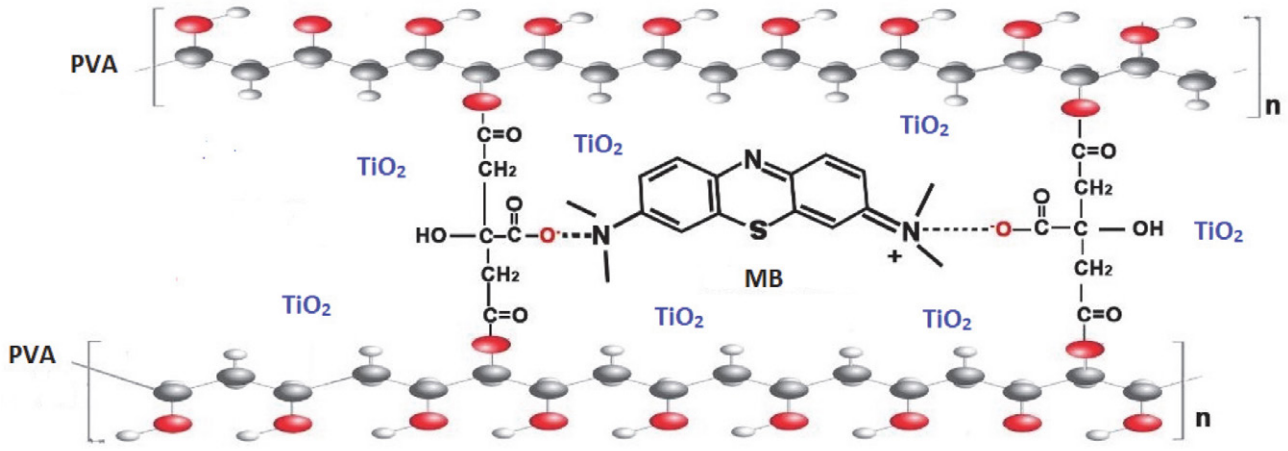

Fig. 6: Illustrate the adsorption site of MB onto PTC mat

Table 1: The previous works for MB batch adsorption

Adsorbent adsorption	Capacity (mg g^{-1})	References
Neem leaf (Azadirachtaindica)	8.76	2005[48]
Bamboo	454.2	2007[34]
Kaolinite	3.05	2009[49]
Bentonite	9.12	2011[50]
Pea shell	246.91	2013[24]
Corn husk	662.25	2013 [51]
Keratin	170	2014[27]
cross-linked chitosan/bentonite composite	142.9	2015[52]
heteroatom-codoped porous carbon	100.2	2018[53]
**VACFF-1300	256.1	2019[54]
VACFF-1600	325.8	2019[54]
Activated carbon from coffee husk	6.82	2020[33]
*DDAB-BC	164	2020[55]
Polylactic acid membrane	97	2020[25]
PLLA/PANI	135	2020[25]
Polyaniline (PAN)	115	2020[25]
PAN/PANI	140	2020[25]
Magnolia denudate leaves(MDL)	185.19	2020[56]
Magnolia grandiflora leaves (MGL)	149.25	2020[56]
Michelia figo leaves *(MFL)*	238.10	2020[56]
PVA/CMC/halloysite nanoclay	8.29	2020[57]
***Nano-Carbon adsorbent	118.98	2022[58]
Molybdenum Disulfide nanomaterials	200	2022[59]
Red mud	147.71	2022[60]
Nano cellulose	4.5	2022[35]
magnetized corn cobs (MCC)	13.23	2023[46]
This work	2.66	

* didodecyldimethylammonium bromide – brown clay. **viscose activated carbon fiber felets. ***zinc gluconate and citric acid

Table 2. Illustrate the kinetic parameter for the linear equation of the kinetic model at optimum conditions and the q_e meas. = 2.6647 mg g^{-1}

Kinetic model	Kinetic parameters		
Pseudo-First order	**$q_e$cal. (mg.g^{-1})**	**K_1 (min^1)**	**R^2**
	1.992	0.0025	0.961
Pseudo-Second order	**$q_e$cal. (mg.g^{-1})**	**K_2 (g.mg^{-1}. min^{-1})**	**R^2**
	2.652481	0.004228	0.995
Elovich model	α (mg.g^{-1} . min^{-1})	β (g. mg^{-1})	R^2
	0.0947	2.1841	0.9697
Intra-particle diffusion	**B_L(mg.g^{-1})**	**K_{dif} (mg g^{-1} $min^{-1/2}$)**	**R^2**
	0.3258	0.0755	0.9268
Part A	**0.0099**	**0.1213**	**0.982**
Part B	**1.4458**	**0.0324**	**0.954**

3. 7. 3. Intra-particle Diffusion (IP) Model

The IP model was used to determine the rate limiting step. Table 2 shows the result of applying this model. Plotting qt against ln(t) gives a straight line with R^2 equal to 0.9268 and the line does not pass through the origin. because the IP model includes a different mechanism that dominance the adsorption process for this reason there are two linear sections (see figure S10) part A: represents the adsorption process from the start to 300 minutes with a very small intercept (B_L = 0.0099) and have high R^2 value

(0.982), that represent the external surface adsorption or instantaneous adsorption stage, while part B: represent the adsorption process from 300 to1035 minutes, which attributed to the gradual adsorption stage, where intra particle diffusion is rate-controlled.[63] At this period the thickness of the boundary layer increase (B_L = 1.4458), so the resistance to the external mass transfer increase as the boundary layer increase.[64] In addition, the rate constant of the intra-particle diffusion K_{dif} will decrease (from 0.1213 to 0.0324) leading to a decrease in the rate of adsorption. At this part, the surface adsorption is more participative in the rate determining step.[65]

3. 8. The Adsorption Isotherm Models

The distribution of the solute molecules between two phases; sold phase (adsorbent) and the liquid phase; at an equilibrium state, can be represented by the isotherm models.

Table S1 shows the entire isotherm models used which include two and three parameters. The obtained results from the applied adsorption isotherm model using Error functions and SNE method for adsorption of MB on (PTC) illustrated in table 4.

a) Two parameter model:

1) Freundlich Isotherm:

Figures S11, S12, and Table 4 show the results of linear and nonlinear Freundlich isotherm equations for the adsorption of MB at ambient temperature. The results show high values of the coefficient of determination R^2 (0.975 and 0.994) for linear and non-linear equations respectively.in addition, the values of Freundlich equations constants (n, K_f) are very close to each other for linear and non-linear expressions. so that the adsorption of MB onto the (PTC) mat obeys the Freundlich isotherm model.

2) Langmuir Isotherm:

The plot of non-linear and linear equations for Langmuir isotherm is shown in figures S13 and S14 respectively. Despite, the Langmuir Isotherm having a higher value of determination coefficient R^2 (0.9998) for linear form (see Table 4) it is not suitable for our adsorption system due to unreasonable values (negative values) of q_{max} and K_L. Also, there are big differences between these values for linear and non-linear forms.

3) Dubinin- Radushkevich isotherm:

Figures (S15-S16) and Table 4 show the results of non-linear and linear Dubinin-Radushkevich isotherm for the adsorption of MB at ambient temperatures. Investigation of these results leads to that the linear regression of Dubinin-Radushkevich isotherm has R^2 values equal to 0.91 for each linear and non-linear. Also, all other parameters are comparable to each other. In addition, the value of adsorption energy (E = 3.75 E + 2 J mol^{-1}) indicates that MB adsorption is a physical adsorption process[66]. But unfortunately, the q_{max} is so small (2.5 mg g^{-1}) and not consistent with practical results.

4) Temkin Isotherm:

For the non-linear form of Temkin isotherm, we plot (q_e) against (C_e), this plot is illustrated in figure (S17) while plot (q_e) against (ln C_e) (figure S18) represents the linear regression of Temkin isotherm. The parameters values for Temkin isotherm (A_t, B_t, b_t) for non-linear; which is obtained according to the SNE method; and linear regression at ambient temperature are shown in Table 4. The values of these parameters are so close and comparable to each other for non-linear and linear regression. Also, the results show an acceptable value of the Coefficient of determination R^2 (0.936, 0.942) for non-linear and linear regression respectively. These results prove that the Temkin isotherm model is a fit with our data.

b) Three parameter model:

The data for the three parameters model; Redlich-Peterson, Sips, and Toth; for linear and non-linear regression at ambient temperature were obtained using trial and error in the solver add-in with Microsoft's spreadsheet, Microsoft Excel. The results show big differences in values for these parameters for linear and non-linear regression for these isotherms that indicate the error does not obey the Gaussian distribution.[67]

1) The Redlich-Peterson Isotherm:

Figure S19 represents the non-linear regression based on the SNE method for the Redlich-Peterson isotherm, while Figure S20 represents the linear form. The values of Redlich-Peterson Isotherm's parameters (K, a, b) for non-linear and linear regression at ambient temperatures are shown in Table 4. In spite of the R^2 value for linear regression being high (0.995) but the exponent parameter value (b) is negative; should be lies between 0 and 1.[68] So the Ridlich Peterson model is not suitable for the adsorption of MB onto (PTC) mat.

2) Sips Isotherm:

The Sips isotherm model is a hybrid model and the most usable three-parameter model for monolayer adsorption[69]. Figures (S21 and S22) represent the non-linear based on the SNE method and the linear regression of Sips isotherm. The results show that the parameters' values (q_{max}, n, b) for the linear and non-linear equations of the Sips Isotherm model at ambient temperature are comparable to each other (see Table 4) and the R^2 values are high (0.995 for non-linear and 0.992 for linear regression). It seems a good fit with our data except the q_m values are so high and not compatible with experimental data.

3) Toth Isotherm:

Figures S24 and S23 illustrate the linear form of the Toth equation which consist of plotting ln $\left(\frac{{q_e}^n}{{q_m}^n - {q_e}^n}\right)$

against (ln C_e) and the non-linear form based on SNE method. (q_{max}, n, K_T) represent the Toth isotherm parameters, and the values of these parameters using a linear and non-linear form of the Toth equation are shown in Table 4. The values of these parameters are so different from each other for linear and non-linear forms and the q_{max} value is very small for the linear form and very high for the non-linear form compared with what we expect from the experimental data, in addition, the Coefficient of determination R^2 values for the linear and non-linear Toth equations are far away from 1 (R^2 = 0.698, 0.865) respectively. So the Toth isotherm is not suitable for application in this adsorption system.

3. 9. Error function

Table 4 shows the value of the sum of the normalized errors SNE for non-linear equations after analyzing five error functions, which are: Sum of squares of the errors (SSE), Chi-square test (χ^2), Derivative of Marquard's Percent Standard Deviation (MPSD), the Average Relative Error (ARE), and Sum of Absolute Error (EABS) using Microsoft Excel solver Add-Ins for minimizing the respective error function across the concentration range studied. Also, the Coefficient of determination R^2 was calculated for linear and non-linear isotherm model equations. The result signed Chi-square test (χ^2) is the best error function according to the SNE method for all non-linear equations (except Dubinin-Radushkevich is MPSD and EABS). This result agrees with Lekan et al.[70] and Neera Singh et al.[71]

3. 10. Carbon Foot Print

The carbon footprint of the optimized composite was calculated using eq 13, where "CO_2-e," "Q," and "F" represent the CO_2 equivalent emission, material amount, and emission factor for producing 1 m^3 of the resultant material, respectively[72,73].

For the improved proposed composites based on citric acid and PVA as the main parameters, the CO_2 equivalent emission is summarized in Table 3. It is clear that all values of CO_2-e is 1.98 kg CO_2-e/m^3. So PTC nanofiber mat is respond to Sustainable Development Goal 17 (SDG 17), especially **6** Clean water and sanitation, **13** climate action.

$$(CO_2 - e) = \sum(Q_1F_1 + Q_2F_2 + Q_nF_n) \quad 13$$

Table 3. CO_2-e Emissions (kg CO_2-e/m^3) for the Proposed PTC

Sample type	Value (kg CO_2-e/m^3) for the PTC	Value (kg CO_2-e/m^3) for the PTC	Total value (kg CO_2-e/m^3)
PVA	2	2 × 0.98 = 1.96	
1.98			
Citric acid	20	20 × 0.01 = 0.2	
TiO_2	0	0.0 × 0.01 = 0.0	

3. 11. Future Prospective

Determination of the optimum conditions for the adsorption of methylene blue. Artificial intelligence (AI)-

Table 4. Parameters of linear and non-linear isotherm models

Isotherm	The parameters for Linear equation				The parameters for nonlinear eqn.					
Two parameters Isotherms										
Frendlich	K_F (mg g^{-1}) (L/mg)$^{1/n}$	N		R^2	K_F (mg g^{-1}) (L/mg)$^{1/n}$	n		R^2	Error function	SNE
	0.0983	0.673		0.975	0.08	0.617		0.994	χ^2	3.683
Langmuir	K_L (L mg^{-1})	q_{max} (mg g^{-1})		R^2	K_L (L mg^{-1})	q_{max} (mg g^{-1})		R^2	Error function	SNE
	–0.0698	–1.97		0.9998	0.0056	42		0.85	χ^2	3.586
Dubinin-Radushkevich	K_{DR} (mol^2 J^{-2})	q_{max} (mg g^{-1})	E (J mol^{-1})	R^2	K_{DR} (mol^2 J^{-2})	q_{max} (mg g^{-1})	E (mol J^{-1})	R^2	Error function	SNE
	3.5E-06	2.5	3.75E+02	0.91	3.55E-06	2.5	3.75E+02	0.91	MPSD,EABS	0.734
Temkin	b_t (J mol^{-1})	A_t (L mg^{-1})	Bt	R^2	b_t (J mol^{-1})	A_t (L mg^{-1})	Bt	R^2	Error function	SNE
	1384	0.3916	1.7897	0.942	1531	0.413	1.618	0.936	χ^2	4.100
Three parameters isotherms										
Redlich-peterson	K(L mg^{-1})	a (L mg^{-1})^b	b	R2	K(L mg^{-1})	a (L mg^{-1})^b	b	R^2	Error function	SNE
	25.78	294.891	–0.575	0.992	0.23	1.00E-05	8.77E-04	0.865	χ^2	3.611
Sips	q_{max}(mg g^{-1})	b(L mg^{-1})	n	R^2	q_{max}(mg g^{-1})	b(L mg^{-1})	n	R^2	Error function	SNE
	200	7.67E-03	0.6256	0.992	316.27	6.15E-03	0.61425	0.995	χ^2	2.221
Toth	q_{max}(mg g^{-1})	K_T (L mg^{-1})	n	R^2	q_{max}(mg g^{-1})	K_T (L mg^{-1})	n	R^2	Error function	SNE
	3	0.117	30	0.698	250	9.18E-04	3.14	0.865	χ^2	3.623

based techniques have been proposed as effective methods for predicting treatment outcomes.

4. Conclusion

A PTC mat with a fiber diameter range of (170nm) was successfully achieved in the electrospinning process, this mat was appropriately used in removing MB dye in two ways; photolytic and adsorption process with optimum conditions (0.03 g of mat, 15 ppm of MB concentration, and pH = 7 at ambient temperature). The Kinetic study of adsorption proves that the adsorption process obeyed the pseudo-second order and good fitting with the Elovich model which indicates the adsorption process is chemical adsorption. Also, the results show the adsorption mechanism follows intra-particle diffusion model. Seven isotherm models having two and three parameters with linear and non-linear regression were investigated and conducted different error functions. The results show that the Freundlich isotherm and Temkin models are the best fit for our data and the Chi-square (χ^2) is the best error function according to the SNE method.

Data Availability:

The figures data used to support the findings of this study are included within the supplementary information file named as the supplementary file; other data are available on request.

Statements and Declaration

On behalf of all authors, the corresponding author states that there is no conflict of interest.

Acknowledgments

The authors would like to thank the Polymer research unit, Mustansiriyah University, Iraq *http://oumustansiriyah.edu.iq* for their support and for providing facilities to accomplish this research work. Also, the authors are thankful for the USAID Partnerships for Enhanced Engagement in Research (PEER) laboratory at the University of Duhok.

5. References

1. Z. H. Mohammad, F. Ahmad, S. A. Ibrahim, S. Zaidi. *Discov. Food.* **2022**, *2,* 12. **DOI:**10.1007/s44187-022-00013-9
2. M. Sirait, Motlan. Innovation in polymer science and technology, IOP Conference, Medan, Indonesia, 2017. *Mater. Sci. Eng.* **2017**, 223. **DOI:**10.1088/1757-899X/223/1/012027
3. D. R. Boverhof, C. M. Bramante, J. H. Butala, S. F. Clancy, M. Lafranconi, J. West S. C. Gordon. *Regul. Toxicol. Pharmacol.* **2015**, *73,*137–150. **DOI:**10.1016/j.yrtph.2015.06.001
4. C. T. Lim, *Prog. Polym. Sci.* **2017**, *70,* 1–17. **DOI:**10.1016/j.progpolymsci.2017.03.002
5. M. Thiruvengadam, G. Rajakumar, I. M. Chung, *3 Biotech.* **2018**, *8,* 1–13. **DOI:**10.1007/s13205-018-1104-7
6. H. Zhong, Z. Li, T. Zhao Y. Chen. *ACS Biomater. Sci. Eng.* **2021**, *7,* 4828–4837. **DOI:**10.1021/acsbiomaterials.1c00982
7. D. H. Kusumawati, K. V. Istiqomah, I. Husnia, N. Fathurin, *J. Phys. : Conf. Ser.* **2021**, 2110. **DOI:**10.1088/1742-6596/2110/1/012010
8. C. Lee, H. Javed, D. Zhang, J. Kim, P. Westerhoff, Q. Li, P. Alvarez. *Environ. Sci. Technol.* **2018**, *52,* 4285–4293. **DOI:**10.1021/acs.est.7b06508
9. J. A. Bhushani, C. Anandharamakrishnan,*Trends Food Sci. Technol.* **2014**, *38,* 21–33. **DOI:**10.1016/j.tifs.2014.03.004
10. R. Sridhara, S. Sundarrajan, J. R. Venugopal, R. Ravichandran**,** S. Ramakrishna, *J. of Biomaterials Sci. Polymer Edition,***2013**, *24,* 365–385. **DOI:**10.1080/09205063.2012.690711
11. S. Parham, A. Z Kharazi, H. R Bakhsheshi-Rad, H. Ghayour, A. F. Ismail, H. Nur, F. Berto, *Materials.* **2020**, *13,* 2153. **DOI:**10.3390/ma13092153
12. M. Kurečič M. S Smole, *Tekstilec,*. **2013**, *56,* 4–12. **DOI:**10.14502/Tekstilec2013.56.4-12
13. J. Rnjak-Kovacina. A. S. Weiss. *tissue Eng.* **2011**, *17,* 365–372. **DOI:**10.1089/ten.teb.2011.0235
14. R. Casasola, N. L Thomas, A. Trybala, S. Georgiadou. *Polymer,* **2014,** *55,* 4728–4737. **DOI:**10.1016/j.polymer.2014.06.032
15. F. Fadil , N. D. N. Affandi , M. I. Misnon, N. N. Bonnia, A. M. Harun M. K. Alam, *Polymers.* **2021**, *13,* 2087. **DOI:**10.3390/polym13132087
16. F. Fadil, F. A Adli, N. D. N Affandi, A. M Harun, M. K. Alam, *Polymers* **2020**, 12, 1–13. **DOI:**10.3390/polym12123043
17. S. Rwei, C. Huang, *Fibers Polym.* **2012**, *13,* 44–50. **DOI:**10.1007/s12221-012-0044-9
18. M. Wang, J. Bai, K. Shao, W. Tang, X. Zhao, D. Lin, S . Huang, C. Chen, Z. Ding , J. YeInt. *J. Polym. Sci.* **2021,** *2021,* 16. **DOI:**10.1155/2021/2225426
19. N. Hasrul, A. Ngadiman, M. Y Noordin, A. Idris, A. S Abdul. I. *Procedia Manuf.* **2015**, *2,* 568–572. ttps://doi.org/10.1016/j.promfg.2015.07.098
20. S. Chen, H. Yang, K. Huang, G. Xiaolong, H. Yao, J. Tang, J. Ren, S. Ren, Y. Ma *Polymers.* **2021**, *13,* 3778. **DOI:**10.3390/polym13213778
21. X. Ji, J. Guo, F. Guan, Y. Liu, Q. Yang, X. Zhang,Y. Xu. *Gels.* **2021**, *7,* 223 **DOI:**10.3390/gels7040223
22. K. Qiu, A. N. Netravali, *Compos. Sci. Technol.* **2012**, *72,* 1588–1594. **DOI:**10.1016/j.compscitech.2012.06.010
23. H. Awada, C. Daneault, *Appl. Sci.* **2015**, *5,* 840–850. **DOI:**10.3390/app5040840
24. Ü, Geçgel, G. Özcan, G. Ç. Gürpınar, *J. of Chemistry*. **2013**, 9.
25. N. Mohammad, Y. Atassi, *Sci. Rep.* **2020**, *10,* 13412. **DOI:**10.1038/s41598-020-69825-y
26. Y. Kuang, X. Zhang, S. Zhou, *Water.* **2020**, *12,* 1–19. **DOI:**10.3390/w12020587
27. A. Aluigi, F. Rombaldoni, C. Tonetti, L. Jannoke, *J. Hazard. Mater.* **2014**, *268,* 156–165.

DOI:10.1016/j.jhazmat.2014.01.012
28. G. Z Kyzas, J. Fu, K. A Matis, *Materials.* **2013**, *6,* 5131–5158. **DOI:**10.3390/ma6115131
29. M. M. Ayad. A. A. El-nasr. *J. Phys. Chem. C.* **2010**, *114,* 14377–14383. **DOI:**10.1021/jp103780w
30. S. A. Yasin, J. A. Abbas, I. A. Saeed, I. H Ahmed. *Polym. Bull.* **2020**, *77,* 3473–3484. **DOI:**10.1007/s00289-019-02919-4
31. A. K. Verma, R. R. Dash, P. A. Bhunia, *J. Environ. Manage.* **2012**, *93,* 154–168. **DOI:**10.1016/j.jenvman.2011.09.012
32. A. Almasia, F. Amirian, M. Mohammadi, A. R. Yari, A. G Dargahi. *Arch Hyg Sci*. **2018**, *7,* 112–118. **DOI:**10.29252/ArchHygSci.7.2.112
33. A. A. Ayalew, T. A. Aragaw, *Adsorption. Sci. Technol.* **2020**, *38,* 205–222. **DOI:**10.1177/0263617420920516
34. B. H. Hameed, A. T. M. Din, A. LAhmed, *J. Hazard. Mater.* **2007**, *141,* 819–825. **DOI:**10.1016/j.jhazmat.2006.07.049
35. A. H. Abdullah, S. Yasin, S. Abdullah, M. Y. Khlaf, I. A. Saeed, *Emergent Mater.* **2022**, *5,* 1199–1212. **DOI:**10.1007/s42247-022-00397-5
36. Y. S. Ho, A. E Ofomaja, *J. Hazard. Mater*. **2006**, *129,* 137–142. **DOI:**10.1016/j.jat.2006.03.012
37. B. Boulinguiez,. P. L. Cloirec, D. Wolbert. *Langmuir*. **2008**, *24,* 6420–6424. ttps://doi.org/10.1021/la800725s
38. K. V Kumar, S. Sivanesan. *J. Hazard. Mater. ,***2006**, *136,* 721–726. **DOI:**10.1016/j.jhazmat.2006.01.003
39. D. W Marquardt, *J. Soc. Ind. Appl. Math. ,*. **1963**, *11,* 431–441. **DOI:**10.1137/0111030
40. B. Subramanyam, A. Das. *J. Environ. Heal. Sci. Eng.* **2014**, *12,* 92. **DOI:**10.1186/2052-336X-12-92
41. Ng, J. C. Y. , W. H. Cheung,G. McKay,*Chemosphere*. **2003**, *6,* 1021–1030. **DOI:**10.1016/S0045-6535(03)00223-6
42. W. K. Biswas, P. Yek, *Renewables Wind. water, Sol.* **2016**, *14,* 1–10.
43. C. Khatuaa, I. Chinyaa, D. Sahab, S. Dasa, R. Sena, A. Dhara, *Int. J. Smart Sens. Intell. Syst.* **2015**, *8,* 1424–1442.
44. E. M Hussein, W. M Desoky, M. F Hanafy, O. W Guirguis, *J. Phys. Chem. Solids*. **2021**, *152,* 109983. **DOI:**10.1016/j.jpcs.2021.109983
45. S. Wang, Y. Boyjoo, A. Choueib, *Chemosphere*. **2005**, *10,* 1401–1407. **DOI:**10.1016/j.chemosphere.2005.01.091
46. N. B Allou, M. A Tigori, A. A Koffi, M. Halidou, N. S. E. P. Atheba, A. Trokourey *Sci. African*. **2023**, *21,* 01828.
47. M. H Abdellah, S. ANosier, A. H El-Shazly, A. A Mubarak, *Alexandria Eng. J.* 2018, *4,* 3727–3735. **DOI:**10.1016/j.aej.2018.07.018
48. G. Krishna. A. S Bhattacharyya, *Dye. Pigment.* **2005**, *65,* 51–59. **DOI:**10.1016/j.dyepig.2004.06.016
49. P. C Mishra, R. K Patel, *J. Hazard. Mater.* **2009**, *168,* 319–325. **DOI:**10.1016/j.jhazmat.2009.02.026
50. C. Perez, D. Fermanndez, A. Bermudez et al. *Chemosphere.* **2011**, *83,* 1028–1034. **DOI:**10.1016/j.chemosphere.2011.01.064
51. M. Khodaie, N. Ghasemi, B. Moradi, M. Rahimi. journal of chemistry. **2013**, 1–6. **DOI:**10.1155/2013/383985
52. Y. Bulut, H. Karaer, *J. Dispersion Sci. Technol.* **2015**, *36,* 61–67. **DOI:**10.1080/01932691.2014.888004
53. B. Chen, Z. Yang, G. Ma, D. Kong, W. Xiong, J. Wang, *Mesoporous Mater*. **2018**, *257,* 1–8. **DOI:**10.1016/j.micromeso.2017.08.026
54. Q. Liu, Y. Zhou, D. Cheng. *Adsorpt. Sci. Technol.* **2019**, *37,* 312–332.
55. M. Munir, M. F. Nazar, M. N. Zafar, et al. *ACS omega*. **2020**, *27,* 16711–16721. **DOI:**10.1021/acsomega.0c01613
56. D. Guo, Y. Li, B. Cui, M. Hu, S. Luo, Y. Liu, *J. Clean. Prod.* **2020**, 267. **DOI:**10.1016/j.jclepro.2020.121903
57. S. Radoor, J. Karayil, J. Parameswaranpillai, S. Siengchin. *J. Environ. Heal. Sci. Eng.* **2020**, *18,* 1311–1327. **DOI:**10.1007/s40201-020-00549-x
58. C. Liang, Q. Shi,J. Feng, et al., *Nanomaterials*. **2022**, 12. **DOI:**10.3390/nano12234235
59. X. Wang, P. Zhang, F. Xu, B. Sun, G. Hong, and L. Bao. *Sustainability*. **2022**, *14,* 7585. **DOI:**10.3390/su14137585
60. Z. Çetinkaya, V. Kalem, *J. Dispers. Sci. Technol.* **2022**, *43,* 1079–1088. **DOI:**10.1080/01932691.2021.1985512
61. S. Z. Roginsky, J. Zeldovich, *J. Acta Physicochim*. **1934**; USSR:554–559.
62. C. W. Cheung, J. F. Porter, G. Mckay, *J. Chem. Technol. Biotechnol.* **2000**, *75,* 963–970. **DOI:**10.1002/1097-4660(200011)75:11<963::AID-JCTB302>3.0.CO;2-Z
63. Y. Li, Q. Du, T. Liu, & A. Wu, *Mater. Res. Bull.* **2012**, *47,* 1898–1904. **DOI:**10.1016/j.materresbull.2012.04.021
64. K. O. Yoro, M. K. Amosa, P. T. Sekoai, J. Mulopo, M. O. Daramola, *Int. J. Sustain. Eng.* **2019**, *13,* 54–67. **DOI:**10.1080/19397038.2019.1592261
65. A. pholosi, E. B. Naidoo, A. E. Ofomaja, *South African J. Chem. Eng.* **2020**, *32,* 39–55. **DOI:**10.1016/j.sajce.2020.01.005
66. J. Monika, V. K. Garg, K. Kadirvelu, *J. Hazard. Mater.* **2009**, *162,* 365–372. **DOI:**10.1016/j.jhazmat.2008.05.048
67. V. Kumar, *Dye. Pigm*. **2007**, *74,* 595–597. **DOI:**10.1016/j.dyepig.2006.03.026
68. N. C. Le, V. P. Dinb, N. C. Le, D. V. Phuc, *Adv. Nat. Sci. Nanosci. Nanotechnol.* **2015**, *6,* 2.
69. R. Saadi, Z. Saadi, R. Fazaeli, N. E. Fard. *Korean J. - Chem. Eng.* **2015**, *32,* 787–799. **DOI:**10.1007/s11814-015-0053-7
70. L. T. Popoola, A. S. Yusuff, O. Adisina, and M. A. Lala. *Journal Environ. Sci. Technol.* **2019**, *12,* 65–80. **DOI:**10.3923/jest.2019.65.80
71. A. Mandal, N. Singh, *J. Environ. Sci. Heal. - Part B Pestic. Food Contam. Agric. Wastes*. **2016**, *51,* 192–203. **DOI:**10.1155/2018/7949741
72. L. F. Jiménez, J. A. Domínguez, R. E. Vega-Azamar, *Adv. Civ. Eng.* **2018**, 2018. **DOI:**10.1021/acsomega.3c00086
73. H. M. Naguib, E. G. Zaki, , D. E. Abdelsattar, A. S. Dhmees, M. A. Azab, S. M. Elsaeed, & U. F. Kandil, *ACS omega,*. **2023**, *8,* 8804–8814.

Povzetek

Oskrba z vodo je velik izziv za podnebne spremembe in prenaseljenost. Podloga iz nanovlaken, sestavljena iz polivinil alkohola (PVA), nanoTiO2 in citronske kisline (PTC), je bila pripravljena s tehniko elektropredenja pri konstantnem pretoku (0,5 ml/h). Morfologijo podlage smo detektirali s tehniko (FESEM) in programsko opremo za slike J. Rezultati kažejo, da ima podlaga morfologijo nanovlaken s povprečnim premerom 170 nm. Ta podlaga je bila uporabljena za odstranjevanje metilen modrega (MB) iz vode na dva načina, s postopkom adsorpcije in s fotodegradacijo z uporabo UV svetlobe. Izvedena je bila kinetična študija adsorpcije metilen modrega MB na PTC podlago. Rezultati kažejo, da je psevdodrugi red najboljši za opis adsorpcije MB, in da je difuzija znotraj delcev korak, ki določa hitrost. Sedem izotermnih modelov; štirje z dvema parametroma in trije s tremi parametri so bili uporabljeni za preučevanje adsorpcijskih eksperimentalnih podatkov z uporabo metod linearne in nelinearne regresije z napako šestih funkcij. Rezultati so pokazali primerljive podatke med linearnimi in nelinearnimi regresijskimi metodami za izoterme dveh parametrov, najboljše ujemanje izoterm s podatki pa sta bila modela Freundlich in Temkin. Nasprotno, izoterme treh parametrov so pokazale moteče podatke med linearnimi in nelinearnimi regresijskimi metodami. Poleg tega rezultati napovedujejo, da je bila najboljša funkcija napovedne napake chi-square test.

Scientific paper

Succinyl Curcumin Conjugated Chitosan Polymer-Prodrug Nanomicelles: A Potential Treatment for Type-II Diabetes in Diabetic Balb/C Mice

Sk Mosiur Rahaman,[1] Gouranga Dutta,[2] Ranu Biswas,[1,*] Abimanyu Sugumaran,[3,*] Mohamed M. Salem,[4] Mohammed Gamal,[5,*] Mohamed AbdElrahman[6] and Mounir M. Salem-Bekhit[7]

[1] *Department of Pharmaceutical Technology, Jadavpur University, Kolkata 700032, West Bengal, India;*

[2] *Department of Pharmaceutics, SRM College of Pharmacy, SRM Institute of Science and Technology, Kattankulathur 603203, Tamilnadu, India;*

[3] *Department of Pharmaceutical Sciences, Assam University (A Central University), Silchar 788011, Assam, India;*

[4] *College of Medicine, Huazhong University of Science and Technology, China;*

[5] *Pharmaceutical Analytical Chemistry Department, Faculty of Pharmacy, Beni-Suef University, AlshaheedShehata Ahmad Hegazy St., 62514, Beni-Suef, Egypt;*

[6] *Clinical Pharmacy Department, College of Pharmacy, Al-Mustaqbal University, Babylon, 51001, Iraq;*

[7] *Department of Pharmaceutics, College of Pharmacy, King Saud University, PO Box 2457, Riyadh 11451, Saudi Arabia.*

** Corresponding author: E-mail: abimanyu.s@aus.ac.in; rbiswas.pharmacy@jadavpuruniversity.in; mgamalm3000@yahoo.com*

Received: 02-05-2024

Abstract

Diabetes mellitus is a chronic metabolic disorder marked by elevated blood sugar levels, leading to organ dysfunction. Curcumin, derived from turmeric, exhibits promise in managing type II diabetes. Amphipathic polymer prodrugs were synthesized by conjugating curcumin with chitosan through succinic anhydride. Nanomicelles, formed via dialysis of amphipathic polymer prodrug, were spherical with an average hydrodynamic size of 57 nm. *In vitro* release studies revealed 97% curcumin release at pH 5 in 7 days. A 21-day experiment on diabetic mice compared nano micelles, standard drugs, and free curcumin's impact on fasting blood glucose. The study showcased gradual, controlled curcumin release from nano micelles, suggesting their potential in type II diabetes treatment.

Keywords: Chitosan, Curcumin, nano micelles, polymer-prodrug, Type-II diabetic

1. Introduction

Diabetes mellitus (DM) is a chronic metabolic disorder marked by persistent high blood glucose levels, termed hyperglycemia. Prolonged hyperglycemia can cause significant harm to the body, impairing function and potentially leading to organ and tissue dysfunction. According to the International Diabetes Federation (IDF) in 2021, approximately 10.5% of adults aged 20 to 79 have diabetes, with nearly half undiagnosed. IDF predicts that by 2045, diabetes prevalence among adults will rise to 1 in 8, affecting around 783 million people, marking a 46% increase from current levels.[1,2] Type 2 diabetes mellitus predominates among major diabetes categories, encompass-

ing around 90% of global diabetes cases.[3,4] Insufficiency of insulin production (Type 1 diabetes) or diminished cellular sensitivity to insulin (Type 2 and gestational diabetes) are the causes of prolonged hyperglycemia. Insulin-producing β cells are autoimmunely destroyed in type 1 diabetes; the destruction was previously linked to a T-cell-mediated attack. Nevertheless, the cause encompasses both environmental and genetic components, including viral infections, altered intestinal microbiota, and dietary patterns, as well as HLA alleles.[5] However, it is hypothesized to be associated with suboptimal dietary patterns characterized by high carbohydrate intake and a sedentary lifestyle. There is a gradual transition from a relative shortfall of insulin and lacking with its sensitivity leads to an absolute deficiency, which eventually requires the injection of exogenous insulin to regulate glucose levels.[3,6,7] Type 2 Diabetes Mellitus (T2DM) traditionally associated with the elderly, is now increasingly prevalent among children and young individuals. This rise is linked to inadequate dietary intake, sedentary lifestyles, and obesity rates. The phytochemical compounds produce a significant therapeutic response in the treatment of metabolic disorders such as diabetes mellitus due to their low toxicity. Curcumin, (CCMN) a polyphenolic phytochemical derived from the rhizome of the turmeric plant (Curcuma longa), has several medicinal properties (like anti-inflammatory, anti-cancer, antioxidant, wound healing, and anti-diabetic etc).[8–10] It has a wide range of potential applications and therapeutic activity. Still, its use is limited due to its very low aqueous solubility, chemical instability, photosensitivity, first-pass metabolism, insufficient tissue distribution, and inadequate absorption, resulting in inadequate bioavailability.[11–13] Studies have demonstrated that CCMN regulates lipid metabolism by suppressing key inflammatory transcription factors (MCP-1, IL-6, HbA1c, TNF-α), reducing hepatic lipogenesis, and enhancing lipid mobilization enzyme activity. In animal models of diabetes, curcumin exhibits anti-hyperglycemic and anti-hyperlipidemic effects. Additionally, its antioxidant properties mitigate oxidative stress, a factor in Type 2 Diabetes Mellitus development. Curcumin has anti-inflammatory properties via its ability to reduce the levels of inflammatory factors, as well as through blocking signalling pathways such as NF-κB.[14,15] Moreover, it plays a crucial function in safeguarding heart health via its ability to mitigate apoptosis and inflammation in individuals with diabetic cardiomyopathy. The cumulative data indicate that curcumin may have therapeutic advantages in managing T2DM and its related problems.[16,17] A variety of approaches, including the encapsulation of CCMN in different lipid nanocarriers or the formation of polymer-prodrug complexes, are intended to address these challenges. Polymer-drug conjugates represent a prevalent and efficacious method for the delivery of hydrophobic drugs. This concept, initially introduced by Ringsdorf et al. in 1975, facilitates controlled drug release, enhances therapeutic efficacy, reduces adverse effects, and improves patient compliance by increasing drug solubility in aqueous solvents.[18,19]

Chitosan (CHT), a biopolymer known for its biocompatibility, biodegradability, and ability to form gel-like structures in acidic conditions, is utilized in drug delivery applications. With its glucosamine unit containing hydroxyl and amine groups, chitosan enables the conjugation of many drugs and other substances.[20] This property can improve the drug's solubility, stability, and toxicity and facilitate the delivery of the drug to specific cells or tissues.[21–23] In this study, we proposed preparing the polymer prodrug conjugate by chemically binding curcumin and chitosan. The conjugation was done in the presence of succinic anhydride, which could act as a bridge between the chitosan and curcumin. This conjugate was converted to nano micelles in an aqueous environment, which may increase CCMN solubility and stability.[24,25] The *in vitro* hemocompatibility and physicochemical characteristics was investigated. The therapeutic potentiality, toxicity, and biochemical parameters of nano micelles was examined in *in-vivo* diabetic Balb/C mice induced by streptozotocin for 21 days.

2. Experimental

2. 1. Materials

Chitosan (low molecular weight ~ 50000 Da) purchased from Sigma-Aldrich, curcumin, succinic anhydride, dimethyl sulfoxide (DMSO), N, N′dicyclohexylcarbodiimide (DCC), 4-dimethylamino pyridine (DMAP), pyrene, pyridine, mono-tetrazolium salt (MTT) and other compounds were purchased from SRL Chem Pvt. Ltd (Mumbai, India). The blood was purchased from the certified blood bank in Kolkata, India. All the chemicals are used as analytical grades.

2. 2. Synthesis of Succinyl-Curcumin Conjugate (SUC-CCMN)

To synthesize SUC-CCMN, initially, CCMN (0.7368 g, 2 mmoL) and succinic anhydride (0.2001 g, 2 mmoL) were dissolved in 30 mL benzene and then added 2mL pyridine consequently refluxed for 36 h at 80 °C. After removal of the solvent under low pressure and lower temperature, the residue was purified by column chromatography, where hexane-ethyl acetate (95:5) was used as the mobile phase and silica gel as a stationary phase to get the final product SUC-CCMN (Yield = 0.32 g, 68.31%).[26]

2. 3. Synthesis of CHT-di(SUC-CCMN) Conjugates

To synthesize CHT-di(SUC-CCMN) conjugate, initially, in 20 mL DMSO carbohydrate polymer CHT

(1.52 gm, 1 mmoL) and SUC-CCMN (0.93 mg, 2 mmoL) were dissolved at room temperature. After both compounds were dissolved entirely, DCC (412 mg, 2 mmoL) and DMAP (116 mg, 1 mmoL) were added to the mixture while stirring continuously. This reaction was carried out in the dark at room temperature for 24 h. Following the completion of the reaction, the product was filtered to precipitate the CHT-di(SUC-CCMN) conjugate. The filtrate was added into a 50 mL solution containing a 1:1 (v/v) ratio of ethanol and ethyl ether to precipitate CHT-di(SUC-CCMN) conjugate. Figure 1 depicts the schematic processes for CHT-di(SUC-CCMN) synthesis.

2. 4. Preparation of CHT-di(SUC-CCMN) Conjugates Micelles

For the preparation of CHT-di(SUC-CCMN) conjugated micelles (CDSCM), 1 mg/mL CHT-di(SUC-CCMN) was prepared with DMSO by proper mixing. Then CHT-di(SUC-CCMN) mixture was taken into a dialysis bag (Mol.Wt 12 kDa), placed into double distilled water for 24 h, and replaced in 4 h intervals. The solvent remained in the reaction process, and other components were eliminated through dialysis. After completion of dialysis, it was passed through a filter of 0.45 μm pore size to avoid the large particles, then lyophilized the product. The final micelles were stored in a cool and dry place for further use.[27] The yield of CDSCM was about 81±6%.

2. 4. Physicochemical Characterizations of CDSCM

2. 4. 1. Characterizations of CDSCM

The structure of synthesized CHT-di(SUC-CCMN) was confirmed by different instrumental analyses, like an FTIR spectrophotometer (Shimadzu Corp No. 01988) with a spectral range of 4000 cm^{-1} to 400 cm^{-1}. ^{1}H-NMR (Bruker–500 MHz spectrometer) spectral analysis was done with the solvent DMSO-d6 and a UV–vis spectrophotometer (Shimadzu, Japan) over 200–700 nm. To know the morphology, hydrodynamic size, and zeta potential of the CDSCM, a zeta seizer (Nano-ZS 90, Malvern Instrument, UK), field emission scanning electron microscope; FEI, Quanta 200 (FE-SEM). To make the SEM sample, 1 mg/mL of lyophilized CDSCM powder was mixed with 1 mL of double distilled water. Then, the dispersion was placed on an aluminum sheet to make the thin film. The air-dried film was then coated with gold and evaluated under the SEM. A high-resolution transmission electron microscope (HR-TEM) (JEOL Japan, JEM-2100 Plus) was used, and TEM samples were prepared by placing a 0.001 mg/mL drop of CDSCM dispersion on the carbon-coated copper grid.

2. 4. 3. Critical Micelle Concentration (CMC) Determination

To determine the CMC of CHT-di(SUC-CCMN), different concentrations of CHT-di(SUC-CCMN) solutions ranging from 0.004 mg/mL to 2.5 mg/mL were vortexed with diluted fluorescent probe pyrene (used as fluorescent dye) solution. The CHT-di(SUC-CCMN) mixture was left overnight to record fluorescence using a fluorescence spectrophotometer at 390 nm emission (Infinite M200, TECAN).[28]

2. 5. Drug Loading Capacity

A specified high concentration of CCMN solution was prepared, and various concentrations of CCMN solution were prepared using the serial dilution procedure using DMSO as a solvent. The absorption was measured at 435 nm, and a standard curve was prepared. Absorption was measured after preparing a known concentration (1mg/mL) of CHT-di(SUC-CCMN) conjugate micelle (CDSCM) in DMSO solvent. The quantity of CCMN in the CHT-di(SUC-CCMN) conjugate micelle was determined using the standard line (equation). The following equation was used to compute the CCMN loading capacity of the CHT-di(SUC-CCMN) conjugate in micelles:

$$\text{CCMN loading capacity } \left(\frac{w}{w}\%\right) = \frac{\text{Ammount of CCMN}}{\text{Ammount of CCMN released from CDSCM}} \times 100 \quad (1)$$

2. 6. Stability of free CCMN and CDSCM in Physiological Conditions

The stability of the compound in different pH is different. The stability of free CCMN and CDSCM were analyzed in PBS buffer pH 7.4 for a specific incubation period at 37 °C, taken absorption by UV–vis spectrophotometer at 427 nm. The change of absorbance in the physiological condition of both compounds was noted and plotted graphically.[29]

2. 7. CCMN Release Study from CDSCM

In CDSCM, CCMN is conjugated with CHT through pH-sensitive succinyl ester bonds. The cumulative releases of CCMN from CDSCM were measured in PBS buffer pH 5.0 and 7.4. A fixed quantity of CDSCM (10 mg) was dispersed in each 10mL of PBS buffer pH 5.0 and 7.4 solutions. All those solutions were taken into two separate dialysis bags and transferred into 90 mL respective buffer solution containing beakers. Those were incubated at 37 °C for 7 days with moderate shaking. During the incubation period, with an increasing time interval, 2 mL of the sample was withdrawn from each beaker and replaced with the respective buffer.[30] A UV-vis spectrophotometer analyzed the concentration of CCMN at 427 nm.

2. 8. Blood Compatibility

A hemolysis study monitored the hemocompatibility of CDSCMs using a blood sample obtained from a local blood bank. RBCs were separated from the blood sample by centrifugation at 2000 rpm for 5 min. The collected RBCs were washed three times in PBS buffer. The stock RBC solution was made by combining 100 µL of washed RBC with 10 mL of PBS (pH 7.4) buffer. To determine the hemoglobin release from RBC by CDSCM, 100 µL of stock RBC solutions were subjected to 100 µL different concentrations of CDSCM ranging from 0.5 to 2 mg/mL for 30 min at 37 °C. Then, all those solutions were centrifuged separately at 1500 rpm for 5 min, and the supernatant was taken for UV–visible absorbance at 541 nm.[31,32] PBS buffer pH 7.4 solution was utilized as a negative control, and distilled water as a positive control. The hemolysis percentage (Hp%) of CDSCM will be determined using the equation shown below:

$$Hp\% = \frac{As-An}{Ap-An} \times 100 \quad (2)$$

Where A_S = absorbance of the sample, the absorbance of the PBS buffer = $A_{n,}$ and absorbance of distilled water = A_p. All the readings were taken in triplicate.

2. 9. *In-vivo* Experimental Protocol

2. 9. 1. Experimental Animals

For the *in vivo* antidiabetic activity study, male Balb/C mice weighing about 25–30 g were obtained from Chakraborty Enterprises (North 24 Parganas PIN-743312 West Bengal), registered breeders.[33,34] Before the start of experiments, they were kept for seven days to adjust standard laboratory conditions with a standard diet according to protocols. This experiment followed the guidelines of the "Institutional Animal Ethics Committee (Registration number: 1805/GO/Re/S/15/ CPCSEA)", Jadavpur University, India (Approval of project proposal No: JU/IAEC-22/30), throughout the study, followed the National Institute of Health (NIH) recommendations.

2. 9. 2. Experiment Design of *In vivo* Study

A total of 30 Animals were taken and equally divided into five groups. Group I: Non-diabetic control animals (NDC) received a high fat-containing regular diet. Group II: Diabetic control (DC) received a high fat-containing regular diet with a single dose of diabetic inducer. Group III: Diabetic control free CCMN (DC-FCUR) received a high fat-containing regular diet with a single dose of diabetic inducer and treated orally with free CCMN at 100 mg/kg body weight for 21 days. Group IV: Diabetic control drug-containing nanoparticle (DC-DCN) received a high fat-containing regular diet with a single dose of diabetic inducer and treated orally with CDSCM equivalent to 100 mg/kg CCMN payload for 21 days. Group V: Diabetic control standard drug (DC-SD), which received a high fat-containing regular diet with a single dose of diabetic inducer and treated orally with 2mg/kg b.w. glibenclamide for 21 days.

2. 9. 3. Induction of Type-II Diabetes Mellitus

To induce Type-II diabetes mellitus, a single intra¬peritoneal injection of STZ (45 mg/kg to overnight fasting animals) followed by a 110 mg/kg intraperitoneal injection of nicotinamide after 15 min.[35–37] both solution was prepared separately by dissolving in citrate buffer pH 4.5 and saline solution, respectively. Non-diabetic control (Group I) animals were injected with saline instead of STZ. FBG levels of all animals were measured by an accu-check glucometer (Roche Diagnostics) on alternate days. Animals with FBG levels ≥ 200 mg/dl for three consecutive days after STZ injection were considered diabetic animals, and animals with blood glucose levels ≤ 145 mg/dl were considered non-diabetic animals and were excluded from the experiment.

2. 9. 4. Sampling of Blood to Estimate FBG Level

Blood samples were collected by pricking the tail and then gently milking it with warm water to evaluate the FBG level of each animal. The direction of milking was from the body side to the tail tip to enhance bleeding. One drop of blood was placed on a strip of the accu-check glucometer to take blood glucose levels, and it was done in duplicate to ensure the consistency of glucometer readings.[38]

2. 9. 5. Measurement of Body Weight

Every four days, the body weight of each animal in each group was measured. The variation in weight was documented. After 21 days, the liver weight of each animal was also recorded.

2. 9. 6. Estimation of Biochemical Parameters Level

For estimating the biochemical parameters, the blood of all animals was collected under mild anesthesia through cardiac puncture on the 21st day of the study. Blood samples were centrifuged for 15 min at 4000 rpm in a cooling centrifuge. Serums were correctly leveled and stored at –80 °C for further analysis. Auto-analyzer (USA) and ELISA kits for estimating the level of a lysosomal enzyme like alkaline phosphatase (ALP) (rAPid Alkaline Phosphatase; Roche), acid phosphatase (ACP) (CS0740, Sigma Aldrich), lipid profile components like HDL, LDL, serum triglycerides (TGL), total serum cholesterol, liver-specific enzymes like serum glutamate oxaloacetic transaminase (SGOT), serum glutamate pyruvic transaminase (SGPT), Hemoglobin A1c (HbA1c) (CS0740, Sigma Aldrich) and serum uric acid.[38,39]

2. 9. 7. Carbohydrate Metabolizing Enzymes Estimation

To estimate the level of hexokinase (HK), glucose-6-phosphate dehydrogenase (G6PD), and lactate dehydrogenase (LDH) parameters in the pancreas, liver, and kidney, all animals were euthanized with thiopental sodium after 21 days of treatment. Those tissues (0.3 g) were taken separately and homogenized in 3 mL of 0.01M Tris-HCL centrifuged at 10000 rpm for 20 min at 4 °C. Supernatants were treated with the corresponding colorimetric assay kits for HK, G6PD, and LDH.[39,40]

2. 10. Statistical Analysis

For the statistical analysis, all the readings were taken more than two times, standard deviation (SD) was calculated from obtained data, and the actual value of the readings was represented as mean ± SD, were it possible. For the statistical processing of obtained results, one-way analysis of variance (ANOVA) with P-value < 0.05 was used to know the groups/category significant changes in another statistical tool, like a student t-test. Different software like Origin Pro 9.0 and GraphPad Prism 6.0 are used for the graphical representation of statistically processed data.

3. Results

The primary objective of our investigation was to synthesize the CHT-CCMN conjugate, which was subsequently synthesized and characterized using various instrumental methods. After confirming the synthesis of the conjugate, it was found that the conjugate was freely soluble in an aqueous and non-aqueous solvent. The tri-molecular conjugated polymer-prodrug, consisting of a hydrophilic polymer and hydrophobic drugs, can enhance aqueous solubility, improve drug targeting, prevent drug resistance, and minimize the toxic effect of the desired drug.[41,42] This study used CHT as a hydrophilic polymer, CCMN as a hydrophobic drug, and succinic anhydride as a bi-molecular pH-sensitive linker. CCMN, when conjugated with CHT via a succinyl ester link, creates an amphiphilic polymer-prodrug known as CHT-di (SUC-CCMN). This prodrug self-assembles into nano micelles when placed in an aqueous media. CHT has several hydroxyl groups that have the capability to form bonds with multiple SUC-CCMN molecules, enabling the transportation of CCMN for drug delivery purposes.

For the formation of CHT-di(SUC-CCMN) prodrug conjugate, CCMN refluxes with succinic anhydride in the presence of pyridine to form SUC-CCMN, which consists of a carboxylic acid group that can further react with a hydroxyl group of CHT to form an ester bond by a condensation reaction in the presence of pyridine, as shown in Figure 1**.** The FT-IR spectrum of CCMN clearly shows characteristic peaks of phenolic O-H stretching at 3507 cm^{-1}, for aromatic moiety C=C stretching peak at 1625 cm^{-1}, benzene ring stretching vibrations peak at 1596 cm^{-1}, for C=O and C=C vibrations peak at 1504 cm^{-1}, for C-H bending vibrations of olefinic (>C=C<) bond peak at 1424 cm^{-1} and for stretching vibrations of the aromatic C-O bonding peak at 1276 cm^{-1} could identify CCMN (Figure 2).[43,44] The FT-IR spectrum of SUC-CCMN shows a peak for phenolic O-H stretching at 3505 cm^{-1}, a peak for aryl

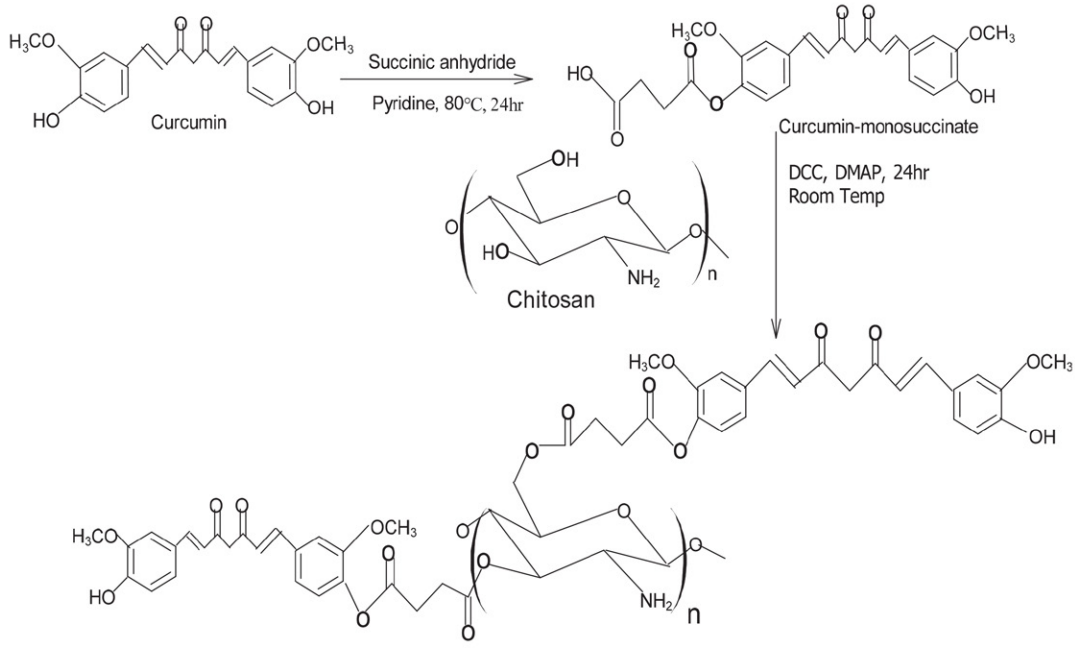

Figure 1. The schematic reactions for synthesizing SUC-CCMN and CHT-di(SUC-CCMN) conjugate.

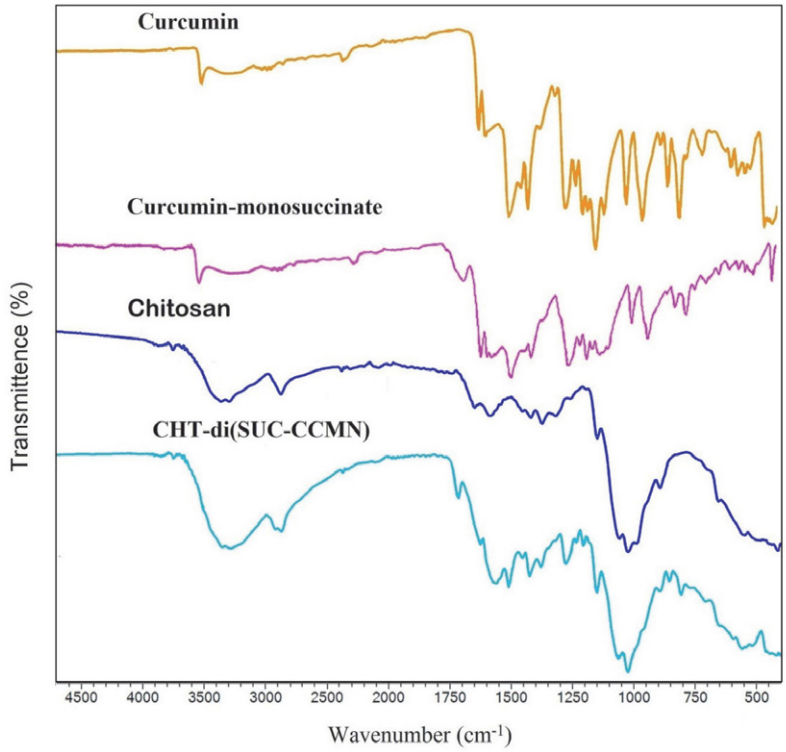

Figure 2: FTIR spectra Curcumin, Curcumin-mono succinate, Chitosan, and CHT-di(SUC-CCMN)

(C-H) stretching at 2942 cm^{-1}, peaks for C=O stretching frequencies of a conjugated succinic acid moiety at 1697cm^{-1}, peak for C=C of CCMN at 1627 cm^{-1}, a peak for stretching frequencies of C=O and C-O (enol) groups of CCMN moiety at 1510cm^{-1} and 1281 cm^{-1}. The peak at 1028 cm^{-1} is attributed to the stretching frequencies of C-O-C. The presence of prominent peaks at 3505 cm^{-1}, 1697 cm^{-1}, and 1510 cm^{-1} corresponding to the –OH, C=O , and C-O bands, respectively, represent the successful conjugation of CCMN to SUC.[25] The FT-IR spectrum (Figure 2) of CHT-di(SUC-CCMN) conjugate exhibits a new peak at 1735 cm^{-1} corresponding to the stretching frequency of the C=O group and a peak at 1510 cm^{-1} corresponding to the C-O (enol) bands stretching frequencies in addition to peaks exhibited by CHT and SUC-CCMN, those peaks represent the existence of newly formed ester bond between CHT and SUC-CCMN.[42] The FTIR analysis demonstrates that the procedure begins with the reaction of CCMN and succinic anhydride, which results in the formation of SUC-CCMN with a reactive carboxylic acid group. The FTIR spectrum reveals that this acid group interacts with the hydroxyl group of CHT in the presence of pyridine to form an ester bond, leading to CHT-di(SUC-CCMN) prodrug-polymer synthesis. The enhanced solubility of curcumin in CHT-di(SUC-CCMN) could potentially be attributed to the formation of a tenuous hydrogen bond between the carbonyl group (C=O) in curcumin and the hydroxyl group in chitosan.[45]

To assure the formation of the conjugated structure of CHT-di(SUC-CCMN), CHT, CCMN, and SUC-CCMN were initially analyzed through ^{1}H-NMR spectroscopy. In Figure 3, it was observed that protons of CCMN show characteristic peaks between 5.4–9.4 ppm;[45,46] CHT shows its distinct peaks between 3.0–4.6 ppm for the protons of β(1–4)-D-glucosamine units,[47] including peak at 1.3 ppm for the presence of acetylated chitosan impurities; SUC-CCMN shows peak at 2.2 and 2.4 ppm for protons of –CH_2-CH_2- (Succinyl moiety) including the peaks at 9.4 and 12.5 ppm for the –OH proton of CCMN and succinyl moiety respectively in addition to peaks of CCMN. CHT-di(SUC-CCMN) conjugate exhibits its peaks consisting of characteristic peaks of CHT (3.0–4.6 ppm), CCMN (5.4–9.4 ppm), and succinyl (2.0 and 2.5 ppm) moiety excluding the peaks 12.5 ppm of succinyl moiety –OH proton were demonstrated the successful synthesis of desire conjugate.[46,48] Analysis of the CHT-di(SUC-CCMN) conjugate by ^{1}H-NMR confirmed its successful synthesis. The characteristic peaks of CCMN, CHT, and SUC-CCMN were evident in their respective spectra. Notably, the conjugate's spectrum displayed peaks from all constituents except the -OH proton of the succinyl moiety. This absence and the presence of all other expected peaks strongly supported the construction of the designed conjugate.

To know the presence of CCMN in the CHT-di(-SUC-CCMN) conjugate, CCMN and CHT-di(SUC-CCMN) were analyzed by UV–vis and fluorescence spectrometer. Both CCMN and CHT-di(SUC-CCMN) conjugate show peak Uv-absorbance at 427 nm (Figure 4a, 4b), but conjugate shows a broader peak than the CCMN peak. The fluorescence emission spectral peak (the excita-

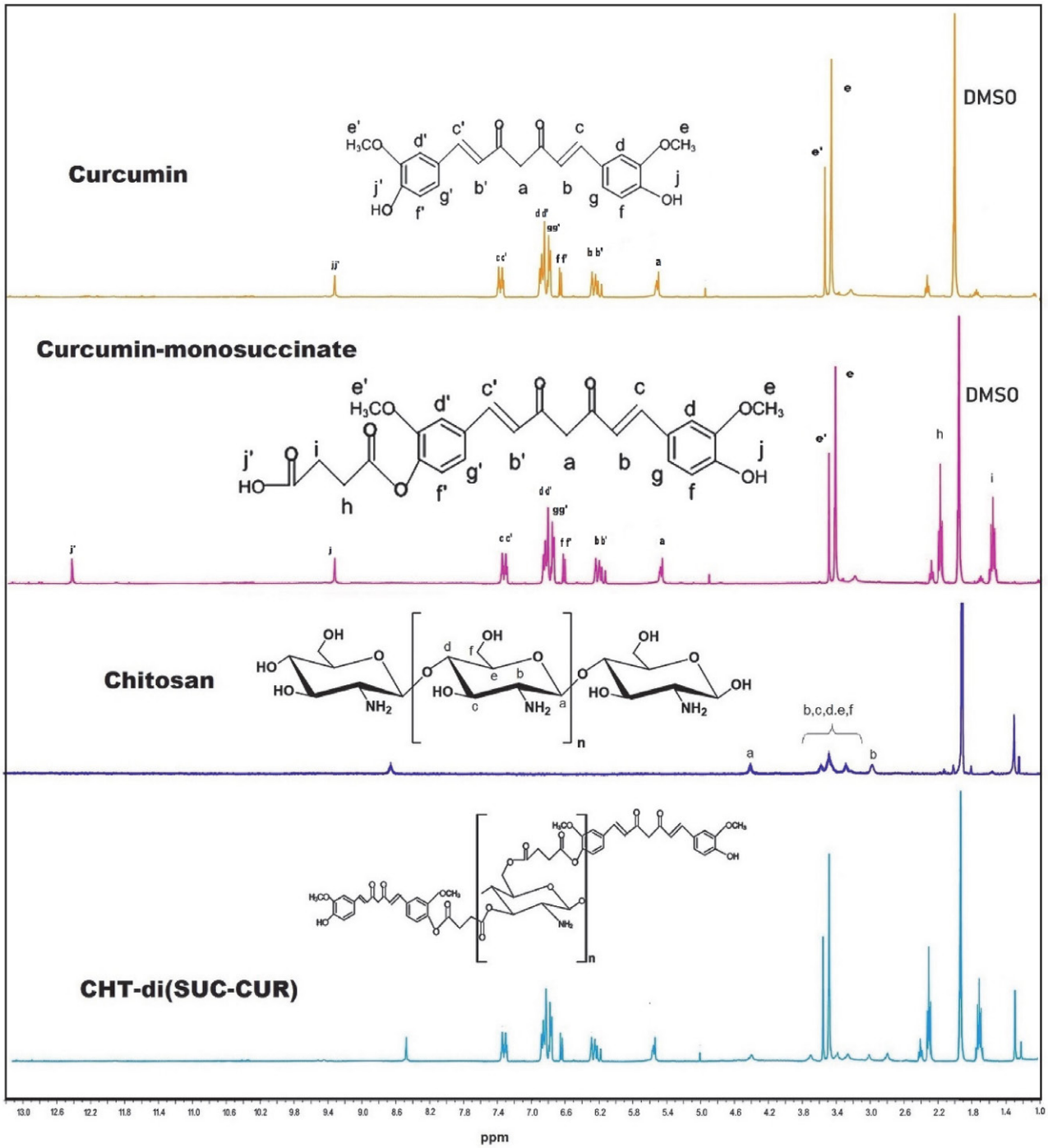

Figure 3: ^{1}H-NMR of spectra of Curcumin, Curcumin-monosuccinate, Chitosan, and CHT-di(SUC-CCMN)

tion wavelength 427 nm) of CCMN and CHT-di(SUC-CCMN) shows at 550 nm and 522 nm, respectively, which help to conclude the formation of the conjugation within CHT and CCMN.[49]

The CHT-di(SUC-CCMN) conjugate consists of a free hydroxyl group containing the CHT moiety, which is the hydrophilic part. The CCMN moiety, the hydrophobic domain, jointly helps the amphiphilic to self-assemble into micelles (CDSCM) in an aqueous medium where the hydrophobic part forms the core and the hydrophilic part remains outside of the micelle. Critical micelle concentration (CMC) signifies a concentration at which the amphiphilic polymeric compound can self-assemble into micelles in the solvent. The CMC of CDSCM was determined by employing the self-quenching agent pyrene as the fluorescence probe in an aqueous medium, and it helps to produce fluorescence for the presence of a lipophilic part of the micellar core. The intensity ratio of pyrene's (I335/I332) peaks depends on the medium's polarity.[50,51] The fluorescence intensity changed rapidly when pyrene transited

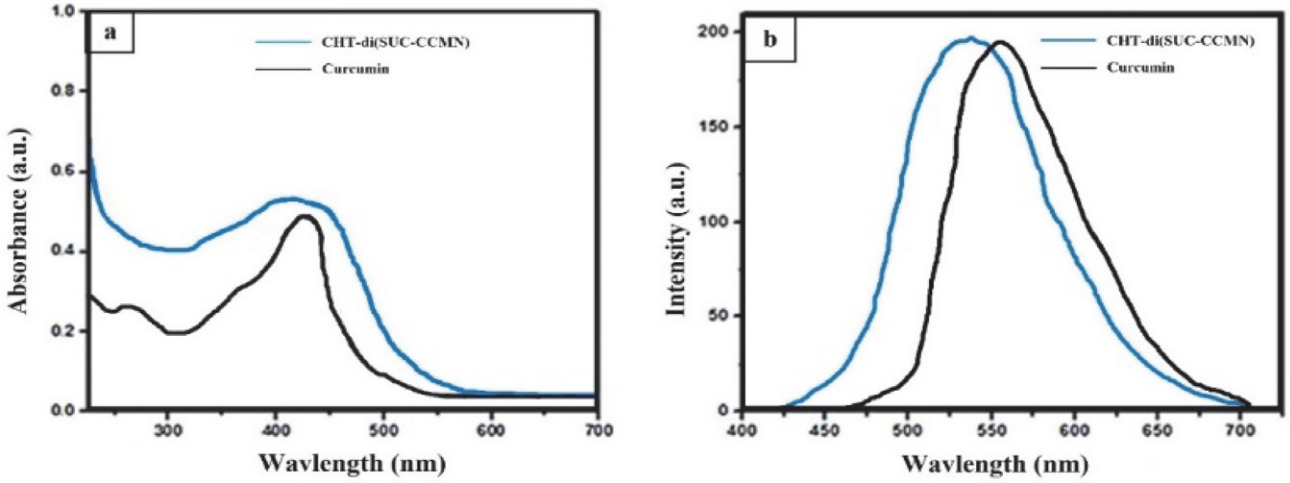

Figure 4: (a) UV–vis and (b) fluorescence spectra of CCMN and CHT-di(SUC-CCMN) conjugate

from hydrophilic media to the lipophilic core of CDSCM. Plotting the logarithm concentration of conjugate vs. intensity ratio constructs two straight lines intersecting at a point called CMC, which was 0.4644 mg/mL (Figure 5A). The lower CMC values signify its stability, prolonging blood circulation and accessibility to the drug's targeting.[52]

The hydrodynamic particle size and zeta potential of the CDSCM were determined by dynamic light scattering (DLS). The hydrodynamic particle size distribution of CDSCM is shown in Figure 5C, and zeta potential is shown in Figure 5B. It was observed that micelles were about 57± 6 nm in size from and polydispersity index was found to be 0.19 Figure 5C**.** The zeta potential of CDSCM was measured to be –34.8 mV, suggesting a significant negative charge. This negative charge is caused by the presence of unbound hydroxyl (-OH) groups in the glucosamine units of the CHT moiety on the surface of CDSCM. This accumulation of hydroxyl groups results in the formation of a highly negatively charged CDSCM surface. This negative change serves to maintain the CDSCM's stability. Higher negative surface charges repel each CDSCM from the other, thereby reducing nano-micelle accumulation.[53] The morphology of CDSCM was also determined through SEM and TEM (Figures 5D, 5E). Figure 5D indicates that CDSCM were roughly spherical and mostly uniform in size. The shape of the particle is distinguishable. For better

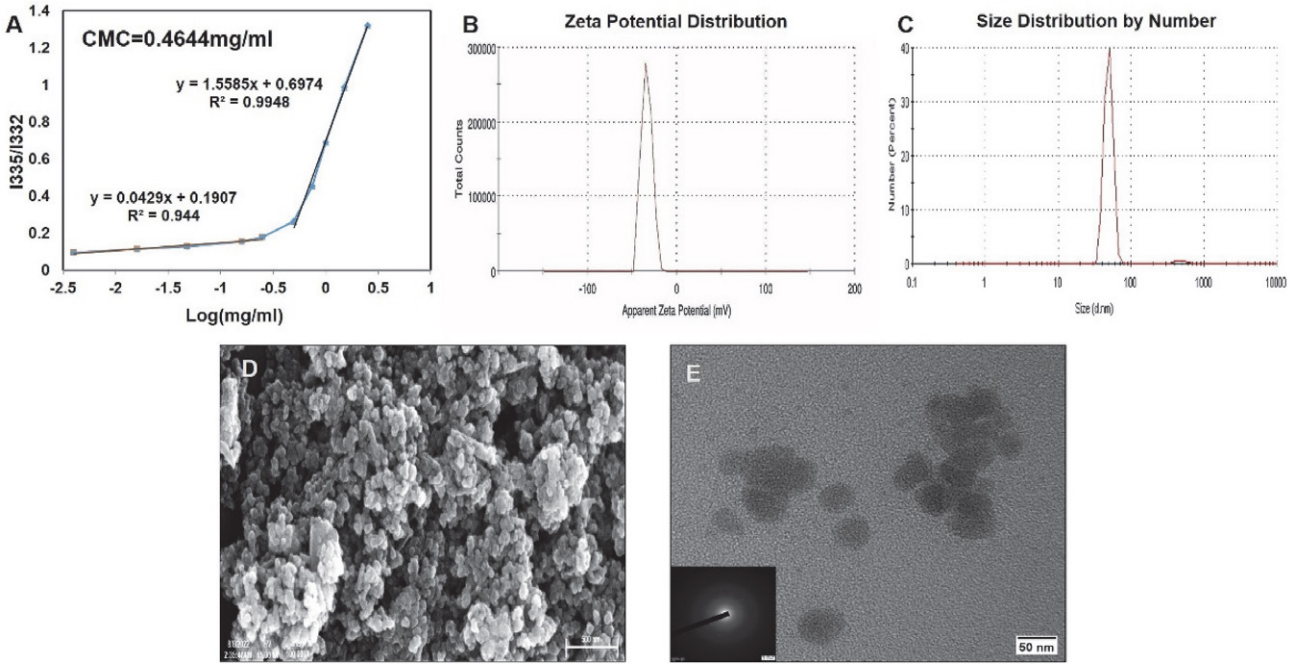

Figure 5. (A) CMC of CHT-di(SUC-CCMN) conjugate; (B) Zeta potential of CDSCM; (C) Particle size distribution of CDSCM; (D) FE-SEM Image of CDSCM; (E) TEM Image of CDSCM

morphological evaluation, another microscopic (TEM) study was done. Figure 5E shows that the CDSCM are spherical in shape and within the size range of 50 nm ±15 nm. The selected area electron diffraction (SAED) pattern in the bottom left corner of the TEM image shows that the CDSCM samples don't have any crystalline particles. Based on the data shown in Figure 5, it is evident that the CDSCM was produced with precision, exhibiting higher zeta potential and smaller particle size. The size of the Nano micelles seen in the TEM analysis was primarily consistent with the hydrodynamic sizes of the Nano micelles determined by DLS analysis. Based on the aforementioned results, it is obvious that the CDSCM has the potential for use in the applications described above.

In physiological pH, the stability of free CCMN and CDSCM was compared. The stability of free CCMN and CCMN in CDSCM was evaluated at pH 7.4. The stability of free and formulated drugs at physiological pH is critical in drug delivery investigations. PBS was used to make a highly concentrated solution of free CCMN and CDSCM (pH 7.4). Absorbance was measured at 427 nm using a UV-vis spectrophotometer at set intervals from both solutions up to a particular period. The percentage of degraded compounds for both compounds was calculated and presented in Figure 6a. It was observed that free CCMN was about to degrade entirely after 8 h, while more than 90% of CCMN in CDSCM was still present at the same time. As a result, conjugated CCMN exist in CDSCM and are much more stable than free CCMN. CCMN micelles developed by conjugation of CCMN with CHT significantly improve CCMN stability (Figure 6a).

The CCMN release pattern from CDSCMs was studied at physiological pH 7.4 and acidic pH 5, as shown in Figure 6b. It was observed that 97% of CCMN was released from CDSCM within 7 days in an acidic (pH 5) condition, whereas 49% of CCMN was released from CDSCM within the same time in a physiological pH 7.4 condition. The complete drug release was observed after 8 days of study in acidic pH 5, and it was observed that the CCMN presence in the CDSCM was about 36.8±2%, calculated using Equation 1. The higher release rate of CCMN in the acidic medium than in the basic medium is due to the acid-catalyzed hydrolysis of the ester linkage.[54,55] As a result, the rate of CCMN release in physiological pH is lower than in acidic

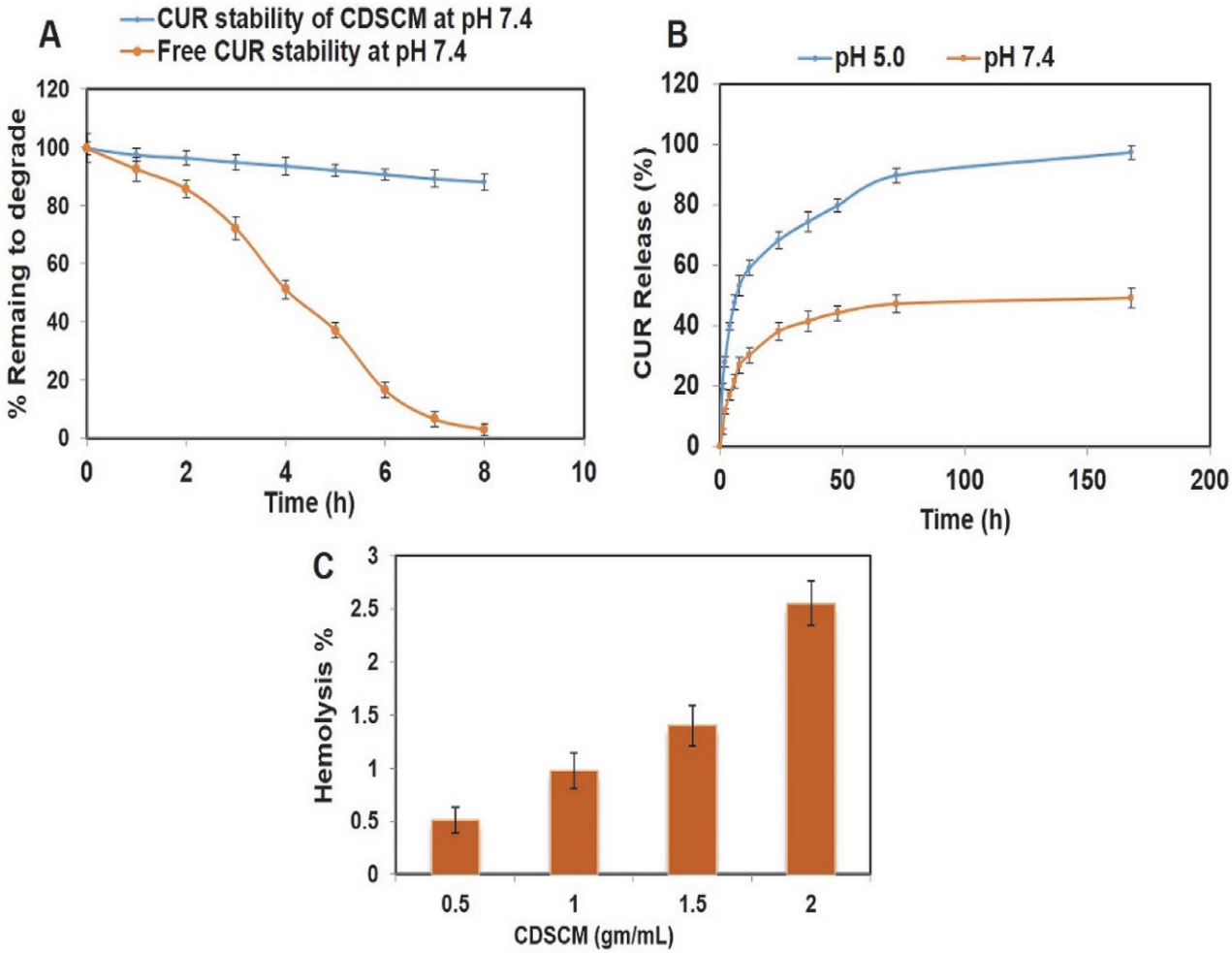

Figure 6: (a) Stability studies of CCMN and CDSCM, (b) Release profiles of CCMN from CDSCM under different conditions, and (c) Hemocompatibility assay of CDSCM

pH. Thus, CDSCM is applicable for sustained CCMN delivery and helps overcome first-pass metabolism.[56,57] The mechanism of drug release from CDSCM may depend on the release pattern in specific pH mediums. Release kinetic models were established for both acidic and basic medium, revealing that in the acidic medium, the release followed the first-order kinetic model, identified by its highest R2 value of 0.943 (Table 1). This indicates that the rate of drug release decreases exponentially over time as the drug concentration in the delivery system decreases. This release mechanism likely involves diffusion through a matrix or dissolution of the drug from a reservoir. The acidic pH may facilitate this diffusion by swelling the nanomicelles and breaking the ester bond, releasing CCMN into the medium. On the other hand, at pH 7.4, a basic medium, CCMN was released from the CDSCM following the Higuchi release kinetic model with the highest R2 value of 0.802 suggests the release of CCMN diffusion through polymeric matrix.

Table 1: The release kinetics from the CDSCM

pH of the medium	pH 5	pH 7.4
	R^2 Value	
Zero Ordar Model	0.5676	0.516
1st Order model	0.9432	0.581
korsmayar peppas model	0.5498	0.722
Higuchi model	0.8371	0.802
Hixson Crowell model	0.8313	0.559

Hemocompatibility is an essential criterion for evaluating compatibility regarding hemoglobin release from RBC by drug-loaded nanoparticles for the safety and biocompatibility of nano-drug formulation. Drugs associated with nanoparticles can damage the RBC partially or fully. A hemolytic study determined the percentage of hemoglobin released from RBC. After CDSCM and RBCs interact, hemoglobin from the damaged RBCs could be released. A UV-visible spectrophotometer measured the absorbance of hemoglobin[30], and was calculated in percentage. After sufficient time of incubation of CDSCMs with RBC, it was observed that around 2.5% of hemoglobin was released at the highest concentration of CDSCM (2mg/mL), as shown in **Figure 6c**. This signifies that our nano-formulation of CDSCM is compatible with RBC and blood, so these nano micelles are also applicable in intravenous administration.[58–60]

After three days of diabetic induction, it was observed that most of the animals had FBG levels of 284±9 mg/dL. Consider those animals as diabetic animals, and those with fasting blood glucose levels ≤145 mg/dL were not considered for the study. After the diabetic induction, a gradual body weight loss was observed (Figure 7C) in group II, but a slight increase in body weight in group III animals was observed. A significant increase in body weight of group-IV (CDSCM receiving group) was observed compared to group-V (diabetic control/standard drug) animals. The findings above highlight the significance of inducing diabetes about body weight and the possible contribution of CDSCM in addressing the alterations in body weight linked to diabetes.

The FBG level of overnight-fasted animals was measured every four days. A gradual increase in FBG level was observed (Figure 7A) in group II, but a gradual decrease in FBG level was observed in groups III, IV, and V. The non-diabetic control group I did not see any substantial alteration in fasting blood glucose (FBG) levels. The decrease in FBG level in users of CDSCM in group IV was substantially greater than in recipients of the conventional medicine in group V. The maximum decrease in blood glucose level was observed (Figure 7B) after 21 days of treatment in CDSCM recipients in group IV. The changes in

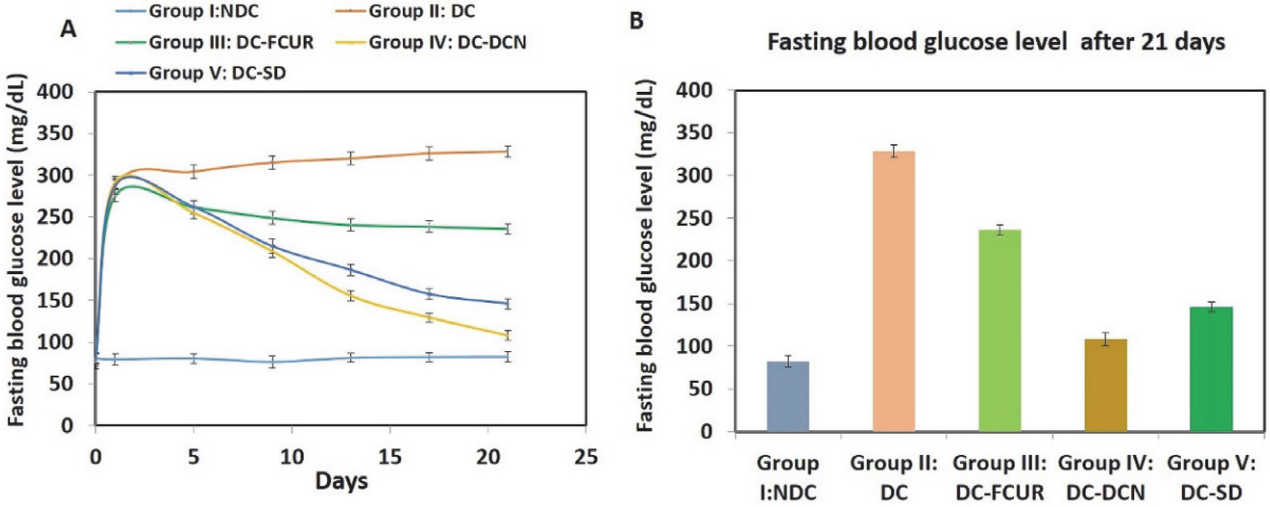

Figure 7: (A) Fasting blood glucose level after 21 days. (B) Change of body weight in 21 days.

Table 2. Biochemical parameters after 21 days of treatment

Parameter	Group I: NDC	Group II: DC	Group III: DC-FCUR	Group IV: DC-DCN	Group V: DC-SD
HbA1c (%)	5.70 ± 0.23	11.03 ± 0.31	8.55 ± 0.22	6.04 ± 0.20	6.89 ± 0.16
Serum creatinine (mg/dL)	0.81 ± 0.05	1.51 ± 0.04*	1.11 ± 0.03*	1.01 ± 0.04	1.17 ± 0.04
Serum uric acid (mg/dL)	3.10 ± 0.40**	5.30 ± 0.20*	4.12 ± 0.31**	3.62 ± 0.27*	4.51 ± 0.52
Serum cholesterol (mg/dL)	83.0 ± 1.1**	157.1 ± 1.7**	109.0 ± 1.2**	91.1 ± 0.9*	124.0 ± 2.1*
Serum triglycerides (mg/dL)	90.0 ± 1.2*	156.3 ± 1.9**	121.7 ± 2.2**	95.0 ± 1.4*	111.0 ± 3.1**
SGPT (IU/L)	70.0 ± 1.1	170.6 ± 3.8**	92.6 ± 3.1**	72.0 ± 1.0	80.1 ± 1.0
SGOT (IU/L)	121.2 ± 2.3**	255.3 ± 4.4**	200.3 ± 2.3**	136.2 ± 2.4**	140.3 ± 2.3**
HDL cholesterol (mg/dL)	51.1 ± 1.3**	32.1 ± 2.1**	38.5 ± 1.4**	44.5 ± 1.5*	43.1 ± 1.4*
LDL cholesterol (mg/dL)	21.0 ± 1.3*	88.8 ± 2.4**	44.2 ± 1.5*	33.5 ± 1.6*	61.8 ± 1.7**
ALP (IU/L)	170.0 ± 1.5**	233.0 ± 3.1**	203.1 ± 2.5**	185.1 ± 2.2**	211.1 ± 2.2**
Hexokinase (U/mL)	1.65 ± 0.11	0.25 ± 0.03	1.04 ± 0.12	1.47 ± 0.21	1.14 ± 0.32
G6PD (U/mL)	22.6 ± 1.4**	85.4 ± 2.1**	62.6 ± 2.5**	29.0 ± 2.8**	38.8 ± 1.8*
LDH (U/mL)	13.6 ± 0.7*	26.8 ± 1.4**	20.8 ± 0.8*	15.8 ± 0.8	17.7 ± 1.0

Data represent mean ± S.D (n = 3). $^{**}p < 0.05$; $^{*}p < 0.01$.

FBG concentrations reflect the effect of interventions on glucose metabolism. The observed reduction in fasting blood glucose (FBG) levels across groups III, IV, and V provides evidence of the potential efficacy of these therapies in managing diabetes. The observed difference in the rate of reduction in fasting blood glucose (FBG) level between group IV (the group receiving the CDSCM treatment) and group V may be attributed to the unique mechanism of action of CDSCM. The faster rate of decrease in FBG levels in the CDSCM group (IV) compared to the conventional drug group (V) demonstrates the potential of CDSCM as a promising strategy for controlling glucose in diabetes management.

Biochemical parameters of all the experimental animals were measured on the 21st days after induction of diabetes and before induction of diabetes (Table 2), which shows that, the levels of HbA1c, serum creatinine, serum uric acid, serum cholesterol, serum triglycerides, SGPT, SGOT, HDL, LDL, ALP, Hexokinase, G6PD, and LDH have no unexpected changes in the non-diabetic control group I but significant increases (except for HDL and Hexokinase) in the group II. Mild increases were observed in the group III animals, and significant inverse phenomena were observed in groups IV and V. Hexokinase and HDL remarkably increased in CDSCM-receiving group IV compared to diabetic control group II and standard drug-receiving group V. The consistency of high FBG levels in the animal group indicates high glycated hemoglobin (HbA1c).[61] After 21 days, the HbA1c levels of animals in group IV treated with CDSCM were lower. This decrease in HbA1c reflects the improved blood sugar management made possible by the administration of CDSCM. In addition, the investigation revealed a correlation between skeletal muscle mass and creatinine levels. As body weight decreased, creatinine levels increased, associated with an increased risk of type II diabetes.[37] Notably, animals treated with CDSCM had significantly lower creatinine levels than those treated with free CCMN and the standard drug. This phenomenon suggests that CDSCM can potentially reduce the incidence of type II diabetes. The uric acid levels in the blood have emerged as valuable markers for various diseases, including stroke, hypertension, cardiac complications, and diabetes.[38,62] CDSCM also decreased serum uric acid levels, suggesting a potential improvement in the associated health risks. The investigation also explored diabetic dyslipidemia, a disorder characterized by abnormal lipid levels, including cholesterol, triglycerides, and distinct lipoprotein fractions. This condition is closely associated with type II diabetes.[38,63] Remarkably, animals treated with CDSCM exhibited fewer lipid abnormalities than the control group, indicating a potential function for CDSCM in diabetic dyslipidemia management.

The enzymatic focus of the investigation was on hexokinase, an enzyme with a negative correlation to diabetes. Notable was the increase in hexokinase levels in animals treated with CDSCM, which may have contributed to enhanced glucose metabolism. G6PD, an enzyme relevant to type II diabetes, is typically characterized by decreased tissue levels that contribute to increased blood levels due to metabolic alterations. Nonetheless, administration of CDSCM decreased blood levels of G6PD, indicating a return to metabolic equilibrium. Type II diabetes includes a variety of metabolic disorders involving enzymes such as hexokinase, G6PD, LDH, SGPT, SGOT, and ALP, among others.[64,65] These enzymes exhibit altered concentrations in associated tissues and blood. The CDSCM treatment significantly decreased the blood levels of these enzymes compared to other treatments, according to the study's findings. Our studies amalgamate chemical synthesis and nanotechnology to increase bioavailability and deliver poorly water-soluble, highly degradable phytochemical curcumin in treating type II diabetes.

4. Discussion

In this study, the CHT-CCMN conjugate was synthesized successfully. The polymer prodrug molecule was then converted to the nano micelles form, a transformation that not only demonstrates the versatility of our research but also its potential for practical applications. The FTIR and NMR evaluation confirms that the polymer and the drug curcumin were chemically conjugated, proving our success. It was discovered that the conjugate was readily soluble in both an aqueous and an organic solvent, a characteristic that enhances its potential applications. After conjugation, the lipophilic compound CCMN and the hydrophilic polymer CHT form an amphiphilic conjugate, a unique feature that further enhances its potential. In an aqueous environment, the amphiphilic conjugate self-assembled into a micelle at a concentration of 0.4644 mg/mL, a finding that underscores its stability and accessibility. Due to the low CMC value, the nano micelles signify its stability, prolonging blood circulation and making it accessible for the drug's targeting. This feature in stills confidence in its potential for drug delivery systems.[66] The nano micelles exhibited an average hydrodynamic size range of 57 ± 6 nm, as measured by a zeta seizer. The majority of the particles were concentrated within a very limited range. The micelle's polydispersity index was found to be 0.19, which signifies the homogeneity of micelle size. From these, it is understood that micelles are not aggregated and create a proper dispersion in aqueous medium. The zeta potential of the micelle was –34.8 mV, which suggests that the micelles' surface are highly negatively charged, which could help them repel each other, accumulate into the aqueous medium, and provide better stability. These negative surface charges and smaller sizes may help micelles escape reticuloendothelial system internalization.[67,68] The SEM and TEM examination were conducted to morphologically characterize the CDSC micelles by microscopic inspection. The scanning electron microscope (SEM) picture revealed that the lyophilized powder of the CDSCM formed a nearly spherical and aggregated thin film. However, in order to get a precise comprehension, these micelles are examined using transmission electron microscopy (TEM), revealing their spherical shape and particle sizes ranging from around 50±10 nm. This provides the similarity with the hydrodynamic size of the prepared nano micelles. The morphological evaluation of the nano micelles provides a clear understanding of the size and shape of the nano micelles, which is acceptable for the *in vivo* characterization, and better homogeneous biodistribution will occur.[69]

The degradation study found that at physiological pH 7.4, more than 90% of CDSCM remained to degrade within eight hours. In comparison, free CCMN degraded almost entirely under the same conditions. This contrast emphasizes the stability of CDSCM to maintain its structural strength in the physiological environment. Moreover, CDSCM showed a longer drug release duration at the physiological pH compared to the medium's acidic pH level. This extended drug release profile presents the potential for achieving controlled drug delivery by assuring a constant drug release from micelles. In addition, CDSCM's ability to release drugs under acidic pH conditions enables its use in various medical conditions where drug release is required in acidic environments, thereby expanding its versatility in drug delivery systems. [70,71] The effect of fasting blood glucose (FBG) levels on animals treated with CDSCM was significantly greater than that of unbound CCMN and the standard drug glibenclamide.

Interestingly, the effects of CDSCM on body weight in diabetic-induced animals were found to be less severe than those of free CCMN and the conventional drug. The difference suggests that CDSCM may have a more targeted and potent effect on glucose regulation, potentially allowing for a more targeted method of treating elevated FBG levels. In addition, the consistent elevation of FBG levels in these animals suggests the presence of an elevated amount of glycated hemoglobin (HbA1c), highlighting the chronic nature of the diabetic condition under study.[72] After 21 days, HbA1c levels were significantly reduced in animals treated with CDSCM, according to this research. This correlation can be explained by the direct relationship between skeletal muscle mass and creatinine levels, where creatinine levels progressively increase as body weight decreases, increasing the risk of type II diabetes.[73] Notably, the creatinine levels of CDSCM-treated animals were substantially lower than those of CCMN-free and standard-drug-treated animals. Notably, treatment with CDSCM increased hexokinase enzyme levels, which may have improved glucose metabolism. Glucose-6-phosphate dehydrogenase (G6PD) is an additional enzyme associated with type II diabetes.

Nevertheless, administration of CDSCM reduced blood glucose-6-phosphate dehydrogenase (G6PD) levels, suggesting a restoration of metabolic equilibrium. Several metabolic disorders involving enzymes such as hexokinase, G6PD, LDH, SGPT, SGOT, and ALP, which exhibit altered concentrations in tissues and blood, are associated with Type II diabetes. Compared to other interventions, the CDSCM treatment substantially decreased blood enzyme levels. The above results could indicate that CDSCM restores the normal metabolic process in group IV more efficiently than in other diabetic groups. The effect of FBG on CDSCM capacity was significantly more than that of accessible CCMN and standard drug glibenclamide, and the impact on body weight of CDSCM-treated animals was less than that of free CCMN and standard drug-treated diabetic induced animals.

5. Conclusion

In this study, we have successfully synthesized a prodrug of chitosan-curcumin conjugate that self-assem-

bled in an aqueous environment as nano-micelles, where chitosan provided the hydrophilic outer backbone and curcumin the lipophilic core of the micelles. The chitosan di-succinyl curcumin micelles have curcumin in their backbone and entrap curcumin in their inner core, enhancing the solubility and stability of curcumin in many folds. Curcumin is sustainably released from micelles at physiological and acidic pH because there are ester bonds between chitosan and curcumin. The micelles play a pivotal role in declining the fasting blood glucose level and normalizing the related biochemical parameters of type II diabetic animals. The findings suggest that nano micelles have a notable effect in restoring the metabolic pathway that is disrupted in Type-II diabetes mellitus, as compared to both glibenclamide (the conventional treatment) and free curcumin. In future studies, these developments explore multidrug delivery in the form of conjugated prodrugs and entrapment in the micelle core. The amount of drug to be delivered can be increased as needed, prolonging the delivery time, and can be used for multiple other chronic biomedical conditions.

Author Contributions: Conceptualization: Sk Mosiur Rahaman and Ranu Biswas, Abimanyu Sugumaran.; Study execution, Data collection, Analysis, and interpretation of results: Sk Mosiur Rahaman, Ranu Biswas and Gouranga Dutta; Writing–original draft: Sk Mosiur Rahaman and Gouranga Dutta; Writing–review and editing: Sk Mosiur Rahaman, Ranu Biswas, Abimanyu Sugumaran, Mohamed M. Salem, Mounir M. Salem-Bekhit, Mohamed Abd El Rahman and Mohammed Gamal. Figures and Tables: Sk Mosiur Rahaman, Gouranga Dutta. All the authors have confirmed the manuscript for the submission proceedings.

Funding: The authors would like to extend their sincere appreciation to the Researchers Supporting Project Number (RSPD2024R986), King Saud University, Riyadh, Saudi Arabia.

Institutional Review Board Statement: The Institutional Animal Ethics Committee of Jadavpur University, Kolkata, India (JU/IAEC-22/30) approved the animal study protocol.

Data Availability Statement: Current study data are available from the corresponding author upon reasonable request

Acknowledgments: The authors are thankful to Head, Department of Pharmaceutical Technology, Jadavpur University, Kolkata, West Bengal, India.

Conflicts of Interest: The author declares that there is no financial or personal conflict of interest associated with the work reported in this paper.

6. Reference

1. QX. Zhang, E. Kupczyk, P. Schmitt-Kopplin, C. Mueller, *Drug Discov. Today.* **2022**, *27*, 103331. **DOI:**10.1016/j.drudis.2022.07.016
2. S. Park, H. Lee, W. Cho, H. G. Woo, H. Lim, S. Kim, S. Y. Rhee, D. K. Yon, *Obes. Rev.* **2024**, *25*, e13714. **DOI:**10.1111/obr.13714
3. N. Esser, S. Legrand-Poels, J. Piette, A. J. Scheen, N. Paquot, *Diabetes Res. Clin. Pract.* **2014**, *105*, 141–150. **DOI:**10.1016/j.diabres.2014.04.006
4. D. A. Domingo-Lopez, G. Lattanzi, L. H. J. Schreiber, E. J. Wallace, R. Wylie, J. O'Sullivan, E. B. Dolan, G. P. Duffy, *Adv. Drug Deliv. Rev.* **2022**, *185*, 114280. **DOI:**10.1016/j.addr.2022.114280
5. L. A. DiMeglio, C. Evans-Molina, R. A. Oram, *Lancet.* **2018**, *391*, 2449–2462. **DOI:**10.1016/S0140-6736(18)31320-5
6. S. E. Kahn, *Diabetologia.* **2003**, *46*, 3–19. **DOI:**10.1007/s00125-002-1009-0
7. Y. Li, W. Zhang, R. Zhao, X. Zhang, *Bioact. Mater.* **2022**, *15*, 392–408. **DOI:**10.1016/j.bioactmat.2022.02.025
8. W. Lu, F. Khatibi Shahidi, K. Khorsandi, R. Hosseinzadeh, A. Gul, V. Balick, *J. Food Biochem.* **2022**, *46*, e14358. **DOI:**10.1111/jfbc.14358
9. B. Salehi, Z. Stojanović-Radić, J. Matejić, M. Sharifi-Rad, N. V. Anil Kumar, N. Martins, J. Sharifi-Rad, *Eur. J. Med. Chem.* **2019**, *163*, 527–545. **DOI:**10.1016/j.ejmech.2018.12.016
10. A. Sugumaran, J. Sadhasivam, P. Gawas, V. Nutalapati, R. Pandian, S. Kumar Perumal, *Mater. Sci. Eng. B.* **2022**, *286*, 116047. **DOI:**10.1016/j.mseb.2022.116047
11. S. Fuloria, J. Mehta, A. Chandel, M. Sekar, N. N. I. M. Rani, M. Y. Begum, V. Subramaniyan, K. Chidambaram, L. Thangavelu, R. Nordin, et al. , *Front. Pharmacol.* **2022**, *13*, 820806. **DOI:**10.3389/fphar.2022.820806
12. N. Agrawal, M. Jaiswal, *Eur. J. Med. Chem. Reports.* **2022**, *6*, 100081. **DOI:**10.1016/j.ejmcr.2022.100081
13. V. Ruiz de Porras, L. Layos, E. Martínez-Balibrea, *Semin. Cancer Biol.* **2021**, *73*, 321–330. **DOI:**10.1016/j.semcancer.2020.09.004
14. Y. Zhong, C. Liu, J. Feng, J. Li, Z. Fan, *Exp. Ther. Med.* **2020**, *20*, 1856–1870. **DOI:**10.3892/etm.2020.8915
15. S. K. Jain, J. Rains, J. Croad, B. Larson, K. Jones, *Antioxid. Redox Signal.* **2009**, *11*, 241–249. **DOI:**10.1089/ars.2008.2140
16. O. Bozkurt, B. Kocaadam-Bozkurt, H. Yildiran, *Food Funct.* **2022**, *13*, 11999–12010. **DOI:**10.1039/D2FO02625B
17. F. Pivari, A. Mingione, C. Brasacchio, L. Soldati, *Nutrients,* **2019**, *11*, 1837. **DOI:**10.3390/nu11081837
18. S. Ibrahim, T. Tagami, T. Kishi, T. Ozeki, *Int. J. Pharm.* **2018**, *540*, 40–49. **DOI:**10.1016/j.ijpharm.2018.01.051
19. H. Ringsdorf, *J. Polym. Sci. Polym. Symp.* **1975**, *51*, 135–153. **DOI:**10.1002/polc.5070510111
20. A. Anand, B. R. Iyer, C. Ponnusamy, R. Pandiyan, A. Sugumaran, *Cardiovasc. Hematol. Agents Med. Chem.* **2020**, *18*, 45–54. **DOI:**10.2174/1871525718666200203112502
21. I. Aranaz, A. R. Alcántara, M. C. Civera, C. Arias, B. Elorza, A. Heras Caballero, N. Acosta, *Polymers (Basel).* **2021**, *13*,

3256. **DOI:**10.3390/polym13193256
22. J. Sharifi-Rad, C. Quispe, M. Butnariu, L. S. Rotariu, O. Sytar, S. Sestito, S. Rapposelli, M. Akram, M. Iqbal, A. Krishna, et al., *Cancer Cell Int.* **2021**, *21*, 318. **DOI:**10.1186/s12935-021-02025-4
23. D. Ghosh Dastidar, S. Saha, G. Dutta, S. Abat, N. Guha, D. Ghosh, *Mater. Res. Express.* **2020**, *7*, 015031. **DOI:**10.1088/2053-1591/ab637f
24. A. Sugumaran, V. Mathialagan, *Curr. Pharm. Des.* **2020**, *26*, 5174–5187. **DOI:**10.2174/1381612826666200625110950
25. V. Krishnaswami, A. Sugumaran, V. Perumal, M. Manavalan, D. P. Kondeti, S. K. Basha, M. A. Ahmed, M. Kumar, S. Vijayaraghavalu, *Curr. Drug Targets.* **2022**, *23*, 1330–1344. **DOI:**10.2174/1389450123666220822094248
26. S. Jain, R. Jain, M. Das, A. K. Agrawal, K. Thanki, V. Kushwah, *RSC Adv.* **2014**, *4*, 29193–29201. **DOI:**10.1039/C4RA04237A
27. M. Li, M. Gao, Y. Fu, C. Chen, X. Meng, A. Fan, D. Kong, Z. Wang, Y. Zhao, *Colloids Surf. B Biointerfaces.* **2016**, *140*, 11–18. **DOI:**10.1016/j.colsurfb.2015.12.025
28. R. Raveendran, C. K. S. Pillai, G. S. Bhuvaneshwar, C. P. Sharma, *J. Nanopharmaceutics Drug Deliv.* **2014**, *2*, 36–51. **DOI:**10.1166/jnd.2014.1046
29. S. Dey, K. Sreenivasan, *Carbohydr. Polym.* **2014**, *99*, 499–507. **DOI:**10.1016/j.carbpol.2013.08.067
30. Sauraj, S. U. Kumar, P. Gopinath, Y. S. Negi, *Carbohydr. Polym.* **2017**, *157*, 1442–1450. **DOI:**10.1016/j.carbpol.2016.09.096
31. S. V. Lale, A. Kumar, S. Prasad, A. C. Bharti, V. Koul, *Biomacromolecules.* **2015**, *16*, 1736–1752. **DOI:**10.1021/acs.biomac.5b00244
32. C. Ponnusamy, A. Sugumaran, V. Krishnaswami, R. Kandasamy, S. Natesan, *IET Nanobiotechnol.* **2019**, *13*, 868–874. **DOI:**10.1049/iet-nbt.2019.0130
33. F. Shafiee, E. Khoshvishkaie, A. Davoodi, A. Dashti Kalantar, H. Bakhshi Jouybari, R. Ataee, *Medicines.* **2018**, *5*. **DOI:**10.3390/medicines5010001
34. M. Wahab, A. Bhatti, P. John, *Polymers (Basel).* **2022**, *14*, 3138. **DOI:**10.3390/polym14153138
35. P. L. Cruz, I. C. Moraes-Silva, A. A. Ribeiro, J. F. Machi, M. D. T. de Melo, F. dos Santos, M. B. da Silva, C. M. C. Strunz, E. G. Caldini, M.-C. Irigoyen, *BMC Endocr. Disord.* **2021**, *21*, 133. **DOI:**10.1186/s12902-021-00795-6
36. P. Rathore, A. Mahor, S. Jain, A. Haque, P. Kesharwani, *RSC Adv.* **2020**, *10*, 43629–43639. **DOI:**10.1039/D0RA07640F
37. G. Chandirasegaran, C. Elanchezhiyan, K. Ghosh, *Biomed. Pharmacother.* **2018**, *99*, 227–236. **DOI:**10.1016/j.biopha.2018.01.007
38. M. U. Akbar, K. M. Zia, M. S. H. Akash, A. Nazir, M. Zuber, M. Ibrahim, *Int. J. Biol. Macromol.* **2018**, *120*, 2418–2430. **DOI:**10.1016/j.ijbiomac.2018.09.010
39. Y. M. El-Far, M. M. Zakaria, M. M. Gabr, A. M. El Gayar, L. A. Eissa, I. M. El-Sherbiny, *Nanomed.* **2017**, *12*, 1689–1711. **DOI:**10.2217/nnm-2017-0106
40. M. F. Elsadek, B. M. Ahmed, *Saudi J. Biol. Sci.* **2022**, *29*, 1402–1406. **DOI:**10.1016/j.sjbs.2021.11.035
41. S. Manandhar, E. Sjöholm, J. Bobacka, J. M. Rosenholm, K. K. Bansal, *J. Nanotheranostics.* **2021**, *2*, 63–81. **DOI:**10.3390/jnt2010005
42. J. Pan, K. Rostamizadeh, N. Filipczak, V. Torchilin, *Molecules.* **2019**, *24*, 1035. **DOI:**10.3390/molecules24061035
43. Sauraj, S. U. Kumar, V. Kumar, R. Priyadarshi, P. Gopinath, Y. S. Negi, *Carbohydr. Polym.* **2018**, *188*, 252–259. **DOI:**10.1016/j.carbpol.2018.02.006
44. J. Wang, J.-Z. Jiang, W. Chen, Z.-W. Bai, *Carbohydr. Polym.* **2016**, *145*, 78–85. **DOI:**10.1016/j.carbpol.2016.03.022
45. A. Praveen, D. Prasad, S. Mishra, S. Nagarajan, S. R. Chaudhari, *Food Chem.* **2021**, *341*, 128646. **DOI:**10.1016/j.foodchem.2020.128646
46. B. N. Waghela, A. Sharma, S. Dhumale, S. M. Pandey, C. Pathak, *PLoS One.* **2015**, *10*, e0117526. **DOI:**10.1371/journal.pone.0117526
47. N. M. L. Hansen, D. Plackett, *Polym. Chem.* **2011**, *2*, 2010–2020. **DOI:**10.1039/c1py00086a
48. M. Huo, Y. Zhang, J. Zhou, A. Zou, D. Yu, Y. Wu, J. Li, H. Li, *Int. J. Pharm.* **2010**, *394*, 162–173. **DOI:**10.1016/j.ijpharm.2010.05.001
49. P. R. Sarika, N. R. James, P. R. A. Kumar, D. K. Raj, T. V. Kumary, *Carbohydr. Polym.* **2015**, *134*, 167–174. **DOI:**10.1016/j.carbpol.2015.07.068
50. A. Sahu, U. Bora, N. Kasoju, P. Goswami, *Acta Biomater.* **2008**, *4*, 1752–1761. **DOI:**10.1016/j.actbio.2008.04.021
51. H. Li, D. Hu, F. Liang, X. Huang, Q. Zhu, *R. Soc. Open Sci.* **2020**, *7*, 192092. **DOI:**10.1098/rsos.192092
52. X. Zhang, Y. Huang, S. Li, *Ther. Deliv.* **2014**, *5*, 53–68. **DOI:**10.4155/tde.13.135
53. Y. Liu, K. Liu, C. Li, L. Wang, J. Liu, J. He, J. Lei, X. Liu, *RSC Adv.* **2017**, *7*, 36256–36268. **DOI:**10.1039/C7RA05913B
54. L. Hu, P. Zhang, X. Wang, X. Cheng, J. Qin, R. Tang, *Carbohydr. Polym.* **2017**, *178*, 166–179. **DOI:**10.1016/j.carbpol.2017.09.004
55. L. Nicolle, C. M. A. Journot, S. Gerber-Lemaire, *Polymers (Basel).* **2021**, *13*, 4118. **DOI:**10.3390/polym13234118
56. J. J. Milligan, S. Saha, *Cancers (Basel).* **2022**, *14*, 1741. **DOI:**10.3390/cancers14071741
57. M. Ghezzi, S. Pescina, C. Padula, P. Santi, E. Del Favero, L. Cantù, S. Nicoli, *J. Control. Release.* **2021**, *332*, 312–336. **DOI:**10.1016/j.jconrel.2021.02.031
58. M. Rai, R. Pandit, S. Gaikwad, A. Yadav, A. Gade, *Nanotechnol. Rev.* **2015**, *4*, 161–172. **DOI:**10.1515/hsz-2015-0001
59. N. Ghalandarlaki, A. M. Alizadeh, S. Ashkani-Esfahani, *Biomed Res. Int.* **2014**, *2014*, 1–23. **DOI:**10.1155/2014/394264
60. Z. Li, M. Shi, N. Li, R. Xu, *Front. Chem.* **2020**, *8*, 589957. **DOI:**10.3389/fchem.2020.589957
61. G. Chao, Y. Zhu, L. Chen, *J. Diabetes Res.* **2021**, *2021*. **DOI:**10.1155/2021/6626587
62. Q. Xiong, J. Liu, Y. Xu, *Int. J. Endocrinol.* **2019**, *2019*, 1–8. **DOI:**10.1155/2019/9691345
63. T. Hirano, *J. Atheroscler. Thromb.* **2018**, *25*, 771–782. **DOI:**10.5551/jat.RV17023
64. M. Taher, T. M. F. S. Tg Zakaria, D. Susanti, Z. A. Zakaria, *BMC Complement. Altern. Med.* **2016**, *16*, 135. **DOI:**10.1186/s12906-016-1118-9

65. S. K. Choudhary, G. Chhabra, D. Sharma, A. Vashishta, S. Ohri, A. Dixit, *Evidence-Based Complement. Altern. Med.* **2012**, *2012*, 1–10. **DOI:**10.1155/2012/293650
66. G. Ottaviani, S. Wendelspiess, R. Alvarez-Sánchez, *Mol. Pharm.* **2015**, *12*, 1171–1179. **DOI:**10.1021/mp5006992
67. K. Xiao, Y. Li, J. Luo, J. S. Lee, W. Xiao, A. M. Gonik, R. G. Agarwal, K. S. Lam, *Biomater.* **2011**, *32*, 3435–3446. **DOI:**10.1016/j.biomaterials.2011.01.021
68. M. Zhang, S. Gao, D. Yang, Y. Fang, X. Lin, X. Jin, Y. Liu, X. Liu, K. Su, K. Shi, *Acta Pharm. Sin. B.* **2021**, *11*, 2265–2285. **DOI:**10.1016/j.apsb.2021.03.033
69. J. M. Caster, S. K. Yu, A. N. Patel, N. J. Newman, Z. J. Lee, S. B. Warner, K. T. Wagner, K. C. Roche, X. Tian, Y. Min, et al. , *Nanomed. :Nanotechnol. Biol. Med.* **2017**, *13*, 1673–1683. **DOI:**10.1016/j.nano.2017.03.002
70. Z. Yu, L. Ma, S. Ye, G. Li, M. Zhang, *Carbohydr. Polym.* **2020**, *236*, 115972. **DOI:**10.1016/j.carbpol.2020.115972
71. N. A. Nasab, H. H. Kumleh, M. Beygzadeh, S. Teimourian, M. Kazemzad, *Artif. Cells Nanomed. Biotechnol.* **2018**, *46*, 75–81. **DOI:**10.1080/21691401.2017.1290648
72. S. I. Sherwani, H. A. Khan, A. Ekhzaimy, A. Masood, M. K. Sakharkar, *Biomark. Insights* **2016**, *11*, 95–104. **DOI:**10.4137/BMI.S38440
73. N. Harita, T. Hayashi, K. K. Sata, Y. Nakamura, T. Yoneda, G. Endo, H. Kambe, *Diabetes Care.* **2009**, *32*, 424–426. **DOI:**10.2337/dc08-1265

Povzetek

Sladkorna bolezen je kronična presnovna motnja, za katero je značilna povišana raven sladkorja v krvi, ki povzroča motnje v delovanju organov. Kurkumin, pridobljen iz kurkume, kaže obetavne lastnosti pri zdravljenju sladkorne bolezni tipa II. Amfipatska polimerna predzdravila so sintetizirali s konjugiranjem kurkumina s hitosanom prek sukcinil anhidrida. Nanomiceli, ki so nastali z dializo amfipatskega polimernega predzdravila, so bili sferični s povprečno hidrodinamsko velikostjo 57 nm. Študije sproščanja *in vitro* so pokazale 97-odstotno sproščanje kurkumina pri pH 5 v 7 dneh. V 21-dnevnem poskusu na diabetičnih miših so primerjali vpliv nanomicel, standardnih zdravil in prostega kurkumina na glukozo v krvi na tešče. Študija je pokazala postopno in nadzorovano sproščanje kurkumina iz nanomicel, kar kaže na njihov potencial pri zdravljenju sladkorne bolezni tipa II.

DRUŠTVENE VESTI IN DRUGE AKTIVNOSTI
SOCIETY NEWS, ANNOUNCEMENTS, ACTIVITIES

Vsebina

Contents

POROČILO PREDSEDNIKA SLOVENSKEGA KEMIJSKEGA DRUŠTVA O DELU DRUŠTVA V LETU 2023

Tudi v letu 2023 je bilo društvo aktivno na številnih področjih. Izvajali smo redne letne aktivnosti, pri katerih je bil glavni poudarek na rednem izdajanju društvene revije *Acta Chimica Slovenica* (ACSi) ter organizaciji največjega letnega dogodka društva, konference »Slovenski kemijski dnevi 2023«.

Društvo je v letu 2023 uvedlo stanovske nagrade društva, ki se bodo prvič podelile v letu 2024. Na 11. seji Glavnega odbora SKD je bil sprejet Pravilnik o nagradah in priznanjih SKD. Prvi mandat Komisije za nagrade in priznanja SKD so dobili Mirela Dragomir (IJS), Dušan Teslić (Lek), Maja Leitgeb (FKKT UM), Irena Kralj Cigić (FKKT LJ), Bogdan Znoj (Helios), Mladen Franko (UNG) in Jože Grdadolnik (KI).

14. septembra smo prav tako v sklopu omenjene konference izvedli redni občni zbor društva, kjer smo spremenili vsebino statuta Slovenskega kemijskega društva. Poleg manjših sprememb je najpomembnejša v 45. členu, v katerem je zavedeno, da SKD podeljuje nagrade in priznanja le-te opredeljuje pravilnik, ki ga sprejme Glavni odbor.

Slovenski kemijski dnevi 2023 *(https://skd2023.chem-soc.si/)* so bili organizirani v Portorožu, v Kongresnem centru Grand hotela Bernardin, in sicer v dneh od 13. do 15. septembra 2023. Programskemu in organizacijskemu odboru je predsedoval znan. svet. dr. Albin Pintar, skupaj s člani odbora v zasedbi prof. dr. Romana Cerc-Korošec, prof. dr. Iztok Devetak, prof. dr. Darja Lisjak, doc. dr. Matic Lozinšek, prof. dr. Zorka Novak Pintarič, dr. Alenka Ristić, prof. dr. Matjaž Valant, dr. Silvo Zupančič in Eva Mihalinec.

Na konferenci je bilo predstavljenih 196 prispevkov v obliki predavanj in posterjev. Delo je potekalo plenarno in v treh vzporednih sekcijah. Udeleženci konference, bilo jih je 305 iz Slovenije in trinajstih drugih držav, so bili zelo zadovoljni s kakovostjo znanstvenih in strokovnih prispevkov ter družabnim programom srečanja. Na konferenci je sodelovalo tudi 23 razstavljalcev laboratorijske in procesne opreme. Sponzorji dogodka so bili Lek (diamantni partner), Vigor (zlati sponzor), Analysis Adria, Chemass, Cinkarna Celje, Kefo, Kemomed, Laboratorij-um, Labtim, LKB, Merck, Mettler Toledo, Optik Instruments, Primalab (srebrni sponzorji), Kemijski inštitut, Krka in Mikro+Polo (bronasti sponzorji). Objavili smo zbornik povzetkov konference, ki je dostopen na USB ključu ter na voljo v NUK-u in strokovnih knjižnicah po Sloveniji.

Plenarni predavatelji na konferenci so bili prof. dr. Ewa Gorecka (University of Warsaw, Poljska), prof. dr. Timo Repo (University of Helsinki, Finska) in prof. dr. Ester Heath (Institut »Jožef Stefan«, Ljubljana). Poleg treh plenarnih predavanj so udeleženci poslušali šest »keynote« vabljenih predavanj, ki so jih izvedli prof. dr. Matej Praprotnik (Kemijski inštitut, Ljubljana), izr. prof. dr. Blaž Likozar (Kemijski inštitut, Ljubljana), prof. dr. Nora Kulak (University of Potsdam, Nemčija), prof. dr. Dana Dvoranová (Slovak University of Technology in Bratislava, Slovaška), dr. Nataša Obermajer (Janssen Pharmaceutica, Beerse, Belgija) in dr. Gerhard J. Mohr (Joanneum Research, Gradec, Avstrija).

Podelili smo tudi nagrade za najboljša študijska dela s področja trajnostne kemije. Strokovno komisijo za izbor najboljših del so sestavljali prof. dr. Marjan Veber, Denis Jahić, dr. Vid Margon, dr. Ema Žagar, doc. dr. Irena Petrinić in doc. dr. Marija Zupančič, ki so se odločili, da nagrado za najboljše diplomsko delo prejme Nika Skušek, nagrado za najboljše magistrsko delo Mitja Kostelec, nagrado za najboljše doktorsko delo in nagrado za največji potencial prenosa v gospodarstvo pa je prejel Gian Claudio Faussone. Sponzor nagrad je bilo podjetje AquafilSLO.

Ob zaključku konference smo že tradicionalno podelili nagrade doktorskim študentom za najboljša predavanja in posterske predstavitve.

Leto 2023 je bilo za revijo Acta Chimica Slovenica jubilejno leto, saj smo obeležili 70-let izhajanja revije. Izdali smo 4 številke revije, v katerih je bilo skupaj objavljenih 69 znanstvenih člankov na skupno 650 straneh z dvokolonskim tiskom. V tretji številki smo v rubriki Društvene novice objavili osem prispevkov ob 70-letnici. V prvem prispevku so zbrani nagovori in čestitke predsednika in častnega predsednika Slovenskega kemijskega društva ter dekanj, dekanov in direktorjev najpomembnejših slovenskih izobraževalnih in raziskovalnih inštitucij. Šest prispevkov podaja zgodovinski pregled delovanja revije, zadnji prispevek pa podaja spomine in vtise področnih nekdanjih in sedanjih urednic in urednikov.

Med objavljenimi članki je bil en Feature Articles (FA) in en Review Article (RA). FA članek je prispevek slovenske raziskovalne skupine, ki pod vodstvom prof. dr. Polonce Trebše z Univerze v Ljubljani raziskuje na področju sinteze, karakterizacije in toksičnosti izbranih UV-A filtrov in ter vlogo antioksidantov kot dodatka v kremah za zaščito pred soncem. RA članek je prispevek indijskih raziskovalcev pod vodstvom prof. dr. Satyanaraya Pattnaika, ki proučuje nanodelce zlata kot nosilce za terapevtske učinkovine.

Članki pokrivajo vsa področja kemije, kemije materialov in kemijskega in biokemijskega inženirstva ter kemijskega izobraževanja. Vseh člankov, ki so bili leta 2023 oddani v uredniški sistem, je bilo 628, kar pomeni, da jih je bilo na koncu sprejetih okoli 11 %. V letu 2023 je revija uvrščena tudi v repozitorij Portico, kjer se v digitalni obliki shranjujejo vsi članki objavljeni v reviji Acta Chimica Slovenica. Z letom 2023 je delo glavnega in odgovornega urednika ACSi prevzel Franc Perdih.

V društvenih vesteh smo poleg prispevkov ob 70-letnici ACSi objavili prispevek A. Godca o uspehih slovenskih dijakov na 55. mednarodni kemijski olimpijadi v Zürichu. Objavili smo tudi seznam diplomskih, magistrskih in doktorskih del FKKT UL, FKKT UM ter Podiplomskega študijskega programa Znanosti o okolju in Fakultete za znanosti okolju, UNG v letu 2022. Objavili smo koledar važnejših znanstvenih srečanj in letna poročila sekcij in author index. V letu 2023 so društvene vesti obsegale 131 strani.

Zahvaljujem se tudi vsem inštitucijam, ki so v letu 2023 finančno podprle izdajanje revije *Acta Chimica Slovenica*. Te so

Fakulteta za kemijo in kemijsko tehnologijo Univerze v Ljubljani, Fakulteta za kemijo in kemijsko tehnologijo Univerze v Mariboru, Univerza v Novi Gorici, Kemijski inštitut in Inštitut »Jožef Stefan«. Sponzorji revije so bili z objavo oglasa Krka d.d., Novo mesto, Donau Lab d.o.o. Ljubljana, Belinka Perkemija in Helios Domžale, d.o.o.

Aktivne so bile tudi naše sekcije in podružnice, saj so njihovi člani v letu 2023 sodelovali pri organizaciji mednarodnih in domačih konferenc, organizirali strokovna srečanja, predavanja, seminarje in webinarje, se udeleževali različnih izobraževanj in tekmovanj, sodelovali pa so tudi v strokovnih in znanstvenih združenjih. Poročila posameznih sekcij in podružnic so priloga temu poročilu.

V letu 2023 smo nadaljevali z aktivnostmi za pridobivanje novih članov. Medse smo jih privabili 20, od tega 12 študentov. Za komunikacijo s člani smo pogosteje uporabljali Facebook, Twitter in LinkedIn ter jih obveščali o dogodkih po elektronski pošti.

V društvu smo ponovno objavili razpis za povezovanje dijakov s strokovnjaki kemijske stroke, pripravili pa smo 2 temi raziskovalnih nalog na različnih institucijah. Kot mentorji dijakom so se predstavili dr. Nina Kostevšek (Institut Jožef Stefan) ter Sebastjan Nemec in doc. dr. Slavko Kralj, Institut Jožef Stefan.

Člani Slovenskega kemijskega društva so bili aktivni tudi na področju mednarodnega sodelovanja. Predvsem je potrebno omeniti članstvo društva v mednarodnih združenjih IUPAC, ECTN, IUCr, EURACHEM, EuChemS, EFCE, EPF, ECA in EFCATS.

dr. Peter Venturini, predsednik društva
dr. Albin Pintar, predsednik organizacijskega odbora konference Slovenski kemijski dnevi
prof. dr. Franc Perdih, glavni urednik ACSi

Poročilo Komisije za slovensko kemijsko terminologijo in nomenklaturo za leto 2023

Komisija za slovensko kemijsko terminologijo in nomenklaturo je tudi v preteklem letu sodelovala pri delu Tehniške komisije Sekcije za terminološke slovarje pri Institutu za slovenski jezik ZRC SAZU. Člana tehniške komisije za področje kemije in kemijske tehnologije sta Andrej Šmalc z ljubljanske ter Peter Glavič z mariborske podružnice Slovenskega kemijskega društva.

V letu 2023 je bila končana strokovna redakcija gradiva s področja kemije, kemijske tehnologije in kemijske tehnike za novo izdajo splošnega tehniškega slovarja, ki je trenutno v fazi dokončne slovaropisne in jezikovne redakcije

Obenem s sodelovanjem pri končni redakciji gradiva za Splošni tehniški slovar je potekalo nadaljnje zbiranje gradiva za novi Kemijski slovar, ki je že nekaj let na spletu in danes obsega že več kot 10 000 gesel ter predstavlja pomembno dopolnitev bodočega Splošnega tehniškega slovarja predvsem s področja kemije kemijske tehnologije in kemijske tehnike, vključuje pa tudi osnovne pojme iz ekonomije in okoljske tehnike (*https://www.fkkt.um.si/kslovar/index.php*: ali kar Google kslovar). Prednost spletne oblike slovarja je prav v tem, da ga je mogoče stalno sproti dopolnjevati in po potrebi tudi popravljati. V letu 2023 je bilo obdelanih 869 gesel, ki bodo v letu 2024 vnesena v slovar.

Poleg dela v zvez s Kemijskim slovarjem bomo še nadalje sodelovali pri prevodu prenovljenega mednarodnega standarda ISO 80000: Veličine in enote s strokovnim pregledom novih prevodov, ki bodo nadomestili sedanje standarde SIST ISO 80000-1 do 80000-13 (dodatne tri dele ISO še razvija).

Ob tej priložnosti se spominjamo tudi sodelavcev skupine za pripravo kemijskega slovarja univ. dipl. inž. Leona Čelika in prof. mag. Antona Stuška, ki sta zaslužna zlasti za zbiranje gradiva in sta žal preminila v letu 2023.

dr. Andrej Šmalc

Poročilo o delu Sekcije za okolje SKD za leto 2023

V letu 2023 sta bili v Sekciji za okolje SKD najbolj aktivni dve delovni skupini, ki sta se ukvarjali s pripravo pregleda slovenskih izobraževalnih institucij, ki imajo v programu tematike s področja kemije okolja, ter s popisom stanja vseh onesnažil v slovenskem vodnem okolju.

Prva skupina pod vodstvom Ester Heath (Institut »Jožef Stefan«, Odsek za znanosti o okolju), v kateri sta sodelovala tudi Janja Vidmar (Institut »Jožef Stefan«, Odsek za znanosti o okolju) in Jan Hočevar (Univerza v Ljubljani, Fakulteta za kemijo in kemijsko tehnologijo), je pripravila pregled slovenskih študijskih programov s področja kemije okolja. Pregled je pokazal, da slovenske izobraževalne ustanove ponujajo veliko število (46) okoljskih študijskih programov, od tega smo jih po 10 identificirali v srednješolskem in višješolskem strokovnem izobraževanju, ter 9 na prvi stopnji (dodiplomski študij), 11 na drugi stopnji (magistrski študij) in 6 na tretji stopnji (doktorski študij) visokošolskega izobraževanja. Opredeljeni okoljski programi z relativno nizkim deležem kemije (<30 %) v učnem načrtu ponujajo širok in raznolik nabor predmetov, zlasti v visokošolskem izobraževanju, kar odraža njihovo interdisciplinarno naravo. Pregled ponuja celovito oceno trenutnega stanja študijskih programov s področja okolja in okoljske kemije v Sloveniji, ki bo koristil tako študentom in šolnikom kot tudi raziskovalcem, ki se zanimajo ali ukvarjajo z okoljskimi znanostmi. Omenjeno delo je bilo predstavljeno na Slovenskih kemijskih dnevih 2023 v Portorožu, na 16. Mednarodni konferenci o prenosu tehnologij v okviru Sekcije za povezovanje znanstvene in šolske sfere ter v obliki znanstvenega članka poslano v revijo Acta Chimica Slovenica, kjer je trenutno v postopku recenzije.

Druga delovna skupina pod vodstvom Vesne Mislej in v sodelovanju z Ester Heath in Janom Hočevarjem, pa je na Slovenskih kemijskih dnevih 2023 predstavila prispevek v obliki posterja z naslovom »Quality status of Slovenian rivers", v katerem so sintetizirali razpoložljive podatke o kemijskem in ekološkem statusu slovenskih površinskih voda, objavljene v uradnih Ocenah stanja voda v Sloveniji, ter s tem širši strokovni javnosti predstavili njihovo kakovost.

Ester Heath in Janja Vidmar sta se v lanskem letu udeležili konference ICCE 2023 Venice (18th EuChemS International Conference on Chemistry and the Environment) v Benetkah, kjer je Ester Heath v obliki predavanja predstavila delo ponovne uporabe prečiščene odpadne vode: privzem in tveganja povezana s kemikalijami, ki vzbujajo zaskrbljenost, Janja Vidmar pa predavanje povezano s privzemom nanoplastike v paradižnike.

Prav tako so se nadaljevale aktivnosti montaže filma o delovanju čistilne naprave, ki ga s svojimi študenti pripravlja režiserka Jasna Hribernik. Pri izvedbi tega projekta prihaja do zamude zaradi težav/pomanjkanja študentov.

V letu 2023 smo imeli tudi namen organizirati ogled Izobraževalnega centra na Igu konec junija 2023, vendar smo se zaradi majhnega odziva/interesa ostalih udeležencev odločili, da te aktivnosti ne bomo izpeljali.

Po podatkih tajništva SKD znaša število članov sekcije 38 na dan 30.1.2024, kar je za 11 več kot pred letom dni, od tega se jih je približno petina aktivno udeleževala in prispevala k aktivnostim sekcije v letu 2023.

dr. Marko Štrok

Poročilo za aktivnosti v letu 2023, Sekcija za živilsko kemijo

Člani Sekcije za živilsko kemijo (SŽK) smo se aktivno udeležili različnih znanstvenih in strokovnih srečanj, kjer smo predstavili svoje raziskovalne dosežke. Aktivni pa smo bili tudi na delavnicah in na področju izobraževanja in popularizacije kemije in še posebej živilske kemije. Sodelovali smo pri organizacijah mednarodnih znanstvenih srečanj.

Aktivno smo sodelovali tudi pri različnih dejavnostih Sekcije za živilsko kemijo (Food Chemistry Division, FCD) Evropskega kemijskega združenja (European Chemical Society - EuChemS), kjer predstavljamo Slovensko kemijsko društvo. V okviru FCD smo sodelovali pri izboru vabljenih predavateljev in oblikovanju programa mednarodnega kongresa »XXII EuroFoodChem Congress« (*https://xxiieurofoodchem.com/*), ki je bil od 14. do 16. 6. 2023 v Beogradu. Na kongresu so bili predstavljeni prispevki mednarodno uveljavljenih raziskovalcev in tudi večjega števila mlajših raziskovalcev. Predstavitve so bile s področij naslednjih aktualnih tematik: kakovost in varnost hrane; hrana in trajnostni razvoj (vključno z valorizacijo stranskih proizvodov); nova živila; hrana in zdravje, funkcionalna živila in sestavine s funkcionalnimi lastnostmi; kemijske reakcije in interakcije med sestavinami v živilih; kemijske spremembe v hrani med predelavo in skladiščenjem; ponarejanje živil, avtentičnost in sledljivost; nove metode analize živil; kontaminanti v hrani. Po kongresu smo se udeležili tudi sestanka FCD, ki je bil 17. 6. 2023 v Beogradu. Na sestanku smo prestavili naše delo in z ostalimi člani FCD naredili načrt dela za prihodnje leto. Za obdobje 2024–2026 smo izvolili novo vodstvo FCD, ki ga sestavljajo prof. Joana Amaral (predsednica), prof. Cristina Todasca (tajnica), dr. Irena Vovk (blagajničarka) in prof. Marco Arlorio (bivši predsednik).

V okviru FCD je potekalo tudi sodelovanje v mednarodni žiriji, ki je ocenjevala prijave na razpis za mednarodno nagrado »The EuChemS Food Chemistry Division Young Researcher Award 2023« za mladega raziskovalca ali mlado raziskovalko za raziskave izvedene v okviru doktorske disertacije na področju živilske kemije in sorodnih področij. Nagrada je bila podeljena na kongresu »XXII EuroFoodChem Congress«.

V okviru Skupine za organizacijo in izvedbo webinarjev, ki od leta 2021 deluje v okviru FCD, smo tudi leta 2023 sodelovali pri izboru tematik in organizaciji webinarjev, pri čemer je bil izveden naslednji webinar:

- »Neurobiological regulation of food intake: Unbiased identification of food bioactives«, prof. dr. Monika Pischetsrieder s Friedrich-Alexander-Universität Erlangen-Nürnberg, Nemčija

V planu za leto 2024 smo predvideli aktivno udeležbo na mednarodnih simpozijih. V okviru FCD bomo sodelovali pri izboru tematik mednarodnega kongresa »XXII EuroFoodChem Congress«, ki bo od 11. do 13. 6. 2025 v Bratislavi. Sodelovali bomo pri izboru tematik in organizaciji webinarjev FCD. Udeležili se bomo tudi sestanka FCD, kjer bomo prestavili naše delo in z ostalimi člani FCD naredili načrt dela za prihodnje leto.

dr. Irena Vovk

Poročilo o delovanju in aktivnostih Mariborske podružnice v letu 2023

V letu 2023 je mariborska podružnica uresničila cilje, ki so bili zastavljeni v preteklem letu. Osrednji dogodek je bila naša udeležba na konferenci Slovenski kemijski dnevi v Portorožu, kjer smo se izkazali v več ključnih vlogah: kot predsedniki sekcij, aktivni predavatelji in avtorji znanstvenih posterjev. Naša prisotnost in strokovni prispevki na konferenci so bili izjemno dobro sprejeti, kar odraža našo predanost in strokovnost na področju kemije.

V skladu z našo zavezo k nenehnemu izobraževanju in profesionalnemu razvoju naših članov, je

podružnica organizirala serijo strokovnih predavanj in seminarjev, ki so jih vodili priznani strokovnjaki s področja kemije, tako iz Slovenije kot iz tujine. Ta dogajanja so pokrivala širok spekter tem od teoretične kemije, kemijskega inženirstva do kemijskega izobraževanja, s čimer smo zagotovili poglobljeno znanje in inovativne pristope našim članom.

Poleg tega smo julija sodelovali pri izvedbi prestižne mednarodne poletne šole "ESS-HPT 2023" (The European Summer School in High Pressure Technology). Ta dogodek, ki ga je soorganiziral naš Laboratorij za separacijske procese in produktno tehniko v sodelovanju s Tehniško Univerzo v Gradcu, je bil osredotočen na

visokotlačne tehnologije in je privabil številne eminentne strokovnjake ter študente z vsega sveta.

Na področju medijske prisotnosti smo se odlikovali z aktivnim sodelovanjem v oddaji RTV Slovenija

Ugriznimo v znanost, kjer smo razpravljali o pomembnosti biobank. Prav tako smo prispevali k članku o superračunalniku Vega in poudarili pomembnost raziskav UM FKKT, kar je dodatno utrdilo našo prisotnost v znanstveni skupnosti.

Izredni dosežek je predstavljala izvolitev red. prof. dr. Željka Kneza v rednega člana Slovenske akademije znanosti in umetnosti (SAZU), kar je priznanje njegovemu

izjemnemu prispevku v znanstveni skupnosti. Poleg tega je izredni profesor dr. Matjaž Finšgar prejel Zoisovo priznanje za njegove prispevke na področju analizne kemije, kar še dodatno potrjuje našo predanost znanstveni odličnosti.

Univerza Stanford je tudi letos objavila seznam 2 % najboljših znanstvenikov na svetu. Na to lestvico so se od sodelavcev UM FKKT uvrstili izr. prof. dr. Matjaž Finšgar, prof. dr. Željko Knez, izr. prof. dr. Maša Knez Marevci, prof. dr. Mojca Škerget in prof. dr. Zdravko Kravanja.

Mednarodno sodelovanje je bilo dodatno okrepljeno s prestižnim obiskom veleposlanika Kraljevine Nizozemske v Sloveniji, kar odraža rastoči mednarodni vpliv in ugled naše fakultete. Dr. Matja Zalar je z intervjujem za Slovensko tiskovno agencijo (STA) še dodatno poudarila naša znanstvena prizadevanja in dosežke.

Vrhunec našega mednarodnega sodelovanja je predstavljal obisk direktorja največje evropske raziskovalne infrastrukture BBMRI-ERIC, prof. dr. Jens Habermanna. Njegov obisk je bil ključen za nadaljnje utrjevanje mednarodnih znanstvenih povezav in izmenjavo znanj, kar je za našo institucijo izjemnega pomena.

dr. Matjaž Finšgar

Poročilo o delu sekcije za katalizo pri Slovenskem kemijskem društvu

Članice in člani sekcije za katalizo smo bili angažirani pri organizaciji mednarodne znanstvene konference z naslovom "9th Conference of the Federation of European Zeolite Associations (FEZA 2023), ki je potekala od 2. do 6. julija 2023 v kongresnem centru Grand hotela Bernardin v Portorožu.

Prav tako smo članice in člani sekcije za katalizo angažirani pri pripravah na izvedbo mednarodne znanstvene konference z naslovom "4th International Conference on Fundamentals and Applications of Cerium Dioxide in Catalysis", ki bo potekala od 17. do 20. septembra 2024 v kongresnem centru Grand hotela Bernardin v Portorožu. Več informacij o dogodku je na voljo na konferenčni spletni strani: *https://ceria2024.chem-soc.si/*.

Izvajamo tudi aktivnosti za pridobitev organizacije mednarodne znanstvene konference "13th European Conference on Solar Chemistry and Photocatalysis: Environmental Applications (SPEA)", ki jo bomo v primeru potrditve kandidature (odločitev bo znana sredi junija 2024) organizirali leta 2026.

Nataša Novak Tušar in Albin Pintar sta kot nacionalna predstavnika sodelovala pri izvajanju aktivnosti pri Evropski federaciji katalitskih združenj (EFCATS). Nataša Novak Tušar je bila v EFCATS federaciji ponovno izvoljena za zakladničarko za naslednje mandatno obdobje.

V sekciji za katalizo smo v lanskem letu sodelovali pri organizaciji predavanj vabljenih tujih raziskovalcev, ki smo jih pripravili v sodelovanju z raziskovalnimi in akademskimi inštitucijami, zelo angažirani pa smo bili pri organizaciji konference "Slovenski kemijski dnevi 2023", kakor tudi pri sodelovanju na dogodku s predstavitvami velikega števila prispevkov.

dr. Albin Pintar

Poročilo sekcije mladih kemikov za leto 2023

Glavni namen sekcije mladih kemikov je vzpostavitev vezi med študenti, mladimi raziskovalci, mladimi doktorji, znanstveno-raziskovalnimi inštitucijami, kemijsko in farmacevtsko industrijo ter pedagoškimi delavci v šolah in fakultetah. Sekcija mladih kemikov je članica v European Young Chemists' Network (EYCN) v okviru EuChemMS in International Young Chemists Network (IYCN) v okviru IUPAC, tako da je ena njenih pomembnejših nalog tudi povezovanje mladih kemikov in delovanje na skupnih projektih v mednarodnem merilu.

V letu 2023 smo izbrali nove predstavnike za združenji EYCN in IYCN, kar sta postala Matjaž Dlouhy in Ervin Rems. V sodelovanju s Študentsko organizacijo UL FKKT smo organizirali ekskurzija v Cinkarno Celje in ekskurzijo v Salonit Anhovo. V sodelovanju s podjetjem Aquafil se je izvedel razpis za nagrade za študentske naloge na področju zelene kemije.

Sara Drvarič Talijan

Poročilo Sekcije za keramiko za leto 2023

V letu 2023 je v Lyonu, Francija, od 2. do 6. julija potekala 18. Konferenca in razstava Evropskega keramičnega združenja (European Ceramic Society, ECerS). Pred dogodkom sta bila s strani organizatorja konference izpeljana sestanka pridruženih držav članic ECerS in stalnega izvršilnega odbora ECerS. Prvi sestanek poteka enkrat, slednji pa dvakrat letno. Izr. prof. Andraž Kocjan je bil po predlogu predsednika ECerS, dr. Francisa Cambierja, imenovan za člana 6-članskega izvršilnega odbora ECerS za dobo dveh let, z možnostjo podaljšanja še za dodatni dve leti. Pred nastopom te funkcije je bil 6 let vodja delovne skupine »Young Ceramists and Training«.

ECerS je za leto 2023 podelil sledeče nagrade:

- Stuijts nagrada (raziskovalki / raziskovalcu, ki pripada državi članici društva, za izjemne prispevke v keramični znanosti, tehnologiji in izobraževalni dejavnosti ali proizvodnji): Prof. Jan Dusza, Institute of materials research, SAS, Slovaška.
- Richard Brook nagrada (raziskovalki / raziskovalcu iz države zunaj Evrope za izjemen prispevek k keramični znanosti ali tehnologiji ter za izboljšanje razumevanja in sodelovanja v mednarodni keramični skupnosti): Prof. Tatsuki Ohji, National Institute of Advanced Industrial Science and Technology, Japonska.
- Nagrada »Mlad znanstvenik / Mlada znanstvenica« (raziskovalki / raziskovalcu, mlajši od 40 let, zaradi izjemnih prispevkov k keramičnim znanostim): Prof. Jesus Gonzalez-Julian, RWTH Aachen University, Nemčija.
- Gian Nicolas Babini nagrada (raziskovalki / raziskovalcu za izjemen tehnični prispevek k razvoju evropske keramične industrije): Dr. Moritz von Witzleben, INMATEC Technologies GmbH, Nemčija.

Oana Andreea Condurache, doktorandka iz Odseka za elektronsko keramiko Instituta »Jožef Stefan«, se je udeležila tekmovanja mladih keramikov ECerS »Student Speech Contest«. Tekmovanje je bilo izpeljano v okviru 18. 18. Konference in razstave ECerS v Lyonu, Francija. Na tekmovanju svoje rezultate predstavijo mladi znanstveniki, kot predstavniki držav pridruženih članic ECerS. Zmagal je predstavnik Avstrije, Abdullah Jabr iz Montanuniversität Leoben, Avstrija.

Odsek za nanostrukturne materiale in Odsek za raziskave sodobnih materialov Instituta »Jožef Stefan« ter Katedra za Stomatološko protetiko Medicinske Fakultete Univerze v Ljubljani so v letu 2023 pridobili najnaprednejši 3D tiskalnik za keramične materiale CeraFab S65 dobavitelja Lithoz GmbH iz Avstrije. Tiskalnik deluje na podlagi sterolitografije, pri kateri keramične komponente oblikujemo s pomočjo foto-občutljive suspenzije z velikim deležem keramičnih delcev. Prednost metode je visoka ločljivostjo (25-50 μm), ki omogoča izdelavo kompleksnih komponent in prototipov. Vrednost investicije je znašala 350.000 €, sofinancirala pa jo je Javna agencija za znanstvenoraziskovalno in inovacijsko dejavnost Republike Slovenije v okviru Paketa opreme 21.

Izr. prof. Matjaž Spreitzer
in *Izr. prof. Andraž Kocjan*

Poročilo Sekcije za kristalografijo pri Slovenskem kemijskem društvu za leto 2023

V letu 2023 so se tudi dejavnosti Sekcije za kristalografijo, potem ko je izzvenela pandemija Korona virusa, vrnile v običajne tirnice.

Glavna dejavnost članov sekcije v letu 2023 je bila organizacija 29. slovensko-hrvaškega kristalografskega srečanja SCCM 2023, ki je potekalo od 14. do 18. junija 2023 v Topolšici. Prijavljenih je bilo 60 udeležencev iz Avstrije, Francije, Nemčije, Maroka, Ukrajine, Velike Britanije, Hrvaške in Slovenije.

Predstavljena so bila štiri plenarna predavanja: Kristalno inženirstvo organskih in kovinsko-organskih večkomponentnih trdnih snovi s halogensko vezjo, Dominik Cinčić, Univerza v Zagrebu, Hrvaška; Red iz nereda: k molekularni arhitekturi sklopa Z-disk mišic, Kristina Djinović-Carugo, EMBL Grenoble; Visokotlačni fazni prehodi v molekulskih kristalih, Simon Parsons, Univerza v Edinburgu, Združeno kraljestvo; in DFT modeliranje materialov in kristalnih struktur z uporabo periodičnih robnih pogojev, Anton Kokalj, Institut Jožef Stefan, Slovenija.

Poleg tega je bilo podanih 45 kratkih ustnih predstavitev, ki so obravnavale sodobne teme v kristalografiji: določanje strukture organskih, anorganskih in koordinacijskih spojin, kristalna arhitektura, inženiring in oblikovanje, fazni prehodi, razmerje med strukturo in lastnostmi, sinergija difrakcijskih in komplementarnih tehnik itd.

Ena od prednosti slovensko-hrvaških srečanj je, da vsi udeleženci svoje delo predstavijo v obliki kratkega ustnega prispevka, kar je še posebej pomembno za mlade znanstvenike, ki imajo tako možnost predstaviti svoje rezultate v prijateljskem, a strokovnem ozračju. Na letošnjem srečanju smo mladim znanstvenikom ponudili možnost, da se prijavijo na tekmovanje za nagrado za najboljšo predstavitev. Prijavilo se je 28 tekmovalcev v treh različnih kategorijah (magistrski študenti / doktorski študenti / po-

doktorski raziskovalci, ki so zagovarjali svoje diplomske naloge pred največ petimi leti. Čeprav so bile vse predstavitve odlične, je žirija soglasno nagradila naslednje:

Doktorandka Lea Čolakić (Univerza v Zagrebu, Hrvaška), Izbirčna halogenska vez v Wernerjevih kompleksih na osnovi izocianata; doktorand Erik Uran (Institut Jožef Stefan, Slovenija), Soli, adukti in kokristali, ki nastanejo pri reakcijah SO2 z organskimi amini, in podoktorski raziskovalec Ivica Cvrtila (Institut Ruđer Bošković, Hrvaška), Kiralna kristalizacija hippurinske kisline iz karvona.

Posebno nagrado za izjemno predstavitev sodobnih tem v kemijski kristalografiji in napredka na področju kristalografskih informacij o majhnih molekulah, ki jo je sponzoriral CCDC, je prejel Klemen Motaln (Institut Jožef Stefan, Slovenija) za prispevek Izmuzljiva kristalna struktura XeOF2.

Predstavniki CCDC so izvedli tudi praktično delavnico, na kateri so se osredotočili na program Mercury in njegove nove funkcije, kot na primer predvidevanje oblike delcev.

Enako kot na vseh dosedanjih srečanjih kotizacije ni bilo, zato se sponzorjem in oglaševalcem, ki so to omogočili (CCDC, Renacon, Rigaku, Aparatura, MettlerToledo, Vigor, Mitegen, Technobis, Dectris, Optik Instruments, Aparatura, Lek-Sandoz, Krka in Scan d.o.o.) iskreno zahvaljujemo.

Slovensko-hrvaško kristalografsko srečanje bomo v Sloveniji spet organizirali v juniju 2025, trenutno pa potekajo priprave na letošnje jubilejno 30. srečanje na Hrvaškem (Veli Lošinj 12.-16. junija 2024). Kot običajno, smo predstavniki Sekcije za kristalografijo vključeni v organizacijski odbor in se skupaj s hrvaškimi kolegi trudimo, da bi tudi to srečanje uspelo vsaj tako dobro, kot so vsa prejšnja.

Hvaležni smo vodstvu in tajništvu SKD, da lahko preko društva plačujemo članarino v evropski (ECA) in svetovni kristalografski zvezi (IUCr), za kar sicer od ARIS običajno dobimo povrnjena sredstva, vendar sta pri tem skrbnost in trud tajništva pri prijavi na ustrezen razpis neprecenljiva.

prof. dr. Anton Meden

Poročilo Sekcije za polimere za leto 2023

V avgustu smo za člane Sekcije za polimere organizirali seminar na Kemijskem inštitutu, kjer je prof. dr. Junpeng Zhao, iz South China University of Technology, Kitajska, imel predavanje z naslovom: "Multidimensionally Controlled Polyether Synthesis through Organocatalysis". Člani sekcije so bili v oktobru povabljeni tudi na predavanje prof. dr. Roberta Liske, iz TU Wien, Avstrija, ki je v sklopu Preglovih predavateljev na Kemijskem inštitutu imel predavanje z naslovom: "Advanced Applications of Photopolymerization: From Frontal Polymerization to new Monomers for 3D Printing".

Na mednarodnem nivoju je predsednik Sekcije za polimere sodeloval pri izvajanju aktivnosti Evropske polimerne federacije (EPF), predsedovanje katere je v letu 2023 prevzela prof. dr. Katja Loos (University of Groningen, Nizozemska).

dr. David Pahovnik

Poročilo sekcije EURACHEM

Na področju meroslovja v kemiji se počasi končuje izjemno dinamično obdobje razvoja konceptov in njihove implementacije, kar se odraža tudi na delu Eurachema in potrebah po novih publikacijah.

V Sloveniji je do sedaj večina preskusnih laboratorijev akreditiranih v skladu z ISO 17025, tako da večjih potreb po izobraževanjih za preskusne laboratorije s področja, ki ga pokriva Eurachem, ni več. Izjema so medicinski laboratoriji, za katere velja ISO 15189. ki se vsebinsko ne razlikuje bistveno od 17025.

Znanja o kakovosti meritev v kemiji in sorodnih vedah pa so potrebne tudi v raziskovalnih in razvojnih laboratorijih, za katere sicer akreditacija ni zakonsko predpisana, tako da je sedaj večina udeležencev izobraževanj s tega področja, ki jih organizira SIQ, prav iz takšnih laboratorijev. Za tiste, ki želijo pridobiti znanja s področja kakovosti merjenj v kemijskih/biokemijskih laboratorijih, je SIQ tudi v letu 2023 organiziral tako Šolo kakovosti za analitske laboratorije, kot tudi celodnevna izobraževanja za posamezne vsebine (meroslovna sledljivost, validacija merilnih postopkov, ovrednotenje merilne negotovosti, notranji in zunanji nadzor kakovosti meritev). Predavatelji sva dr. Monika Inkret in jaz. Pri izvedbi teh izobraževanj uporabljava tudi gradivo pripravljeno v okviru evropskega sodelovanja v prejšnjem desetletju, pri oblikovanju katerega smo imeli slovenski strokovnjaki vodilno vlogo.

dr. Nineta Hrastelj

Poročilo Analizne sekcije v okviru Slovenskega kemijskega društva za leto 2023

Osnovna dejavnost sekcije za Analizno kemijo v okviru Slovenskega kemijskega društva je organiziranje mednarodnih in domačih znanstvenih ter strokovnih srečanj, predavanj domačih in tujih strokovnjakov ter izvedba različnih delavnic, seminarjev in simpozijev. Člani sekcije so aktivni tudi znotraj delovnih skupin Eurachem in drugih združenj v evropskem prostoru (DAC, FECS) in tako dodatno prispevajo k prepoznavnosti Slovenskega kemijskega društva.

Aprila smo v okviru Analizne sekcije povabili dr. Tonya Edga iz podjetja VWR, ki je del skupine Avantor, da predstavi novosti in trende na področju kromatografije. Dobro obiskanega predavanja so se udeležili raziskovalci iz inštitutov in akademske sfere, študenti ter strokovnjaki iz industrije.

Med 25. in 28. 6. 2023 smo izvedli tradicionalno 28. mednarodno srečanje podiplomskih študentov in njihovih mentorjev YISAC (Young Investigators Seminar on Analytical Chemistry). Potekalo je na Fakulteti za kemijo Univerze v Beogradu v Srbiji. Poudariti velja, da je med vsemi predstavitvami najboljše ocenjeno predavanje predstavil prav slovenski doktorski študent Maksimiljan Dekleva iz Fakultete za kemijo in kemijsko tehnologijo Univerze v Ljubljani.

Med aktivnostmi sekcije v Sloveniji velja izpostaviti 29. jubilejno konferenco »Slovenski kemijski dnevi 2023«, ki se je odvijala septembra 2023 v Portorožu. Področje analizne kemije je bilo tradicionalno zelo dobro zastopano, konference se je udeležilo veliko kolegov iz različnih institucij, ki so predstavili številne zanimive raziskave s področij spektroskopije, kromatografije, elektrokemije, materialov in okolja. Veseli nas veliko število razstavljavcev analitske opreme, nekateri so bili na konferenci prvič ali po daljšem obdobju. Posledično je bilo predstavljenih res veliko pomembnih novosti za področje analizne kemije.

V prihodnje si bo sekcija aktivno prizadevala za izvedbo in organizacijo ter so-organizacijo domačih ter tujih srečanj, predavanj in konferenc. Posebej želimo vključiti mlade člane v delovanje sekcije ter okrepiti povezovanje in prenos znanja iz univerzitetnih in raziskovalnih laboratorijev v industrijo.

prof. dr. Mitja Kolar

KOLEDAR VAŽNEJŠIH ZNANSTVENIH SREČANJ S PODROČJA KEMIJE IN KEMIJSKE TEHNOLOGIJE

SCIENTIFIC MEETINGS – CHEMISTRY AND CHEMICAL ENGINEERING

2024

July 2024

1 – 5	50TH WORLD POLYMER CONGRESS – MACRO2024 Coventry, United Kingdom
Information:	https://www.macro2024.org/
2 – 5	7TH INTERNATIONAL CONGRESS CHEMISTRY FOR CULTURAL HERITAGE 2024 (CHEMCH 2024) Bratislava, Slovakia
Information:	https://chemch2024.educell.sk/
7 – 11	9TH EUCHEMS CHEMISTRY CONGRESS (ECC9) Dublin, Ireland
Information:	https://euchems2024.org/
7 – 10	BALTICUM ORGANICUM SYNTHETICUM 2024 (BOS2024) Riga, Latvia
Information:	https://boschem.eu/
14 – 19	29TH IUPAC SYMPOSIUM ON PHOTOCHEMISTRY Valencia, Spain
Information:	https://www.photoiupac2024.com/

August 2024

12– 16	TRANSFORMING CHEMISTRY AND INTERDISCIPLINARY RESEARCH TO INNOVATION Online
Information:	https://sites.google.com/uom.ac.mu/vcca-2024

September 2024

9 – 11	26TH INTERNATIONAL SYMPOSIUM FOR HIGH-PERFORMANCE THIN-LAYER CHROMATOGRAPHY Budapest, Hungary
Information:	https://akcongress.com/hptlc2024/
9– 13	21ST INTERNATIONAL SYMPOSIUM ON SOLUBILITY PHENOMENA AND RELATED EQUILIBRIUM PROCESSES Novi Sad, Serbia
Information:	https://issp2024.pmf.uns.ac.rs/

17– 20	4TH INTERNATIONAL CONFERENCE ON FUNDAMENTALS AND APPLICATIONS OF CERIUM DIOXIDE IN CATALYSIS Portorose, Slovenia
Information:	https://ceria2024.chem-soc.si/
18– 20	SCS ANNUAL MEETING 2024 Portorose, Slovenia
Information:	https://skd2024.chem-soc.si/en/
18 – 20	25TH CONGRESS ON ISOPRENOIDS Naples, Italy
Information:	https://isoprenoids25.org/
22 – 25	28TH INTERNATIONAL SYMPOSIUM ON SEPARATION SCIENCES (ISSS) Messina, Italy
Information:	https://www.sepscisoc.com/isss2024
25	3RD GLOBAL CONVERSATION ON SUSTAINABILITY
Information:	https://www.gcs-day.org/
25 – 28	27TH CONGRESS OF SCTM Ohrid, N. Macedonia
Information:	https://congress.sctm.mk/event/4/
23 – 27	EUROPEAN FORUM FOR ENGINEERING AND CATALYSIS TOWARDS SUSTAINABILITY (EFFECTS) Karlsruhe, Germany
Information:	https://www.youngcatalysis.net/effects-2024

Acta Chimica Slovenica

Author Guidelines

Submissions

Submission to ACSi is made with the implicit understanding that neither the manuscript nor the essence of its content has been published in whole or in part and that it is not being considered for publication elsewhere. All the listed authors should have agreed on the content and the corresponding (submitting) author is responsible for having ensured that this agreement has been reached. The acceptance of an article is based entirely on its scientific merit, as judged by peer review. There are no page charges for publishing articles in ACSi. The authors are asked to read the Author Guidelines carefully to gain an overview and assess if their manuscript is suitable for ACSi.

Additional information

- Citing spectral and analytical data
- Depositing X-ray data

Submission material

Typical submission consists of:

- full manuscript (PDF file, with title, authors, abstract, keywords, figures and tables embedded, and references)
- supplementary files
  - ***Full manuscript*** (original Word file)
  - ***Statement of novelty*** (Word file)
  - ***List of suggested reviewers*** (Word file)
  - ***ZIP file containing graphics*** (figures, illustrations, images, photographs)
  - ***Graphical abstract*** (single graphics file)
  - ***Proposed cover picture*** (optional, single graphics file)
  - ***Appendices*** (optional, Word files, graphics files)

Incomplete or not properly prepared submissions will be rejected.

Submission process

Before submission, authors should go through the checklist at the bottom of the page and prepare for submission.

Submission process consists of 5 steps.

Step 1: Starting the submission

- Choose one of the journal sections.
- Confirm all the requirements of the ***checklist.***
- Additional plain text comments for the editor can be provided in the relevant text field.

Step 2: Upload submission

- Upload full manuscript in the form of a Word file (with title, authors, abstract, keywords, figures and tables embedded, and references).

Step 3: Enter metadata

- First name, last name, contact email and affiliation for all authors, in relevant order, must be provided. Corresponding author has to be selected. Full postal address and phone number of the corresponding author has to be provided.
- ***Title and abstract*** must be provided in plain text.
- Keywords must be provided (max. 6, separated by semicolons).
- Data about contributors and supporting agencies may be entered.
- ***References*** in plain text must be provided in the relevant text filed.

Step 4: Upload supplementary files

- Original Word file (original of the PDF uploaded in the step 2)
- ***List of suggested reviewers*** with at least five reviewers with two recent references from the field of submitted manuscript must be uploaded as a Word file. At the same time, authors should declare (i) that they have no conflict of interest with suggested reviewers and (ii) that suggested reviewers are experts in the field of the submitted manuscript.
- All ***graphics*** have to be uploaded in a single ZIP file. Graphics should be named Figure 1.jpg, Figure 2.eps, etc.
- ***Graphical abstract image*** must be uploaded separately
- ***Proposed cover picture*** (optional) should be uploaded separately.
- Any additional ***appendices*** (optional) to the paper may be uploaded. Appendices may be published as a supplementary material to the paper, if accepted.
- For each uploaded file the author is asked for additional metadata which may be provided. Depending of the type of the file please provide the relevant title (Statement of novelty, List of suggested reviewers, Figures, Graphical abstract, Proposed cover picture, Appendix).

Step 5: Confirmation

- Final confirmation is required.

Article Types

Feature Articles are contributions that are written on Editor's invitation. They should be clear and concise summaries of the author's most recent work written with the broad scope of ACSi in mind. They are intended to be general overviews of the authors' subfield of research but should be written in a way that engages and informs scientists in other areas. They should contain the following (see also general guidelines for article structure below): (1) an introduction that acquaints readers with the authors' research field and outlines the important questions for which answers are being sought; (2) interesting, novel, and recent contributions of the author(s) to the field; and (3) a summary that presents possible future directions. Manuscripts should normally not exceed 40 pages of one column format (font size 12, 33 lines per page). Generally, experts who have made an important contribution to a specific field in recent years will be invited by the Editor to contribute a **Feature Article**. Individuals may, however, send a proposal (of no more than one page) for a **Feature Article** to the Editor-in-Chief for consideration.

Scientific articles should report significant and innovative achievements in chemistry and related sciences and should exhibit a high level of originality. They should have the following structure:

1. Title (max. 150 characters),
2. Authors and affiliations,
3. Abstract (max. 1000 characters),
4. Keywords (max. 6),
5. Introduction,
6. Experimental,
7. Results and Discussion,
8. Conclusions,
9. Acknowledgements,
10. References.

The sections should be arranged in the sequence generally accepted for publications in the respective fields and should be successively numbered.

Short communications generally follow the same order of sections as Scientific articles, but should be short (max. 2500 words) and report a significant aspect of research work meriting separate publication. Editors may decide that a Scientific paper is categorized as a Short Communication if its length is short.

Technical articles report applications of an already described innovation. Typically, technical articles are not based on new experiments.

Preparation of Submissions

Text of the submitted articles must be prepared with Microsoft Word. Normal style set to single column, 1.5 line spacing, and 12 pt Times New Roman font is recommended. Line numbering (continuous, for the whole document) must be enabled to simplify the reviewing process. For any other format, please consult the editor. Articles should be written in English. Correct spelling and grammar are the sole responsibility of the author(s). Papers should be written in a concise and succinct manner. The authors shall respect the ISO 80000 standard [1], and IUPAC Green Book [2] rules on the names and symbols of quantities and units. The Système International d'Unités (SI) must be used for all dimensional quantities.

Graphics (figures, graphs, illustrations, digital images, photographs) should be inserted in the text where appropriate. The captions should be self-explanatory. Lettering should be readable (suggested 8 point Arial font) with equal size in all figures. Use common programs such as MS Excel or similar to prepare figures (graphs) and ChemDraw to prepare structures in their final size. Width of graphs in the manuscript should be 8 cm. Only in special cases (in case of numerous data, visibility issues) graphs can be 17 cm wide. All graphs in the manuscript should be inserted in relevant places and **aligned left**. The same graphs should be provided separately as images of appropriate resolution (see below) and submitted together in a ZIP file (Graphics ZIP). Please do not submit figures as a Word file. In **graphs**, only the graph area determined by both axes should be in the frame, while a frame around the whole graph should be omitted. The graph area should be white. The legend should be inside the graph area. The style of all graphs should be the same. **Figures and illustrations** should be of sufficient quality for the printed version, i.e. 300 dpi minimum. **Digital images and photographs** should be of high quality (minimum 250 dpi resolution). On submission, figures should be of good enough resolution to be assessed by the referees, ideally as JPEGs. High-resolution figures (in JPEG, TIFF, or EPS format) might be required if the paper is accepted for publication.

Tables should be prepared in the Word file of the paper as usual Word tables. The captions should appear above the table and should be self-explanatory.

References should be numbered and ordered sequentially as they appear in the text, likewise methods, tables, figure captions. When cited in the text, reference numbers should be superscripted, following punctuation marks. It is the sole responsibility of authors to cite articles that have been submitted to a journal or were in print at the time of submission to ACSi. Formatting of references to published work should follow the journal style; please also consult a recent issue:

1. J. W. Smith, A. G. White, *Acta Chim. Slov.* **2008**, *55*, 1055–1059.
2. M. F. Kemmere, T. F. Keurentjes, in: S. P. Nunes, K. V. Peinemann (Ed.): Membrane Technology in the Chemical Industry, Wiley-VCH, Weinheim, Germany, **2008**, pp. 229–255.
3. J. Levec, Arrangement and process for oxidizing an aqueous medium, US Patent Number 5,928,521, date of patent July 27, **1999**.
4. L. A. Bursill, J. M. Thomas, in: R. Sersale, C. Collela, R. Aiello (Eds.), Recent Progress Report and Discussions: 5th International Zeolite Conference, Naples, Italy, 1980, Gianini, Naples, **1981**, pp. 25–30.
5. J. Szegezdi, F. Csizmadia, Prediction of dissociation constant using microconstants, http://www. chemaxon.com/conf/Prediction_of_dissociation _constant_using_microco nstants.pdf, (assessed: March 31, 2008)

Titles of journals should be abbreviated according to Chemical Abstracts Service Source Index (CASSI).

Special Notes

- Complete characterization, **including crystal structure**, should be given when the synthesis of new compounds in crystal form is reported.
- Numerical **data should be reported with the number of significant digits corresponding to the magnitude** of experimental uncertainty.
- **The SI system of units and IUPAC recommendations** for nomenclature, symbols and abbreviations should be followed closely. Additionally, the authors should follow the general guidelines when citing spectral and analytical data, and depositing crystallographic data.
- **Characters** should be correctly represented throughout the manuscript: for example, 1 (one) and l (ell), 0 (zero) and O (oh), x (ex), D7 (times sign), B0 (degree sign). Use Symbol font for all Greek letters and mathematical symbols.
- The rules and recommendations of the **IUBMB** and the **International Union of Pure and Applied Chemistry (IUPAC)** should be used for abbreviation of chemical names, nomenclature of chemical compounds, enzyme nomenclature, isotopic compounds, optically active isomers, and spectroscopic data.
- **A conflict of interest** occurs when an individual (author, reviewer, editor) or its organization is in-

volved in multiple interests, one of which could possibly corrupt the motivation for an act in the other. Financial relationships are the most easily identifiable conflicts of interest, while conflicts can occur also as personal relationships, academic competition, etc. **The Editors** will make effort to ensure that conflicts of interest will not compromise the evaluation process; potential editors and reviewers will be asked to exempt themselves from review process when such conflict of interest exists. When the manuscript is submitted for publication, **the authors** are expected to disclose any relationships that might pose potential conflict of interest with respect to results reported in that manuscript. In the Acknowledgement section the source of funding support should be mentioned. The statement of disclosure must be provided as Comments to Editor during the submission process.

- **Published statement of Informed Consent.** Research described in papers submitted to ACSi must adhere to the principles of the Declaration of Helsinki (***http://www.wma.net/e/policy/b3.htm***). These studies must be approved by an appropriate institutional review board or committee, and informed consent must be obtained from subjects. The Methods section of the paper must include: 1) a statement of protocol approval from an institutional review board or committee and 2), a statement that informed consent was obtained from the human subjects or their representatives.
- **Published Statement of Human and Animal Rights.**When reporting experiments on human subjects, authors should indicate whether the procedures followed were in accordance with the ethical standards of the responsible committee on human experimentation (institutional and national) and with the Helsinki Declaration of 1975, as revised in 2008. If doubt exists whether the research was conducted in accordance with the Helsinki Declaration, the authors must explain the rationale for their approach and demonstrate that the institutional review body explicitly approved the doubtful aspects of the study. When reporting experiments on animals, authors should indicate whether the institutional and national guide for the care and use of laboratory animals was followed.
- To avoid conflict of interest between authors and referees we expect that not more than one referee is from the same country as the corresponding author(s), however, not from the same institution.
- Contributions authored by **Slovenian scientists** are evaluated by non-Slovenian referees.
- Papers describing **microwave-assisted reactions** performed in domestic microwave ovens are not considered for publication in *Acta Chimica Slovenica.*
- *Manuscripts that are **not prepared and submitted** in accord with the instructions for authors are not considered for publication.*

Appendices

Authors are encouraged to make use of supporting information for publication, which is supplementary material (appendices) that is submitted at the same time as the manuscript. It is made available on the Journal's web site and is linked to the article in the Journal's Web edition. The use of supporting information is particularly appropriate for presenting additional graphs, spectra, tables and discussion and is more likely to be of interest to specialists than to general readers. When preparing supporting information, authors should keep in mind that the supporting information files will not be edited by the editorial staff. In addition, the files should be not too large (upper limit 10 MB) and should be provided in common widely known file formats to be accessible to readers without difficulty. All files of supplementary materials are loaded separately during the submission process as supplementary files.

Proposed Cover Picture and Graphical Abstract Image

Graphical content: an ideally full-colour illustration of resolution 300 dpi from the manuscript must be proposed with the submission. Graphical abstract pictures are printed in size 6.5 x 4 cm (hence minimal resolution of 770 x 470 pixels). Cover picture is printed in size 11 x 9.5 cm (hence minimal resolution of 1300 x 1130 pixels)

Authors are encouraged to submit illustrations as candidates for the journal Cover Picture*. The illustration must be related to the subject matter of the paper. Usually both proposed cover picture and graphical abstract are the same, but authors may provide different pictures as well.

* The authors will be asked to contribute to the costs of the cover picture production.

Statement of novelty

Statement of novelty is provided in a Word file and submitted as a supplementary file in step 4 of submission process. Authors should in no more than 100 words emphasize the scientific novelty of the presented research. Do not repeat for this purpose the content of your abstract.

List of suggested reviewers

List of suggested reviewers is a Word file submitted as a supplementary file in step 4 of submission process. Authors should propose the names, full affiliation (department, institution, city and country) and e-mail addresses of five potential referees. Field of expertise and at least two references relevant to the scientific field of the submitted manuscript must be provided for each of the suggested reviewers. The referees should be knowledgeable about the subject but have no close connection with any of the authors. In addition, referees should be from institutions other than (and countries other than) those of any of the authors. Authors declare no conflict of interest with suggested reviewers. Authors declare that suggested reviewers are experts in the field of submitted manuscript.

How to Submit

Users registered in the role of author can start submission by choosing USER HOME link on the top of the page, then choosing the role of the Author and follow the relevant link for starting the submission process.

Prior to submission we strongly recommend that you familiarize yourself with the ACSi style by browsing the journal, particularly if you have not submitted to the ACSi before or recently.

Correspondence

All correspondence with the ACSi editor regarding the paper goes through this web site and emails. Emails are sent and recorded in the web site database. In the correspondence with the editorial office please provide ID number of your manuscript. All emails you receive from the system contain relevant links. **Please do not answer the emails directly but use the embedded links in the emails for carrying out relevant actions.** Alternatively, you can carry out all the actions and correspondence through the online system by logging in and selecting relevant options.

Proofs

Proofs will be dispatched via e-mail and corrections should be returned to the editor by e-mail as quickly as possible, normally within 48 hours of receipt. Typing errors should be corrected; other changes of contents will be treated as new submissions.

Submission Preparation Checklist

As part of the submission process, authors are required to check off their submission's compliance with all of the following items, and submissions may be returned to authors that do not adhere to these guidelines.

1. The submission has not been previously published, nor is it under consideration for publication in any other journal (or an explanation has been provided in Comments to the Editor).
2. All the listed authors have agreed on the content and the corresponding (submitting) author is responsible for having ensured that this agreement has been reached.
3. The submission files are in the correct format: manuscript is created in MS Word but will be **submitted in PDF** (for reviewers) as well as in original MS Word format (as a supplementary file for technical editing); diagrams and graphs are created in Excel and saved in one of the file formats: TIFF, EPS or JPG; illustrations are also saved in one of these formats. The preferred position of graphic files in a document is to embed them close to the place where they are mentioned in the text (See ***Author guidelines*** for details).
4. The manuscript has been examined for spelling and grammar (spell checked).
5. The ***title*** (maximum 150 characters) briefly explains the contents of the manuscript.
6. Full names (first and last) of all authors together with the affiliation address are provided. Name of author(s) denoted as the corresponding author(s), together with their e-mail address, full postal address and telephone/fax numbers are given.
7. The ***abstract*** states the objective and conclusions of the research concisely in no more than 150 words.
8. Keywords (minimum three, maximum six) are provided.
9. ***Statement of novelty*** (maximum 100 words) clearly explaining new findings reported in the manuscript should be prepared as a separate Word file.
10. The text adheres to the stylistic and bibliographic requirements outlined in the ***Author guidelines***.
11. Text in normal style is set to single column, 1.5 line spacing, and 12 pt. Times New Roman font is recommended. All tables, figures and illustrations have appropriate captions and are placed within the text at the appropriate points.
12. Mathematical and chemical equations are provided in separate lines and numbered (Arabic numbers) consecutively in parenthesis at the end of the line. All equation numbers are (if necessary) appropriately included in the text. Corresponding numbers are checked.
13. Tables, Figures, illustrations, are prepared in correct format and resolution (see ***Author guidelines***).
14. The lettering used in the figures and graphs do not vary greatly in size. The recommended lettering size is 8 point Arial.
15. Separate files for each figure and illustration are prepared. The names (numbers) of the separate files are the same as they appear in the text. All the figure files are packed for uploading in a single ZIP file.
16. Authors have read ***special notes*** and have accordingly prepared their manuscript (if necessary).
17. References in the text and in the References are correctly cited. (see ***Author guidelines***). All references mentioned in the Reference list are cited in the text, and vice versa.
18. Permission has been obtained for use of copyrighted material from other sources (including the Web).
19. The names, full affiliation (department, institution, city and country), e-mail addresses and references of five potential referees from institutions other than (and countries other than) those of any of the authors are prepared in the word file. At least two relevant references (important recent papers with high impact factor, head positions of departments, labs, research groups, etc.) for each suggested reviewer must be provided. Authors declare no conflict of interest with suggested reviewers. Authors declare that suggested reviewers are experts in the field of submitted manuscript.
20. Full-colour illustration or graph from the manuscript is proposed for graphical abstract.
21. ***Appendices*** (if appropriate) as supplementary material are prepared and will be submitted at the same time as the manuscript.

Privacy Statement

The names and email addresses entered in this journal site will be used exclusively for the stated purposes of this journal and will not be made available for any other purpose or to any other party.

ISSN: 1580-3155

Koristni naslovi

Slovensko kemijsko društvo
www.chem-soc.si
e-mail: chem.soc@ki.si

Wessex Institute of Technology
www.wessex.ac.uk

SETAC
www.setac.org

European Water Association
http://www.ewa-online.eu/

European Science Foundation
www.esf.org

European Federation of Chemical Engineering
https://efce.info/

International Union of Pure and Applied Chemistry
https://iupac.org/

Novice europske zveze kemijskih društev EuChemS najdete na:

Brussels News Updates
http://www.euchems.eu/newsletters/

DONAU LAB Ljubljana
Member of LPPgroup

BÜCHI

NOVOST

Rotavapor® R-80

Kompaktna rešitev za evaporacije

www.donaulab.si
+386 (0)1 24 182 09
office-si@donaulab.com

Odkrijte več
na naši spletni strani

NATIONAL INSTITUTE OF **CHEMISTRY**

Hajdrihova 19,
1000 Ljubljana
Slovenia
www.ki.si

_research EXCELENCE

Basic and applied research in materials, life sciences, biotechnology, chemical engineering, structural and theoretical chemistry, analytical chemistry and environmental protection.

In line with EU research and innovation priorities: nanotechnology, genomics and biotechnology for health, sustainable development, climate change, energy efficiency and food quality and safety.

We expand knowledge and technology transfer to domestic and foreign chemical, automotive and nanobiotechnology industries.

We are aware of the power of youth, so we transfer our knowledge to younger generations and offer many opportunities for cooperation.

contact: mladi@ki.si

MAGNEZIJ Krka

MAGNEZIJ + B-KOMPLEKS

BODITE NEUSTAVLJIVI

- **Manj utrujenosti**
- **Normalno delovanje mišic**

NOVO

ENOSTAVNO, BREZ TEKOČINE

www.magnezijkrka.si

Prehransko dopolnilo ni nadomestilo za uravnoteženo in raznovrstno prehrano.
Skrbite za uravnoteženo in raznovrstno prehrano ter zdrav način življenja.

KRKA | 70let

THE SECRET INSIDE
EXCELLENT PRODUCTS

Helios Resins – specialists for reliable coating and composite solutions since 1908.

SILVER 2023 ecovadis Sustainability Rating

ISCC International Sustainability & Carbon Certification

www.resinshelios.com

HELIOS RESINS

Acta Chimica Slovenica

17βHSD1 represents an emerging drug target for breast cancer treatment. Here, an efficient protocol for expression, purification and activity screening of human recombinant 17βHSD1 from is described, which can be used as a ready source of enzyme for screening new 17βHSD1 inhibitors.

Year 2024, Vol. 71, No. 2